Tinh Quoc Bui
Le Thanh Cuong
Samir Khatir *Editors*

Structural Health Monitoring and Engineering Structures

Select Proceedings of SHM&ES 2020

Springer

Lecture Notes in Civil Engineering

Volume 148

Lecture Notes in Civil Engineering (LNCE) publishes the latest developments in Civil Engineering - quickly, informally and in top quality. Though original research reported in proceedings and post-proceedings represents the core of LNCE, edited volumes of exceptionally high quality and interest may also be considered for publication. Volumes published in LNCE embrace all aspects and subfields of, as well as new challenges in, Civil Engineering. Topics in the series include:

- Construction and Structural Mechanics
- Building Materials
- Concrete, Steel and Timber Structures
- Geotechnical Engineering
- Earthquake Engineering
- Coastal Engineering
- Ocean and Offshore Engineering; Ships and Floating Structures
- Hydraulics, Hydrology and Water Resources Engineering
- Environmental Engineering and Sustainability
- Structural Health and Monitoring
- Surveying and Geographical Information Systems
- Indoor Environments
- Transportation and Traffic
- Risk Analysis
- Safety and Security

To submit a proposal or request further information, please contact the appropriate Springer Editor:

– Pierpaolo Riva at pierpaolo.riva@springer.com (Europe and Americas);
– Swati Meherishi at swati.meherishi@springer.com (Asia - except China, and Australia, New Zealand);
– Wayne Hu at wayne.hu@springer.com (China).

All books in the series now indexed by Scopus and EI Compendex database!

More information about this series at http://www.springer.com/series/15087

Tinh Quoc Bui · Le Thanh Cuong ·
Samir Khatir

Editors

Structural Health Monitoring and Engineering Structures

Select Proceedings of SHM&ES 2020

Springer

Editors
Tinh Quoc Bui
Department of Civil and Environmental
Engineering
Tokyo Institute of Technology
Tokyo, Japan

Le Thanh Cuong
Department of Civil engineering
Ho Chi Minh City Open University
Ho Chi Minh, Vietnam

Samir Khatir
Soete Laboratory, Department of Electrical
Energy, Metals, Mechanical Constructions
and Systems, Faculty of Engineering and
Architecture
Ghent University
Ghent, Belgium

Organization

Head of Organization Committee

Dr. Le Thanh Cuong
Dr. Samir Khatir

Conference Chairs

Prof. Dr. Nguyen Trong Phuoc, Ho Chi Minh City Open University, Vietnam
Ph.D. Dr. Le Thanh Cuong, Ho Chi Minh City Open University, Vietnam
Prof. Dr. Bui Quoc Tinh, Tokyo Institute of Technology, Japan
Ph.D. Dr. Samir Khatir, Ghent University, Belgium

International Scientific Committee

Prof. Roberto Capozucca (Italy)
Prof. Nguyen Xuan Hung (Vietnam)
Prof. Gholamreza Ghodrati Amiri (Iran)
Prof. Li Hua (Singapore)
Prof. Nguyen Trung Kien (Vietnam)
Dr. Muhamad Norhisham (Malaysia)
Prof. Magd Abdel Wahab (Belgium)
Prof. Luong Van Hai (Vietnam)
Dr. Nadeem Ali Bhatti (Pakistan)
Prof. Yusuf Sahin (Turkey)
Prof. Idir Belaidi (Algeria)
Prof. Nguyen Thoi Trung (Vietnam)

Preface

This volume contains the proceedings of the First International Conference on Structural Health Monitoring and Engineering Structures (SHM&ES). Structural Health Monitoring and Engineering Structures (SHM&ES) conference was organized in Ho Chi Minh Open University, Vietnam, during the period 15–16 December. The overall objective of the conference is to bring together international scientists and engineers in academia and industry in fields related to advanced numerical techniques, such as FEM, machine learning, optimization techniques, and their applications to engineering structures. The conference covers industrial engineering applications of numerical simulations to civil engineering, materials engineering, aerospace engineering, and mechanical engineering.

The presentations of NME 2018 are divided into five main sessions:

- Optimization and Machine Learning for Engineering Structures.
- Crack Analysis for Engineering Structures.
- Application for Structural Health Monitoring.
- Geotechnical and Geoenvironmental Engineering.
- Experimental and Numerical Investigation for Engineering Structure

The organizing committee is grateful to keynote speakers, Prof. Fu-Kuo Chang—Stanford University (USA), for his keynote speech entitled 'Structural Health Monitoring (SHM) for Smart Cities,' and Prof. Dr. R. Venkata Rao—Department of Mechanical Engineering, S. V. National Institute of Technology (SVNIT), Surat, India, for his keynote speech entitled 'Weight Optimization of a Truss Structure using Rao Algorithms and their Variants.'

Big thanks to members of the Scientific Committee of SHM&ES for reviewing the articles published in this volume and for judging their scientific merits. Based on the comments of reviewers and the scientific merits of the submitted manuscripts, the articles were accepted for publication in the conference proceedings and

for presentation at the conference venue. The accepted papers are of a very high scientific quality and contribute to the advancement of knowledge in all research topics relevant to SHM&ES conference.

Finally, the organizing committee would like to appreciate all the contributors for their efforts writing good research papers.

<div align="right">

SHM&ES Chairs

</div>

Tokyo, Japan   Tinh Quoc Bui
Ho Chi Minh, Vietnam   Le Thanh Cuong
Ghent, Belgium   Samir Khatir

Contents

Application for Structural Health Monitoring

Editors and Contributors

About the Editors

Dr. Tinh Quoc Bui is currently an Associate Professor at the Department of Civil and Environmental Engineering, Tokyo Institute of Technology, Japan. He holds other academic positions including Visiting Professor (Dalian University of Technology, China) and Visiting Associate Professor (NTUST, Taiwan). Prof. Bui received his Ph.D. in Mechanical Engineering, Vienna University of Technology, Austria, 2009. He serves Editor for Applied Mathematical Modelling, Thin-Walled Structures; Engineering Analysis with Boundary Elements; Scientific Reports, SN Applied Sciences. He was awarded "The 2018 JACM Award for Young Investigators in Computational Mechanics" from Japan Association for Computational Mechanics. He is authored and co-authored of over 150 ISI peer-reviewed articles. Prof. Bui's research interests are computational mechanics, fracture mechanics, composites, computational inelasticity, and numerical methods.

Dr. Le Thanh Cuong is lecturer at the Faculty of Civil Engineering, Ho Chi Minh City Open University, Vietnam. He received his Ph.D. from Ghent University of Belgium in 2019. His research focuses on computational science and engineering, structural stability, dynamic analysis, plates and shell, optimization and structural health monitoring. He has published papers in Computer Methods in Applied Mechanics and Engineering, Composite structures, and Thin-Walled Structures.

Dr. Samir Khatir is currently a Doctor assistant at Ghent University Belgium and adjunct Doctor assistant at Ho Chi Minh Open university Vietnam. He received Ph.D. in Civil engineering at Ghent University and another Ph.D. in Mechanical engineering from UMBB Algeria. Dr. Samir Khatir improved and created many techniques for damage identification. He is authored and co-authored of over 40 ISI peer-reviewed articles. His primary research interest is in the areas of Civil and Mechanical engineering such as FEM, XFEM, Iso-Geometric Analysis (IGA), Extended Iso-Geometric analysis (XIGA), Dynamic, Static, Damage identification, Fracture mechanics, Optimization, Inverse problem, Wear, Friction, Laminated composites, Delamination, Transmissibility, Fatigue, Bridge, Civil engineering structures, Machine Learning, Model Reduction, Deep Learning, and experimental modal analysis. He is also on the editorial board in many scientific journals.

Contributors

M. Abdel Wahab Soete Laboratory, Faculty of Engineering and Architecture, Ghent University, Zwijnaarde, Gent, Belgium

Magd Abdel Wahab Soete Laboratory, Faculty of Engineering and Architecture, Ghent University, Zwijnaarde, Belgium

Nguyen Truong An Le Quy Don Technical University, Hanoi, Vietnam

A. Behtani Laboratory of Mechanics, Structure and Energetics (LMSE), Mouloud Mammeri University of Tizi-Ouzou, Tizi Ouzou, Algeria

Ferhat Bekhoucha Polytechnic National School, El Harrach, Algeria

Faiza Boumediene University of Sciences and Technology Houari Boumediene, Bab Ezzouar, Algeria

Hadjila Bournine University of Sciences and Technology Houari Boumediene, Bab Ezzouar, Algeria

Djilali Boutchicha Laboratory of Applied Mechanics, University of Science and Technology of Oran Mohamed Boudiaf, BP 1505 Oran, Algeria

Anh Kiet Bui Faculty of Civil Engineering, Ho Chi Minh City Open University, Ho Chi Minh City, Vietnam

Linh Van Hong Bui Faculty of Civil Engineering, Ho Chi Minh City Open University, Ho Chi Minh City, Vietnam

Tung Thanh Bui University of Transport and Communications, Hanoi, Vietnam

Anh-Tuan Cao Department of Civil and Environmental Engineering, Kunsan National University, Gunsan-si, Jeollabuk-do, Republic of Korea

Thi Nguyen Cao Faculty of Civil Engineering, Tien Giang University, My Tho City, Vietnam

Xiao-hui Cao School of Mechanical and Electrical Engineering, Wuhan University of Technology, Wuhan, China

Truong Linh Chau University of Science and Technology, The University of Da Nang, Da Nang, Vietnam

Thanh Cuong Le Faculty of Civil Engineering, Ho Chi Minh City Open University, Ho Chi Minh City, Vietnam

Thanh Cuong-Le Faculty of Civil Engineering, Ho Chi Minh City Open University, Ho Chi Minh City, Vietnam

Minh Hung Dam Training, Construction and Human Resource Development JS Company No 6, Hanoi, Vietnam

Duy Khanh Doan National University of Forestry—Southern Campus, Hanoi, Vietnam

Q. X. Do Faculty of Civil Engineering, University of Transport and Communications, Hanoi, Vietnam

Tin V. Do Karagozian & Case Australia Pty Ltd., Bondi Junction, NSW, Australia;
Ho Chi Minh Open University, Ho Chi Minh City, Vietnam

Tin Van Do Faculty of Civil Engineering, Ho Chi Minh City Open University, Ho Chi Minh City, Vietnam

Trang Nhu Do Faculty of Civil Engineering, University of Transport Technology, Hanoi, Vietnam

Nguyen Nhu Dung Hanoi Architectural University, Hanoi, Vietnam

Tham H. Duong Ho Chi Minh City Open University, Ho Chi Minh City, Vietnam

Lai Dang Giang Le Quy Don Technical University, Hanoi, Vietnam

Vu Thi Thuy Giang Faculty of Civil Engineering, Hanoi Architectural University, Hanoi, Vietnam

Minh-Nhat Ha University of Danang, University of Science and Technology, Da Nang, Vietnam

Le Quang Hai University of Fire Prevention and Fighting, Hanoi, Vietnam

Ngoc-Duc Han Faculty of Building and Industrial Construction, National University of Civil Engineering, Hanoi, Vietnam

Q. Hoan Pham Faculty of Civil Engineering, Vietnam Maritime University, Hai Phong, Vietnam

Tran Duc Hoan Le Quy Don Technical University, Hanoi, Vietnam

Bac An Hoang University of Architecture Ho Chi Minh City, Ho Chi Minh City, Vietnam

Quoc Long Hoang Institute of Special Construction Engineering, Le Quy Don Technical University, Hanoi, Vietnam

Tuan-Nghia Hoang Faculty of Building and Industrial Construction, National University of Civil Engineering, Hanoi, Vietnam

Duc-Duy Ho Vietnam National University Ho Chi Minh City, Ho Chi Minh City, Vietnam

Vo Nguyen Phu Huan Ho Chi Minh City Open University, Ho Chi Minh City, Vietnam

Le Phuoc Son Huynh Centre of Computational Mechanics, Department of Engineering Mechanics, Ho Chi Minh City University of Technology, Ho Chi Minh City, Vietnam

Thanh-Canh Huynh Faculty of Civil Engineering, Institute of Research and Development, Duy Tan University, Da Nang, Vietnam

Ramazan-Ali Jafari-Talookolaei Department of Mechanical Engineering, Babol Noshirvani University of Technology, Babol, Mazandaran Province, Iran

Pitcha Jongvivatsakul Innovative Construction Materials Research Unit, Department of Civil Engineering, Chulalongkorn University, Pathumwan, Bangkok, Thailand

H. Katsuchi Faculty of Civil Engineering, Yokohama National University, Yokohama, Japan

S. Khatir Faculty of Civil Engineering, Ho Chi Minh City Open University, Ho Chi Minh City, Vietnam;
Soete Laboratory, Faculty of Engineering and Architecture, Ghent University, Zwijnaarde, Ghent, Belgium

Samir Khatir Soete Laboratory, Faculty of Engineering and Architecture, Ghent University, Zwijnaarde, Belgium;
Faculty of Civil Engineering, Ho Chi Minh City Open University, Ho Chi Minh City, Vietnam

T. Khatir Department of Technology, University Centre of Naama—Salhi Ahmed, Naama, Algeria

Nguyen Tan Khoi Danang University of Science and Technology, The University of Danang, Da Nang, Vietnam

Dookie Kim Department of Civil and Environmental Engineering, Kongju National University, Seobuk-gu Cheonan, Chungcheongnam-do, Republic of Korea

Nguyen Lan Danang University of Science and Technology, The University of Danang, Da Nang, Vietnam

C. Le Thanh Faculty of Civil Engineering, Ho Chi Minh City Open University, Ho Chi Minh City, Vietnam

Luu Xuan Le Faculty of Civil Engineering, Yokohama National University, Yokohama, Japan;
Faculty of Civil Engineering, University of Transport and Communications, Hanoi, Vietnam

Thanh-Cao Le Faculty of Civil Engineering, Ho Chi Minh City University of Technology (HCMUT), Ho Chi Minh City, Vietnam;
Vietnam National University Ho Chi Minh City, Ho Chi Minh City, Vietnam;
Faculty of Civil Engineering, Nha Trang University, Nha Trang, Vietnam

Thi-Mai-Trang Le Faculty of Technology and Technique, Quy Nhon University, Quy Nhon, Binh Dinh, Vietnam;
Department of Ocean Science and Engineering, Kunsan National University, Gunsan-si, Jeollabuk-Ddo, Republic of Korea

Chong-hui Li Chongqing Research Institute, Zhongxing Telecommunication Equipment Corporation, Shenzhen, China

Cun-rong Li School of Mechanical and Electrical Engineering, Wuhan University of Technology, Wuhan, China

B. X. Luong Faculty of Civil Engineering, University of Transport and Communications, Hanoi, Vietnam

Van Hai Luong Faculty of Civil Engineering, Ho Chi Minh City University of Technology (HCMUT), District 10, Ho Chi Minh City, Vietnam;
Vietnam National University Ho Chi Minh City (VNU-HCM), Thu Duc, Ho Chi Minh City, Vietnam

Tran-Huu-Tin Luu Faculty of Civil Engineering, Ho Chi Minh City University of Technology (HCMUT), Ho Chi Minh City, Vietnam;
Vietnam National University Ho Chi Minh City, Ho Chi Minh City, Vietnam

Erica Magagnini Structural Section DICEA, Polytechnic University of Marche, Ancona, Italy

Hoang-Le Minh Faculty of Civil Engineering, Ho Chi Minh City Open University, Ho Chi Minh City, Vietnam

Tran Tuan Nam Ho Chi Minh City University of Technology (HUTECH), Ho Chi Minh City, Vietnam

Djamel Nedjar Faculty of Architecture and Civil Engineering, Department of Civil Engineering, Laboratory of Mechanic of Structures and Stability of Constructions LM2SC, University of Science and Technology of Oran Mohamed Boudiaf, BP 1505 Oran, Algeria

Nhi K. Ngo Laboratory of Applied Mechanics (LAM), Ho Chi Minh City University of Technology, HCMUT, Ho Chi Minh City, Vietnam;
Ho Chi Minh National University, Ho Chi Minh City, Vietnam

Dinh-Hoa Nguyen Faculty of Building and Industrial Construction, National University of Civil Engineering, Hanoi, Vietnam

Dinh-Tuan Nguyen University of Danang, University of Science and Technology, Da Nang, Vietnam

Duc-Anh Nguyen University of Danang, University of Science and Technology, Da Nang, Vietnam

Duc-Trong Nguyen Campus in Ho Chi Minh City, University of Transport and Communications, Ho Chi Minh City, Vietnam

Duc Hieu Nguyen University of Transport and Communications, Hanoi, Vietnam

Duc Minh Nguyen Graduate student, Ho Chi Minh City Open University, Ho Chi Minh City, Vietnam

Duy-Liem Nguyen Faculty of Civil Engineering, Ho Chi Minh City University of Technology and Education, Ho Chi Minh City, Vietnam

Hai H. Nguyen University of Danang, University of Science and Technology, Danang City, Vietnam

Hung Q. Nguyen Laboratory of Applied Mechanics (LAM), Ho Chi Minh City University of Technology, HCMUT, Ho Chi Minh City, Vietnam;
Ho Chi Minh National University, Ho Chi Minh City, Vietnam

Huu Hung Nguyen University of Transport and Communications, Hanoi, Vietnam

Lan Nguyen The University of Da Nang, University of Science and Technology, Da Nang, Vietnam

N. T. Nguyen Faculty of Civil Engineering, Ho Chi Minh City Open University, Ho Chi Minh City, Vietnam

Phu-Cuong Nguyen Advanced Structural Engineering Laboratory, Faculty of Civil Engineering, Ho Chi Minh City Open University, Ho Chi Minh City, Vietnam

Phuc Q. Nguyen University of Transport and Communications, Hanoi City, Vietnam

Phuoc Trong Nguyen Faculty of Civil Engineering, Ho Chi Minh City Open University, Ho Chi Minh City, Vietnam

Thanh-Truong Nguyen Industrial Maintenance Training Center, Ho Chi Minh City University of Technology (HCMUT), Ho Chi Minh City, Vietnam;
Vietnam National University Ho Chi Minh City, Ho Chi Minh City, Vietnam

Thanh Quang Nguyen University of Science and Technology, The University of Da Nang, Da Nang, Vietnam

Thao D. Nguyen Laboratory of Applied Mechanics (LAM), Ho Chi Minh City University of Technology, HCMUT, Ho Chi Minh City, Vietnam;
Ho Chi Minh City Department of Transportation, Ho Chi Minh City, Vietnam

Thuy Linh Nguyen University of Transport and Communications, Hanoi, Vietnam

Trong Chuc Nguyen Institute of Special Construction Engineering, Le Quy Don Technical University, Hanoi, Vietnam

Trong Phuoc Nguyen Ho Chi Minh City Open University, Ho Chi Minh City, Vietnam

Trung-Kien Nguyen Faculty of Building and Industrial Construction, National University of Civil Engineering, Hanoi, Vietnam

Tuong Long Nguyen Centre of Computational Mechanics, Department of Engineering Mechanics, Ho Chi Minh City University of Technology, Ho Chi Minh City, Vietnam

Van-My Nguyen University of Danang, University of Science and Technology, Da Nang, Vietnam

Yen Thi Hai Nguyen Faculty of Civil Engineering, Ho Chi Minh City Open University, Ho Chi Minh City, Vietnam

Mohammad Hadi Pashaei Department of Mechanical Engineering, Babol Noshirvani University of Technology, Babol, Mazandaran Province, Iran

R. B. Pawar Department of Mechanical Engineering, Sardar Vallabhbhai National Institute of Technology, Surat, Gujarat, India

Sy Pham-Van Faculty of Civil Engineering, Vietnam Maritime University, Hai Phong, Vietnam

Hung Huy Pham The University of Da Nang, University of Science and Technology, Da Nang, Vietnam

Phuong N. Pham University of Danang, University of Science and Technology, Danang City, Vietnam

Toan B. Pham Laboratory of Applied Mechanics (LAM), Ho Chi Minh City University of Technology, HCMUT, Ho Chi Minh City, Vietnam;
Ho Chi Minh National University, Ho Chi Minh City, Vietnam

Hoang-Nam Phan University of Danang, University of Science and Technology, Da Nang, Vietnam

Thanh-Hoang Phan School of Mechanical Engineering, Pusan National University, Busan, South Korea

R. V. Rao Department of Mechanical Engineering, Sardar Vallabhbhai National Institute of Technology, Surat, Gujarat, India

Morteza Saadatmorad Department of Mechanical Engineering, Babol Noshirvani University of Technology, Babol, Mazandaran Province, Iran

Meriem Seguini Faculty of Architecture and Civil Engineering, Department of Civil Engineering, Laboratory of Mechanic of Structures and Stability of Constructions LM2SC, University of Science and Technology of Oran Mohamed Boudiaf, BP 1505 Oran, Algeria

Mostafa Siavashi Department of Mechanical Engineering, Babol Noshirvani University of Technology, Babol, Mazandaran Province, Iran

M. Slimani Laboratory of Mechanics, Structure, and Energetics (LMSE), Mouloud Mammeri University of Tizi-Ouzou, Tizi-Ouzou, Algeria

Boonchai Stitmannaithum Innovative Construction Materials Research Unit, Department of Civil Engineering, Faculty of Engineering, Chulalongkorn University, Pathumwan, Bangkok, Thailand

Nguyen Minh Tam Ho Chi Minh City Open University, Ho Chi Minh City, Vietnam

Le Trong Tan Le Quy Don Technical University, Hanoi, Vietnam

Cuong-Le Thanh Faculty of Civil Engineering, Ho Chi Minh City Open University, Ho Chi Minh City, Vietnam

Nguyen Trung Thanh Le Quy Don Technical University, Hanoi, Vietnam

Do Minh Thao University of Fire Prevention and Fighting, Hanoi, Vietnam

Nguyen Thi Bich Thuy Ho Chi Minh City Open University, Ho Chi Minh City, Vietnam

S. Tiachacht Laboratory of Mechanics, Structure, and Energetics (LMSE), Mouloud Mammeri University of Tizi-Ouzou, Tizi-Ouzou, Algeria

Nguyen Manh Tien Le Quy Don Technical University, Hanoi, Vietnam

L. G. To Faculty of Civil Engineering, University of Transport and Communications, Hanoi, Vietnam

Thoi H. Tra University of Technology, Ho Chi Minh City, Vietnam

Ngoc-Thanh Tran Faculty of Civil Engineering, Ho Chi Minh City University of Transport, Ho Chi Minh City, Vietnam

Ngoc Hoa Tran University of Transport and Communications, Hanoi, Vietnam

Thanh-Tuan Tran Institute of Offshore Wind Energy, Kunsan National University, Gunsan-si, Jeollabuk-do, Republic of Korea;
Faculty of Technology and Technique, Quy Nhon University, Quy Nhon, Binh Dinh, Vietnam

Thanh Danh Tran Ho Chi Minh City Open University, Ho Chi Minh City, Vietnam

Thao T. T. Tran University of Danang, University of Science and Technology, Danang City, Vietnam

The Truyen Tran University of Transport and Communications, Hanoi, Vietnam

Van Than Tran Ho Chi Minh City Open University, Ho Chi Minh City, Vietnam

Viet T. Tran University of Danang, University of Science and Technology, Danang City, Vietnam

Do Nhu Trang Faculty of Civil Engineering, University of Transport Technology, Hanoi, Vietnam

Khuc Quang Trung University of Fire Prevention and Fighting, Hanoi, Vietnam

Viet-Hung Truong Thuyloi University, Dong Da, Hanoi, Vietnam

Sy Quan Tu University of Transport and Communications, Hanoi, Vietnam

Nguyen Anh Tuan Le Quy Don Technical University, Hanoi, Vietnam

Linh Van Hong Bui Faculty of Civil Engineering, Ho Chi Minh City Open University, Ho Chi Minh City, Vietnam

Dao Van Luu Le Quy Don Technical University, Hanoi, Vietnam

Nam Van Nguyen Faculty of Civil Engineering, Ho Chi Minh City Open University, Ho Chi Minh City, Vietnam

Nam Van Nguyen Faculty of Civil Engineering, Ho Chi Minh City Open University, Ho Chi Minh City, Vietnam

Thanh Au Vo Testing Lab, HCMC Technical Center of Standards Metrology and Quality, Ho Chi Minh City, Vietnam

T. Vu-Huu Faculty of Civil Engineering, Vietnam Maritime University, Hai Phong, Vietnam

Anh-Tuan Vu Faculty of Building and Industrial Construction, National University of Civil Engineering, Hanoi, Vietnam

Giang Thi Thuy Vu Faculty of Civil Engineering, Ha Noi Architectural University, Hanoi, Vietnam

Zhi-cheng Wang School of Mechanical and Electrical Engineering, Wuhan University of Technology, Wuhan, China

S. E. H. A. M. Zarbaf The University of Cincinnati, Cincinnati, OH, USA

Optimization and Machine Learning for Engineering Structures

Weight Optimization of a Truss Structure Using Rao Algorithms and Their Variants

R. V. Rao, R. B. Pawar, S. Khatir, and Thanh Cuong Le

1   Introduction

The optimization of truss structures is a challenging task in the field of structural engineering due to its complex design with numerous design variables and design constraints. The structural optimization problems are classified into three groups as: (i) topology optimization, (ii) shape optimization, and (iii) size optimization. The location of links, the nodal coordinates, and the cross-section areas of the members are considered as design variables in the problems of topology optimization, shape optimization, and size optimization, respectively.

In this work, the size optimization of a 10-bar truss structure is considered. The stresses induced in the members and the displacements occurred at nodes of a truss structure are considered as design constraints. The design variables in this study are considered as discrete as well as continuous type variables individually. The researchers have been taking efforts to solve such complex truss optimization problems using various advanced optimization algorithms. Some of the studies are discussed here.

Luh and Lin [1] utilized the two-stage particle swarm optimization (PSO) algorithm for weight minimization of truss structures while satisfying kinematic stability, deflection, and stress constraints. Sonmez [2] applied the artificial bee colony (ABC) algorithm for the weight minimization of truss structures.

R. V. Rao (✉) · R. B. Pawar
Department of Mechanical Engineering, Sardar Vallabhbhai National Institute
of Technology, Surat, Gujarat, India

S. Khatir
Soete Laboratory, Ghent University, Ghent, Belgium

T. Cuong Le
Faculty of Civil Engineering, Ho Chi Minh City Open University, Ho Chi Minh City,
Vietnam
e-mail: ravipudirao@gmail.com

Sadollah et al. [3] presented the optimization of truss structures with discrete variables using the mine blast algorithm (MBA). Kaveh and Khayatazad [4] used the ray optimization algorithm for shape and size optimization of truss structures. Eskandar et al. [5] carried out the optimization of truss structures with weight as an objective using the water cycle algorithm (WCA). Zuo and Li [6] presented a hybrid method with optimality criteria and genetic algorithm (GA) for optimization of trusses with frequency constraints. Dede [7] applied the teaching-learning-based optimization (TLBO) algorithm for the optimization of trusses with discrete variables.

Ho-Huu et al. [8] studied the layout optimization of trusses with discrete variables using improved constrained differential evolution (DE). Pham [9] proposed the enhanced DE algorithm based on adaptive directional mutation and nearest neighbor comparison for optimization of truss structures with frequency constraints. Farshchin et al. [10] optimized truss structures for shape and size using a collaborative optimization strategy with consideration of frequency constraints. Stolpe [11] reviewed developed theory, models, and optimization methods for optimization of trusses with discrete design variables. Kanarachos et al. [12] presented truss optimization with frequency constraints using the fruit fly optimization algorithm. Assimi et al. [13] applied a genetic programming approach for simultaneous sizing and topology optimization of truss structures. Mortazavi and Togan [14] presented the design optimization of truss structures with static and dynamic constraints using an integrated particle swarm optimization (PSO) algorithm. Lieu et al. [15] proposed the optimization of truss structures using an adaptive hybrid evolutionary firefly algorithm. Kaveh and Mahdavi [16] studied the muti-objective optimization of trusses using the multi-objective colliding bodies optimization algorithm. Li and Yan [17] applied an improved bat algorithm for truss optimization. Kaveh and Seddighian [18] presented the multi-objective optimization of trusses using an enriched firefly algorithm.

In this paper, the performance of nine novel advanced optimization algorithms, namely the Rao-1 algorithm, Rao-2 algorithm, Rao-3 algorithm, self-adaptive multi-population Rao-1 (SAMP Rao-1) algorithm, SAMP Rao-2 algorithm, SAMP Rao-3 algorithm, quasi-oppositional-based Rao-1 (QO Rao-1) algorithm, QO Rao-2 algorithm, and the QO Rao-3 algorithm, is investigated to solve a 10-bar truss optimization problem. These algorithms were implemented in previous studies to solve various optimization problems such as Rao [19], Wang et al. [20], Jabir et al. [21], Kalemci and Ikizler [22], Ravipudi [23], Rao and Keesari [24], and Rao and Pawar [25–28]. The results obtained in previous studies revealed that the superiority of these Rao algorithms and their variants over other advanced optimization algorithms considered. The main advantage of these Rao algorithms and their variants is that they do not have algorithm-specific control parameters. Hence, the efforts required to tune algorithm-specific parameters have vanished. These algorithms are simple to understand and ease efforts to implement. The next section presents a brief description of Rao algorithms and their variants.

2 Optimization Algorithms Considered

2.1 Rao Algorithms

Rao [19] recently proposed three metaphor-less algorithms named as the Rao-1 algorithm, Rao-2 algorithm, and the Rao-3 algorithm. These Rao algorithms do not have algorithm-specific control parameters. Similar to other population-based algorithms, these algorithms also start with an initial randomly generated population. Then, these algorithms calculate objective function values for the initial population. The initial population is updated using any one of the following three equations.

$$X'_{c,v,i} = X_{c,v,i} + r_{1,c,v,i}(X_{\text{best},v,i} - X_{\text{worst},v,i}), \tag{1}$$

$$X'_{c,v,i} = X_{c,v,i} + r_{1,c,v,i}(X_{\text{best},v,i} - X_{\text{worst},v,i}) + r_{2,c,v,i}(|X_{c,v,i} \text{ or } X_{r,v,i}| - |X_{r,v,i} \text{ or } X_{c,v,i}|), \tag{2}$$

$$X'_{c,v,i} = X_{c,v,i} + r_{1,c,v,i}(X_{\text{best},v,i} - |X_{\text{worst},v,i}|) + r_{2,c,v,i}(|X_{c,v,i} \text{ or } X_{r,v,i}| - (X_{r,v,i} \text{ or } X_{c,v,i})), \tag{3}$$

where subscripts c, v, and i represent the number of candidate solution, variable, and iteration, respectively. $X_{\text{best},v,i}$ is the value of the best candidate, and $X_{\text{worst},v,i}$ is the value of the worst candidate for the variable v during the ith iteration. $X'_{c,v,i}$ is the updated value of $X_{c,v,i}$, and $r_{1,c,v,i}$ and $r_{2,c,v,i}$ are the two random numbers in the range of 0–1.

In Eqs. (2) and (3), the term $X_{c,v,i}$ or $X_{r,v,i}$ represents that there is an interaction of cth candidate solution with the randomly selected rth candidate solution, and their objective function values are compared. If the objective function values of a cth candidate solution are better than the rth candidate solution, then the term "$X_{c,v,i}$ or $X_{r,v,i}$" becomes $X_{c,v,i}$, and the term "$X_{r,v,i}$ or $X_{c,v,i}$" becomes $X_{r,v,w}$. Otherwise vice versa.

Equation (1) is used in the Rao-1 algorithm, Eq. (2) in the Rao-2 algorithm, and Eq. (3) in the Rao-3 algorithm. Then, the updated candidate solutions are compared with initial candidate solutions one-by-one, and the best candidate solutions are carried forward in the next iteration. These best candidate solutions forwarded in next iteration become initial population for this iteration. These steps are repeated until the termination criteria satisfied.

For more details and the MATLAB codes of the Rao algorithms, readers may refer to the Web site https://sites.google.com/view/raoalgorithms/.

2.2 Self-adaptive Multi-population (SAMP) Rao Algorithms

Rao and Pawar [28] proposed new variants of basic Rao algorithms with some modifications and named as "self-adaptive multi-population (SAMP) Rao algorithms". In SAMP Rao algorithms, the complete population splits into number of subpopulations at initial stage of each iteration. This feature diversifies the search process of algorithms. The number of subpopulations is decided by these algorithms based on the value of best solution obtained in each iteration.

These subpopulations are updated individually in the same way as used in basic Rao algorithms. Equation (1) is used in the SAMP Rao-1 algorithm, Eq. (2) is used in the SAMP Rao-2 algorithm, and Eq. (3) is used in the SAMP Rao-3 algorithm to update candidate solutions of each subpopulation in every iteration. The updated subpopulations are merged in a single population at the end of each iteration. If the objective function value of the best solution in the current iteration is better than same in the previous iteration, the number of subpopulations is increased by 1 in the next iteration to explore the search process. Otherwise, the number of subpopulations is decreased by 1 in the next iteration to exploit the search process of the algorithm.

Each subpopulation must have at least three candidate solutions. Also, the duplicate candidate solutions are replaced by the new random solutions to again explore the search process of the algorithm. These steps are repeated until the termination criteria satisfied.

2.3 Quasi-Oppositional-Based (QO) Rao Algorithms

The opposition-based learning concept is incorporated in the basic Rao algorithms to diversify the search process, and these new variants of Rao algorithms named as "QO Rao algorithms" [27]. A population opposite to the current population is generated in each iteration of these algorithms. Then, the quasi-opposite population is obtained using Eqs. (4)–(6) to maintain the stochastic nature of Rao algorithms.

$$X_{c,v,i}^q = \text{rand}(a, b) \tag{4}$$

$$a = \frac{X_v^{\text{LL}} + X_v^{\text{UL}}}{2} \tag{5}$$

$$b = X_v^{\text{L}} + X_v^{\text{U}} - X_{c,v,i} \tag{6}$$

$$c = 1, 2, \ldots, P; \quad v = 1, 2, \ldots, d; \quad i = 1, 2, \ldots, n$$

where $X^q_{c,v,i}$ is the quasi-opposite value of $X_{c,v,i}$ which is randomly generated between a and b; a is the center of the search space; b is the opposite value of $X_{c,v,i}$; X^{LL}_v is the lower limit, and X^{UL}_v is the upper limits of the vth variable.

The quasi-opposite population is merged with the current population. Then, the first half of the best candidate solutions is selected. These candidate solutions are then updated in the same way as used in basic Rao algorithms. The rest procedure of these algorithms is the same as the Rao algorithms. The next section gives the optimization problem considered in this study.

3 Optimization Problem of a 10-bar Truss Structure

In this work, the weight optimization of a 10-bar truss structure as shown in Fig. 1 is considered. This problem was previously solved by various researchers. Some of them are Shih and Yang [29], Kaveh and Rahami [30], Li et al. [31], Kaveh and Malakoutirad [32], Sadollah et al. [3], and Eskandar et al. [5].

The material properties used for a truss structure such as the modulus of elasticity and the density of the material are 10^7 psi (68,947.57 MPa) and 0.1 lb/in^3, respectively. The cross-section area of each bar is taken as a design variable. There are limitations for the stress induced in each member of a truss, and the displacement takes place at each node. Hence, this problem consists of ten design variables and 36 design constraints.

The mathematical model for optimization of a 10-bar truss structure is as follows:

Design variables:

$$X = [A_1, A_2, \ldots, A_{10}] \tag{7}$$

Fig. 1 Schematic diagram of a 10-bar truss structure [31]
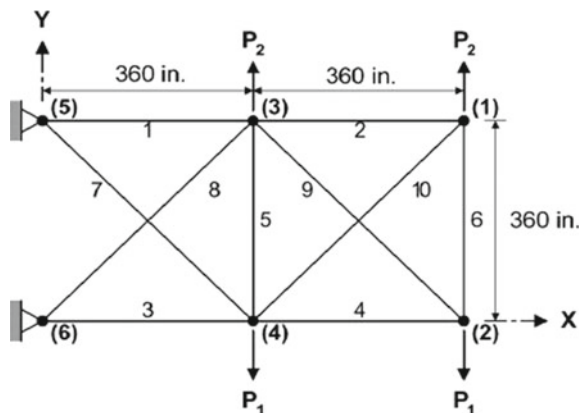
Objective function:

$$\text{Minimize, } f(x) = \sum_{i=1}^{10} \rho A_i L_i \tag{8}$$

Design constraints:

$$-25 \le \sigma_i \le 25 \, \text{ksi} \quad i = 1, 2, \ldots, 10 \tag{9}$$

$$-2 \le u_i \le 2 \, \text{in} \quad i = 1, 2, 3, 4 \tag{10}$$

$$-2 \le v_i \le 2 \, \text{in} \quad i = 1, 2, 3, 4 \tag{11}$$

Here, A_i is the cross-section area of the ith member, ρ is the density of material, L_i is the length of the ith member, σ_i is the stress induced in ith member, u_i is the horizontal displacement takes place at ith node, and v_i is the vertical displacement takes place at ith node.

Search space: In this work, three different cases of search space are considered as follows:

Case 1 In this case, all design variables are to be considered as discrete type variables belong to the following set of values.

$$A_i \in [1.62, 1.80, 1.99, 2.13, 2.38, 2.62, 2.63, 2.88, 2.93, 3.09, 3.13,$$
$$3.38, 3.47, 3.55, 3.63, 3.84, 3.87, 3.88, 4.18, 4.22, 4.49, 4.59,$$
$$4.80, 4.97, 5.12, 5.74, 7.22, 7.97, 11.5, 13.5, 13.9, 14.2, 15.5,$$
$$16, 16.9, 18.8, 19.9, 22, 22.9, 26.5, 30, 33.5] (\text{in}^2)$$

Case 2 In this case also, all design variables are to be considered as discrete type variables belong to the following set of values.

$$A_i \in [0.1, 0.5, 1.0, 1.5, 2.0, 2.5, 3.0, 3.5, 4.0, 4.5, 5.0, 5.5, 6.0, 6.5,$$
$$7.0, 7.5, 8.0, 8.5, 9.0, 9.5, 10.0, 10.5, 11.0, 11.5, 12.0, 12.5,$$
$$13.0, 13.5, 14.0, 14.5, 15.0, 15.5, 16.0, 16.5, 17.0, 17.5, 18.0,$$
$$18.5, 19.0, 19.5, 20.0, 20.5, 21.0, 21.5, 22.0, 22.5, 23.0, 23.5,$$
$$24.0, 24.5, 25.0, 25.5, 26.0, 26.5, 27.0, 27.5, 28.0, 28.5, 29.0,$$
$$29.5, 30.0, 30.5, 31.0, 31.5] (\text{in}^2)$$

Case 3 In this case, all design variables are to be considered as continuous type variables as,

$$0.1 \leq A_i \leq 35 \, \text{in}^2 \quad i = 1, 2, \ldots, 10$$

The next section presents the computational results obtained in this work using Rao algorithms, SAMP Rao algorithms, and QO Rao algorithms.

4   Optimization Results and Discussion

In this work, the Rao algorithms and their variants are coded in the MATLAB-R2016b tool. A laptop with configuration of 8 GB RAM and Intel Core i3-4030U 1.90 GHz processor is used to run considered algorithms. A static penalty approach is used in this work to handle numerous design constraints. In this work, the optimization of a 10-bar truss is carried out for three different cases of search space mentioned in Sect. 3, and the optimal designs of a 10-bar truss obtained using nine advanced optimization algorithms such as three Rao algorithms, three SAMP Rao algorithms, and three QO Rao algorithms are presented in following subsections. Each algorithm considered in this study is executed for 50 individual runs to obtain optimal solutions.

4.1   Case 1

For case 1, the maximum number of function evaluations considered is 10,000 for all Rao algorithms and their variants. The population size considered for Rao algorithms and SAMP Rao algorithms is 20, while the same for QO Rao algorithms is 10. Table 1 presents the optimal designs of a 10-bar truss for case 1 got using Rao algorithms, SAMP Rao algorithms, and QO Rao algorithms. Also, the results obtained using Rao algorithms and their variants are compared with the results achieved by other researchers and optimization methods for case 1 such as GA [29, 30, 33]; PSO, PSOPC and HPSO [31]; ACO [34]; MBA[3]; and WCA [5].

The Rao algorithms and their variants got the same results as given by WCA and Kaveh and Rahami as shown in Table 1. The results achieved by Rao algorithms and their variants are superior to the results given by GA, Shih and Yang, PSO, PSOPC, HPSO, ACO, and MBA. The weight of a 10-bar truss structure given by Rao algorithms and their variants are less by 2.19, 1.83, 1.63, 0.74, 0.49, 0.31, and 0.018% than the same given by GA, PSOPC, PSO, HPSO, ACO, MBA, and Shih and Yang.

The QO Rao-2 algorithm has required less number of function evaluations than other considered algorithms to reach an optimal solution of a 10-bar truss for case 1.

Table 1 Comparison of optimal designs of a 10-bar truss structure for case 1

Methods used	Objective W (lb)	Design variables										Function evaluations
		A_1	A_2	A_3	A_4	A_5	A_6	A_7	A_8	A_9	A_{10}	
GA*	5613.8	33.5	1.62	22	15.5	1.62	1.62	14.2	19.9	19.9	2.62	N.A.
Shih and Yang*	5491.7	33.5	1.62	22.9	15.5	1.62	1.62	7.97	22	22	1.62	N.A.
Kaveh and Rahami*	**5490.738**	33.5	1.62	22.9	14.2	1.62	1.62	7.97	22.9	22	1.62	N.A.
PSO*	5581.76	30	1.62	30	13.5	1.62	1.8	11.5	18.8	22	1.8	N.A.
PSOPC*	5593.4	30	1.8	26.5	15.5	1.62	1.62	11.5	18.8	22	3.09	N.A.
HPSO*	5531.9	30	1.62	22.9	13.5	1.62	1.62	7.97	26.5	22	1.8	20,000
ACO*	5517.72	33.5	1.62	22.9	14.2	1.62	1.62	11.5	22	19.9	1.62	N.A.
MBA*	5507.7	30	1.62	22.9	16.9	1.62	1.62	7.97	22.9	22.9	1.62	3600
WCA*	**5490.73**	33.5	1.62	22.9	14.2	1.62	1.62	7.97	22.9	22	1.62	2200
Rao-1	**5490.73**	33.5	1.62	22.9	14.2	1.62	1.62	7.97	22.9	22	1.62	2980
Rao-2	**5490.73**	33.5	1.62	22.9	14.2	1.62	1.62	7.97	22.9	22	1.62	980
Rao-3	**5490.73**	33.5	1.62	22.9	14.2	1.62	1.62	7.97	22.9	22	1.62	2460
SAMP Rao-1	**5490.73**	33.5	1.62	22.9	14.2	1.62	1.62	7.97	22.9	22	1.62	2840
SAMP Rao-2	**5490.73**	33.5	1.62	22.9	14.2	1.62	1.62	7.97	22.9	22	1.62	1060
SAMP Rao-3	**5490.73**	33.5	1.62	22.9	14.2	1.62	1.62	7.97	22.9	22	1.62	2200
QO Rao-1	**5490.73**	33.5	1.62	22.9	14.2	1.62	1.62	7.97	22.9	22	1.62	2400
QO Rao-2	**5490.73**	33.5	1.62	22.9	14.2	1.62	1.62	7.97	22.9	22	1.62	**840**
QO Rao-3	**5490.73**	33.5	1.62	22.9	14.2	1.62	1.62	7.97	22.9	22	1.62	1240

*Sources GA—Rajeev and Krishnamoorthy [33]; Shih and Yang [29]; Kaveh and Yang [29]; Kaveh and Rahami [30]; PSO, PSOPC and HPSO—Li et al. [31]; ACO—Kaveh and Hassani [34]; MBA—Sadollah et al. [3]; and WCA- Eskandar et al. [5]

Bold values indicate the best values

Fig. 2 Convergence plot of the optimal solution for case 1 of a 10-bar truss problem

Figure 2 illustrates the plot of convergence for the optimal solution of a case 1 obtained using the QO Rao-2 algorithm. The QO Rao-2 algorithm reached the optimal solution of a 10-bar truss for case 1 within 42 iterations.

4.2 Case 2

For case 2, the maximum number of function evaluations considered is 10,000 for all Rao algorithms and their variants. The population size considered for Rao algorithms and SAMP Rao algorithms is 20, while the same for QO Rao algorithms is 10. Table 2 presents the optimal designs of a 10-bar truss structure for case 2 got using Rao algorithms, SAMP Rao algorithms, and QO Rao algorithms. Also, the results obtained using Rao algorithms and their variants are compared with the results achieved by other researchers and optimization methods for case 2 such as Branch and Bound [35]; PSO, PSOPC and HPSO [31]; MBA [3]; and WCA [5].

The Rao algorithms and their variants got the same results as given by WCA and MBA algorithm as shown in Table 2. The solution given by the Branch and Bound method for case 2 is an infeasible solution due to violation of the vertical displacement constraint at node 1. Hence, the results achieved by Rao algorithms and their variants are superior to the results given by Branch and Bound, PSO, PSOPC, and HPSO. The weight of a 10-bar truss structure given by Rao algorithms and their variants for case 2 are less by 3.36, 1.28, and 0.12% than the same given by PSO, PSOPC, and HPSO algorithm.

The SAMP Rao-3 algorithm has required less number of function evaluations than the remaining Rao algorithms and their variants to reach optimal solution of a 10-bar truss structure for case 2. Figure 3 illustrates the plot of convergence for the

Table 2 Comparison of optimal designs of a 10-bar truss structure for case 2

| Methods used | Objective | Design variables | | | | | | | | | | Function |
	W (lb)	A_1	A_2	A_3	A_4	A_5	A_6	A_7	A_8	A_9	A_{10}	evaluations
Branch and Bound	5059.9	30.5	0.1	23	15.5	0.1	0.5	7.5	21	21.5	0.1	N.A.
PSO	5243.71	24.5	0.1	22.5	15.5	0.1	1.5	8.5	21.5	27.5	0.1	N.A.
PSOPC	5133.16	25.5	0.1	23.5	18.5	0.1	0.5	7.5	21.5	23.5	0.1	N.A.
HPSO	5073.51	31.5	0.1	24.5	15.5	0.1	0.5	7.5	20.5	20.5	0.1	25,000
MBA	**5067.33**	29.5	0.1	24	15	0.1	0.5	7.5	21.5	21.5	0.1	3000
WCA	**5067.33**	29.5	0.1	24	15	0.1	0.5	7.5	21	22	0.1	1800
Rao-1	**5067.33**	30.5	0.1	23.5	14.5	0.1	0.5	7.5	21.5	21.5	0.1	5060
Rao-2	**5067.33**	30.5	0.1	23.5	14.5	0.1	0.5	7.5	21.5	21.5	0.1	2900
Rao-3	**5067.33**	29.5	0.1	23.5	15.5	0.1	0.5	7.5	21.5	21.5	0.1	2740
SAMP Rao-1	**5067.33**	30.5	0.1	23.5	14.5	0.1	0.5	7.5	21.5	21.5	0.1	4660
SAMP Rao-2	**5067.33**	30.0	0.1	23.5	15.0	0.1	0.5	7.5	21.5	21.5	0.1	2440
SAMP Rao-3	**5067.33**	29.5	0.1	23.5	15.5	0.1	0.5	7.5	21.5	21.5	0.1	**2100**
QO Rao-1	**5067.33**	30.0	0.1	23.5	15.0	0.1	0.5	7.5	21.5	21.5	0.1	3640
QO Rao-2	**5067.33**	29.5	0.1	24.0	15.0	0.1	0.5	7.5	21.5	21.5	0.1	2300
QO Rao-3	**5067.33**	31.0	0.1	22.5	15.0	0.1	0.5	7.5	20.5	22.5	0.1	2280

*Sources GA—Branch and Bound—Ringertz [35]; PSO, PSOPC and HPSO—Li et al. [31]; MBA—Sadollah et al. [3]; and WCA—Eskandar et al. [5]
Bold values indicate the best values

Fig. 3 Convergence plot of the optimal solution for case 2 of a 10-bar truss problem
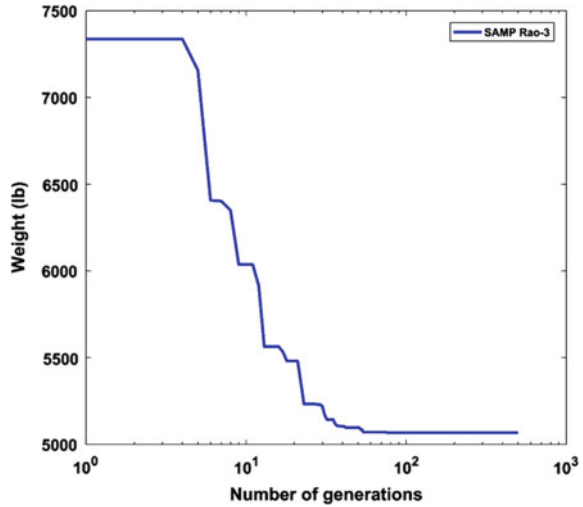
optimal solution of a case 2 obtained using the SAMP Rao-3 algorithm. The SAMP Rao-3 algorithm reached nearer to the optimal solution of a 10-bar truss problem for case 2 within 50 iterations approximately.

4.3   Case 3

For case 3, the maximum number of function evaluations considered is 50,000 for all Rao algorithms and their variants. The population size considered for Rao algorithms and SAMP Rao algorithms is 20, while the same for QO Rao algorithms is 10. Table 3 presents the optimal designs of a 10-bar truss for case 3 got using Rao algorithms, SAMP Rao algorithms, and QO Rao algorithms. Also, the results obtained using Rao algorithms and their variants are compared with the results achieved by other researchers and optimization methods for case 1 such as [36–43]; GA [30, 33, 44, 45]; ACO [34]; HGAPSO [32]; PSO and WCA [5].

The SAMP Rao-2 algorithm has achieved best design of a 10-bar truss for case 3 as compared to the other optimization methods considered. The weight of a 10-bar truss given by the SAMP Rao-2 algorithm is less by 8.47, 1, 0.68, 0.68, 0.55, 0.47, 0.38, 0.31, 0.31, 0.13, 0.13, 0.12, 0.02, and 0.01% than the same given by PSO, Gellatly and Berke, Ghasemi et al., ACO, Schmit and Farshi, Venkayya, Dobbs and Nelson, Schmit and Miura, Rizzi, GA, Kaveh and Kalatjari, Khan et al., Kaveh and Rahami, and HGAPSO.
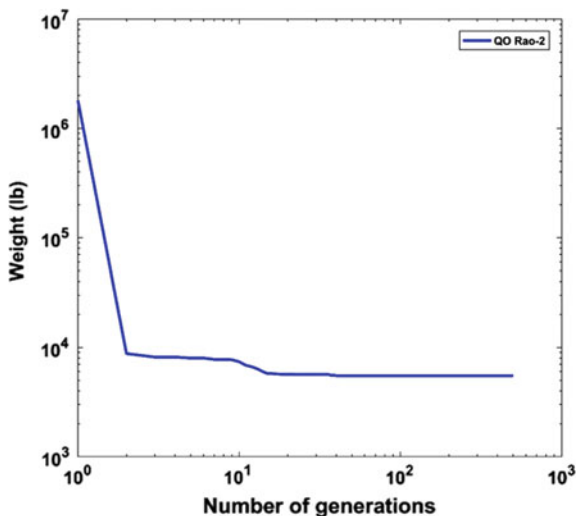
Figure 3 illustrates the plot of convergence for the optimal solution of a case 3 achieved using the SAMP Rao-2 algorithm. The SAMP Rao-2 algorithm reached nearer to the optimal solution of a 10-bar truss problem for case 3 within 200 iterations (Fig. 4).

Table 3 Comparison of optimal designs of a 10-bar truss structure for case 3

Methods used	Objective W (lb)	Design variables										Function evaluations
		A_1	A_2	A_3	A_4	A_5	A_6	A_7	A_8	A_9	A_{10}	
Venkayya*	5084.9	30.42	0.13	23.41	14.91	0.1	0.1	8.7	21.08	21.08	0.19	N.A.
Gellatly and Berke*	5112	31.35	0.1	20.03	15.6	0.14	0.24	8.35	22.21	22.06	0.1	N.A.
Schmit and Farsi*	5089	33.43	0.1	24.26	14.26	0.1	0.1	8.39	20.74	19.69	0.1	N.A.
Rizzi*	5076.66	30.73	0.1	23.93	14.73	0.1	0.1	8.54	20.95	21.84	0.1	N.A.
Dobbs and Nelson*	5080	30.5	0.1	23.29	15.43	0.1	0.21	7.65	20.98	21.82	0.1	N.A.
Schmit and Miura*	5076.85	30.67	0.1	23.76	14.59	0.1	0.1	8.59	21.07	20.96	0.1	N.A.
Khan et al.*	5066.98	30.98	0.1	24.17	14.81	0.1	0.41	7.54	21.05	20.94	0.1	N.A.
Haug and Arora*	5060.92	30.03	0.1	23.27	15.28	0.1	0.55	7.46	21.19	21.61	0.1	N.A.
GA*	5067.31	28.92	0.1	24.07	13.96	0.1	0.56	7.69	21.95	22.09	0.1	N.A.
Ghasemi et al.*	5095.65	25.73	0.1	24.85	16.35	0.1	0.1	8.7	21.41	22.3	0.12	N.A.
Kaveh and Kalatjari*	5067.3	29.5	0.1	23.5	15.5	0.1	0.5	7.5	21.5	21.5	0.1	N.A.
Kaveh and Rahami*	5061.9	30.67	0.1	22.87	15.34	0.1	0.46	7.48	20.96	21.7	0.1	N.A.
ACO*	5095.46	30.86	0.1	23.55	15.01	0.1	0.22	7.63	21.65	21.32	0.1	N.A.
HGAPSO*	5061.4	30.63	0.1	23.06	15.01	0.1	0.59	7.49	21.1	21.56	0.1	N.A.
PSO*	5529.5	33.46	0.11	23.17	15.47	3.64	0.11	8.32	23.34	23.01	0.19	150,000
WCA*	5061.02	30.53	0.1	23.05	15.03	0.1	0.56	7.48	21.12	21.63	0.1	12,500
Rao-1	5060.9568	30.5227	0.1002	23.2368	15.1605	0.1000	0.5661	7.4616	21.0822	21.4870	0.1000	44,520
Rao-2	5060.9248	30.4316	0.1003	23.1870	15.2439	0.1000	0.5556	7.4588	21.0671	21.5524	0.1000	39,700
Rao-3	5060.914809	30.4940	0.1000	23.1769	15.1519	0.1001	0.5565	7.4655	21.0929	21.5473	0.1000	49,440
SAMP Rao-1	5060.9179	30.4397	0.1000	23.2744	15.2244	0.1000	0.5673	7.4478	21.0285	21.5401	0.1000	40,460

(continued)

Table 3 (continued)

Methods used	Objective	Design variables										Function evaluations
	W (lb)	A_1	A_2	A_3	A_4	A_5	A_6	A_7	A_8	A_9	A_{10}	
SAMP Rao-2	**5060.8901**	**30.5175**	**0.1000**	**23.2595**	**15.2282**	**0.1001**	**0.5422**	**7.4495**	**21.0131**	**21.5238**	**0.1000**	**42,080**
SAMP Rao-3	5060.9056	30.6059	0.1000	23.1606	15.2676	0.1000	0.5430	7.4659	21.0492	21.4506	0.1000	26,800
QO Rao-1	5060.9274	30.4877	0.1002	23.1442	15.3299	0.1000	0.5624	7.4581	21.0228	21.5225	0.1000	38,320
QO Rao-2	5060.9113	30.6113	0.1000	23.2193	15.1663	0.1000	0.5696	7.4580	21.0216	21.4938	0.1000	36,020
QO Rao-3	5060.9136	30.5902	0.1001	23.1012	15.1722	0.1000	0.5560	7.4675	21.0354	21.5743	0.1000	48,180

*Sources Venkayya [36]; Gellatly and Berke [37]; Schmit and Farshi [38]; Rizzi [39]; Dobbs and Nelson [40]; Schmit and Miura [41]; Khan et al. [42]; Haug and Arora [43]; GA—Rajeev and Krishnamoorthy [33]; Ghasemi et al. [44]; Kaveh and Kalatjari [45]; Kaveh and Rahami [30]; ACO—Kaveh and Hassani [34]; HGAPSO—Kaveh and Malakoutirad [32]; PSO and WCA—Eskandar et al. [5]
Bold values indicate the best values

Fig. 4 Convergence plot of the optimal solution for case 3 of a 10-bar truss problem
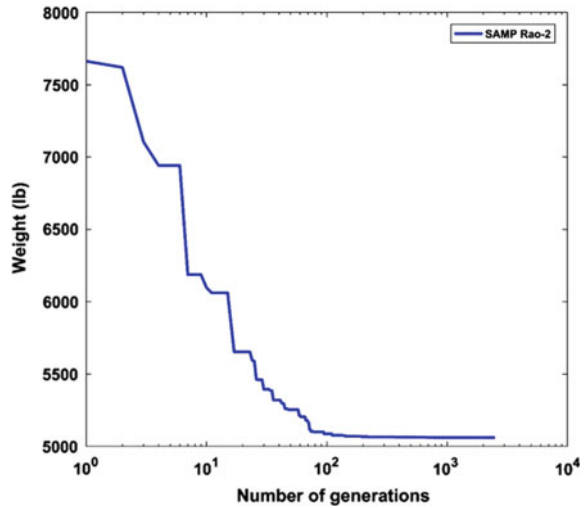
5   Conclusions

In this work, the weight optimization of a 10-bar truss is proposed using nine recently developed advanced optimization algorithms namely Rao-1 algorithm, Rao-2 algorithm, Rao-3 algorithm, SAMP Rao-1 algorithm, SAMP Rao-2 algorithm, SAMP Rao-3 algorithm, QO Rao-1 algorithm, QO Rao-2 algorithm, and QO Rao-3 algorithm. The comparison of results in this study concluded that the Rao algorithms and their variants are effective in solving the optimization problems of truss structures. Also, these algorithms can handle optimization problems with numerous design variables and design constraints. These Rao algorithms and their variants do not need algorithm-specific parameters to search the optimum solution. Hence, these algorithms reduce the efforts of researchers and designers required to adjust algorithm-specific parameters. Besides, the concept of these Rao algorithms and their variants is simple to understand and easy to implement. In future studies, these Rao algorithms and their variant will be used to solve different structural optimization problems.

References

1. Luh, G.-C., Lin, C.-Y.: Optimal design of truss-structures using particle swarm optimization. Comput. Struct. **89**(23–24), 2221–2232 (2011)
2. Sonmez, M.: Artificial Bee Colony algorithm for optimization of truss structures. Appl. Soft Comput. **11**(2), 2406–2418 (2011)
3. Sadollah, A., Bahreininejad, A., Eskandar, H., Hamdi, M.: Mine blast algorithm for optimization of truss structures with discrete variables. Comput. Struct. **102–103**, 49–63 (2012)

4. Kaveh, A., Khayatazad, M.: Ray optimization for size and shape optimization of truss structures. Comput. Struct. **117**, 82–94 (2013)
5. Eskandar, H., Sadollah, A., Bahreininejad, A.: Weight optimization of truss structures using water cycle algorithm. Int. J. Optim. Civil Eng. **3**(1), 115–129 (2013)
6. Zuo, W., Li, B.: A hybrid OC–GA approach for fast and global truss optimization with frequency constraints. Appl. Soft Comput. **14**, 528–535 (2014)
7. Dede, T.: Application of teaching-learning-based-optimization algorithm for the discrete optimization of truss structures. KSCE J. Civil Eng. **18**, 1759–1767 (2014)
8. Ho-Huu, V., Nguyen-Thoi, T., Nguyen-Thoi, M.H., Le-Anh, L.: An improved constrained differential evolution using discrete variables (D-ICDE) for layout optimization of truss structures. Expert Syst. Appl. **42**(20), 7057–7069 (2015)
9. Pham, H.A.: Truss optimization with frequency constraints using enhanced differential evolution based on adaptive directional mutation and nearest neighbor comparison. Adv. Eng. Softw. **102**, 142–154 (2016)
10. Farshchin, M., Camp, C.V., Maniat, M.: Optimal design of truss structures for size and shape with frequency constraints using a collaborative optimization strategy. Expert Syst. Appl. **66**, 203–218 (2016)
11. Stolpe, M.: Truss optimization with discrete design variables: a critical review. Struct. Multidiscip. Optim. **53**, 349–374 (2016)
12. Kanarachos, S., Griffin, J., Fitzpatrick, M.E.: Efficient truss optimization using the contrast-based fruit fly optimization algorithm. Comput. Struct. **182**, 137–148 (2017)
13. Assimi, H., Jamali, A., Nariman-zadeh, N.: Sizing and topology optimization of truss structures using genetic programming. Swarm Evol. Comput. **37**, 90–103 (2017)
14. Mortazavi, A., Togan, V.: Sizing and layout design of truss structures under dynamic and static constraints with an integrated particle swarm optimization algorithm. Appl. Soft Comput. **51**, 239–252 (2017)
15. Lieu, Q.X., Do, D.T.T., Lee, J.: An adaptive hybrid evolutionary firefly algorithm for shape and size optimization of truss structures with frequency constraints. Comput. Struct. **195**, 99–112 (2018)
16. Kaveh, A., Mahdavi, V.R.: Multi-objective colliding bodies optimization algorithm for design of trusses. J. Comput. Des. Eng. **6**(1), 49–59 (2019)
17. Li, Y., Yan, Z.: Application of improved bat algorithm in truss optimization. KSCE J. Civil Eng. **23**, 2636–2643 (2019)
18. Kaveh, A., Seddighian, M.R.: Simultaneously multi-material layout, and connectivity optimization of truss structures via an enriched firefly algorithm. Structures **27**, 2217–2231 (2020)
19. Rao, R.V.: Rao algorithms: three metaphor-less simple algorithms for solving optimization problems. Int. J. Ind. Eng. Comput. **11**, 107–130 (2020)
20. Wang, L., Wang, Z., Liang, H., Huang, C.: Parameter estimation of photovoltaic cell model with Rao-1 algorithm. Optik **210**, 163846 (2020)
21. Jabir, H.A., Kamel, S., Selim, A., Jurado, F.: Optimal coordination of overcurrent relays using metaphor-less simple method. In: 2019 21st International Middle East Power Systems Conference (MEPCON), Cairo, Egypt, pp. 1063–1067 (2019)
22. Kalemci, E.N., Ikizler, S.B.: Rao-3 algorithm for the weight optimization of reinforced concrete cantilever retaining wall. Geomech. Eng. **20**(6), 527–536 (2020)
23. Ravipudi, J.L.: Synthesis of linear, planar, and concentric circular antenna arrays using Rao algorithms. Int. J. Appl. Evol. Comput. **11**(3) (2020). https://doi.org/10.4018/ijaec.2020070103
24. Rao, R.V., Keesari, H.S.: Rao algorithms for multi-objective optimization of selected thermodynamic cycles. Eng. Comput. (2020). https://doi.org/10.1007/s00366-020-01008-9
25. Rao, R.V., Pawar, R.B.: Constrained design optimization of selected mechanical system components using Rao algorithms. Appl. Soft Comput. **89**, 106141 (2020)
26. Rao, R.V., Pawar, R.B.: Optimal weight design of a spur gear train using Rao algorithms. In: Intelligent Computing Applications for Sustainable Real-World Systems, ICSISCET 2019:

Proceedings in Adaptation, Learning and Optimization, vol. 13. Springer, Cham (2020). https://doi.org/10.1007/978-3-030-44758-8_33

27. Rao, R.V., Pawar, R.B.: Quasi-oppositional-based Rao algorithms for multi-objective design optimization of selected heat sinks. J. Comput. Des. Eng. (2020). https://doi.org/10.1093/jcde/qwaa060

28. Rao, R.V., Pawar, R.B.: Self-adaptive multi-population Rao algorithms for engineering design optimization. Appl. Artif. Intell. **34**(3), 187–250 (2020)

29. Shih, C.J., Yang, Y.C.: Generalized Hopfield network based structural optimization using sequential unconstrained minimization technique with additional penalty strategy. Adv. Eng. Softw. **33**, 721–729 (2002)

30. Kaveh, A., Rahami, H.: Analysis, design and optimization of structures using force method and genetic algorithm. Int. J. Numer. Meth. Eng. **65**, 1570–1584 (2006)

31. Li, L.J., Huang, Z.B., Liu, F.: A heuristic particle swarm optimization method for truss structures with discrete variables. Comput. Struct. **87**, 435–443 (2009)

32. Kaveh, A., Malakoutirad, S.: Hybrid genetic algorithm and particle swarm optimization for the force method-based simultaneous analysis and design. Iranian J. Sci. Technol., Tran. B: Eng. **34**(B1), 15–34 (2010)

33. Rajeev, S., Krishnamoorthy, C.S.: Discrete optimization of structures using genetic algorithms. J. Struct. Eng. **118**(5), 1233–1250 (1992)

34. Kaveh, A., Hassani, M.: Simultaneous analysis, design and optimization of structures using force method and ant colony algorithms. Asian J. Civil Eng. **10**(4), 381–396 (2009)

35. Ringertz, U.T.: On methods for discrete structural constraints. Eng. Optim. **13**(1), 47–64 (1988)

36. Venkayya, V.B.: Design of optimum structures. Comput. Struct. **1**, 265–309 (1971)

37. Gellatly, R.A., Berke, L.: Optimal structural design, AFFDLTR-70-165. Air Force Flight Dynamics Laboratory, Wright-Patterson AFB, OH (1971)

38. Schmit Jr., L.A., Farshi, B.: Some approximation concepts for structural synthesis. AIAA J. **12**, 692–699 (1974)

39. Rizzi, P.: Optimization of multi-constrained structures based on optimality criteria. In: AIAA/ASME/SAE 17th Structures, Structural Dynamics, and Materials Conference, King of Prussia, PA (1976)

40. Dobbs, M.W., Nelson, R.B.: Application of optimality criteria to automated structural design. AIAA J. **14**, 1436–1443 (1976)

41. Schmit Jr., L.A., Miura, H.: Approximation Concepts for Efficient Structural Synthesis, NASA CR-2552. NASA, Washington, DC (1976)

42. Khan, M.R., Willmert, K.D., Thornton, W.A.: An optimality criterion method for large-scale structures. AIAA J. **17**, 753–761 (1979)

43. Haug, E., Arora, J.: Applied Optimal Design. Wiley, New York (1979)

44. Ghasemi, M., Hinton, E., Wood, R.: Optimization of trusses using genetic algorithms for discrete and continuous variables. Eng. Comput. **16**, 272–301 (1997)

45. Kaveh, A., Kalatjari, V.: Genetic algorithm for discrete-sizing optimal design of trusses using the force method. Int. J. Numer. Meth. Eng. **55**, 55–72 (2002)

Model Updating of Frame Structure Using Equilibrium Optimizer (EO) and Cuckoo Search (CS) Algorithms

S. Tiachacht, S. Khatir, M. Slimani, A. Behtani, C. Le Thanh, and M. Abdel Wahab

1 Introduction

Over their lifetime, any local damage can occur to many structural systems. Unless the local damage is not detected quickly, it may lead to a disastrous outcome. Moreover, damage detection is an important topic for structural engineering and has provided considerable attention in recent years. The identification of structural damage consists of three separate stages to define the presence, position, and quantification of the damage. The MCI was developed by Tiachacht et al. [1] for damage detection, localization, and quantification in complex structures. The results showed that MCI provided better results than CI. For more accuracy, the authors used MCI as an objective function to quantify correctly the damaged elements. Ghannadi and Kourehli [2] presented an inverse problem of damage detection using artificial neural network. The study of sensitivity analysis carried out for each example showing the performance of an artificial neural network after mode shape expansion was efficiently improved. Khatir et al. [3, 4] studied the inverse analysis using genetic algorithm (GA) and particle swarm optimization (PSO) for damage detection, localization, and quantification in composite beams based on inverse problem. Measured and calculated frequencies were used in the objective function. Nobahari and Seyedpoor [5] investigated an efficient technique for multiple dam-

S. Tiachacht (✉) · M. Slimani · A. Behtani
Laboratory of Mechanics, Structure, and Energetics (LMSE), Mouloud Mammeri University of Tizi-Ouzou, B.P.N 17 RP, 15000 Tizi-Ouzou, Algeria
e-mail: Samir.tiachacht@ummto.dz

S. Khatir · M. Abdel Wahab
Soete Laboratory, Faculty of Engineering and Architecture, Ghent University, Technologiepark Zwijnaarde 903, 9052 Zwijnaarde, Belgium

C. Le Thanh
Faculty of Civil Engineering, Ho Chi Minh City Open University, Ho Chi Minh City, Vietnam

19

ages in simple and complex structures. The new technique is named flexibility strain energy-based index (FSEBI). The results showed that the proposed indicator could accurately estimate the location and of the severity damage. A two-step approach to determine the location and level of multiple damages based on the information fusion technique and GA was investigated in [6]. Ghannadi et al. [7] used gray wolf optimization (GWO) algorithm for SHM of 3D structures. The objective function was based on frequencies and mode shapes. Two experimental examples were studied using a cantilever beam and a truss tower to validate the proposed approach. Multiverse optimizer (MVO) was used to address the issue of damage detection by Ghannadi and Kourehli [8]. Two objective functions were used to solve the inverse problem based on the modal assurance criterion (MAC) and modified total modal assurance criterion (MTMAC).

In this paper, a convergence study and CPU time analysis of CS and EO are considered. Model reduction of FE frame structure is combined with CS and EO for model updating based on experimental measurements. The results show that EO has good convergence and less CPU compared with CS based on the selected number of populations and iterations.

2   Methodology

2.1   Cuckoo Search (CS) Algorithm

Cuckoo search (CS) [9] is an algorithm inspired by nature, Cuckoo birds' brood reproductive strategy to raise their population. Thus, each Cuckoo lays one egg at a time and dumps it in a randomly chosen host nest. Normally, the eggs Cuckoo will hatch quicker than the other eggs in the same nest. The number of available host nests is fixed, and the egg laid by a cuckoo is discovered by the host bird with a probability $p_a \in [0, 1]$. When this happens, the host cuckoo would remove the non-hatched eggs by moving the eggs out of the nest or leaving the nest to build a completely new nest in a new location. This feature satisfies the reducing the probability of the legitimate eggs from hatching. Furthermore, the foreign cuckoo chick can gain access to more food by mimicking the call of the host chicks. To explore the new feasible search space, the movement strategy of CS algorithm using Lévy flight distribution (LFD) which is random walk whose direction is random and their step length is derived from the Lévy distribution. A random walk is a random process, which consists of taking a series of consecutive random steps. After a large number of steps, the distance from the origin of the random walk tends to a stable distribution. In exploring large-scale search zones, Lévy flights are more successful. This is mostly because the variation in Lévy flights rises much faster than the usual random walk. The main concept of movement updating of CS algorithm is expressed in Eq. 1.

$$X_i^{t+1} = X_i^t + \alpha s \otimes H(p_a - \varepsilon) \otimes \left(X_j^t - X_k^t \right)$$

$$X_i^{t+1} = X_i^t + \alpha L(s, \lambda) \tag{1}$$

where

α	Positive step size scaling factor.
s	Step size (normally equal $L/100$ with L is levy step).
$\otimes$	Entry-wise product of two vectors.
H	Heavy-side function.
P_a	Used to switch between local and global random walks.
ε	Uniform distribution.
$L(s, \lambda)$	Lévy distribution and used to define the step size of a random walk.

2.2 Equilibrium Optimizer (EO) Algorithm

The source of EO approach is a basic well-mixed dynamic mass balance on a control volume, in which a mass balance equation is used to describe the concentration, of a nonreactive constituent in a control volume as a function of its various source and sink mechanisms [10]. For the conservation of mass entering, leaving, and generated in a control volume, the mass balance equation provides the underlying physics. The change in mass in time is equal to the amount of mass entering the system plus the amount created inside minus the amount leaving the system, i.e.,

$$V \frac{dC}{dt} = Q C_{eq} - QC + G \tag{2}$$

C	Concentration inside the control volume (V).
$V \frac{dC}{dt}$	Level of change of mass in the volume of control.
Q	Volumetric flow rate into and out of the control volume.
C_{eq}	Concentration at an equilibrium state in which there is no iteration inside the control volume.
G	Rate of mass iteration within the volume of control.

Equation (2) can also be rearranged to solve, as a function of time (t), the concentration in the control volume (C):

$$\frac{dC}{\lambda C_{eq} - \lambda C + \frac{G}{V}} = dt \tag{3}$$

$$\int\limits_{C_0}^{C} \frac{\mathrm{d}C}{\lambda C_{\mathrm{eq}} - \lambda C + \frac{G}{V}} = \int\limits_{t_0}^{t} \mathrm{d}t \tag{4}$$

$$C = C_{\mathrm{eq}} + \left(C_0 - C_{\mathrm{eq}}\right)e^{-\lambda(t-t_0)} + \frac{G}{\lambda V}\left(1 - e^{-\lambda(t-t_0)}\right) \tag{5}$$

The initial starting time and concentration are t_0 and C_0.

Based on the number of particles and dimensions with uniform random initialization in the search space, the initial concentrations are constructed as follows:

$$C_i^{\mathrm{initial}} = C_{\min} + \mathrm{rand}_i(C_{\max} - C_{\min}) \quad i = 1, 2, \ldots, n \tag{6}$$

Equilibrium pool and candidates (C_{eq}) can be expressed in the following formulation:

$$\vec{C}_{\mathrm{eq,pol}} = \left\{ \vec{C}_{\mathrm{eq}(1)} \quad \vec{C}_{\mathrm{eq}(2)} \quad \vec{C}_{\mathrm{eq}(3)} \quad \vec{C}_{\mathrm{eq}(4)} \quad \vec{C}_{\mathrm{eq(ave)}} \right\} \tag{7}$$

More details are described in [10].

3 Experimental Modal Analysis

Experimental modal analysis is conducted on a four-story steel frame as presented in Fig. 1. To investigate the performance of the inverse analysis in both healthy and damaged frame structures, the frequencies are used into the objective function to compare the calculated and measured ones. This frame was analyzed at Columbia University in New York. This structure was analyzed for structural damage detection in [7, 11].

In the first stage, a hydraulic shake table was used to excite the frame structure, and the structural responses were measured by sensors located in each story as shown in Fig. 1b. Four floors were incorporated into the structure, with an inter-story height of 533 mm, floor plate dimensions of $610 \times 457 \times 12.7$ mm^3, and column cross-sectional dimensions of 50.8×9.5 mm^2. The full structure is connected with bolt for fast replacement. Natural frequencies of the undamaged steel frame FEM and experimental results are provided in Table 1. In the second stage, structural damage detection is investigated after reducing 66% of the cross section of one column in the third story, resulting in 22.2% reduction of stiffness at inter-story. In Fig. 1b, the damaged element is shown. To calibrate the story rigidity of the numerical model, the FE model updating is applied based on the difference
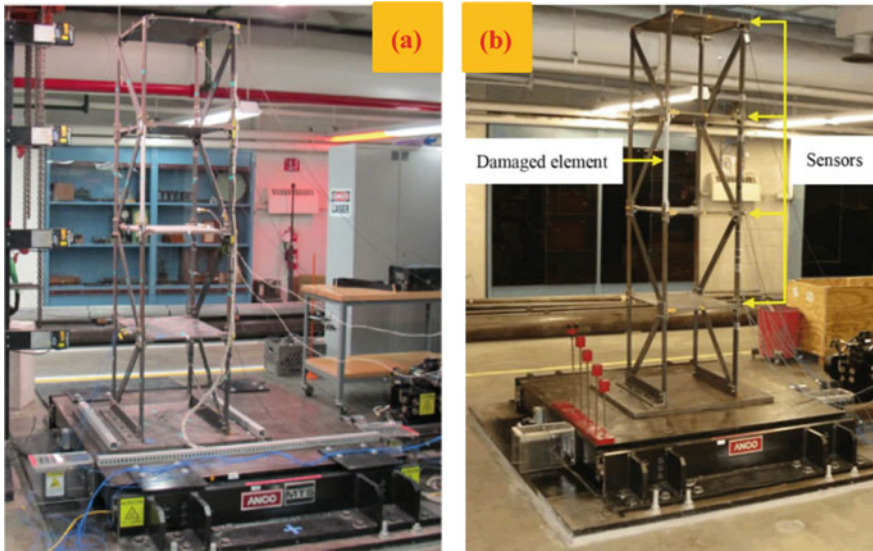
Fig. 1 Four-story shear-type steel frame [11]; **a** healthy and **b** damaged

Table 1 Natural frequencies (Hz) of a healthy steel frame with 50 iterations and different population

Mode		1	2	3	4	Error mean (%)	CPU time (s)
Initial		3.747	10.788	16.528	20.275		
Experimental		3.902	10.980	18.645	26.243		
100 populations	CS	3.865	10.997	18.720	26.231	0.39	1.352
	Error %	0.95	0.16	0.40	0.05		
	EO	3.906	10.971	18.655	26.238	0.07	0.169
	Error %	0.10	0.09	0.05	0.02		
500 populations	CS	3.934	11.005	18.675	26.193	0.35	2.399
	Error %	0.83	0.22	0.16	0.19		
	EO	3.902	10.980	18.645	26.243	0.00	0.843
	Error %	0.00	0.00	0.00	0.00		
1000 populations	CS	3.908	10.952	18.649	26.237	0.12	3.787
	Error %	0.16	0.26	0.02	0.02		
	EO	3.902	10.980	18.645	26.243	0.00	1.560
	Error %	0.00	0.00	0.00	0.00		
2000 populations	CS	3.903	10.968	18.651	26.229	0.05	6.273
	Error %	0.03	0.11	0.03	0.05		
	EO	3.902	10.980	18.645	26.243	0.00	3.193
	Error %	0.00	0.00	0.00	0.00		
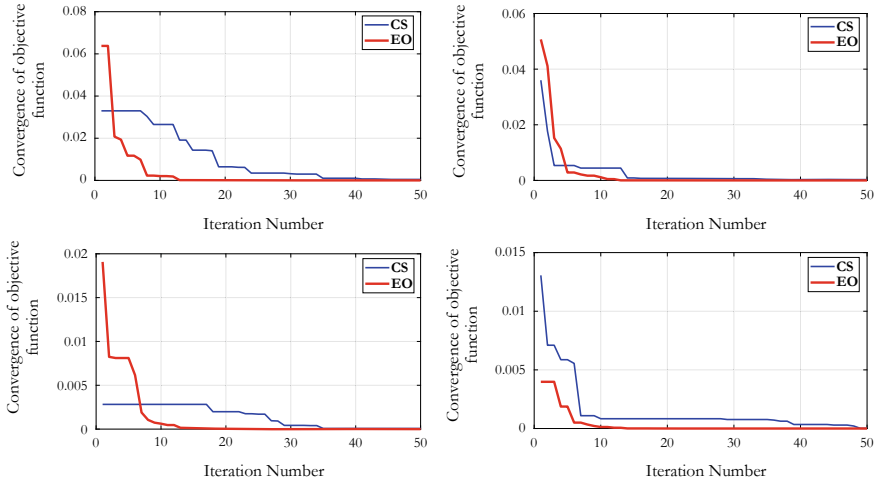
Fig. 2 Convergence study of different population sizes (healthy frame structure)

Table 2 Natural frequencies (Hz) of a healthy steel frame with 200 population and different iterations

Mode		1	2	3	4	Error mean (%)	CPU Time (s)
Initial		3.747	10.79	16.528	20.275		
Experimental		3.902	10.980	18.645	26.243		
50 iterations	CS	3.954	10.989	18.576	26.297	0.50	1.668
	Error %	1.34	0.08	0.37	0.20		
	EO	3.892	10.999	18.626	26.263	0.15	0.309
	Error %	0.25	0.17	0.10	0.08		
100 iterations	CS	3.898	10.983	18.648	26.241	0.04	2.658
	Error %	0.11	0.02	0.02	0.01		
	EO	3.902	10.980	18.645	26.243	0.00	0.663
	Error %	0.00	0.00	0.00	0.00		
500 iterations	CS	3.903	10.980	18.644	26.243	0.01	7.838
	Error %	0.01	0.00	0.01	0.00		
	EO	3.902	10.980	18.645	26.243	0.00	3.303
	Error %	0.00	0.00	0.00	0.00		

between the first four natural frequencies obtained from the FE analysis and measured from the experiments. Equation (8) is used during the process for both optimizations CS and EO. CPU time analysis and convergence study are carried out to study the effectiveness of both optimization techniques.

$$OF = \sum_{i=1}^{r} \frac{\left(\omega_i^c - \omega_i^m\right)^2}{\left(\omega_i^m\right)^2} \quad i = 1, \dots, r \tag{8}$$

where ω_i^c and ω_i^m are the calculated and measured frequency, respectively, and r denotes the number of modes.

4 Results and Discussion

For the healthy frame structure, two scenarios are investigated. Firstly, the number of iteration is fixed and next, the population size is modified for CS and EO. The results are presented in Table 1.

The provided results show that EO has less CPU time compared with CS. The convergence study of each population size is presented in Fig. 2.

In the second scenario, the population size is fixed to 200, and next, different numbers of iterations are used 50, 100, and 500 iterations. Table 2 summarizes all the results using CS and EO.

The results show that EO provides more accurate results and less CPU time compared with CS. The convergence study of each test is shown in Fig. 3.

In the second scenario, the inverse problem is used to predict damage in story 3. Different population sizes are analyzed to study the accuracy of CS and EO.
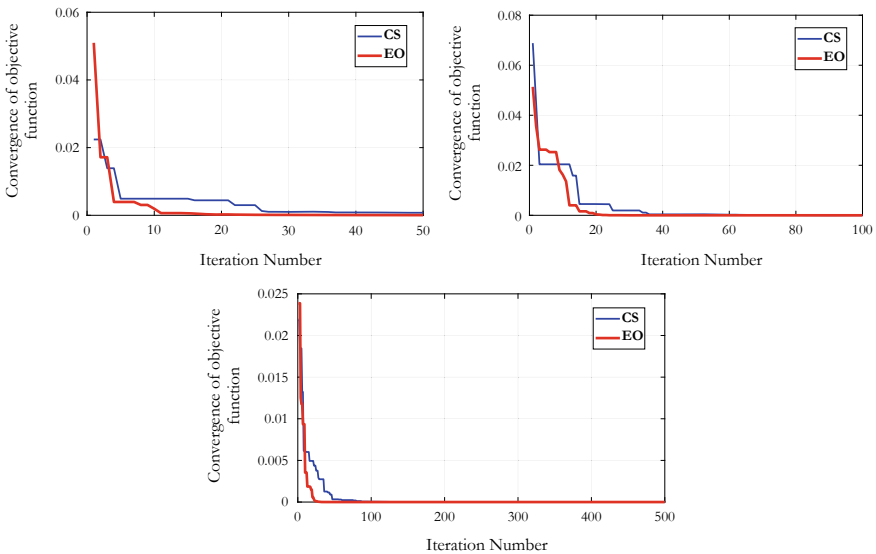
Fig. 3 Convergence study using a different number of iteration (healthy frame structure)

Table 3 Natural frequencies (Hz) of damaged steel frame with 50 iterations and different population sizes

Mode		1	2	3	4	Error mean (%)	CPU time (s)
Initial		3.747	10.788	16.528	20.275		
Experimental		3.902	10.980	18.645	26.243		
Experimental Damaged		3.856	10.808	18.327	25.442		
100 populations	CS	3.825	10.881	18.419	25.363	0.57	1.508
	Error %	0.80	0.67	0.50	0.31		
	EO	3.749	10.924	18.471	25.390	1.21	0.193
	Error %	2.77	1.08	0.79	0.20		
500 populations	CS	3.841	10.880	18.337	25.367	0.35	2.762
	Error %	0.39	0.67	0.05	0.29		
	EO	3.856	10.809	18.326	25.442	0.01	0.858
	Error %	0.01	0.01	0.00	0.00		
1000 populations	CS	3.870	10.788	18.337	25.444	0.15	3.638
	Error %	0.35	0.18	0.05	0.01		
	EO	3.856	10.808	18.327	25.442	0.00	1.649
	Error %	0.00	0.00	0.00	0.00		
2000 populations	CS	3.858	10.833	18.298	25.424	0.13	7.753
	Error %	0.05	0.23	0.16	0.07		
	EO	3.856	10.808	18.327	25.442	0.00	3.252
	Error %	0.00	0.00	0.00	0.00		

Table 3 presents the results after different population sizes using CS and EO. The obtained results showed that EO has good accuracy and less CPU time. Figure 4 shows that EO has a good convergence study compared with CS.

In this section, the results are investigated after different numbers of iterations. Table 4 summarized the provided results of CS and EO.

The results show that EO has good convergence as it can be seen from Fig. 5 and less CPU time even with less number of iteration.

5   Conclusion

This paper presents a convergence study of CS and EO based on model updating of healthy and damaged frame structures. The inverse problem is used to study the effectiveness of both algorithms. The objective function compares the measured and calculated frequencies by CS and EO. The results showed that EO had less CPU time, and the best convergence was achieved by using different populations and iterations.
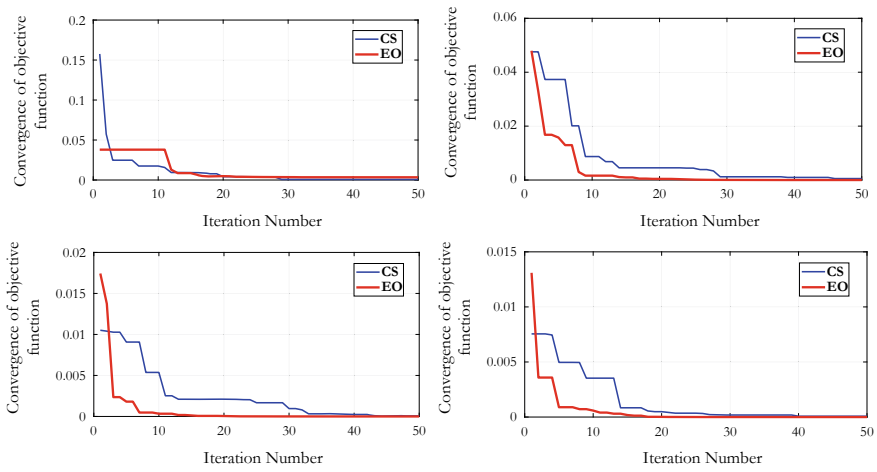
Fig. 4 Convergence study based on a different number of population—damaged experimental steel frame

Table 4 Natural frequencies (Hz) of the damaged steel frame with 200 population and different iterations

Mode		1	2	3	4	Error mean (%)	CPU time (s)
Initial		3.747	10.788	16.528	20.275		
Experimental		3.902	10.980	18.645	26.243		
Experimental damaged		3.856	10.808	18.327	25.442		
50 iterations	CS	3.832	10.854	18.330	25.382	0.33	1.635
	Error %	0.63	0.42	0.02	0.24		
	EO	3.852	10.814	18.319	25.441	0.05	0.317
	Error %	0.10	0.06	0.04	0.00		
100 iterations	CS	3.848	10.819	18.368	25.435	0.14	2.778
	Error %	0.21	0.11	0.22	0.03		
	EO	3.856	10.808	18.327	25.442	0.00	0.617
	Error %	0.00	0.00	0.00	0.00		
500 iterations	CS	3.857	10.808	18.326	25.442	0.01	8.410
	Error %	0.01	0.00	0.00	0.00		
	EO	3.856	10.808	18.327	25.442	0.00	3.319
	Error %	0.00	0.00	0.00	0.00		
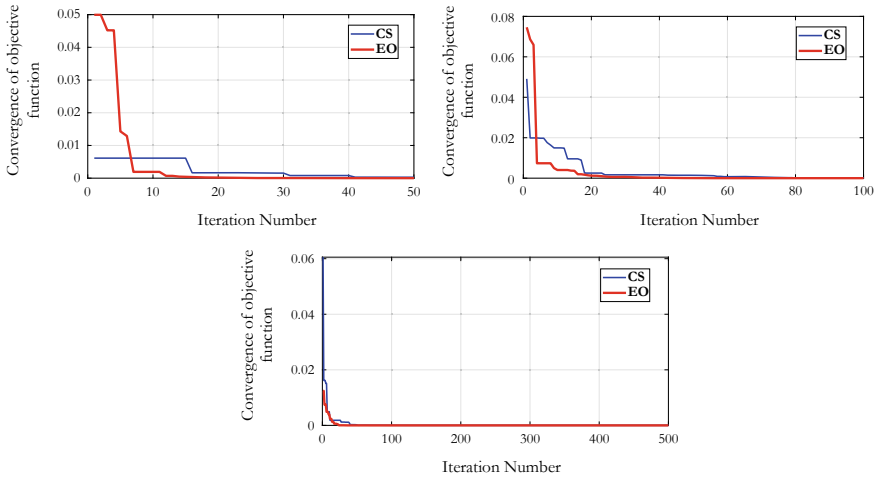
Fig. 5 Convergence study based on a different number of iterations—damaged experimental steel frame

References

1. Tiachacht, S., et al.: Damage assessment in structures using combination of a modified Cornwell indicator and genetic algorithm. Eng. Struct. **177**, 421–430 (2018)
2. Ghannadi, P., Kourehli, S.S.: An effective method for damage assessment based on limited measured locations in skeletal structures. Adv. Struct. Eng., 1369433220947193 (2020)
3. Khatir, S., et al.: Damage detection and localization in composite beam structures based on vibration analysis. Mechanics **21**(6), 472–479 (2015)
4. Khatir, S., et al.: Multiple damage detection in composite beams using particle swarm optimization and genetic algorithm. Mechanika **23**(4), 514–521 (2017)
5. Nobahari, M., Seyedpoor, S.M.: An efficient method for structural damage localization based on the concepts of flexibility matrix and strain energy of a structure. Struct. Eng. Mech. **46**(2), 231–244 (2013)
6. Guo, H., Li, Z.: A two-stage method to identify structural damage sites and extents by using evidence theory and micro-search genetic algorithm. Mech. Syst. Signal Process. **23**(3), 769–782 (2009)
7. Ghannadi, P., et al.: Efficiency of grey wolf optimization algorithm for damage detection of skeletal structures via expanded mode shapes. Adv. Struct. Eng., 1369433220921000 (2020)
8. Ghannadi, P., Kourehli, S.S.: Multiverse optimizer for structural damage detection: numerical study and experimental validation. In: The Structural Design of Tall and Special Buildings, p. e1777 (2020)
9. Yang, X.-S., Deb, S.: Cuckoo search via Lévy flights. In: 2009 World Congress on Nature and Biologically Inspired Computing (NaBIC). IEEE (2009)
10. Faramarzi, A., et al.: Equilibrium optimizer: a novel optimization algorithm. Knowl. Based Syst. **191**, 105190 (2020)
11. Chatzis, M.N., Chatzi, E.N., Smyth, A.W.: An experimental validation of time domain system identification methods with fusion of heterogeneous data. Earthquake Eng. Struct. Dynam. **44**(4), 523–547 (2015)

Multilayer Perceptron Neural Network for Damage Identification Based on Dynamic Analysis

**Morteza Saadatmorad, Mostafa Siavashi,
Ramazan-Ali Jafari-Talookolaei, Mohammad Hadi Pashaei,
Samir Khatir, and Cuong-Le Thanh**

1   Introduction

Because of the importance of structural health monitoring, vibration-based damage detection methods have been widely investigated over the last few decades to prevent various structures' failure. These methods are considered as efficient and reliable non-destructive techniques for damage detection of structures. In general, two common types of problems related to the analysis of damaged structures are forward problems and inverse problems. The forward problems aim to find the natural frequencies and mode shapes of a damaged structure using the damage's severity and location. The inverse problems' contribution is to obtain the severity and location of damage using modal parameters such as the natural frequencies and mode shapes [1].

In the forward problems, an empirical method such as the finite element method (FEM) or modal impact hammer experiment is usually used to obtain the modal characteristics such as natural frequencies and mode shapes of a damaged structure. For example, Jafari-Talookolaei et al. [2] investigated modal characteristics of generally laminated composite curved beams with damage called single through-the-width delamination. Liang et al. [3] presented the effect of crack on crack-induced eigenfrequency changes in beam structures.

M. Saadatmorad · M. Siavashi · R.-A. Jafari-Talookolaei (✉) · M. H. Pashaei
Department of Mechanical Engineering, Babol Noshirvani University of Technology,
Babol, Mazandaran Province, Iran
e-mail: ra.jafari@nit.ac.ir

S. Khatir
Soete Laboratory, Faculty of Engineering and Architecture, Ghent University,
Technologiepark Zwijnaarde 903, 9052 Zwijnaarde, Belgium

C.-L. Thanh
Faculty of Civil Engineering, Ho Chi Minh City Open University,
Ho Chi Minh City, Vietnam

Also, various methods have been developed in the inverse problem in the literature. One of the most recent inverse damage detection methods is computational intelligence techniques such as genetic algorithms and artificial neural networks (ANNs) for detecting damage's severity and location [4].

ANN is a prominent tool for detecting patterns in the data. Researchers usually used modal parameters such as mode shapes and natural frequencies as the input layer of artificial neural networks to detect the severity of damages in structures [5, 6]. However, some researchers applied the derivative of mode shapes as the input layer of ANNs. Other researchers also used the modal strain energy-based damage index for the input layer of ANNs [7]. Liu et al. [8] used normalized flexibility change vectors as the input layer of ANNs to detect the location and severity of damages in multiple damage scenarios. In [9], both modal strain energy and natural frequencies were applied as the input layer of the extreme learning machine to detect the size and location of damage; however, there were remarkable errors in the detection of damage in for multiple damage scenarios.

In this paper, a new model is developed to predict damage severity in beam-like structures based on the FEM as well as MLP neural network. In this way, empirical data are obtained using FEM, then MLP neural network is used to predict damage's severity for single-damage scenarios.

The rest of this study is organized as follows. Section 2 deals with the proposed methodology in the current study. In this section, first, the mathematical formulation is introduced, and then the proposed model for predicting damages using the MLP neural network is presented. Section 3 addresses three computational dynamic examples to evaluate the proposed model's performance for various single-damage scenarios. In Sect. 4, results are presented and discussed. Finally, Sect. 5 concludes the present paper.

2   Methodology

2.1   *Mathematical Formulation*

Consider the beams indicated in Fig. 1. As shown in this figure, there are two beams, one beam is an intact one (a), and the other is a damaged one (b). In this study, the mathematical formulation for the governing equation of the beam-like structure's free vibration is based on the finite element method (FEM). In this way, the beam-like structure as a continuous is discretized into several finite elements. Then local matrices for each element's mass and stiffness are written to be assembled and form global matrices for the beam's mass and stiffness.

The governing equation of motion in a FEM-based multidegree system for the intact beam is expressed as [10]:
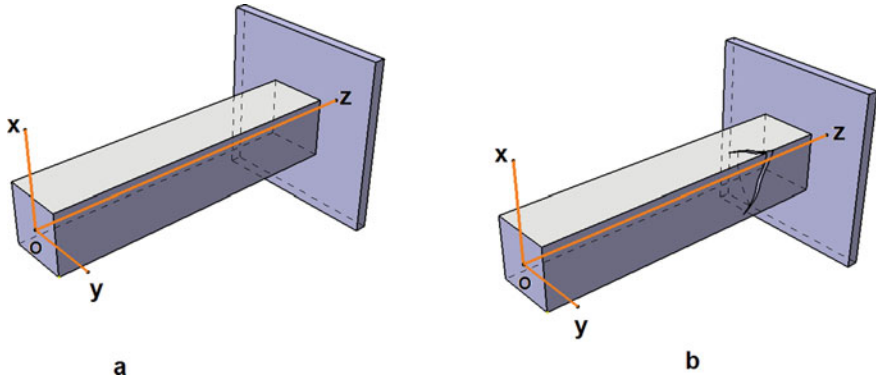
Fig. 1 Geometry model of two beams: **a** an intact beam and **b** a damaged beam

$$[M]\{\ddot{x}(t)\} + [K]\{x(t)\} = F(t) \tag{1}$$

where $[M]$ and $[K]$ are the global mass and stiffness matrices, respectively. $\{\ddot{x}(t)\}$ is the acceleration velocity, and $\{x(t)\}$ is the displacement vector caused by the applied force $F(t)$. If $F(t) = 0$, then the governing equation of motion of free vibration for the intact beam is obtained as follows:

$$[M]\{\ddot{x}(t)\} + [K]x(t) = 0 \tag{2}$$

By considering the harmonic response $\{x\} = \{\varphi\}e^{i\omega t}$ and the corresponding acceleration $\{\ddot{x}\} = -\omega^2\varphi e^{i\omega t}$, Eq. (2) can be obtained as:

$$[M]\{-\omega^2\{\varphi\}\} + [K]\{\varphi\} = 0 \tag{3}$$

For ith vibration mode, Eq. (3) is written as

$$[M]\{-\omega_i^2\{\varphi_i\}\} + [K]\{\varphi_i\} = 0 \tag{4}$$

where ω is the natural frequency of the system, and φ_i is its corresponding mode shape vector in ith mode. Equation (4) is called the ith eigenvalue equation. If $\omega_i^2 = \lambda_i$, Eq. (4) can be expressed in a standard form as follows:

$$[M]\{-\lambda_i\{\varphi_i\}\} + [K]\{\varphi_i\} = 0 \tag{5}$$

Finally, for the intact beam, Eq. (5) can be rewritten as:

$$|\{-\lambda_i[M]\} + [K]| = 0 \tag{6}$$

Using the finite element method, the global stiffness matrix $[K]$ can be written as follows:

$$[K] = \sum_{j=1}^{m} [k]_j \tag{7}$$

where m represents the number of elements and the local stiffness matrix for the jth element is denoted by $[k]_j$.

In this paper, the global stiffness matrix of a damaged structure is denoted by $[K_d]$. Thus, Eq. (6) for the damaged structure can be rewritten as:

$$[K_d] = \sum_{j=1}^{m} [\alpha_j][k]_j \tag{8}$$

where $\alpha_j \in [0, 1]$ represents a reduction of rigidity. If the value α_j is 1, then the jth element is undamaged and in the case $\alpha_j = 0$, the jth element is completely damaged, and when $0 < \alpha_j < 1$, the jth element is partially damaged.

By definition presented in Eq. (7), ith eigenvalue equation of a damaged structure can be obtained as:

$$[M]\{-\lambda_{di}\{\varphi_{di}\}\} + [K_d]\{\varphi_{di}\} = 0 \tag{9}$$

where φ_{di} is the ith mode shape vector of the damaged structure, and λ_{di} is the natural frequency of damaged structure in the ith mode. It should also be noted that the global mass matrix $[M]$ remains unchanged after occurring damage because physically, the reduction of mass of structure caused by occurring crack or damage is intangible.

Also, for the intact beam, Eq. (5) can be rewritten as:

$$|-\lambda_{di}[M] + [K_d]| = 0 \tag{10}$$

2.2 Multilayer Perceptron (MLP) Neural Network

In this paper, a type of feed-forward ANN called MLP is used to detect damage severity in beam-like structures. Figure 2 shows that an MLP includes at least three layers of nodes called the input layer, hidden layer, and output layer. Nodes in hidden and output layers use activation function [11].

Fig. 2 Topology of a typical MLP [12]
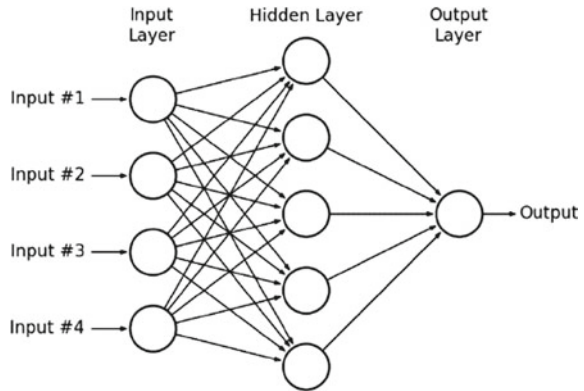
The weighted sum of input data is computed as follows [4, 13]:

$$\text{input}_k = \sum_{i,k=1}^{n,m} b_k + w_{ik} * x_i; \quad k = (1:m); \; i = (1:n) \tag{11}$$

where w_{ik} indicates weight between the ith neurons and the kth neurons, and b_k denotes the bias ratio between hidden layers and inputs; x_i is the output in ith neurons of the input layer; m and n represent the number of the neurons in hidden and input layers, respectively. Also, input$_k$ represents the input of kth neurons in the hidden layer.

In this paper, after computing the input$_k$ for a typical neuron in a layer, a nonlinear activation function is used through the following expression to calculate the output for the jth neuron:

$$\text{Output}_j = \left(\frac{2}{1 + \frac{1}{e^{2\text{input}_q}}} \right) - 1 \tag{12}$$

The above function is named hyperbolic tangent sigmoid transfer function or simply Tan-Sigmoid transfer function. The graph of this function is indicated in Fig. 3.

It is noted that, in (12), input$_q$ is input related to qth neuron in the output layer, and output$_j$ denotes jth neuron of the output layer.

2.3 Proposed Algorithm

The application of the MPL neural network in the proposed method is demonstrated in Fig. 4.
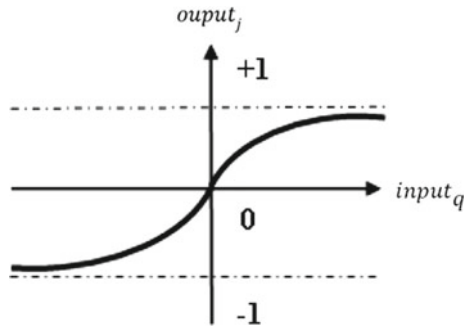
Fig. 3 Graph of Tan-Sigmoid activation function [14]
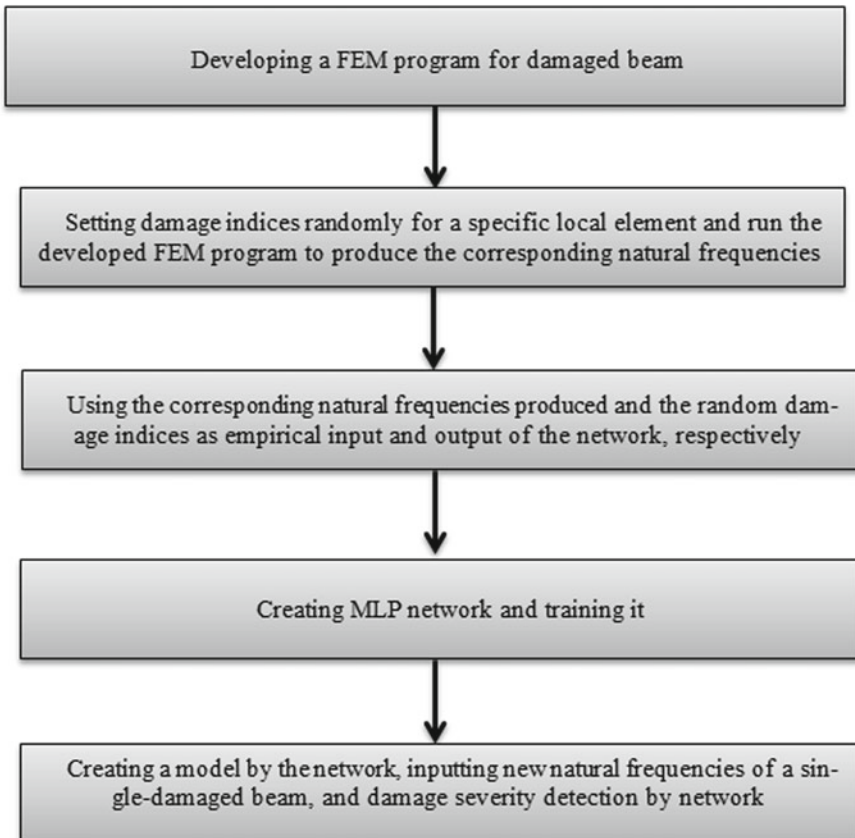
Fig. 4 Proposed algorithm of this paper

3   Computational Examples

In this section, three computational examples are presented to validate the proposed methodology for damage severity detection of beam-like structures. These three computational examples act as three single-damage scenarios. A cantilever beam with characteristics shown in Table 1 is discretized into five finite elements in these scenarios, as seen in Fig. 5.

The effective stiffness matrix $[K^e]$ and the effective mass matrix $[m^e]$ for each element of beams are written as follows:

$$[K^e] = \begin{bmatrix} \frac{12EI}{l_e^3} & \frac{6EI}{l_e^2} & \frac{-12EI}{l_e^3} & \frac{6EI}{l_e^2} \\ \frac{6EI}{l_e^2} & \frac{4EI}{l_e} & \frac{-6EI}{l_e^2} & \frac{2EI}{l_e} \\ \frac{-12EI}{l_e^3} & \frac{6EI}{l_e^2} & \frac{12EI}{l_e^3} & \frac{-6EI}{l_e^2} \\ \frac{6EI}{l_e^2} & \frac{2EI}{l_e} & \frac{-6EI}{l_e^2} & \frac{4EI}{l_e} \end{bmatrix} \tag{13}$$

$$[m^e] = \begin{bmatrix} \frac{156\rho Al_e}{420} & \frac{22\rho Al_e^2}{420} & \frac{54\rho Al_e}{420} & \frac{-13\rho Al_e^2}{420} \\ \frac{22\rho Al_e^2}{420} & \frac{4\rho Al_e^3}{420} & \frac{13\rho Al_e^2}{420} & \frac{-3\rho Al_e^3}{420} \\ \frac{54\rho Al_e}{420} & \frac{13\rho Al_e^2}{420} & \frac{156\rho Al_e}{420} & \frac{-22\rho Al_e^2}{420} \\ \frac{-13\rho Al_e^2}{420} & \frac{-3\rho Al_e^3}{420} & \frac{-22\rho Al_e^2}{420} & \frac{4\rho Al_e^3}{420} \end{bmatrix} \tag{14}$$

In each scenario, one element of the beam is subjected to a set of random percentage of damages. This is performed by changing random values of one of the

Table 1   Constant properties of the considered beams

Property	Symbol	Value (unit)
Cross-sectional area (m^2)	A	1.82×10^{-4}
Moment of inertia (m^4)	I	1.46×10^{-9}
Density (kg/m^3)	ρ	2685
Total length of beams (m)	L	0.5
Length of each element (m)	l_e	0.1

Fig. 5   Finite element model of the considered beam
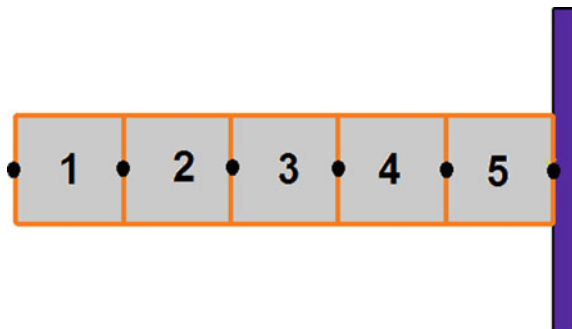
arrays of the matrix $[\alpha_j]$ to produce corresponding empirical natural frequencies as real input data of the MLP neural network. For each scenario, 100 single damages (100 data) are assigned. Seventy data belong to train the MLP network, and 30 data belong to test it.

3.1 Scenario 1: Single Damages Located at the End of the Right of the Beam

As shown in Fig. 6, in this scenario, single damages are located at the end of the beam's right. This is equivalent to locating single damages in element number 5.

3.2 Scenario 2: Single Damages Located at the Mid-Span of the Beam

As shown in Fig. 7, in this scenario, single damages are located at the mid-span of the beam. This is equivalent to locating single damages in element number 3.

3.3 Scenario 3: Single Damages Located at the Free End of the Beam

As shown in Fig. 8, in this scenario, single damages are located at the free end of the beam. This is equivalent to locating single damages in element number 1.

Fig. 6 Typical single damages are located at the end of the beam's right
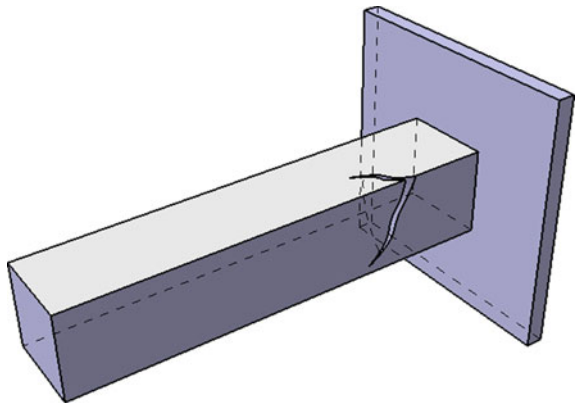
Fig. 7 Typical single damages are located at the mid-span of the beam
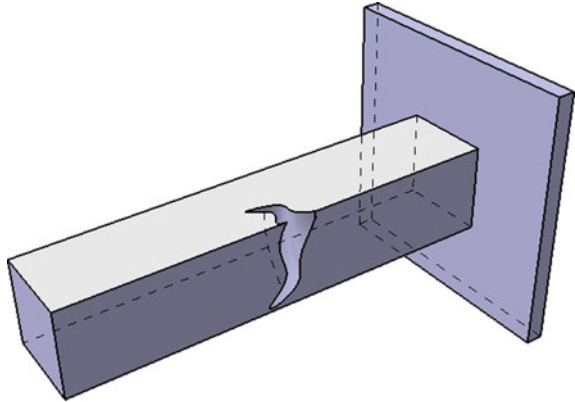
Fig. 8 Typical single damages located at the free end of the beam
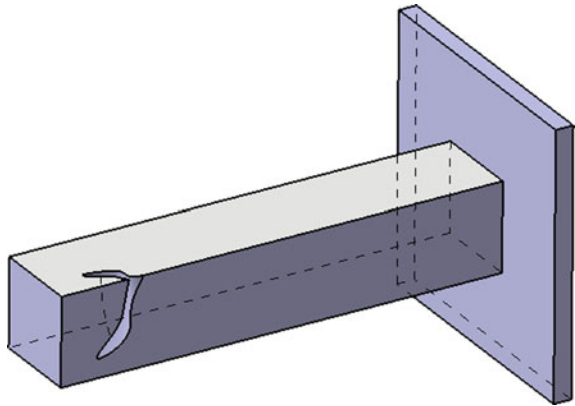
4 Results

In this section, the results of the current study are reported in terms of data matching between training and testing data and the regression index for the three different single-damage scenarios (Fig. 8).

4.1 Scenario 1

Figure 9 indicates the real train data (red) versus predicted train data by MLP network (blue) for scenario 1. According to this figure, for scenario 1, it is clear that the actual training data and the training data predicted by the network are highly consistent. Also, Fig. 10 shows the real test data (red) versus predicted test data by the MLP network (blue) for scenario 1. According to this figure, for scenario 1, it is

Fig. 9 Real train data (red) versus predicted train data by MLP network (blue) for scenario 1

Fig. 10 Real test data (red) versus predicted test data by MLP network (blue) for scenario 1

Fig. 11 Regression representation relationship between real train data versus predicted train data by MLP network (ANN or MLP ANN output) for scenario 1

clear that the actual test data and the test data predicted by the network are highly consistent.

Figure 11 presents the regression representation relationship between real train data versus predicted train data by MLP network for scenario 1. It shows that the real train data versus predicted train data by MLP network are entirely consistent because R-value is equal to 1. Figure 12 indicates the regression representation relationship between real test data versus predicted test data by MLP network for scenario 1. It shows that the real train data versus predicted train data by MLP network are highly consistent ($R = 0.99996$).

4.2 Scenario 2

Figure 13 indicates the real train data (red) versus predicted train data by MLP network (blue) for scenario 2. According to this figure, for scenario 2, it is clear that the actual training data and the training data predicted by the network are highly consistent. Also, Fig. 14 shows the real test data (red) versus predicted test data by the MLP network (blue) for scenario 2. According to this figure, for scenario 2, it is clear that the actual test data and the test data predicted by the network are highly consistent.

Fig. 12 Regression representation relationship between real test data versus predicted test data by MLP network (ANN or MLP ANN output) for scenario 1

Fig. 13 Histogram representation relationship between real test data versus predicted test data by MLP network (ANN or MLP ANN output) for scenario 1

Fig. 14 Histogram representation relationship between real train data versus predicted train data by MLP network (ANN or MLP ANN output) for scenario 1

Figure 15 presents the regression representation relationship between real train data versus predicted train data by MLP network for scenario 2. It shows that the real train data versus predicted train data by MLP network are highly consistent because *R*-value is equal to 99,961. Figure 16 indicates the regression representation relationship between real test data versus predicted test data by MLP network for scenario 2. It shows that the real train data versus predicted train data by MLP network are highly consistent ($R = 0.99977$).

4.3 Scenario 3

Figure 17 indicates the real train data (red) versus predicted train data by MLP network (blue) for scenario 3. According to this figure, for scenario 3, it is clear that the actual training data and the training data predicted by the network are highly consistent. Also, Fig. 18 shows the real test data (red) versus predicted test data by the MLP network (blue) for scenario 3. According to this figure, for scenario 3, it is clear that the actual test data and the test data predicted by the network are highly consistent.

Figure 19 presents the regression representation relationship between real train data versus predicted train data by MLP network for scenario 3. It shows that the real train data versus predicted train data by MLP network are highly consistent because *R*-value is equal to 99,977. Figure 20 indicates the regression
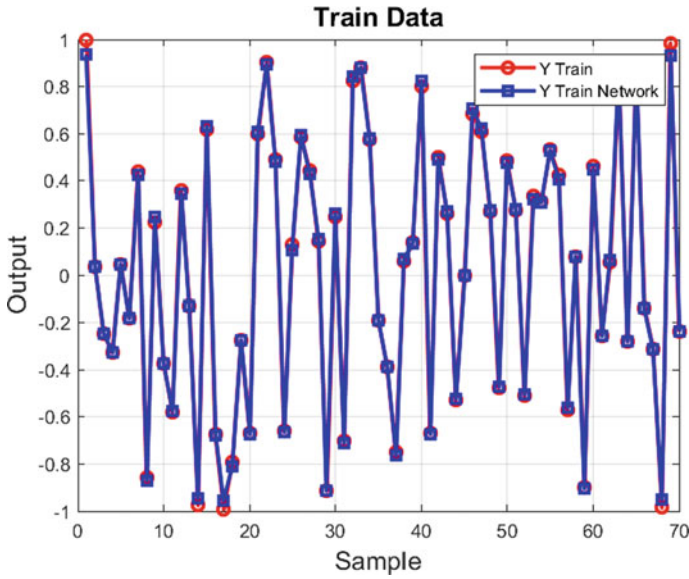
Fig. 15 Real train data (red) versus predicted train data by MLP network (blue) for scenario 2
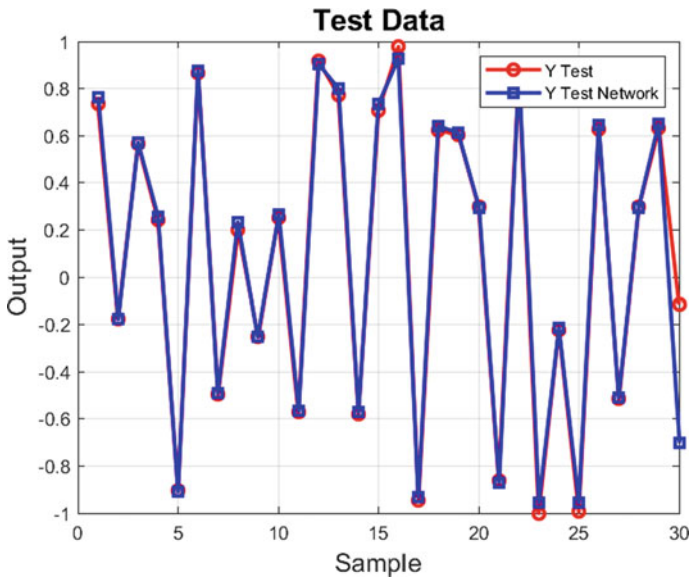
Fig. 16 Real train data (red) versus predicted train data by MLP network (blue) for scenario 2

representation relationship between real test data versus predicted test data by MLP network for scenario 3. It shows that the real train data versus predicted train data by MLP network are highly consistent ($R = 0.98549$) (Figs. 21, 22, 23, 24, 25, 26).
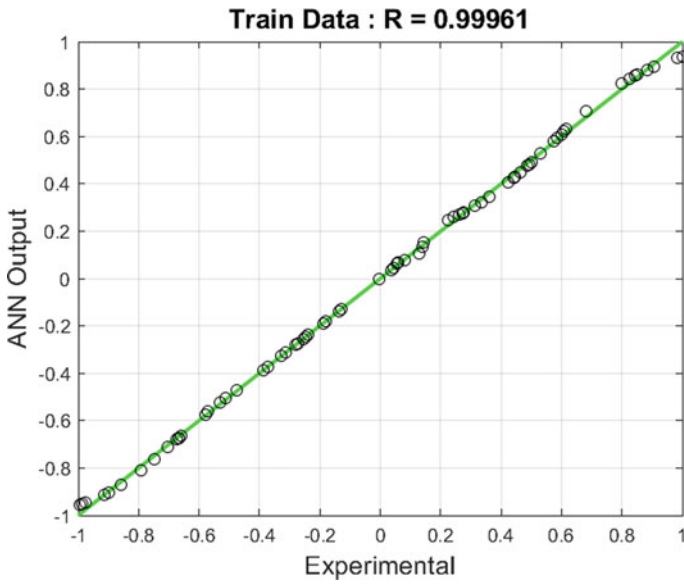
Fig. 17 Regression representation relationship between real train data versus predicted train data by MLP network (ANN or MLP ANN output) for scenario 2
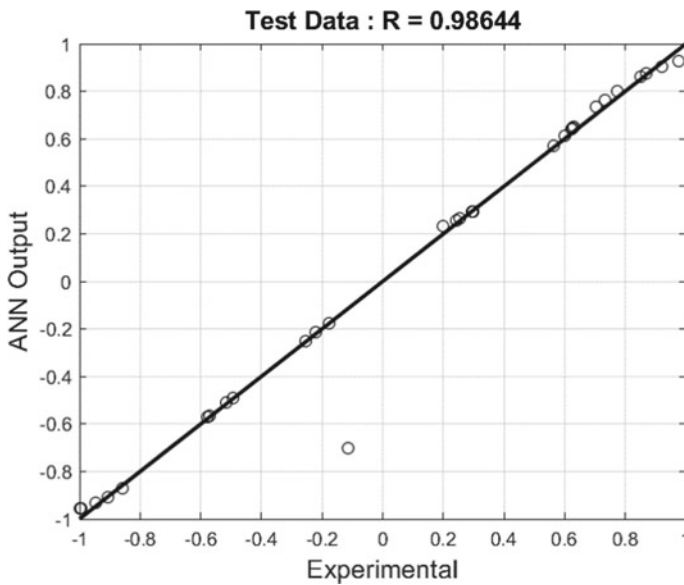
Fig. 18 Regression representation relationship between real test data versus predicted test data by MLP network (ANN or MLP ANN Output) for scenario 2
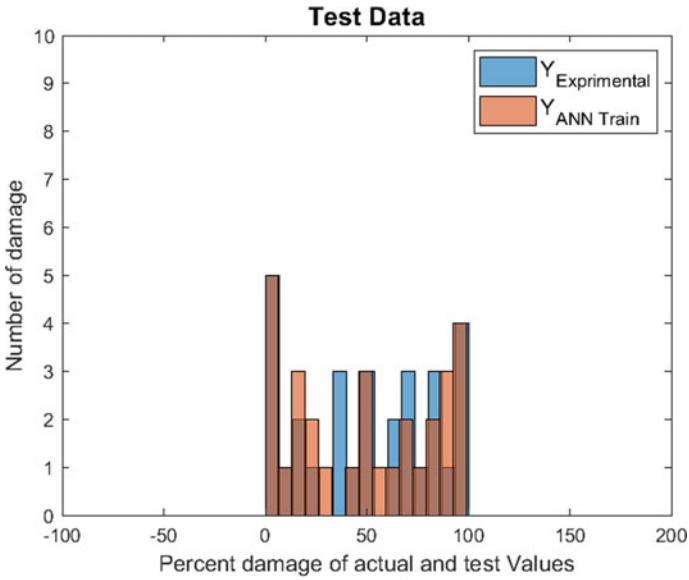
Fig. 19 Histogram representation relationship between real test data versus predicted test data by MLP network (ANN or MLP ANN output) for scenario 2
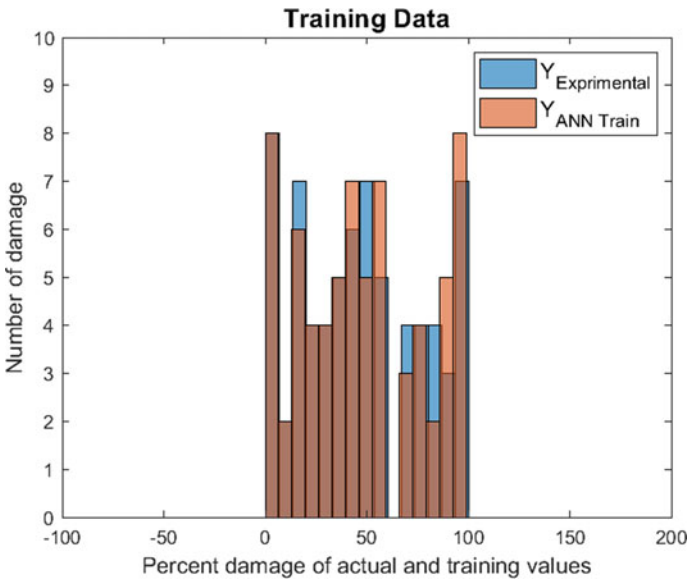
Fig. 20 Histogram representation relationship between real train data versus predicted train data by MLP network (ANN or MLP ANN output) for scenario 2
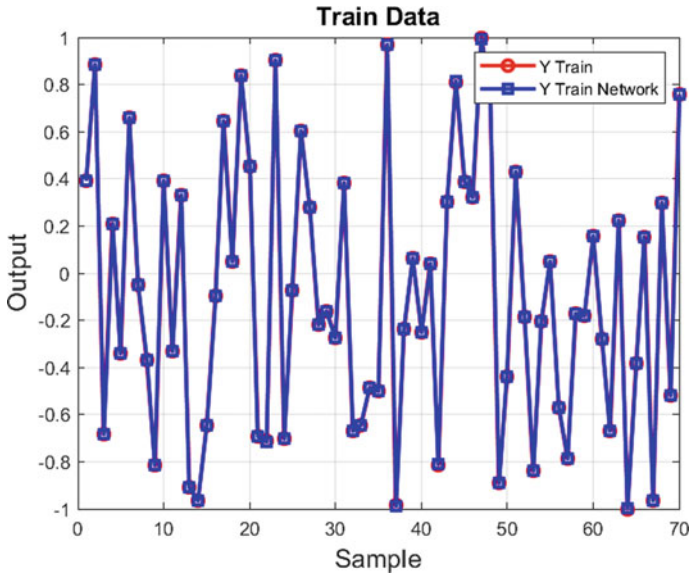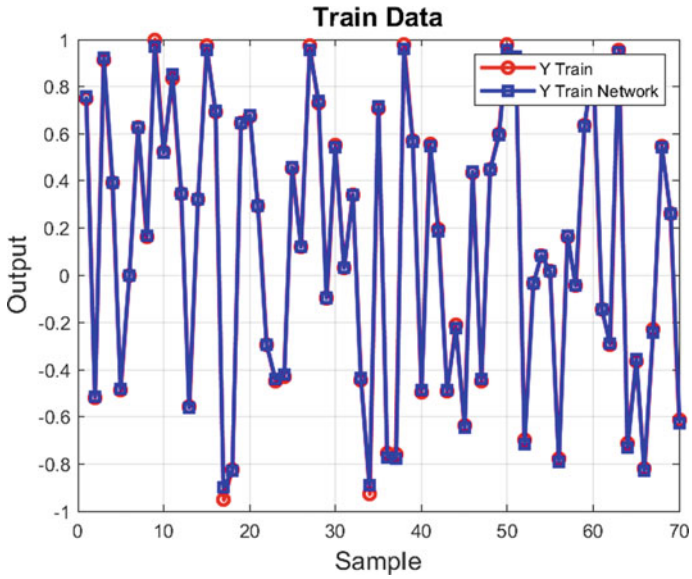
Fig. 21 Real train data (red) versus predicted train data by MLP network (blue) for scenario 3
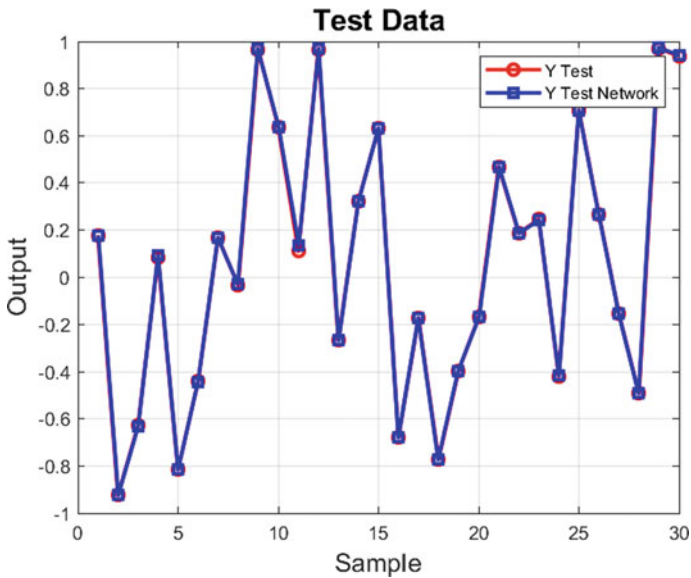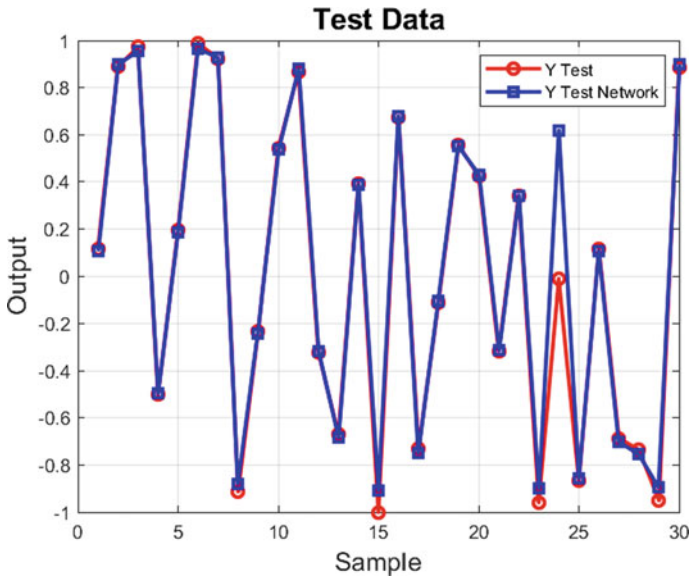

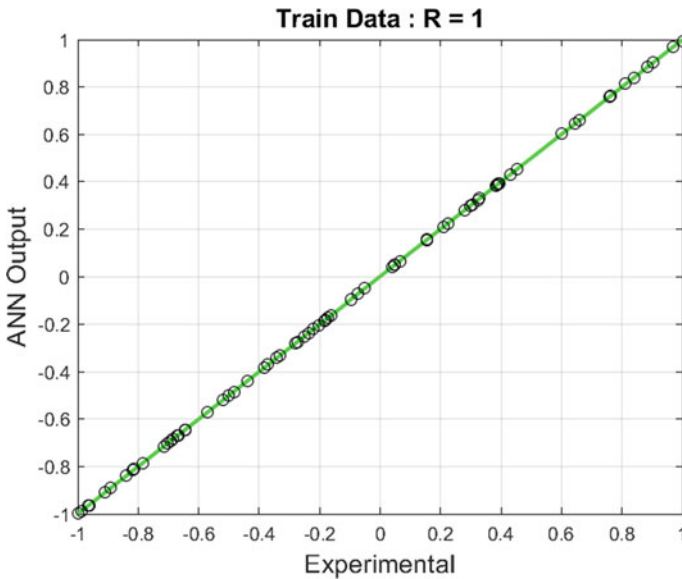**Fig. 22** Real train data (red) versus predicted train data by MLP network (blue) for scenario 3
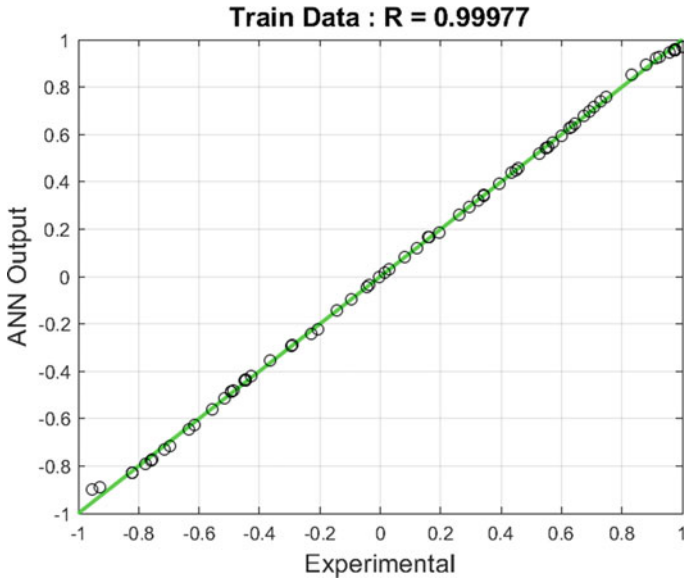
Fig. 23 Regression representation relationship between real train data versus predicted train data by MLP network (ANN or MLP ANN output) for scenario 3
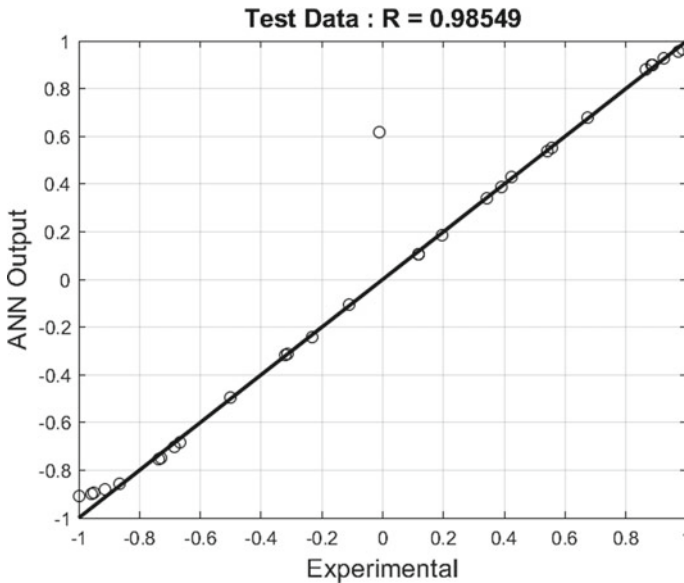
Fig. 24 Regression representation relationship between real test data versus predicted test data by MLP network (ANN or MLP ANN output) for scenario 3
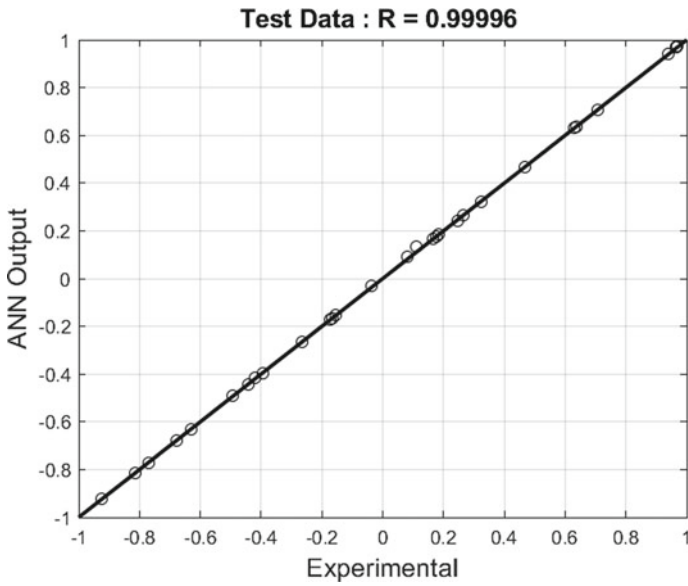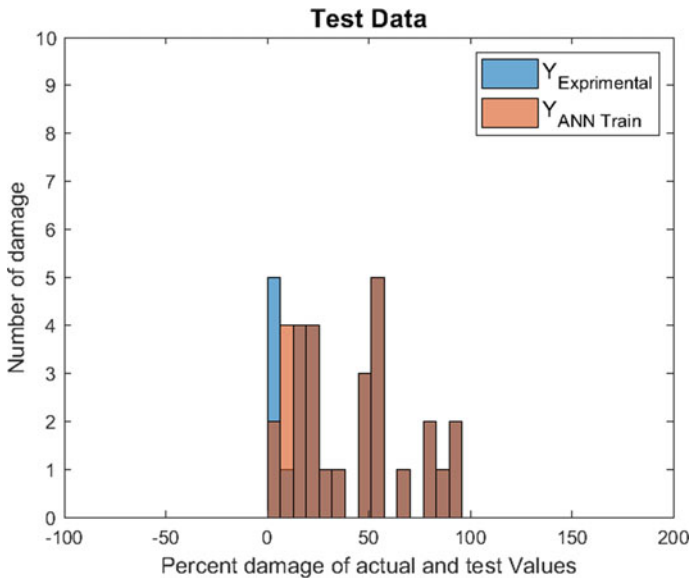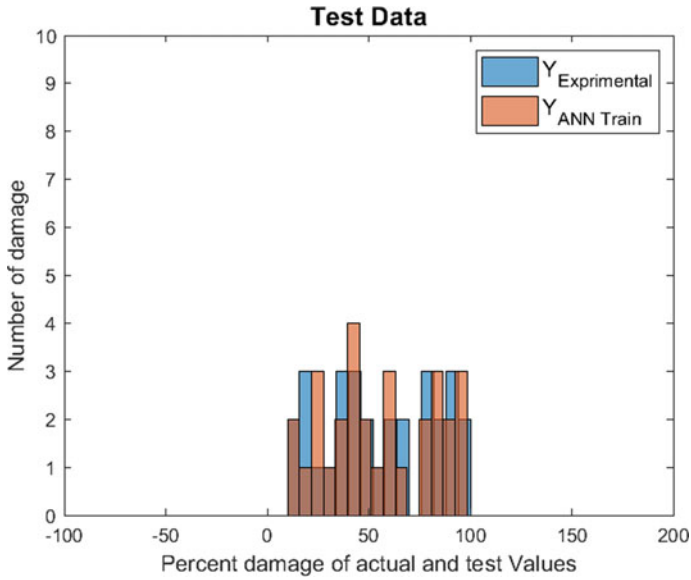
Fig. 25 Histogram representation relationship between real test data versus predicted test data by MLP network (ANN or MLP ANN output) for scenario 3
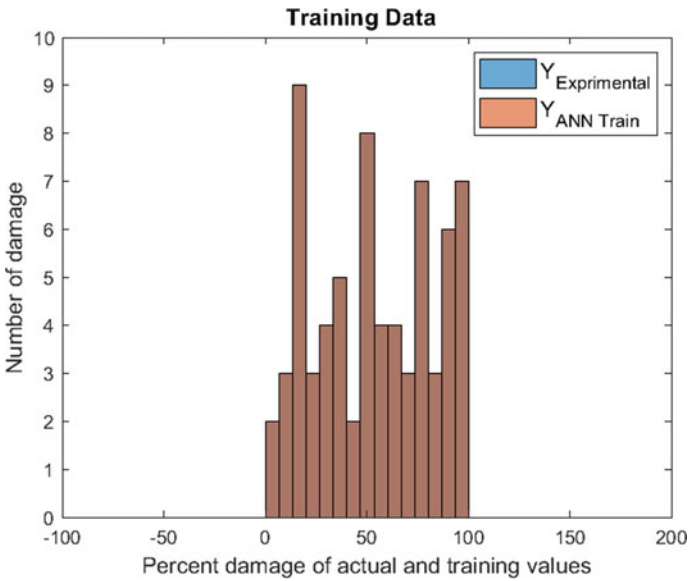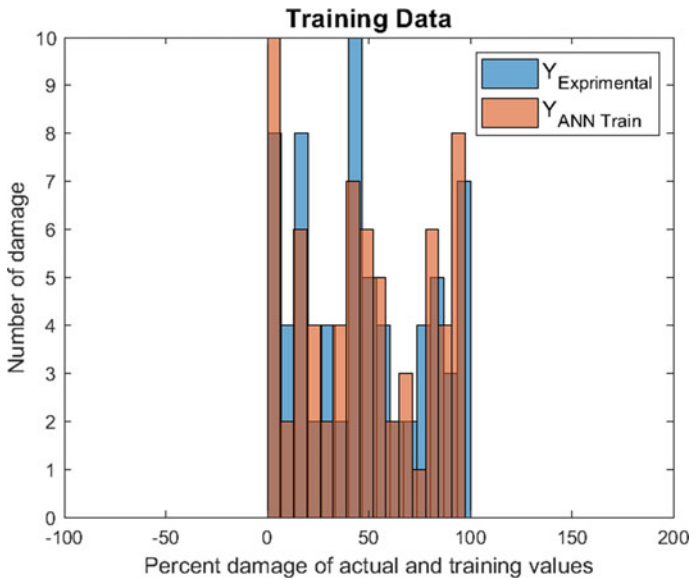

Fig. 26 Histogram representation relationship between real train data versus predicted train data by MLP network (ANN or MLP ANN output) for scenario 3

5 Conclusions

In this study, a novel and high-performance damage detection methodology to detect single damages in beam-like structures. This methodology is based on random producing damages indices ($[\alpha_j]$) in one element of the beam to obtain the corresponding natural frequencies of beam-like structures and then used them for training an MLP neural network. The finding of this paper shows that the proposed damage detection methodology can predict single damages in beam-like structures with high accuracy.

References

1. Yang, J.Y., Xia, B.H., Chen, Z., Li, T.L., Liu, R.: Vibration-based structural damage identification: a review. Int. J. Robot. Autom. **35**(2) (2020)
2. Jafari-Talookolaei, R.A., Abedi, M., Hajianmaleki, M.: Vibration characteristics of generally laminated composite curved beams with single through-the-width delamination. Compos. Struct. **138**, 172–183 (2016)
3. Liang, R.Y., Hu, J., Choy, F.: Theoretical study of crack-induced eigenfrequency changes on beam structures. J. Eng. Mech. **118**(2), 384–396 (1992)
4. Tran-Ngoc, H., Khatir, S., De Roeck, G., Bui-Tien, T., Wahab, M.A.: An efficient artificial neural network for damage detection in bridges and beam-like structures by improving training parameters using cuckoo search algorithm. Eng. Struct. **199**, 109637 (2019)
5. Mehrjoo, M., Khaji, N., Moharrami, H., Bahreininejad, A.: Damage detection of truss bridge joints using artificial neural networks. Expert Syst. Appl. **35**(3), 1122–1131 (2008)
6. Rosales, M.B., Filipich, C.P., Buezas, F.S.: Crack detection in beam-like structures. Eng. Struct. **31**(10), 2257–2264 (2009)
7. Dackermann, U., Li, J., Samali, B.: Dynamic-based damage identification using neural network ensembles and damage index method. Adv. Struct. Eng. **13**(6), 1001–1016 (2010)
8. Liu, H., Song, G., Jiao, Y., Zhang, P., Wang, X.: Damage identification of bridge based on modal flexibility and neural network improved by particle swarm optimization. Math. Probl. Eng. (2014)
9. Ghadimi, S., Kourehli, S.S.: Multiple crack identification in Euler beams using extreme learning machine. KSCE J. Civil Eng. **21**(1), 389–396 (2017)
10. Miguel, L.F.F., Miguel, L.F.F., Kaminski Jr., J., Riera, J.D.: Damage detection under ambient vibration by harmony search algorithm. Expert Syst. Appl. **39**(10), 9704–9714 (2012)
11. Rhim, J., Lee, S.W.: A neural network approach for damage detection and identification of structures. Comput. Mech. **16**(6), 437–443 (1995)
12. Zainal-Mokhtar, K., Mohamad-Saleh, J.: An oil fraction neural sensor developed using electrical capacitance tomography sensor data. Sensors **13**(9), 11385–11406 (2013)
13. Khatir, S., Boutchicha, D., Le Thanh, C., Tran-Ngoc, H., Nguyen, T.N., Abdel-Wahab, M.: Improved ANN technique combined with Jaya algorithm for crack identification in plates using XIGA and experimental analysis. Theor. Appl. Fract. Mech., 102554 (2020)
14. Dorofki, M., Elshafie, A.H., Jaafar, O., Karim, O.A., Mastura, S.: Comparison of artificial neural network transfer functions abilities to simulate extreme runoff data. Int. Proc. Chem. Biol. Environ. Eng. **33**, 39–44 (2012)

Optimization of Processing Parameters of Primary Phase Particle Size of Cooling Slope Process for Semi-solid Casting of ADC 12 Al Alloy

Nguyen Anh Tuan, Dao Van Luu, and Lai Dang Giang

1 Introduction

Semi-solid metal processing (SSMP) was invented by Fleming et al. in 1973, since it was born this method has been proved a lot of advantages compared with conventional technique, such as lightweight potential resulting from enhanced mechanical properties, superior weldability and pressure tightness, near net shape casting, enhanced surface quality… [1]. The key feature of this processing is preparation globular structure before forming, because it is directly influent to behave of thixotropy of billet in semi-solid state.

Currently, semi-solid billet production methods are electromagnetic stirring, mechanical stirring, gas-induced semi-solid, etc. These methods have disadvantages such as complex design and high operating costs, but the obtaining billet has the heterogeneous microstructure. The cooling slope method is a simple but highly effective method because it has a simple design, low equipment and operating cost, and easy control of processing parameters, besides good effective in creating a globular microstructure with high homogeneity and is commonly used in the creation of semi-solid billet for the thixoforming [2].

The billet preparation technology for semi-solid forming process is usually based on two main hypotheses: Creating multiple nucleation near the liquidus temperature with limited and multidirectional growth, excessive nucleation [2–4]. In addition to eutectic alloy to accelerate the process of nucleation based on the creation theory irregular eutectic solidification [5]. According to this theory, in order for the solidification process to be favorable for the α-Al phase to appear, the velocity of cooling process must have an appropriate speed.

In experimental optimization techniques, the design of experiment is one of the most influential statistical techniques for analyzing the process variables affecting the responses. Besides, using surface response method (RSM) and experimental

N. A. Tuan (✉) · D. Van Luu · L. D. Giang
Le Quy Don Technical University, Hanoi, Vietnam

design according to central composite design (CCD) in experimental design brings high efficiency in saving cost and time. The greatest advantage of this test setup is the reduction in the number of test units required while still delivering statistically significant results and acceptability. Das et al. [6] used Taguchi method to study the effect of processing parameters on microstructure when creating billet by cooling slope method. The author concludes that the slope length has the greatest influence on the α-Al grain morphology compared to other parameters (pouring temperature, slope angle, and wall temperature). Khosravi et al. [7] experimentally used D-optimal design method to optimize input parameters of inclined cooling method for casting semi-liquid billet of aluminum alloy A356. They concluded that the pouring temperature was an important parameter affecting grain size and globularity of primary phase of the alloy. Hajihashemi et al. [8] studied the effects of parameters on the microstructure and mechanical properties of Al 6061 alloy in semi-solid casting. They used a two-level factorial design method to determine the effect of input parameters (pouring temperature, pouring rate, slope length, and slope angle) and output parameters (grain size number and hardness values). The author concluded that the influence of the interaction variables (slope length and the pouring rate; pouring temperature, the pouring rate and slope length) and slope length had the greatest influence on the number of grain size.

ADC 12 has excellent cast ability with high fluidity and low shrinkage rate [5, 9, 10], so it is widely used in industry, especially in automotive and motorcycle piston casting. ADC 12 (Si 11.6 wt%) has high strength and low ductility (about 1%) because it is an eutectic alloy with eutectic dendrite microstructure. Few investigators have attempted to modify the cast structure of ADC 12 Al alloy using gas-induced semi-solid technique (GISS), strain-induced metal activation (SIMA), and mechanical rotational barrel (MRB) [11–13]. In this study, the cooling slope method is used to change the eutectic dendrite to a globular microstructure with small particle size to change the mechanical properties of ADC 12 alloy and study the effect of process parameters on average particle size. ADC 12 with globular microstructure increases the ductility of this alloy during the semi-solid forming process while remaining mechanical properties lead to an increase in the quality of finished parts such as the piston, increasing the reliability of the internal combustion engine. The research organized experiments according to central composite design (CCD) with an expansion of experimental factors $\alpha = 1.68$ and used the surface response method to study average particle size of primary phase of this alloy.

2 Material and Method

2.1 Material

Chemical composition of aluminum ADC 12 alloy was determined by Spectrolab machine in Laboratory of Institute of Technology which present in Table 1. It is

Table 1 Chemical composition of ADC12 alloy

Element	Si	Fe	Cu	Mn	Mg	Cr	Ni	Zn	Ti	Pb	Al
wt%	11.58	0.63	2.09	0.17	0.081	0.023	0.055	0.77	0.048	0.056	84.5
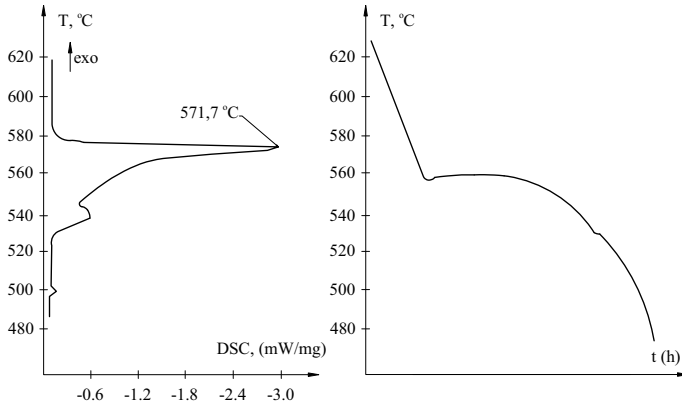
Fig. 1 DSC curve of ADC 12 aluminum alloy

worth noting that the silicon content is 11.6%. This proves that this is an eutectic alloy of aluminum–silicon and some alloys have other significant components such as Cu 2% (this metal was added to increase the strength and machinable [5]), Fe, Zn, Mg ….

To create a semi-solid state, the most important thing is to accurately determine the solidification and melting temperatures of the alloy. In this study, the method of differential thermal calorimetry (DSC) is analyzed. This is the method commonly used to determine the material transition temperature that show in Fig. 1. Cube 2 mm^3 reheated to 800 °C with velocity 10 °C/min and then cooling with the same velocity in DSC 2500 at physic department in Le Quy Don University. The result shows that the melting and solidus temperature of ADC 12 are 571.7 °C and 500 °C, respectively.

2.2 Procedure of Experiment

In once of experiment, 1100 g aluminum alloy was put in a graphite crucible and melted by an Nabertherm electric resistance furnace and then cooling to pouring temperature. It is then poured onto the surface of cooling slope plate made of stainless steel with a water-circulating cooling system and slurry of alloy out of the plate collected into stainless steel mold. The mold is placed in the oven to keep the
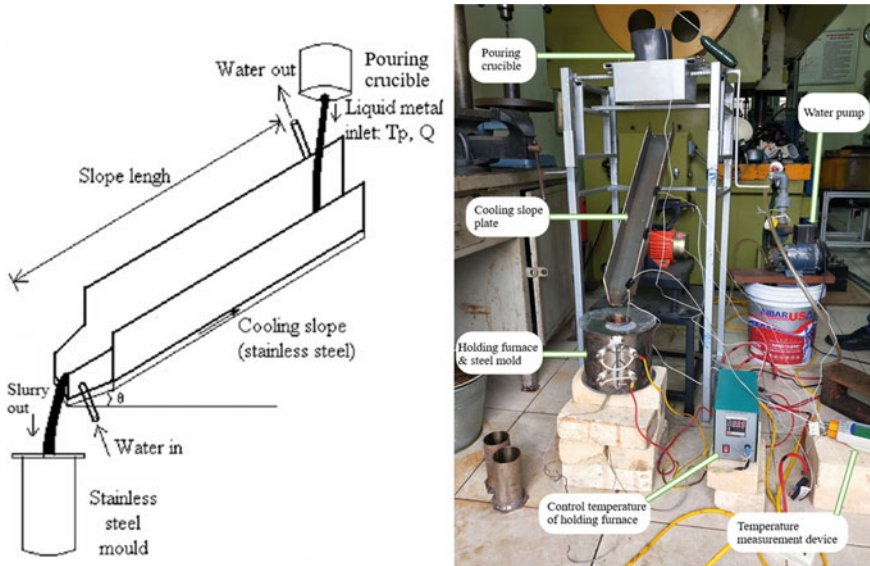
Fig. 2 Schematic diagram of cooling slope

temperature at 400 within 5 min then quenched in water. K-type thermocouple was placed at different location of cooling slope to measure the temperature, schema of cooling slope presented in Fig. 2.

2.3 Organization of Experiment

In order to effectively use the experiments and save costs during the experiment process but still ensure the accuracy of the experiments, the research uses the central composite design method and response surface method. This is also the method used by many authors to study the effect of input parameters on many output parameters [14]. In this study, factors investigated in the process of forming a globules microstructure include pouring temperature, denoted by x_1; length of travel of the melting alloy on cooling plate is called slope length, denoted x_2; angle of the cooling slope to the horizontal (θ in Fig. 2) denoted x_3. The level of the corresponding factors is shown in Table 2. Experimental layout optimized for primary phase particle size was carried out according to CCD model with three factors and five levels. Thus, the study was conducted with 20 experiments including 8 factorial points, 6 axial points (with $\alpha = \pm 1.68$), and 6 center points.

Table 2 Factors and level of survey in the experiment

Symbol	Factor	Unit	Processing parameter				
			−1.68	−1	0	1	1.68
x_1	Pouring temp	°C	573	580	590	600	606
x_2	Slope length	mm	197	300	450	600	702
x_3	Slope angle	deg	38	45	55	65	71

2.4 Analysis of Samples

Sample obtained from experiment was shown in Fig. 3 and then cut by CNC wire-cutting machine to size $1 \times 1 \times 1$ cm. The cut sections were subject to mechanical grinding and polishing and etched by 0.5% HF solution. The etched samples were investigated using an Carl Zeiss microscope. For image processing of the resulted microstructures, for each image was obtained, conducted image analysis by ImageJ software and using Eq. (1) [15].

$$d_{\mathrm{Ave}} = \frac{\sum_{i=1}^{n} \sqrt{\frac{4A}{\pi}}}{n} \tag{1}$$

where d_{Ave} is average particle size, A and n are area of one particle and total particle in the microscopic, respectively.

Data collected from the experiment process was statistically processed and built a response surface model, using Software Design-Expert version 11.1. The general model has the following form

Fig. 3 Billet casting and simples was cut by CNC wire-cutting machine

$$y = b_0 + \sum_{j=1}^{n} b_j x_j + \sum_{i,j=1}^{n} b_{ij} x_i x_j + \sum_{j=1}^{n} b_{jj} x_j^2 + \varepsilon \tag{2}$$

where response variable of cooling slope experiment is average particle size y; b_0 is a constant, b_j, b_{ij}, b_{jj} are the linear, interaction and quadratic coefficients, respectively, and ε is a random error term.

Analysis of variance (ANOVA) is used to assess the suitability of the model. From the model obtained, optimization of the parameters was performed with the amplitude of the margins in the range [−1.68; 1.68] in Table 2. Evaluating the goodness of fit in models was carried out using the coefficient of determination (R^2), while its statistical significance was checked by the F-test, selecting the option with the highest level of desirability (smallest average particle size).

3   Result and Discussion

3.1   Experimental Result

Experimental matric according CCD shows in Table 2 and microscopic of 20 samples (1–20) in standard order mention in Table 3 is presented in Fig. 4. In this experimental result, including three columns x_1, x_2 and x_3 are three columns corresponding to three input factors: pouring temperature, slope length, and slope angle. The last column is response value particle size. In this table, eight experiments are numbered from 1 to 8 at the factorial points, the next six experiments are six extended experiments and the last six experiments are six experiments at the center.

As shown in Fig. 4, the experiment was successful in creating a globules microstructure. The microstructure of the eutectic aluminum–silicon billet usually takes the form of eutectic dendrite which is replaced by globules microstructure of α-Al, silicon became plate-like which concentrated into slabs. The formation of that microstructure can be explained as follows. After the liquid metal has passed through the inclined plate, a large number of nucleation are formed, These nucleation grew under conditions of low cooling and near isotherms, they tended to grow into a sphericity of primary α-Al particles and push other crystals to cluster at the grain boundary.

Table 3 Experimental result

Experimental information		Processing parameter			Response
Std. order	Run order	x_1: pouring temperature (°C)	x_2: slope length (mm)	x_3: slope angle (deg)	y: particle size (μm)
1	4	580	300	45	62.5
2	11	600	300	45	72.6
3	9	580	600	45	55
4	15	600	600	45	51.5
5	2	580	300	65	48.8
6	10	600	300	65	58.5
7	13	580	600	65	57.1
8	5	600	600	65	53.2
9	20	573.182	450	55	58.2
10	12	606.818	450	55	64.6
11	7	590	197.731	55	57.2
12	16	590	702.269	55	50.3
13	17	590	450	38.1821	59.6
14	14	590	450	71.8179	51.6
15	6	590	450	55	57.7
16	18	590	450	55	56.9
17	8	590	450	55	57
18	3	590	450	55	57.3
19	1	590	450	55	56.2
20	19	590	450	55	56

3.2 Optimization of Particle Size

The process of globules is based on grain fragmentation rate of dendrite on cooling slope to create nucleation in steel mold. The statistical analysis results in Table 4 show that the regression model obtained includes linear coefficients, interaction coefficients, and quadratic coefficients. These coefficients show significant level of $p < 0.05$. A value of F 523.27 and a value of $p < 0.0001$ proves that the obtained model is highly statistically significant.

The following equation is the final empirical models in terms of coded factors for particle size:

$$y = 56.56 + 1.7x_1 - 2.72x_2 - 2.74x_3 - 3.4x_1x_2 + 3.95x_2x_3 + 1.74x_1^2 - 0.961x_2^2 \tag{3}$$

While the following equation is final empirical model in terms of actual factor for particle size, P:
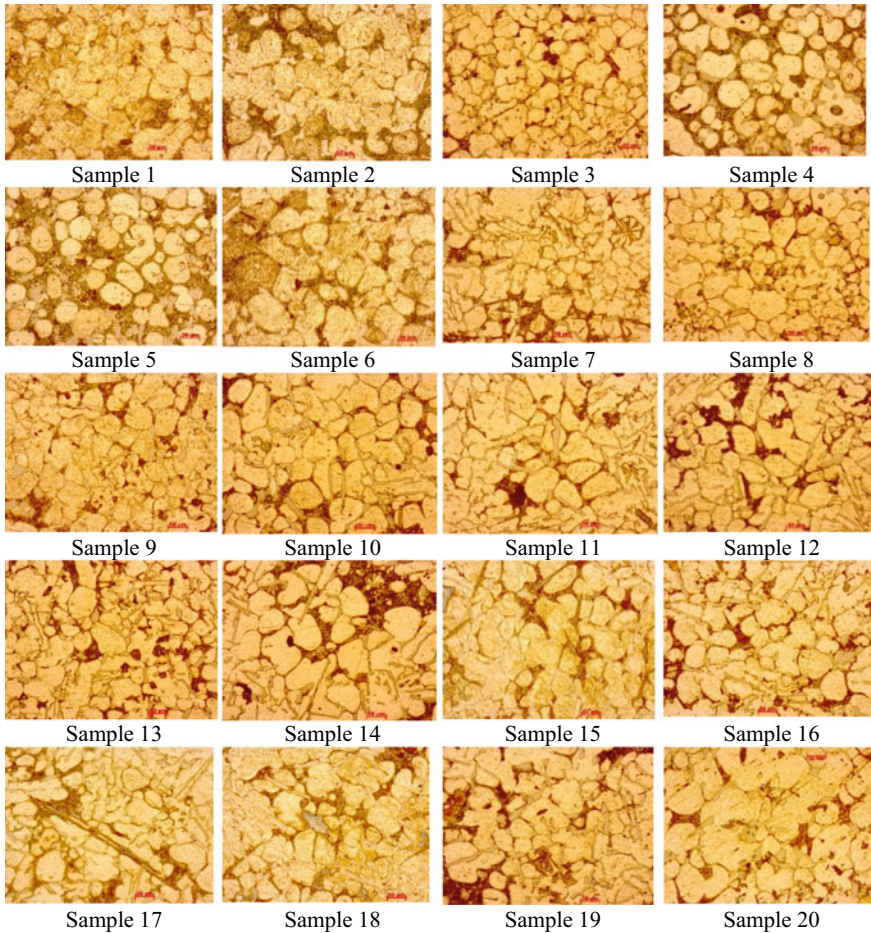
Fig. 4 Twenty simples in standard order in Table 3

$$P = 5504 - 19.38545 \times \text{Pouring temp} + 1.21278 \times \text{Slope length}$$
$$- 1.45925 \times \text{Slope angle} - 0.002267 \times \text{Pouring temp}$$
$$\times \text{Slope length} + 0.002633 \times \text{Slope length} \times \text{Slope angle} \tag{4}$$
$$+ 0.017436 \times \text{Pouring temp}^2 - 0.000043 \times \text{Slope length}^2$$

The suitability of the model was also assessed by the F value of lack of fit. Good regression models need to fit between actual and theoretical data. Therefore, the model obtained with the lack of fit test is not statistically significant, confirming the model found is very significant. According to Paskevich and Wies [14], a good regression model needs a determination coefficient R^2 greater than 0.8 and an Adeq precision coefficient greater than 4. The regression model obtained from the test has

Table 4 ANOVA for reduced quadratic model

Source	Sum of squares	df	Mean square	F-value	p-value	
Model	523.27	7	74.75	84.25	<0.0001	Significant
x_1-pouring temperature	39.29	1	39.29	44.28	<0.0001	
x_2-slope length	101.35	1	101.35	114.23	<0.0001	
x_3-slope angle	102.72	1	102.72	115.77	<0.0001	
$x_1 x_2$	92.48	1	92.48	104.23	<0.0001	
$x_2 x_3$	124.82	1	124.82	140.68	<0.0001	
x_1^2	44.25	1	44.25	49.87	<0.0001	
x_2^2	13.44	1	13.44	15.15	0.0021	
Residual	10.65	12	0.8872			
Lack of fit	8.55	7	1.22	2.92	0.1284	Not significant
Pure error	2.09	5	0.4190			
Cor total	533.92	19				
Std. Dev.	0.9419		R^2		0.9801	
Mean	57.09		Adjusted R^2		0.9684	
C.V. %	1.65		Predicted R^2		0.9292	
			Adeq precision		39.5770	

satisfied the above conditions with high R-squared parameter ($R^2 = 0.98$ means 98% of the total variability observed in this model) and Adeq precision are 39.57, showing the model is accurate enough to predict the average particle size.

3.3 Effect of Processing Parameters on the Particle Size

Effect of pouring temperature

Effect of pouring temperature on the particle size was showed in Fig. 5. The effect of pouring temperature x_1 shows that as the pouring temperature increases, the size of the resulting particle increases. As the pouring temperature increases, the too undercooling the cooling slope decreases, the ability of metal to solidify on the surface of plate decreases, leading to the ability to solidify on the plate to reduce the number of nucleation generated, resulting in an increase in the particle size. In addition, according to Eq. (3) pouring temperature is the variable that has the greatest impact on particle size, reducing pouring temperature means reducing particle size. But if the pouring temperature drops too low, the metal solidifies too quickly on the slope directly affecting the flow on the slope plate [4].
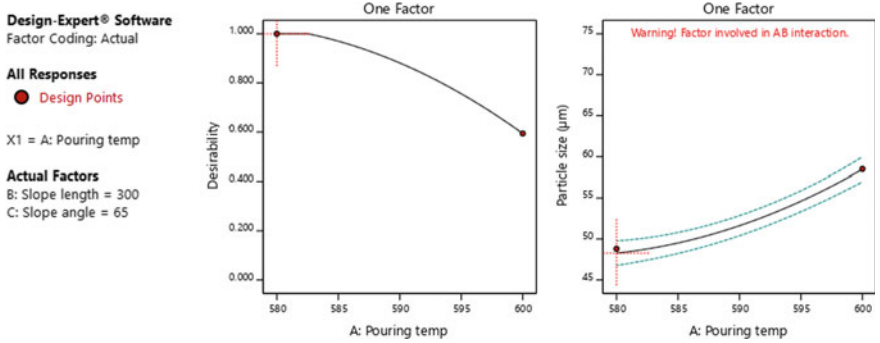
Fig. 5 Effect of pouring temperature on particle size

Effect of slope length

Effect of slope length on the particle size was showed in Fig. 6. As the length of the slope increases, the average size of the grain tends to increase. The length of the slope is directly affected by the pouring temperature shown by the two variables $x_1 x_2$ in Eq. (3). This can be explained as follows. When molten metal is poured onto the surface of plate, the nucleation and growth start on the surface of cooling slope and its detachment due to the fluid motion is responsible for nucleation. Thus, length of travel of the melting alloy on cooling plate has a influence on number of nucleation. Further, increase in slope length over the optimum value (i.e., 300 mm) results in solid liquid metal adhering to the surface not being detachment by the fluid motion that reduces the number of nucleates produced leading to increased particle size.

Effect of slope angle

Effect of slope angle on the particle size was showed in Fig. 7. The reduced slope angle reduces the particle size. When reducing the slope angle directly affects the
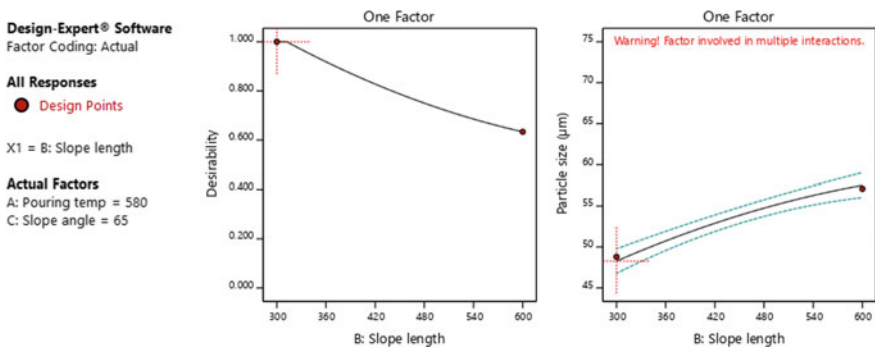
Fig. 6 Effect of slope length on particle size
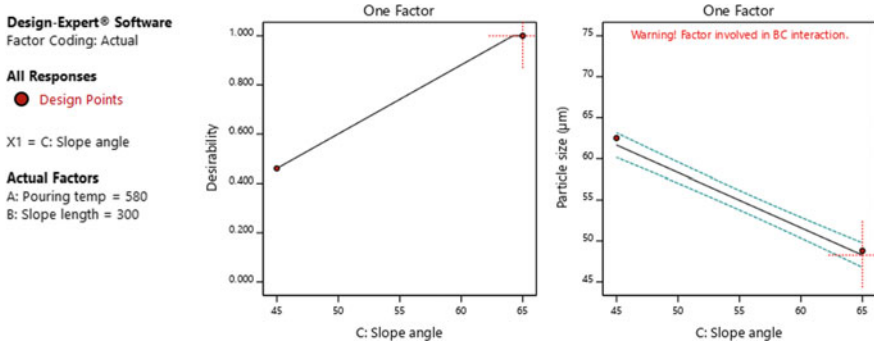
Fig. 7 Effect of slope angle on particle size

velocity of molten metal flow on the cooling plate or in other words directly affects the speed of fragmentation eutectic dendrite on the plate reduces the number of nucleation generated in steel mold. The slope angle is less influenced by pouring temperature, but more influenced by the slope length through two variables x_2x_3 in Eq. (3).

3.4 Optimization of Parameters

In this experimental study, optimization study of the cooling slope method is aimed to minimize the average grain size of the α-Al grain using desirability function optimization. The main goal was to find the optimal technological parameters under experimental conditions to obtain the smallest particle size. The optimal solution for each response is reported in Table 5 with higher desirability level. It can be observed that at pouring temperature of 580 °C, slope length 300 mm and slope angle of 65° optimal value with the desired level of 0.97 for the value of minimum particle size. A successful semi-solid processing could be carried out under these conditions.

Table 5 Optimal parameters

Number	Pouring temp	Slope length	Slope angle	Particle size	Desirability	
1	580.000	300.000	65.000	48.274	0.979	Selected
2	580.000	300.066	64.901	48.343	0.976	

4   Conclusions

The surface response method has been used to find reasonable parameters in the casting process by cooling slope. The model of particle size regression based on experimental arrangement according to the central composite design method has high accuracy. Based on statistical results, experimental models and optimal values presented have drawn the following conclusions:

- Changing the experimental parameters changes the microscopic structure of the cast aluminum ADC 12. The optimum value in this casting process when the pouring temperature is 580 °C, the pouring length 300 mm, and the inclined angle of the trough is 65°.
- Pouring temperature is the parameter most influencing on average particle size followed by slope angle and slope length.
- The regression model was found to have average particle size with very large coefficient of variation R^2, proving that the model found was very meaningful.

References

1. Winklhofer, J.: Semi-solid casting of aluminium from an industrial point of view. Solid State Phenom. **285**, 24–30 (2019)
2. Nafisi, S., Ghomashchi, R.: Semi-solid Processing of Aluminum Alloys. Springer (2016)
3. Fan, Z.: Semisolid metal processing. Int. Mater. Rev. **47**(2), 49–85 (2013)
4. Eskin, D.G., Mi, J.: Solidification Processing of Metallic Alloys Under External Fields. Springer (2018)
5. Barrirero, J.: Eutectic modification of Al–Si casting alloys. Linköping University Electronic Press (2019)
6. Das, P., Samanta, S.K., Das, R., Dutta, P.: Optimization of degree of sphericity of primary phase during cooling slope casting of A356 Al alloy: Taguchi method and regression analysis. Measurement **55**, 605–615 (2014)
7. Khosravi, H., Eslami-Farsani, R., Askari-Paykani, M.: Modeling and optimization of cooling slope process parameters for semi-solid casting of A356 Al alloy. Trans. Non-ferr. Metal Soc. China **24**(4), 961–968 (2014)
8. Hajihashemi, M., Niroumand, B., Shamanian, M.: The effect of process parameters on the microstructure and mechanical properties of semisolid cast Al6061. Metall. Mater. Trans. B **46**(2), 780–792 (2014)
9. Zhao, H., Wang, F., Li, Y., Xia, W.: Experimental and numerical analysis of gas entrapment defects in plate ADC12 die castings. J. Mater. Process. Technol. **209**(9), 4537–4542 (2009)
10. Elliot, R.: Eutectic Soldification Processing: Crystalline and Glassy Alloys. Butterworths & Company (1983)
11. Janudom, S., Rattanochaikul, T., Burapa, R., Wisutmethangoon, S., Wannasin, J.: Feasibility of semi-solid die casting of ADC12 aluminum alloy. Trans. Non-ferr. Metal Soc. China **20**(9), 1756–1762 (2010)
12. Wang, Z., Ji, Z., Hu, M., Xu, H.: Evolution of the semi-solid microstructure of ADC12 alloy in a modified SIMA process. Mater. Charact. **62**(10), 925–930 (2011)

13. Hu, Z.H., Xiang, P.E., Wu, G.H., Cheng, D.Q., Liu, W.C., Zhang, L., Ding, W.J.: Microstructure evolution and mechanical properties of rheo-processed ADC12 alloy. Trans. Non-ferr. Metal Soc. China **26**(12), 3070–3080 (2016)
14. Paskevich, A., Wies, T.: Verified Software. Theories, Tools, and Experiments: 9th International Conference, VSTTE 2017, Heidelberg, Germany, 22–23 July, Revised Selected Papers. Springer (2017)
15. Kolahdooz, A., Dehkordi, S.A.: Effects of important parameters in the production of Al-A356 alloy by semi-solid forming process. J. Mater. Res. Technol. **8**(1), 189–198 (2019)

Application of Artificial Neural Network for Recovering GPS—RTK Data in the Monitoring of Cable-Stayed Bridge Deformation

Thuy Linh Nguyen and Huu Hung Nguyen

1 Introduction

For cable-stayed bridges, bridge deformation is an important indicator of the structure to assess the quality of the bridge. Large deformation or unfavorable deformation can cause danger to the traffic on the bridge, affecting the integrity of the structure. The GPS in the cable-stayed bridge continuous monitoring system is used to determine the overall deformation of the bridge. Research on the application of GPS technology in monitoring the deformation of the bridge has been interested in many scientists over the world.

Kaloop and Li [1] GPS were used for deformation monitoring. Two main analytical methods: Kalman filter (KF) and parametric least square (PLS) were used for the adjustment of these data. Kaloop et al. [2] presented the recent development in structural health monitoring (SHM) applications for monitoring the dynamic behavior of structures using the GPS technique. GPS monitoring systems for real-time kinematic (RTK), precise point positioning (PPP), and the sampling frequency development of GPS measurements are summarized for time series analysis. Recently proposed time series GPS monitoring systems, error sources, and mitigation, as well as system analysis and identification, are presented and discussed. Yunus et al. [3] reviewed previous research on bridge dynamic displacement monitoring using GPS and an accelerometer for SHM of the bridge. These include the review of the advantages and disadvantages of the measurement as well as the methodology of the measurements used in the recent research study.

However, during operation, GPS data may be lost due to many factors such as wind, temperature, signal transmission, cause of intermittent interruption of the measurement results, affecting the analysis and assessment of the bridge condition. The document [2, 3] investigated the applicability of the polynomial method to

T. L. Nguyen · H. H. Nguyen (✉)
University of Transport and Communications, Hanoi, Vietnam
e-mail: nhhunggttp@utc.edu.vn.com

interpolate lost GPS data of the cable-stayed bridge. It is also suggested that the polynomial method is only suitable when applying up to 5 lost GPS values. The disadvantage of the polynomial method is that if the value to be interpolated is large, the degree of the interpolation polynomial is also very large, leading to difficulties in the calculation. At the same time, some articles also show that this method is only convenient in linear problems. Compared to the above method, the artificial neural network method has the advantage of being able to process and analyze with large data, and more importantly, it can easily solve nonlinear and complex problems. ANN incorporates a Kalman filter, an adaptive filter method, an autoregressive moving average (ARMA) method to filter data, reduce noise, improve GPS-RTK accuracy, and predict the displacement of the bridge [4–7].

In Vietnam, in the field of structural monitoring, there are not much scientific research on the application of ANN in processing and analyzing measurement data. The article [8] uses an artificial neural network to build a settlement model of the Yaly hydropower dam. In the study [9], the author applied ANN in the prediction of surface subsidence due to pit mining. Scientific publication [10] has only studied the application of ANN in the prediction of vertical displacement of the cable-stayed bridge under the effect of wind, air temperature without considering the horizontal displacement, the longitudinal displacement, and the effect of the load. Currently, in Vietnam, there is no scientific research on the recovery of GPS —RTK cable-stayed bridge displacement measurement data by the ANN method. At the same time [11] has demonstrated that the influence of air temperature, wind speed on the displacement of the mid-span of the cable-stayed bridge is very large.

So the authors' research on the application of the ANN method to recover lost GPS—RTK data with three directions X, Y, Z at the mid main span of the actual cable-stayed bridge based on the influence of wind speed, air temperature, and structural stresses. First, the monitoring data for 3 days including wind speed, air temperature, structural stress, GPS displacement of the actual cable-stayed bridge in Vietnam were extracted for study. After that, we apply ANN to recover lost GPS data. Interpolation results by the ANN method are compared with actual monitoring data to evaluate the accuracy. Obtained results demonstrated that the ANN method completely guarantees accuracy and reliability in recovering GPS—RTK data.

2 Theoretical Basis

2.1 Working Principle of GPS—RTK Measurement Technology

Global positioning system—real-time kinematic (GPS—RTK) is a dynamic GPS measurement method in real-time, measuring results for the instantaneous coordinate value and elevation of the measurement point. The working principle of this method consists of a base station located at a point of known coordinates, elevation,

or connected to the point of known coordinates, elevation and one or more rover located at points need to determine coordinates, elevation. Both devices simultaneously receive signals from satellites. At the base station, the machine has a radio link transmitter or a 3G wave that continuously emits a rectification signal, and this correction number will be transmitted to mobile devices (rover) to adjust the position to achieve accuracy high. The range of the rover station to a base station is up to 10 km with radio link wave and greater with 3G wave under favorable conditions. The bridge health monitoring system (BHM) installed on the bridge usually includes GPS antenna, wind speed sensor, traffic camera, structural temperature sensor, air temperature sensor, rainfall sensor, accelerometer, and cable tension force measurement sensor measured data are transmitted via optic cable to the data storage department and the office of the management center. The real-time measurement results of the SHM system will be averaged over the period 1 min, 10 min, 1 h, 1 day, as the basis for analysis, evaluation, and reporting of the bridge condition. During the displacement monitoring of the cable-stayed bridge, lost GPS data may be causing the intermittently interrupted monitoring results affecting the accuracy of the measurement results and the analysis and evaluation of the bridge performance [12]. Figure 1 shows the GPS—RTK data lost during displacement monitoring.

2.2 Introduction to an Artificial Neural Network (ANN)

The artificial neural network can be "learning" and parallel process. It calculates the value of the output variable with a given set of information of the input variable. The ANN method will be "trained" in order to be able to "learning" from past information. From there, the network gives computational results based on what has been learned. This process is carried out by a network training method of supervised learning and backpropagation algorithm.
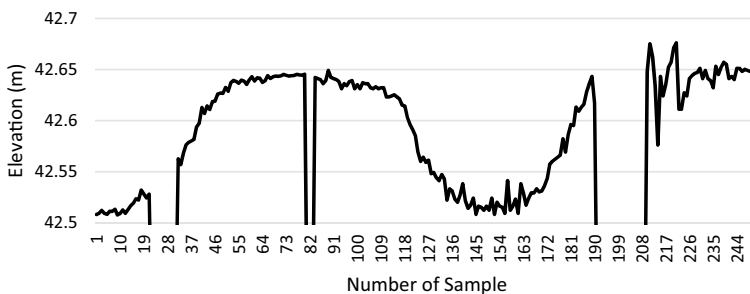
Fig. 1 Case of lost data [13]

2.2.1 Feedforward Neural Network

Feedforward neural network is arranged including an input layer, hidden layers, and an output layer. The input layer will be the receiver of the input signals, be it a constant, raw data, or the output of another neural network. These values will affect the hidden layer neurons through the w_{ij} weights. In the hidden layer, the signal of the input layer will be handled by an activate function, usually the Sigmoid function or the hyperbolic tangent function, then the signal will be passed through the output layer via the w_{jk} weights. Hidden layers link between the input layer and the output layer, making the neural network capable of simulating nonlinear relationships.

2.2.2 Backpropagation Algorithm

To compute the output signal according to the input signal, an activation function in hidden layers is required. Two commonly used activation functions are the Sigmoid function and the hyperbolic tangent function. For a single hidden layer ANN, the input signal is X_i and the weights w_{ij} will have the output signal at neuron H_j is

$$H_j = f \sum_{i=1}^{n} X_i w_{ij} \tag{1}$$

After obtaining signals in hidden layers value $\widehat{Y_k}$ (estimated) will be calculated as follows

$$\widehat{Y_k} = f\left(\sum_{j=1}^{q} H_j * w_{jk}\right) = f\left(\sum_{j=1}^{q} f\left(\sum_{i=1}^{n} X_i w_{ij}\right) * w_{jk}\right) \tag{2}$$

For a t-th observation ($t = 1 \div T$), the output signal of the network is denoted by $\widehat{Y_{k,t}}$, the actual signal is denoted by $Y_{k,t}$, the deviation between $\widehat{Y_{k,t}}$ and $Y_{k,t}$ called error. The estimation of the model parameters is to find the weights w_{ij} and w_{jk} so that the sum of squared errors is the smallest or find the minimum value of the objective function E(w):

$$E(w) = \frac{1}{2} \sum_{t=1}^{T} \sum_{k=1}^{n} (Y_{k,t} - \widehat{Y_{k,t}})^2 \tag{3}$$

Since the function $E(w)$ is a nonlinear function in terms of w, it is necessary to calculate these weights w using the error backpropagation algorithm. Backpropagation algorithms and supervised learning methods are commonly used in multilayered neural networks. This algorithm is implemented in principle that when the weight (w) changes, the objective function E will change, and for a function E there will be a set of values of the weights w that makes function

E smallest. To do that, the backpropagation algorithm performs two steps of information transmission. First, the input signal x_i is passed from input to output, the result of data transmission in the forward direction is to produce the signal y_i at the output of the network. Then the error between the actual data (t_i) and the output data (calculated from the y_i network) is transmitted back from the output layer back to the previous layer to adjust the weights of the network so that the weights set make the target function E smaller. The process of finding the right weights for the network is also known as the "learning" process. The learning process will be repeated until the objective function reaches a minimum value [14, 15].

2.2.3 Evaluating the Quality of the ANN Method in Data Interpolation

To evaluate the accuracy of GPS—RTK data interpolation, several indicators are used later in the paper:

Mean square error:

$$\text{MSE} = \frac{1}{n}\sum_{i=1}^{n}\left(Y_i - \widehat{Y_k}\right)^2 \tag{4}$$

Root mean square error:

$$\text{RMSE} = \sqrt{\frac{\sum_{k=1}^{n}\left(Y_k - \widehat{Y_k}\right)}{n}} \tag{5}$$

Regression coefficient between the actual measured value and the interpolation value R^2:

$$R^2 = \frac{\sum_{k=1}^{n}\left(Y_k - \overline{Y_k}\right)\left(Y_k - \overline{\widehat{Y_k}}\right)}{\sqrt{\sum_{k=1}^{n}\left(Y_k - \overline{Y_k}\right)^2\sum_{k=1}^{n}\left(\widehat{Y_k} - \overline{\widehat{Y_k}}\right)^2}} \tag{6}$$

In which: Y_k: Actual measured values; $\widehat{Y_k}$: Interpolation value (value calculated from the network).

2.3   Experimental Calculations

Interpolating GPS—RTK data during displacement monitoring at the mid main span of the cable-stayed bridge by ANN method from experimental data at Can Tho bridge, Vietnam.

2.3.1   Description of Bridge

Can Tho bridge is a cable-stayed bridge with two cable plane, width 26 m, the length of the main bridge is 2750 m, the tower is 164.8 m high. The main span of the bridge is 550 m long with 210 m of mid-span with a prefabricated steel box girder and assembled with a concrete part cast in place at both ends.

   In the SHM system, GPS is installed on Can Tho bridge, including two base stations, nine rover stations and is monitored continuously by using real-time kinematic (RTK) technology. According to the catalog, the measurement accuracy is ±(10 mm + 1 ppm) horizontally, ±(20 mm + 1 ppm) vertically. Anemometer used to determine wind speed, wind direction includes two sets installed at the top of the south tower, in the middle of the bridge with an accuracy of measuring wind speed of 0.3 m/s. The temperature measuring devices were installed at the center point of the deck with a temperature measurement accuracy of ±0.5 °C to determine the air temperature. The stress measuring devices to determine the strain of the bridge deck and the main girder to detect strain under the impact of vehicles [13]. The installation locations of the devices are shown in Fig. 2.
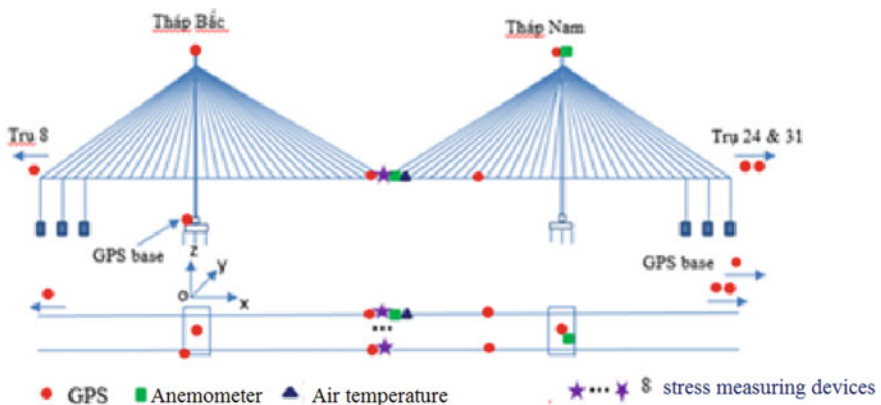
Fig. 2   Installed location of GPS, anemometer, air temperature, and stress [13]

2.3.2 Experimental Results

GPS—RTK measurement data lost during the displacement monitoring of the cable-stayed bridge is recovered by the ANN method according to the following steps:

Collecting and processing measured data

In order to interpolate the displacement in three directions of the point at the mid main span of Can Tho bridge by ANN, it is necessary to collect data related to the displacement of the bridge, which is air temperature, wind speed, and structural stress. GPS, wind, temperature, and stress sensors are measured at the same time, and the sampling frequency of these devices is 10 min/1 time. With a measuring time of 4 days from February 13 to 16, 2016, there were 419 samples constructed to model displacement in the X, Y, Z directions at the midpoint of the main span. Then, the wind, temperature, and stress data on February 18, 2016, equivalent to 5, 15, 40, 80 samples, respectively, were put into the network to recover the lost GPS—RTK measurement data. After being recovered, these data were compared with actual measured GPS—RTK data.

The data collected from the above measuring devices at the midpoint of the main span are shown in the following Fig. 3.

The architecture of a neural network

After collecting measurement data, three-layer backpropagation neural networks are designed with the input layer, the hidden layer, and the output layer. The activation function used is the sigmoid nonlinear function, supervised learning, and the training algorithm is Levenberg–Marquardt (Fig. 4).

The input layer has 10 neurons, of which one neuron is the air temperature; two input neurons are the wind speed; eight input neurons are stress; the hidden layer has one layer of 10 neurons; the output layer has one neuron, in turn, is the GPS value measuring displacement in the longitudinal, horizontal, and vertical direction of the bridge. The dataset was divided into two main subsets. Set 1 is a network training dataset that has 419 input samples. Set 2 is used to recover lost GPS data including 5, 15, 40, 80 samples, respectively. The training dataset will be divided into three small data groups including network training accounts for 70% of the dataset, corresponding to 293 samples. Network validation accounts for 15% of the data with 63 samples. Network testing accounts for 15% of the dataset with 63 samples.

Training ANN network

With the network architecture selected in step 2, continue with the network training. Network training is the process of adjusting weights. These link weight values will be randomly assigned at the start of network construction, then, during network training, the algorithms will adjust the weight values above.

Check the accuracy of the network

The results of the network training will display the MSE and the regression coefficient (R^2) of the three sub-datasets (training, validating, and verifying the network)
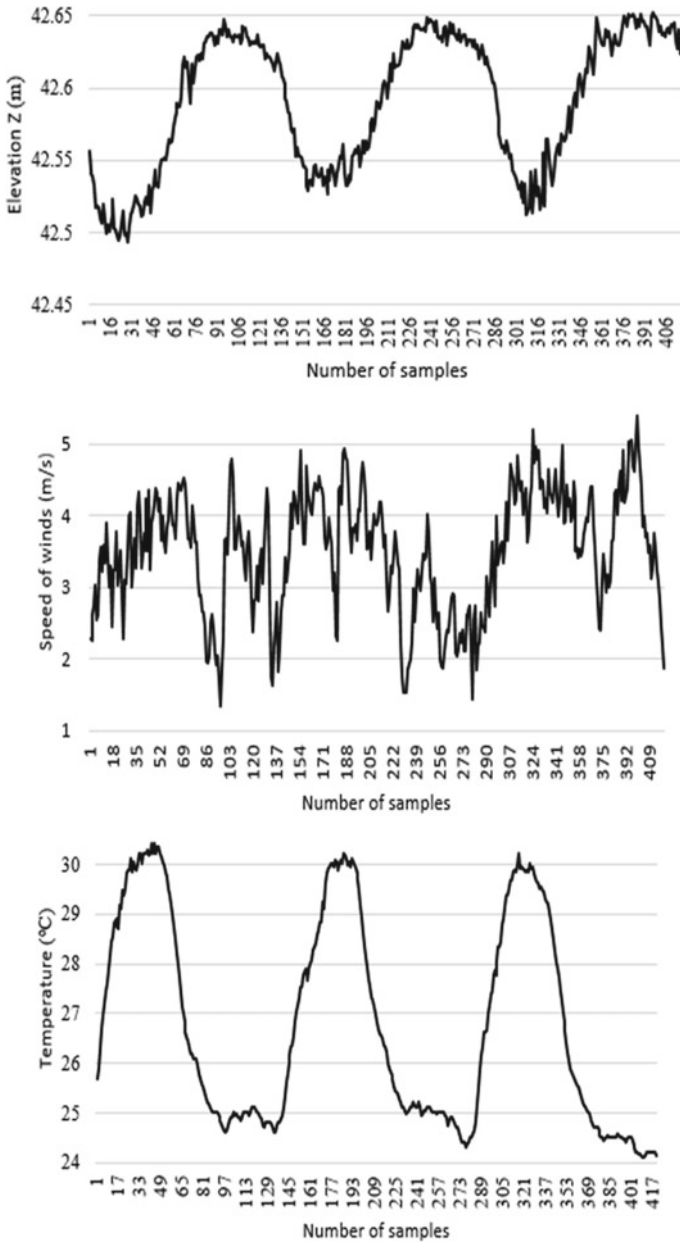
Fig. 3 Measurement data of GPS—RTK, wind, and air temperature [13]
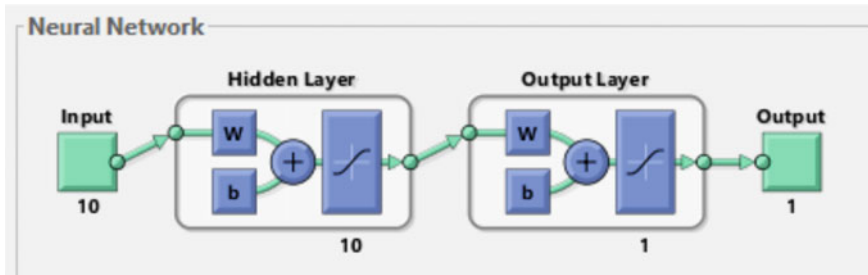
Fig. 4 Architecture of a neural network [13]

divided from the input dataset, which is training dataset error, validating error, and verifying error. The best recovery results when the MSE equal 0 and the regression coefficient R^2 equal 1. If the reliability of the network after testing does not reach the desired result, do one of the following two ways:

- Way 1: Continue retraining the network for better results by reselecting the network parameters such as learning rate, learning process (epochs) …,
- Way 2: Go back to step 2, adjust the number of neurons in the hidden layer or network architecture, and then train the network again.

Table 1 shows that the MSE of training is very small, close to zero. That demonstrates the trained network is very good.

Results of calculating regression coefficient R^2 in the cases of loss of 5, 15, 40, 80 samples are shown in Table 2.

Table 2 shows the regression coefficient between the recovery displacement value calculated from the input data as the air temperature, wind speed, structural stress, and actual displacement measured value according to the three directions X, Y, Z. The regression coefficient in the Z-direction is close to 1, showing the recovered data consistent with the actual measured data. The regression coefficient in the Y-direction is greater than 0.7, showing the reliability of good interpolation. The regression coefficient in the X direction about $0.4 < 0.5$ has very poor interpolation reliability.

Table 1 MSE value [13]

The case	MSE of direction X (m)	MSE of direction Y (m)	MSE of direction Z (m)
Loss of five samples	2×10^{-5}	9×10^{-5}	7×10^{-5}
Loss of 15 samples	9×10^{-6}	6×10^{-6}	6×10^{-5}
Loss of 40 samples	10^{-5}	9×10^{-5}	4×10^{-5}
Loss of 80 samples	2×10^{-5}	6×10^{-6}	5×10^{-5}

Table 2 Regression coefficient [13]

	Direction	R^2
Loss of five samples	X	0.389
	Y	0.772
	Z	0.989
Loss of 40 samples	X	0.405
	Y	0.772
	Z	0.991
Loss of 15 samples	X	0.435
	Y	0.791
	Z	0.989
Loss of 80 samples	X	0.435
	Y	0.791
	Z	0.989

Through checking the accuracy of the network, it can be seen that the ANN method is completely capable of recovering GPS data based on the close relationship between the inputs that are meteorological factors (wind and ambient temperature), structural stress, and the output that are the displacements in the Y, Z directions of the midpoint of the main span. In the X-direction, although the MSE is calculated very small, the regression coefficient is small, the interpolation reliability is poor, so it is impossible to use the inputs above to interpolate the data.

Recover lost GPS—RTK data

Use the ANN method to recover 5, 15, 40, 80 GPS—RTK samples lost with corresponding input data such as wind speed, air temperature, and structural stress. The recovery results in the Y and Z directions are shown in the following figure.

Calculate deviation between interpolation value and actual measured value. Get the maximum deviation v_{imax}, the minimum deviation v_{imin}, then determine the amplitude between the maximum deviation and the minimum deviation in the Y-direction, the Z-direction is shown in Table 3.

From Figs. 5, 6 and Table 3, it is found that the interpolation results in the GPS data loss cases are very close to the actual measured GPS value. The displacement interpolation results are quite accurate with the real displacement measurement results.

Table 3 Maximum and the minimum deviation in the Y, Z directions [13]

The case	Y-direction (m)			Z-direction (m)		
	v_{imax}	v_{imin}	Amplitude	v_{imax}	v_{imin}	Amplitude
Loss of five samples	0.011	0.003	0.008	0.004	−0.005	0.009
Loss of 15 samples	0.009	−0.010	0.020	0.014	−0.015	0.029
Loss of 40 samples	0.011	−0.010	0.021	0.009	−0.025	0.034
Loss of 80 samples	0.009	−0.010	0.019	0.014	0.026	0.040
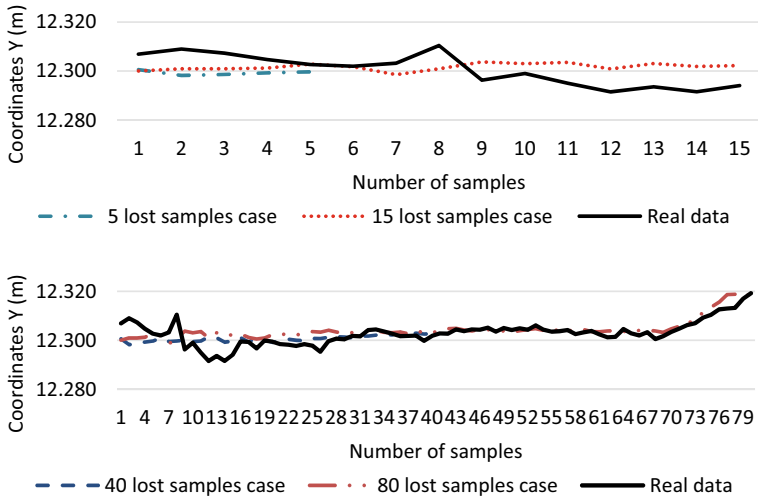
Fig. 5 Results of Y-direction interpolated GPS data [13]
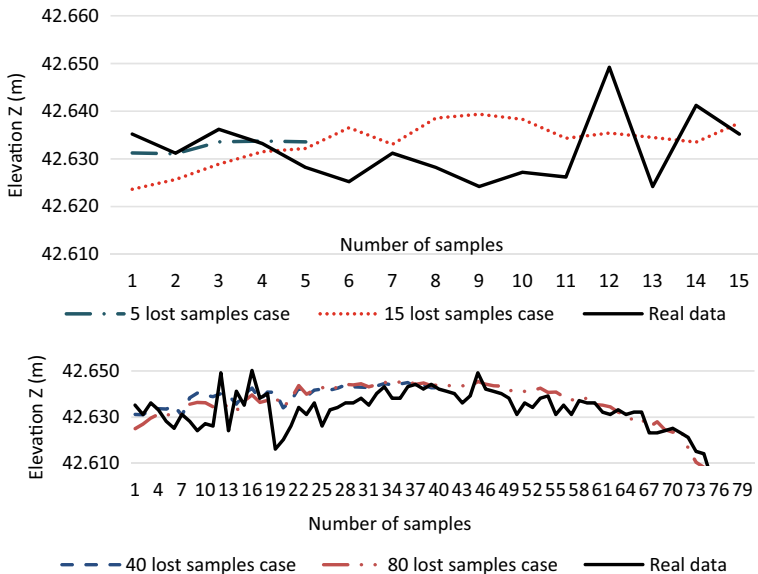
Fig. 6 Results of Z-direction interpolated GPS data [13]

Then, determine RMSE to evaluate the accuracy of the ANN method, the results of recovering GPS—RTK data when monitoring displacement in the Y, Z directions of the cable-stayed bridge are shown in Table 4.

Table 4 RMSE value [13]

The case	RMSE Y (m)	RMSE Z (m)
Loss of five samples	0.003	0.003
Loss of 15 samples	0.007	0.008
Loss of 40 samples	0.005	0.007
Loss of 80 samples	0.004	0.007

Table 4 shows that RMSE when recovering data in the Y and Z directions is very small or in other words, the accuracy of data recovery by the ANN method is very good. The ANN method is an effective method, which can be used as an alternative to the polynomial method when interpolating GPS—RTK data in monitoring the displacement of the cable-stayed bridge based on random and complex impacts such as wind velocity, air temperature, and structural stress.

3 Conclusion

Air temperature, wind velocity, and structural stress are strongly related to the horizontal and vertical displacement at the midpoint of the main span of a cable-stayed bridge and these factors can be supplied lost GPS—RTK data.

With a simple calculation method, high accuracy, the ANN method can be applied to recover GPS—RTK data in displacement monitoring of the cable-stayed bridge and replace the polynomial method.

However, the authors also recommend that for an objective assessment of the ANN method, it is recommended to calculate more with a larger amount of data and with data in many other bridges.

References

1. Kaloop, M.R., Li, H.: Monitoring of bridge deformation using GPS technique. KSCE J. Civil Eng. **13**(6), 423–431 (2009)
2. Kaloop, M.R., Elbeltagi, E., Hu, J.W., Elrefai, A.: Recent advances of structures monitoring and evaluation using GPS-time series monitoring systems: a review. ISPRS Int. J. Geo-Inf. **6**, 382 (2017)
3. Yunus, M.Z.M., Ibrahim, N., Ahmad, F.S.: A review on bridge dynamic displacement monitoring using global positioning system and accelerometer. Int. Conf. Eng. Technol. (IntCET) (2017)
4. Jwo, D.J., Huang, H.C.: Neural network aided adaptive extended Kalman filtering approach for DGPS positioning. J. Navig. (2004)
5. Elnabwy, M.T., Kaloop, M.R., Elbeltagi, E.: Talkha steel highway bridge monitoring and movement identification using RTK-GPS technique. Measurement **46**, 4282–4292 (2013)
6. Kaloop, M.R., Kim, D.: GPS-structural health monitoring of a long span bridge using neural network adaptive filter. Survey Rev. **46** (2014)

7. Kaloop, M.R., Hu, J.W.: Optimizing the de-noise neural network model for gps time-series monitoring of structures. Sensors (2015)
8. Khanh, P.Q., Manh, N.V.: Research on the application of artificial neural networks to predict the settlement of hydropower projects. J. Sci. Technol. Min. Geol. **60**(4) (2019)
9. Long, N.Q.: Evaluation of the applicability of neural networks to predict mine surface subsidence due to pit mining. Min. Sci. Technol. J. **55**, 79–88 (2016)
10. Linh, N.T., Huong, H.T.L., Hung, N.H.: Artificial intelligence (AI) application research to build a model for predicting displacement in the vertical direction of the cable-stayed bridge. J. Transp., 72–77 (2019)
11. Huong, H.T.L., Hien, L.V.: Study on the correlation between wind, temperature, and displacement of some locations on Can Tho bridge. J. Transp. Sci. **54**, 45–53 (2016)
12. Trung, N.V., Hoc, B.X.: Cable-Stayed Bridge Monitoring System and Hammock Bridge. Construction Publishing House (2017)
13. Nippon Koei Co. Ltd, Chodai Co, Ltd., Tedi South: Summary of design technical report for Can Tho bridge structure monitoring system (May 2010)
14. Waszczyszyn, Zenon: Neural Networks in the Analysis and Design of Structures. Springer-Verlag Wien GmbH, Udine (1999)
15. Dreyfus, G.: Neural Networks Methodology and Applications. Springer-Verlag, Berlin Heidelberg, Germany (2005)

Estimation of Cable Tension with Unknown Parameters Using Artificial Neural Networks

Luu Xuan Le, H. Katsuchi, L. G. To, S. E. H. A. M. Zarbaf, and Cuong-Le Thanh

1 Introduction

Accurate identification of cable tension in cable structures is of paramount important in the construction stage or health monitoring of structure to evaluate the serviceability of bridges. It becomes quite challenging to pinpoint precisely cable forces in existing cables of cable-stayed bridges owing to the uncertainties of the cable properties like bending stiffness or actual boundary conditions at cable ends. Direct determination of cable tension with a set of measurement devices such as hydraulic jacks, pressure, and displacement meters often yields high accuracy, but costly [1]. Alternatively, vibration-based tension estimation provides engineers with a simpler and cheaper tool, in which tension forces are commonly determined through the measured frequency data of existing cables along with cable geometrical and mechanical parameters.

Vibration-based cable tension identification is effective, even so, its accuracy depends heavily on groups of issues including (1) analytical cable model (e.g., cable inclination, sag-extensibility, and bending stiffness), (2) technique to excite and record data of existing cables to reduce noise in output signals during the

L. X. Le · H. Katsuchi
Faculty of Civil Engineering, Yokohama National University, Yokohama, Japan

L. X. Le (✉) · L. G. To
Faculty of Civil Engineering, University of Transport and Communications, Hanoi, Vietnam
e-mail: luusbvl@utc.edu.vn

C.-L. Thanh (✉)
Faculty of Civil Engineering, Ho Chi Minh City Open University, Ho Chi Minh City, Vietnam
e-mail: cuong.lt@ou.edu.vn

S. E. H. A. M.Zarbaf
The University of Cincinnati, Cincinnati, OH, USA

measurement, and (3) uncertainties of cable working conditions (e.g., boundary conditions at cable ends, degradation of bending stiffness and cracks).

Many efforts have been made to take these above concerns into account. Irvine and Caughey [2] proposed a cable model with and without sag effect but neglected cable bending stiffness. Ceballos and Prato [3], Fang and Wang [4] introduced solutions for tension estimation of a bend-stiff cable by vibration method. Some others showed models with a simultaneous combination of cable sag and bending stiffness such as Zui et al. [5], Mehrabi and Tabatabai [6], and Ricciardi and Saitta [7]. On the question of cable uncertainties, some models with uncertain boundary conditions, in which cable ends are theoretically treated as rotational and/or translational restraint boundaries which represent for complexity at cable supports, have recently been proposed [3, 8–10]. In addition to the uncertain boundary conditions, bending stiffness of an actual cable is also an unknown input. To alleviate that, Liao et al. [11] introduced multiple-parameter identification with the updates of cable bending by minimizing the error function which describes the differences between measured frequencies and frequencies obtained from the model. In a similar manner, Zarbaf et al. [12] minimized the error function by means of GA and PSO, in which cable bending stiffness was treated as one unknown parameter of the error function.

In practice, boundary conditions at cable ends of existing cables are quite complex relying heavily on anchorage types, configurations of the supports, anchoring techniques, and more. Apparently, the boundary conditions should be in the type of imperfectly hinged or imperfectly fixed ends rather than pure ones. Therefore, a cable model with rotational restraint ends should be developed and used for the estimation of cable tension by vibration method, especially for such short and medium length cables of cable-supported bridges like the cables of the An Dong Bridge as shown in this paper.

Recently, a novel application of artificial neural networks (ANNs) on vibration-based cable condition assessment was proposed by Zarbaf et al. [13]. The discretized cable with fixed ends was used to generate datasets for training, validation, and testing of ANNs. Following this novel approach, the present paper herein proposes a discretized cable model with rotational restraint end conditions. Finite difference formulation for the cable vibration was derived to generate datasets for training, validation, and testing in ANNs. During the training in ANNs, cable bending stiffness and rotational restraint stiffness at cable ends were inactivated and treated as the unknown parameters. The proposed method was applied to identify tensions in the typical cables of the An Dong Bridge in Vietnam as a case study.
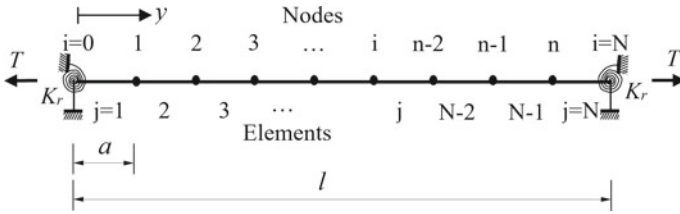
Fig. 1 Discretized cable with rotational restraint ends

2 Finite Difference Model of a Cable with Rotational Restraint Ends

A discretized cable with rotational restraints at cable ends is schematically shown in Fig. 1.

Coordinate y starts from the left end of the cable. The cable has chord length l, mass per unit length m, bending stiffness EI, and chord tension T. The rotational restraint stiffness at cable ends is assumed with proportionally elastic stiffness K_r. The cable is discretized into N elements with n internal nodes in which the element length is a. An assumption is made that the initial chord tension T of the cable is large enough compared to its self-weight, thus sag-extensibility is neglected. The bending stiffness of the cable EI is included in this study. By considering the cable as an undamped system, the in-plane transverse free vibration of the cable is derived as

$$T\frac{\partial^2 v(y,t)}{\partial y^2} - \text{EI}\frac{\partial^4 v(y,t)}{\partial y^4} - m\frac{\partial^2 v(y,t)}{\partial t^2} = 0 \qquad (1)$$

solution of vibration

$$v(y,t) = \tilde{v}(y)e^{\omega i t} \qquad (2)$$

where $i^2 = -1$; ω = cable circular frequency; $\tilde{v}(y)$ = mode shape of the cable. Substitution of the cable vibration deflection $v(y, t)$ from Eq. (2) into Eq. (1) gives

$$\text{EI}\frac{d^4 \tilde{v}(y)}{dy^4} - T\frac{d^2 \tilde{v}(y)}{dy^2} - m\omega^2 \tilde{v}(y) = 0 \qquad (3)$$

By discretizing the cable into N elements as depicted in Fig. 1, the mode shape equation Eq. (3) can be rewritten in the form of discretized formulation as

$$[K]\{\tilde{v}\} - \omega^2[M]\{\tilde{v}\} = 0 \tag{4}$$

in which $[K]$ = cable stiffness matrix; $[M]$ = cable mass matrix; $\{\tilde{v}\}$ = vector of nodal displacements.

The transformation from Eq. (3) to (4) is conducted using finite difference method (FDM). The FDM means the replacement of such derivatives of the differential equation, Eq. (3) with corresponding difference quotients. In this study, the central finite difference scheme is used to approximate the second and fourth derivatives in Eq. (3) with quotients as shown in Eqs. (5) and (6).

$$\frac{d^2\tilde{v}(y)}{dy^2} = \frac{(\tilde{v}_{i+1} - 2\tilde{v}_i + \tilde{v}_{i-1})}{a^2} \tag{5}$$

$$\frac{d^4\tilde{v}(y)}{dy^4} = \frac{(\tilde{v}_{i+2} - 4\tilde{v}_{i+1} + 6\tilde{v}_i - 4\tilde{v}_{i-1} + \tilde{v}_{i-2})}{a^4} \tag{6}$$

Substitution of the difference quotients from Eqs. (5) and (6) into Eq. (3) yields the finite difference formulation (FDF) of cable vibration. Then, mass matrix $[M]$ and stiffness matrix $[K]$ are assembled by applying FDF to each internal node. It is noted that boundary conditions at cable ends are needed when working with node 1 and node n. The completed matrices of $[M]$ and $[K]$ are corresponding as shown in Eqs. (7) and (8), noting that each matrix row corresponds to each node.

$$[M] = \begin{bmatrix} m_1 & 0 & 0 & 0 & 0 & 0 \\ 0 & m_2 & 0 & 0 & 0 & 0 \\ 0 & 0 & \cdots & 0 & 0 & 0 \\ 0 & 0 & 0 & m_i & 0 & 0 \\ 0 & 0 & 0 & 0 & \cdots & 0 \\ 0 & 0 & 0 & 0 & 0 & m_n \end{bmatrix} \tag{7}$$

where m_i = mass per unit length at node i.

$$[K] = \frac{T}{a^2}\left(\frac{1}{\xi^2}\right) \begin{bmatrix} \beta n^2 + 2\xi^2 & -4n^2 - 1\xi^2 & n^2 & 0 & 0 & 0 & 0 & 0 \\ -4n^2 - \xi^2 & 6n^2 + 2\xi^2 & -4n^2 - \xi^2 & n^2 & 0 & 0 & 0 & 0 \\ n^2 & -4n^2 - \xi^2 & 6n^2 + 2\xi^2 & -4n^2 - \xi^2 & n^2 & 0 & 0 & 0 \\ 0 & n^2 & -4n^2 - \xi^2 & 6n^2 + 2\xi^2 & -4n^2 - \xi^2 & n^2 & 0 & 0 \\ 0 & \cdots & \cdots & \cdots & \cdots & \cdots & \cdots & 0 \\ 0 & 0 & 0 & 0 & n^2 & -4n^2 - \xi^2 & 6n^2 + 2\xi^2 & -4n^2 - \xi^2 \\ 0 & 0 & 0 & 0 & 0 & n^2 & -4n^2 - 1\xi^2 & \beta n^2 + 2\xi^2 \end{bmatrix} \tag{8}$$

where $\xi = l\sqrt{T/EI}$ characterizes the non-dimensional parameter of bending stiffness; β = factor of boundary conditions.

$$\beta = \frac{K_r a \xi^2 - 2Tl^2}{K_r a \xi^2 + 2Tl^2} + 6 \tag{9}$$

It is recognizable that a cable with hinged ends ($K_r = 0$) leads to $\beta = 5$, and a cable with fixed ends ($K_r \to \infty$) results in $\beta = 7$. In such conventional cases of the cable supports, the stiffness matrix $[K]$ shown here is the same as one proposed by Mehrabi and Tabatabai [6]. A non-dimensional form of rotational restraint stiffness is also introduced as Eq. (10), in which $0 \leq k_r \leq 1$ corresponding to the stiffness from hinged to fixed ends.

$$k_r = \frac{K_r \times l}{K_r \times l + e^5 \text{EI}} \tag{10}$$

The eigenfrequencies ω of Eq. (4) are obtained by tackling the eigen formulation as

$$\left| [K] - \omega^2 [M] \right| = 0 \tag{11}$$

This formulation is used in the next section to generate datasets for training, validation, and testing in ANNs.

3 Estimation of Cable Tension with Unknown Parameters Using Artificial Neural Networks

Artificial neural networks (ANNs), by definition, are multi-layer fully connected neural nets. It contains several layers including an input layer, multiple hidden layers, and an output layer. Every node in one layer is connected to other nodes in the next layer. Along with the historical development of neural network theories, ANNs have been applied to many aspects of civil engineering such as for pattern recognition in structural analysis, optimization, structural condition assessment and

Fig. 2 Element of neural networks
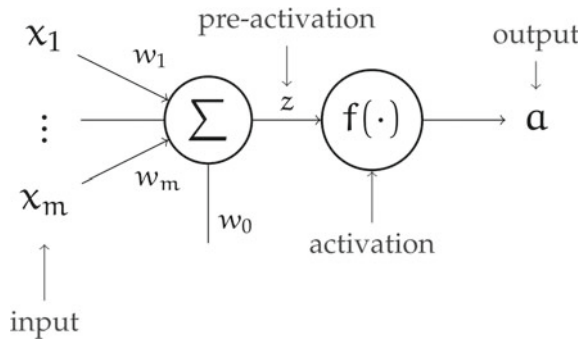
monitoring, and structural system identification. A basic information-passed mechanism of the neural networks is displayed schematically in Fig. 2.

In this study, the inputs of training, validation, and testing in ANNs are cable length l, mass per unit length m, and fundamental natural frequencies f while the output is cable tension T. It raises the question that how to treat cable bending stiffness and boundary conditions as unknown parameters. Before training in ANNs, a dataset with a wide range of rotational restraint stiffness values at cable end is generated which covers all possible states of cable ends from hinged to fixed supports. Also, a certain range of cable bending stiffness, with values varied surrounding the design flexural rigidity of a cable, is generated. Data points of rotational restraint stiffness and cable bending stiffness EI are shuffled and employed to compute the corresponding data points of cable natural frequency f $(=\omega/2\pi)$ according to Eq. (11). Since the cable supports and flexural rigidity are considered as the unknown parameters, they will be inactivated during the ANNs processing.

In ANNs algorithm, a given node takes the weighted sum of its inputs and passes it through a nonlinear activation function. This is the output of the node, which then becomes the input of another node in a next layer. The activation function used in this study is the Sigmoid function. The function of an output signal as shown in Fig. 2 is described as

$$a = f(z) = f\left(\sum_{j=1}^{m} x_j w_j + w_0\right) = f\left(w^T x + w_0\right) \tag{12}$$

where a = an output; f = an activation function; x_1 to x_m= inputs; w_1 to w_m = weights; and, w_0 = a bias.

Training, validation, and testing of datasets in ANNs in this study are conducted using the neural fitting tool in MATLAB, which allows mapping between the input signals with a target one. Figure 3 depicts the steps to identify tension in a stay cable using the application of ANNs.

In order to increase the accuracy of cable tension estimation, datasets for each cable among selected cables will be individually generated. For that, a sample of γ data points of each cable property including cable length l, tension T, weight per unit length w, bending stiffness parameter ξ will be generated with a variance of around 15% compared to the initial designs. Also, γ data points of dimensionless rotational restraint stiffness k_r are created within the range from 0 to 1 (from hinged to fixed end behavior). These datasets are shuffled individually in their subsets before being used to calculate γ data points of the cable natural frequency f.

Training, validation, and testing are executed in the neural network toolbox in MATLAB. Since the cable bending stiffness and rotational restraint stiffness at cable ends are considered as unknown parameters, the input data contains just three features of the cable properties (length l, mass per unit length m, and fundamental natural frequency f), and output will be estimated cable tension T. Datasets are randomly divided into three packages with N_1% for training, N_2% for validation, and N_3% for testing. During training, the network is adjusted according to the error
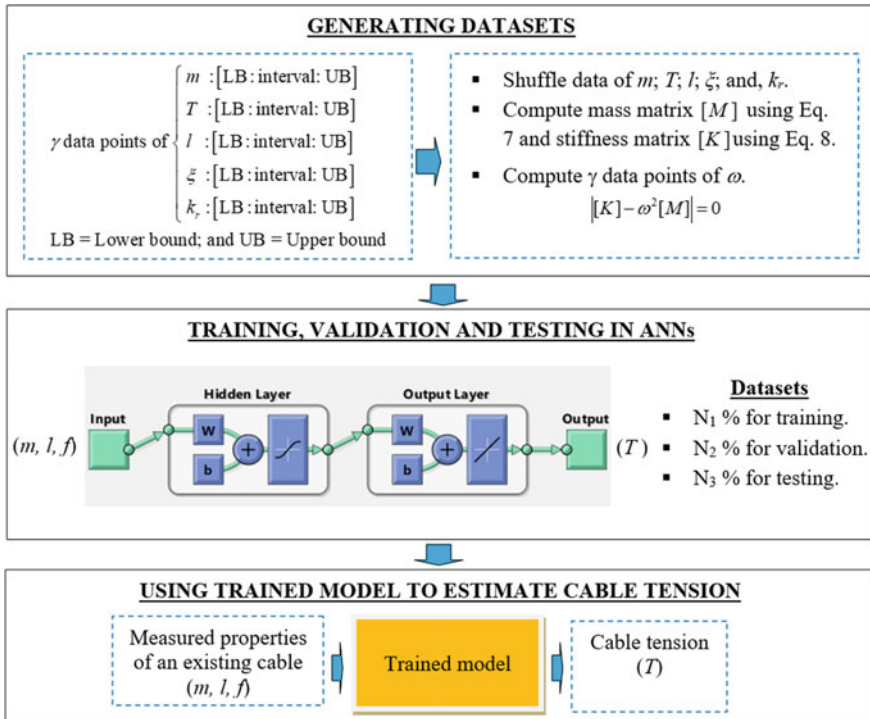
Fig. 3 Procedures of estimation of a cable tension using ANNs

between predicted and target tensions. The subset of validation is used here to measure network generalization and to halt training when generalization stops improving. The subset of testing provides an independent measure of network performance during and after training. The number of hidden neurons in the hidden layer will be gradually increased until reaching the desired accuracy. The Levenberg–Marquardt algorithm is selected for the training of the network to fit the inputs and output. In this algorithm, the weights will be updated after each iteration. In order to evaluate the accuracy of the algorithm in ANNs, the correlation factor R shows the correlation between predicted tensions and a target one.

$$R = \frac{\text{cov}(P, E)}{\sigma_P \sigma_E} \tag{13}$$

where cov(P,E) = covariance between predicted tensions and a target one; σ_P and σ_E = corresponding standard deviations.

After successfully training in ANNs, a well-trained model is created and ready to be used for the identification of tension in an existing cable. In this step, the inputs are composed of the measured properties of an existing cable including cable length

l, mass per unit length m, and the measured fundamental natural frequency f whereas cable tension T is the output. The suggested methodology herein is applied to assess cable tensions of selected cables of the An Dong Bridge in Vietnam to verify the feasibility and applicability of the proposed approach.

4 A Case Study

The An Dong Bridge is crossing the Dinh river in Ninh Thuan province, Vietnam. The total length of the bridge is 1018 m in which the main bridge is an extradosed structure with a length of 580 m. The cross section of the main bridge is three-cell box girder type that is supported by 48 stay cables as depicted in Fig. 4.

Six typical stay cables C-01, C-02, C-03, C-04, C-05, and C-06 as flagged in Fig. 4 were selected for identification of cable tension based on the foregoing ANNs algorithms. The cable properties including measured fundamental natural frequencies f of these selected cables are shown in Table 1. It is noted that cable bending stiffness EI shown in the table is the designed value. It is only used for generating the data points of the datasets. During training, validation, and testing in ANNs, cable bending stiffness is inactivated and considered as an unknown parameter.

For the measurement of cable vibration, an acceleration transducer ARF-20A which was supplied by Tokyo Sokki Kenkyujo Co., Ltd was attached to a cable and connected to a recorded device SDA-7910. Cables were excited using ropes with pull and release technique by technicians. The vibration data in time series was converted into frequency domain representation using fast Fourier transformation (FFT). The frequency spectrums of six selected cables, from C-01 to C-06, are shown in Fig. 5, in which the value of the fundamental frequency is marked at the first peak of the corresponding dominant spectrums.

The trained model is built for each selected cable to increase the accuracy of the proposed solution. The datasets of 1000 data points for each property in each cable are randomly generated within a suitable range as shown in Table 2. The datasets consist of cable length l, mass per unit length m, cable tension T, bending stiffness parameter ξ, and rotational restraint stiffness parameter k_r. As a result, the sample of

Fig. 4 An-Dong Bridge in Vietnam (source: picture taken by the 3rd author)

Table 1 Cable properties

Cable	Length l (m)	Mass per unit length m (kg/m)	Flexural rigidity EI (kNm^2)	Measured 1st frequencies f (Hz)
C-01	55.50	47.9	514.75	2.44
C-02	47.90	47.9	514.75	2.85
C-03	40.60	47.9	514.75	3.29
C-04	33.20	47.9	514.75	4.00
C-05	26.00	47.9	514.75	4.90
C-06	19.70	47.9	514.75	6.20

(a) C-01   (b) C-02   (c) C-03

(a) C-04   (b) C-05   (c) C-06
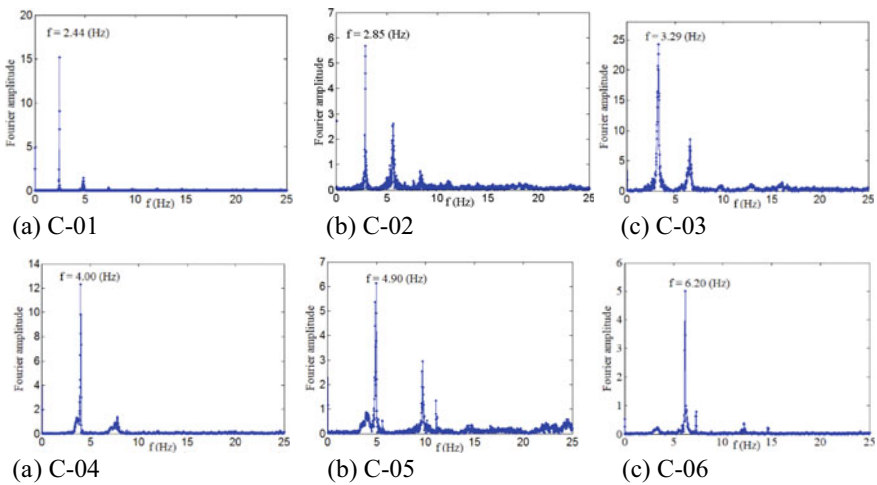
Fig. 5 Frequency spectrums of cable vibration in six selected cables

1000 data points of the first natural frequencies f is correspondingly calculated, using the finite difference formulation Eq. (11). For ANNs, datasets herein were randomly divided into three parts with 70% for training, 15% for validation, and 15% for testing, in which the input features are composed of cable length l, mass per unit length m, and model circular frequency ω. The output was cable tension T. Figure 6 shows the results of training, validation, and testing in ANNs for the cable C-01. It showed a high correlation, almost 99%, between predicted tensions and target ones. Noted that, target tensions were values from datasets of cable forces T, which were generated corresponding to the cable C-01. The predicted values were tensions that were estimated using ANNs. The results of the five remaining cables were not shown here but they all had the correlation of 99%. After training, validation, and testing, a well-trained model was created and ready to be used to estimate tension in an existing cable with the measured parameters.

Tensions in the six selected cables are estimated by using the successfully trained models. In this step, the input parameters of the trained model are m, l and

Table 2 Ranges of cable parameters for generating datasets

	Length l (m)		Mass per unit length m (kg/m)		Tension T (kN)		Bending stiffness parameter ξ		Rotational stiffness parameter k_r	
	LB	UB	LB	UB	LB	UB	LB	UB	LB	UB
C-01	47	63	40.87	55.35	3100	4200	120	170	0.1	0.9
C-02	40	55	40.87	55.35	3000	4100	100	150	0.1	0.9
C-03	34	46	40.87	55.35	2900	3950	80	120	0.1	0.9
C-04	28	38	40.87	55.35	2800	3900	70	100	0.1	0.9
C-05	22	29	40.87	55.35	2600	3600	50	75	0.1	0.9
C-06	16	22	40.87	55.35	2400	3300	40	55	0.1	0.9

Note LB = Lower bound; and *UB* = Upper bound
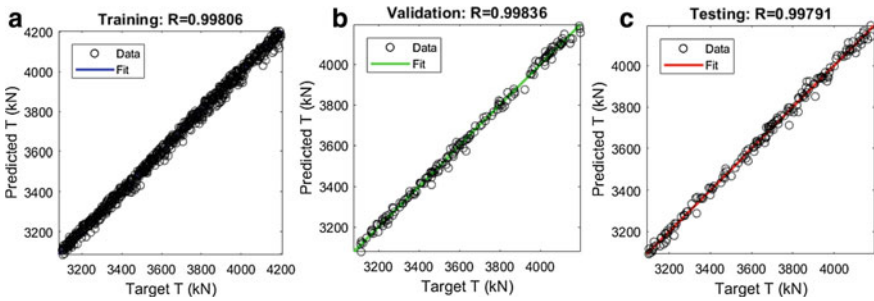
Fig. 6 Correlation between predicted and target tensions of the C-01 cable for **a** training, **b** validation, and **c** testing in ANNs

the first natural frequency of cable while the output is an estimated cable tension T. It is worth noting that cable bending stiffness EI and rotational restraint stiffness at cable ends K_r are inactivated and treated as unknown parameters. The results are illustrated in Fig. 7. It shows that a cable model with hinged end support leads to the highest value of tension while fixed end boundary conditions result in the lowest tension. As discussed, the boundary conditions at cable ends should be in a type of rotational restraint ends rather than perfectly hinged or completely fixed supports. With the perspective that boundary conditions are the uncertain factors, they are represented here through rotational restraint boundaries, but the values of rotational stiffness are also unknown. Therefore, it is inactivated before training in ANNs. Consequently, tensions in the selected cables with rotational restraints are shown in Fig. 7. For the stay cables of the An Dong Bridge, tensions were successfully identified with the values quite close to those of the fixed support cases. It is understandable because the length of stay cables in this bridge is quite short (from 19.7 to 55.5 m) compared to the common lengths of cables in cable-stayed bridges.

	C-01	C-02	C-03	C-04	C-05	C-06
■ T (fixed ends)	3600	3465	3294	3224	2914	2601
■ T (rotational restraint ends)	3626	3500	3309	3251	2954	2630
▪ T (hinged ends)	3704	3586	3433	3393	3123	2870
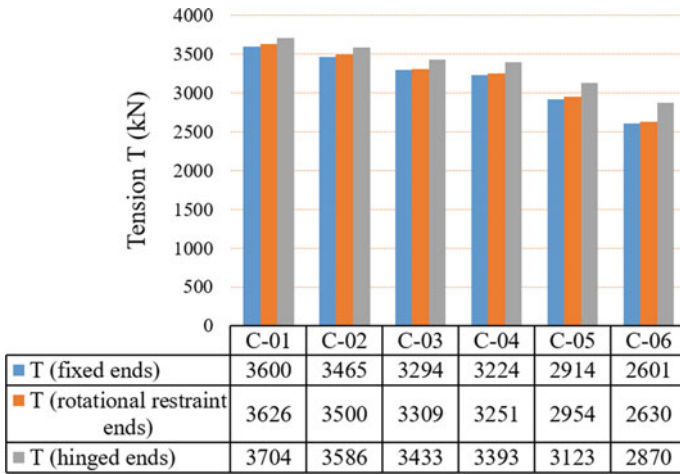
Fig. 7 Tensions in six selected cables

5 Conclusions

The application of artificial neural networks (ANNs) was used to estimate tension in a stay cable regardless of unknown cable bending stiffness and uncertain boundary conditions at cable ends. The datasets for training, validation, and testing in ANNs were generated using the finite difference model. Results showed that the ANNs algorithm is highly capable of matching inputs (available cable properties) with output (estimated tension), having the correlation of 99%. Cable tensions in the six typical cables of the An Dong Bridge in Vietnam were successfully identified on the basis of the proposed solution, showing the feasibility and applicability of the suggested methodology.

References

1. Cho, S., Yim, J., Shin, S.W., Jung, H.-J., Yun, C.-B., Wang, M.L.: Comparative field study of cable tension measurement for a cable stayed bridge. J. Bridge Eng. **18**(8), 748–757 (2012)
2. Irvine, H.M., Caughey, T.K.: The linear theory of free vibrations of a suspended cable. Proc. R. Soc. London A. **341**(1626), 299–315 (1974)
3. Ceballos, M.A., Prato, C.A.: Determination of the axial force on stay cables accounting for their bending stiffness and rotational end restraints by free vibration tests. J. Sound Vib. **317**(1), 127–141 (2008)
4. Fang, Z., Wang, J.Q.: Practical formula for cable tension estimation by vibration method. J. Bridge Eng. **17**(1), 161–164 (2012)
5. Zui, H., Shinke, T., Namita, Y.: Practical formulas for estimation of cable tension by vibration method. J. Struct. Eng. **122**(6), 651–656 (1996)

6. Mehrabi, A.B., Tabatabai, H.: Unified finite difference formulation for free vibration of cables. J. Struct. Eng. **124**(11), 1313–1322 (1998)

7. Ricciardi, G., Saitta, F.: A continuous vibration analysis model for cables with sag and bending stiffness. Eng. Struct. **30**(5), 1459–1472 (2008)

8. Chen, C.C., Wu, W.H., Chen, S.Y., Lai, G.: A novel tension estimation approach for elastic cables by elimination of complex boundary condition effects employing mode shape functions. J. Eng. Struct. **166**, 152–166 (2018)

9. Le, X.L., Katsuchi, H.: Estimation of cable tension based on shape function of cable and energy approach. In: Proceedings of Constructional Steel, Japan, vol. 26, pp. 432–439 (2018)

10. Yan, B.F., Chen, W., Yu, J.Y., Jiang, X.: Mode shape-aided tension force estimation of cable with arbitrary boundary conditions. J. Sound Vib. **440**, 315–331 (2019)

11. Liao, W., Ni, Y., Zheng, G.: Tension force and structural parameter identification of bridge cables. Adv. Struct. Eng. **15**(6), 983–996 (2012)

12. Zarbaf, S.E.H.A.M., Norouzi, M., Allemang, R., Hunt, V., Helmicki, A.: Stay cable tension estimation of cable-stayed bridges using genetic algorithm and particle swarm optimization. J. Bridge Eng. **22**(10), 05017008 (2017)

13. Zarbaf, S.E.H.A.M., Norouzi, M., Allemang, R., Hunt, V., Helmicki, A., Venkatesh, C.: Vibration-based cable condition assessment: a novel application of neural networks. Eng. Struct. **177**, 291–305 (2018)

Effect of Static Wind Loads on Reduction of Damping in a Stay Cable with a Damper

Luu Xuan Le, H. Katsuchi, Cuong-Le Thanh, B. X. Luong, Q. X. Do, and N. T. Nguyen

1 Introduction

In the design of cables in cable-stay bridges, a certain level of damping in cables is required to suppress extreme vibrations such as rain-wind-induced vibration or vortex-excited vibration. For example, PTI guide specification [1] suggested that a cable damping ratio equal to 0.5–1.0% would be needed to suppress rain-wind induced. Since intrinsic damping in a stay cable is quite low 0.01–0.2% [2], a damper becomes an alternative to mitigate extreme vibrations of a cable by means of providing additional damping in the cable. Damper attached to a cable plays a role as an energy absorber, and the emerging energy caused by cable vibration will be partially dissipated by installed damper leading to fast decay of cable vibration. Magnetorheological (MR) damper, viscous damper, friction damper, tuned mass damper (TMD) and high damping rubber (HDR) damper are typical options in practice. For many years, such studies on the vibration of a stay cable with a damper have been widely implemented in the context of proposing formulation of added damping, e.g., Pacheco et al. [3], Tabatabai and Mehrabi [4], Krenk [5], Main and Jones [6], Hoang and Fujino [7], and Fujino and Hoang [8]. However, the measured damping in actual cables showed lower damping values than the theoretical ones. For instance, efficiency ratios of 0.6 and 0.3 for viscous damper and HDR damper, respectively, have been reported in an experimental study by Zhou et al. [9]. There are some factors that can be mentioned as the culprits of damping

L. X. Le · H. Katsuchi
Faculty of Civil Engineering, Yokohama National University, Yokohama, Japan

L. X. Le (✉) · B. X. Luong · Q. X. Do
Faculty of Civil Engineering, University of Transport and Communications, Hanoi, Vietnam
e-mail: luusbvl@utc.edu.vn

C.-L. Thanh (✉) · N. T. Nguyen
Faculty of Civil Engineering, Ho Chi Minh City Open University, Ho Chi Minh City, Vietnam

reduction in a cable such as cable sag-extensibility, cable bending stiffness, damper support stiffness or damper stiffness. Recently, Le et al. [10, 11] proposed the reduction of damping in cable triggered by rotational restraint between a cable and damper at a damper location.

In this paper, the reduction of added damping in a cable caused by static wind loads acting on the cable is proposed here for the first time. The results show that in the presence of static wind loads, the global stiffness of a cable increases, leading to an increase in vibration frequency and a significant decrease in the added cable damping.

Based on the best knowledge of the authors, there are two points which make this paper to considerably differ from others: (1) The effect of static wind loads on damper effectiveness is discussed here for the first time; (2) without having static wind loads, reduction of cable damping due to cable self-weight has been raised and solved previously, but such impacts of damper support stiffness, cable bending stiffness and restraint boundary conditions at cable ends on the exact configuration of cable static profile (cable sag) have not been scrupulously and completely discussed.

2 Equation of Motion

Figure 1 shows transverse vibration of a cable with a viscous damper, in which the coordinate system with x-axis passes along the cable length, and y-axis is perpendicular to x. The cable has a chord length l, mass per unit length m, bending stiffness EI, chord tension of cable T and cable inclination angle θ. Restraints at cable ends are assumingly treated as the linear rotational springs with the stiffness k_r. An external viscous damper with damper coefficient c and damper stiffness k_d is attached to the cable at location $y = L_d$.

The cable is depicted in two different configurations: (a) a static deformed shape of a cable under static loads (static state) and (b) cable configuration due to cable motion (dynamic state). For static state, the cable is subjected to the dead loads f (x) which include cable self-weight and static wind load components. Under the dead loads, the cable has the static deflection $y(x)$ as shown in Fig. 1a. For dynamic state, cable starts to vibrate under the dynamic load $g(x, t)$, resulting in the dynamic displacement $v(x, t)$. It is noted that $v(x, t)$ is measured from the reference state $y(x)$.

In this study, the dead loads are composed of cable self-weight and static component of wind loads.

$$f(x) = \frac{1}{2}\rho C_\mathrm{D} D U^2 (\sin \varphi)^2 + mg \times \cos \varphi \tag{1}$$

in which ρ = air density which is set to 1.23 kg/m³; C_D = drag coefficient; D denotes cable diameter; and U = mean wind velocity.

(a) Static state (b) Dynamic state
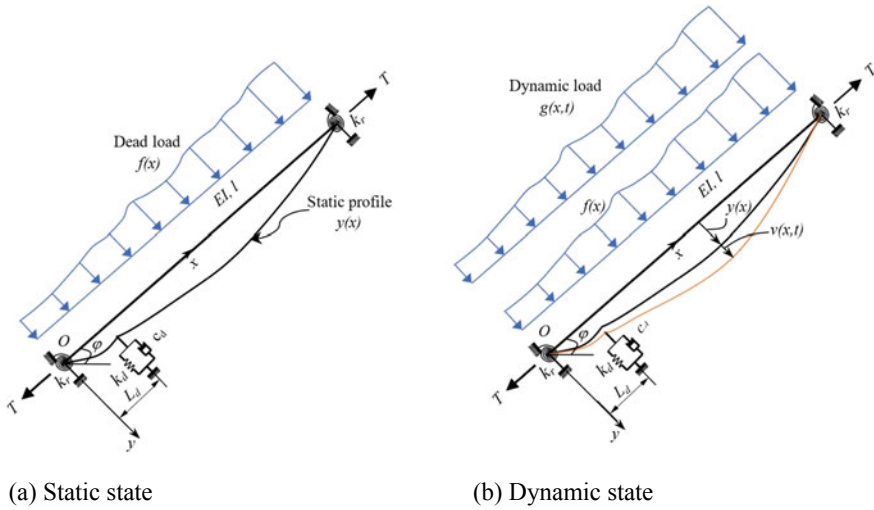
Fig. 1 Schematic diagram of cable with a viscous damper accounting for influence of static wind loads

Although wind flows in many directions, only along wind velocity components are considered in this study, and the impact of its static loads in transverse in-plane vibration of the cable is the objective because the damper is installed for this plane. Figure 2 displays forces acting on cable elements at its position of the static and dynamic equilibrium.

- Equation of equilibrium at rest (static state)

A small cable element is with a length ds, in which dx and dy are lengths of the element along the x and y directions, correspondingly. Under the dead loads $f(x)$, the

(a) Static state (b) Dynamic state
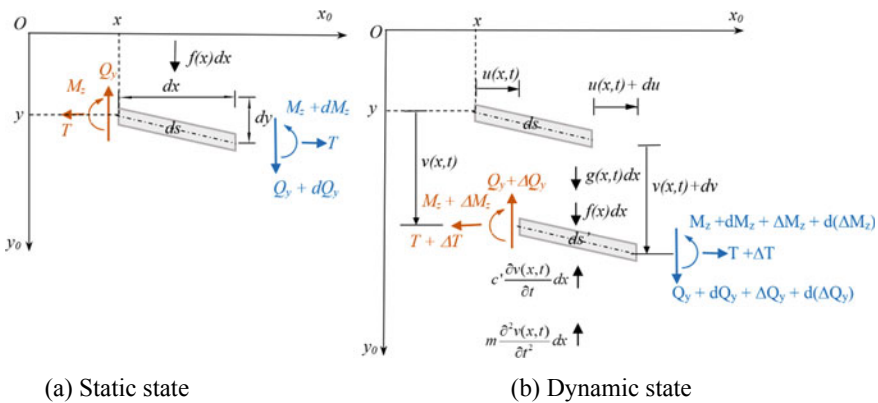
Fig. 2 Cable elements

forces acting on the left-hand side cross section of the element ds are T, Q_y and M_z, and the corresponding forces in the right-hand side of the element ds are T, $Q_y + dQ_y$ and $M_z + dM_z$. It is can be noted that the force equilibrium in the x-direction yields a constant cable force T. Taking force equilibrium along y-axis and bending moment at the centroid of the right-hand side cross section of the element ds give

$$\sum F_y = 0 \Rightarrow dQ_y + f(x)dx = 0 \tag{2}$$

$$\sum M = 0 \Rightarrow Q_y = \frac{dM_z}{dx} + T\frac{dy}{dx} \tag{3}$$

Combination of Eqs. (2) and (3) gives

$$EI\frac{d^4y}{dx^4} - T\frac{d^2y}{dx^2} = f(x) \tag{4}$$

The static profile of the cable will be determined using Eq. (4) under the dead loads $f(x)$ that should satisfy boundary conditions at cable ends and continuity conditions at a damper location.

- Equation of motion (dynamic state)

In dynamic state, the external forces subjected to the cable elements and resulting forces action on the cross sections of the element are illustrated in Fig. 1b, in which ds' is new length of the element; c' is the coefficient of viscous damping per unit length; prefix Δ denotes the increment caused by dynamic effects; and $v(x, t)$ and $u(x, t)$ are transverse and horizontal time-dependent displacements.

$$(ds')^2 = (dx + du)^2 + (dy + dv)^2 \tag{5}$$

Taking force equilibrium along y-axis and bending moment at the centroid of the right-hand side of the cross sections of the element ds'.

$$\sum F_y = 0 \Rightarrow d\Delta Q_y = c'\frac{\partial v(x,t)}{\partial t}dx + m\frac{\partial^2 v(x,t)}{\partial^2 t}dx - g(x,t)dx \tag{6}$$

$$\sum M = 0 \Rightarrow \frac{d\Delta Q_y}{dx} = T\frac{d^2v(x,t)}{dx^2} + \Delta T\frac{d^2y(x)}{dx^2} + \frac{d^2\Delta M_z}{dx^2} \tag{7}$$

Combination of Eqs. (6) and (7) gives equation of motion as

$$m\frac{\partial^2 v(x,t)}{\partial t^2} + c'\frac{\partial v(x,t)}{\partial t} - T\frac{\partial^2 v(x,t)}{\partial x^2} - \Delta T\frac{d^2y(x)}{dx^2} + EI\frac{\partial^4 v(x,t)}{\partial x^4} = g(x,t) \tag{8}$$

in which ΔT = time-dependent additional chord tension caused by vibration of cable.

It is worth noting that for a taut string cable (without sag), this additional force $\Delta T = 0$. In this study, sag-extensibility of a cable is considered owing to the influence of the dead loads on initial cable static profile. It can verify that equation of motion Eq. (8) has the same form of a governing equation of a sagging bending-stiff cable derived by Mehrabi and Tabatabai [12] when static wind loads are not included. So far, equation of motion of a flexural cable has been derived accounting for the effect of dead loads including cable self-weight and static wind loads on cable sag, and these dead loads directly intervene in the cable static deformation $y(x)$ and additional chord tension ΔT.

3   Finite Difference Formulation for Cable Vibration

A finite difference formulation of equation of motion Eq. (8) will be developed here, so that characteristics of cable vibration including the natural frequencies and added cable damping can be determined as results. First of all, the additional cable tension ΔT needs to be derived. The axial strain ε measured from the position of static configuration of the cable is

$$\varepsilon = \frac{ds' - ds}{ds} \tag{9}$$

where

$$ds = \sqrt{dx^2 + dy^2} \tag{10}$$

By expanding Eq. (5) in combination with ds gives

$$ds' = ds\left\{1 + \frac{1}{2}\left[2\frac{\partial u}{\partial s}\frac{dx}{ds} + 2\frac{dy}{ds}\frac{\partial v}{\partial s} + \left(\frac{\partial u}{\partial s}\right)^2 + \left(\frac{\partial v}{\partial s}\right)^2\right]\right\} \tag{11}$$

From which,

$$\varepsilon = \frac{1}{2}\left[2\frac{\partial u}{\partial s}\frac{dx}{ds} + 2\frac{dy}{ds}\frac{\partial v}{\partial s} + \left(\frac{\partial u}{\partial s}\right)^2 + \left(\frac{\partial v}{\partial s}\right)^2\right] \tag{12}$$

On neglecting high-order terms of Eq. (12), one obtains

$$\varepsilon = \left(\frac{dx}{ds}\right)^2\left(\frac{\partial u}{\partial x} + \frac{dy}{dx}\frac{\partial v}{\partial x}\right) \tag{13}$$

The time-dependent additional chord tension ΔT can be expressed as

$$\Delta T = \Delta T(x,t)\frac{\mathrm{d}x}{\mathrm{d}s} \tag{14}$$

where $\Delta T(x, t) = \mathrm{EA} \times \varepsilon$ characterizes the added axial tension due to vibration and EA = cable axial rigidity.

Combination of Eq. (14) with Eq. (13) gives

$$\Delta T \left(\frac{\mathrm{d}s}{\mathrm{d}x}\right)^3 = \mathrm{EA}\left(\frac{\partial u}{\partial x} + \frac{\mathrm{d}y}{\mathrm{d}x}\frac{\partial v}{\partial x}\right) \tag{15}$$

Integration of Eq. (15) with respect to x yields

$$\Delta T = \frac{\mathrm{EA}}{L_e} \int \left[\frac{\partial u}{\partial x} + \frac{\mathrm{d}y}{\mathrm{d}x}\frac{\partial v}{\mathrm{d}x}\right]\mathrm{d}x \tag{16}$$

in which $L_e = \int(\mathrm{d}s/\mathrm{d}x)^3\mathrm{d}x \approx \int[1 + (\mathrm{d}y/\mathrm{d}x)^2]^{3/2}\mathrm{d}x$ denotes the cable length in the static deformed configuration.

For free vibration of a cable, cable deformations and additional tension can be expressed in term of the harmonic forms as

$$v(x,t) = \tilde{v}(x)e^{pt}; \ u(x,t) = \tilde{u}(x)e^{pt}; \ \text{and } \Delta T = \Delta T_0 e^{pt} \tag{17a, b, c}$$

in which $\tilde{v}(x)$ and $\tilde{u}(x)$ are the transverse and axial mode shapes of the cable, respectively; ΔT_0 = time-independent additional tension; and p = complex number.

$$p = -\xi\omega \pm i\omega\sqrt{1 - \xi^2} \tag{18}$$

where ξ = damping ratio and ω = natural angular frequency of undamped vibration.

Substitution of Eqs. (17), (18) and (19) into Eq. (16) gives

$$\Delta T_0 = -\frac{\mathrm{EA}}{L_e}\left[\int \left(\frac{\mathrm{d}^2 y(x)}{\mathrm{d}x^2}\right)\tilde{v}(x)\mathrm{d}x\right] \tag{19}$$

It is noted that Eq. (19) is only valid for non-movable end cable.

By inserting cable solution $v(x, t)$ and additional tension ΔT from Eq. (17) into Eq. (8), free vibration of the cable is obtained as

$$\text{EI}\frac{\partial^4 \tilde{v}(x)}{\partial x^4} - T\frac{\mathrm{d}^2 \tilde{v}(x)}{\partial x^2} - \Delta T_0 \frac{\mathrm{d}^2 y(x)}{\mathrm{d}x^2} + pc'\tilde{v}(x) + p^2 m\tilde{v}(x) = 0 \qquad (20)$$

Finite difference method (FDM) is properly applied in this study to formulate a discretized expression of cable governing equation. To do that, the cable is divided into N elements corresponding to n internal nodes with element length of a, and then, Eq. (20) can be rewritten in the form of the discretized formulation as

$$[K]\{\tilde{v}\} + p[C]\{\tilde{v}\} + p^2[M]\{\tilde{v}\} = 0 \qquad (21)$$

where $[K]$ = cable stiffness matrix; $[C]$ = cable damping matrix; $[M]$ = cable mass matrix; and $\{\tilde{v}\}$ = vector of the nodal displacements.

The transformation from Eq. (20) to Eq. (21) is conducted using finite difference method (FDM). The principle of FDM is to replace such derivatives of the differential equation, Eq. (20), with suitable difference quotients. In this study, the central finite difference scheme is used to approximate the second and fourth derivatives of Eq. (20). Mass matrix $[M]$ and damping matrix $[C]$ are defined as

$$[M] = \begin{bmatrix} m_1 & 0 & 0 & 0 & 0 & 0 \\ 0 & m_2 & 0 & 0 & 0 & 0 \\ 0 & 0 & \cdots & 0 & 0 & 0 \\ 0 & 0 & 0 & m_i & 0 & 0 \\ 0 & 0 & 0 & 0 & \cdots & 0 \\ 0 & 0 & 0 & 0 & 0 & m_n \end{bmatrix}; \text{ and } [C] = \begin{bmatrix} 0 & 0 & 0 & 0 & 0 & 0 \\ 0 & 0 & 0 & 0 & 0 & 0 \\ 0 & 0 & \cdots & 0 & 0 & 0 \\ 0 & 0 & 0 & c/a & 0 & 0 \\ 0 & 0 & 0 & 0 & \cdots & 0 \\ 0 & 0 & 0 & 0 & 0 & 0 \end{bmatrix}$$

$$(22a, b)$$

where m_i = mass per unit length at node i and c = coefficient of viscous damper.

It is noted that damping matrix $[C]$ is a diagonal matrix containing only one component corresponding to the internal node where the viscous damper is attached. In addition, each row of these matrices represents to one node of the discretized cable started from the first node in the left-hand end to the last node of the remaining end.

The stiffness matrix $[K]$ is

$$[K] = [K_1] + [K_2] + [K_3] \qquad (23)$$

where $[K_1]$ = stiffness matrix owing to bending stiffness and static cable tension, $[K_2]$ = stiffness matrix due to additional cable tension and $[K_3]$ = stiffness matrix sourced from damper stiffness.

$$[K_1] = \frac{T}{a^2}\left(\frac{1}{\lambda^2}\right) \begin{bmatrix} \beta n^2 + 2\lambda^2 & -4n^2 - \lambda^2 & n^2 & 0 & 0 & 0 & 0 & 0 \\ -4n^2 - \lambda^2 & 6n^2 + 2\lambda^2 & -4n^2 - \lambda^2 & n^2 & 0 & 0 & 0 & 0 \\ n^2 & -4n^2 - \lambda^2 & 6n^2 + 2\lambda^2 & -4n^2 - \lambda^2 & n^2 & 0 & 0 & 0 \\ 0 & n^2 & -4n^2 - \lambda^2 & 6n^2 + 2\lambda^2 & -4n^2 - \lambda^2 & n^2 & 0 & 0 \\ 0 & \cdots & \cdots & \cdots & \cdots & \cdots & \cdots & 0 \\ 0 & 0 & 0 & 0 & n^2 & -4n^2 - \lambda^2 & 6n^2 + 2\lambda^2 & -4n^2 - \lambda^2 \\ 0 & 0 & 0 & 0 & 0 & n^2 & -4n^2 - \lambda^2 & \beta n^2 + 2\lambda^2 \end{bmatrix}$$

$$(24)$$

where $\lambda = l\sqrt{T/EI}$ characterizes the nondimensional parameter of bending stiffness and β = factor of boundary condition.

$$\beta = \frac{\lambda^2 \bar{k}_r(a/l) - 2}{\lambda^2 \bar{k}_r(a/l) + 2} + 6 \tag{25}$$

in which $\bar{k}_r = k_r/(Tl)$ denotes the dimensionless rotational stiffness at cable ends

It is recognizable that for a cable with hinged ends, $(\bar{k}_r = 0)$ leads to $\beta = 5$, and for a cable with fixed ends, $(\bar{k}_r \to \infty)$ results in $\beta = 7$. In such conventional cases of the cable supports, the stiffness matrix $[K_1]$ shown here is the same as one proposed by Mehrabi and Tabatabai [12].

Stiffness matrix $[K_2]$

$$[K_2] = \mathbf{rs}^T \tag{26}$$

in which vectors $\mathbf{r}$ and $\mathbf{s}$ are defined as

$$\mathbf{s} = [s_1 \ s_2 \ \ldots \ s_i \ \ldots \ s_n]^T; \quad s_i = \left(\frac{y_{i+1} - 2y_i + y_{i-1}}{a^2}\right) \tag{27}$$

$$\mathbf{r} = [r_1 \ r_2 \ \ldots \ r_i \ \ldots \ r_n]^T; \quad r_i = \frac{s_i}{\sum_{i=1}^{n} \frac{\left[\left(\frac{y_{i+1} - y_{i-1}}{2a}\right)^2 + 1\right]^{3/2}}{EA_i}} \tag{28}$$

Stiffness matrix $[K_3]$ is diagonal matrix in which only one value sourced from damper stiffness k_d, corresponding to the internal node containing an attached damper.

$$[K_3] = \begin{bmatrix} 0 & 0 & 0 & 0 & 0 & 0 \\ 0 & 0 & 0 & 0 & 0 & 0 \\ 0 & 0 & \ldots & 0 & 0 & 0 \\ 0 & 0 & 0 & k_d/a & 0 & 0 \\ 0 & 0 & 0 & 0 & \ldots & 0 \\ 0 & 0 & 0 & 0 & 0 & 0 \end{bmatrix} \tag{29}$$

For the eigenvalue problem, Eq. (21) can be rewritten in the following form

$$[\bar{K}]_{2n\times 2n}\{\bar{v}\}_{2n} + p[\bar{M}]_{2n\times 2n}\{\bar{v}\}_{2n} = 0 \qquad (30)$$

where

$$\{\bar{v}\}_{2n} = \begin{Bmatrix} \tilde{v} \\ p\tilde{v} \end{Bmatrix}; \quad [\bar{K}]_{2n\times 2n} = \begin{bmatrix} K & 0 \\ 0 & I \end{bmatrix}; \quad [\bar{M}]_{2n\times 2n} = \begin{bmatrix} C & M \\ -I & 0 \end{bmatrix} \qquad (31a, b, c)$$

By solving Eq. (30), the complex eigenvalues p can be determined which contain the damping ratio ξ and natural frequency ω. According to Eq. (18), these vibration characteristics can be obtained as

$$\omega = \sqrt{(\mathrm{Re}[p])^2 + (\mathrm{Im}[p])^2}; \text{ and } \xi = \frac{-\mathrm{Re}[p]}{|p|} \qquad (32a, b)$$

4 Numerical Investigations

4.1 Verification of the Present Study for a Cable Without Static Wind Effects

The previous studies, especially a work of Tabatabai and Mehrabi [4], presented vibration of a cable with a viscous damper in which sag-extensibility due to cable self-weight was considered. Most of the previous works assumed the cable static profile under self-weight with a simple configuration based on the taut string theory. Cable static deflection derived from the taut string theory takes a second-order parabola without having any effect of cable bending stiffness. Because bending stiffness of a stay cable is often small, the general shape of cable profile might not significantly differ from that of the taut string theory. However, the deflection of a cable near cable ends, especially for fixed supports, relies heavily on cable bending stiffness because of boundary effect. Most importantly, a damper is often practically mounted to a cable at a location very near one cable end; hence, the effect of bending stiffness on the exact static deformed shape, which results in the performance of a damper, should be scrupulously discussed. For that reason, this section will not only verify with the previous study but also take the influence of the cable bending stiffness on attainable damping into account.

Figure 3 shows the static configurations of a cable under its self-weight for small bending stiffness of the cable. It is worth noting that Tabatabai and Mehrabi [4] used a simple form of the cable profile based on the taut string theory (without cable bending stiffness). As can be seen that for a small bending stiffness cable, cable profile developed herein highly coincides with one proposed by Tabatabai and
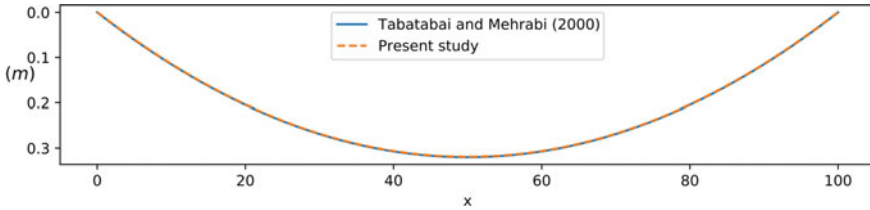
Fig. 3 Cable static profile under self-weight for small bending stiffness ($\lambda = 1000$)
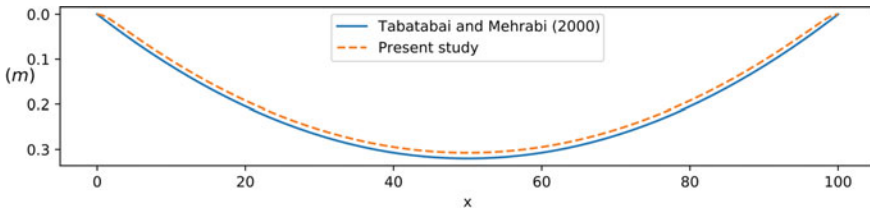
Fig. 4 Cable static profile under self-weight for large bending stiffness ($\lambda = 100$)

Mehrabi [4] whereas it has slight difference in the cable configuration when cable flexural rigidity is large as shown in Fig. 4.

The added damping in a cable versus damper locations is presented in Fig. 5. It appears that for a cable with small bending stiffness, e.g., $\lambda = 1000$, cable sag which used configuration introduced by Tabatabai and Mehrabi [4] without bending stiffness and cable sag with bending stiffness used in this study had the same effects on the cable damping with the error less than 1% between two solutions. However, there was a significant distinction in cable damping between two solutions when cable flexural rigidity is large as depicted in Fig. 5b; for example, the discrepancy of around 10, 5.7 and 4% corresponding to damper locations $L_d/l = 0.01$, 0.02 and 0.03 was found between approaches. It had that difference, especially for a damper

(a) small bending stiffness ($\lambda = 1000$)   (b) large bending stiffness ($\lambda = 100$)
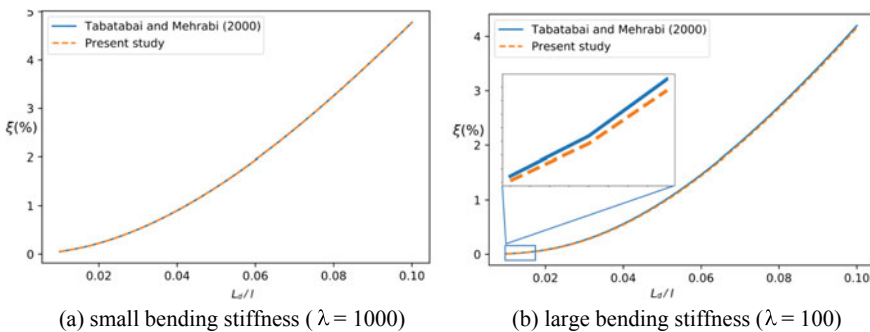
Fig. 5 Cable damping versus damper location (L_d/l)

near cable ends because cable bending stiffness is considered in this paper; hence the static displacement of a cable at cable ends is more constrained in comparison with cable shape developed by string theory which has no ability to fully reflect cable shape with different boundary conditions. As a result, using a simple type of the cable sag without bending stiffness will trigger overestimation the added damping in a stay cable.

4.2 Effect of Static Wind Loads on Cable Frequency and Reduction of Attainable Damping

Cables in cable-stayed bridges are low inherent damping, low rigidity and low-weight structure. Hence, a cable is so susceptible to vibration under external loads, leading to lager amplitude of vibration, excessive stress and fatigue. Although, dampers, one of the countermeasures for mitigation of extreme vibration, are often attached to cable, it shows less effective than expected. When related to cable structure problems, the wind is a flow fundamentally characterized by three time-dependent components. Each wind component includes a mean wind velocity such as U and the fluctuating component such as $u(t)$. For example, wind velocity

$$U(t) = U + u(t) \tag{33}$$

In the presence of wind, the dead loads acting on cable, as shown in Eq. (1), consist of cable self-weight and mean wind forces which represent the static component of wind loads caused by U. It is noted that the mean wind velocity U is only a function of the height above the ground, and in this study, the power law wind profile is used to calculate the mean wind velocity U acting on each cable element.

$$U = U_0 \left(\frac{Z_i}{Z_0} \right)^\alpha \tag{34}$$

in which U_0 = wind speed at the bridge desk level; Z_0 = desk level above the ground, assumed 40 m; Z_i = level of the cable nodes where the mean wind velocity is calculated; and α = the power law exponent which relies on the terrain condition, assumed 0.143 for the open terrain condition.

A cable with the following properties is used in this investigation: length l = 100 m, tension $T = 3 \times 10^6$ N, bending stiffness $EI = 6.75 \times 10^6$ Nm^2, axial stiffness EA = 2.70×10^9 N, mass per unit length m = 78.30 kg/m, cable diameter D = 0.20 m, cable inclination angle $\varphi = 30^0$ and drag coefficient C_d = 1.20. A viscous damper with damper coefficient c = 30,000 N/m/s and damper stiffness k_d = 50 000 N/m is assumingly attached to the cable at the location L_d/l = 0.04.
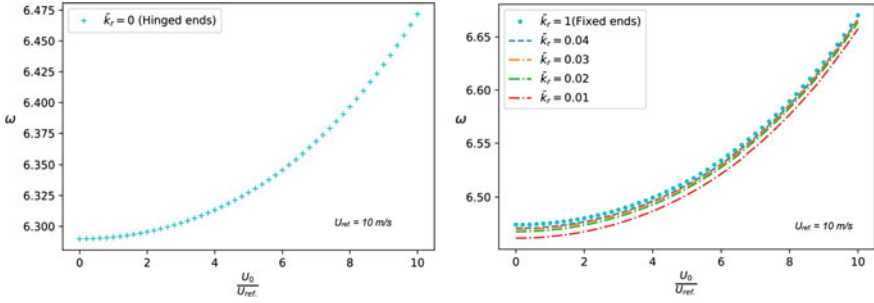
Fig. 6 Increase in cable frequency versus the mean wind speeds
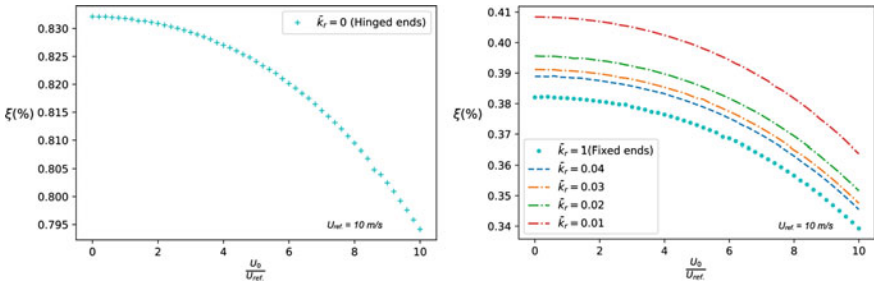
Fig. 7 Reduction of cable damping versus the mean wind speeds

Figure 6 shows the change in cable frequency caused by static wind load component acting on the cable, accounting for various types of boundary conditions including hinged ends, fixed ends and rotational restraint ends. As can be seen, the increase in mean wind speeds results in an increase in cable frequency. This result is also understandable because in the appearance of static wind loads, the global stiffness of the cable is stiffer leading to higher vibration frequency of a cable.

Figure 7 shows the reduction of the added damping in cable due to static wind load effects. In other words, the static component of wind loads existing on a cable triggers the ineffectiveness of damper performance.

5   Conclusions

The present study proposes a solution to determine the natural frequency and attainable damping in a stay cable with a viscous damper, in which effects of cable bending stiffness, damper stiffness and static wind loads on the static configuration of the cable are properly considered.

For a cable with large bending stiffness, cable sag developed from the string theory (without cable bending stiffness) triggers the overestimation of the damping in a cable with a damper installed near a cable end.

In the existence of static wind loads acting on a cable, damper works ineffectively. The reduction of the added damping in a cable depends on the wind velocity and aerodynamic properties of the cable. Cable natural frequency, on the other hand, increases when static wind loads increase.

References

1. PTI Guide Specification: Recommendations for stay cable design, testing and installation. In: Post-Tensioning Institute Committee on Cable-Stayed Bridges, 5th ed. Phoenix, AZ (2007)
2. Gimsing, N.J., Georgakis, C.T.: Cable Supported Bridges: Concept and Design, 3rd edn. Wiley, Chichester, UK (2012)
3. Pacheco, B.M., Fujino, Y., Sulekh, A.: Estimation curve for modal damping in stay cables with viscous damper. J. Struct. Eng. **119**(6), 1961–1979 (1993)
4. Tabatabai, H., Mehrabi, A.B.: Design of mechanical viscous dampers for stay cables. J. Bridge Eng. **5**(2), 114–123 (2000)
5. Krenk, S.: Vibrations of a taut cable with an external damper. J. Appl. Mech. **67**(4), 772–776 (2000)
6. Main, J.A., Jones, N.P.: Free vibrations of taut cable with attached damper. I: Linear viscous damper. J. Eng. Mech. **128**(10), 1062–1071 (2002)
7. Hoang, N., Fujino, Y.: Analytical study on bending effects in a stay cable with a damper. J. Eng. Mech. **133**(11), 1241–1246 (2007)
8. Fujino, Y., Hoang, N.: Design formulas for damping of a stay cable with a damper. J. Struct. Eng. **134**(2), 269–278 (2008)
9. Zhou, H., Xiang, N., Huang, X., Sun, L., Xing, F., Zhou, R.: Full-scale test of dampers for stay cable vibration mitigation and improvement measures. Struct. Monit. Maint. **5**(4), 489–506 (2018)
10. Le, L.X., Katsuchi, H., Yamada, H.: Effect of rotational restraint at damper location on damping of a taut cable with a viscous damper. J. Bridge Eng. **25**(2), 04019139 (2020)
11. Le, L.X., Katsuchi, H., Yamada, H.: Damping of cable with HDR damper accounting for restraint boundary conditions. J. Bridge Eng. **25**(12), 04020105 (2020)
12. Mehrabi, A.B., Tabatabai, H.: Unified finite difference formulation for free vibration of cables. J. Struct. Eng. **124**(11), 1313–1322 (1998)

Characteristics of Semi-rigid Steel Frames with Fuzzy Variables

Viet-Hung Truong and **Phu-Cuong Nguyen**

1 Introduction

In a common structural design, the parameters of geometry, materials, and applied loads of the structure are often considered as deterministic values. However, through the health monitoring of structures, these parameters are confirmed to be uncertain. Lots of studies have been published in the literature to account for the effects of uncertain parameters of the structure and applied loads on structural behaviors and design results (refer [1–5], among others). The results of these works show that these uncertainties considerably influence the structural responses and should be considered in the structural design. It should be noted that, in most of these works, the uncertainty of the structural parameters is assumed to have probabilistic distributions such as normal, log-normal, Gumbel, etc. This assumption is incorrect in the practical design of structure since some structural parameters may not be collected with sufficient information to develop appropriate probabilistic distributions. To solve this issue, these parameters can be represented as fuzzy variables where only the range of their values are known based on limited statistics and engineer design experience. Obviously, since the structural parameters are fuzzy variables, structural responses are fuzzy. To find the range of the structural responses, the method based on optimization algorithms has been considered as a powerful method since it requires much smaller computational effort [6].

Steel frames have been widely used in the construction industry so this structural type has attracted significant interest of the researchers. It is well-known that there

V.-H. Truong (✉)
Thuyloi University, 175 Tay Son, Dong Da, Hanoi, Vietnam
e-mail: truongviethung@tlu.edu.vn

P.-C. Nguyen
Faculty of Civil Engineering, Ho Chi Minh City Open University, Ho Chi Minh City, Vietnam
e-mail: cuong.pn@ou.edu.vn

are several nonlinear inelastic behaviors of a steel frame that come from the stress–strain behaviors of materials, the axial force–bending moment interaction in beams and columns, and the moment–rotation nonlinear relationship in beam–to–column joints [7–10]. Therefore, the steel frame is now usually modeled as a semi-rigid steel frame in order to increase the accuracy in the analysis of the structure [11–15]. Regarding the analysis method for a semi-rigid steel frame, direct analysis is preferred to conventional design methods since this approach allows direct capture of structural load-carrying capacity without requiring the individual member capacity check. Although semi-rigid steel frames have been widely studied, there have been few works concerning the fuzzy behaviors of structural parameters. Eventually, no studies considering fuzzy structural parameters and direct analysis have been done.

To fill this gap of the literature, in this work, we present a method for estimating the fuzzy responses of semi-rigid steel frames with fuzzy variables. A nonlinear inelastic analysis method based on the refined plastic hinge method is employed to predict the load-carrying capacity and displacements of the structure. In addition, the nonlinear behaviors of semi-rigid joints are modeled by using the zero-length element and the Kishi–Chen three-parameter power model. The α-cut method, where the lower- and upper-bounds are calculated by using the micro-genetic algorithm (micro-GA), is used to present the fuzzy characteristics of the structure. The Monte Carlo simulation method is employed to verify the efficiency and accuracy of the proposed method. A semi-rigid two-story frame example is investigated.

2   Direct Analysis of Semi-rigid Steel Frames

To model a semi-rigid steel frame, most direct analysis methods can be divided as finite element and beam–column types. In finite element methods (or plastic-zone methods), the nonlinear responses along the elements are accurately captured by dividing the structural members into many small elements and using interpolation functions. These methods often require much computation time, so they have not been widely applied for the actual design of steel frames. In contrast, in the beam–column methods, the structural members are divided into only one to two elements, and hence, the computational efforts are greatly reduced. Consequently, semi-rigid steel frames are modeled by using beam–column methods in this work.

Beams and columns of the semi-rigid steel frame are modeled as beam–column elements where stability functions are used to predict second-order effects. A refined plastic hinge model in which a member is integrated as an elastic element and the hinges at two of its ends are employed to estimate the inelastic responses. In addition, the nonlinear behaviors of semi-rigid joints are modeled by using the zero-length element [11] and the three-parameter power model [14]. In the zero-length element model, a semi-rigid connection is modeled as three rigid translational springs, two nonlinear bending springs, and one rigid torsional spring as presented in Fig. 1. The three-parameter power model [14] is employed to

present nonlinear moment-rotation relations of semi-rigid joints. The moment M of the connection is calculated as

$$M = \frac{R_{ki}|\theta_r|}{[1 + (|\theta_r|/\theta_0)^n]^{1/n}}, \quad \theta_0 = \frac{M_u}{R_{ki}} \quad (1)$$

where θ_r is the connection rotation; θ_0 is defined as the reference plastic rotation; M_u is the ultimate moment capacity of the connection; R_{ki} is the initial connection stiffness; and, n is the shape parameter.

The generalized displacement control (GDC) algorithm is applied to solve the nonlinear equilibrium equations [1]. Details on this approach can be found in [7–15].

3 Fuzzy Concept for Uncertainties

The concept of fuzzy logic was first introduced in 1965 by Zazeh [16] as follows:

$$A = \{x, \mu_A(x)\}, \quad x \in X \quad (2)$$

where **A** is a subset of **X** that includes all values x having the probability $\mu_A(x) \in [0, 1]$ belongingness to the fuzzy set **A**. If $\mu_A(x) = 1$, x absolutely belongs to **A**. $\mu_A(x)$ may include discrete values or a curved "smooth" line, called the S-type "grade of membership", such as the probability density function of probability distributions. In these cases, the representation of $\mu_A(x)$ function is often very complicated. Therefore, $\mu_A(x)$ is often simplified by expressing in a linear form with many straight lines and called the membership function with a linear conversion. Commonly, a membership function has the trapezoid or triangle diagram. Besides that, owing to the variation of the membership function, the α-cut method is often employed to solve the fuzzy problem design of structures. In the α-cut method, a fuzzy variable that has a complicated membership function is converted
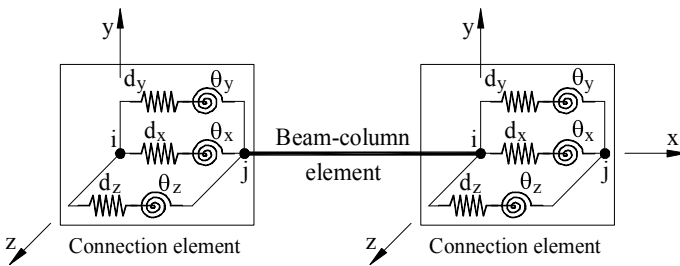
Fig. 1 Zero-length element model for semi-rigid connection

to an interval variable with a specific range. Since then, the output parameter of the fuzzy problem, which is well-known as a fuzzy variable, is estimated by determining the lower- and upper-bounds of its interval. Figure 2 illustrates the α-cut method. With a random value of α in [0,1], a confidence fuzzy interval, A_α is defined as:

$$\mathbf{A} = \{x, \mu_A(x)\} \geq \alpha, \quad x \in \mathbf{X} \tag{3}$$

Furthermore, a fuzzy variable, x, is defined as:

$$x = \{x_L, x_m, x_U\} \tag{4}$$

where x_m is the value of x corresponding to $\alpha = 1$.

4 Fuzzy Analysis of Load-Carrying Capacity of Semi-rigid Frames

By using the direct analysis method presented in Sect. 2, the load-carrying capacity, R, of a semi-rigid frame is directly determined. The safety of the structure is then checked by comparing R with the applied load, S. If R is greater than S, the frame is safe and vice versa. For simplicity, the ratio lf $= R/S$ is defined as the ultimate load factor of the structure. And then, if lf is greater than 1.0, the frame is safe and vice versa.

Assuming $(x_1, x_2, \ldots, x_N)$ are N fuzzy variables of the frame which have triangular membership function. Obviously, lf is a fuzzy variable where its distribution

$$\mu_A(x) = \begin{cases} 0 & \text{if} \quad x < x_L \text{ or } x > x_U \\ \dfrac{x - x_L}{x_m - x_L} & \text{if} \quad x_L \leq x \leq x_m \\ \dfrac{x_U - x}{x_U - x_m} & \text{if} \quad x_L \leq x \leq x_m \end{cases}$$
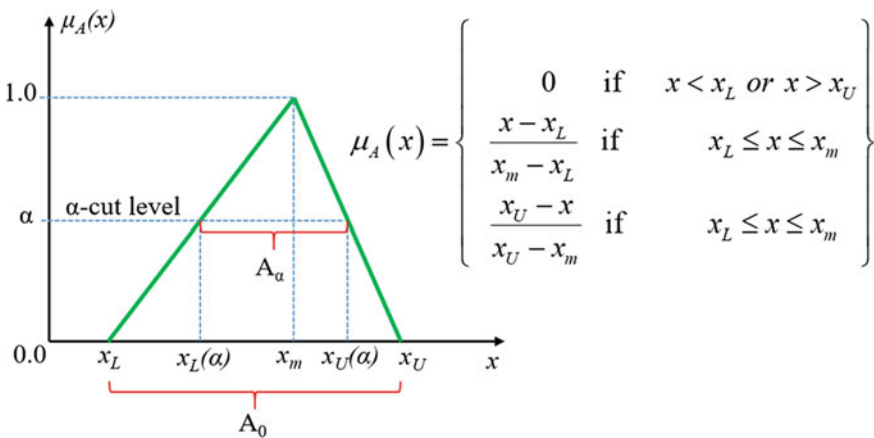
Fig. 2 α-cut method schematic

can be found by using the α-cut method. Corresponding to each α-cut, the interval value of lf is calculated by finding the lower-bound, $lf_L(\alpha)$, and the upper-bound, $lf_U(\alpha)$. The process to determine $lf_L(\alpha)$ and $lf_U(\alpha)$ can be described as an optimization problem to find the minimum and maximum values of lf with the design variables of $(x_1, x_2, \ldots, x_N)$ as follows:

$$
\begin{aligned}
lf_L(\alpha) = \text{minimize}: \quad & lf = \frac{R(x_1, x_2, \ldots, x_N)}{S(x_1, x_2, \ldots, x_N)} \\
f_U(\alpha) = \text{maximize}: \quad & lf = \frac{R(x_1, x_2, \ldots, x_N)}{S(x_1, x_2, \ldots, x_N)} \\
\text{With}: \quad & x_i \in \left[x_{i,L}(\alpha), x_{i,U}(\alpha) \right] \quad i = 1, \ldots, N
\end{aligned}
\tag{5}
$$

The optimization problems described in Eq. (5) are the optimization problems with continuous variables and without the constraints. To solve these optimization problems, there are many different methods that can be used such as direct optimization methods and meta-heuristic algorithms. Due to the highly nonlinear behaviors of the semi-rigid steel frames, meta-heuristic algorithms are often preferred since these methods can balance between finding locally and globally optimal solutions better than direct optimization methods. In this study, micro-GA is used since this method is very efficient in finding promising sectors with a small number of populations. The basic idea of micro-GA is to use a small number of populations in order to increase the convergence speed and then restarting a new population where only the best individual is kept. In this way, the population is restarted several times during the optimization process that can help micro-GA prevent premature convergence. The content of micro-GA can be found in Refs. [4–8, 14, 15], and [17–19].

5 Case Study

A two-story space semi-rigid steel frame is as presented in Fig. 3. The columns and beams are made from A992 steel with the elastic modulus of 200 GPa and the yield stress of 344.5 MPa. With each cross section type of beams and columns, two parameters are considered as fuzzy variables such as cross-sectional area (A) and moment inertial with the strong axis (I). The wind load (W) is acting in the x-direction as the concentrated loads located at the frame nodes. The dead load (DL) and live loads (LL) are considered as the distributed loads on the beams. There are a total of 12 fuzzy variables considered in this case study as presented in Table 1. The considered load combination is (1.2DL + 0.5LL + 1.6W). The parameters for Mimro-GA are the number of individuals = 20; the maximum number of generations = 200. Note that, the objective function to find $lf_U(\alpha)$ is presented as (10-lf). Monte Carlo simulation (MCS) method is employed for comparison with the sample number of 100,000.
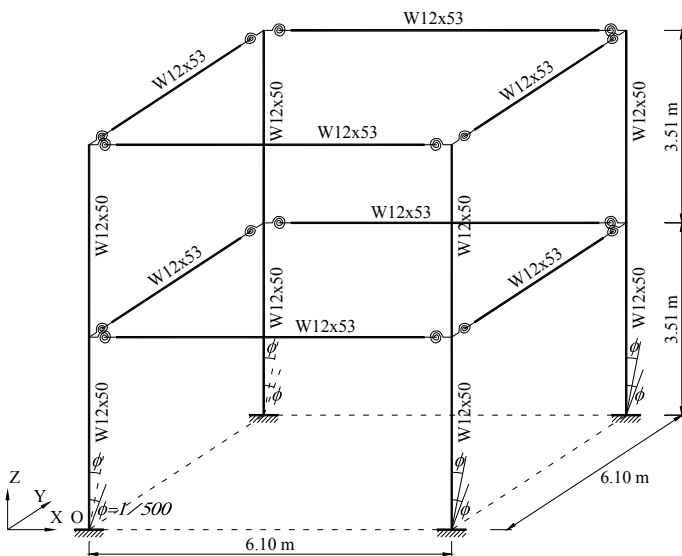
Fig. 3 Two-story space semi-rigid steel frame

Table 1 Fuzzy variable data of two-story space frame

Properties	Variables	Lower-bound	Main value ($\mu = 1$)	Upper-bound	Shape
Material	F_y (Mpa)	310.50	345.0	379.50	Isosceles triangle, dev. = 10%
	E (Gpa)	180	200,000	220,000	Isosceles triangle, dev. = 10%
Column	A (mm^2)	9090	10,100	11,110	Isosceles triangle, dev. = 10%
	I (mm^4)	159,300,000	177,000,000	194,700,000	Isosceles triangle, dev. = 10%
Beam	A (mm^2)	9054	10,060	11,066	Isosceles triangle, dev. = 10%
	I (mm^4)	159,300,000	177,000,000	194,700,000	Isosceles triangle, dev. = 10%
Connection	R_{ki} (kNm/ rad)	42,480	47,200	51,920	Isosceles triangle, dev. = 10%
	M_u (kNm)	74.52	82.80	91.08	Isosceles triangle, dev. = 10%
	n	0.792	0.880	0.968	Isosceles triangle, dev. = 10%
Loading	DL (kN/m)	5.90	6.56	7.21	Isosceles triangle, dev. = 10%
	LL (kN/m)	4.43	4.67	5.41	Triangle, dev. = 10%
	W (kN)	12	13.5	18.0	Triangle, dev. = 20%
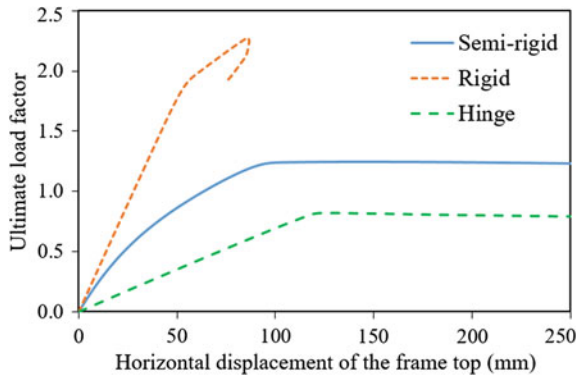
Fig. 4 Load–displacement curves of the frame with different connection types

Figure 4 presents the load–displacement curves of the frame with three types of beam-to-column connections such as rigid, semi-rigid, and hinge. The frame with rigid connections has the greatest ultimate load factor and smallest displacement since this connection type allows fully transferring moments from beams to columns and vice versa. Contrastery, the frame with hinge connections has the smallest ultimate load factor because the connections prevent the transfer moments from the columns to beams.

Figure 5 presents the membership functions approximated by five α-cuts for the ultimate load factor of the frame. As can be seen in this figure, the lower- and upper-bounds of lf obtained by using the proposed method are smaller and greater
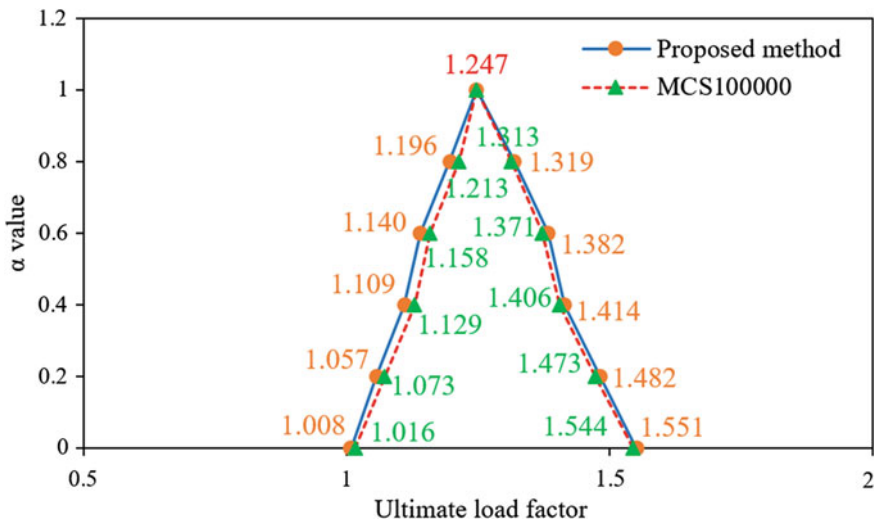
Fig. 5 Fuzzy distribution of the ultimate load factor of the frame

than those of MCS, respectively. It implies that the membership functions of lf obtained by using the proposed method are better than the results of MCS. Furthermore, with each α-cut, the proposed method requires only 8000 structural analyses while MCS spends 100,000. This means that the proposed method is much computationally efficient than MCS.

6 Conclusion

A micro-GA-based method was presented to estimate the load-carrying capacity of semi-rigid steel frames considering fuzzy variables. The fuzzy variables of the frame were presented as triangular fuzzy variables. The load-carrying capacity of the frame was calculated by modeling columns and beams as beam–column elements and semi-rigid connections as the zero-length elements with six springs. The fuzzy characteristics of the structural load-carrying capacity were then predicted by using the α-cut method, where the lower- and upper-bounds were calculated by using the micro-GA algorithm. The efficiency of the proposed method was demonstrated by comparing with the results obtained by using the Monte Carlo simulation method. A semi-rigid two-story space frame example was studied. The numerical results showed that the proposed method was efficient, so it could be considered as an alternative tool for engineers in practical design tasks.

References

1. Truong, V.H., Kim, S.E.: An efficient method of system reliability analysis of steel cable-stayed bridges. Adv. Eng. Softw. **114**, 295–311 (2017)
2. Truong, V.H., Kim, S.E.: An efficient method for reliability-based design optimization of nonlinear inelastic steel space frames. Struct. Multidiscip. Optim. **56**(2), 331–351 (2017)
3. Kim, S.E., Truong, V.H.: Reliability evaluation of semi-rigid steel frames using advanced analysis. J. Struct. Eng. **146**(5), 04020064 (2020)
4. Truong, V.H., Kim, S.E.: Reliability-based design optimization of nonlinear inelastic trusses using improved differential evolution algorithm. Adv. Eng. Softw. **121**, 59–74 (2018)
5. Truong, V.H., Ha, H.M.: Reliability-based design optimization of steel frames using direct design. IOP Conf. Ser.: Mater. Sci. Eng. **869**(5), 052009 (2020)
6. Chakraborty, D., Guha, D., Dutta, B.: Multi-objective optimization problem under fuzzy rule constraints using particle swarm optimization. Method. Appl. **20**, 2245–2259 (2016)
7. Ha, M.H., Vu, Q.V., Truong, V.H.: Optimization of nonlinear inelastic steel frames considering panel zones. Adv. Eng. Softw. **142**, 102771 (2020)
8. Truong, V.H., Ha, M.H., Anh, P.H., Hoc, T.D.: Optimization of steel moment frames with panel-zone design using an adaptive differential evolution. J. Sci. Technol. Civil Eng. (STCE)-NUCE **14**(2), 65–75 (2020)

9. Truong, V.H., Vu, Q.V., Thai, H.T., Ha, M.H.: A robust method for safety evaluation of steel trusses using gradient tree boosting algorithm. Adv. Eng. Softw. **147**, 102825 (2020)
10. Truong, V.H., Vu, Q.V., Dinh, V.T.: A deep learning-based procedure for estimation of ultimate load carrying of steel trusses using advanced analysis. J. Sci. Technol. Civil Eng. (STCE)-NUCE **13**(3), 113–123 (2019)
11. Nguyen, P.C., Kim, S.E.: Investigating effects of various base restraints on the nonlinear inelastic static and seismic responses of steel frames. Int. J. Non-linear Mech. **89**, 151–167 (2017)
12. Nguyen, P.C., Kim, S.E.: A new improved fiber plastic hinge method accounting for lateral-torsional buckling of 3D steel frames. Thin-Walled Struct. **127**, 666–675 (2018)
13. Nghia-Nguyen, T., Shukla, S.K., Nguyen, D.D.C., Lam, L.G., H-Dang, P., Nguyen, P.C.: A new discrete method for solution to consolidation problem of ground with vertical drains subjected to surcharge and vacuum loadings. Eng. Comput.; ahead-of-print (2019)
14. Truong, V.H., Kim, S.E.: A robust method for optimization of semi-rigid steel frames subject to seismic loading. J. Constr. Steel Res. **145C**, 184–195 (2018)
15. Truong, V.H., Nguyen, P.C., Kim, S.E.: An efficient method for optimizing space steel frames with semi-rigid joints using practical advanced analysis and the micro-genetic algorithm. J. Constr. Steel Res. **128**, 416–427 (2017)
16. Zadeh, L.A.: Fuzzy sets. Inf. Control **8**(3), 338–353 (1965)
17. Carroll, D.L: Fortran genetic algorithm (GA) driver v1.7.0. Available http://www.cuaerospace.com/carroll/ga.html
18. Ghannadi, P., Kourehli, S.S.: Model updating and damage detection in multi-story shear frames using salp swarm algorithm. Earthq. Struct. **17**(1), 63–73 (2019)
19. Ghannadi, P., Kourehli, S.S., Noori, M., Altabey, W.A.: Efficiency of grey wolf optimization algorithm for damage detection of skeletal structures via expanded mode shapes. Adv. Struct. Eng. **23**(13), 2850–2865 (2020)

Optimization of Rigid Steel Frames Using Direct Analysis and Improved Differential Evolution Considering Frequency Constraints

Viet-Hung Truong and **Phu-Cuong Nguyen**

1 Introduction

The computing technology development has enabled the use of more refined and complex methods for structural analysis and design such as direct analysis using nonlinear inelastic analysis. Compared to the conventional design methods such as allowable stress design (ASD) and load and resistance factor design (LRFD), direct analysis methods can predict directly the whole system behavior, and hence, capacity check for individual structural members is eliminated [1–5]. Most of the direct analysis methods can be divided into plastic-hinge and plastic-zone methods. Plastic-hinge methods require much smaller computational efforts, while the accuracy of the results is acceptable [6, 7]. Besides that, structural optimization design has attracted significant researchers' interest since it can save much structural cost while design requirements are satisfied. Many works on structural optimization designs have been done in the literature, and they indicated that using direct analysis can yield more realistic and lighter optimum designs [8–14]. In most of these works, constraints of the optimization are the strength and serviceability conditions defined in the standards. To improve the performance of the structure and prevent resonance phenomena, dynamic constraints are also considered by using the conditions relating to structural frequencies [15, 16]. However, according to the authors' knowledge, no studies considering the above constraints simultaneously in the optimization of rigid steel frames have been done, especially using direct analysis.

V.-H. Truong (✉)
Thuyloi University, 175 Tay Son, Dong Da, Hanoi, Vietnam
e-mail: truongviethung@tlu.edu.vn

P.-C. Nguyen
Faculty of Civil Engineering, Ho Chi Minh City Open University,
Ho Chi Minh City, Vietnam
e-mail: cuong.pn@ou.edu.vn

To fill this gap in the literature, we develop a new optimization design problem of rigid steel frames using direct analysis in this work. In this new one, the constraints include the conditions of strengths, service abilities, and structural frequencies. The objective function is the total structural weight. To reduce computational efforts, the plastic-hinge approach using the beam–column element is employed to evaluate the serviceability and strength constraints. An improved DE method is used to solve the proposed optimization problem. A three-bay five-story planar frame is considered to illustrate this work.

2 Direct Analysis of Steel Frames

For performing nonlinear inelastic analysis of steel frames, in this study, beams and columns are modeled as beam–column elements by using the refined plastic-hinge method [17]. In this method, an element is simplified as a beam and two hinges at the ends as presented in Fig. 1. The element is assumed that the beam is always elastic and the yielding is only developed two plastic hinges. Second-order effects are considered by using stability functions [18]. Inelastic effects are estimated by using the tangent modulus concept [18] with the Orbison's yield surfaces [19]. To solve nonlinear equations, the GDC method is used [20]. More information about the refined plastic-hinge method can be found in [17]. Based on the direct analysis, the structural load-carrying capacity, R, can be estimated. The safety of the frame is then checked by comparing R and the factored load combination, S. If R is greater than S, the frame is safe and vice versa. For simplicity, we define $lf = \frac{R}{S}$ as the ultimate load factor of the structure. Now, if lf is greater than 1.0, the frame is safe and vice versa.

Fig. 1 Beam–column element model
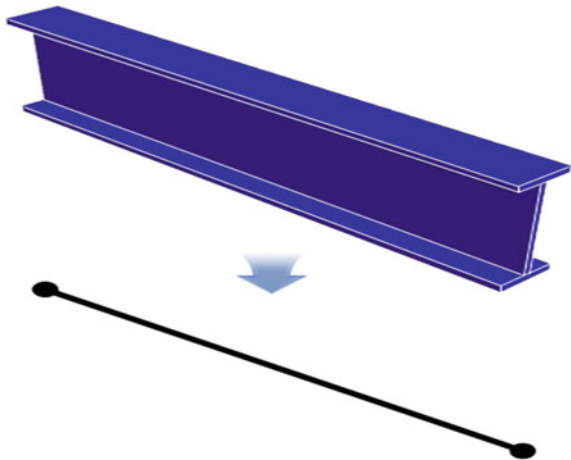
3 Formulation of Optimization of Steel Frames

The optimization of rigid steel frames using direct analysis considering structural frequency constraints can be summarized as

$$\text{Min}: \quad W(\mathbf{X}) = \rho \sum_{i=1}^{N} A_i L_i$$

$$\text{Subjected to}: \quad \begin{cases} 1 - \mathrm{lf}_j \leq 0 & j = 1, \ldots, M_1 \\ \frac{|d_{l,k}|}{[d_{l,k}]} - 1 \leq 0 & l = 1, \ldots, M_2; \ k = 1, \ldots, M_3 \\ \frac{f_t}{[f_t]} - 1 \leq 0 & t = 1, \ldots, M_4 \end{cases} \tag{1}$$

where W is the total weight of the frame; ρ is the material density; L and A are the element's length and cross-sectional area, respectively; $\mathrm{X} = (x_1, x_2, \ldots, x_D)$ is the design variable vector, where x_i represents the order of cross section i in the predefined list; lf is the ultimate load factor of the structure; $d, f, [d]$, and $[f]$ are the inner-story drift, structural frequency, and their allowances, respectively; N and M_3 are the numbers of beam and column groups and structural stories, respectively; M_1, M_2, and M_4 are the numbers of strength, serviceability, and structural frequency constraints, respectively.

To use meta-heuristic algorithms to solve the constrained optimization problem presented in Eq. (2), the penalty function method is used to transform it to unconstrained one as

$$W_{\mathrm{un}}(\mathbf{X}) = \left(1 + \sum_{j=1}^{M_1} \alpha_{1,j} \gamma_{1,j} + \sum_{k=1}^{M_2} \alpha_{2,k} \gamma_{2,k} + \sum_{t=1}^{M_4} \alpha_{3,t} \gamma_{3,t} \right) \times W(\mathbf{X}) \tag{2}$$

In which

$$\begin{cases} \gamma_{1,j} = \max\left(1 - \mathrm{lf}_j, 0\right) \\ \gamma_{2,k} = \sum_{l=1}^{M_2} \max\left(\frac{|d_{k,l}|}{[d_{k,l}]} - 1, 0\right) \\ \gamma_{3,t} = \max\left(\frac{f_t}{[f_t]} - 1, 0\right) \end{cases} \tag{3}$$

where $\alpha_{1,j}$, $\alpha_{2,k}$, and $\alpha_{3,t}$ are the penalty factors for the strength constraint jth, the serviceability constraint kth, and the structural frequency constraint tth, respectively.

4   Improved Differential Evolution Method

The unconstrained optimization problem presented in Eq. (3) is highly nonlinear owing to the discrete characteristics of design variables and nonlinear inelastic behaviors of the structure. For this such optimization problem, meta-heuristic optimization algorithms are preferred since these methods efficiently search the global optimum solutions [8–14, 21, 22]. Among many meta-heuristic algorithms, an improved differential evolution (DE) [12], named as EapDE, is used in this study since it is very efficient for optimizing steel frames. Compared to the original DE method, EapDE is integrated with some improvements to increase its performance for optimizing steel frames using direct analysis. These improvements are as follows.

The first improvement in EapDE is that the mutation strategy used in EapDE is an adaptive strategy which is developed based on "DE/pbest/1" by using the following equation:

$$p = \frac{1}{\text{NP}} + \left(1 - \frac{1}{\text{NP}}\right) \times \frac{DI_{(t)}}{DI_{(0)}} \qquad (4)$$

$$\text{With} \qquad DI_{(t)} = \frac{1}{\text{NP}} \sum_{k=1}^{\text{NP}} \sqrt{\sum_{i=1}^{D} \left(\frac{x_{k,i} - x_{C,i}}{x_i^{\text{UB}} - x_i^{\text{LB}}}\right)^2}, \; x_{C,i} = \frac{1}{\text{NP}} \sum_{k=1}^{\text{NP}} x_{k,i} \qquad (5)$$

where NP and D are the numbers of individuals and design variables, respectively; i, k, and t are the ordinal numbers of the variable, individual, and iteration, respectively; x_i^{UB} and x_i^{LB} are upper- and lower-bounds of x_i. Equations (4) and (5) imply that when $DI_{(t)}$ is large, individuals in the current population may be highly dispersed, so the diversity of individuals should be maintained by using a larger value of p and vice versa.

Besides that, to reduce structural analyses used for evaluating the constraints in the optimization process, EapDE is used multi-comparison technique (MCT) [3]. In MCT, the strength and serviceability load combinations are evaluated in turn to update the unconstrained objective function continuously. If in any analysis steps of load combinations the unconstrained objective function of the trial design variable is greater than that of the target individual, the trial design variable is neglected immediately. By this approach, lots of redundant structural analyses are prevented.

5   Case Study

A three-bay five-story planar steel frame in Fig. 2 is considered. The columns and beams are made from A992 steel with the elastic modulus of 200 GPa and the yield stress of 344.5 MPa. The wind load (W) is acting in the x-direction as the

concentrated loads located at the frame nodes. The dead load (DL) and live loads (LL) are considered as the distributed loads on the beams. Cross sections of columns and beams are divided into 12 design variables as presented in Fig. 2. W10–W44 with 267 sections are used for beams and W12, W14, W18, W21, W24, and W27 with 158 sections are for columns. (1.2DL + 0.5LL + 1.6W) and (1.2DL + 1.6LL) are considered for the strength constraints, while (1.2DL + 0.5LL + 1.6W) is for the serviceability condition. The limit of inter-story is $h/400$. The first three structural frequencies (f_1, f_2, f_3) must be not smaller than 1, 3, and 7 (Hz), respectively. The parameters used for EapDE are: NP = 25, max_iteration = 1000; scale factor = 0.7; and, crossover rate = random in (0,1).

Table 1 shows the best optimum designs of frame among 20 independent optimization times. Two case studies are considered such as considering (1) and neglecting (2) the structural frequency constraints. Table 1 shows that the best optimum design in case 1 is 10,982 (kg) which is much greater than 5699 (kg) of case 2 owing to the effects of structural frequency constraints. The robustness of EapDE is also performed since it requires only 7916 and 9218 structural analyses in cases 1 and 2, respectively. Notes that, with two strength and one serviceability load combinations considered, the traditional approaches require 75,000 structural analyses.

Figure 3 shows the best optimum designs' optimization process. Obviously, the convergence speed of case 2 is better than case 1 since structural frequency constraints are not considered in case 2. In other words, the optimization problem with structural frequency constraints is more complicated. Furthermore, Fig. 4 shows the direct analysis of the best optimum frame in case 1 to present structural nonlinear

Fig. 2 Three-bay five-story frame
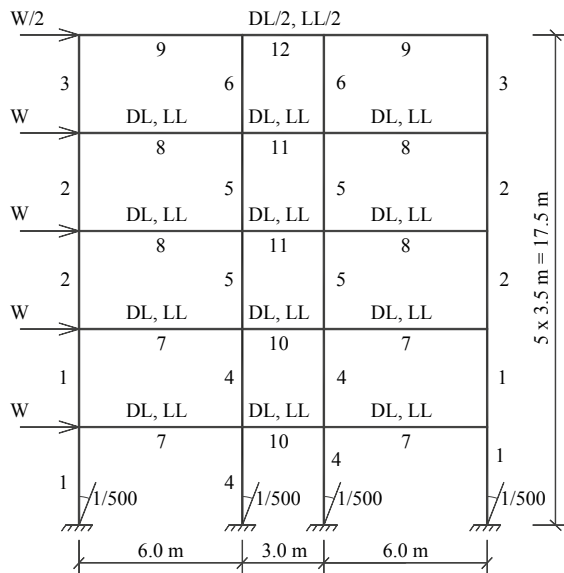
Table 1 Best optimum designs of the frame

Variable group	Considering frequency constraint	Neglecting frequency constraint
1	W18 × 35	W14 × 22
2	W12 × 14	W14 × 22
3	W10 × 17	W12 × 14
4	W30 × 99	W18 × 40
5	W33 × 118	W16 × 26
6	W33 × 118	W10 × 12
7	W16 × 26	W16 × 31
8	W16 × 31	W16 × 26
9	W12 × 19	W12 × 19
10	W24 × 94	W21 × 50
11	W21 × 62	W12 × 26
12	W21 × 55	W12 × 14
Total weight (kg)	10,982	5699
f_1	1.064	–
f_2	3.536	–
f_3	7.037	–
Load factor of (1.2DL + 1.6LL)	1.427	1.069
Load factor of (1.2DL + 0.5LL + 1.6W)	1.012	1.014
Inter-story drift ratio	0.379	0.99
Structural analyses	7916	9218
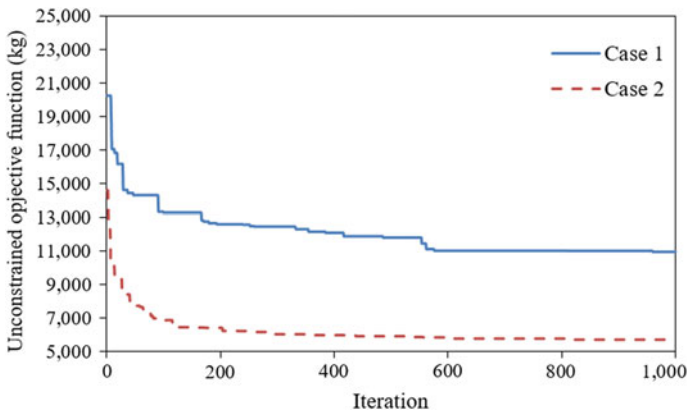
Fig. 3 Optimization process history of the best optimum designs
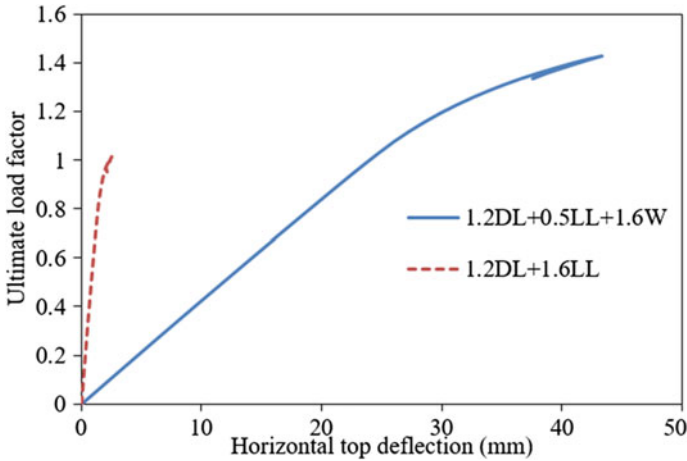
Fig. 4 Nonlinear inelastic behaviors of best optimum design of Case 1

inelastic responses. As can be seen in this figure, the ultimate load factors of both strength load combinations (1.2DL + 0.5LL + 1.6W) and (1.2DL + 1.6LL) are greater than 1.0. This means the frame is satisfied with strength constraints.

6 Conclusion

A new optimization problem of nonlinear inelastic steel frames was proposed. Objective function was the frame weight, while the considered constraints included the strength, serviceability, and structural frequency conditions. The plastic-hinge was employed to estimate nonlinear inelastic behaviors of the frame. An improved DE method, named as EapDE, was employed for optimizer with its robustness in saving computation efforts. A three-bay five-story planar frame with 12 design variables was studied. The numerical results showed that EapDE considerably reduces the required structural analyses for optimization. Furthermore, the proposed optimization problem was more complicated than the optimization problem without considering structural frequency constraints. This opens up a new class of optimization problems that are more complex and more realistic than the optimization problems considered earlier.

References

1. Nghia-Nguyen, T., Shukla, S.K., Nguyen, D.D.C., Lam, L.G., H-Dang, P., Nguyen, P.C.: A new discrete method for solution to consolidation problem of ground with vertical drains subjected to surcharge and vacuum loadings. Eng. Comput.; ahead-of-print (2019)
2. Truong, V.H., Kim, S.E.: An efficient method of system reliability analysis of steel cable-stayed bridges. Adv. Eng. Softw. **114**, 295–311 (2017)
3. Kim, S.E., Truong, V.H.: Reliability evaluation of semi-rigid steel frames using advanced analysis. J. Struct. Eng. **146**(5), 04020064 (2020)
4. Truong, V.H., Vu, Q.V., Thai, H.T., Ha, M.H.: A robust method for safety evaluation of steel trusses using gradient tree boosting algorithm. Adv. Eng. Softw. **147**, 102825 (2020)
5. Truong, V.H., Vu, Q.V., Dinh, V.T.: A deep learning-based procedure for estimation of ultimate load carrying of steel trusses using advanced analysis. J. Sci. Technol. Civil Eng. (STCE)-NUCE **13**(3), 113–123 (2019)
6. Nguyen, P.C., Kim, S.E.: Investigating effects of various base restraints on the nonlinear inelastic static and seismic responses of steel frames. Int. J. Non-linear Mech. **89**, 151–167 (2017)
7. Nguyen, P.C., Kim, S.E.: A new improved fiber plastic hinge method accounting for lateral-torsional buckling of 3D steel frames. Thin-Walled Struct. **127**, 666–675 (2018)
8. Kim, S.E., Truong, V.H.: Reliability-based design optimization of nonlinear inelastic trusses using improved differential evolution algorithm. Adv. Eng. Softw. **121**, 59–74 (2018)
9. Truong, V.H., Kim, S.E.: An efficient method for reliability-based design optimization of nonlinear inelastic steel space frames. Struct. Multidiscip. Optim. **56**(2), 331–351 (2017)
10. Truong, V.H., Ha, H.M.: Reliability-based design optimization of steel frames using direct design. IOP Conf. Ser.: Mater. Sci. Eng. **869**(5), 052009 (2020)
11. Ha, M.H., Vu, Q.V., Truong, V.H.: Optimization of nonlinear inelastic steel frames considering panel zones. Adv. Eng. Softw. **142**, 102771 (2020)
12. Truong, V.H., Ha, M.H., Anh, P.H., Hoc, T.D.: Optimization of steel moment frames with panel-zone design using an adaptive differential evolution. J. Sci. Technol. Civil Eng. (STCE)-NUCE **14**(2), 65–75 (2020)
13. Truong, V.H., Kim, S.E.: A robust method for optimization of semi-rigid steel frames subject to seismic loading. J. Constr. Steel Res. **145C**, 184–195 (2018)
14. Truong, V.H., Nguyen, P.C., Kim, S.E.: An efficient method for optimizing space steel frames with semi-rigid joints using practical advanced analysis and the micro-genetic algorithm. J. Constr. Steel Res. **128**, 416–427 (2017)
15. Kaveh, A., Zolghadr, A.: Democratic PSO for truss layout and size optimization with frequency constraints. Comput. Struct. **130**, 10–21 (2014)
16. Farshchin, M., Camp, C.V., Maniat, M.: Multi-class teaching–learning-based optimization for truss design with frequency constraints. Eng. Struct. **106**, 355–369 (2016)
17. Thai, H.T., Kim, S.E.: Practical advanced analysis software for nonlinear inelastic dynamic analysis of space steel structures. J. Constr. Steel Res. **67**(3), 453–461 (2011)
18. Kim, S.E., Park, M.H., Choi, S.H.: Direct design of three-dimensional frames using practical advanced analysis. Eng. Struct. **23**(11), 1491–1502 (2001)
19. Orbison, J.G.: Nonlinear static analysis of three-dimensional steel frames. Report No. 82-6, Department of Structural Engineering, Cornell University, Ithaca, New York (1982)
20. Yang, Y.B., Shieh, M.S.: Solution method for nonlinear problems with multiple critical points. AIAA J. **28**(12), 2110–2116 (1990)
21. Ghannadi, P., Kourehli, S.S.: Multiverse optimizer for structural damage detection: Numerical study and experimental validation. Struct. Des. Tall Special Build. **29**(13), e1777 (2020)
22. Ghannadi, P., Kourehli, S.S.: Structural damage detection based on MAC flexibility and frequency using moth-flame algorithm. Struct. Eng. Mech. **70**(6), 649–659 (2019)

A Chimp Optimization Algorithm (ChOA) for Vibration-Based Damage Detection of a Damaged Steel Truss

M. Slimani, S. Tiachacht, T. Khatir, S. Khatir, A. Behtani, C. Le Thanh, and M. Abdel Wahab

1 Introduction

In civil engineering structures, structural health monitoring (SHM) plays an important role in damage detection applications. The identification of structural damage is based on three separate stages to define the presence, location, and size of damage. Improved indicator for complex structures, namely modified Cornwel indicator (MCI) was created by Tiachacht et al. [1] for damage detection, localization, and quantification. The provided results were more accurate than the original indicator CI. For more accuracy, the authors used MCI as an objective function to reduce the errors between the exact and estimated results. Khatir et al. [2, 3] used particle swarm optimization (PSO) and genetic algorithm (GA) for damage detection, localization, and quantification in composite beams based on inverse problem. Nobahari and Seyedpoor [4] created an efficient technique for multiple damages detection in simple and complex structures. The results showed that a proposed indicator could accurately estimate the location of damage and its severity. A two-step approach to determine the location and level of multiple

M. Slimani · S. Tiachacht (✉) · A. Behtani
Laboratory of Mechanics, Structure and Energetics (LMSE), Mouloud Mammeri University of Tizi-Ouzou, B.P.N°17 RP, 15000 Tizi Ouzou, Algeria
e-mail: samir.tiachacht@ummto.dz

T. Khatir
Department of Technology, University Centre of Naama—Salhi Ahmed, P.O. Box 66, 45000 Naama, Algeria

S. Khatir · C. Le Thanh
Faculty of Civil Engineering, Ho Chi Minh City Open University, Ho Chi Minh City, Vietnam

M. Abdel Wahab
Soete Laboratory, Faculty of Engineering and Architecture, Ghent University, Technologiepark Zwijnaarde 903, B-9052 Gent, Belgium

damages based on the information fusion technique and GA was investigated in [5]. Ghannadi et al. [6] used grey wolf optimization (GWO) algorithm for SHM of 3D structures. The objective function was based on frequencies and mode shapes to compare measured and calculated values by GWO. Two experimental examples were studied using a cantilever beam and a truss tower to validate the proposed approach. Multiverse optimizer (MVO) is used to address the issue of damage detection by Ghannadi and Kourehli [7]. Two objective functions were used to solve the inverse problem based on the modal assurance criterion (MAC) and modified total modal assurance criterion (MTMAC).

In this paper, a convergence study and CPU time analysis of chimp optimization algorithm (ChOA) are presented. Two structures are used to test the accuracy of ChOA using frequencies and mode shapes as modal parameters.

2 A Chimp Optimization Algorithm (ChOA)

Khishe and Mosavi [8] created a novel metaheuristic algorithm called chimp optimization algorithm (ChOA) extracted by the individual intelligence and sexual motivation of chimps in their group hunting, which is different from the other social predators (Fig. 1). ChOA is intended to further alleviate the two problems of the slow speed of convergence and local optima trapping in solving high-dimensional problems. Mathematical model of diverse intelligence and sexual motivation of chimps is presented based on Ref. [8].

Fig. 1 First phase of the hunting process [8]

In this due regard, during the exploration and exploitation phases, the prey is hunted. Equation (1) is provided to model the driving and chasing of prey mathematically.

$$\begin{cases} d = \left| c \cdot \chi_{\text{prey}}(t) - m \cdot \chi_{\text{chimp}}(t) \right| \\ \chi_{\text{chimp}}(t+1) = \chi_{\text{prey}}(t) - a \cdot d \end{cases} \tag{1}$$

where t denotes the number of the current iteration, a, m and c are the coefficient vectors, χ_{prey} represents the vector of prey position and χ_{chimp} represents the position vector of a chimp. a, m and c vectors can be calculated by using Eq. (2), i.e.:

$$\begin{cases} a = 2 \cdot f \cdot r_1 - f \\ c = 2 \cdot r_1 \\ m = \text{Chaotic\_value} \end{cases} \tag{2}$$

where r_1 and r_2 are the random vectors in the range of [0,1]. Finally, m is a chaotic vector calculated based on a various chaotic map so that this vector represents the effect of the sexual motivation of chimps in the hunting process. We assume that there is a probability of 50% to choose between either the normal updating position mechanism or the chaotic model to update the position of chimps during optimization. The mathematical model is expressed by the following formulation.

$$x_{\text{chimp}}(t+1) = \begin{cases} x_{\text{prey}}(t) - a \cdot d & \text{if } \mu < 0.5 \\ \text{Chaotic\_value} & \text{if } \mu \geq 0.5 \end{cases} \tag{3}$$

where μ is a random number in the range [0,1].

3 Numerical Examples

Two different structures, namely 10 and 25-bar plane trusses, are used to examine the effectiveness and accuracy of the ChOA for damage identification based on natural frequencies and mode shapes.

3.1 FEM of Truss Structures

In this section, the details of the two structures are explained. Firstly, 10-bar planar truss with a non-structural mass of 454.0 kg is attached to the free nodes. This structure has been used as an example in the field of structural optimization by

several researchers, e.g. Kaveh and Zolghadr [9]. The structure has 8 DOFs as shown in Fig. 2a. Table 1 presents the mechanical and geometrical properties of this structure. Secondly, 25-bar plane truss is modelled in MATLAB software using FEM. The structure consists of 25 elements and 21 DOFs. Truss elements are made from a steel material with Young's modulus $E = 200$ GPa, Poisson's ratio $\upsilon = 0.3$, density $\rho = 7.8 \times 10^3$ Kg m^{-3}, and cross-sectional areas are given ($A_{1-6} = 18$ cm^2; $A_{7-12} = 15$ cm^2; $A_{13-17} = 10$ cm^2 and $A_{18-25} = 12$ cm^2). A numerical model of the truss structure is described in Fig. 2b.

Several damage scenarios with different damage levels are considered for both structures as presented in Table 2 to investigate the robustness of ChOA for the detection of location, severity, and number of the damaged elements.

The frequencies of both structures for healthy and damaged cases are listed in Tables 3 and 4.

4 ChOA for Damage Detection and Quantification

4.1 Objective Functions

For more accuracy, two objective functions based on frequencies and mode shapes are considered to test the robustness of ChOA. In all cases, the population size is
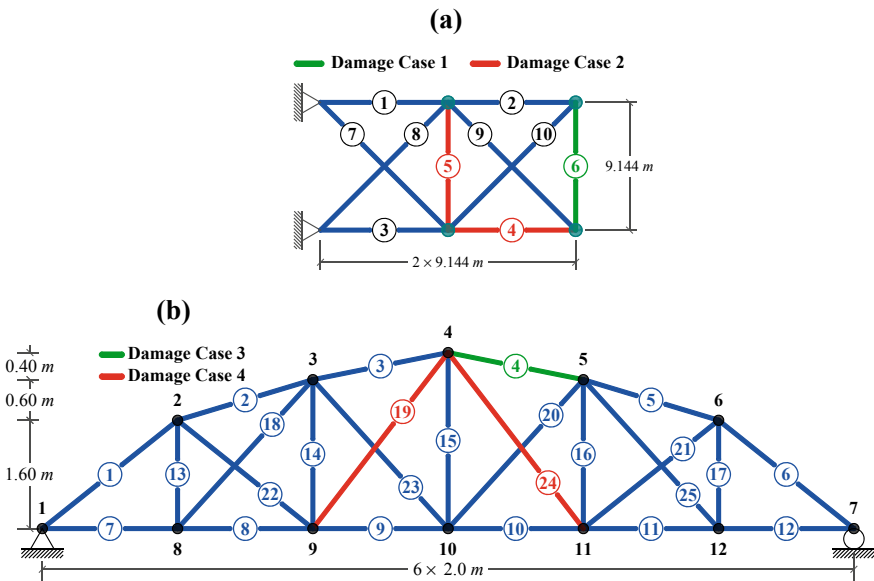
Fig. 2 FE model of planner truss: **a** a 10-bar plane truss and **b** a 25-bar plane truss

Table 1 Material properties of the 10-bar planar truss

Property (unit)	Value
E, modulus of elasticity (N/m^2)	6.98×10^{10}
S, cross-sectional area of the members (m^2)	0.0025
Added mass (kg)	454.0
ρ, material density (kg/m^3)	2770.0
L, main bar's dimension (m)	9.144

Table 2 Different damage scenarios

10-bar plane truss				25-bar plane truss			
Case 1	Element no.	6	–	Case 3	Element no.	4	–
	Damage ratio (%)	20	–		Damage ratio (%)	20	–
Case 2	Element no.	4	5	Case 4	Element no.	19	24
	Damage ratio (%)	25	35		Damage ratio (%)	25	35

Table 3 Frequencies (Hz) of damaged and undamaged structures (10-bar planar truss)

Mode no.	Undamaged		Damage	
	FEM [9]	FEM	Case 1	Case 2
1	6.6421	6.6421	6.6421	6.6102
2	19.9916	19.9916	19.9772	19.1983
3	21.4192	21.4192	21.4192	21.0964
4	37.8057	37.8057	37.8057	37.4086
5	43.2929	43.2929	39.8818	39.6510

Table 4 Frequencies (Hz) of damaged and undamaged structures (25-bar plane truss)

Mode no.	Undamaged		Damage	
	FEM [10]	FEM	Case 3	Case 4
1	30.30	30.25	29.93	30.24
2	69.00	68.73	68.02	68.56
3	96.30	96.04	96.03	95.45
4	181.80	181.18	181.06	180.32
5	223.20	222.53	214.91	222.28
6	275.60	274.72	273.89	268.87
7	321.60	320.53	320.37	318.01
8	352.00	350.91	350.88	346.70
9	357.70	356.51	356.39	352.87
10	373.00	371.78	371.12	363.65

fixed to 2000 and 100 iterations are used. The first objective function provided for damage detection and quantified is presented in the following formulation:

$$OF1 = \sqrt{\frac{1}{r}\sum_{i=1}^{r}\frac{(\omega_i^c - \omega_i^m)^2}{(\omega_i^m)^2}} \quad i = 1,\ldots,r \tag{4}$$

where ω_i^c is the frequency computed by optimization technique, ω_i^m is the measured frequency and r denotes the order number of modes used. The second objective function is based on the mode shape using MAC formulation as mentioned in the following formulation:

$$OF2 = \sum_{j=1}^{r}\left|MAC_j^{Measured} - MAC_j^{Calculated}\right| \tag{5}$$

where $MAC_j^{Measured}$ represents the modal assurance criteria calculated from numerical or experimental analysis and $MAC_j^{Calculated}$ represents the modal assurance criteria calculated in the process of ChOA based on a reduction in stiffness.

The changes of mode shapes can be evaluated quantitatively using a well-known correlation measure, and the modal assurance criteria (MAC), between two mode shapes measured $\left(\psi_i^m\right)$ and calculated $\left(\psi_j^c\right)$, which is defined as:

$$MAC = \frac{\left|\left(\psi_i^m\right)^T \cdot \psi_i^c\right|^2}{\left(\left(\psi_i^m\right)^T \psi_i^m\right)\left(\left(\psi_i^c\right)^T \psi_i^c\right)} \tag{6}$$

4.2   10-Planar Bar Truss

Two cases are considered using both objective functions. The results are plotted based on fitness and convergence of damaged elements in Figs. 3, 4, 5 and 6.

The results of ChOA are accurate and fast for single and multiple damaged elements with a different damage rate for simple 2D structure using frequencies and mode shapes as an objective function.

4.3   25-Planar Bar Truss

In the second structure, two cases are considered and the results are presented in Figs. 7, 8, 9 and 10.
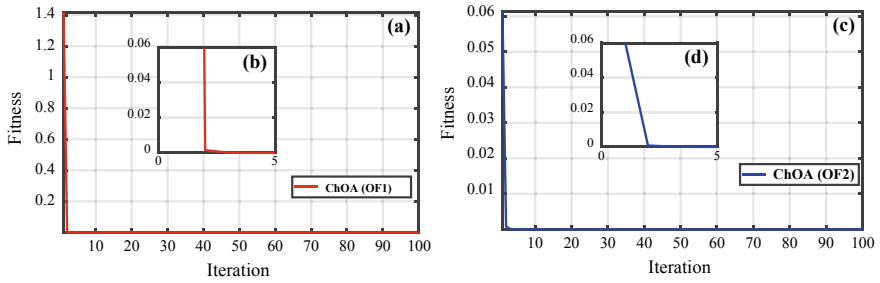
Fig. 3 10-planar bar truss—case 1—convergence study of the fitness: **a** ChOA (OF1), **b** zoom in area ([0–5]^x; [0–0.06]^y), (c) ChOA (OF2), and (d) zoom in area ([0–5]^x; [0–0.06]^y)
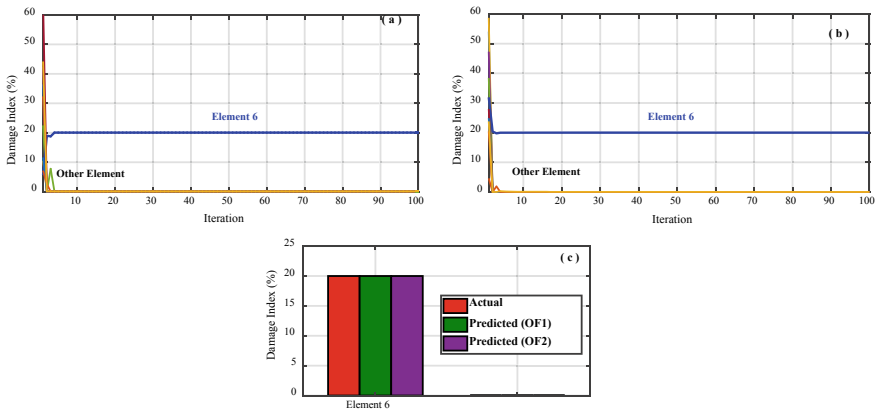
Fig. 4 10-planar bar truss—case 1—damage index: **a** ChOA (OF1), **b** ChOA (OF2), and **c** severity
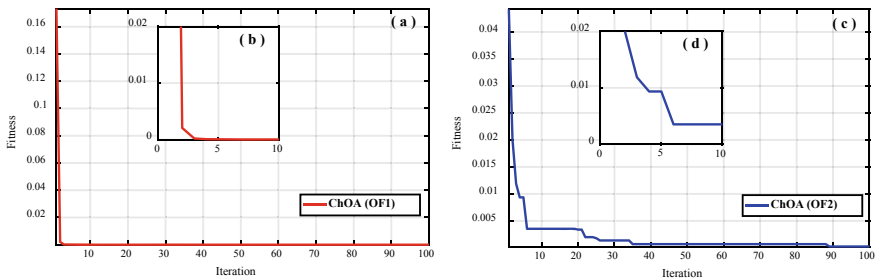
Fig. 5 10-planar bar truss—case 2—convergence study of the fitness: **a** ChOA (OF1), **b** zoom in area ([0–10]^x; [0–0.02]^y), **c** ChOA (OF2), and **d** zoom in area ([0–10]^x; [0–0.02]^y)
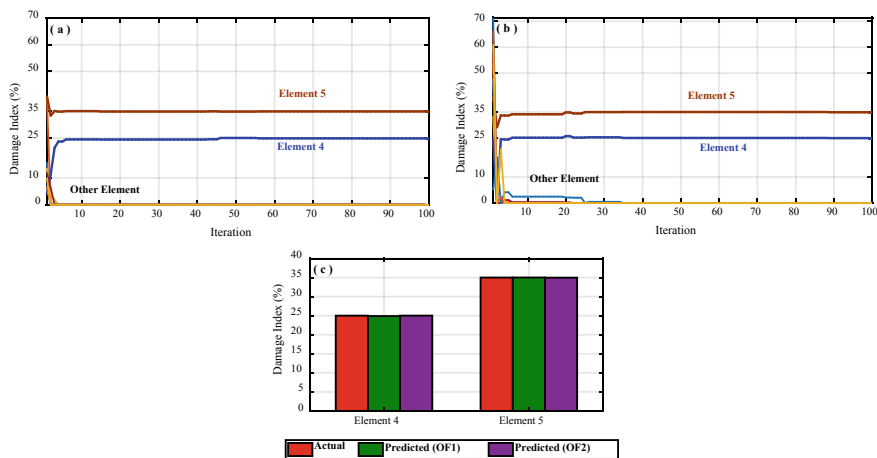
Fig. 6 10-planar bar truss—case 2—damage index: **a** ChOA (OF1), **b** ChOA (OF2), and **c** severity
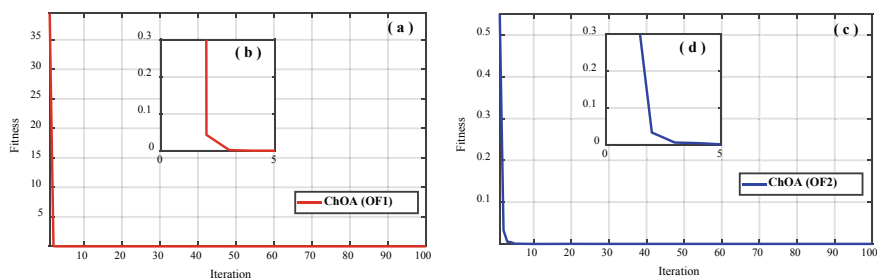
Fig. 7 25-planar bar truss—case 3—convergence study of the fitness: **a** ChOA (OF1), **b** zoom in area ($[0–5]^x$; $[0–0.3]^y$), **c** ChOA (OF2), and **d** zoom in area ($[0–5]^x$; $[0–0.3]^y$)

The results of ChOA for 25-bar truss structure are effective and fast for single and multiple damaged elements with a different damage rate for simple 2D structure using frequencies and mode shapes as an objective function. Table 5 presents CPU time of ChOA convergence study for both structures based on the two objective functions.

The CPU time for each case using both objective functions are very close. This proves the robustness of ChOA during the processes. More details for the convergence study are presented in Table 6.
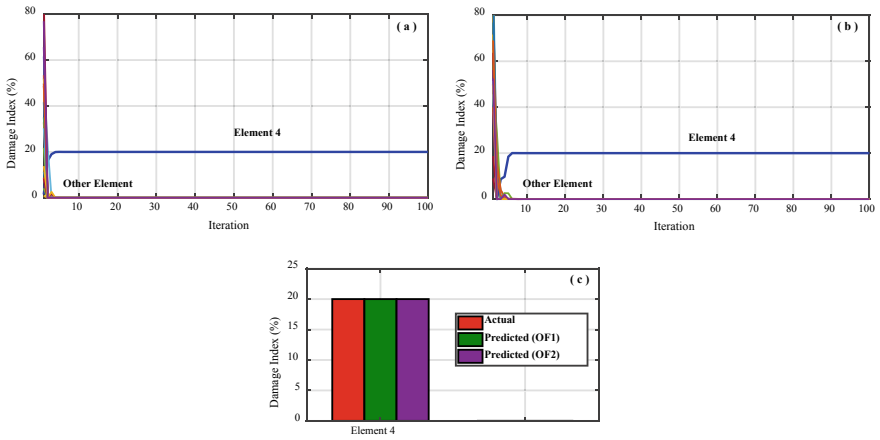
Fig. 8 25-planar bar truss—case 3—damage index: **a** ChOA (OF1), **b** ChOA (OF2), and **c** severity
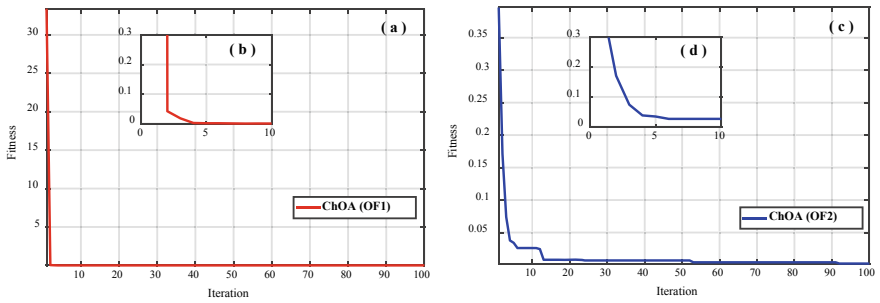
Fig. 9 25-planar bar truss—case 4—convergence study of the fitness: **a** ChOA (OF1), **b** zoom in area ($[0–10]^x$; $[0–0.3]^y$), **c** ChOA (OF2), and **d** zoom in area ($[0–10]^x$; $[0–0.3]^y$)
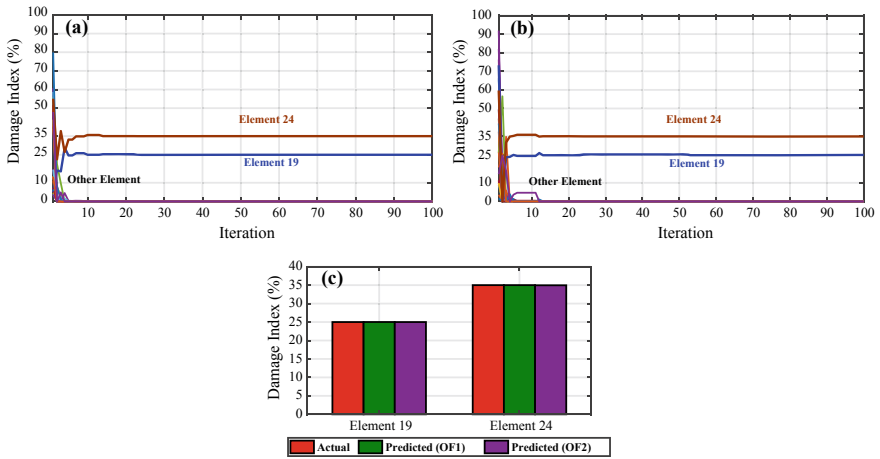
Fig. 10 25-planar bar truss—case 4—damage index: **a** ChOA (OF1), **b** ChOA (OF2), and **c** severity

Table 5 CPU time compared with ChOA

10-planar bar truss			25-planar bar truss		
	ChOA (OF1)	ChOA (OF2)		ChOA (OF1)	ChOA (OF2)
Case 1	199.304335	217.939051	Case 3	714.136983	708.122492
Case 2	213.259931	217.341468	Case 4	669.281186	734.439839

Table 6 Evolution of a different objective function

Iteration no.	10-planar bar truss				25-planar bar truss			
	Case 1		Case 2		Case 3		Case 4	
	ChOA (OF1)	ChOA (OF2)	ChOA (OF1)	ChOA (OF2)	ChOA (OF1)	ChOA (OF2)	ChOA (OF1)	ChOA (OF2)
1	1.4187	0.0613	0.1733	0.0442	39.4898	0.5505	33.4080	0.3965
10	2.35E−08	3.41E−06	1.29E−05	0.0035	1.96E−08	6.46E−07	0.00014	0.0261
20	3.47E−09	1.01E−06	1.13E−05	0.0034	8.34E−10	4.78E−07	3.74E−05	0.0080
30	3.94E−11	1.01E−06	1.13E−05	0.0014	8.34E−10	3.17E−07	1.41E−06	0.0070
40	3.94E−11	8.12E−07	1.13E−05	0.0007	8.34E−10	3.17E−07	3.86E−08	0.0070
50	3.94E−11	8.12E−07	1.10E−06	0.0007	9.45E−11	3.17E−07	3.86E−08	0.0070
60	3.94E−11	8.12E−07	4.60E−07	0.0007	3.29E−12	3.17E−07	3.86E−08	0.0041
70	4.46E−12	2.19E−07	4.60E−07	0.0007	3.29E−12	3.17E−07	3.86E−08	0.0041
80	4.46E−12	2.19E−07	4.60E−07	0.0007	3.29E−12	3.17E−07	3.86E−08	0.0041
90	4.46E−12	2.19E−07	3.78E−07	0.0003	2.08E−12	3.17E−07	3.86E−08	0.0041
100	2.25E−12	2.19E−07	3.78E−07	0.0003	2.08E−12	3.17E−07	3.86E−08	0.0022

5   Conclusion

This paper studies the damage identification in 10 and 25-bar plane truss structures based on inverse problem using ChOA. MATLAB software using FEM is used to build models for both structures. Single and multiple damages cases with different levels are investigated to study the effectiveness of ChOA. The objective function is based on the measured and calculated frequencies and mode shapes to study the convergence of fitness and damaged elements. The ChOA provided good results for both structures after a few iterations.

References

1. Tiachacht, S., et al.: Damage assessment in structures using combination of a modified cornwell indicator and genetic algorithm. Eng. Struct. **177**, 421–430 (2018)
2. Khatir, S., et al.: Damage detection and localization in composite beam structures based on vibration analysis. Mechanics **21**(6), 472–479 (2015)
3. Khatir, S., et al.: Multiple damage detection in composite beams using particle swarm optimization and genetic algorithm. Mechanika **23**(4), 514–521 (2017)
4. Nobahari, M., Seyedpoor, S.M.: An efficient method for structural damage localization based on the concepts of flexibility matrix and strain energy of a structure. Struct. Eng. Mech. **46**(2), 231–244 (2013)
5. Guo, H., Li, Z.: A two-stage method to identify structural damage sites and extents by using evidence theory and micro-search genetic algorithm. Mech. Syst. Signal Process. **23**(3), 769–782 (2009)
6. Ghannadi, P., et al.: Efficiency of grey wolf optimization algorithm for damage detection of skeletal structures via expanded mode shapes. Adv. Struct. Eng., 1369433220921000 (2020)
7. Ghannadi, P., Kourehli, S.S.: Multiverse optimizer for structural damage detection: Numerical study and experimental validation. Struct. Des. Tall Special Build., e1777 (2020)
8. Khishe, M., Mosavi, M.R.: Chimp optimization algorithm. Expert Syst. Appl., 113338 (2020)
9. Kaveh, A., Zolghadr, A.: An improved CSS for damage detection of truss structures using changes in natural frequencies and mode shapes. Adv. Eng. Softw. **80**, 93–100 (2015)
10. Esfandiari, A., et al.: Structural model updating using frequency response function and quasi-linear sensitivity equation. J. Sound Vib. **326**(3–5), 557–573 (2009)

Comparison of Swarm Intelligence Algorithms for Optimization Problems

Hoang-Le Minh, Van Hai Luong, and Cuong-Le Thanh

1 Introduction

In the two last decades, the optimization algorithms have become more and more attractive. New algorithms have been presented such as particle swarm optimization (PSO) [1], artificial bee colony (ABC) [2], firefly algorithm (FA) [3], genetic algorithm (GA) [4], differential evolution (DE) [5], evolution strategy (ES) [6], ant colony optimization (ANT) [7], cuckoo search (CS) [8], and gray wolf optimizer (GWO) [9]. The common features of these algorithms are all inspired by the animals' search for food in nature. This process attempted to simulate mathematical formulas. All algorithms have outstanding features such as simple programming, fast convergence speed, and accuracy with acceptable errors. These algorithms appeared in almost fields including the economic system, engineering problem. It leads to finding that a remarkable algorithm that can solve the problem with suitable and high reliability is necessary. For that, in this paper, comparing the reliability of four algorithms PSO, ABC, CS, and GWO, in which, PSO and ABC algorithms are known as classical algorithms, and their significant features are widely acknowledged. CS and GWO algorithms are recently proposed as the new algorithms, and the main characteristic of these algorithms is improved accuracy. In order to comprehensively evaluate the advantages and disadvantages of the above algo-

H.-L. Minh · C.-L. Thanh (✉)
Faculty of Civil Engineering, Ho Chi Minh City Open University, Ho Chi Minh City, Vietnam
e-mail: cuong.lt@ou.edu.vn

V. H. Luong
Faculty of Civil Engineering, Ho Chi Minh City University of Technology (HCMUT), 268 Ly Thuong Kiet Street, Ward 14, District 10, Ho Chi Minh City 70000, Vietnam

V. H. Luong
Vietnam National University Ho Chi Minh City (VNU-HCM), Linh Trung Ward, Thu Duc, Ho Chi Minh City 70000, Vietnam

rithms, the paper investigated the search space having 30 dimensions to compare the performance of all four algorithms in two terms; the convergence rate and accuracy level.

2 Swarm Intelligence Algorithms

Particle Swarm Optimization (PSO)

Particle swarm optimization (PSO) is proposed by Eberhart and Kennedy [1]. The feature of this algorithm is based on the balance of global best (G_{best}) and local best ($L_{\text{best},i}$) during the velocity update. Thus, each candidate solution $X_i (i = 1, 2, \ldots, n)$ at the step of movement $(t + 1)$th registers the new position which is closer to the local best or global best position. During their movement, solution candidates also expand the new search spaces through the two factors defined as learning factors c_1, c_2. The process of updating the new velocity and position of the PSO algorithm is described in Eqs. 1 and 2.

$$V_i^{t+1} = wV_i^t + c_1 r_1 \left(L_{\text{best},i} - X_i^t \right) + c_2 r_2 \left(G_{\text{best}} - X_i^t \right) \tag{1}$$

$$X_i^{t+1} = X_i^t + V_i^{t+1} \tag{2}$$

where r_1, r_2 register the value in the range [0,1], w is denoted an inertia weight to control the velocity.

Artificial Bee Colony (ABC)

The artificial bee colony (ABC) [2] algorithm is a swarm-based meta-heuristic algorithm that was introduced by Karaboga in 2005. The search process of ABC has three major steps:

- Send the employed bees to a food source and estimate their nectar quality following Eq. 3;

$$v_{i,j} = x_{i,j} + \phi_{i,j} \left(x_{i,j} - x_{k,j} \right) \tag{3}$$

  where $k \in \{1, 2, \ldots, \text{SN}\}$ is randomly chosen index; k is determined randomly and should differ from i. $\phi_{i,j}$ register the value in the range [0,1].

- Onlooker bees select the food sources based on information collected from employed bees and estimate their nectar quality expressed in Eq. 4;

$$p_i = \frac{\text{fit}_i}{\sum_{i=1}^{\text{SN}} \text{fit}_i} \tag{4}$$

  where fit_i is the fitness value of the solution ith.

- Determine the scout bees and employ them on possible food sources for exploitation.

The general structure of the algorithm is introduced as follows.

The food source of which the nectar is abandoned by the scout bees is replaced with a new food source by the scouts by Eq. (7) in case the position cannot be improved further. The parameter *limit* is the control parameter to determine the abandonment of the food sources within the predetermined number of cycles.

Cuckoo search Algorithm (CS)

Cuckoo search algorithm (CS) is also a nature-inspired algorithm, lied on the development of the population of cuckoo bird in nature. This algorithm was introduced by Yang and Deb [8]. This algorithm lied on Lévy flights having the step length s to orient the new direction. An outstanding advantage of this algorithm is that it can produce a suitable distribution in which its values can be registered positive or negative. Thus, at the step of movement, $(t + 1)$th follows Eq. 5

$$X_i^{t+1} = X_i^t + \alpha L(s, \lambda) \tag{5}$$

where

α: Scaling factor;
X_i^{t+1} and X_i^t are new position and current position of cuckoo bird.
$L(s, \lambda)$: is Lévy distribution, used to define the step size of random walk.

Gray Wolf Optimizer (GWO)

Gray wolf optimizer (GWO) is proposed by Mirjalili et al. [9]. Based on the hunting characteristics of wolves, with a division of tasks for each of the wolves, the leader in the swarm is called alpha (α). The alpha considers the best solution, the second and third best solution namely beta (β) and delta (δ). The process of hunting and attract toward the prey can simulate in mathematical form as:

$$\overrightarrow{D_a} = \left| \overrightarrow{C_1} \cdot \overrightarrow{X_a} - \overrightarrow{X} \right|, \ \overrightarrow{D_\beta} = \left| \overrightarrow{C_2} \cdot \overrightarrow{X_\beta} - \overrightarrow{X} \right|, \ \overrightarrow{D_\delta} = \left| \overrightarrow{C_3} \cdot \overrightarrow{X_\delta} - \overrightarrow{X} \right| \tag{6}$$

$$\overrightarrow{X_1} = \overrightarrow{X_a} - \vec{A_1}(\vec{D_\alpha}), \ \overrightarrow{X_2} = \overrightarrow{X_\beta} - \vec{A_2}(\vec{D_\beta}), \ \overrightarrow{X_3} = \overrightarrow{X_\delta} - \vec{A_3}(\vec{D_\delta}) \tag{7}$$

$$\vec{X}(t+1) = \frac{\vec{X_1} + \vec{X_2} + \vec{X_3}}{3} \tag{8}$$

Table 1 First ten classical benchmark functions

Function	Solution space (S)	$f_{\min}$
$F_1(x) = \sum_{i=1}^n x_i^2$	$[-100,100]^D$	0
$F_2(x) = \sum_{i=1}^n |x_i| + \prod_{i=1}^n |x_i|$	$[-100,100]^D$	0
$F_3(x) = \sum_{i=1}^n \left(\sum_{j=1}^i x_j\right)^2$	$[-100,100]^D$	0
$F_4(x) = \max\{|x_i|, 1 \leq i \leq n\}$	$[-100,100]^D$	0
$F_5(x) = \sum_{i=1}^{n-1}\left[100(x_{i+1}-x_i^2)^2 + (x_i-1)^2\right]$	$[-30,30]^D$	0
$F_6(x) = \sum_{i=1}^n ([x_i+0.5])^2$	$[-100,100]^D$	0
$F_7(x) = \sum_{i=1}^n i x_i^4 + \text{rand}(0,1)$	$[-1.28,1.28]^D$	0
$F_8(x) = \sum_{i=1}^n -x_i \sin\left(\sqrt{|x_i|}\right)$	$[-500,500]^D$	$-418.9829 \times D$
$F_9(x) = \sum_{i=1}^n [x_i^2 - 10\cos(2\pi x_i) + 10]$	$[-5.12,5.12]^D$	0
$F_{10}(x) = -20\exp\left(-0.2\sqrt{\frac{1}{n}\sum_{i=1}^n x_i^2}\right) - \exp\left(\frac{1}{n}\sum_{i=1}^n \cos(2\pi x_i)\right)$ $+ 20 + e$	$[-32,32]^D$	0

Note n is the dimension of function, $f_{\min}$ is the minimum value of the function, and S is a subset of R^n
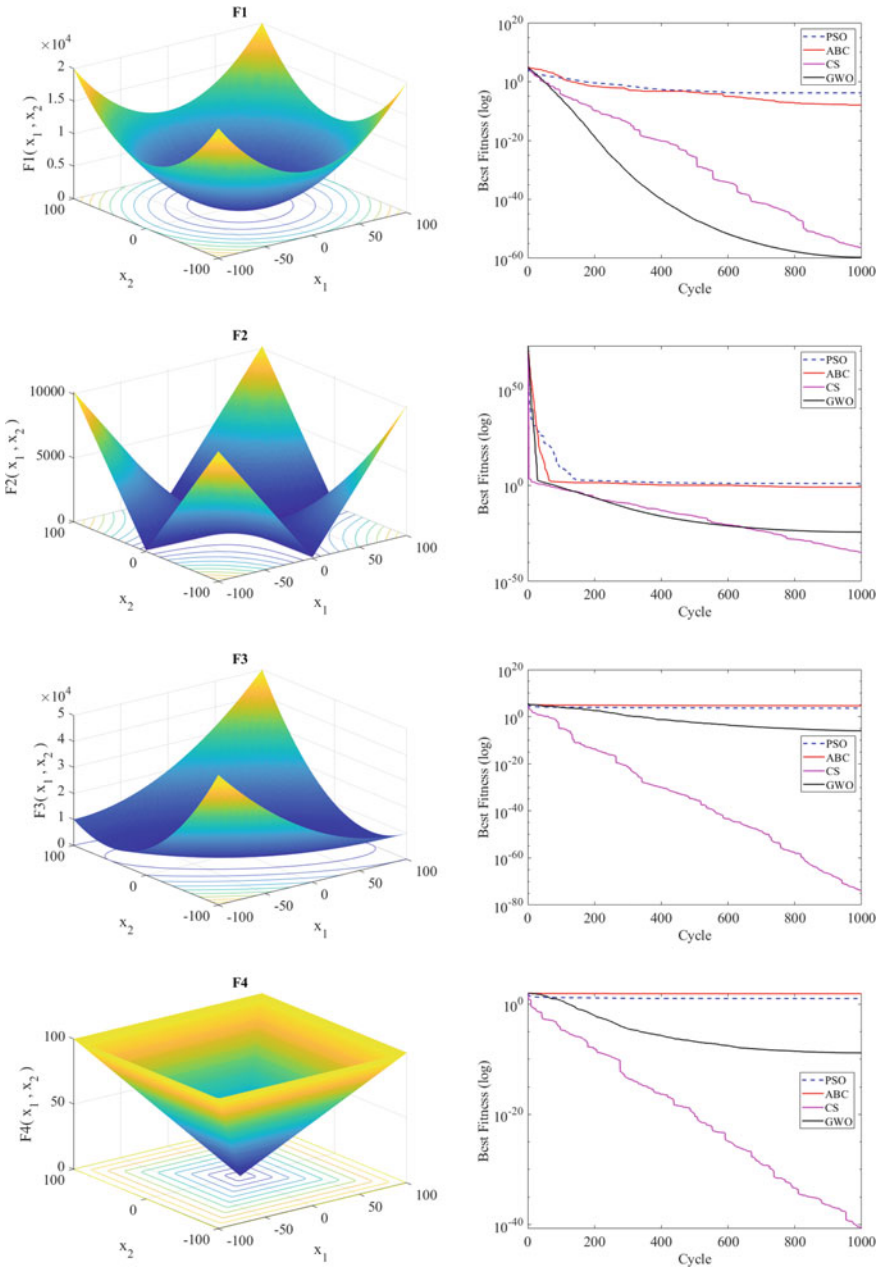
Fig. 1 Convergence trends of the 15 benchmark functions
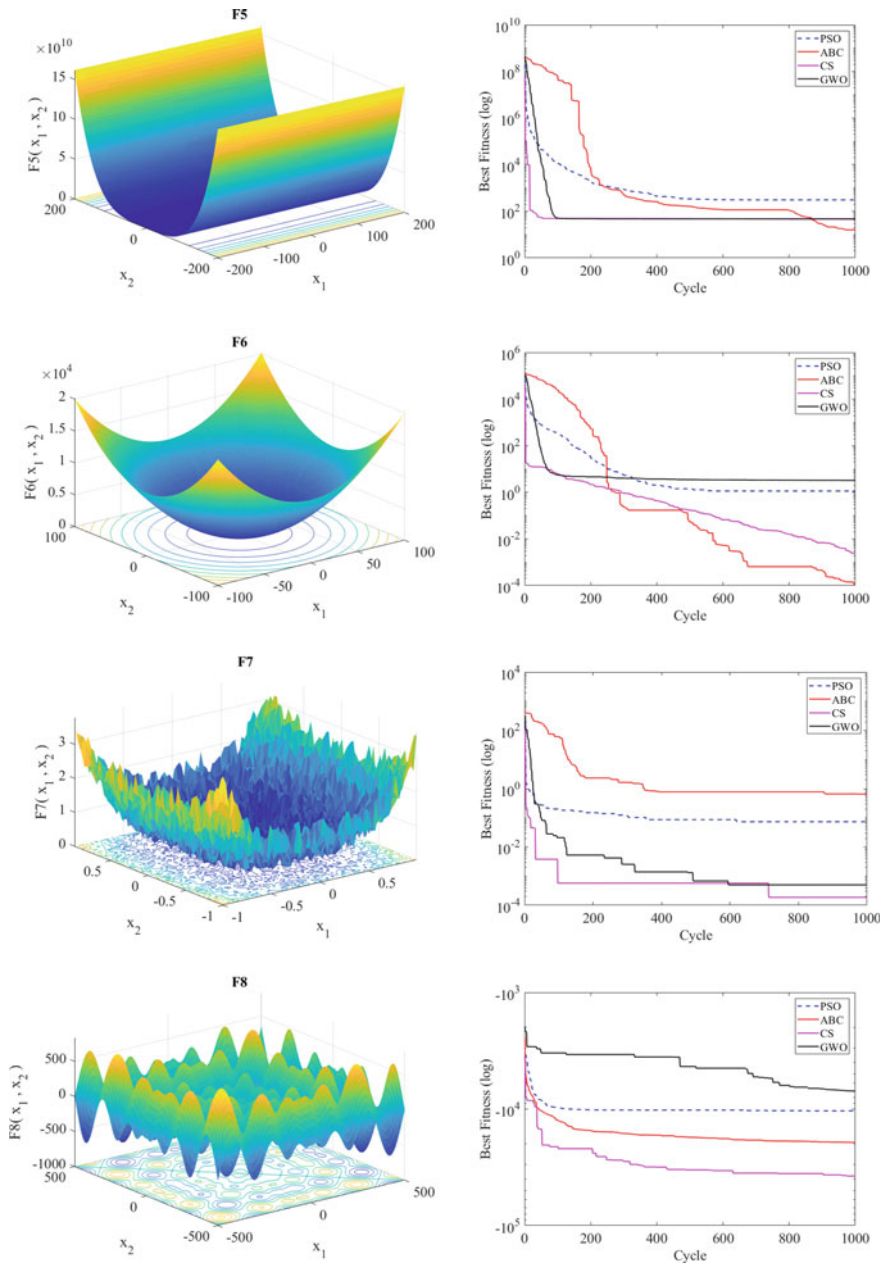
Fig. 1 (continued)
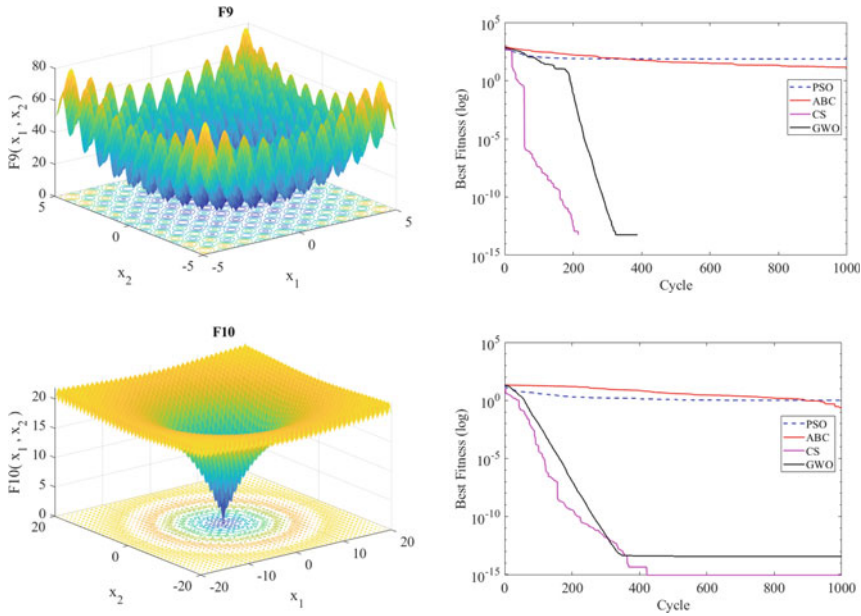
Fig. 1 (continued)

where

$$A_{1,2,3}^{\rightarrow} = 2\vec{a}\vec{r}_1 - \vec{a}$$
$$C_{1,2,3}^{\rightarrow} = 2\vec{r}_2$$

$$(9)$$

In Eq. 9, the vector $\vec{a}$ is a reduction function from 2 to 0. $\vec{r}_1$ and $\vec{r}_2$ are random scalar having a value in range [0,1].

3   Numerical Examples

To compare the efficiency of algorithms PSO, ABC, CS, and WGO, the first ten benchmark test functions were selected to examine and are given in Table 1. All functions have the same search space with $n = 30$ dimension, the results are presented in two terms; comparing the convergence rate and accuracy level for each function.

For fair in comparison, all algorithms have the same initial solution candidates $N = 30$, and a total of iterations are 1000. The convergence trend of all functions is shown in Fig. 1. The comparison results obtained from 30 runs randomly in both algorithms are given in Table 2 in the case of 30 dimensions. Terms of best fitness,

Table 2 Results of ten benchmark functions in comparison between other algorithms with dimension $n = 30$

Functions		Algorithms			
		PSO	ABC	CS	GWO
F_1	Best fitness	6.766E−15	8.691E−10	7.286E−63	4.507E−61
	Mean best	8.062E−09	4.939E−09	3.357E−54	3.866E−59
	Standard deviation	1.718E−08	2.834E−09	1.051E−53	7.328E−59
F_2	Best fitness	4.492E+01	5.395E−02	2.583E−42	1.975E−25
	Mean best	2.143E+02	1.075E−01	2.393E−37	8.889E−25
	Standard deviation	1.812E+02	5.030E−02	5.652E−37	6.630E−25
F_3	Best fitness	2.370E+03	3.840E+04	2.039E−86	1.389E−10
	Mean best	3.602E+03	4.766E+04	2.867E−73	9.081E−07
	Standard deviation	9.782E+02	6.160E+03	8.540E−73	1.442E−06
F_4	Best fitness	8.011E+00	6.303E+01	9.555E−44	1.194E−10
	Mean best	9.558E+00	7.309E+01	9.866E−39	2.677E−09
	Standard deviation	1.108E+00	5.507E+00	2.384E−38	3.763E−09
F_5	Best fitness	1.962E+02	5.553E+00	4.482E+01	4.608E+01
	Mean best	2.758E+02	5.416E+01	4.566E+01	4.719E+01
	Standard deviation	6.909E+01	4.062E+01	4.948E−01	9.445E−01
F_6	Best fitness	2.245E−05	6.944E−06	2.795E−03	1.004E+00
	Mean best	2.351E−02	4.407E−05	4.999E−03	2.339E+00
	Standard deviation	6.120E−02	3.231E−05	2.584E−03	6.083E−01
F_7	Best fitness	4.794E−02	5.844E−01	6.479E−05	5.927E−04
	Mean best	7.211E−02	7.055E−01	4.646E−04	1.326E−03
	Standard deviation	1.587E−02	1.075E−01	2.649E−04	8.006E−04
F_8	Best fitness	−1.181E+04	−1.974E+04	−5.181E+04	−1.139E+04
	Mean best	−9.137E+03	−1.926E+04	−4.659E+04	−9.530E+03
	Standard deviation	1.586E+03	2.759E+02	3.588E+03	1.071E+03
F_9	Best fitness	3.980E+01	5.074E+00	0.000E+00	0.000E+00
	Mean best	5.435E+01	1.035E+01	0.000E+00	5.092E−01
	Standard deviation	1.417E+01	2.333E+00	0.000E+00	1.610E+00
F_{10}	Best fitness	1.566E+00	1.102E−02	8.882E−16	2.931E−14
	Mean best	2.312E+00	7.359E−02	8.882E−16	3.393E−14
	Standard deviation	4.393E−01	6.909E−02	0.000E+00	4.447E−15

mean, and standard deviation are investigated after obtaining the results from 30 runs randomly.

Based on the convergence trend shown in Fig. 1, it can be realized that two algorithms, CS and GWO, illustrate the better performance of convergence rate at functions F_1–F_5, F_9–F_{10}. Especially, at the F_9 function, the CS and GWO algorithms achieved the best value which are registered around 200 and 400 of iterations, respectively. Meanwhile, the ABC algorithm shows a good convergence rate at F_8 functions. And PSO records the worst convergence rate among the algorithms.

Based on the results statistics given in Table 2, it can be seen that the CS and GWO algorithms are given the best level of accuracy response in almost functions investigated. Especially at the functions F_1–F_5, the CS algorithm has shown superiority when the best fitness value is far ahead of the other algorithms. Meanwhile, the accuracy of PSO and ABC still recorded worse performance in comparison with the CS and GWO algorithms. However, at function F_6, the ABC algorithm achieved the most accurate level.

4 Conclusion

In this paper, a comparison between the algorithms presented such as PSO, ABC, CS, and GWO to analyze optimization problems. The first ten benchmark functions are used as numerical examples to investigate the convergence rate and accuracy response of the algorithms. Through the achieved results, the CS algorithm is considered to be a stable and highly reliable algorithm in solving the real works, while the PSO and ABC algorithms recognize an instability in some cases particular problems.

References

1. Kennedy, J., Eberhart, R.: Particle swarm optimization. In: Proceedings of ICNN'95 International Conference on Neural Networks. IEEE (1995)
2. Karaboga, D., Basturk, B.: On the performance of artificial bee colony (ABC) algorithm. Appl. Soft Comput. **8**(1), 687–697 (2008)
3. Yang, X.-S.: Firefly algorithm, stochastic test functions and design optimisation. Int. J. Bio-inspired Comput. **2**(2), 78–84 (2010)
4. Mühlenbein, H.: Genetic algorithms (1997)
5. Storn, R., Price, K.: Differential evolution–a simple and efficient adaptive scheme for global optimization over continuous spaces. J. Glob. Optim. **11**(4), 341359 (1997)
6. Rechenberg, I.: Evolution strategy: nature's way of optimization. In: Optimization: Methods and Applications, Possibilities and Limitations, pp. 106–126. Springer (1989)

7. Dorigo, M., Gambardella, L.M.: Ant colony system: a cooperative learning approach to the traveling salesman problem. IEEE Trans. Evol. Comput. **1**(1), 53–66 (1997)
8. Yang, X.-S., Deb, S.: Cuckoo search via Lévy flights. In: 2009 World Congress on Nature and Biologically Inspired Computing (NaBIC). IEEE (2009)
9. Mirjalili, S., Mirjalili, S.M., Lewis, A.: Grey wolf optimizer. Adv. Eng. Softw. **69**, 46–61 (2014)

Genetic and Particle Swarm Optimization Algorithms for Damage Detection of Beam-like Structures Using Residual Force Method

Morteza Saadatmorad, Mostafa Siavashi, Ramazan-Ali Jafari-Talookolaei, Mohammad Hadi Pashaei, Samir Khatir, and Cuong-Le Thanh

1 Introduction

Due to the importance of preventing unexpected structural failures, vibration-based damage detection methods have been widely investigated over the last few decades to monitor the health of various structures. These methods are considered as efficient and reliable non-destructive techniques for damage detection of structures. Generally, damaged structures problems can be divided into two main categories including forward problems and inverse problems. In the forward problems, the natural frequencies and mode shapes of a damaged structure are determined using damage size and location. In contrast, in the inverse problems, the damage size and location are determined using modal parameters of the damage [1]. In the forward problems, an experimental method is usually used to find the natural frequencies and mode shapes of a damaged structure. In addition, there are other methods, such as the finite element method (FEM) and damage modeling method to model and find the natural frequencies and mode shapes of a damaged structure. Also, in recent decades, many methods have been developed for solving inverse problems.

One of the most popular inverse damage detection methods is the optimization-based method. In this method, the optimization problem is formulated using the objective function based on modal parameters such as natural frequencies,

M. Saadatmorad · M. Siavashi · R.-A. Jafari-Talookolaei (✉) · M.-H. Pashaei
Department of Mechanical Engineering, Babol Noshirvani University of Technology, Babol, Mazandaran Province, Iran
e-mail: ra.jafari@nit.ac.ir

S. Khatir
Soete Laboratory, Faculty of Engineering and Architecture, Ghent University, Technologiepark Zwijnaarde 903, 9052 Zwijnaarde, Belgium

C.-L. Thanh
Faculty of Civil Engineering, Ho Chi Minh City Open University, Ho Chi Minh City, Vietnam

143

mode shapes, and other modal damage indicators. Various researches have presented different optimization algorithms for finding optimum values of the optimization-based damage detection problems.

Dinh-Cong et al. [2] used the Jaya algorithm for detecting damage in plate-like structures. Gomes et al. [3] applied a sunflower optimization algorithm (SFOA) in order to identify damage in laminated composite plates. Mishra et al. [4] presented an antlion optimization algorithm (ALO) in order to identify damages in structures based on vibration data. Maity et al. [5] proposed a genetic algorithm (GA) for evaluating damages in structures based on changes in natural frequencies. In this study, it was demonstrated that GA can find damages with proper precision. Alexandrino et al. [6] presented a multi-objective GA in order to detect damages in a plate structure. In this robust optimization, authors demonstrated that using the multi-objective GA, artificial neural network (ANN), and fuzzy set theory as a tool for decision making in order to the best solution can be very useful. In Barman et al. [7], the performance of particle swarm optimization (PSO) algorithm and continuous ant colony optimization (ACOr) in order to detect damages in plane and space truss structure was compared. The proposed objective function was based on frequency and mode shapes. Another optimization-based algorithm is imperialist competitive (IC) algorithm. Gerist et al. [8] used the IC algorithm to detect damage in structures using a new objective function based on mode shapes. In Kim et al. [9], an optimization-based algorithm called differential evolution (DE) was applied to identify locations and severities in structures with multiple damages. Ding et al. [10] artificial bee colony (ABC) algorithm was applied to optimize the damage detection problem of a plate and a truss. A novel algorithm called P-NMA was proposed in order to damage the detection of structure based on vibration data [11]. The objective function used in this study was based on changes in frequencies before and after occurring damage in the structure. In a study [12], harmony search (HS) algorithm was proposed to identify damage under ambient vibration. Zhong et al. [13] utilized a method based on the MUSIC algorithm to identify near-field damage in a composite structure. Abdalla et al. [14] used the PSO algorithm for detecting damage in a cantilever beam. Yuan et al. [15] using an improved genetic algorithm and residual force method performed damage detection optimization.

According to the above cite references and literature review on damage detection using optimization algorithms, there is no study on compression of performance of PSO and GA in a vibration-based damage detection problem.

In this paper, a novel objective function based on the residual force vector is proposed. Then, the performance of two powerful algorithms called particle swarm optimization (PSO) algorithm and genetic algorithm (GA) for optimization of the proposed objective function is evaluated in terms of accuracy and computational time. The results are reported for several damage scenarios.

The rest of this study is organized as follows. Section 2 deals with the dynamic model for vibration-based damage detection. In this section, first, the residual force method (RFM) is introduced, and then the proposed objective function based on RFM is formulated. Section 3 presents the implementation of PSO and GA

algorithms. In Sect. 4, numerical examples are presented to compare the performance of PSO and GA algorithms with the proposed objective function in various single and multiple damage scenarios. Finally, Sect. 5 concludes the current paper.

2 Dynamic Model for Vibration-Based Damage Detection

2.1 The Residual Force Method (RFM)

In this study, a new objective function inspired by the RFM is proposed to formulate damage detection optimization problem as an inverse problem. The proposed objective function does not require the mode shapes commonly used in conventional RFM-based objective function for damage detection of structures. Here, the main idea RFM is considered.

The governing equation of motion in a FEM-based multi-degree system is expressed as [16]:

$$[M]\{\ddot{x}(t)\} + [K]\{x(t)\} = F(t) \tag{1}$$

where $[M]$ and $[K]$ are the global mass and stiffness matrices, respectively. $\{\ddot{x}(t)\}$ is the acceleration velocity, and $\{x(t)\}$ is the displacement vector caused by the applied force $F(t)$. If $F(t) = 0$, then the governing equation of motion of free vibration for the considered system is obtained as follows:

$$[M]\{\ddot{x}(t)\} + [K]x(t) = 0 \tag{2}$$

By considering the harmonic response $\{x\} = \{\varphi\}e^{i\omega t}$ and the corresponding acceleration $\{\ddot{x}\} = -\omega^2 \varphi e^{i\omega t}$, Eq. (2) can be obtained as:

$$[M]\{-\omega^2\{\varphi\}\} + [K]\{\varphi\} = 0 \tag{3}$$

For ith vibration mode, Eq. (3) is written as:

$$[M]\{-\omega_i^2\{\varphi_i\}\} + [K]\{\varphi_i\} = 0 \tag{4}$$

where ω is the natural frequency of the system, and φ_i is its corresponding mode shape vector in ith mode. Equation (4) is called the ith eigenvalue equation. If $\omega_i^2 = \lambda_i$, Eq. (4) can be expressed in a standard form as follows:

$$[M]\{-\lambda_i\{\varphi_i\}\} + [K]\{\varphi_i\} = 0 \tag{5}$$

Using the finite element method, the global stiffness matrix $[K]$ can be written as follows:

$$[K] = \sum_{j=1}^{m} [k]_j \qquad (6)$$

where m represents the number of elements and the local stiffness matrix for the jth element is denoted by $[k]_j$.

In this paper, the global stiffness matrix of a damaged structure is denoted by $[K_d]$. Thus, Eq. (6) for the damaged structure can be rewritten as:

$$[K_d] = \sum_{j=1}^{m} \alpha_j [k]_j \qquad (7)$$

where $\alpha_j \in [0, 1]$ represents a reduction of rigidity. If the value α_j is 1, then the jth element is undamaged and in the case $\alpha_j = 0$, the jth element is completely damaged, and when $0 < \alpha_j < 1$, the jth element is partially damaged.

By definition presented in Eq. (7), ith eigenvalue equation of a damaged structure can be obtained as:

$$[M]\{-\lambda_{di}\{\varphi_{di}\}\} + [K_d]\{\varphi_{di}\} = 0 \qquad (8)$$

where φ_{di} is the ith mode shape vector of the damaged structure, and λ_{di} is the natural frequency of damaged structure in the ith mode. It should also be noted that the global mass matrix $[M]$ remains unchanged after occurring damage because physically, the reduction of mass of structure caused by occurring crack or damage is intangible.

Substituting Eq. (7) in Eq. (8), the following expression may be written:

$$R_i = [M]\{-\lambda_{di}\{\varphi_{di}\}\} + \sum_{j=1}^{m} \alpha_j [k]_j \{\varphi_{di}\} = 0 \qquad (9)$$

In the above equation, R_i is called the residual force vector for the ith mode. It is obvious that by setting a proper set of α_j and having λ_{di} and φ_{di}, the value of the residual force vector R_i will be 0.

2.2 Proposed Objective Function Based on RFM

Due to $\{\varphi_{di}\} \neq 0$, Eq. (9) can be simplified as follows:

$$F_i = [M]\{-\lambda_{di}\} + \sum_{j=1}^{m} \alpha_j [k]_j = 0 \qquad (10)$$

In this paper, the proposed objective function based on Eq. (10) is expressed as:

$$F_i = \sqrt{\sum_{e=1}^{n}\left([M]\{-\lambda_{ie}\} + \sum_{j=1}^{m}\alpha_j[k]_{je} - [M]\{-\lambda_{die}\} - \sum_{j=1}^{m}\alpha_{dj}[k]_{je}\right)^2} \qquad (11)$$

where e is element number, and n is the total number of elements in the considered structure. Also, i is vibration mode number. Therefore, the proposed optimization objective function of this study is formulated as follows:

Minimize

$$F_i = \sqrt{\sum_{e=1}^{n}\left([M]\{-\lambda_{ie}\} + \sum_{j=1}^{m}\alpha_j[k]_{je} - [M]\{-\lambda_{die}\} - \sum_{j=1}^{m}\alpha_{dj}[k]_{je}\right)^2} \qquad (12)$$

subjected to

$$\alpha_j \in [0, 1]$$

where α_j is design variables of the above objective function for damage detection problem, and also, d stands for '*damage.*'

3 Implementation of PSO and GA Algorithms

3.1 PSO Algorithm

Particle swarm optimization (PSO) is an optimization method inspired by social behavior between birds in a flock. This algorithm uses swarm intelligence in order to optimize objective functions [17]. In PSO, each bird is symbolically represented as a particle (solution) in the n-dimensional search space.

The first step of this technique is initialization with a random population and then evolving over a generation in order to find an optimum solution. In this process, each particle has a changing velocity and position. Changing particle's position is done using information obtained from the previous position as well as its current velocity. Particles know their best position (personal best) and the best position among personal bests (global best). This principle is mathematically expressed as follows [18]:

$$V_{in}^{k+1} = wV_{in}^k + c_1 \times rand_1\left(p_{in} - X_{in}^k\right) + c_2 \times rand_2\left(p_{gn} - X_{in}^k\right) \qquad (13)$$

$$X_{in}^{k+1} = X_{in}^k + V_{in}^{k+1} \qquad (14)$$

In the above expressions, w is the inertia weight factor; V_{in}^k is particle's velocity i at iteration k in the dimension of the search space n; p_{in} denotes the best personal position experienced by the particle i considering its fitness value; c_1 and c_2 denotes acceleration coefficients, $rand_1$ and $rand_2$ represent random values (between 0 and 1) to ensure converging PSO algorithm around an extended search space; X_{in}^k is particle's current position i at iteration k in the dimension of the search space n; and p_{gn} is the global best position of the particle in search space.

Equations (13) and (14) express that at every iteration $k + 1$ the new position of the particle i is determined through adding its current velocity (V_{in}^{k+1}) to its position (X_{in}^k).

3.2   GA Algorithm

The genetic algorithm (GA) is an optimization inspired by Charles Darwin's theory of evolution. Using GA, the process of natural selection is numerically simulated to solve an optimization problem. The aim of GA is to find an approximate optimal solution by presenting a set of optimal points. This process is started with selecting the fittest individuals in a population. Then, the selected individuals produce offspring that inherit the features of their parents. Then, the produced offspring is added to the next generation. The parents that have better relative fitness their offspring have more chance of surviving. The process continues to the end of the process to obtain the fittest and best individuals. Here, each individual represents a solution for the optimization problem; therefore, the fittest individual corresponds to the best solution for the optimization problem [19]. Generally, there are five main phases in the structure of the genetic algorithm, namely initial population, fitness function, selection, crossover, and mutation.

In the initial population phase, initialization is performed to set individuals as an initial population. Each individual in this population is considered as a solution for the optimization problem. Each individual is described by a series of variables called genes. A set of genes form a string that is named a string or chromosome. In other words, each chromosome represents a corresponding solution. In the fitness function phase, individuals are fitted in order to obtain a fitness score for each individual. The fitness score is the criteria for selecting individuals to be reproduced [20]. The fittest individuals are selected in the selection phase for transmitting them to the next generation. In this phase, two pairs of parents are selected according to their corresponding fitness scores. There is more chance for individuals that have high fitness for being chosen to reproduce [21]. Crossover phase is one of the most important phases in the structure of the genetic algorithm. A crossover point randomly is selected in order to mate between all pair of parents [22]. The final phase in the structure of the genetic algorithm is related to mutation. In a few offspring, some genes are subjected to the mutation randomly. It occurs for maintaining

diversity among individuals and preventing premature convergence. The GA algorithm terminates if the generation has converged and the produced offspring are remarkably distinct from the prior generation. In such a condition, the genetic algorithm provides a solution to the optimization problem.

4 Numerical Examples

Four cantilever beams shown in Fig. 1 are considered in order to compare the performances of GA and PSO algorithms with experimental data obtained from FEM. Two types of damage scenarios called single damage scenarios (cases 1 and 2) and multiple damage scenarios (cases 1 and 2) are addressed. In the first case of the single damage scenario, element 3 is damaged by reducing 30% in damage index. The second case of the single damage scenario, element 2 is damaged by reducing 10% in damage index. In the first case of the multiple damage scenario, element 1, element 2, and element 5 are damaged by reducing 80%, 30%, and 70% in damage index, respectively.

The finite element method is used in order to obtain frequencies of damaged beams in different mentioned scenarios. Beams are divided into five elements. The effective stiffness matrix $[K^e]$ and the effective mass matrix $[m^e]$ for each element of beams are written as follows:
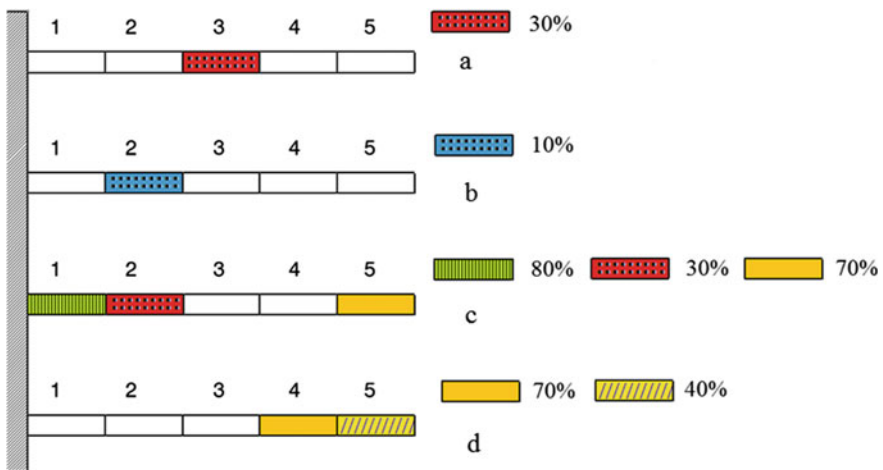
Fig. 1 Damage scenarios in four studied beams in details: **a** single damage scenario—case 1, **b** single damage scenario—case 2, **c** multiple damage scenario—case 1, **d** multiple damage scenario—case 2

$$[\mathbf{K}^e] = \begin{bmatrix} \frac{12EI}{l_e^3} & \frac{6EI}{l_e^2} & \frac{-12EI}{l_e^3} & \frac{6EI}{l_e^2} \\ \frac{6EI}{l_e^2} & \frac{4EI}{l_e} & \frac{-6EI}{l_e^2} & \frac{2EI}{l_e} \\ \frac{-12EI}{l_e^3} & \frac{-6EI}{l_e^2} & \frac{12EI}{l_e^3} & \frac{-6EI}{l_e^2} \\ \frac{6EI}{l_e^2} & \frac{2EI}{l_e} & \frac{-6EI}{l_e^2} & \frac{4EI}{l_e} \end{bmatrix} \tag{15}$$

$$[m^e] = \begin{bmatrix} \frac{156\rho A l_e}{420} & \frac{22\rho A l_e^2}{420} & \frac{54\rho A l_e}{420} & \frac{-13\rho A l_e^2}{420} \\ \frac{22\rho A l_e^2}{420} & \frac{4\rho A l_e^3}{420} & \frac{13\rho A l_e^2}{420} & \frac{-3\rho A l_e^3}{420} \\ \frac{54\rho A l_e}{420} & \frac{13\rho A l_e^2}{420} & \frac{156\rho A l_e}{420} & \frac{-22\rho A l_e^2}{420} \\ \frac{-13\rho A l_e^2}{420} & \frac{-3\rho A l_e^3}{420} & \frac{-22\rho A l_e^2}{420} & \frac{4\rho A l_e^3}{420} \end{bmatrix} \tag{16}$$

The constant properties of the considered beams are listed in Table 1. After producing frequencies of damaged beams using FEM in order to generate corresponding objective functions, GA and PSO algorithms are used in order to detect damages in the mention scenarios.

Parameters settings in PSO and GA algorithms are listed in Tables 2 and 3, respectively.

Results obtained from FEM, GA, and PSO for the single damage scenario and multiple damage scenarios are listed in Tables 4 and 5, respectively. As mentioned, represents a reduction of rigidity. If the value of the damage index α_j is 1, then the jth element is undamaged and in the case $\alpha_j = 0$, the jth element is completely damaged, and when $0 < \alpha_j < 1$, the jth element is partially damaged.

The results of the current study are graphically presented in Figs. 2, 3, 4, 5, 6, 7, 8, 9.

Results reported in Tables 4 and 5 as well as Figs. 2, 3, 4, 5, 6, 7, 8, 9 demonstrate that the PSO algorithm can detect the location and severity of damaged areas of the beam in all four cases with high accuracy. Therefore, in terms of the accuracy of the solution, the PSO algorithm is a more efficient algorithm than the GA algorithm for detecting damages through the proposed objective function. This is because of the nature of the discreteness of the PSO algorithm and the proposed objective function. Also, in terms of convergence of the two compared algorithms, according to results, PSO indicates better convergence to the optimum solution over 700 generations in all scenarios than the GA algorithm. Finally, in terms of run

Table 1 Constant properties of considered beams

Property	Symbol	Value (unit)
Cross-sectional area (m^2)	A	1.82×10^{-4}
Moment of inertia (m^4)	I	1.46×10^{-9}
Density (kg/m^3)	ρ	2685
Total length of beams (m)	L	0.5
Length of each element (m)	l_e	0.1

Table 2 PSO parameters setting

Parameters	Value
Number of variables	5
Population size (Swarm size)	1000
Maximum iteration	700
Acceleration coefficients	$c_1 = c_2 = 1.5$
Inertia weight factor	$w = 0.73$

Table 3 GA parameters setting

Parameters	Value
Number of variables	5
Number of population	1000
Maximum iteration	700
Percent of crossover	0.5
Percent of mutation	0.5

Table 4 Damage index obtained GA and PSO compared with those determined in FEM for the single damage scenario

Case	Method	Damage index (α_j)				
		Element 1	Element 2	Element 3	Element 4	Element 5
1	FEM	1	1	0.7	1	1
	GA	1	1	0.70045	1	0.99935
	PSO	1	1	0.7	1	1
2	FEM	1	0.9	1	1	1
	GA	1	0.79831	1	1	1
	PSO	1	0.9	1	1	1

Table 5 Damage index obtained GA and PSO compared with those determined in FEM for the multiple damage scenario

Case	Method	Damage index (α_j)				
		Element 1	Element 2	Element 3	Element 4	Element 5
1	FEM	0.2	0.7	1	1	0.3
	GA	0.54079	0.36022	0.49243	0.49407	0.96525
	PSO	0.2	0.7	1	1	0.3
2	FEM	1	1	1	0.3	0.6
	GA	0.88061	0.4759	0.61068	1	0.87403
	PSO	1	1	1	0.3	0.6

Fig. 2 Damage indices for single damage scenario, case 1

Fig. 3 Evolutionary process in single damage scenario, case 1
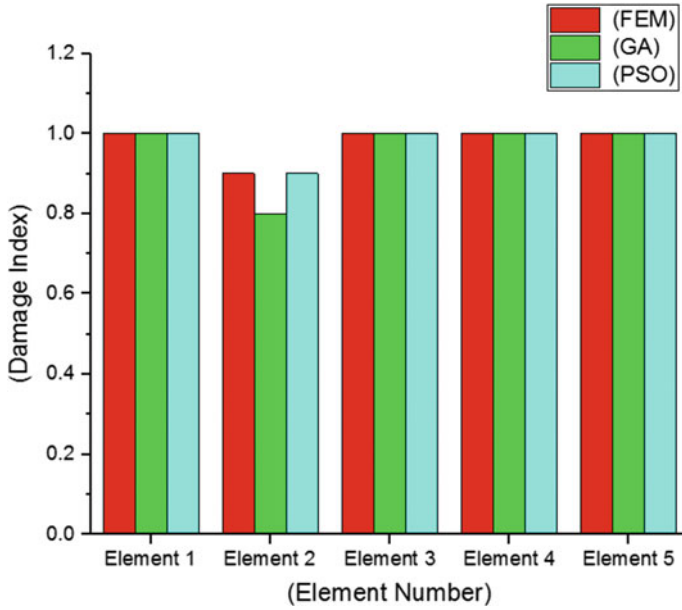
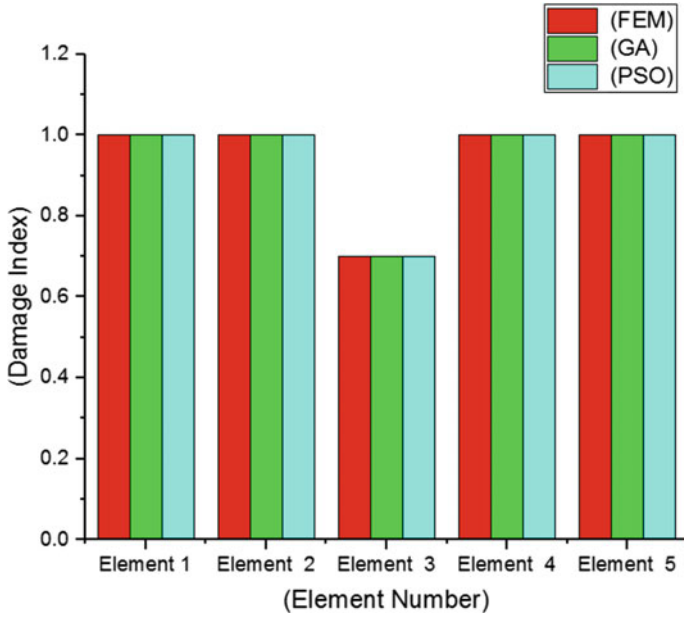**Fig. 4** Damage indices for single damage scenario, case 2
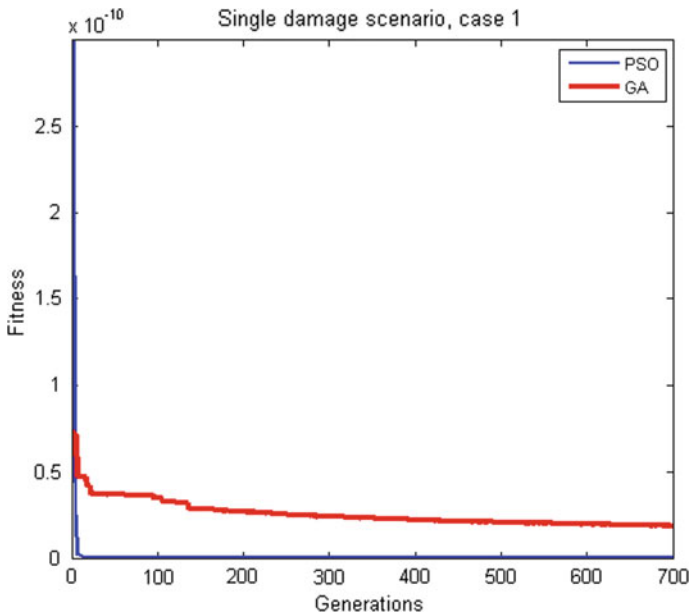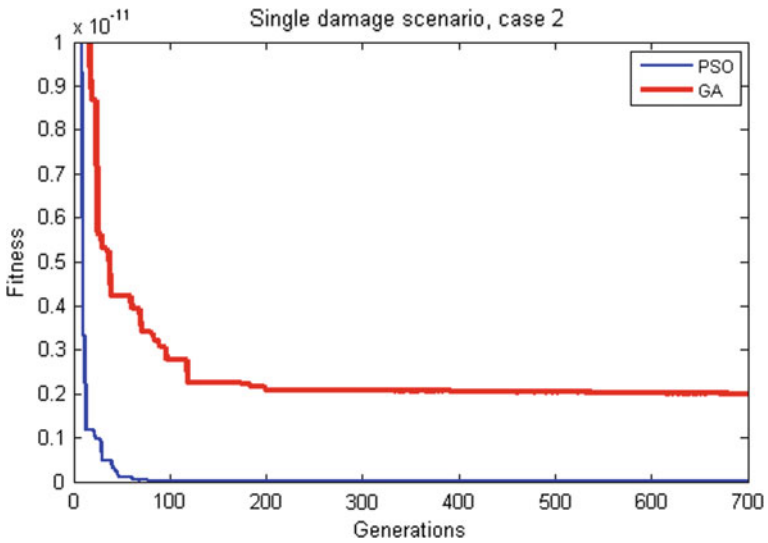

Fig. 5 Evolutionary process in single damage scenario, case 2
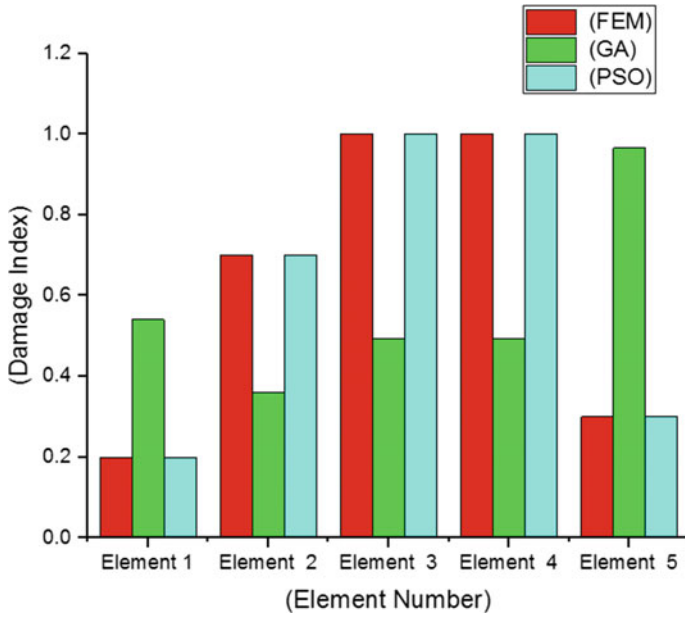
Fig. 6 Damage indices for multiple damage scenario, case 1
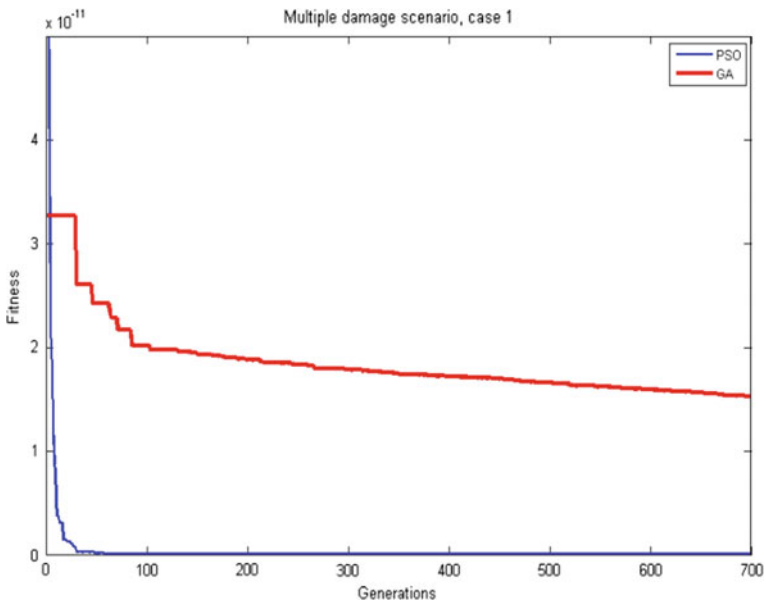
Fig. 7 Evolutionary process in multiple damage scenario, case 1
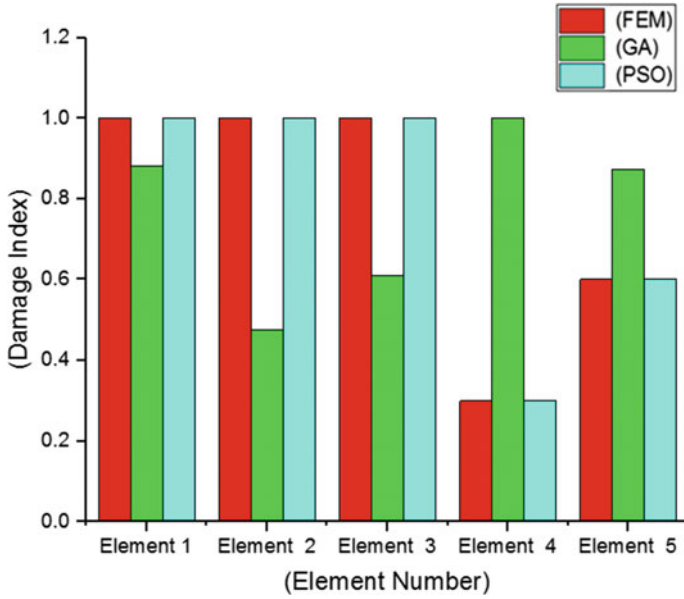
Fig. 8 Damage indices for multiple damage scenario, case 2
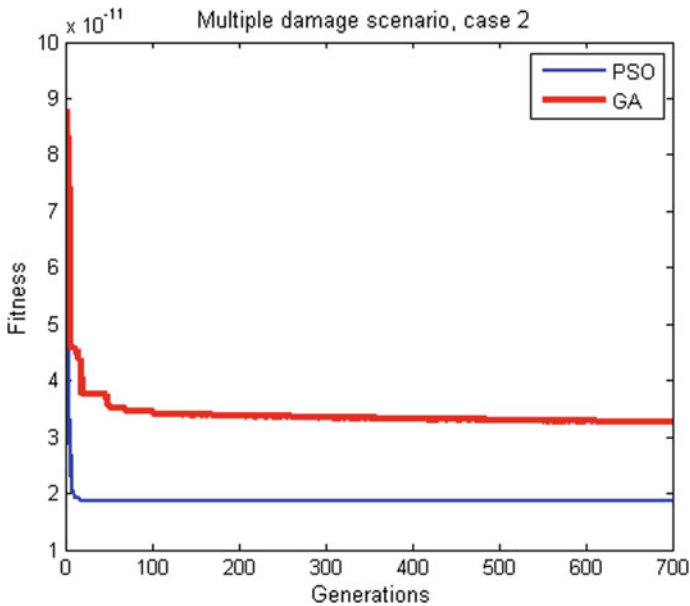
Fig. 9 Evolutionary process in multiple damage scenario, case 2

Table 6 Time elapsed by GA and PSO algorithms for different damage scenarios

Scenario	Case	Elapsed time by PSO (s)	Elapsed time by GA (s)
Single damage	1	149.8140	34.291
	2	166.957736	36.0126
Multiple damage	1	155.8581	108.4314
	2	168.630856	106.1746

time, according to Table 6, the GA algorithm indicates less elapsed time, but in trading off between accuracy, convergence, and elapsed times of the two algorithms, it is concluded that the PSO algorithm is further efficient than GA algorithm.

5 Conclusions

In this study, a damage detection method is presented in order to compare and estimate the performance of the PSO algorithm with the GA algorithm for a proposed objective function based on the residual force method. Two damage scenarios called the single damage scenario and the multiple damage scenario in the form of four damage cases are considered in order to find the location and severity of damages in damaged elements. The experimental data are obtained from FEM as a criterion for comparing the results of PSO and GA algorithms. PSO and GA algorithms optimize the proposed objective function and achieve different results. Findings indicated high efficiency of the proposed method using the PSO algorithm in all damage cases. It is concluded that the PSO algorithm is more suitable than the GA algorithm.

References

1. Yang, J.Y., Xia, B.H., Chen, Z., Li, T.L., Liu, R.: Vibration-Based structural damage identification: a review. Int. J. Robot. Autom. **35**(2) (2020)
2. Dinh-Cong, D., Vo-Duy, T., Ho-Huu, V., Nguyen-Thoi, T.: Damage assessment in plate-like structures using a two-stage method based on modal strain energy change and Jaya algorithm. Inverse Prob. Sci. Eng. **27**(2), 166–189 (2019)
3. Gomes, G.F., da Cunha, S.S., Ancelotti, A.C.: A sunflower optimization (SFO) algorithm applied to damage identification on laminated composite plates. Eng. Comput. **35**(2), 619–626 (2019)
4. Mishra, M., Barman, S.K., Maity, D., Maiti, D.K.: Ant lion optimisation algorithm for structural damage detection using vibration data. J. Civil Struct. Health Monit. **9**(1), 117–136 (2019)
5. Maity, D., Tripathy, R.R.: Damage assessment of structures from changes in natural frequencies using genetic algorithm. Struct. Eng. Mech. **19**(1), 21–42 (2005)

6. Alexandrino, P.D. S.L., Gomes, G.F., Cunha Jr, S.S.: A robust optimization for damage detection using multiobjective genetic algorithm, neural network and fuzzy decision making. Inverse Prob. Sci. Eng. 1–26 (2019)
7. Barman, S.K., Maiti, D.K., Maity, D.: Damage detection of truss employing swarm-based optimization techniques: a comparison. In Advanced Engineering Optimization Through Intelligent Techniques, pp. 21–37. Springer, Singapore (2020)
8. Gerist, S., Maheri, M.R.: Structural damage detection using imperialist competitive algorithm and damage function. Appl. Soft Comput. **77**, 1–23 (2019)
9. Kim, N.I., Kim, S., Lee, J.: Vibration-based damage detection of planar and space trusses using differential evolution algorithm. Appl. Acoust. **148**, 308–321 (2019)
10. Ding, Z.H., Huang, M., Lu, Z.R.: Structural damage detection using artificial bee colony algorithm with hybrid search strategy. Swarm Evol. Comput. **28**, 1–13 (2016)
11. Nhamage, I.A., Lopez, R.H., Miguel, L.F.F.: An improved hybrid optimization algorithm for vibration based-damage detection. Adv. Eng. Softw. **93**, 47–64 (2016)
12. Miguel, L.F.F., Miguel, L.F.F., Kaminski Jr., J., Riera, J.D.: Damage detection under ambient vibration by harmony search algorithm. Expert Syst. Appl. **39**(10), 9704–9714 (2012)
13. Zhong, Y., Yuan, S., Qiu, L.: Multiple damage detection on aircraft composite structures using near-field MUSIC algorithm. Sens. Actuators, A **214**, 234–244 (2014)
14. Abdalla, M.O.: Particle swarm optimization (PSO) for structural damage detection. In: ASMCSS'09 Proceedings of the 3rd International Conference on Applied Mathematics, Simulation, Modelling, Circuits, Systems and Signals, pp. 29–31) (2009)
15. Yuan, Y., Lin, G., Yan, D.M., Zhou, A.H.: Study on structural damage identification based on residual force method and improved genetic algorithm. Chinese J. Comput. Mech. **24**(2), 224–230 (2007)
16. Slimani, M., Tiachacht, S., Khatir, S., Behtani, A., Mansouri, L., Bouazzouni, A., Wahab, M. A.: Damage localization and quantification in structures using residual force indicator. In: Proceedings of the 13th International Conference on Damage Assessment of Structures, pp. 213–224. Springer, Singapore (2020)
17. Yu, L., Wan, Z.Y.: An improved PSO algorithm and its application to structural damage detection. In: 2008 Fourth International Conference on Natural Computation, vol. 1, pp. 423–427. IEEE (2008)
18. Deng, W., Yao, R., Zhao, H., Yang, X., Li, G.: A novel intelligent diagnosis method using optimal LS-SVM with improved PSO algorithm. Soft. Comput. **23**(7), 2445–2462 (2019)
19. Pinto, B.Q., Ribeiro, C.C., Rosseti, I., Noronha, T.F.: A biased random-key genetic algorithm for routing and wavelength assignment under a sliding scheduled traffic model. J. Global Optim. 1–25 (2020)
20. Jenkins, W.M.: Towards structural optimization via the genetic algorithm. Comput. Struct. **40** (5), 1321–1327 (1991)
21. Camp, C., Pezeshk, S., Cao, G.: Optimized design of two-dimensional structures using a genetic algorithm. J. Struct. Eng. **124**(5), 551–559 (1998)
22. Guo, H.Y., Li, Z.L.: A two-stage method to identify structural damage sites and extents by using evidence theory and micro-search genetic algorithm. Mech. Syst. Signal Process. **23**(3), 769–782 (2009)

Crack Analysis for Engineering Structures

Studying the Wave Propagating Characteristics of a Defected Semi-rigid Structure (Near Field and Far Field)

Tham H. Duong and Thoi H. Tra

1 Introduction

Structure Health Monitoring (SHM) has a wide range of topics. The substructure is a very complicated aspect in which the vaguest part is the properties of soil dynamics. A model may be valid just in a narrow category.

For solving a geotechnical engineering problem, there are a lot of solutions from thoroughly or partly studying, from theoretical to the empirical approach. Questions like: what a relevant model to use for a specific purpose? .... have still been vague.

Pile is a reinforced concrete shaft penetrating into the soil foundation to support the load transmitting from the superstructure. For higher bearing capacity and a smaller density of piles (i.e., the total area of pile section over the area of construction), bored or drilled pile with big diameter should be used. Because it is built in place, these piles should be tested at site to evaluate its quality. The inconsistency between the measured data and the real responses would lead to misunderstand the real condition of the structural health and inaccurately assess the failure probability of the structure. Combined with uncertainties in collecting data of loading conditions, structural rigidity, and others taken from the observation, it is a complex task to be tackled, especially in soil medium [1]. One of the common ways to get closer to the real response, statistical data should be collected to enough big amount, and a proper approach for error removal is necessary [2]. The change in structural impedance is a good indicator for detecting damages and deficiencies in structure [3].

Damage or defects in a structure can be detected by applying some vibrational excitation to the structure. For randomly located defects or damages [4] such as void, cracks, bulging, necking or lack of integrity, the pile impedance would change

T. H. Duong (✉)
Ho Chi Minh City Open University, Ho Chi Minh City, Vietnam
e-mail: tham.dh@ou.edu.vn

T. H. Tra
University of Technology, Ho Chi Minh City, Vietnam

due to either the decrease in stiffness, the changes in cross-section, or velocity of the longitudinal wave in the structure.

This article would study the characteristics of the wave propagation within the pile shaft or near field and the transmission to soil medium in the far field and the changes in the impedance of the structure when the module of elasticity decreases. Both analyses in the time domain and frequency domain are considered.

2 Method

2.1 Model

A single reinforced concrete pile is modeled as in Fig. 1. Its material properties and cross section are described in Table 1. Springs in both horizontal directions are prescribed of which the stiffness is computed by Eqs. 1 and 2. For modeling a point bearing pile, a spring and a dashpot are assigned at the pile tip, as in Fig. 1.

For the dynamic analysis, the load case would be of time history in a corporation with a dead load. An excitation as a time-dependent loading is $P(t) = P_o. \sin(2\pi ft + \theta)$ in which f is the excitation frequency. The excitation plays a role as an input impact applied to detect the damages via the response curves in both time domain (TD) and frequency domain (FD) analysis. Five factors which govern the problem are the time-dependent load, the continuity of the structural medium, the
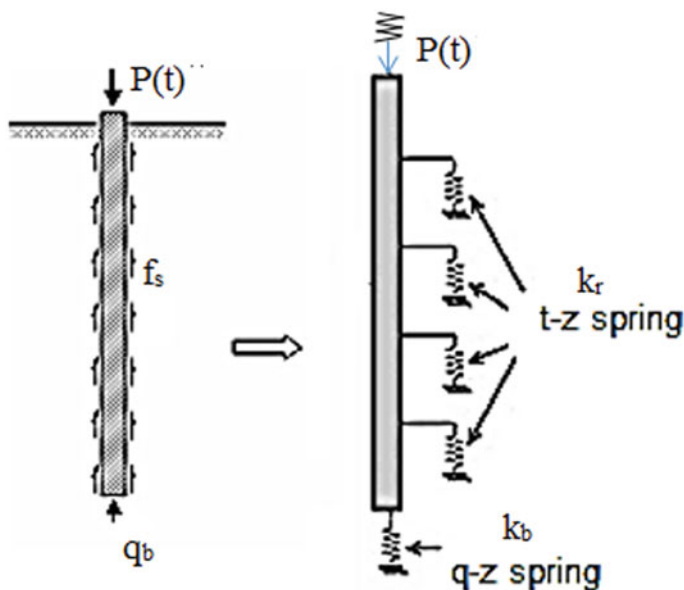
Fig. 1 Model of the single pile subjected to a dynamic excitation at the pile head

Table 1 Kinds of defects to be considered in the study

Kinds of defects	Properties	Modeling in SAP2000		Notation
Materials or geometry modification				
X1 reduced area/inertia	Geometry	X		
X2 Loss of friction	Material	X		
X3 discontinuity	Geometry	X		
X4 low quality	Material		X	
X5 excitation source	External action	–	–	
Uncontrollable factors				
N1	=1 (uniform)	=2 stratified foundation		
N2	=1, L/d < 10	=2, L/d > 20**		

soil–structure interaction (i.e., shaft friction or bearing capacity), the quality of materials, and restraints (simply supported or springs) standing for the soil–structure interaction.

In this study, spring stiffness is computed to the classical formula [5]

For the pile mantle, the stiffness is

$$k_v = 2.3G_s; \quad c_v = 2\pi\rho_s.V_s.d; \quad K_b = \frac{4G_s d}{(1 - v_s)}; \quad C_b = \frac{0.85K_b d}{V_s} \quad (1)$$

where k_v c_v, respectively, is the vertical stiffness and vertical damping component for the pile mantle, K_b C_b, respectively, is the vertical stiffness and vertical damping component for the pile tip, ρ_s is the soil bulk density, v_s is the Poisson's ratio of the soil, d is the pile diameter, and V_s is the shear wave propagating velocity, determined by the formula as below:

$$V_s = \sqrt{\frac{G_s}{\rho_s}} \quad (2)$$

where G_s is the shear modulus of the soil and $G_s = E_s/2(1 + v_s)$ with E_s is the modulus of elasticity of the soil. The stiffness of skin friction spring will be assigned as the link/support element in SAP2000 [9] as illustrated in Fig. 2. In this study, for a practical purpose, the V_s shear wave velocity of soil is computed by taking a modulus of elasticity $E = 12,500$ kN/m^2, i.e., V_s is 50–150 m/s.

In the second stage, defects are deliberately created at random locations within the pile, and a process of collecting data is planned systematically. The response that is obtained, including the time plot displacement and internal forces, will be analyzed in the frequency domain (FD). Defects may be defined with a symbolic character, for instance, the reduction ratio of cross section X1 (due to necking or bulging), loss in friction due to any bad adhesive effect of the surrounding soil on the skin friction X2, discontinuity X3 (i.e., void or full cracks into segments, or partially connected segments), low material stiffness X4 and the frequency of the
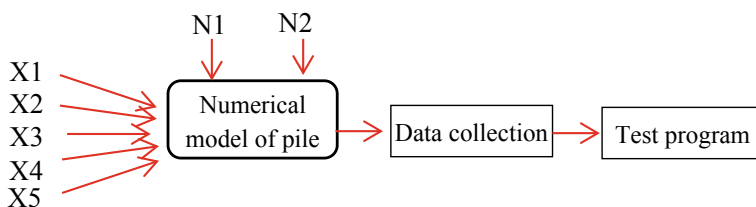
Fig. 2 Process of analyzing with input factors, uncontrollable factors, and the outcome

excitation X5. In this study, for modeling a discontinuity, a thin interface element having a very small stiffness is assigned; for modeling a partially cracked segment: a reduced stiffness, associated with a weakened cross-section (EA/l). Two uncontrollable factors are encountered, the stratification of the soil foundation N1, and the weakness of the wave signal N2 due to the pile slenderness (i.e., the ratio of length to diameter is greater than 30). The strategy for analyzing the problem is in Fig. 2.

For modeling the confining effect of the soil around the 0.6-meter diameter pile shaft, very high stiffness of springs in both x-direction and y-direction is assigned, and to investigate how the wave originates and propagates from the pile shaft, an axisymmetric 2D model with 2D mesh is created. An impulse excitation force P (t) with some specifications is as follows: amplitude $P_o = 50$ kN; the time of wave transfer is planned to examine within a duration $t = 2$ s. The time step is $\Delta t = 0.01$ ms and the number of steps is 200 (to display a 2 sec-plotting).

For modeling the defects, some techniques of assigning the material properties and modification for the cross-section are applied, as follows:

For plotting the time domain response of the wave propagating, we use the built-in tool of SAP 2000 software, written as the text file, and then, the file will be converted into a spreadsheet to be analyzed in frequency domain by the fast Fourier transform (FFT) algorithm. Each style of defect is assumed to have a specific curve, both in TD and FD. The model would be calibrated by assigning data of prior research work, comparing the responsive curves.

2.2 Data for Analysis in Near Field

Soil data. Data of soil brought into this study are described in Table 2. There are two kinds of uncontrollable factors: the stratification of the soil foundation (N1, value = 1 if homogenous layer; = 2 if strongly stratified) and the structure slenderness L/d (N2, = 1 for short pile, = 2 for slender pile). In other words, noise N1 relates wave diffraction or wave absorption that we cannot take into account; N2 relates the ability of attenuation of the compressive wave due to weak signals traveling through the long-distance. Data for collection are described in Table 1.

Table 2 Soil description for the model

List of factors	Layer 1	Layer 2
Classification		
$\gamma_{unsat}/\gamma_{sat}$ (kN/m^3)	16/17	18/20
Cohesion (kPa)	5	1
Friction angle (degree)	1	31
Modulus of elasticity (kPa)	1.25ẽ	5e4
SPT (average value)	7	14
Wave characteristics		
Shear wave (m/s)	50–150	<180

Method. All the defects are assigned randomly, deliberately, and of the two-level factors, i.e., low and high. For quantifying the intensity of defects, low risk is below 10% and high level is of more than 30%, and this percentage is for factors X1 through X4 using the modification tool in the package SAP2000; for factor X5, the level is unity for low frequency and equals to 2 for high-frequency continuous sinus wave. For ensuring a statistically sufficient data set, it is well-proved that the Taguchi method is suitable to apply in which for 5 two-level factors, combined with two uncontrolled factors, it is necessary to conduct total eight trials, and 32 outcomes are obtained [6]. This content is beyond the scope of this paper.

Models will serve for studying wave propagation in both near field and far field. The former is for the wave characteristics within the medium of the structure as the rigidity changes, and the latter is for the dynamic effects on the surrounding free domain of ground or existing structures in the vicinity. The impedance is computed as below:

$$Z_D = \frac{EA}{C} \propto \frac{\rho A.V_p}{g} \tag{3}$$

in which V_p is the wave propagation velocity in the axial direction, ρ/g is the specific weight of the material, and A is the cross section of the structure. The formula (3) is based on some authors' research works [7]. By analyzing the curves of the mobility, the length of the structure and the cross section could be identified quantitatively. In this study, spectral velocity is taken into account instead of the absolute velocity in the time domain. The amplitude of spectral velocity is given by the output of SAP2000, in the pull-down menu 'Display > Show Response Spectrum Curves.'

In Fig. 3, the mobility of a pile can be used to compute the defected area of the cross section. Δf is the peak-peak difference in the frequencies corresponding to the consecutive peak mobility value. With the maximum or minimum N value in the plot, together with a value of the velocity V_p, the maximum and minimum cross-sectional area A_{max}/A_{min} is computed using the formula (3).
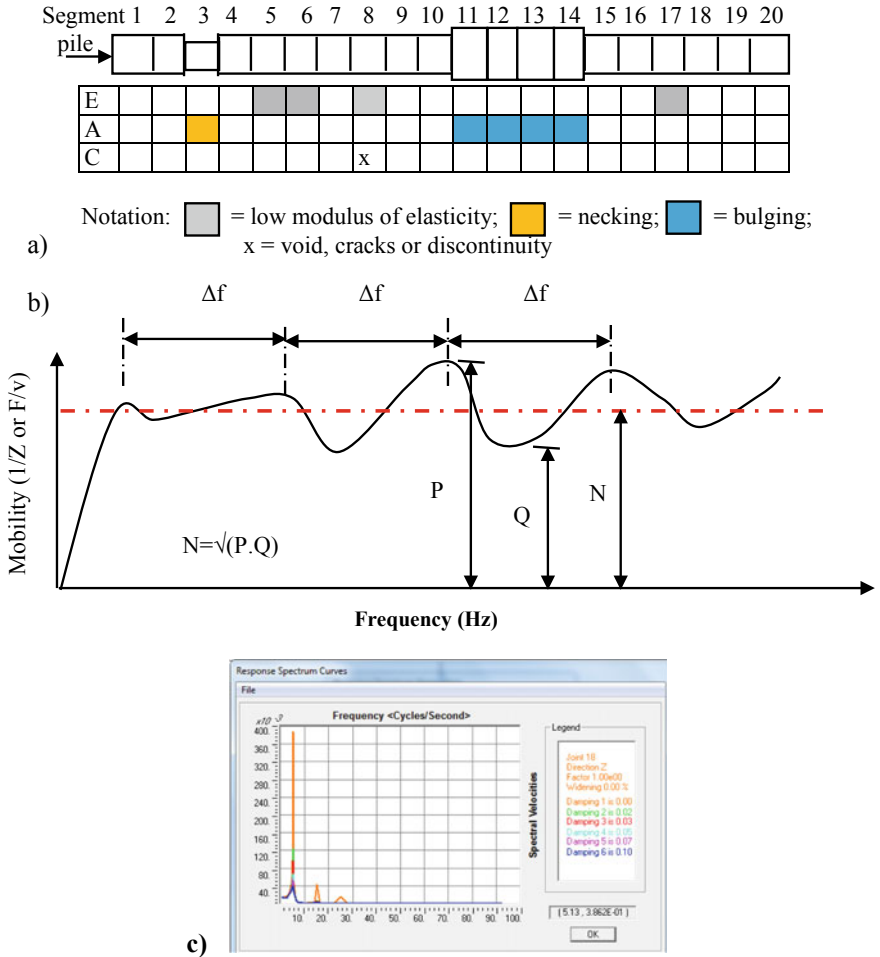
Fig. 3 **a** Randomly distributed positions of impedance changes and their symbols; **b** mobility plot for determining the change in the structure impedance and the length of the structure; **c** spectral velocity of a point along the pile shaft, that is used to compute the impedance

3   Results

3.1   Impedance Curve in Case of Rigid and Semi-rigid Structures

Based on the material stiffness, cross section, and the integrity of the structure (i.e., density), the theoretical curve of impedance has the shape as in Fig. 4.
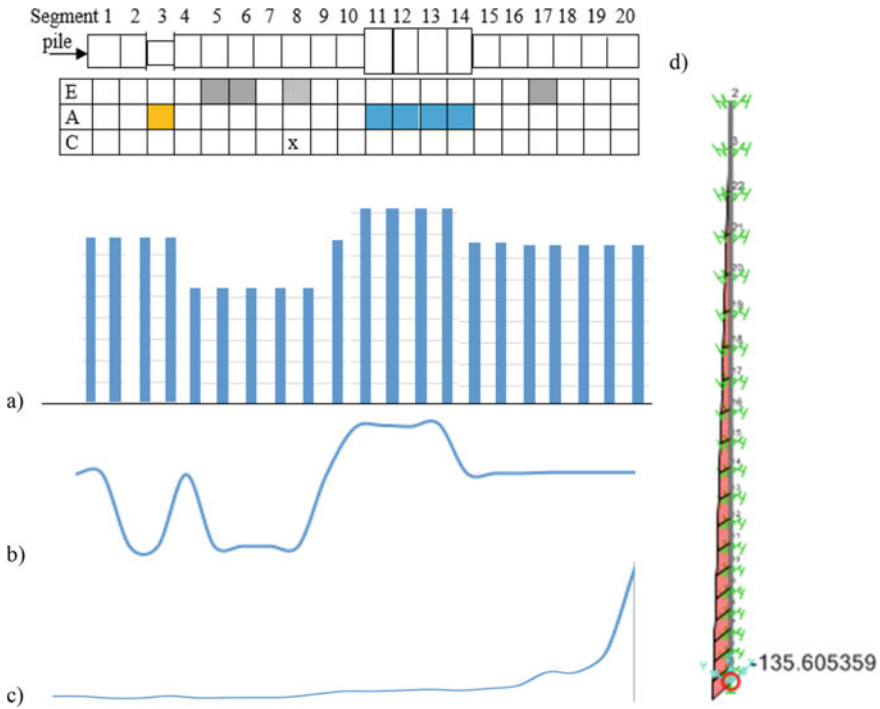
Fig. 4 Compatible shape of the impedance curve for a pile with different of defects (i.e., necking, low E, and bulging), **a** theoretical impedance; **b** results of impedance plotted from output data of SAP2000 [9], rigid pile; **c** impedance curve, semi-rigid columns; **d** Sap2000 model

The results of the semi-rigid model are shown in Fig. 4c, providing the material stiffness E is reduces to more than 10^3 times and the geometry has the same defects as a rigid pile. It is recognized that:

- The dominant frequency decreases from 5.15 Hz for the rigid pile to 1.54 Hz for the semi-rigid soil–cement column (unit weight $\gamma = 17.5$ kN/m^3 and the modulus of elasticity $E = 3.4e4$ kPa);
- In the low rigidity structure, the velocity decreases from the head (i.e., ground surface) to the tip. In another model conducted with a 12 m long pile, the same results indicate the velocity varies from 3.5 m/s at pile head to 0.01 m/s at the pile tip. The velocity decreases to the square of the depth (trend line is a parabolic curve with $R^2 = 0.9946$).
- Although there are defects along the shaft of the column (the same in pile case), no variation in the impedance of the semi-rigid column is identified, especially the rapid increase of the impedance at the pile tip. The heterogeneous medium of the soil–cement mixing might be the major reason for this.

3.2   *Wave Emitted from Pile and Column*

For studying the wave propagation in the far field, a Plaxis 2D axisymmetric model is developed as in Fig. 5. For simplicity and more reality, the soil model is two layers and hardening soil is used as in [8]. Pile is a point bearing one when the harmonic load on 40 cm diameter pile is taken to have an amplitude P_o = 100 kN instead of 5000 kN [8], and the frequency of the impact driving load is modified to be 1.5 Hz (i.e., 90 impacts per minute).

The dominant frequency of the pile response is f_o = 4.98 Hz, and the computed velocity of a longitudinal wave in the pile is $V \approx 4800$ m/s (the time is 0.0025 s for a length 12 m). For a pile with necking or bulging, the dominant frequencies are a shift to the right side of the frequency axis and result in higher frequencies. A frequency domain analysis for the spectral velocity at pile head B and tip A is given in Fig. 6 and a comparison to that of normal structure; for comparing to that of semi-rigid structure (soil-cement column), the FD spectral velocity of the column is shown in the right of Fig. 6 (The x-axis in all plots of Fig. 6 shows the frequency in Hz).

Necking or bulging of columns at the same position as pile cause higher frequencies, (i.e., $f1$ = 88 Hz, $f2$ = 118 Hz or 123 Hz, etc.) and the spectral velocity differ totally as compared to that of pile/column head (i.e., a single dominant frequency).
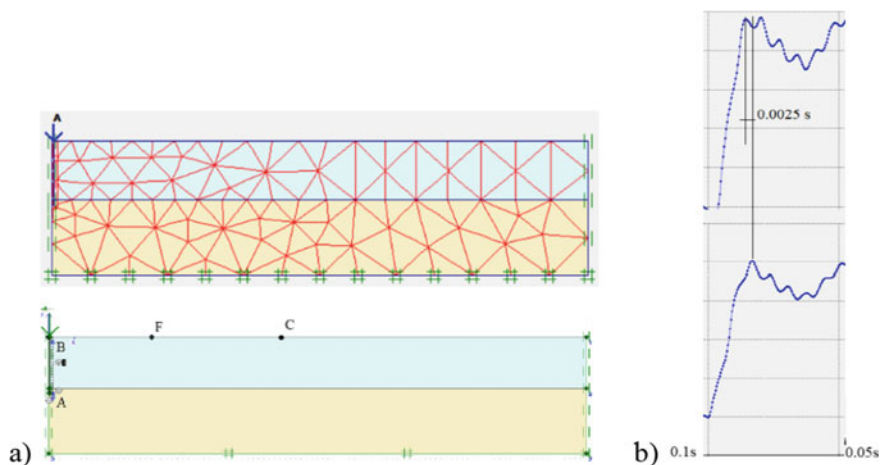
Fig. 5   a Far field with pick-up sensor at a distance 20, and 50 m points in free domain of the ground surface; **b** time domain displacement between point B and A (12 m long pile)

a) Undefected pile and soil-cement column
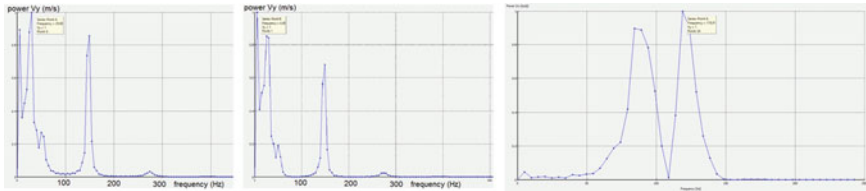
b) Pile/column with Necking in the middle of the shaft
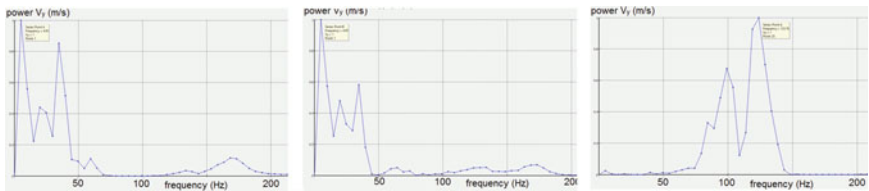
c) Pile/Column with Bulging in the middle of the shaft
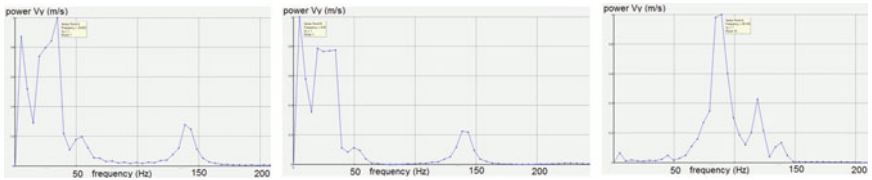
d) Pile with low modulus of elasticity (E=6e6 kPa)/ Soil cement column (E=1.0 e4 kPa)
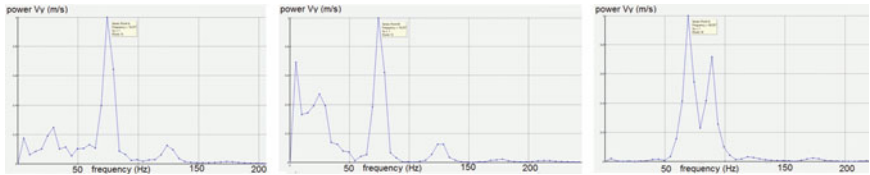
Fig. 6 FD analysis for spectral velocity at the pile head (point B, right) and pile tip (point A, left), corresponding to different kinds of defects: **a** normal condition; **b** necking; **c** bulging; **d** low E. (*Note* The pile is the left and centered plot, and the column is in the right)

3.3 Effects of the Reduced Stiffness on the Vibration in the Far Field

Point C is at the 50 m, and F is at the 20 m from the source of vibration. By reviewing the response output at this point, it is recognized that all the responses are very small, much lower than the value of the source. The maximum displacement is recorded to be around 1.25e–8 m, meanwhile the recorded maximum acceleration in the model is 3.37 m/s^2 (or 0.34G); especially at the point F, the acceleration is about const $\times$ 10^{-4} m/s^2.
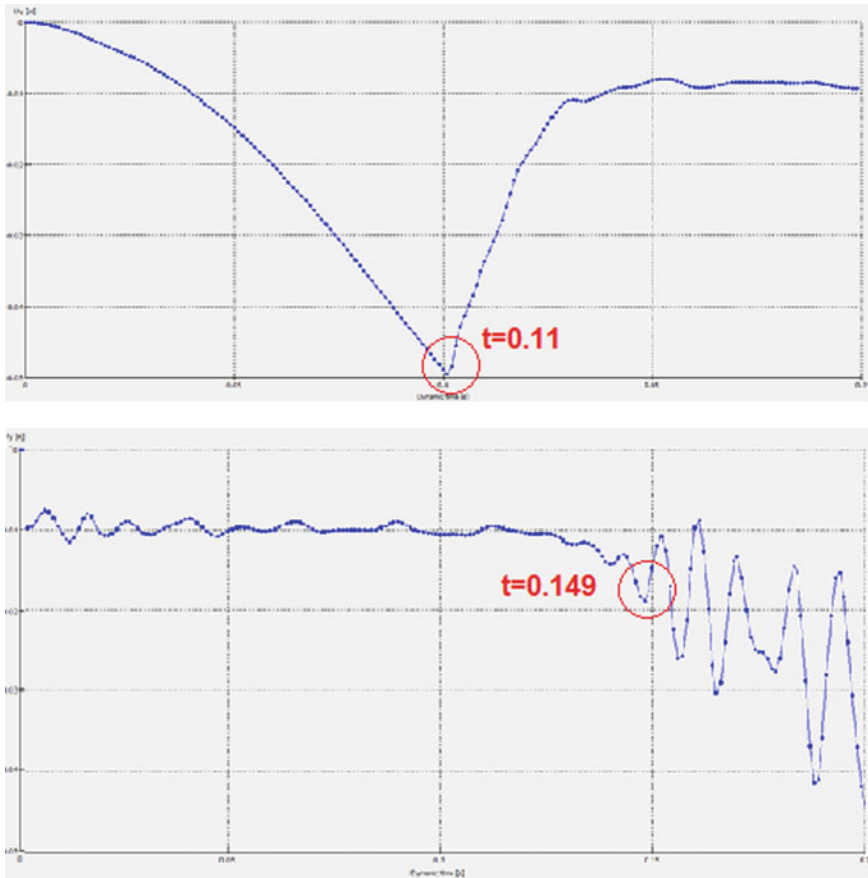
Fig. 7 Velocity of wave propagation in the semi-rigid column under studying

The wave velocity can be estimated from the displacement of the head and the tip of the column, as in Fig. 7. For the 12 m of pile length, the velocity of longitudinal wave is about 308 m/s, higher than the soil, but much lower than that of concrete pile.

Vibration originates from the soil–cement column which attenuates rapidly to a very small value (i.e., constant $\times$ 10^{-4}) of the free domain displacement, velocity, and acceleration at a distance not exceeding the *F* point or 20 m from the source (Table 3).

Table 3 Far-field study, displacement at points in the far field (at $t = 0.2$ s)

Point	Displacement (m)		f_n (Hz)	Normal stress (kPa)
	F	*C*		Tip
Concrete pile	1.8e-6	3.6e-8	4.98	340.34
Soil–cement column	3e-7	9e-9	4.95	162.10

The effective normal stress in column is rather acceptable as compared to that in reality.

4 Discussions

Some key points need to have further consideration as follows:

- In the model of a single pile, spring stiffness and damping are computed by the theory of elasticity. Keeping the spring stiffness to be constant and change the material stiffness is not a rigorous approach. There are several formulas for determining the spring stiffness at pile tip (q–z spring) and pile shaft (t–z spring). From the practical point of view, the stiffness and damper of a soil–cement column should be obtained from experiments using small-scale model or site static load test.
- The pile driving load exerted on the rigid pile head causes a small deformation (displacement $U_y \approx 0.0012$ m, $V_y \approx 0.17$ m/s), but keeping this load to use for the semi-rigid may not be suitable to make a small deformation ($U_y \approx 0.05$ m, $V_y \approx 3,6$ m/s). The big value of the displacement and velocity at the pile head confirms this. As such, this is not absolutely a kind of small deformation test. The Rayleigh damping is not considered in the model.
- In this study, the responsive velocity is selected to be the main variable to analyze for avoiding the errors from integrating twice to obtain the displacement of response; this quantity can be used for evaluating the impedance of the structure.
- For studying in the near field, a 0.6 diameter 20-meter long pile is used and then lower its stiffness to turn out to be a semi-rigid structure; the slenderness is more than 30; but in the model of the far field, 0.4 diameter pile is studied with the length to be 12 m of length. These are slender structures. The reason for this is to modify suitably as instructed in the Plaxis manual for simplicity.
- The contents regarding the effects of the each factor X1 to X5 or uncontrollable factor on the wave propagation as mentioned in Fig. 2 and Table 1 still need further studies in both experimental and theoretical aspect.

5 Conclusion

This study aims to study the wave propagating characteristics of the semi-rigid structure. By using the finite element model, the structure and its effect on the near and far field are investigated. Defects in the structure are the necking (i.e., 50% reduction in cross-sectional area) or bulging (i.e., 20% of the diameter for studying in the near-field and 50% for the far-field), the discontinuity due to cracks and void (partly in one segment of pile or column, equals 50% cavity), and the reduced

material stiffness (i.e., reducing 30% the value of the modulus of elasticity) due to heterogeneity due to mixing the materials at the site. The assumption to be verified is that the defects cause the impedance change in the way that the model could be calibrated by data of the real test. The results indicate that the semi-rigid soil–cement column with defects reflects weakly variation in the impedance; wave traveling in semi-rigid is hundreds m/s, much lower than that of concrete. Furthermore, the response in far field decays at the closer distance (i.e., 20 m) than that of pile (50 m). The mechanism of the wave transmission via the shaft of the semi-rigid structure, i.e., soil–cement column, is rather weak and the zone of wave transmission into far field is much smaller than that of a rigid pile, even with a heavy driving load as in this study. The soil–cement column cannot be the same as pile to name 'soil–cement pile' as usual. Based on the abovementioned features, the mechanism of load transmission and wave characteristics for semi-rigid, i.e., soil–cement columns as described in this study, is not recognized clearly. This study also suggests finding other methods of integrity test for this structure.

References

1. Edip, K., Grevski, M., Sesov, V.: Numerical simulation of wave propagation in soil medium, http://ebooks.iospress.nl/publication/31124, https://doi.org/10.3233/978-1-60750-808-3-140-145 (2018)
2. Catbas, F.N.: Structural Health Monitoring, Applications and Data Analysis. Chapter 1. 1–39. Woodhead Publishing. http://www.knovel.com (copyright © 2009)
3. Diogo, R., Roberto, M.F.N., Valder, S. Jr.: Impedance-based structural health monitoring. The 23rd ABCM Intl Congress of Mechanical Engineering Rio de Janeiro, RJ, Brazil (2015). https://www.researchgate.net/publication/315550109. Last Update 2017
4. Lai, JR, Yu, C.-P., Liao, S.-T.: Assessment of the integrity of piles by impedance log technique. Paper https://doi.org/10.4028/www.scientific.net/KEM.321-323.340 (2006)
5. Mladen, C., Boris, F., Radomia, F.: Numerical Simulation of The Pile Integrity Test on Defected Piles. https://www.researchgate.net/publication/279080437. Uploaded 2015
6. Tham, D.H.: Some statistical techniques applied to engineering mechanics problems. Vietnam J. Sci. Technol. **57**(6A). https://doi.org/10.15625/2525-2518/57/14006 (2019)
7. Varma, S.J., Gopalakrishnan, N., Sathish Kumar, K., Eapen Sakaria, P.: Structural integrity evaluation of pile foundations by pile integrity test. Int. J. Struct. Civil Eng. Res. **2**(3) 133–140 (2013)
8. Plaxis 2D 2011. Tutorial Manual, session 13, pp. 117–123. https://www.plaxis.com/support/manuals/plaxis-2d-manuals/
9. Sap2000 User Manual. https://www.civilax.org/sap2000-manual/

Bonding-Based Approach for Calculation of Shear Resistance of ETS FRP Bars in ETS-Strengthened Beams

Linh Van Hong Bui[ID], **Tin Van Do**[ID], **Phuoc Trong Nguyen**[ID], **and Boonchai Stitmannaithum**

1 Introduction

Recently, the vicinity to the novel methods for strengthening of the reinforced concrete (RC) structures has opened to the great potential for the structural intervention. One of the newly strengthening methods for enhancing the shear performance of RC beams is the embedded through-section (ETS) method. The ETS technique utilizes an amount of adhesive composite to glue the steel or fiber-reinforced polymer (FRP) bars along the holes predrilled through the section of the beam. However, the advantages of the ETS method for strengthening/retrofitting of the beams have not fully understood with only few studies can be found [1–5]. It was reported in previous studies that the members intervened in shear with ETS bars resulted in the substantial efficiency in comparison with the earlier retrofitting technologies [4, 5]. Several prominent efficiencies have also been found in the literature, i.e., the ETS retrofitting system enhanced the ductility of the members through the yielding phenomenon of the tension steel bars or the substantial crushing at concrete compressive zone of the beam. In addition, the premature debonding of the ETS retrofitting in the beams was avoidable using the solid anchorage screwed the ends of the ETS retrofitting elements [5].

To estimate the shear carrying forces by the ETS strengthening system in the RC beams, the previous studies have attempted to use the models offered in the

L. V. H. Bui · T. V. Do · P. T. Nguyen (✉)
Faculty of Civil Engineering,
Ho Chi Minh City Open University, Ho Chi Minh City 70000, Vietnam
e-mail: phuoc.nguyen@ou.edu.vn

L. V. H. Bui
e-mail: linh.bvh@ou.edu.vn

B. Stitmannaithum
Department of Civil Engineering, Faculty of Engineering, Chulalongkorn University,
Bangkok 10330, Thailand

American Concrete Institute (ACI) [6] as well as the recommendation by the Japan Society of Civil Engineers (JSCE) [7], which were proposed in predicting of the shear capacity of the RC beams reinforced with ordinary FRP shear reinforcement. However, Bui et al. [4] indicated that the shear resisting forces of the ETS FRP elements made by the aforementioned guidelines underestimated substantially the experimental measurement. Thereby, Bui et al. [4] proposed a simple approach for calculation of the shear carrying capacity of the ETS retrofitting bars. The approach was fundamental to the bonding-based approach, which illustrated the shear performance of the strengthening bars via the bond response of the intervening system to concrete. In that study, the ETS FRP shear contribution using the proposed bonding-based approach and considering the regression procedure has been successfully computed. The results obtained from the proposed model were adequately reliable in comparison to the experimental monitoring. However, the larger deviation in the regressing process might reduce the accuracy of the model. Therefore, the current study aims to provide a bonding-based approach considering mainly the mathematical and mechanical aspects for prediction of the ETS FRP shear strengths.

The structures of this paper are described as follows. (1) The validation of the bond model developed in Bui et al. [4] against the bond test results is provided; (2) the bonding-based approach to analyze the shear properties of the ETS intervening systems in the members is diagrammed; (3) the predictions for the shear carrying forces of the ETS FRP retrofitting are made through comparison of the results calculated by the bonding-based approach incorporating with the mechanical approach and the regressing approach.

2   Experimental Database

2.1   Description of Bond Tests

In this section, the bond tests are related to the ETS technique, which were conducted in the previous studies [4, 8, 9]. Bui et al. [4] investigated the bond properties of anchored ETS glass FRP (GFRP) rods to concrete to develop the bond model representing for the ETS FRP–concrete interface. In the studies by Godat et al. [8] and Caro et al. [9], the pullout tests were provided to examine the bond behaviors of the ETS carbon FRP (CFRP) bars embedded in concrete blocks. Various factors including the types of ETS, concrete strength, the embedment length, and the presence of anchorage were analyzed in the studies. Figure 1 presents the general illustration for the ETS bonding tests conducted in the mentioned literatures. In the study by Bui et al. [4], the gauges for measuring the strain trace were attached along the embedded bars to gain into insight the interfacial

Fig. 1 General scheme for
bond tests
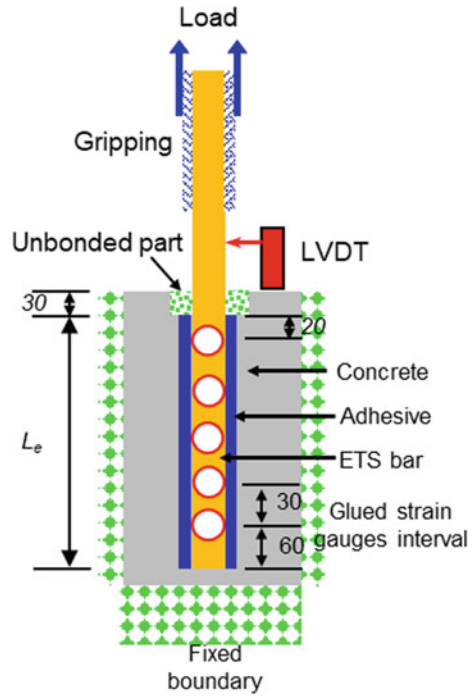
mechanism of the deep-embedment retrofitting system to concrete. Table 1 demonstrates the specimen details of the experiments and the tested results from the three tests. As can be observed in the table that the maximum bond forces generally increased with the elastic modulus and the embedment length of the ETS bars. This is because those parameters decreased the strain trace in the ETS FRP bars, triggering in the great capacity.

2.2 Bond Model for ETS FRP–Concrete Interfaces

In this section, the validations of the bond law are made by comparing to the experimental results obtained by Bui et al. [4]. The input data in Table 1 will be used for the estimation of the ETS contribution in Sect. 3. Based on the mathematical consideration, the bond stress (τ_i) and interfacial slip (s_i) at each strain gauge (SG) glued in the ETS bars are expressed as follows.

$$\tau_i = \frac{E_r A_r}{p_r} \frac{\varepsilon_i - \varepsilon_{i-1}}{\Delta x} \tag{1}$$

Table 1 Specimen details and experimental results [4]

Study	Specimens	f'_c (MPa)	E_r (GPa)	d_b (mm)	L_e (mm)	P_{max} Exp. (kN)	s_{max} (mm)	τ_{max} (MPa)
Bui et al. [4]	C1	38	50	10	150	26.5	0.21	5.62
	C2	38	50	10	150	30.3	0.34	6.43
	C3	38	50	10	120	37.9	0.12	10.05
	C4	38	50	8	150	32.1	0.18	8.51
	C5	38	50	10	200	39.2	0.19	6.24
	C6	38	50	10	250	37.4	0.08	4.76
	C8	38	50	10	120	35.0	0.09	9.28
	C9	38	50	10	120	37.1	0.20	9.84
Godat et al. [8]	D1*	20.7	120	9.52	143	35.7	0.06	8.35
	D2	20.7	144	12.7	143	57	NA	9.99
	D3	42.7	155	9.52	143	80.4	NA	18.80
	D4	42.7	155	9.52	143	91.2	0.06	21.32
	D5	42.7	155	9.52	143	78.5	NA	18.35
Godat et al. [8]	D6	42.7	155	9.52	48	42.8	0.06	29.81
	D7	42.7	155	9.52	71	57.4	NA	27.03
	D8	42.7	155	9.52	95	63.4	0.03	22.31
	D9	42.7	155	9.52	119	71	NA	19.95
	D10	42.7	155	9.52	166	100.7	NA	20.28
	D11	42.7	155	9.52	190	102.4	0.13	18.02
Caro et al. [9]	E1*	26.1	130	12	180	73.3	3.20	10.80
	E2	26.1	130	10	150	56.2	1.60	11.93
	E3	24.8	40	12	120	36.3	1.90	8.02
	E4	24.8	130	12	120	49.6	1.50	10.96
	E5	24.8	40	12	60	22.8	1.40	10.08

Table 1 (continued)

Study	Specimens	f'_c (MPa)	E_r (GPa)	d_b (mm)	L_e (mm)	P_{max} Exp. (kN)	s_{max} (mm)	τ_{max} (MPa)
	E6	24.8	40	12	60	27.1	2.10	11.98
	E7	24.8	130	12	60	31.6	1.00	13.97
	E8	24.8	130	12	60	30.1	1.20	13.31
	E9	45.6	130	10	150	74.8	2.20	15.87
	E10	45.6	40	10	100	40.4	2.80	12.86
	E11	45.6	130	10	100	43.5	1.20	13.85
	E12	45.6	40	10	50	21.6	1.70	13.75
	E13	45.6	130	10	50	21.1	1.10	13.43

*Specimens were renamed

Notes f'_c (MPa) is the strength of concrete in compression, L_e (mm) is the embedment length of the ETS elements, d_b (mm) is the diameter of ETS rods, E_r (GPa) is the elastic moduli of FRP, P_{max} (kN) is maximum bond force measured from the tests, s_m (mm) is slip value at maximum interfacial stress, τ_m (MPa) is maximum interfacial stress

$$s_i = \frac{\Delta x}{2}\left(\varepsilon_0 + 2\sum_{j=1}^{i-1}\varepsilon_j + \varepsilon_i\right) \tag{2}$$

where E_r (GPa) is the FRP elastic moduli, A_r (mm^2) is the sectional area of the FRP reinforcement, p_r (mm) is the FRP bar perimeter, Δx (mm) is the interval amongst glued strain gauges spaced 30 mm, ε_0 (µm/m) is the strain measured at the bar end, and ε_i (µm/m) is the values of the strain recorded at the ith-order gauge.

Figure 2 presents the strain trace along the bonded length of the ETS bar in the test specimen C1 under the increase of the loads. It is obvious that the strain profile was nonlinearly distributed along the length. In addition, the values of the transfer length and the strain increased as the increasing of the gripping tensile forces. Further, the maximum strain was achieved at the gauge nearest to the loaded end.

It was revealed in the researches by Dai et al. [10] and Bui et al. [11] that the τ–s curves are distinct at the varying interfacial positions due to the characteristics of the bonded surface and the defection of the interfacial layers, where the epoxy was filled improperly. Those phenomena exhibit the scatters and the deviations of the strain values at the high load level. Therefore, one of the τ–s curves was unable to represent the bond property and mechanism of the ETS bars to concrete. Thereby, Bui et al. [11] developed a bond model that could be reasonable to express the τ–s relationships of the ETS FRP intervening bars embedded in concrete specimen.

According to the model formulated by Bui et al. [11], the bond–slip relationship can be expressed as below.

$$\tau = \frac{E_r A_r}{p_r} A^2 B e^{-Bs}\left(1 - e^{-Bs}\right) \tag{3}$$

By taking the integration of the bond–slip formulation, the interfacial energy (G_f^∞) and the peak bond force (P_{max}) are written by the following equations.

Fig. 2 Distribution of strain along embedment length for specimen C1
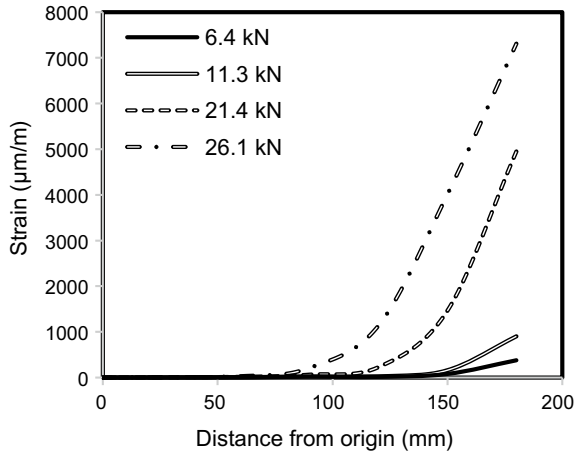
$$G_f^{\infty} = \int\limits_0^{\infty} \tau ds = \frac{A^2}{2} \frac{E_r A_r}{p_r} \tag{4}$$

$$P_{\max} = E_r A_r \varepsilon_{\max} = E_r A_r A = E_r A_r \sqrt{2 G_f \frac{p_r}{E_r A_r}} \tag{5}$$

where $\varepsilon_{\max} = A$ (µm/m) is the largest strain measured in the ETS strengthening bars, $B = \ln 2/s_m$ (1/mm) is defined as the interfacial bond ductility.

Figure 3a shows the comparison on the interfacial stress–slip relations between the measured data and bond model for the specimens in the study of Bui et al. [4]. The measured data for the τ–s curves are plotted by utilizing Eqs. (1) and (2), while the bond model described above is used to compare with the test results. Figure 3a indicates that the curves obtained by the proposed bond constitutive law fitted reasonably with the plots derived from the integration of the strain values. It means that the bond model offered by Bui et al. [4] is acceptable to express the response at the interfacial profile of the ETS embedding rods to concrete through the τ–s law. Although the developed bond formulation agreed with the experimental curves in the ascending trend, the descending resulted in some deviations owing to the scatter of the monitoring results at the high load level. Figure 3b shows comparison of the validation of the results obtained from the bond model against the experiments in terms of the maximum pullout forces. From Fig. 3b, the mean by 0.96 is the average of the ratio of the ultimate pullout forces obtained by the bond model to the maximum bond forces measured from the tests, and the coefficient of variation (COV) of the mean is 12.1%. This finding indicates the reliability of the proposed interfacial constitutive law in predicting the bond strengths of the ETS GFRP retrofitting bar to concrete.

3 Bonding-Based Approach for Estimation of Shear Resisting Forces of ETS FRP Retrofitting System

3.1 Proposed Approach

This section summarizes briefly two approaches, i.e., mechanical expression and regression procedure [4], based on the bonding behavior for estimating the shear resistance of ETS FRP strengthening bars in the ETS-intervened beams. Figure 4 presents the scheme to analyze the shear carrying capacity of the ETS FRP strengthening in the beams via the bond behaviors of the ETS intervening bars to concrete. As illustrated in Fig. 4, Bui et al. [4] indicated that ETS bars passed the main crack plane resisted to the shear via the interfacial mechanism between ETS

Fig. 3 Validations of bond
model against the pullout test
results: **a** bond stress-slip
curves; **b** maximum bond
forces

Although the bond
model agreed well
with the monitoring
data in the ascending
trend, the descending
branch resulted in
some deviations.
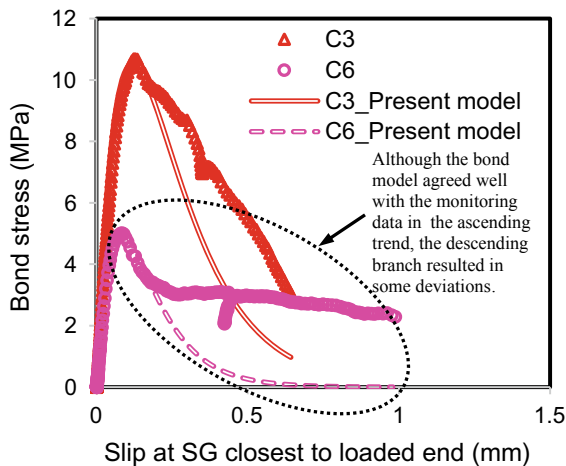
(a)
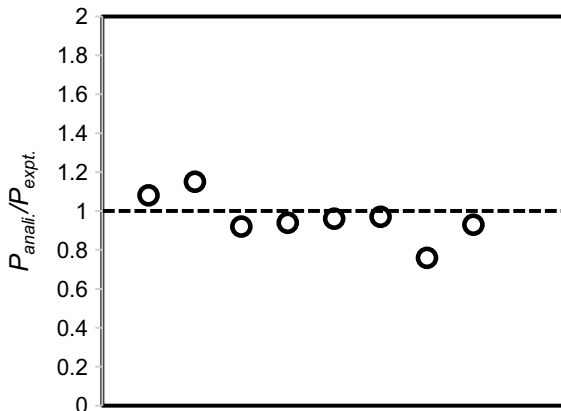
(b)

rods–adhesive–concrete embedded in an equivalent concrete block. Since the bond
model has been identified for the cases without failing by FRP bar rupture, the
ETS-strengthened beams failed with no rupture of the strengthening system are
satisfied to utilize the proposed shear model.

To determine the shear contribution based on the bonding consideration, the
configurations of the equivalent bond specimen are built as follows. First, the
amount of ETS bars (N_f) carried by the shear is estimated as Eq. (6). The
embedment length (L_{fi}) in the zone where concrete was covered the ETS bar is
expressed as Eq. (7).
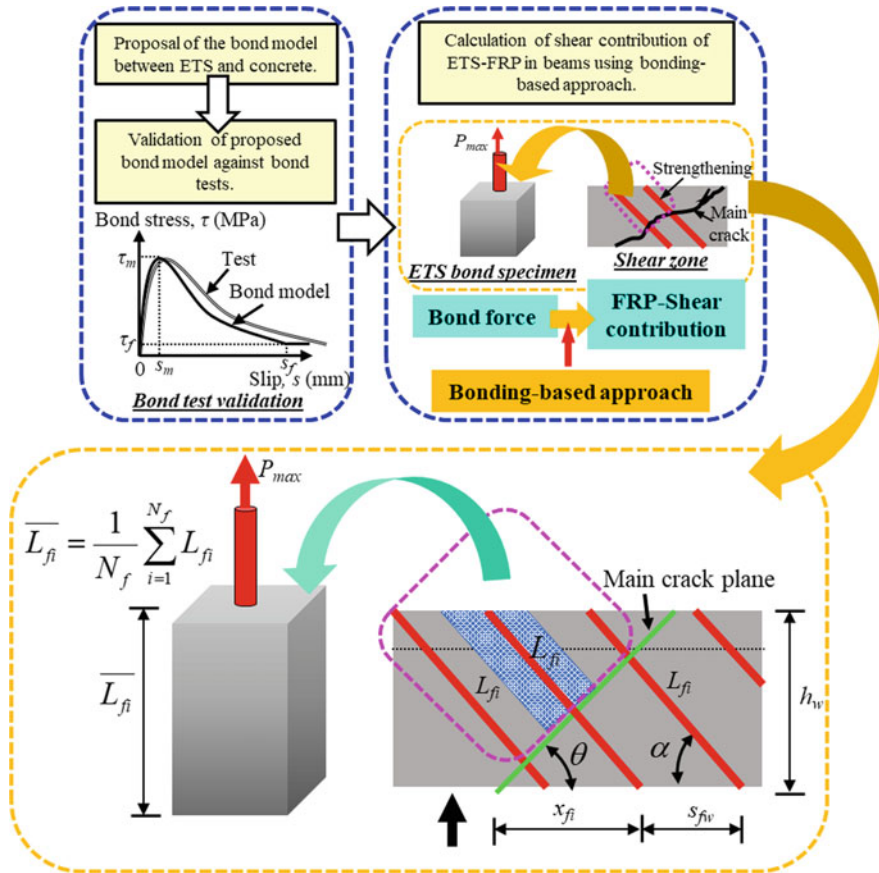
Fig. 4 Shear bonding-based model of ETS rods in ETS-retrofitted beams

$$N_f = \text{round off}\left[h_w \frac{\cot\theta + \cot\alpha}{s_{fw}}\right] \tag{6}$$

$$L_{fi} = \begin{cases} is_{fw}\dfrac{\sin\theta}{\sin(\theta+\alpha)} & \text{for } x_{fi} < \dfrac{h_w}{2}(\cot\theta + \cot\alpha) \\[2ex] L_f - is_{fw}\dfrac{\sin\theta}{\sin(\theta+\alpha)} & \text{for } x_{fi} \geq \dfrac{h_w}{2}(\cot\theta + \cot\alpha) \end{cases} \tag{7}$$

where $x_{fi} = is_{fw}$, s_{fw} (mm) is the interval of the ETS bars located in the shear region of the beams, and h_w (mm) is the height of the beam; θ (°) and α (°) are, respectively, the angle of the main crack and the inclination of the transverse reinforcement.

Whole effective strengthening system in the beam will be converted into an equivalent concrete prism embedded by the ETS FRP bar. Equation (8) describes the average bond length computed from the mean of ETS single bond lengths. The bond force corresponding to the resistance of the intervening system in the RC beams is the bond capacity of the equivalent concrete block. The formulation to calculate the shear strengths of the ETS retrofitting rods via the bonding-based approach is displayed as Eq. (8).

$$\overline{L_{fi}} = \frac{1}{N_f} \sum_{i=1}^{N_f} L_{fi} \tag{8}$$

$$V_f^b = N_f P_{\max} = N_f E_r A_r \sqrt{2 G_f \frac{p_r}{E_r A_r}} \tag{9}$$

For the mechanical approach which mainly considering the mathematical aspects without using empirical coefficients, the test values on the bond behaviors of the ETS intervening bars to concrete have to be collected, while the regressing approach utilizes the regression procedure to obtain the bond parameters.

For the mechanical approach, the interfacial energy (G_f) is determined in Eq. (10). The experimental values of the bond factors maximum bond stress (τ_m), slip at ultimate interfacial bond stress (s_m), maximum slip (s_f) are collected in the bond test results [1, 8, 9] considering the equivalent configurations of the specimens. Table 1 also partially displays the necessary information regarding the factors for the mechanically bonding-based approach.

$$G_f = \int_0^{s_f} \tau ds = \frac{E_r A_r}{p_r} \times A^2 \times \left(\frac{1}{2} e^{-2 s_f B} - e^{-s_f B} + \frac{1}{2} \right) \tag{10}$$

For the regressing approach, based on the regressing procedure formulated by Bui et al. [4] and Nakares et al. [12] (in Fig. 5), the interfacial energy (G_f) is analytically expressed as follows.

$$G_f = 5 \times 10^{-5} \times (1/L_e)^{-1.179} \times (f_c')^{1.5651} \times (E_r A_r / p_r)^{0.042} \tag{11}$$

3.2 Validation of Model

The accuracy of the bonding-based model is validated in this study by considering the comparison on the ETS FRP shear contributions between the monitoring and the calculated results. All RC beams retrofitted in transverse region with ETS bars analyzed in the previous works by Bui et al. [5], Breveglieri et al. [13] and Mofidi et al. [14] are examined for the model validation. The failures of the investigated
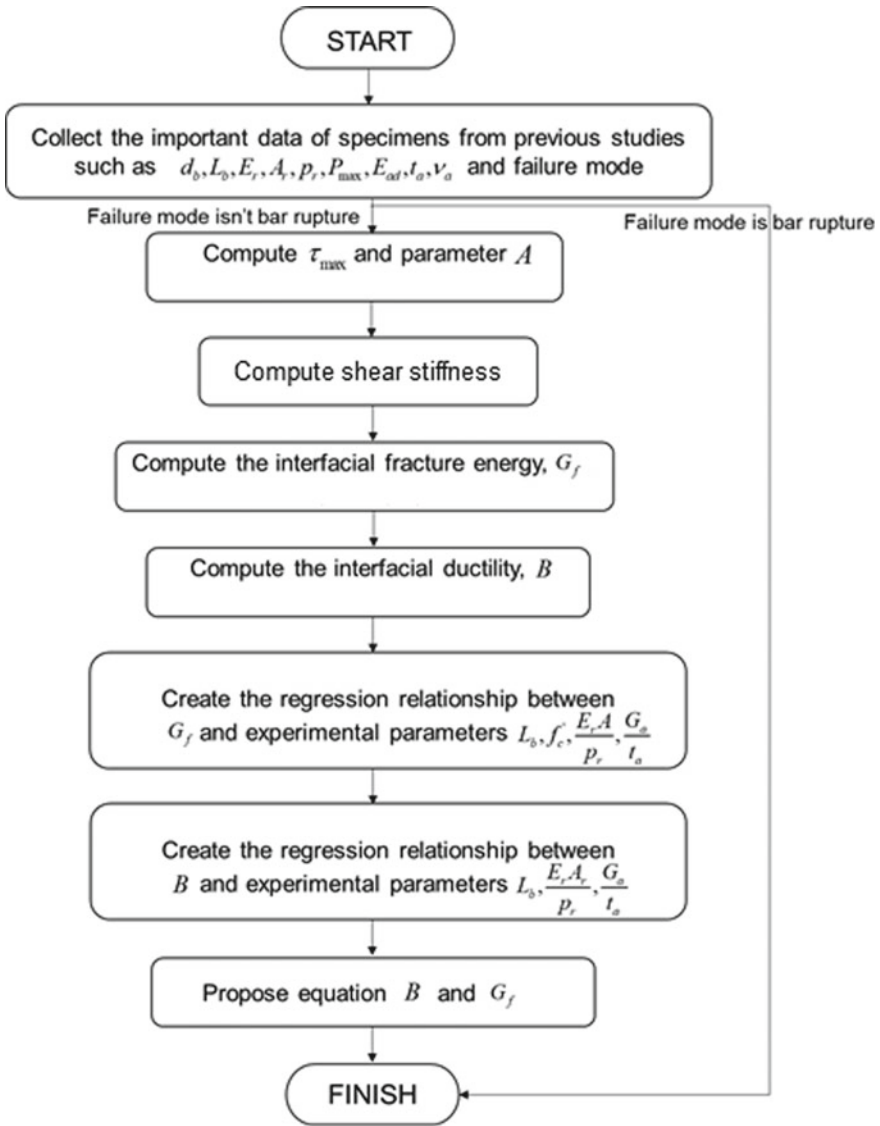
Fig. 5 Regression procedure considering all parameters (adapted from Nakares et al. [12])

beams occurred mainly by the fractures of concrete in the shear region of members. The details for the beam configurations, the beam properties, and the measured data could also be found in the open literature [5, 13, 14].

Figure 6 depicts the comparison in the FRP-strengthening shear contributions between the results achieved by the mechanical approach and the regressing approach. It is worth mentioning that the proposed model is strongly governed by the bond responses of the ETS FRP retrofitting to concrete. Thus, the bond factors

Fig. 6 Validation of the proposed model against the experimental data
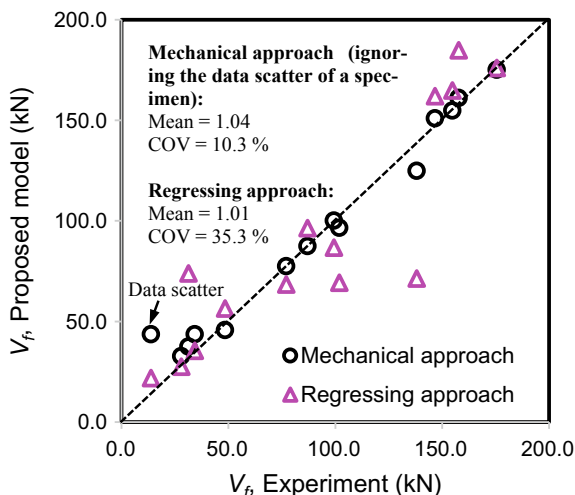
(i.e., the maximum bond stress and its peak slip) affected substantially the pre-
diction. Figure 6 indicates that the mechanical approach provides the good agree-
ment compared to the experiments rather than the regressing approach. In fact, the
means of the ratios of the predicted shear contributions to the monitored shear
resistances are 1.04 and 1.01 for the mechanical approach and regressing approach,
respectively. The coefficients of variation (COV) of the means for two aforemen-
tioned approaches are 10.3% and 35.3%, respectively. The possible reason for these
findings is the reduction of the accuracy in the regression procedure. Meanwhile,
the mechanical approach considered the mathematical aspects and the actual test
values, thereby the estimation of the ETS FRP shear contribution in the strength-
ened beams made by the bonding-based approach with mechanical considerations is
highly feasible. In addition, the predicted results obtained from the proposed shear
resisting method reflected reasonably the real responses of the retrofitting in the RC
beams. Indeed, for both tests and model, the shear contributions of the strength-
ening system are increased by increasing the shear reinforcement content.

4   Conclusions

This is the novel and promising study to estimate the shear strengths of the ETS
strengthening/retrofitting systems in the RC beams through the bonding-based
approach. In this study, the method to convert the shear mechanism of the ETS
retrofitting systems in the RC members into the bond response of the ETS FRP
intervening bar embedded in concrete is successfully proposed. In addition, the
regression procedure is also provided to carry out the regressing approach to
incorporate with the bonding-based method. For the mechanical approach, which

considering accurately the τ_m and s_m, the proposed model demonstrates the substantial efficiency in predicting of the shear carrying strengths of the ETS FRP strengthening rods. Although the regressing approach shows the less accuracy than the mechanical approach compared to the tests, it is still reasonable for calculation of the shear revisiting strength of the ETS FRP retrofitting bars in cases the accurate bond factors are unknown. The authors will conduct the further study to enhance the broad application and reliability of the bonding-based approach for estimation of the shear contribution of various shear strengthening types (i.e., not only ETS but also others) in the strengthened beams.

References

1. Bui, L.V.H., Boonchai, S., Ueda, T.: Mechanical performance of concrete beams strengthened by embedded-through section bars. In: The Thirtieth KKHTCNN Symposium on Civil Engineering, November 2–4, 2017, Taiwan
2. Bui, L.V.H., Boonchai, S., Ueda, T.: Bond behavior between embedded through-section bars and concrete. Int. J. Adv. Sci. Eng. Inf. Technol. **8**(4), 1008–1014 (2018)
3. Bui, L.V.H., Boonchai, S., Ueda, T.: Bond response of embedded through section GFRP bars to concrete. In: The JSCE International Summer Symposium in 2018. Hokkaido, Japan
4. Bui, L.V.H., Boonchai, S., Pitcha, J.: Comprehensive investigation on bond mechanism of embedded through-section fiber-reinforced polymer bars to concrete for structural analysis. J. Build. Eng. **29**, 101180 (2020)
5. Bui, L.V.H., Boonchai, S., Ueda, T.: Experimental investigation of concrete beams strengthened in shear with embedded through-section steel and FRP bars. J. Compos. Constr. **24**(5), 1–14 (2020)
6. ACI: Guide for the design and construction of structural concrete reinforced with FRP bars. American Concrete Institute, ACI 440.1R-15 (2015)
7. JSCE: Recommendations for design and construction of concrete structures using continuous fiber reinforcing materials. Tokyo: Japan Society of Civil Engineers, vol. C, p. 325. Concrete E, Japan (1997)
8. Godat, A., L'Hady, A., Chaallal, O., Neale, K.: Bond behavior of the ETS FRP bar shear-strengthening method. J. Compos. Constr. **16**, 529–539 (2012)
9. Caro, M., Jemaa, Y., Dirar, S., Quinn, A.: Bond performance of deep embedment FRP bars epoxy-bonded into concrete. Eng. Struct. **147**, 448–457 (2017)
10. Dai, J.G., Sato, Y., Ueda, T.: Development of the nonlinear bond stress–slip model of fiber reinforced plastics sheet–concrete interfaces with a simple method. J. Compos. Constr. **9**(1), 52–62 (2005)
11. Bui, L.V.H., Boonchai, S., Ueda, T.: Simulation of concrete beams strengthened by embedded through-section steel and GFRP bars with newly developed bond model. J. Adv. Concrete Technol. **18**(7), 364–385 (2018)
12. Nakares, K., Bui, L.V.H., Pitcha, J.: Analytical investigation on bond behavior between concrete and FRP bars of near-surface mounted and embedded through-section strengthening methods. In: The 25th National Convention on Civil Engineering, Thailand (2020)
13. Breveglieri, M., Aprile, A., Barros, J.A.O.: Embedded through-Section shear strengthening technique using steel and CFRP bars in RC beams of different percentage of existing stirrups. Compos. Struct. **126**, 101–113 (2015)
14. Mofidi, O.C., Brahim, B., Kenneth, N.: Experimental tests and design model for RC beams strengthened in shear using the embedded through-section FRP method. J. Compos. Constr. **16**(5), 540–550 (2012)

Effect of Damage by Notches in the Vibration Response of Homogeneous and Heterogeneous Beam Models

Erica Magagnini and Samir Khatir

1 Introduction

The detection of damage of structural components for many years has been the focus of various studies and research [1]. Assessment of structures by the response to vibration has gained popularity in recent years [2–4].

The study of effects of damages on the stiffness and strength of materials and structures interest also the new composite materials [5–7], which represent a large part of more recent material, employed in recent years also in civil engineering. The behavior of damaged beams built with homogeneous material has been analyzed by many authors by dynamic analysis with useful theoretical results [2]. Few works have been developed considering damaged elements built with heterogeneous material [8–10]. In general, the damage of the concrete by cracking that interests RC beams reduces its strength and influences the ductility of the sections [3]. In the case of localized deep damage, the loss of bending stiffness was evident [11].

In this paper, experimental vibration tests and numerical approach have been carried out to detect the response of damaged homogeneous and heterogeneous beam models with different concentrated damage degree [11–13]. The fundamental concept behind monitoring by vibration is that the structures' physical properties

E. Magagnini (✉)
Structural Section DICEA, Polytechnic University of Marche, Ancona, Italy
e-mail: e.magagnini@univpm.it

S. Khatir
Soete Laboratory, Faculty of Engineering and Architecture, Ghent University, Technologiepark Zwijnaarde 903, B-9052 Zwijnaarde, Belgium
e-mail: Khatir_samir@hotmail.fr

S. Khatir
Faculty of Civil Engineering, Ho Chi Minh City Open University, Ho Chi Minh City, Vietnam

influence the dynamic characteristics, so when a structural element is subjected to damage, its dynamic response will change [14–17].

The authors present experiments based on vibration tests and results obtained to evaluate different damages. The experimental behavior of damaged beam models has been analyzed by dynamic tests of free vibration adopting two beam models: a homogeneous beam model, undamaged and with three different configurations of damage by notches, and RC beam model as heterogeneous beam again damaged by notches. The damage is located in the middle of the span and the vibration tests make it possible to define the fall of the frequency values when the degree of damage is increased.

On the other hand, finite element (FE) numerical simulation is performed in order to obtain the frequencies of the device and modal shapes for the variation of the degree of damage of beams. The numerical analysis has been developed assuming constraints adopted in the tests: simply supported beam for homogeneous model and with free-free ends for RC beam model.

A comparison of experimental and numerical results made it possible to receive helpful suggestions on the adoption of non-destructive method of vibration tests in the detection of damaged beams, made by homogeneous and heterogeneous materials.

2 Dynamic Tests on Beam Models with Localized Damage

2.1 Experimental Test on Homogeneous Models

A slender homogeneous beam made by marble from Carrara (Italy) has been subjected to experimental tests [17].

The dimensions of the beam are summarized in Table 1. In order to simulate the hinge conditions at the ends the mechanical apparatus shown in Fig. 1a has been adopted.

The experimental campaign is organized in a way to carry out testing on a beam without damage, indicated as damage degree D0 (Fig. 1a), and on three specimens with a localized damage realized by notches at the midspan: n1–n1b–N1 (Fig. 1b, c, d).

The experimental dynamic test is performed by means of a technique where the acceleration of the structural element caused by an impact of a hammer at a fixed

Table 1 Geometrical and mechanical parameters of marble beam without damage [18]

Width b	Height h	Distance L between hinges	Young's modulus E	Density ρ	Moment of inertia I
30.6 mm	19 mm	325 mm	67.00 kN/mm^2	2.80·10^{-9} Ns^2/mm^4	19.20·10^3 mm^4
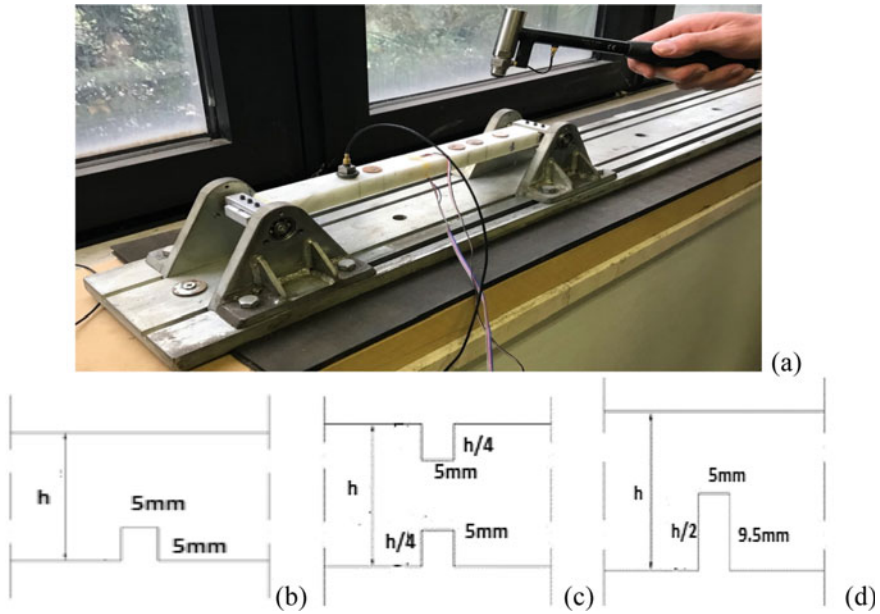
Fig. 1 a Setup for vibration tests and instruments adopted; detail of damage by notch at midspan section for homogeneous beam model: **b** damage degree n_1 **c** damage degree n_{1b}; **d** damage degree N_1 [17]

point is calculated by an accelerometer. The impact point is placed at a distance of 37.50 mm; with the piezoelectric accelerometer is positioned at a succession of points labeled as $a_i = 1,\ldots, 5$ placed at different intervals.

For each location a_i of the accelerometer, a set of 10 hits is made and the average value is obtained. A function referred to as coherence was elaborated during dynamic tests in order to monitor the absence of noise in the vibration results.

The suitability of the experimental setup is checked by the evaluation of the theoretical values of the natural frequencies for the first three modes of vibration $r = 1,\ldots, 3$, carried out prior to the experimental study. The Euler–Bernoulli expression, valid for any boundary condition, can be utilized for the evaluation of the circular frequency of a beam, supposed as slender and homogeneous [19]:

$$\omega_r^f = \left(\alpha_r \cdot \frac{r\pi}{L}\right)^2 \cdot \sqrt{\frac{EI}{\rho A}} \tag{1}$$

being EI the flexural stiffness, ρ the density, r the index of vibration mode and $\lambda_r = \frac{r\pi}{L}$ the eigenvalue.

The natural frequency can be evaluated as:

$$f_r = \frac{\omega_r}{2\pi} \tag{2}$$

The geometrical and mechanical parameters adopted for the calculation of the theoretical frequencies are summarized in Table 1.

Table 2 shows a comparison between the natural frequencies obtained experimentally, on undamaged beam model, theoretically considering the Eqs. (1) and (2) and by modeling with FE. It is possible to notice a good agreement between the data obtained by the experimentation and the ones given by theoretical analysis that confirms the validity of the system used for the simulation of the constraint conditions.

The results of the experimental vibration tests on damaged beams were gained in terms of frequency response functions (FRFs), composed of complex matrices from which the variables that characterized the dynamic behavior of the system were extracted. Table 3 gives the experimental data obtained by tests together with the variations in percent of frequency values $\frac{\Delta f_r}{f_{r,exp}^{D0}} = 100 \frac{f_{r,exp}^{D0} - f_{r,exp}^{Di}}{f_{r,exp}^{D0}}$ in relation to the evolution of damage degree. From the analysis of the data reported it is possible to verify that the localized damage causes the experimental frequency values to be reduced. In particular, it is possible to notice a relevant variation Δf_1 of about 25%, for the first mode $r = 1$.

Table 2 Theoretical and experimental frequencies obtained for beam without damage and beams under configuration of damage n1–n1b–N1 [17]

	f_1 [Hz]	Δf_1 [%]	f_2 [Hz]	Δf_2[%]	f_3 [Hz]	Δf_3 [%]
Euler–Bernoulli uniform beam	411.70	–	1646.75	–	3705.20	–
Theor. values by FEM	406.70	–	1398.54	–	3561.16	–
Exp. average values—D0	420.00	–	1246.00	–	3822.00	–
Exp. average values—n1	396.00	5.7	1350.00	−8.3	3826.00	−0.10
Exp. average values—n1b	314.00	25.2	1344.00	−7.8	3378.00	11.60
Exp. average values—N1	334.00	20.4	1406.00	−12.8	3544.00	7.27

Table 3 Geometrical and mechanical parameters for RC beam model

Width b	Height h	Length L	Young's modulus E	Density ρ	Moment of inertia I
b_1 = 75 mm; b_2 = 85 mm	80 mm	1000 mm	36.00 kN/mm^2	2.453 Ns^2/mm$^4 \cdot 10^{-9}$	3409 mm$^4 \cdot 10^3$

2.2 Vibration Test on Heterogeneous RC Beam Model

RC beam model with free-free ends is tested under free vibration (Fig. 2a). RC beam model (Table 3) had a trapezoidal cross section with widths of 85–75 mm, height of 80 mm, and length of 1000 mm. The RC beam is reinforced with longitudinal steel rods having a diameter of 6 mm at the extrados and of 12 mm at intrados without the presence of stirrups. The concrete was characterized by an experimental value of Young's modulus equal to about $E_c \approx 36.0$ kN/mm^2; while the steel bars was identified by an average yielding stress equal to $f_{y,av} \approx 500$ N/mm^2 with Young's modulus $E_s = 2.1 \cdot 105$ N/mm^2.

With the aim to obtain the theoretical frequency values, for a first approximation, the undamaged RC beam model is supposed to be a uniform slender beam neglecting gravitational forces, the effects of rotating inertia, shear deformation and damping.

In the case of a beam with free ends, the eigenvalue at the mode r $\lambda_r = \frac{r\pi}{L}$ given by Eq. (1) may be associated to the value λ_r for a simply supported beam [18]:

$$\lambda_r^f = \alpha_r \cdot \lambda_r \tag{3}$$

where a_r is a coefficient that is related to the various mode of vibration r, and it is equal to 1.506, 1.25, 1.167, and 1.125, respectively, for the first four modes.

The first four theoretical frequencies obtained for undamaged beam model with mechanical parameters given in Table 3 using Eq. (3) are summarized in Table 4.

The dynamic response of the RC beam was acquired by measuring the acceleration of the system with an accelerometer after having triggered the model with an impulsive force given by an impact hammer (Fig. 2a). The response of the structure
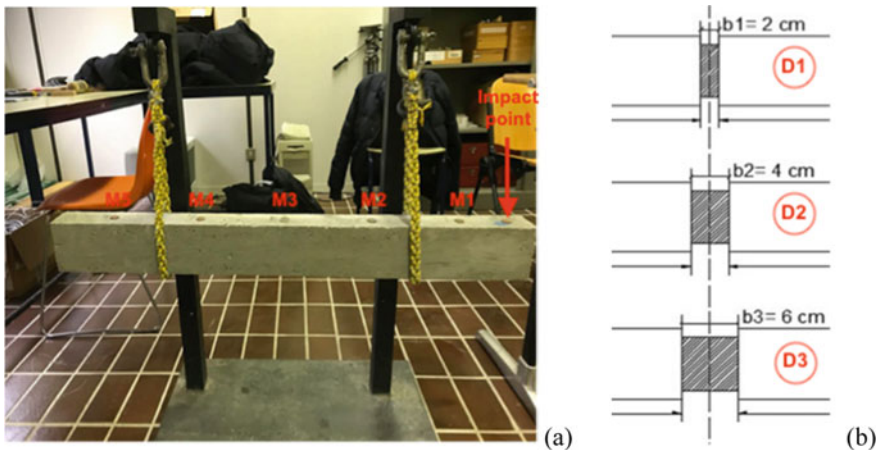
Fig. 2 a Setup of dynamic tests for RC beam; b damage conditions with a notch at the middle of the length

Table 4 Theoretical and experimental frequencies for RC beam model without damage

	f_1 [Hz]	Δf_1 [%]	f_2 [Hz]	Δf_2 [%]	f_3 [Hz]	Δf_3 [%]	f_4 [Hz]	Δf_4 [%]
Euler–Bernoulli uniform beam	314.63	–	867.01	–	1700.3	–	2809.11	–
FEM	270.21	–	690.39	–	1348.8	–	2339.02	–
Experimental average values	272	0.66	664	−3.97	1412	4.48	2340	0.04

is acquired by a piezoelectric accelerometer placed in one fixed position; while the impact force is imparted in five different positions, M_i $i = 1,\ldots, 5$, considering the average of 10 beach for each point. In a first phase of experimentation, the undamaged beam model (D0) is analyzed based on free vibration test. During the test, the experimental results are confirmed by comparing the experimental data with the preliminary theoretical data evaluated by FEM (Table 4), in terms of variation of frequency value $\frac{\Delta f_r}{f_{r,\exp}^{D0}} = 100 \frac{f_{r,\exp}^{D0} - f_{r,\text{FEM}}}{f_{r,\exp}^{D0}}$ in order to limit dynamic error of response due to experimental apparatus' defects.

Then, the effect of localized damage by notch all over the midspan section of the RC beam model was experimentally evaluated. Three different damage steps D1– D2 and D3, increasing the width of notch, were considered (Fig. 2b). Dynamic tests were performed and, for each damage phase, natural frequency values were acquired. Figure 3 shows the experimental diagrams of FRFs at various states of damage Di $i = 1,\ldots,3$, with the vibration measurements recorded by the accelerometer at a number of impact mark points. In Table 5 average values between measurements of frequencies for each positions of the impact point are summarized together with the percent variations of frequencies $\frac{\Delta f_r}{f_{r,\exp}^{D0}} = 100 \frac{f_{r,\exp}^{D0} - f_{r,\exp}^{Di}}{f_{r,\exp}^{D0}}$ in relation to the various degree of damage. The summary of the evolution of experimental frequency values evaluated for each damage step, for the four vibration modes $r = 1,\ldots, 4$, is given in Fig. 4a.

It can be seen how the increase of the notch's width causes a decrease of the frequency value. Figure 4b gives a comparison between the variations of frequency for the four vibration modes, as damage increases, with reference to the D0 condition. In relation to the diagrams reported in Fig. 4b, it is possible to see that also for low damage degrees, the variation is significant, showing a level equal to about 24%, for $r = 1$, and 8.5%, for $r = 2$. In correspondence of final damage level D3, the peak was reached, with a value of about 58%, for $r = 1$, and 15%, for $r = 2$.
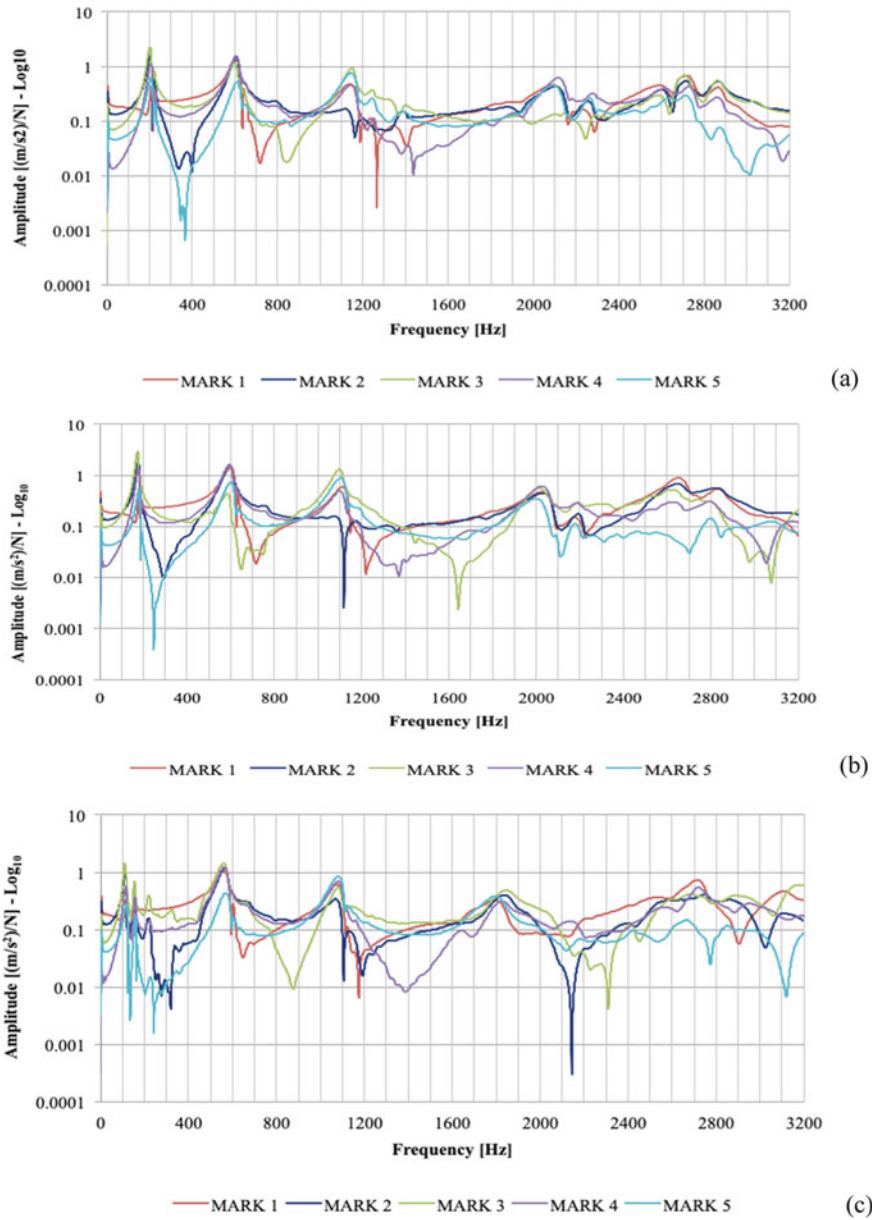
Fig. 3 Exp. envelope of FRF diagrams for RC beam model for different mark points, *Mi i* = 1,…, 5 at damage degrees **a** D1, **b** D2 and **c** D3

Table 5 Experimental and FE frequencies at different levels of damage for homogeneous beam [17]

Damage degree	exp f_1 [Hz]	FEM f_1 [Hz]	exp f_2 [Hz]	FEM f_2 [Hz]	exp f_3 [Hz]	FEM f_3 [Hz]
Un-damage D0	420.000	406.743	1246.000	1398.538	3822.002	3561.161
$n1$	396.001	390.232	1350.000	1464.031	3826.000	3354.156
$n1b$	314.000	312.229	1344.000	1451.602	3378.003	3212.068
$N1$	334.000	333.781	1406.000	1482.291	3544.000	3056.485
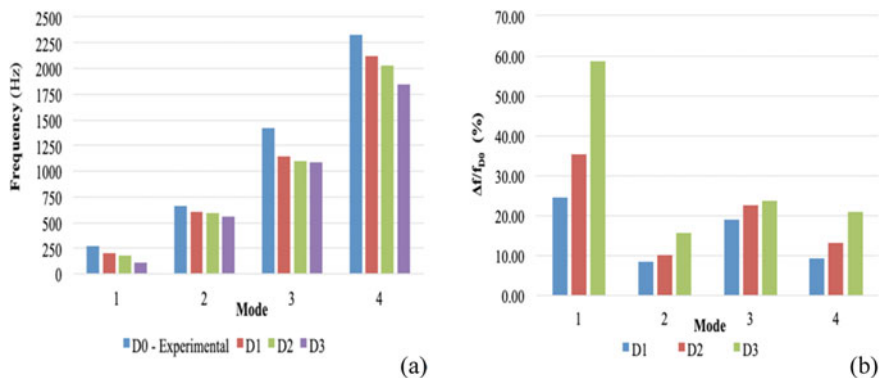
Fig. 4 **a** Values of frequency at each degree of damage; **b** variation of values of frequency at step of damage degree for RC beam

3   FE Modeling of Beam Models

The 3D ANSYS code is used for the modeling by FE of the homogeneous and heterogeneous beam models. Elements made by solid bricks are used to model all the materials adopted including marble and aluminum at the ends, for the homogeneous beam, concrete and steel, for the heterogeneous RC beam. Marble and concrete are modeled using the brick element, labeled as Solid65 [19]. The aluminum is reproduced using Solid185 element, having Young's modulus and Poisson's ratio equal, respectively, to ≈ 70.0 kN/mm^2 and 0.3. The steel reinforcement is modeled with the use of Beam188 element. The numerical analysis has been developed assuming constraints adopted in the tests: simply supported beam for homogeneous models and with free-free ends for RC beam models. In addition to the above components, element Combin14, defined by two nodes, a spring constant k and damping coefficients, is used in the numerical modeling in order to model the suspension springs of the beams, simulating the same free beam conditions during vibration tests (Fig. 5). Finally, during the modeling procedure also the mass of the accelerometer is considered. The accelerometer has been taken into account in a simplified way as a point with a mass of 15 g (Fig. 5).
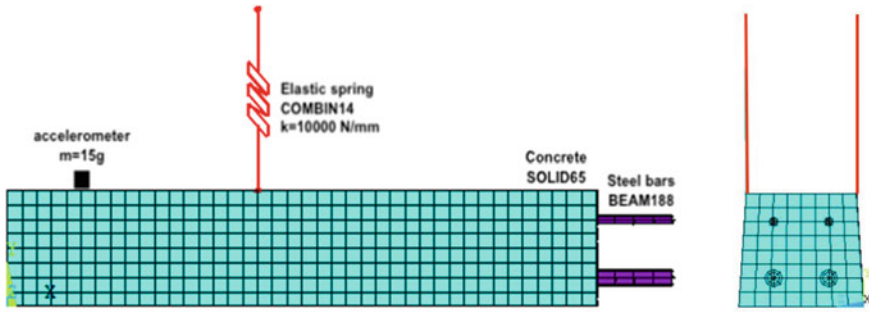
Fig. 5 Typical FE mesh with cross sections of heterogeneous RC beam

The purpose of the analytical study is to extract the frequencies of the device and the modular shapes as the degree of damage increases. The FE mesh adopted for RC beam model with different level of damage by notch is shown in Fig. 6. For each FE beam model, modal analysis was performed to derive the first four natural frequencies of beams corresponding to the experimental modes measured by the dynamic experiments. The first four values of frequency obtained by FE analysis without damage are presented in Table 2, for homogeneous marble beam, and in Table 4, for heterogeneous RC beam, together with the experimental results. Figure 7 shows the mode shapes provided by the FE modeling of damaged RC beam model for the first four modes of natural vibration $r = 1,…, 4$, at damage
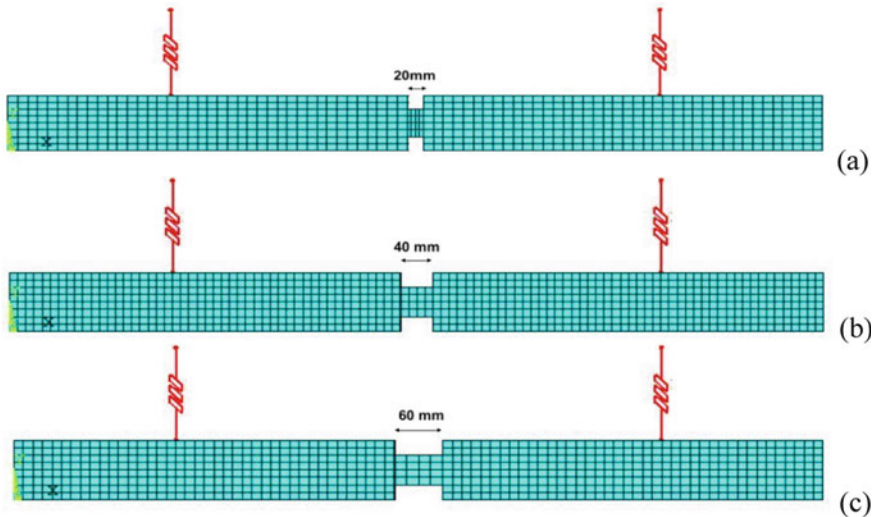
Fig. 6 FE mesh for heterogeneous RC damaged beam with different damage degree: **a** D1, **b** (D2) and **c** D3
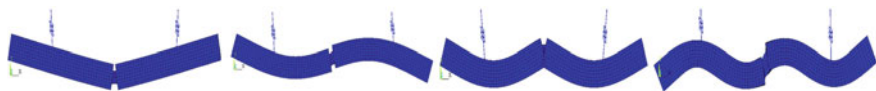
Fig. 7 First four modes of vibration $r = 1,\ldots, 4$ for heterogeneous RC beam evaluated with FEM —damage degree D1

Table 6 Experimental and FE frequencies at different levels of damage Di for heterogeneous RC beam

Damage degree	exp	FEM	exp	FEM	exp	FEM	exp	FEM
	f_1 [Hz]	f_1 [Hz]	f_2 [Hz]	f_2 [Hz]	f_3 [Hz]	f_3 [Hz]	f_4 [Hz]	f_4 [Hz]
D0	271.998	270.211	664.003	690.385	1411.573	1348.768	2340.000	2339.022
D1	206.983	201.463	607.764	575.882	1139.000	1138.655	2082.211	2153.229
D2	179.000	178.779	594.881	559.929	1097.772	1069.402	2018.964	2054.330
D3	114.997	113.702	563.597	551.668	1077.632	1060.931	1820.716	1806.767

degree D1. Tables 5 and 6 contain the values of frequency evaluated for each level of damage by FEM for homogeneous and heterogeneous beam models.

Table 5 gives a comparison between the values of frequency obtained by FE modeling of the homogeneous model and by experimentation considering the first three modes of vibration. It is possible to notice that the approximation of numerical results is adequate, with variations varying from 0.07 to 13.75%, in relation to the experimental results.

In Table 6 the values of frequency evaluated by experimental tests and FE modeling are compared for heterogeneous RC beam model. In this case for the first mode, the numerical modeling gives results that are in good agreement with the ones obtained experimentally, with a percent deviation for damage degree D0 and D3, equal to, respectively, 0.6% and 1.13%. Similar values of variations were obtained for the other first four modes, with variation in percent varying between 0.04 and 5.89%.

4   Conclusions

The paper deals about the experimental and numerical behavior of beam models undamaged and damaged by notches. Main results obtained are following synthesized:

- The reduction of the value of frequencies is connected to the increase of level of damage with a shift of experimental FRF diagrams;
- In the homogeneous beam models, the comparison between experimental and FEM results permits to verify an adequate agreement taking into account the

difficulty to simulate in the FE model the mechanical imperfections of the measurement apparatus;

- In the case of heterogeneous beams as RC beam models, the comparison between experimental and theoretical data by FEM permits to verify a perfect agreement.

References

1. Capozucca, R.: Damage to reinforced concrete due to reinforcement corrosion. Constr. Build. Mater. **9**, 295–303 (1995)
2. Salawu, O.S.: Detection of structural damage through changes in frequency: a review. Eng. Struct. **19**, 718–723 (1997)
3. Capozucca, R., Magagnini, E.: Analysis of cracked RC beams under vibration. J. Phy. Conf. Series **842**, 012076 (2017)
4. Cawley, P., Adams, R.D.: The location of defects in structures from measurements of natural frequencies. J. Strain Anal. Eng. Des. **14**, 49–57 (1979)
5. Arduini, M., Di Tommaso, A., Nanni, A.: Brittle failure in FRP plate and sheet bonded beams. ACI Struct. J. **94**(4), 363–370 (1997)
6. Capozucca, R., Bonci, B.: Notched CFRP laminates under vibration. Compos. Struct. **122**, 367–375 (2015)
7. Hassan, N.M., Batra, R.C.: Modelling damage in polymeric composites. Compos. Part B: Eng. **39**, 66–82 (2008)
8. Capozucca, R., Bossoletti, S.: Static and free vibration analysis of RC beams with NSM CFRP rectangular rods. Compos. B Eng. **67**, 95–110 (2014)
9. Capozucca, R.: A reflection on the application of vibration tests for the assessment of cracking in PRC/RC beams. Eng. Struct. **48**, 508–518 (2013)
10. Capozucca, R., Magagnini, E.: RC beam models damaged and strengthened with GFRP strips under bending loading and free vibration. Compos. Struct. **253**, 112730 (2020)
11. Capozucca, R.: Assessment of CFRP strengthened RC beams through dynamic tests. Compos. B Eng. **46**, 69–80 (2013)
12. Wahab, M.A., De Roeck, G., Peeters B.: On the application of FE model updating to damaged concrete beams. Identification in engineering systems: In: Proceedings of the Second International Conference Held in Swansea, pp. 578–587. Wales, UK, (1999)
13. Khatir, S., Brahim, B., Capozucca, R., Wahab, M.A.: Damage detection in CFRP composite beams based on vibration analysis using proper orthogonal decomposition method with radial basis functions and cuckoo search algorithm. Compos. Struct. **187**, 344–353 (2018)
14. Khatir, S., Wahab, M.A.: Fast simulations for solving fracture mechanics inverse problems using POD-RBF XIGA and Jaya algorithm. Eng. Fract. Mech. **205**, 285–300 (2019)
15. Khatir, S., Wahab, M.A.: A computational approach for crack identification in plate structures using XFEM, XIGA, PSO and Jaya algorithm. Theoret. Appl. Fract. Mech. **103**, 102240 (2019)
16. Khatir, S., Wahab, M.A., Boutchicha, D., Khatir, T.: Structural health monitoring using modal strain energy damage indicator coupled with teaching-learning-based optimization algorithm and isogoemetric analysis. Sound Vib. **448**, 230–246 (2019)
17. Capozucca, R., Magagnini, E.: Experimental vibration response of homogeneous beam models damaged by notches and strengthened by CFRP lamina. Compos. Struct. **206**, 563–577 (2018)
18. Warburton, G.B.: The dynamical behaviour of structures. Pergamon Press, Oxford (1964)
19. ANSYS Inc. 2019. ANSYS manual. USA: Southpoint (2019)

Reducing Shrinkage and Improving Cracking Resistance of Concrete by Using Fly Ash

Nguyen Thi Bich Thuy

1 Introduction

Concrete, one of the most popular materials, is used in the construction due to a low cost and easy availability of its ingredients [1]. However, concrete easily cracks due to its low tensile strength. Shrinkage strain occurs in concrete due to the loss of moisture from the fresh concrete stage until hardened stage. It is the volume of concrete which is changed. When tensile strength of concrete is higher than its tensile strength capacity, cracks occur in concrete. The cracks in concrete lead to reduce both the quality and the service life of building.

In order to prevent cracks due to shrinkage strain in concrete, many methods are applied. The use of nanocarbon is to enhance the tensile strength capacity of concrete. Fly ash used as a replacing cement material can reduce the shrinkage of concrete. The improved curing method is also noticed. Besides supplying water to concrete through the external curing methods, minimization of water loss from concrete is also considered by using the internal curing methods with internal curing materials. The good curing condition makes the hydration continues and shrinkage of concrete decreases, especially in hot weather in tropical regions.

Many researches have investigated the influence of fly ash on the properties of concrete, especially shrinkage of concrete. The compressive strength of concrete at early age is decreased by using low CaO fly ash. However, it is improved gradually at long term due to the pozzolanic reaction of fly ash. The use of fly ash decreases drying shrinkage and also decreases the porosity of concrete matrix [2]. Using fly ash also can improve the cracking resistance of SCC relative to the control mix. In order to improve the cracking resistance of concrete, the replacing cement can be up to 50% in low degree of restraint case and up to 35% for high degree of restraint case [3]. When observed the effect of fly ash on the damage of concrete, test results

N. T. B. Thuy (✉)
Ho Chi Minh City Open University, Ho Chi Minh City, Vietnam
e-mail: thuy.ntbich@ou.edu.vn

show that the fly ash to binder ratio from 20 to 30% indicates significant effect on the resulting damage. The number of crack per 100 cm^2 decreases sharply from about 153–29 [4].

In this paper, the effect of fly ash on the length changes of concrete under free and internal restrained conditions is evaluated. In order to examine the cracking resistance of concrete by using fly ash, cracking age and cracking width of concrete in the restrained ring test are observed according to ASTM C1581 [5].

2 Experimental Program

2.1 Materials

Portland cement type I and high CaO fly ash (class C) were used as binder in this study. Chemical composition and physical properties of the tested cement and fly ash (FA) are given in Table 1.

2.2 Mix Proportions

Concretes with a controlled water to binder ratio of 0.5 are used in this study. The percentages of fly ash replacing binder are 0% and 30%. The mix proportions of concrete are presented in Table 2.

Table 1 Chemical compositions and physical properties of the tested cement and fly ash

Chemical compositions (% by weight)	OPC	FA
SiO_2	18.93	37.09
Al_2O_3	5.51	19.69
Fe_2O_3	3.31	14.18
CaO	65.53	19.36
MgO	1.24	2.32
Na_2O	0.15	0.35
K_2O	0.31	2.92
SO_3	2.88	3.24
Free lime	–	2.36
LOI	–	0.01
Specific gravity	3.15	2.20
Blaine's fineness (g/cm^2)	3,100	2,790

Table 2 Mix proportions of concrete

Mix	w/b	Unit of weight (kg/m^3)			
		OPC	FA	Sand	Gravel
C100FA0	0.50	340	0	722	1129
C70FA30	0.50	238	102	722	1129

2.3 Test Procedure

Compressive strength. The concrete specimens have size of $100 \times 100 \times 100$ mm. The specimens were cured in water and measured at 1 day, 7 days, 28 days and 91 days after casting.

Length Changes. The free expansion of concrete was conducted according to ASTM 157 [6] and measured by a length comparator. Steel prisms with a size of $75 \times 75 \times 285$ mm were used to cast concrete specimens for this test. After casting 8 h, concretes were demoulded and the initial readings were recorded immediately. The curing condition was moist curing. The free expansion of concretes was tested until 7 days. On the other hand, the restrained specimens simulated the condition of reinforced concrete in real structures (see Fig. 1). The restraint condition was created by using two steel plates at both ends were fixed by nuts. The strains of the restrained specimens were recorded immediately after casting by using a data logger. Concrete specimens were demolded at 24 h after casting and then cured in moist curing until 7 days in a control curing room having a temperature of 28 ± 2 °C.

Cracking Resistance. The ring test is a common method used to examine the shrinkage cracking potential of concrete and follow the ASTM C1581 [5]. In this study, the steel ring strain and cracking age of concretes with and without fly ash were examined. Two strain gauges were attached opposite on the interior surface of the inner ring along a diameter. Fresh concrete was compacted in a circular mould around the steel ring, seen in Fig. 2. The specimen surface was flat and covered by plastic sheet. After finishing surface around 10 min, the bolts were immediately
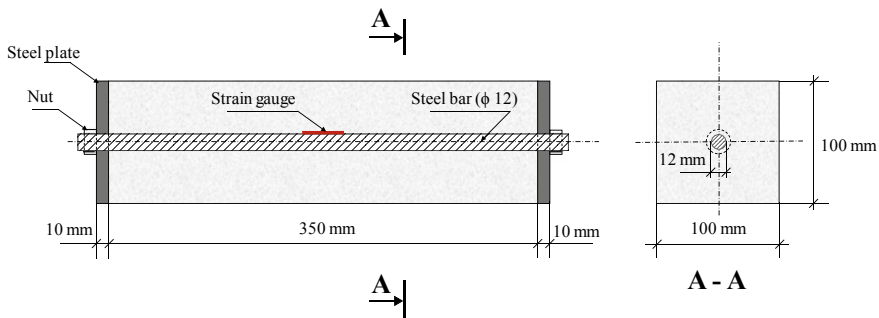
Fig. 1 Profiles of a specimen for testing internal restrained shrinkage

loosen with eccentric washers. The steel ring strain was recorded immediately after loosening the bolts with eccentric washers by data logger. After casting of 1 day, the outer ring was removed and the top surface of specimen was sealed by paraffin layers. Cracking age of concrete was indicated by a sudden decrease in the steel ring strain.

3 Results and Discussion

3.1 Compressive Strength

Compressive strength of concrete is decreased by using fly ash, as seen in Fig. 3. However, the compressive strength of concrete containing fly ash continually increases until later ages when compared to that of concrete without fly ash, as seen in Fig. 4. It is due to the pozzolanic reaction of fly ash.

3.2 Length Changes

Length changes of concretes with and without fly ash under free condition and internal restrained condition are shown in Figs. 5 and 6, respectively. The expansion of concrete during 7 days of moist curing condition is enhanced by using fly ash. The expansion of concretes occurs mainly during first day and slowly at later days. The development of compressive strength from the first day to the 7th day of

Fig. 2 Ring mould with attacked strain gauge
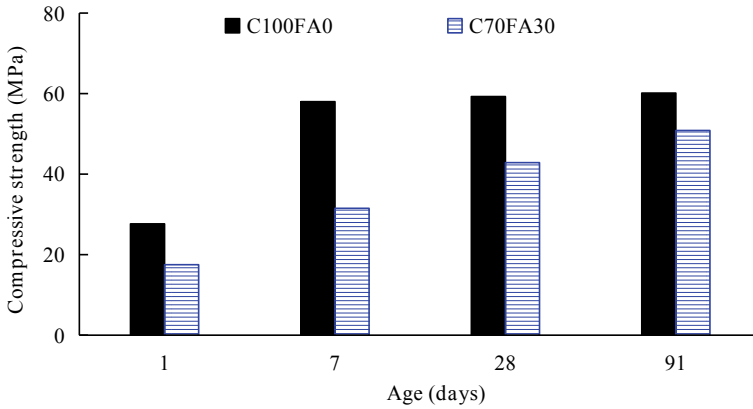
Fig. 3 Compressive strength of concrete
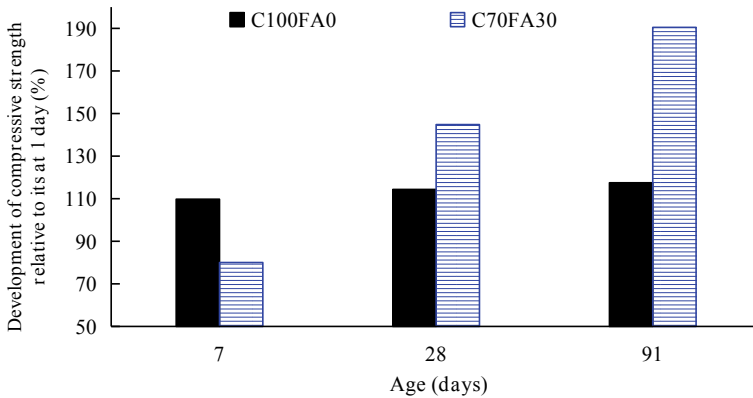
Fig. 4 Development of compressive strength relative to its at 1 day

fly ash concrete is lower when compared to that of non-fly ash concrete. Thus, fly ash concrete with lower stiffness leads to a higher expansion when compared to that of non-fly ash concrete [7].

Shrinkage of concrete was measured when all specimens were uncovered and cured in the air-curing condition. The use of fly ash decreases shrinkage of concrete in the air-curing condition. The role of the maximum expansion is very important on the shrinkage of concrete. It is obviously seen that concrete with higher expansion has a lower shrinkage at long term. This is because a higher expansion at early age compensates well the shrinkage at later age. Therefore, concrete needs a proper curing condition and mix proportions to enhance the early expansion.
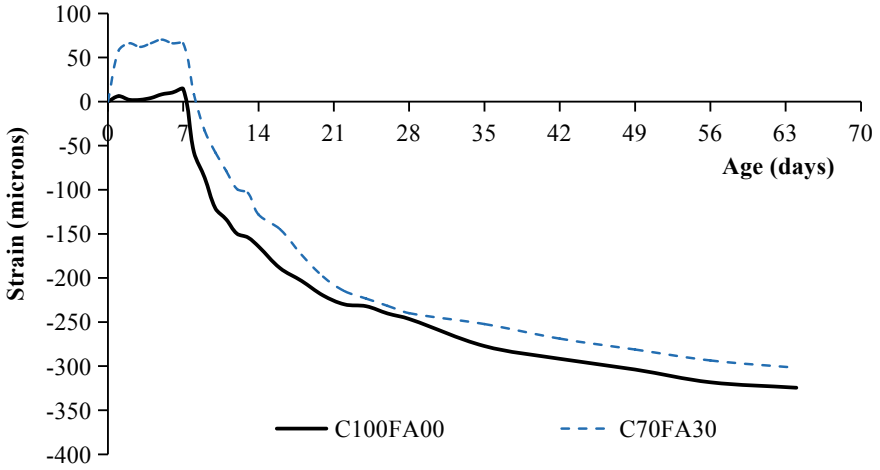
Fig. 5 Length changes under free condition
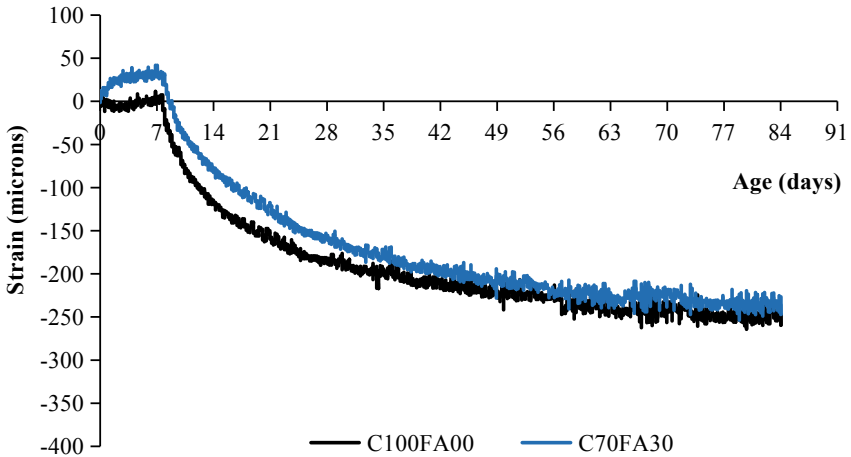
Fig. 6 Length changes under internal restrained condition

3.3 Cracking Resistance

The cracking resistance of concrete is evaluated by the ring test (external restrained condition). Cracks occur in concrete when the steel ring strain is suddenly decreased, as seen in Fig. 7. The tensile strain of all mixes become larger according to the elapsed time. Especially, strain of OPC shows the largest shrinkage in the first 2 weeks and cracks appears around 19 days. By using fly ash, the strain of concrete is decreased and the cracking age is delayed, and it is around 43 days.
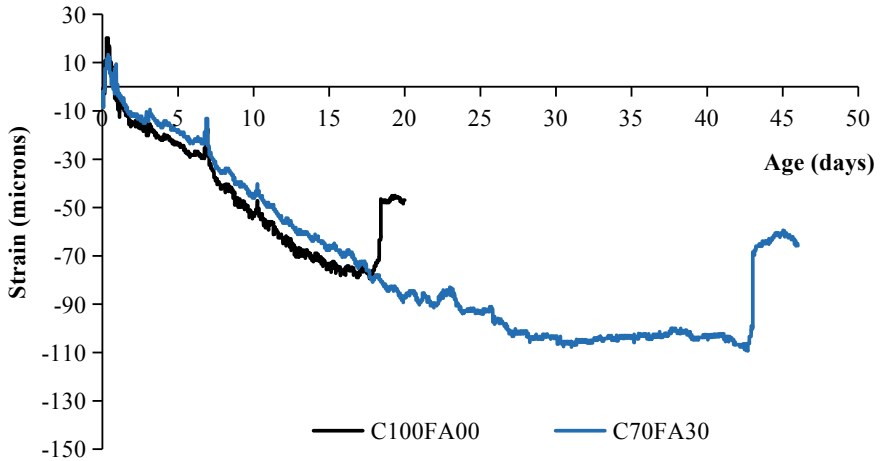
Fig. 7 Restrained strain during the ring test

4 Conclusions

From this study, some conclusions can be drawn as follows:

1. Compressive strength of fly ash concrete is lower than that of non-fly ash concrete. However, the development of compressive strength continually increases in fly ash concrete at later ages due to the pozzolanic reaction of fly ash.
2. The use of fly ash increases the expansion of concrete in moist curing condition and decreases shrinkage of concrete in the air-curing condition.
3. The cracking resistance of concrete evaluated by the ring test is enhanced by using fly ash. The cracking age of fly ash concrete is significantly delayed compared to non-fly ash concrete.

References

1. Rashad, A.M.: A brief on high-volume class F fly ash as cement replacement—a guide for civil engineering. Int. J. Sustain Built Environ **4**(2), 278–306 (2015)
2. Saha, A.K.: Effect of class F fly ash on the durability properties of concrete. Sustain. Environ. Res. **28**(1), 25–31 (2018)
3. Altoubat, S., Junaid, M.T., Leblouba, M., Badran, D.: Effectiveness of fly ash on the restrained shrinkage cracking resistance of self-compacting concrete. Cem. Concr. Compos. **79**, 9–20 (2017)
4. Rodrigue, A., Duchesne, J., Fournier, B., Bissonnette, B.: Influence of added water and fly ash content on the characteristics, properties and early-age cracking sensitivity of alkali-activated slag/fly ash concrete cured at ambient temperature. Constr. Build. Mater. **171**, 929–941 (2018)

5. ASTM 1581.: Standard test method for determining age at cracking and induced tensile stress characteristic of mortar and concrete under restrained shrinkage. In: ASTM International, West Conshohocken, PA (2003)
6. ASTM 157.: Standard test method for length change of hardened hydraulic cement mortar and concrete. Annual Book of ASTM Standards. ASTM International, West Conshohocken, PA (2008)
7. Nguyen, T.B.T., Chatchawan, R., Saengsoy, W., Tangtermsirikul, S., Sugiyama, T.: Influences of different types of fly ash and confinement on performances of expansive mortars and concretes. Constr. Build. Mater. **209**, 176–186 (2019)

Response of Concrete-Filled Double Skin Tube Segmental Columns Under Blast Loads

Tin V. Do and Trong Phuoc Nguyen

1 Introduction

With the development of the precast construction method and the prestress technologies, precast segmental structures (PSS), e.g. RC columns and RC beams, have been commonly built-in both building and bridge construction over the last few decades. PSSs offer numerous advantages including reducing the construction period, increasing construction quality, providing more cleaning and safe working environment for workers on-site as compared to conventional construction techniques. However, the structural behaviours of PSSs under hazardous loads, i.e. impact, vehicle collision, and blast events, have not fully understood due to the lack of studies on this field. Recently, few studies on the impact and blast response of the precast segmental columns (PSC) have been investigated [1–3]. It is found that under impact and blast loads, the PCS may exhibit higher maximum lateral displacement as compared to a monolithic column due to the relatively smaller lateral stiffness but smaller residual lateral displacement [4]. Under lateral loads, i.e. cyclic, impact and blast loads, the PSC allows the segmental joints to be opened which thus significantly reduces the flexural cracks and the residual displacement [1–6]. However, due to the stress concentration at the segment corner when opening, concrete crushing is normally observed on the reinforced concrete (RC) segment. Additionally, diagonal shear to the impacted segment and localised concrete spalling may occur when the PSC is impacted by a moving vehicle or blast pressures [1, 3]. In order to prevent the localised damage of the RC segment which may lead to the failure of the entire PSC, steel confinement and Fibre Reinforced Polymer (FRP) wrapping were usually incorporated into the PSC to boost the dynamic

T. V. Do (✉)
Karagozian & Case Australia Pty Ltd., Bondi Junction, NSW, Australia
e-mail: tin.do@ou.edu.vn

T. V. Do · T. P. Nguyen
Ho Chi Minh Open University, District 3, Ho Chi Minh City, Vietnam

capacity and enhance the dynamic performance of the segment [4, 7]. The contribution of these presented techniques in improving the impact and blast resistance capacity of the concrete segments has been reported in the recent research works [1, 7]. This study forms a part of the previous works of the authors and continues to investigate the dynamic performance of concrete-filled double skin tube segmental columns (CFDST-SC) under blast loads. The numerical model of the CFDST-SC is carefully developed and calibrated against the available data in the open literature. The numerical model developed in this study is then utilised to investigate the effects of the column critical parameters, i.e. number of segments, initial prestress force, and hollow ratio on its blast response.

2 Numerical Simulation

2.1 Numerical Model

Column configuration and simulation process

In this study, a detailed three-dimensional (3D) model of CFDST-SC is built in the commercial software LS-DYNA as shown in Fig. 1. The column is 2500 mm tall with the outer and inner diameter are 210 mm and 100 mm, respectively. The thickness of both inner and outer tubes is 5 mm with the tensile strength of steel material is 300 MPa. The compressive strength of concrete used in the numerical model is 30 MPa. The overall dimension of the column and its property are adopted from Zhang et al. [8]. The column is divided into five separate segments with the length of each segment is 500 mm. The segments are connected based on the initial compressive prestress from the tendon which is placed in the middle of the segment, see in Fig. 1. The yield strength of the prestress tendon used in this study is 1750 MPa while its diameter is 26 mm. Based on the column properties and suggestions from the previous studies [1, 7], the initial tensile force in the tendon is designed at approximately 380 kN.

In the numerical model, concrete, steel tubes and prestress tendon elements are modelled by solid elements. The mesh sensitivity analysis is also conducted in this study to achieve the optimal mesh size of elements. The numerical results converge when the column has meshed with 10 mm along its height and 80 points along the cross-section circumferential direction. The top and footing steel anchors are also simulated in the model by using solid elements, as shown in Fig. 1.

The numerical simulation process in this study consists of two separate stages, i.e. dynamic relaxation (DR) and explicit stage in order to accurately simulate the real behaviour of the CFDST-SC under blast load event where it usually comprises of two phases, i.e. prestress phase and blast phase. In the DR stage, the prestress load and gravity load will apply on the column through the Load_Thermal_Load_Curve and Load_Body_Z keywords, respectively. The DR stage will stop when the dynamic effects caused by these vertical loads on structures, i.e. stress and
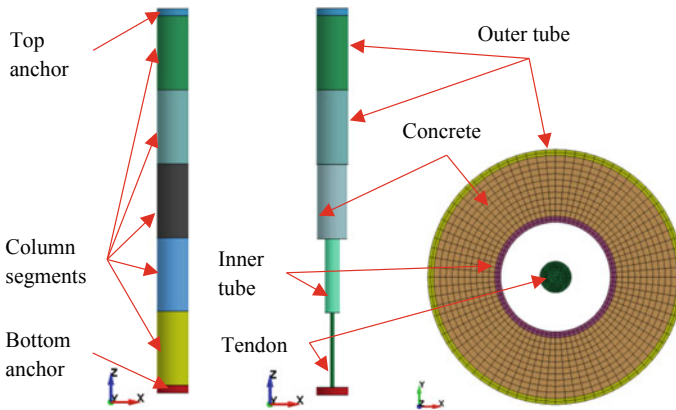
Fig. 1 3D model of CFDST-SC with prestress tendon in LS-DYNA

displacement variation, are eliminated from the model. The numerical results from the DR phase will then automatically pass to the second stage where the blast load is generated and applied on the front surface of the column. It is noted that the prestress force in the tendon is generated based on a temperature-induced shrinkage method with the detailed information for this modelling technique was introduced in the previous studies [1, 2, 7].

In the numerical model, all the footing elements are constrained in all directions and rotations, while the top part is constrained against horizontal displacements. It is worth mentioning that the top of the column is allowed to move in the vertical direction in order to apply the compressive load on the column through the tendon.

The LS-DYNA *Contact_Automatic_Surface_To_Surface keyword is adopted in the model to simulate the contact between the column segments, between columns and support parts, between concrete and steel tubes, between the tendon and column. This contact algorithm is usually used in the previous study to simulate the contact between two solid parts [1]. The dynamic and static coefficients of this contact algorithm are 0.5 and 0.6, respectively [1, 7, 9].

Material model

In this study, K&C concrete model i.e. Mat_072R3 is used to model concrete material. The accuracy of this material model in predicting blast response as well as failures of RC structures has been presented in many previous works [1, 3, 7, 9]. Dynamic increase factor (DIF) is also allowed to be incorporated in this material model to consider the strength increment of concrete under dynamic loads. In this study, the strength increase of concrete in tension and compression is accounted by using Hao and Hao [10]'s DIF models. Moreover, the dynamic response of the steel material is simulated by using Plastic_Kinematic (*Mat_003) material model with the Cowper and Symonds DIF model [11] is incorporated. For the prestress tendon, the Elastic_Plastic_Thermal material (*Mat_004) is required for the DR phase as

Table 1 Input parameters for LS-DYNA material models

Element/Material model	Input parameter	Value	Unit
Concrete—*Mat072R3	Mass density	2400	kg/m^3
	Compressive strength	30	MPa
	Poisson's ratio	0.19	
Steel tubes—*Mat_003	Mass density	7850	kg/m^3
	Young's Modulus	200	GPa
	Poisson's ratio	0.3	
	Yield strength	300	MPa
	Tangent modulus	2	GPa
	Strain rate parameter—C	40	
	Strain rate parameter—P	5	
Steel tendon—*Mat_004	Mass density	7850	kg/m^3
	Young's Modulus	200	GPa
	Poisson's ratio	0.3	
	Yield strength	1750	MPa
	Tangent modulus	2	GPa
	Coefficient of thermal expansion	10^{-4}	

presented above. Input parameters for the material models in the simulation are given in Table 1.

Simulation of blast loads

The LS-DYNA keyword namely *Load_Blast_Enhanced (LBE) is adopted in the model to simulate the blast event and calculate the blast pressure applied on the column. It is worth indicating that the use of this blast function in simulating the dynamic performance of RC and steel structures under the relatively far-field blast load, i.e. 1500 mm standoff distance with 250 mm cross-section diameter and 2500 mm column height, has been verified in the previous studies [7, 8]. In this study, the standoff distance of 1500 mm is also used to investigate the blast response of the 210 mm diameter CFDST-SC. Thus, it is reasonable to adopt this blast function in the simulation. The loading surface of the column is defined through *Load_Blast_Segment_Set keyword.

2.2 Numerical Verification

Since no available field blast tests of CFDST-SC can be found in the open literature, the response of CFDSTs under blast load conducted by Zhang et al. [8] will be used to verify the presented numerical approach, i.e. contact and material models, DIF, and blast function. The overall properties of the monolithic CFDST are similar to the CFDST-SC presented in the previous section. Figure 2 shows the comparison

Fig. 2 Comparison of blast response of the two columns
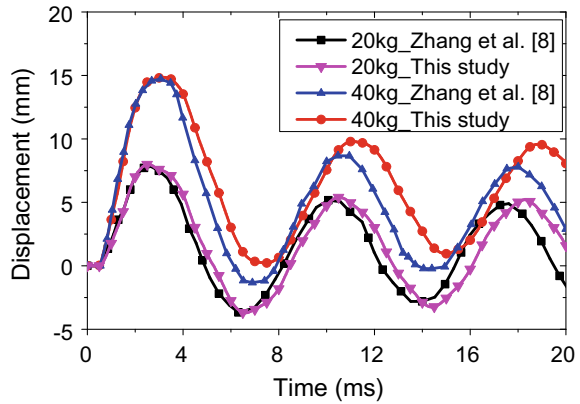
between the numerical model developed in this study and the numerical model developed by Zhang et al. [8]. As can be seen that the column responses under 20 kg TNT and 40 kg TNT blast, i.e. maximum and residual displacement, global displacement curve are well simulated by this modelling technique as compared to the previous model.

It is noted that by using the above numerical techniques, the blast response of concrete-filled steel tube (CFST) column and the impact response of the PSC have been fully calibrated in the previous studies [1, 2]. The calibrations indicate that the presented simulation technique can reasonably estimate the dynamic response of CFDST-SC structures under blast loads. Thus, the numerical model will then be used to investigate the blast response of the CFDST-SC in the subsequent sections.

3 Numerical Results and Discussions

Figure 3 shows damage to concrete and displacement time histories of the CFDST-SC under 10 kg TNT, 20 kg TNT and 40 kg TNT in comparison with the monolithic CFDST. As can be seen that under the same blast loading pressure, the CFDST-SC shows its advantages compared to the monolithic one with less concrete cracks and lower residual displacement owing to the joint opening mechanism and the residual capacity of the prestress tendon. The CFDST exhibits flexural cracks on both sides of the column at the two ends and mid-height while that is minor concrete damage at the joint corner, i.e. bottom segment, top segment, and mid-height segment, in the CFDST-SC. However, due to the smaller lateral stiffness caused by the discontinuous of the steel tubes and concrete at the segment joint, the CFDST-SC exhibits higher maximum lateral displacement than the CFDST, as shown in Fig. 3b. The numerical results are similar to the previous experiment test of the PSC under impact loads [4] where the maximum displacement of the PSC was also higher than that of the monolithic one.

(a) Damage to concrete

(b) Displacement time histories
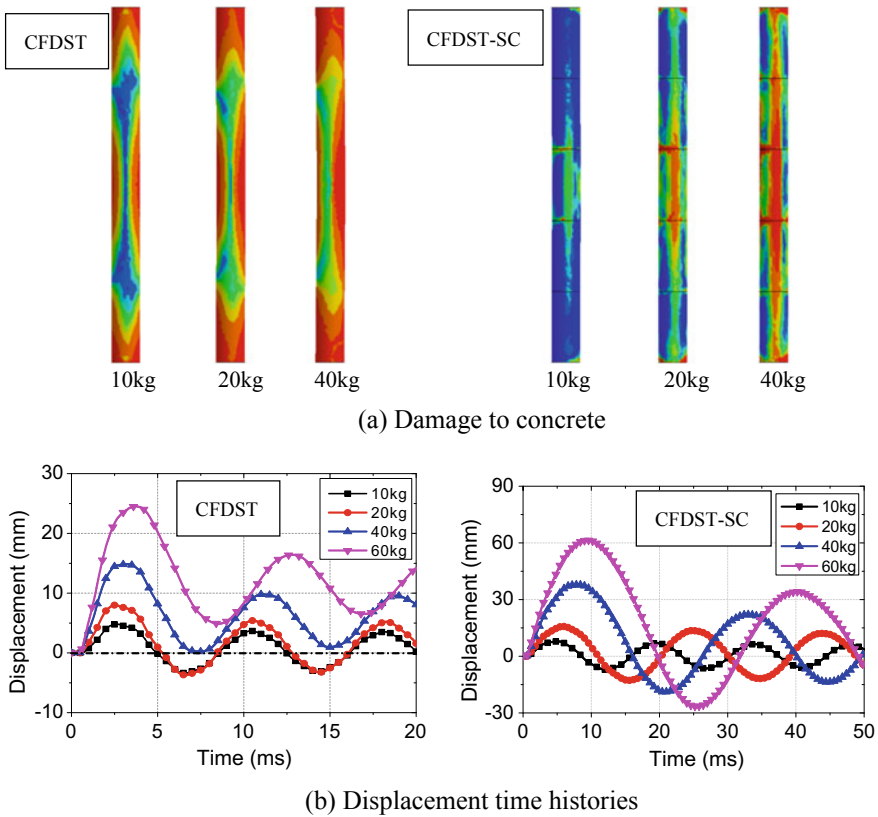
Fig. 3 Damage to concrete and displacement time histories of CFDST and CFDST-SC

Additionally, under high blast pressure, the axial force in the tendon increases significantly compared to the initial prestress level, as shown in Fig. 4, due to the openings at the joints. In the CFDST-SC the tensile force caused by the bending effect is only carried by the prestress tendon which is placed in the centre of the column while that is the steel tubes in the CFDST. The area of the prestress tendon in the CFDST-SC is usually smaller than the total area of the steel tubes in the tension side of the CFDST. Thus, the failure of the tendon in the CFDST-SC, e.g. tensile fracture as observed in the previous studies [7], is likely to occur prior to the failure of the steel tubes CFDST. Therefore, for the CFDST-SC under blast loads, external energy dissipation devices, e.g. Li et al. [6], are recommended to use in the CFDST-SC at critical segment joints, i.e. base and top joints, mid-height joint, to alleviate possible fracture of the tendon.

The numerical model of the CFDST-SC is then used to investigate the effects of the three-column parameters including number of segments, hollow ratio, and steel tube thickness on the blast response of the column.

Fig. 4 Tensile force in the tendon of the CFDST-SC
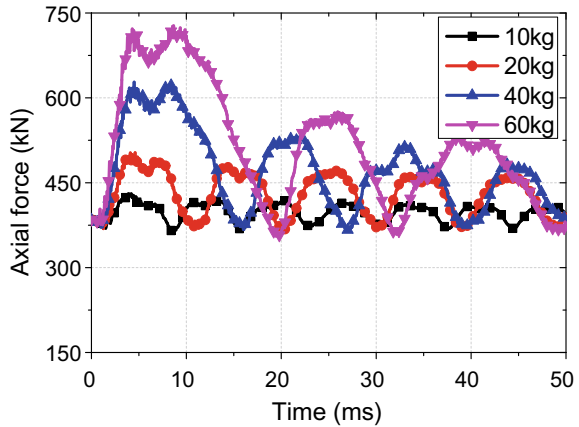
4 Parametric Studies

4.1 Number of Segments

Figures 5 and 6 present the numerical results and compare the blast responses of the CFDST-SC with different number of segments, i.e. 3 segments, 5 segments, and 7 segments under blast loads. Three columns are considered under two different blast scenarios, i.e. 20 kg TNT and 40 kg TNT. As shown in Fig. 5a that under the same blast conditions, the number of segments has minor effects on the variation of tensile force in the tendon when the three columns exhibit the similar peak values under the two prescribed blast scenarios. Since the variation of the tensile force in the tendon is associated with the total opening accumulated along the segmental column, the numerical results indicate that even with different number of opening joints, the total opening gap of the three columns is identical. It was previously mentioned that the relation between the total joint opening and the tendon axial force is one of the most challenges in the segmental column when an analytical approach is adopted to investigate its dynamic response, i.e. seismic and impact response [1, 6, 7]. This finding thus considerably contributes to understand the dynamic response of the segment columns.

Figure 6 shows that increasing the number of segments contributes to reduce the concrete damage at the segment corner. This is because in the column with more segments, e.g. 7 segments, more joint openings are observed along the column height under lateral blast load, which thus contributes to reduce the compressive stress on the segment corner, while the openings are mostly concentrated at the mid-height and column ends on the less segment column, e.g. 3 segments. With the similar total opening gap, as explained previously, the openings at the mid-height and column ends of the less segment column are wider. Thus, the compressive stress on the concrete segment is higher, and thus more concrete damage is observed. However, increasing the number of segments reduces the lateral stiffness
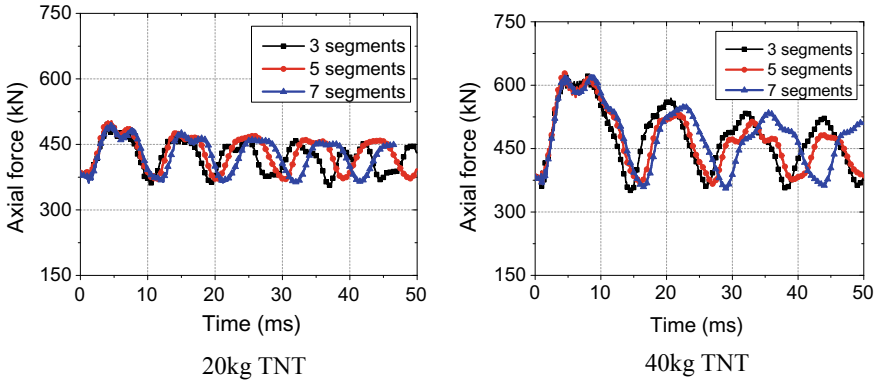
Fig. 5 Time histories of the tensile force in the tendon during the blast load

(a) Damage to concrete

(b) Displacement time histories
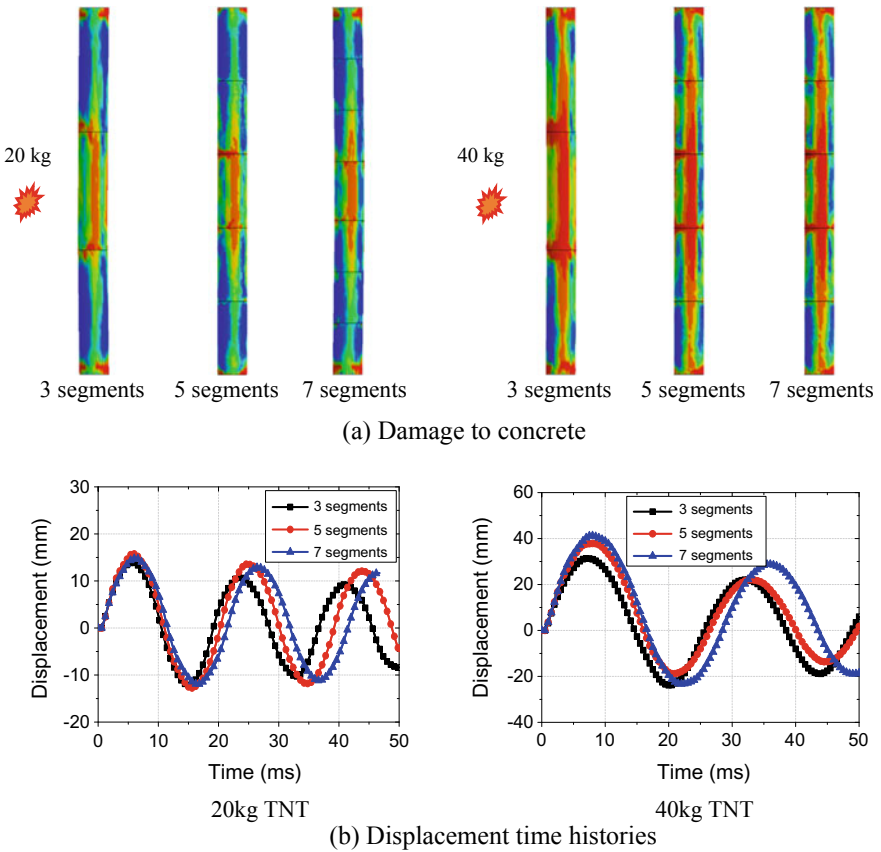
Fig. 6 Blast response of the CFDST-SC with different number of segments

of the CFDST-SC, therefore the column with more segments exhibits higher lateral displacement as compared to its counterpart under the same blast condition. Therefore, the number of segments has to be carefully considered in the design process in order to optimise its blast performance.

4.2 Hollowness Ratios

Figure 7 and Table 2 compare the blast responses of the CFDST-SC with three different hollowness ratios (HR), i.e. HR = 0.25, HR = 0.5 and HR = 0.75, subjected to the two prescribed blast scenarios. The hollowness ratio is defined based on the ratio between the outer diameter and the inner diameter of the concrete section, as shown in Fig. 1.

The figure and table show that the increase of HR increases concrete damage at the sides of the column (see Fig. 7a) and also increases the lateral displacement at the column mid-height (see Table 2). It is worth mentioning that under lateral blast pressure the column section exhibits the concrete expansion at two sides resulted from stress wave propagation from the front face to the rear face of the column [2]. The expansion at the sides of the cross-section causes the tensile stress and thus concrete damage as shown in Fig. 7a. The column with higher HR has thinner concrete layer, since more concrete damage is observed at the column sides. Additionally, the reduction of concrete area in the high HR column decreases the axial stiffness of the segment, which thus increases the opening at the segment-to-segment joints when they are open under the lateral blast pressure. Therefore, under similar blast conditions, the column with higher HR exhibits higher maximum axial force in the tendon, as shown in Table 2.
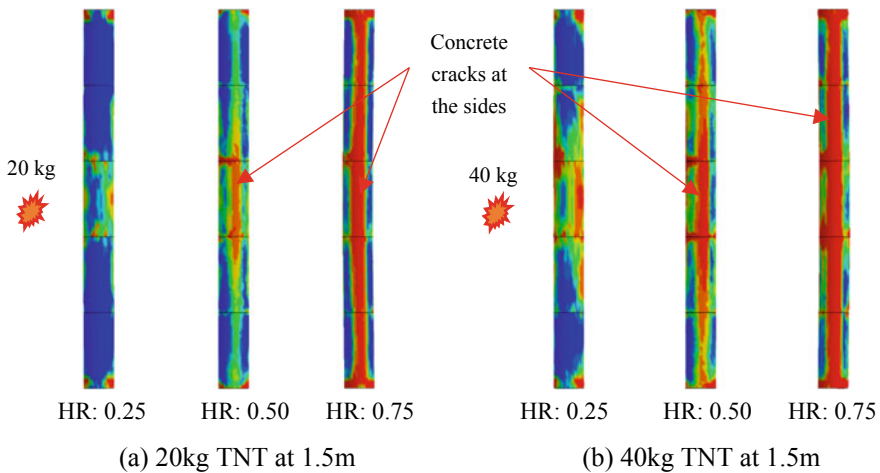
Fig. 7 Blast response of the CFDST-SC with different hollowness ratios

Table 2 Responses of the CFDST-SC with different hollowness ratios under blast loads

Column	Concrete outer diameter (mm)	Concrete inner diameter (mm)	TNT charge (kg)	Maximum displacement (mm)	Peak axial force in tendon (kN)
HR 0.25	200	50	20	15.1	491.5
HR 0.50	200	100	20	15.8	503.0
HR 0.75	200	150	20	19.7	526.5
HR 0.25	200	50	40	32.9	617.7
HR 0.50	200	100	40	37.9	627.8
HR 0.75	200	150	40	46.8	687.4

4.3 Steel Tube Thicknesses

Figure 8 presents damage to the concrete of the CFDST-SC with different steel tube thicknesses (STT) under the two blast scenarios. The thickness of the steel tubes in the three considered columns is given in Table 3. It is noted that the three columns are designed with the same area in the steel material. As shown in the figure that changing the steel tube thickness has a minor influence on concrete damage when the concrete crack patterns on the columns are similar. All the columns exhibit concrete damage at the sides due to the section expansion and at the segment corners caused by the joint opening.

Additionally, the variation of the steel tubes' thicknesses slightly affects the blast responses of the CDFST-SC as summarised in Table 2. The increase of the outer tube's thickness from 3 to 6.25 mm while decreasing the inner tube's thickness

STT1   STT2   STT3   STT1   STT2   STT3

(a) 20kg TNT   (b) 40kg TNT
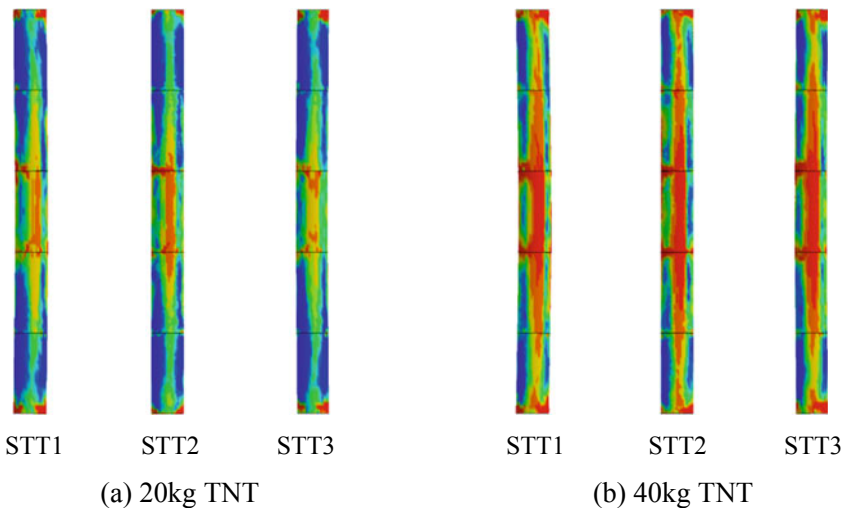
Fig. 8 Blast response of the CFDST-SC with steel tube thicknesses

Table 3 Responses of the CFDST-SC with different steel tube thicknesses under blast loads

Column	Outer tube (mm)	Inner tube (mm)	TNT charge (kg)	Maximum displacement (mm)	Peak axial force in the tendon (kN)
STT1	3.00	9.00	20	18.4	490.1
STT2	5.00	5.00	20	16.7	503.4
STT3	6.25	2.50	20	16.4	503.8
STT1	3.00	9.00	40	43.4	617.7
STT2	5.00	5.00	40	37.9	627.8
STT3	6.25	2.50	40	36.8	641.0

from 9 to 2.5 mm reduces the maximum horizontal displacement at the column by 15% but increases the peak tensile force in the tendon by 3.7%. It is because the contribution of the outer tube to the lateral stiffness of the column is more significant than the inner one. Thus, increasing the outer tube's thickness and reducing the inner tube's thickness but keeping the same area of the steel material will increase the column stiffness and thus reduce the column lateral displacement. However, under the lateral blast load, the column deformation and joint openings mainly contribute to dissipate the blast energy. With similar input blast energy, the column with smaller lateral displacement will have higher joint opening. Therefore, the column which has lower lateral displacement will exhibit higher tensile force in the tendon.

5   Conclusions

This study investigates the blast response of the concrete-filled double skin tube segmental column (CFDST-SC) by using the numerical model developed in LS-DYNA. Under the blast pressure, the CFDST-SC exhibits less concrete damage, i.e. only compressive damage concentrated at the segment corners due to joint opening, but higher lateral displacement as compared to the monolithic one. The effects of the column parameters, i.e. number of segments, hollowness ratios, and steel tubes' thicknesses on the column response have also been considered. It has been found that the column with more segments exhibits higher lateral displacement but less concrete damage at the corner as compared to the column with fewer segments. However, the change of the column segments shows a minor influence on the peak tensile force in the tendon. Furthermore, increasing the hollowness ratio of the CFDST-SC will increase the lateral displacement, cause higher axial force in the tendon, and induce more concrete damage in the columns. Last but not least, the variation of the steel thicknesses, i.e. varying from 3 to 9 mm, has an insignificant effect on the damage level of the CFDST-SC.

References

1. Do, T.V., Pham, T.M., Hao, H.: Impact response and capacity of precast concrete segmental versus monolithic bridge columns. J. Bridge Eng. **24**(6) (2019)
2. Do, T.V., Pham, T.M., Hao, H.: Stress wave propagation and structural response of precast concrete segmental columns under simulated blast loads. Int. J. Impact Eng. **143** (2020)
3. Li, J., Hao, H., Wu, C.: Numerical study of precast segmental column under blast loads. Eng. Struct. **134** (2017)
4. Hao, H., et al.: Impact response and mitigation of precast concrete segmental columns. In: 12th International Conference on Shock and Impact Loads on Structures, Singapore (2017)
5. Ou, Y.-C.: Precast Segmental Post-Tensioned Concrete Bridge Columns for Seismic Regions. State University of New York at Buffalo (2007)
6. Li, C., et al.: Cyclic test and numerical study of precast segmental concrete columns with BFRP and TEED. Bulletin of Earthquake Engineering (2019)
7. Do, T.V., Pham, T.M., Hao, H.: Effects of steel confinement and shear keys on the impact responses of precast concrete segmental columns. J. Construct. Steel Res. **158** (2019)
8. Zhang, F., et al.: Numerical modeling of concrete-filled double-skin steel square tubular columns under blast loading **29**(5) (2015)
9. Do, T.V., Pham, T.M., Hao, H.: Numerical investigation of the behavior of precast concrete segmental columns subjected to vehicle collision. Eng. Struct. **156** (2018)
10. Hao, Y., Hao, H.: Influence of the concrete DIF model on the numerical predictions of RC wall responses to blast loadings. Eng. Struct. **73** (2014)
11. Cowper, G.R., Symonds, P.S.: Strain-Hardening And Strain-Rate Effects in the Impact Loading of Cantilever Beams. Brown Univ Providence Ri (1957)

The Superplastic Behavior of AA7075 al Alloy Under the Impacts of the Temperature and Strain Rate

**Nguyen Manh Tien, Nguyen Truong An, Tran Duc Hoan,
Nguyen Trung Thanh, and Le Trong Tan**

1 Introduction

Superplastic materials have the deformation ability with a large extent without being fractured under the impact of low yield stress and depending on the strain rate [1]. Superplastic phenomenon of materials is characterized by three basic signs. The degree of plastic deformation is large, it can reach hundreds or even thousands of percent without destroying the material. The stress required to deform the material in the superplastic state is very small compared to the plastic deformation in normal conditions. Superplastic deformation stress is very sensitive to changes in strain rate.

In order to appear structural superplastic, three conditions must be ensured: microstructure of material, deformation temperature, and strain rate. Metals and alloys have a fine and stable microstructure (usually between $5 \div 15$ μm) and the particle size is almost unchanged during deformation. The temperature range of deformation to superplastic deformation is quite wide, usually ranging from $(0.5 \div 0.9)$ T_{nc} (T_{nc}—melting point of the material in degrees Kelvin). The deformation temperature must ensure no change during deformation and uniformity throughout the workpiece. The strain rate must be small enough for diffusion to occur and must be large enough at high temperatures to ensure that the particles do not grow during machining. Normally, the strain rate of superplastic deformation usually ranges from $(10^{-4} \div 10^{-2})$ s^{-1} [2].

The superplastic deformation studies found that the ability of superplastic deformation depends largely on factors such as particle size and deformation temperature. In case, the superplastic deformation temperature will be lower with smaller particle size, smaller yield stress, higher strain rate.

In the publication of Barnes [3] and Rambabu et al. [4] shows that the deformed aluminum alloy has been applied widely in engineering and life (the automotive,

N. M. Tien (✉) · N. T. An · T. D. Hoan · N. T. Thanh · L. T. Tan
Le Quy Don Technical University, 236 Hoang Quoc Viet, Hanoi, Vietnam

aerospace, and ship industries). The application of the superplastic materials was recently published by Backofen et al. [5]. In which, for the first time, a detail was pneumatically formed from a sheet of superplastic Al–Zn eutectoid alloy (70% Zn, 21% Al Sheet). From the published scientific reports show that a commercially useful superplastic aluminum alloy was possible, many aluminum alloys are used to produce engineering products from sheet material [6]. In recent years, more and more research works have confirmed the superplastic deformation ability of aluminum alloys such as AA2004, AA5083, AA7075, AA7475, AA8090.

The goal of the paper is to assess the effect of technology factors on superplastic deformation of AA7075 sheet. The factors considered include strain temperature (470, 500, 530, 530 °C) and initial strain rate (5×10^{-4} s^{-1}, 10^{-3} s^{-1} and 1.5×10^{-3} s^{-1}), while the response is maximum superplastic elongation (δ). From the research results allowed to determine the reasonable process parameters for superplastic deformation of AA7075 aluminum alloy.

2   Experimental Procedure

The composition of chemical elements of AA7075 alloy is presented in Table 1. The AA7075 aluminum alloys are highly durable aluminum alloys and have superplasticity properties. The superplasticity of AA7075 alloy at different strain rates and temperatures were studied by Yang et al. [7]. The degree of deformation and yield stresses of superplastic materials are sensitively dependent on strain rate.

The initial workpieces were used to perform the thermomechanical process to prepare the material microstructure for superplastic deformation with an initial thickness of 5 mm. The Taharsahraoui's method were used to reduce the thermomechanical treatment processing time [8].

The thermomechanical treatment of AA7075 alloy consists of different stages (Fig. 1): Firstly, the initial workpieces is solution treatment at 500 °C to dissolve all dispersed phases. Subsequently, the alloy is cooled with the furnace to retain the dissolved substance in the solution, the furnace is kept heat at 380 °C for two hours to create an even distribution of phase Al_2CuMg (S), $Al_2Mg_3Zn_3$ (T). Next, the samples are warm rolled at 180 °C to the level of 80% deformation (Table 2). On heavy warm working, these particles are violently intense localized deformation and lattice rotation which provide sites for discontinuous recrystallization. Rapid heating to 500 °C results in many recrystallization nuclei in the locally deformed regions adjacent to the coarse precipitates and the result obtained is microstructural features of material with fine stable and grain size.

Table 1 The composition of chemical elements of AA7075 alloy (in weight percent)

Zn	Mg	Cu	Fe	Cr	Ti	Mn	Si	Al
5.35	2.34	1.32	0.30	0.22	0.04	0.024	0.05	Balance

Source The datas are surveyed by the research team
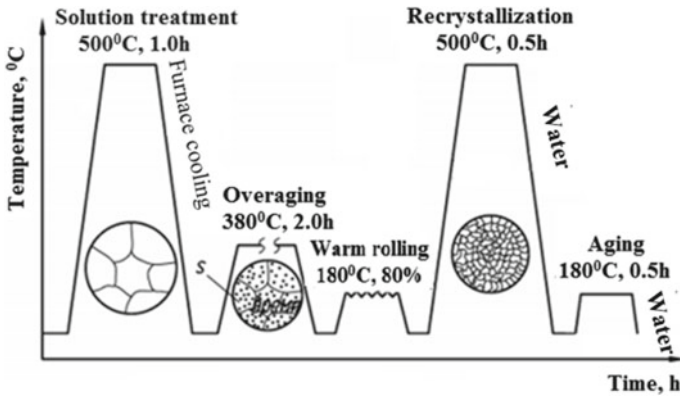
Fig. 1 The thermomechanical treatment process of AA7075 alloy [9]

Table 2 The warm rolling process

Steps	Rolling temperature [°C]	The sample thickness [mm]		Strain		Total deformation [%]
		Before	After	mm	ε[%]	
1	180	5.0	4.5	0.5	10	10
2	180	4.5	4.0	0.5	11.1	20
3	180	4.0	3.5	0.5	12.5	30
4	180	3.5	3.0	0.5	14.3	40
5	180	3.0	2.5	0.5	16.7	50
6	180	2.5	2.0	0.5	20	60
7	180	2.0	1.5	0.5	25	70
8	180	1.5	1.2	0.3	20	76
9	180	1.2	1.0	0.2	16.7	80

Tensile tests were carried out with various process parameters including temperatures of 470, 500, 530 and 550 °C, and strain rates 5×10^{-4}, 10^{-3}, 1.5×10^{-3} s^{-1}. The total number of experiments performed was twelve. Tensile testing mode in superplastic condition is shown in Table 3.

The Devotrans DVT FU/RDNN 50kN—CKS testing machine (the working speed from 0.001 to 500 mm/min) is used in the tensile tests. The temperature deformation is guaranteed by furnace Nabertherm B180 (Fig. 2).

Table 3 The tensile test mode

Samples	Strain rate [s^{-1}]	Temperature [°C]
1	5×10^{-4}	470
2	10^{-3}	470
3	1.5×10^{-3}	470
4	5×10^{-4}	500
5	10^{-3}	500
6	1.5×10^{-3}	500
7	5×10^{-4}	530
8	10^{-3}	530
9	1.5×10^{-3}	530
10	5×10^{-4}	550
11	10^{-3}	550
12	1.5×10^{-3}	550

Fig. 2 The test equipment

3   Results and Discussions

The microstructure of AA7075 cast aluminum alloy is shown in Fig. 3a. The results show that the sample microstructure after casting has dendrite structure. Aluminum alloys often have an unbalanced distribution around the grain. With this microstructure, it adversely affects the mechanical properties and plasticity of the aluminum alloy. Figure 3b–d show the microstructure during thermomechanical treatment.

After the overage process: The dissolution of solid solutions of common alloy elements such as Zn, Mg, Cu, etc. and even component in cast ingot occurs. In addition, after overaging, the phase S (Al_2CuMg) was fine microstructure about 1 μm (Fig. 3b). The S-phase increases the deformation effect of the workpiece during the warm rolling process, ensuring a total deformation of about 80%.

After recrystallization process: Obtained AA7075 alloy microstructural features (especially fine stable and grain size) shown in Fig. 3c. The grain size is about
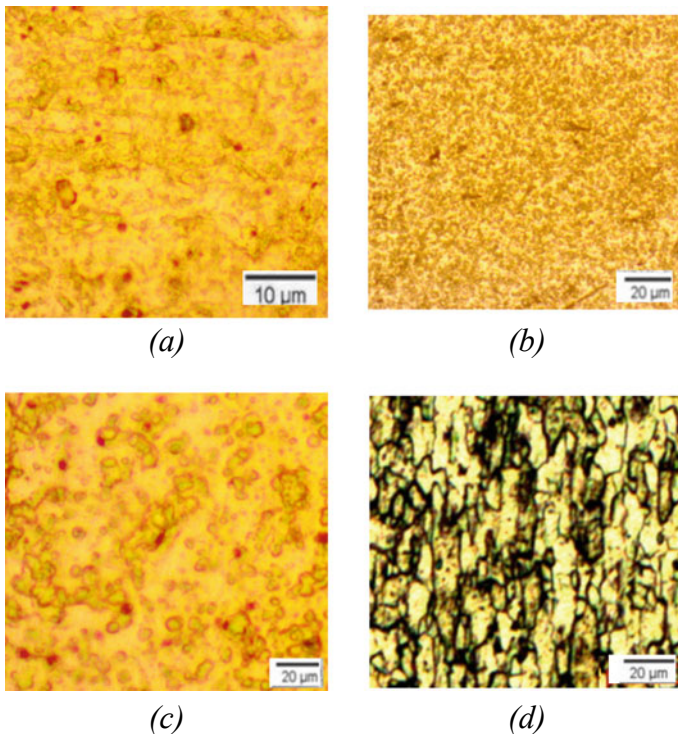
Fig. 3 Microstructure of AA7075 aluminum alloy (before and after thermomechanical treatment), **a** micrograph of AA7075 cast aluminum alloy; **b** after overaging; **c** after warm rolling; **d** after recrystallization

10–13 µm. This is one of the conditions for AA7075 alloy can be performed superplastic deformation process. The experimental results are shown in Table 4.

The samples after tensile test process are shown in Fig. 4. The experimental results for different initial strain rates and the different temperatures are shown in Figs. 5 and 6.

Based on the results of the tensile tests, maximum stresses were below 10 MPa. With the value of constant strain rate, when reducing the temperature stress, the maximum stress will increase. With the value of constant strain temperature, the maximum stress decreases when the strain rate decreased. However, through the maximum stress results obtained, it was found that maximum stress value is relatively small and the difference is not much (5.0 and 10 MPa). In Fig. 5, with deformation temperature of 530 °C and initial strain rate of 10^{-4} s^{-1}, the stress reaches lowest value. The highest maximum stress was obtained at 470 °C and 1.5×10^{-3} s^{-1}.

Found that, with the value of constant strain rate, when the deformation temperature increases, the deformation ability increases ($\delta = 280\%$). The elongation to fracture reaches the maximum value for temperature of 530 °C and initial strain rate of 10^{-3} s^{-1}. In deformation temperature for 470, 500 and, 550 °C, the test results obtained lower elongations [2, 10].

Besides, with the value of constant strain temperature, when the strain rate increased, the elongation to fracture increases. However, the elongation to fracture is reduced when the strain rate is greater 10^{-3} s^{-1} [10].

Table 4 The experimental results

N°	Elongation to fracture δ [%]	Maximum stress σ [MPa]
1	130	8.0
2	170	8.4
3	130	10
4	150	7.4
5	240	8.0
6	150	9.8
7	170	5.0
8	280	7.6
9	180	8.3
10	140	4.6
11	180	7.0
12	140	7.8

Fig. 4 The samples after tensile tests
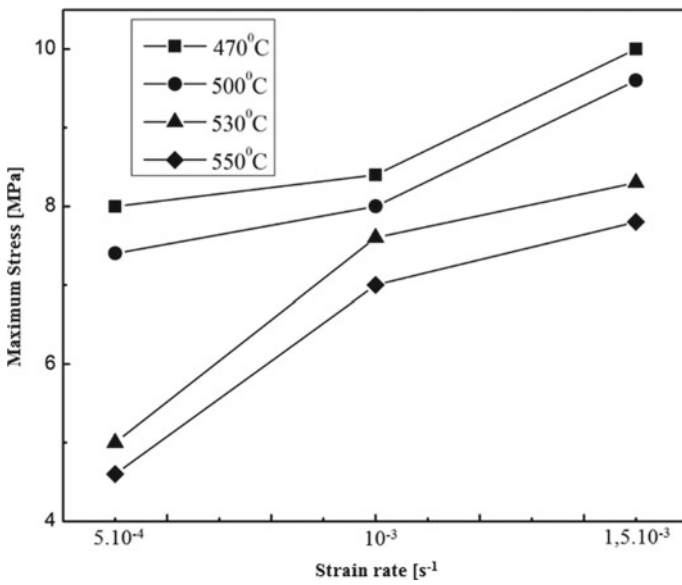
Fig. 5 The maximum stresses
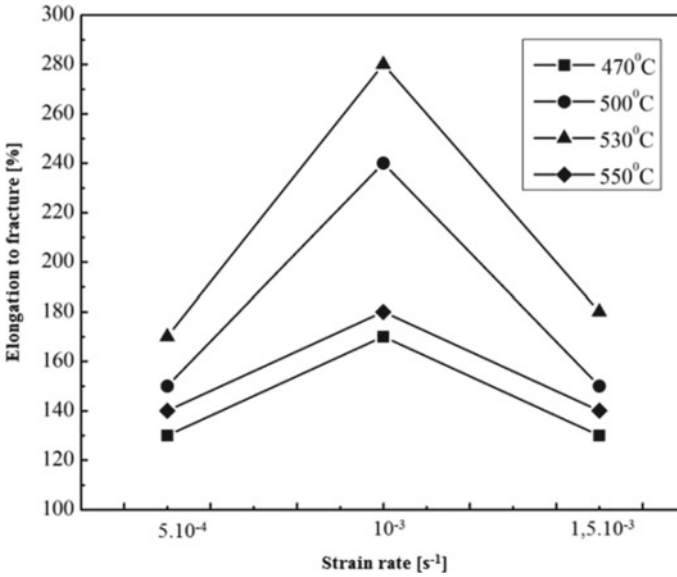
Fig. 6 The elongation to fracture

4 Conclusion

This work has identified the thermomechanical regime and experiments in preparing microstructure for superplastic deformation of AA7075 aluminum alloy. Samples of aluminum alloy AA7075 were prepared by thermomechanical regime producing with average grain size of 13 μm. This is an important and prerequisite condition for the appearance of superplasticity of the material.

These tensile experiments were tested at temperatures for 470, 500, 530, 550 °C and initial strain rates from 5×10^{-4} s^{-1}, 10^{-3} s^{-1}, 1.5×10^{-3} s^{-1} to assess superplastic deformation ability. The response is maximum superplastic elongation (δ) and maximum stresses (σ).

Through the experimental results and analysis of the results, assess the impact of process parameters (strain rate, strain temperature) on the yield stress and deformation ability of the test samples. The positive results were obtained for 530 °C and 10^{-3} s^{-1}, achieving 280% elongation to fracture and 7.6 MPa of maximum stress. The results of the paper are the basis for the next step of superplastic deformation process from AA7075 aluminum alloy.

This work is expected as a significant contribution to improve the superplastic deformation ability of AA7075. The process of forming superplastic will be studied in subsequent studies.

References

1. Giuliano, G.: Superplastic Forming of Advanced Metallic Material. Woodhead Publishing Limited (2011)
2. Nieh, T.G., Wadsworh, J., Sherby, O.D.: Superplasticity in Metals and Ceramics. Cambridge University press (2005)
3. Barnes, A.J.: Superplastic forming 40 years and still growing. J. Mater. Eng. Perform. **16**(4), 440–454 (2007)
4. Rambabu, P., Eswara Prasad, N., Kutumbarao, V.V., Wanhill, R.J.H.: Aerospace Materials and Material Technologies. Indian Institute of Metals Series (2017)
5. Backofen, W.A., Avery, D.H., Turner, J.R.: Superplasticity in Al–Zn alloy. Trans. Am. Soc. Metals **57**, 980 (1964)
6. Grimes, R.: Superplastic forming: evolution from metallurgical curiosity to major manufacturing tool. Mater. Sci. Technol. **19**, 3–10 (2003)
7. Yang, Xuyue, Miura, Hiomi, Sakai, Taku: Continuous dynamic recystallization in a superplastic 7075 aluminum alloy. Mater. Trans. **43**(10), 2400–2407 (2002)
8. Kumaresan, Kalaichelvan, K.: Experimental studies of a rectangular cup formation of Al 7075 alloy in superplastic forming process. In: 3rd International Conference on Materials Processing and Characterisation (ICMPC 2014), Procedia Materials Science vol. 6, pp. 892–896 (2014)
9. Sahraoui, T., Hadji, M., Bacha, N., Badji, R.: Superplastic deformation behavior of 7075 aluminum alloy. J. Mater. Eng. Perform. **12**, 398–401 (2003)
10. Mahidhara, R.K.: Effect of grain size on the superplastic behavior of a 7475 alloy. J. Mater. Eng. Perform. **4**(6), 674–678 (1995)

Thermal Cracks in Concrete Structure—The Basic Issues to Be Understood

Trong Chuc Nguyen📍, **Anh Kiet Bui, and Quoc Long Hoang**

1 Introduction

Thermal cracks occur in concrete structures caused by the temperature difference between locations in the structure exceeding the allowable limit. The cooler portion at the concrete block surface contacting with air ambient cools down quickly and tends to contract more than that at the warmer portion inside the mass concrete block. Thermal cracks occur when the restraint resulting in tensile stresses exceeds the tensile strength of concrete [1–3]. It is noted that thermal cracks not only occur on mass concrete structures but also others, such as pavements, concrete structures working in high-temperature environments, etc.

To find out the reason why thermal cracks appear, the following reasons need to be distinguished.

The cement hydration process: the chemical reaction between cement and water accompanies an exothermic process [4, 5]. The heat dissipation rate of cement decreases with time. For small and thin structures, the amount of heat generated during hydration is quickly diffused into the air and cracks do not occur at an early age. However, for the mass concrete structures, the amount of internal hydration heat of the concrete block increases and decreases slowly due to the low thermal conductivity of concrete, while the concrete zone nearby the surface cools down quickly and exposes directly to the air ambient. This leads to the contraction of the surface elements of the concrete block, but they are limited by the internal expansion of the concrete block. Therefore, uneven contraction, expansion between

T. C. Nguyen · Q. L. Hoang
Institute of Special Construction Engineering, Le Quy Don Technical University,
Hanoi, Vietnam

A. K. Bui (✉)
Faculty of Civil Engineering, Ho Chi Minh City Open University,
Ho Chi Minh City, Vietnam
e-mail: kiet.ba@ou.edu.vn

elements in concrete blocks causes the formation of thermal cracks. In most cases in construction, thermal cracks in mass concrete structures often occur at an early age [6–9].

Effect of ambient temperature and solar radiation: when the elements of the concrete block are exposed to a hot (or cold) ambient temperature, it leads to a thermal contraction (or expansion) changing the volume of concrete blocks. Thermal cracks may occur if the volume change is restraint [10–12].

2 Materials and Methods

2.1 Object of Study

Mass concrete: there are several different definitions of mass concrete based on the standard of each country. However, the main factor for determining a mass concrete block structure is depended on its minimum size. According to ACI 301, mass concrete structures include mat foundations, dams, and other concrete structures with a width or depth exceeding 4 feet (1.3 m) [13]. Besides, the ratio of surface area to volume of concrete blocks is also given by many documents to define mass concrete [14]. Besides, structures that are small in size but use large amounts of cement or high-heat cement should also take measures to prevent the formation of thermal cracks at an early age.

The main concern with mass concrete is the thermal gradient formed as discussed above. From the above reason, thermal cracks on the surface of concrete blocks are formed at an early age (due to hydration of cement) and later (due to changes in ambient temperature).

Other concrete structures: thermal cracks can occur not only for mass concrete structures but also for structures, such as pavement, concrete slabs working in high-temperature environments, etc.

For cement concrete pavement with a large surface area, it receives heat directly from the sun and the heat is transmitted downward and heats up. The temperature of cement concrete pavement is transmitted to the environment by convection form (the surface). Part of the heat is transferred to the ground through the bottom of the cement concrete pavement. The heat transfer from the sun to the surface of cement concrete pavement is described as Fig. 1 [15].

Especially, during the exploitation process, the cement concrete pavements are affected by the variation of environmental temperature. Thus, the change of ambient temperature leads to the temperature difference between the surface and the bottom of the cement concrete pavement. As a result, the temperature difference in the cement concrete pavement causes contraction and expansion.

The deformation process of cement concrete pavement is prevented from moving laterally due to friction between the concrete slab and its foundation. Therefore, thermal stresses are formed on cement concrete pavement [16].

Fig. 1 Cement concrete pavement is affected by environmental temperature [15]
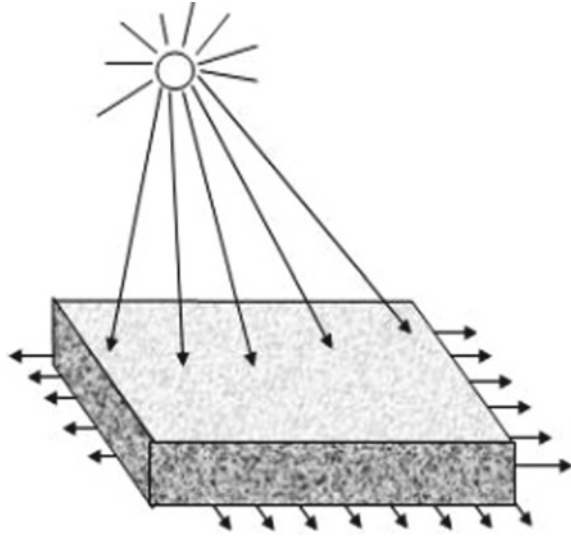
2.2 How to Recognize Thermal Cracking?

Thermal cracks are caused by temperature differences exceeding permissible values. Thereafter they appear randomly on the surface of the concrete block. Thermal cracks due to temperature effects usually appear within a few days after removing the formwork.

Cracks related to temperature changes impact the surface of cement concrete pavement often like cracks due to shrinkage. These cracks usually occur perpendicular to the longest axis of the concrete slab. This type of cracking occurs any time after the concrete is poured but usually occurs in the first summer or winter of the first year.

2.3 Several Criteria Are Used to Evaluate Thermal Cracks

To control crack formation, it is necessary to control the maximum temperature difference in concrete structures. Usually, the permissible temperature difference is taken as 20 °C and does not depend on the construction area and the type of concrete.

In Vietnam, according to TCVN 305.2004 "Mass concrete—code of practice of construction and acceptance", two factors should be controlled to prevent cracking in mass concrete structures. First, the temperature difference (ΔT) between the center of the mass concrete and its surface should be less than 20 °C. The second, module of temperature gradient (M_T) should be less than 50 °C/m.

According to the CIRIA C600 standard (Great Britain) points out that the maximum temperature difference between the inner zone of the mass concrete and its outer surface $\Delta T_{\max}$ is determined by the Eq. (1).

$$\Delta T_{\max} = \frac{3.7\varepsilon}{\alpha} \tag{1}$$

where ε—ultimate tensile strength of early age concrete; α—is the coefficient of thermal expansion of concrete.

In Japan, the assessment of the formation of cracks in concrete mass can be made using the cracking index, defined as described in Eq. (2).

$$I_{cr} = \frac{f_t(\tau)}{f_{sp}(\tau)} \tag{2}$$

where I_{cr} is the index of thermal cracking; $f_t(\tau)$—tensile strength, corresponding to the age of concrete τ; $f_{sp}(\tau)$—is the maximum temperature stress caused by the cement hydration process per day τ.

The cracking can be estimated by Thermal Cracking Index as presented in Table 1.

2.4 A Method to Solve the Temperature Problem in the Concrete Structures

To solve the thermal problems including temperature field and thermal stress in mass concrete structures, the finite element simulation has been used as an optimized option.

The numerical solution of the problem is based on the solution of the differential equation of the theory of thermal conductivity [14, 15].

$$\frac{\partial}{\partial x}\left(k_x \frac{\partial T}{\partial x}\right) + \frac{\partial}{\partial y}\left(k_y \frac{\partial T}{\partial y}\right) + \frac{\partial}{\partial z}\left(k_z \frac{\partial T}{\partial z}\right) + q_v = \rho c \frac{\partial T}{\partial \tau} \tag{3}$$

where k_x, k_y, and k_z—coefficient of heat diffusion of the material in the directions of the axis X, Y, and Z in the Cartesian coordinate system, respectively, m²/s; q_v—

Table 1 Cracking index criteria for controlling thermal crack formation [25]

Crack control criteria	Thermal crack index (I_{cr})
The prevention of cracks	$I_{cr} \geq 1.5$
Possibility of limited cracks	$1.2 \leq I_{cr} \leq 1.5$
Limiting the occurrence of dangerous cracks	$0.7 \leq I_{cr} \leq 1.2$

internal heat source due to cement hydration (W/m^3); c—specific heat of concrete, kJ/kg.°C; ρ—density of concrete, kg/m^3; T—temperature, (°C); τ—time, (day).

When solving the temperature regime, the following boundary condition as shown in Eq. (4) is used.

$$k_x\frac{\partial T}{\partial_x}n_x + k_y\frac{\partial T}{\partial_y}n_y + k_z\frac{\partial T}{\partial_z}n_z + q_v + h\left(T_s - T_f\right) = 0 \tag{4}$$

where n_x, n_y, and n_z—vector normal to X, Y, and Z direction of heat transfer, respectively; T_s and T_f—nodal temperature at the boundary points and air temperature, respectively; h—convection coefficient.

3 Results and Discussion

3.1 How to Minimize Thermal Cracks?

3.1.1 Massive Concrete Structures

To minimize thermal crack development in mass concrete structures, it is important to know which characteristic parameters affect the appearance of thermal cracks. These are the maximum temperature and temperature difference in mass concrete blocks. Therefore, the determining maximum temperature in concrete blocks is necessary to provide appropriate measures to control thermal cracks. Besides, the reduction of the temperature difference between the inner zone and the concrete zone at the surface of the concrete block contacting the air ambient should also be considered. Previous studies indicated that the allowable temperature difference should not exceed 20 °C [17, 18]. In rare cases, cracks may occur when the temperature difference is lower or higher than the allowable value. The determination of the maximum temperature and temperature difference in mass concrete block can be measured by using Finite Element simulation or using thermal sensors inserted inside the concrete block.

Minimizing crack formation is recommended by designers and contractors. The main factors causing the formation of thermal cracks should be considered, such as the initial temperature of the concrete mixture, cement content, cement type, the time of concreting, curing conditions, etc. [19].

A few measures to minimize cracking formation for mass concrete.

Using cement replacement materials to reduce hydration heat source in mass concrete structures.

According to Tang et al. [20], the results showed that the replacement of cement by class F of natural pozzolan (PU) significantly reduces the maximum temperature in mass concrete structures. Maximum temperatures at the center of concrete blocks with a composition using 100% cement and with a composition using 20% PU

replacing cement are 65.76 and 52.44 °C after 48 h of hardening, respectively. The results of the temperature distribution in concrete blocks are shown in Fig. 2.

Hence, it is necessary to optimize the composition of the concrete mixture by using cement replacement materials, such as fly ash, slag, or using low-heat cement.

Using chemical admixtures to delay the moment the temperature reaches its maximum value in mass concrete block.

Lower the initial temperature of the concrete mixture: the initial temperature of the concrete mixture greatly affects the maximum temperature value in mass concrete blocks. To reduce the initial temperature of the concrete mixture, there are many measures, such as: reducing the temperature of the aggregate of concrete mixture, using ice instead of a part of water, using liquid nitrogen to cool down the concrete mixture. When using measures to reduce the initial temperature of the concrete mixture, it is necessary to calculate in detail the economic feasibility of the given measures [21–24].

According to the principle of conserving the heat before and after mixing the concrete mixture, the temperature of the concrete mixture after mixing is determined by the formula (5) [25].

$$T_{\text{mix}} = \frac{0.2(m_a T_a + m_c T_c) + m_w T_w}{0.2(m_a + m_c) + m_w} \tag{5}$$

where m_a, m_c, and m_w—mass (kg/m^3) of aggregate, cement, and water, respectively; T_a, T_c, and T_w,—temperature (°C) of aggregate, cement, and water, respectively; specific heat capacity of aggregate (or cement) and water approximate 0.2 kJ/kg.°C and 1.0 kJ/kg.°C, respectively.

Guidelines for controlling cracked concrete mass 2016 [24] indicates that: to decrease 1 °C of concrete mixture, it normally needs to reduce the temperature of cement, aggregate, and water corresponding to 8 °C, 2 °C, and 4 °C, respectively.
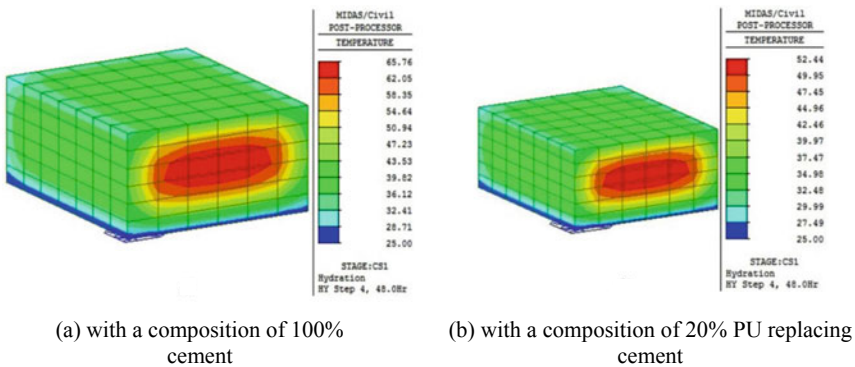

(a) with a composition of 100% cement

(b) with a composition of 20% PU replacing cement

Fig. 2 Distribution of temperature in concrete blocks after 48 h of concrete hardening [20]

When a part of ice water is used to replace concrete mixing water, the temperature reduction of the concrete mixture compared to when not using ice water is determined by the formula (6) [25].

$$\Delta T_{\text{mix}} = \frac{m_{\text{ice}}\{79.6 + (T_w - 0)\}}{0.2(m_a + m_c) + m_w} E_f \tag{6}$$

where m_{ice}—weight of ice water, kg/m³; E_f—cooling effect, varying in a range of (0.7–0.8).

Besides, lowering the temperature of the aggregates in the concrete mixture, the method of using liquid nitrogen can be used to reduce the temperature at casting the concrete. This method is applied by injecting liquid nitrogen directly into the concrete mixture during mixing.

Selection of the moment of placing concrete is important to control the maximum temperature in the concrete block. In particular, placing concrete at night or in the early morning has many advantages, such as: minimize the risk of heavy traffic congestion to the construction site, reduce solar radiation during construction.

Using cooling systems: one of the most effective ways to prevent cracking is to use a cooling pipe system. This method has been used for mass concrete structures, such as dams, foundations, piers bridges, etc. The first cooling pipe system was used in the construction of the Hoover Dam (USA). The same procedure was applied for other projects, i.e., Xiang Hong Dian Dam (China), Bureyskaya hydroelectric plant (Russia), Seo-He Bridge (South Korea), Tuyen Quang Dam (Vietnam) [26–30].

Besides, the cooling pipes method can adjust the maximum temperature in concrete blocks by changing the working time of cooling pipes, water temperature. This method allows to reduce the maximum temperature in mass concrete to the appropriate value.

According to [6], it is quite effective to use the cooling pipe system to control the formation of thermal cracks in the mass concrete structures. Also, the study evaluated the effect of cooling water temperature on the maximum temperature in mass concrete structures as shown in Fig. 3. It can be seen that when using a cooling pipe system with cooling water temperature $T_w = 25$ °C, the temperature in the center of the concrete block significantly decreases 15.71% when compared to the case without using a cooling pipe system.

However, when the cooling water temperature changes from 25 to 10 °C, the maximum temperature at the center of the concrete block only decreases from 60.01 to 55.4 °C (4.61 °C). It can be concluded that the maximum temperature of the concrete block is not significantly dependent on the temperature of the cooling pipe.

Use surface insulation: the main purpose of this method is to reduce the temperature difference between the inner zone and the surface of the concrete block. The surface insulation layer can be used during construction in both winter season (preventing rapid cooling of concrete block surface) and summer season conditions (reducing the warming of concrete block surface). Currently, there are many types of surface insulation, i.e. polyethylene, polystyrene foam, water or sand layer,
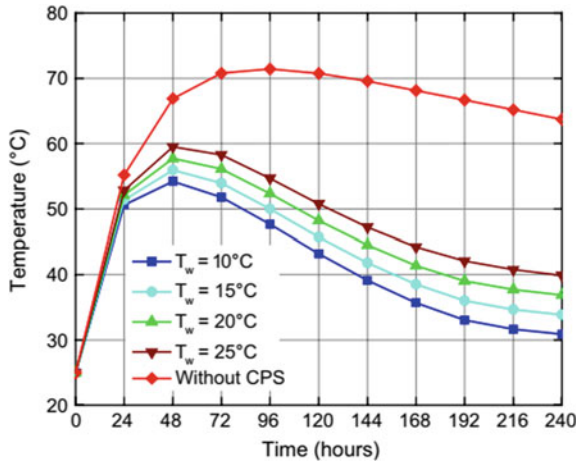
Fig. 3 The temperature at the center of the concrete block changes over time [6]

burlap [30–33]. The change in insulation thickness affects the maximum temperature and the temperature difference between the center and the surface of the concrete block [32].

The results showed that it can reduce the risk of cracking occurring when the temperature difference between the center and surface of the concrete block is 16.65 °C with using an insulation thickness of 1 cm while the temperature difference is 26.31 °C in the case without using insulation (Fig. 4).

a) Without using insulation

b) With using 1 cm thickness of
polystyrene insulation
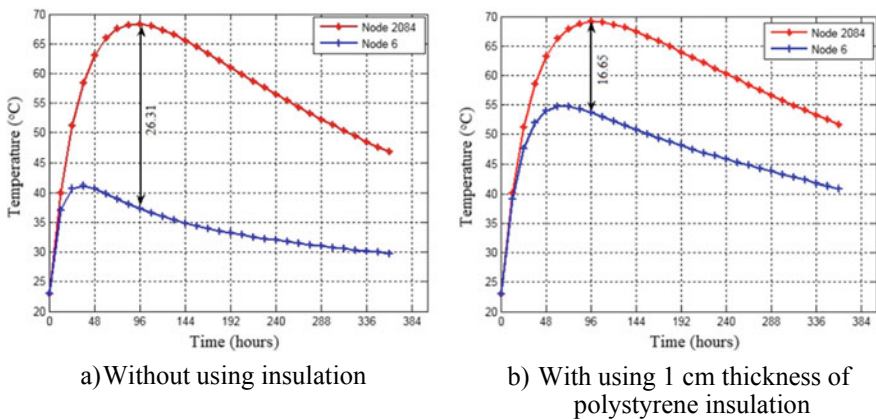
Fig. 4 Temperature variation in the center and surface of the concrete block [33]
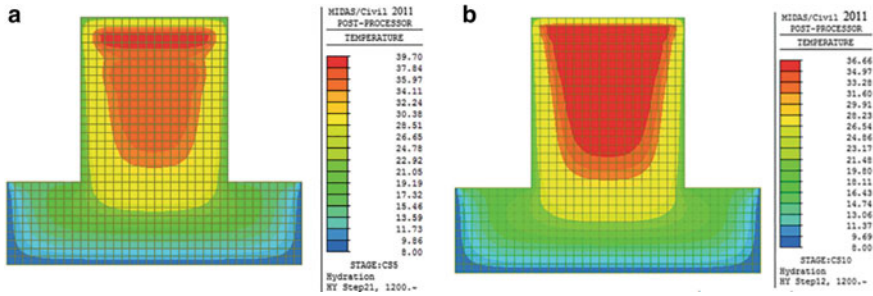
Fig. 5 Temperature distribution in the concrete block: case 1 (**a**); case 2 (**b**) [34]

Reduce the thickness of the concrete casting block: the thickness of the concrete casting block greatly affects the maximum temperature in mass concrete structures.

As indicated in Aniskin et al. [34], the thickness of the concrete casting affects the maximum temperature of the concrete block. Two concreting cases: (a) case 1—using the layer thickness of 2 m; (b) case 2—using the layer thickness of 4 m were presented. The temperature distribution in concrete blocks in two cases above are shown in Fig. 5. As can be seen, the maximum temperature in the concrete block in case 1 is 36.66 °C while that in case 2 is 39.70 °C. Hence, pouring with a smaller thickness of concrete block can reduce the maximum temperature in the concrete block.

3.1.2   Other Concrete Structures

To prevent the formation of cracks in cement concrete pavement structures under the effect of environmental temperature changes, it is needed to determine the temperature difference between the surface and the bottom of the cement concrete pavement. Based on that basis, a proper design of the length-thickness and width-thickness ratios of cement concrete pavement can be made.

3.2   How to Repair Thermal Cracks?

To repair the cracks on concrete structures should be consulted by experts and designers to avoid damage later on. For cement concrete pavement, it may be repaired by using compatible materials or demolition of the cracked and dumped area replaced by new cement concrete. For the mass concrete, the repair process depends on the crack width, the crack depth, and the later operation. If the crack width is small, it does not affect the strength and workability of the structure. In contrast, if the crack width is large, spraying epoxy, as a suitable option, is necessary to be used.

4 Conclusions

1. From the above discussions, the mechanism of thermal crack formation in concrete structures in general needs to be understood. At last, the research directions are proposed to control the formation of cracks for each type of structure.
2. To control and prevent the formation of thermal cracks, some alternatives based on the type of structure are proposed:

For large concrete structures: these factors affecting the temperature distribution and stress field, such as cement content, type of cement, the initial temperature of the concrete mixture when pouring, etc., should be optimized.

For cement concrete pavement, the thickness and dimensions of the concrete slab are carefully determined.

References

1. Korea Concrete Institute.: Thermal Crack Control of Mass Concrete, Concrete Practices Manual. Korea. (2010)
2. Bofang, Z.: Thermal stresses and temperature control of mass concrete. Printed in the United States of America. p. 518 (2014). https://doi.org/10.1016/C2012-0-06038-3
3. Barbara, K., Maciej, B., Maciej, P., Aneta, Z.: Analysis of cracking risk in early age mass concrete with different aggregate types. Procedia Eng. **197**, 234–241 (2019). https://doi.org/10.1016/j.proeng.2017.06.209
4. Aneta, Ż., Barbara, K., Miguel, A., Dirk, S.: Consideration of soil temperature in the modeling of early age mass concrete slab. IOP Conf. Series: Mater. Sci. Eng. **603**(022095), (2019). https://doi.org/10.1088/1757-899x/603/2/022095
5. Do, T.M.D., Lam, T.Q.K.: Solutions to improve the quality of mass concrete construction in climate conditions of Southern Vietnam. Int. J. Innovative Technol. Exploring Eng. (IJITEE) **8**(6C2), 188–192 (2019)
6. Nguyen, T.C., Huynh, T.P., Tang, V.L.: Prevention of crack formation in mass concrete at early age by cooling pipe system. Asian J. Civil Eng. **20**(8), 1101–1107 (2019). https://doi.org/10.1007/s42107-019-00175-5
7. Nguyen, C.T., Aniskin, N.A.: Temperature regime during the construction massive concrete with pipe cooling. Mag. Civil Eng. **89**(5), 156–166 (2019). https://doi.org/10.18720/MCE.89.13
8. TCXDVN 305:2004.: Mass Concrete—code of practice of construction and acceptance. Hanoi, Vietnam. p. 80 (2004)
9. Muneer, K.S., Muhammad, K.R., Mohammed, H.B., Lutf, A.T.: Cracking in concrete water tank due to restrained shrinkage and heat of hydration: field investigations and 3D finite element simulation. J. Perform. Constructed Facil. **34**(1), 12 (2020). https://doi.org/10.1061/(ASCE)CF.1943-5509.0001356
10. Arangi, S.R., Jain, R.K.: Review paper on pavement temperature prediction model for Indian climatic condition. Int. J. Innovative Res. Adv. Eng. (IJIRAE) **8**(2), 1–9 (2014)
11. Mohammad, H.A., Medhat, M.H.: A mathematical model for the distribution of heat through pavement layers in Makkah roads. J. King Saud Univ.—Eng. Sci. **26**, 41–48 (2014)

12. Bui, K.A., Sancharoen, P., Tanapornraweekit, G., Tangtermsirikul, S., Nanakorn, P.: An evaluation of thermal effects on behavior of a concrete arch dam. Songklanakarin J. Sci. Technol. **41**(5) (2019)
13. ACI 207.5R-11.: Report on roller-compacted mass concrete. American Concrete Institute, p. 75 (2007)
14. ACI Committee 311.: ACI Manual of Concrete Inspection, SP-2(07). American Concrete Institute, Farmington Hills, MI, p. 199 (2007)
15. Harik, I. E., Jianping, P., Southgate, H., Allen, D.: Temperature Effects on Rigid Pavements. Journal of Transportation Engineering 120(1), (1994)
16. Mirambell, E.: Temperature and stress distributions in plain concrete pavements under thermal and mechanical loads. In: Proceedings, 2nd International Workshop on Design and Rehabilitation of Concrete Pavements, Sigiienza, Spain, pp. 121–135 (1990)
17. Zhu, H., Hu, Y., Li, Q., Ma, R.: Restrained cracking failure behavior of concrete due to temperature and shrinkage. Constr. Build. Mater. **224**, (2020). https://doi.org/10.1016/j.conbuildmat.2020.118318
18. Makeeva, A., Amelina, A., Semenov, K., Yuriy, B.: Temperature action in analysis of thermal stressed state of massive concrete and reinforced concrete structures. MATEC Web of Conferences **245**(03016), (2018). https://doi.org/10.1051/matecconf/201824503016
19. Struchkova, A.Y., Barabanshchikov, Yu. G., Semenov, K.S., Shaibakova, Al. A.: Heat dissipation of cement and calculation of crack resistance of concrete massifs. Mag. Civil Eng. **78**(2), 128–135 (2018). https://doi.org/10.18720/mce.78.10
20. Tang, V.L., Nguyen, T.C., Ngo, X.H., Dang, V.P., Bulgakov, B., Bazhenova, S.: Effect of natural pozzolan on strength and temperature distribution of heavyweight concrete at early ages. MATEC Web of Conferences **193**, 03024 (2018)
21. Aniskin, N.A., Nguyen, T.C.: Mathematical model of temperature regime and thermal stress state of roller-compacted concrete gravity dam. IOP Conf. Series: J. Phy. Conf. Series **1425** (2020) 012051 (2019). https://doi.org/10.1088/1742-6596/1425/1/012051
22. Kim, S.G.: Effect of heat generation from cement hydration on mass concrete placement. Iowa State University. p. 126 (2010)
23. Chen, H., Liu, Z.: Temperature control and thermal-induced stress field analysis of GongGuoQiao RCC dam. J. Therm. Anal. Calorim. **135**(3), 11 (2018). https://doi.org/10.1007/s10973-018-7450-1
24. Bui, A.K., Nguyen, T.C.: The temperature field in mass concrete with different placing temperatures. Civil Eng. Archit. **8**(2), 94–100 (2020). https://doi.org/10.13189/cea.2020.080207
25. Japan Concrete Institute.: Guidelines for control of cracking of mass concrete 2016. Tokyo, Japan, p. 302 (2017)
26. Chen, S., Su, P., Shahrour, I.: Composite element algorithm for the thermal analysis of mass concrete Simulation of cooling pipes. Int. J. Numer. Meth. Heat Fluid Flow **21**(4), 434–447 (2011). https://doi.org/10.1108/09615531111123100
27. Zheng, Wenyi, Pan, Peng, Ye, Lieping: Study on thermal stress and temperature cracks control of Longlin roller-compacted concrete gravity dam. Appl. Mech. Mater. **212**(213), 912–916 (2012). https://doi.org/10.4028/www.scientific.net/AMM.212-213.912
28. Li, C., Li, Y.: Optimization of cooling pipes inside mass concrete bridge pile cap. In: The 2nd World Conference on Humanities and Social Sciences, 25–30 (2017). https://webofproceedings.org/proceedings_series/ESSP/WCHSS%202017/WCHSS005.pdf
29. Liu, X., Zhang, C., Chang, X., Zhou, W., Cheng, Y., Duan, Y.: Precise simulation analysis of the thermal field in mass concrete with a pipe water cooling system. Appl. Therm. Eng. **78**, 449–459 (2015). https://doi.org/10.1016/j.applthermaleng.2014.12.050
30. Qiu, Y., Zhan, G.: Stress and damage in concrete induced by pipe cooling at mesoscopic scale. Adv. Mech. Eng. **9**(2), 1–17 (2017). https://doi.org/10.1177/1687814017690509
31. Nguyen, T.C., Luu, X.B.: Reducing temperature difference in mass concrete by surface insulation. Mag. Civil Eng. **4**(88), 70–79 (2019). https://doi.org/10.18720/MCE.88.7

32. Chen, Y.-Y., Chen, S.-Y., Yang, C.-J., Chen, H.-T.: Effects of insulation materials on mass concrete with Pozzolans. Constr. Build. Mater. **137**, 261–271 (2017). https://doi.org/10.1016/j.conbuildmat.2017.01.059
33. Nguyen, T.C., Pham, V.T., Bui, A.K.: The effects of insulation thickness on temperature field and evaluating cracking in the mass concrete. Electron. J. Struct. Eng. **18**(2), 128–132 (2018)
34. Aniskin, N.A.: Nguyen Trong Chuc: the problem of temperature cracking in concrete gravity dams. Vestnik MGSU **15**(3), 380–398 (2020)

Experimental Investigation on Flexural Behavior of Reinforced Lightweight Concrete Slabs Using Recycled Expanded Polystyrene

**Dinh-Hoa Nguyen, Ngoc-Duc Han, Anh-Tuan Vu,
Trung-Kien Nguyen, and Tuan-Nghia Hoang**

1 Introduction

Expanded PolyStyrene concrete (EPS-C) has been investigated and used for building heat and sound insulation, contributing to energy-saving and sustainable development. This kind of material, environment-friendly, has been widely used for building construction in recent years [1–4]. EPS-C is formed by a mixture of different components such as cement, light aggregate (EPS - Expanded Polystyrene Beads), water, and admixtures [5, 6]. It is classified as lightweight concrete. As an important component of its composition, EPS beads are impermeable with a normal density range of 10–20 kg/m^3. Thanks to its properties, EPS-C showed a good characteristic in thermal and acoustic insulation. Besides, EPS-beads help to significantly reduce the weight of such concrete material. EPS-C can be thus an interesting solution for the supportive structure in building areas [5, 7, 8]. Regarding this aspect, it can be cited herein the work of Colombo et al. [9] on bending behavior of textile reinforced concrete sandwich beam which placed a thick internal expanded polystyrene foam as an insulation layer. They showed that the tangential non-linear behavior of EPS foam played significant role in bending behavior. Fernando et al. [2] investigated EPS sandwich wall panel as a walling material for building while Assaad et al. [10] studied the non-structural EPS sandwich panel subjected to winds and seismic loading. Both reveal that the feasibility of using EPS-C as a non-structural material for building construction. To the author's knowledges, there are few studies on using EPS concrete for structural members so far. This remains an interesting question, especially in the Vietnam condition.

D.-H. Nguyen · N.-D. Han · A.-T. Vu (✉) · T.-K. Nguyen · T.-N. Hoang
Faculty of Building and Industrial Construction, National University of Civil Engineering, 55 Giai Phong Road, Hanoi, Vietnam
e-mail: tuanva@nuce.edu.vn

Moreover, even EPS-C has been engaged in research and application in Vietnam in recent years, most of them used commercial EPS beads, which account for a large proportion of the cost of EPS-C. Also, the amount of EPS waste is growing in the current environment, which is very dangerous because there is no effective treatment. Therefore, to ensure the environment-friendly aspect of the sustainable development and reduce the EPS-C manufacturing cost, in this study, we proposed to use recycled geofoam instead of commercial EPS beads. Besides, the research aims to test the ability of reinforced lightweight concrete using recycled polystyrene as a structural component in form of EPS-C slab.

To achieve this goal, an experimental campaign has been carried out to investigate the flexural behavior of one-way slabs made of reinforced EPS-C. The findings reveal that load-bearing capacity of 100 mm thickness slab reaches over 4 kN/m^2 with EPS-C density lower than 1200 kg/m^3.

2 Materials and Method

2.1 Materials

The material used in this study is lightweight concrete, which was produced in replacing coarse aggregate by recycled expanded polystyrene beads in concrete composition. These specimens were fabricated at the laboratory of NUCEWALL factory, Hung Yen province in Vietnam (Fig. 1). The EPS-C making materials used in the present study include cement, EPS beads recycled from waste foam (the diameter of EPS grains varied from 4 to 6 mm and the density was about 10 kg/m^3), and superplasticizer admixtures. The density of the investigated EPS-C was 1200 kg/m^3, its composition is shown in Table 1.

EPS beads are mixed with cement, water according to a specified ratio. After casting into the steel mold, the samples were cured at room temperature (around 24°) for the first 24 h. Subsequently, the specimens were removed and stored under
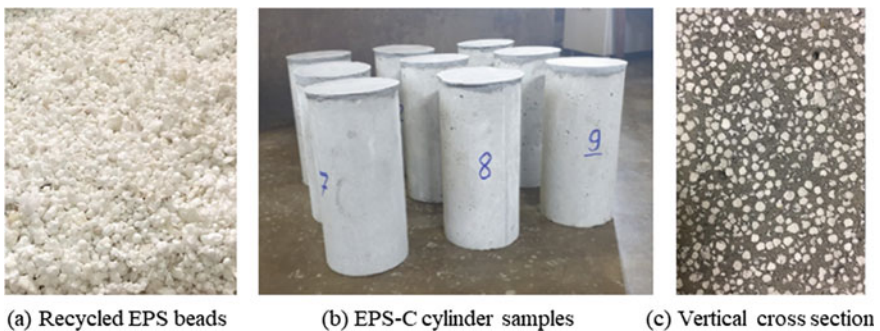

(a) Recycled EPS beads   (b) EPS-C cylinder samples   (c) Vertical cross section

Fig. 1 EPS-C specimen's preparation

Table 1 Composition of EPS-C making-materials (for 1 m^3 EPS-C, density of 1200 kg/m^3)

Cement (kg)	EPS (l)	Superplasticizer (l)	Water (l)
845	455	5.5	270

ambient conditions until they reached the 28 day-strength before testing. The cubes, cylinders, and slab specimens were all prepared with the same concrete composition, with an average density of 1200 kg/m^3. This value was slightly variable due to variations in the distribution of the EPS beads during casting. The slabs measured 2000 × 500 × 100 mm while cube dimensions were 150 × 150 × 150 mm and the cylindrical specimens with dimensions of 150 mm in diameter and 300 mm in height.

To determine the compressive strength of EPS-C, 10 cubes specimens of 150 × 150 × 150 mm were prepared and subjected to uniaxial compression test. Meanwhile, Young's modulus of EPS-C was determined through the compression of 6 cylindrical specimens with dimensions of 150 mm in diameter and 300 mm in height. These specimens had the same composition and were mixed in the same batch with the concrete used in manufacturing slabs (described in Sect. 2.2). The mechanical properties of EPS-C are summarized in Table 2.

2.2 Four-Point Bending Flexural Test: An Experimental Campaign

The dimensions of reinforced EPS-C slab were 2000 × 500 × 100 mm in length, width, and thickness, respectively. The one-way slab specimens were reinforced with rebar type welded wire mesh, with main reinforcement in longer direction consisted of 3 bars φ6a200 and reinforcement in shorter direction consisted of 8 bars φ4a200. Cold drawn steel with tensile strength of 630 MPa, and Young's modulus of 186 GPa was used. Welded wire meshes were placed on the upper and lower layers. Reinforcement arrangement and formwork installation are shown in Fig. 2.

Three slab specimens, named M1, M2, M3, were tested as one-way slab system with clear span 1900 mm between two supports. Four-point bending scheme was applied. The slab was installed on the support system while loading was performed in displacement, controlled by hydraulic jack with a capacity of 50 kN, splitting into 2 concentrated forces via beam system as displayed in Fig. 3. For each test, three dis-placement transducers (LVDT—Linear Variable Differential Transformer)

Table 2 Mechanical properties of EPS-C

Compressive strength (MPa)	Tensile strength (MPa)	Young's modulus (MPa)
6.7	0.8	6343

(a) Welded wire mesh   (b) Form work installation   (c) EPS-C casting vertically
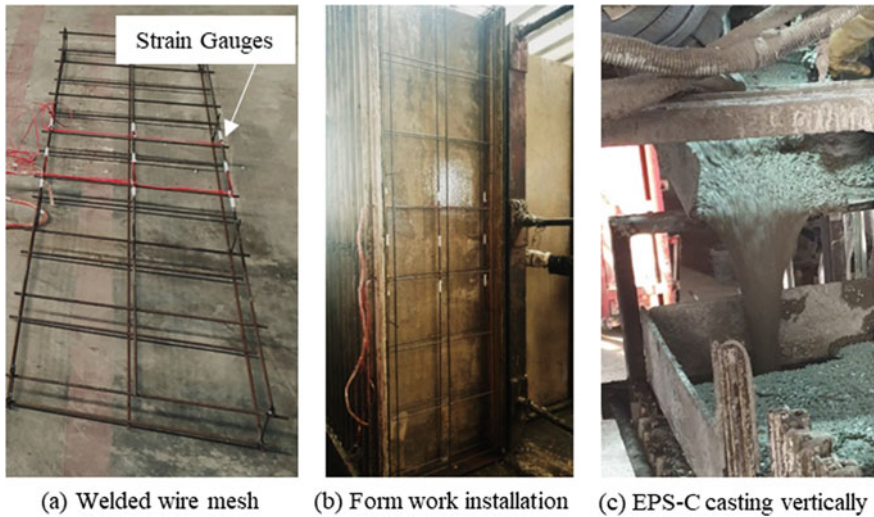
Fig. 2 Rebar wired mesh and EPS-C casting

were placed at 2 support positions (LVDT1 and LVDT3), and mid-span of the slab (LVDT2). Extensometer strain gauges were also attached to the rebar to calculate the reinforcement deformation inside the slab. LVDT, extensometer strain gauges, and load-cell were connected to the Datalogger to enable automatic and simultaneous recording. The deflection of the slab was calculated from the measured displacement data of the three LVDTs. The load-deflection relationship obtained from the experimental campaign was then used to investigate and analyze the flexural mechanical behavior such as stiffness, failure mechanism, etc. of reinforced EPS-C slab. The flexural tests were implemented at the Construction Testing Laboratory (LAS-125) of National University of Civil Engineering, Hanoi, Vietnam.

The loading process was divided into small steps to avoid the dynamic effect. During the loading process, first crack occurrence and crack pattern were recorded by visual inspection and specific optical equipment which can measure the minimum crack opening of 0.01 mm (Fig. 4).

3   Experimental Results and Discussion

3.1   Load-Deflection Relationship

Three full-scale reinforced EPS-C slabs subjected to four-point bending flexural conditions were performed up to failure. The load was applied gradually, and LVDTs measured the deflections in the mid-span of the specimen as defined in the

(a) Schematic diagram

(b) Experimental set-up
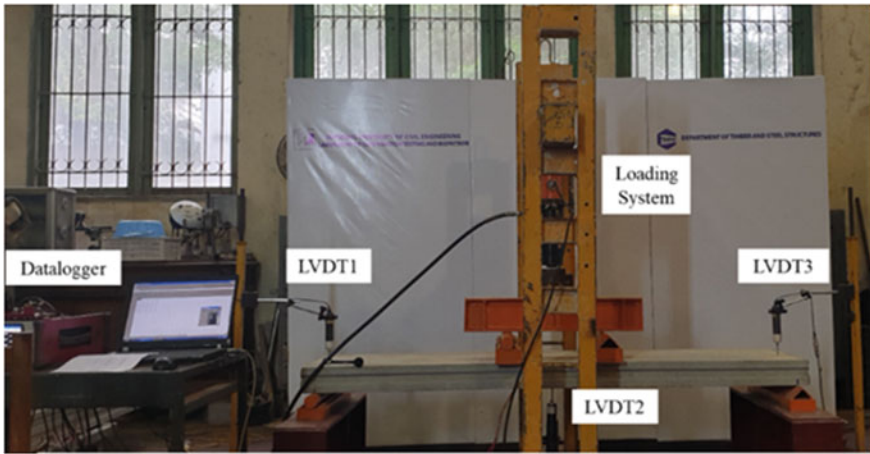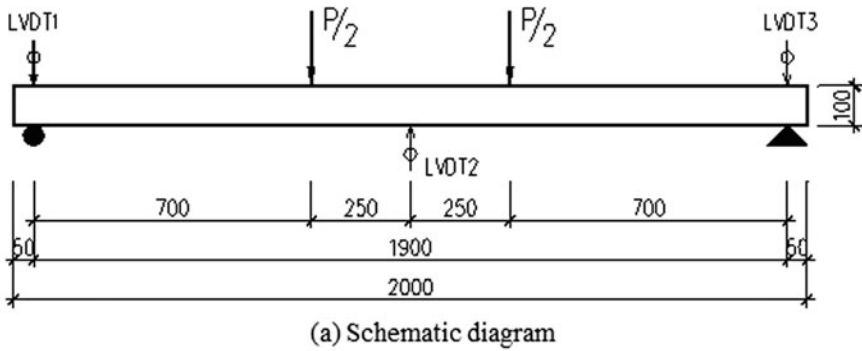
Fig. 3 4-point bending flexural test

previous section. The load-deflection relationships of the three slab specimens (M1, M2, and M3) were obtained from the experiments, as shown in Fig. 5. The cracking event was detected, and the ultimate load was then evaluated.

It can be seen from Fig. 5 that the experimental findings between the three experiments are well consistent. The loading path attains peak at 9 kN, which corresponds to a deflection of about 25 mm in the mid-span. To obtain further insight into the flexural behavior of the EPS-C slab, further analyzes are carried out on the result of M1 specimen.

Figure 6 shows the behavior of reinforced EPS-C slabs, load-deflection relationship of M1 specimen characterized by cracking load P_{cr}, serviceability load P_{ser} (representing the maximum serviceability in deflection), and ultimate load P_{ult}. In addition to the evolution in the load-deflection relationship, the behavior of steel reinforcement within the slabs is also studied thanks to nine strain gauges connected

Fig. 4 Slab deformation and crack pattern

Fig. 5 Load-deflection
relationship at mid-span of
reinforced EPS-C slab
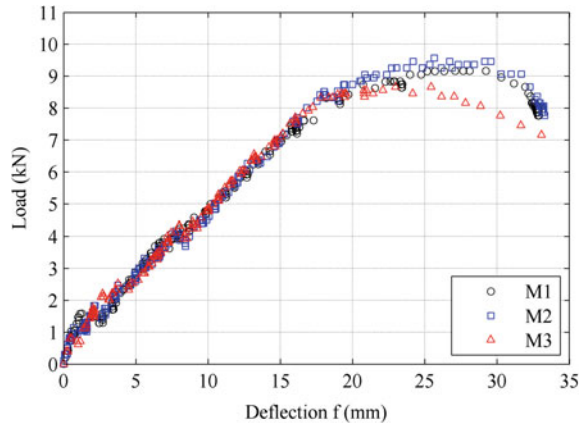
to each specimen at longitudinal rebar. Figure 7 illustrates the relationship between
load and steel reinforcement strain in the M1 specimen. The result obtained from
specimen M1 as shown in Fig. 6 reveals that reinforced EPS-C slab behavior can be
categorized into three regimes, as follows:

Regime 1 (before the first crack appearance): This stage corresponds to the OA
segment where the load applied remains relatively low, steel reinforcement and slab
concrete still behave in the elastic phase, the load-deflection relationship is nearly
linear. This stage ends at point A, when the load applied meets the cracking load
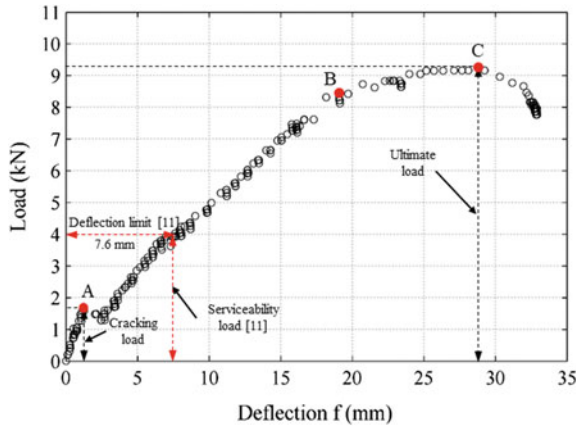
Fig. 6 Load-deflection relationship in specimen M1 and limit values
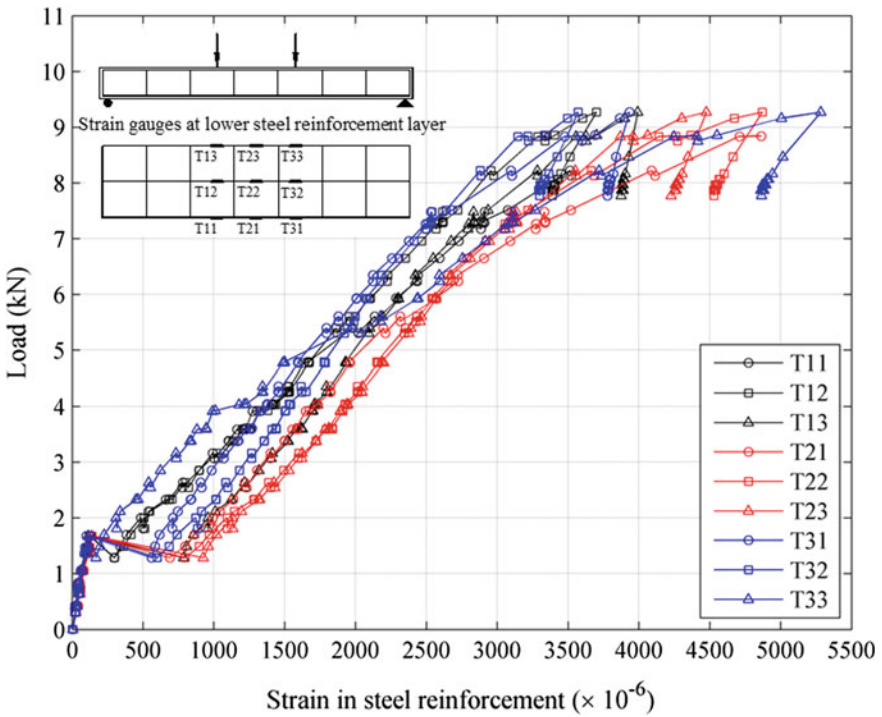
Fig. 7 Load and steel reinforcement strain relationship in M1 specimen

P_{cr}. At the transition from regime 1 to regime 2, the curve is almost horizontal. It can be stated that the tensile stress in concrete reaches the extensional strength at this point which induces the occurrence of the first crack in the specimen. Consequently, the cross-sectional area of the slab reduces, and its geometrical features decrease as well. At this point, the entire loading is transmitted from the concrete section to the rebar which explains a sudden increase in steel reinforcement stress-strain behavior as observed in Fig. 7.

Regime 2 (After crack occurrence): This regime is demonstrated in the AB segment. The crack grows at this stage with increasing load. The relation between load and deflection is highly non-linear. Tensile force in reinforced EPS-C slab is mostly supported by steel reinforcement. Regime 2 terminates at point B when the load applied exceeds over 8.5 kN, at which the steel reinforcement rapidly reaches its yielding limits. The loading value of 8.5 kN is well consistent with steel reinforcement behavior (Fig. 7).

Segment BC reflects regime 3. The deflection of the reinforced EPS-C slab increases rapidly as the applied load continues to increase. It is evidently due to the reduction of slab stiffness caused by the rapid development of the multi-cracking phenomenon. Stress increases with loading applied in the compressive zone. This regime ends at point C corresponding to the rapid decreasing of load applied. The slab specimen starts not being able to sustain the loading after this point. Point C refers to the average load-bearing capacity of the reinforced EPS-C slab, allowing the maximum ultimate load P_{ult} to be determined.

3.2 Cracking, Ultimate, and Serviceability Loads

The cracking load (P_{cr}) is determined experimentally from load-deflection curves. Be-fore crack appearance, the load-deflection relationship is almost linear due to the linear elastic behavior of materials, and the flexural strength of cross-section remains constant. After cracking, the behavior of reinforced EPS-C changes to the plastic phase with some residual strain, efficient cross-sectional height decreases as well as deformation modulus, *i.e., deformation modulus of materials is lower than the elastic Young's modulus*. For this reason, the slab's overall stiffness unexpectedly reduces, jump in the deflection curve can be observed. The cracking load and ultimate load-bearing capacity for specimen M1 are 1.58 kN and 9.37 kN, respectively. The cracking load corresponds approximately to 16% of the ultimate load, in line with typical concrete slab behavior.

From Fig. 6, the serviceability loads (P_{ser}) corresponding to the allowable deflection of slab specimen can be calculated. The allowable deflection for slabs is L/250, with L is slab's span [11]. The span of reinforced EPS-C slab specimens in this study is 1.9 m which implies that the slab deflection cannot exceed 7.6 mm. Consequently, the serviceability loads (P_{ser}) for the slab is 4.10 kN, equivalent to 45% of the ultimate load. Crack width for reinforced concrete slabs is restricted to 0.4 mm based on the indication provided by [11]. The value of the ultimate

cracking load ($P_{crc,u}$) which corresponds to the limit of crack width is about 4.06 kN. It can be noted that in this case, P_{ser} and $P_{crc,u}$ have almost the same value. It can be concluded that the serviceability limit loading of the reinforced EPS-C slab to ensure the condition of normal use reaches over 4 kN (equivalent to 4.2 kN/m^2).

4 Conclusions

The paper has presented an experimental campaign to investigate the flexural behavior of reinforced EPS-C slabs. Three different full-scale 4 point-bending flexural tests were performed. The relationship between load and deflection as well as the cracking, serviceability, and ultimate load limit has been discussed.

The results suggest that the behavior of reinforced EPS-C slabs is similar to that of conventional reinforced concrete slabs, characterizing by failure regime and load-bearing capacity refers to normal use conditions. For slabs spanning less than 2 m, based on Eurocode 2 requirements [11], the serviceability load (P_{ser}), determined by conditions of allowable deflection and maximum crack-opening width, is approximately 45 percent of the ultimate load. The results also showed that the load-bearing capacity of 100 mm thickness reinforced EPS-C slab made from EPS-C with a density of 1200 kg/m^3 reached 4 kN/m^2. This observation leads to conclude that it is possible to use EPS-C slab as a structural component in civil engineering applications.

References

1. Cui, C., Huang, Q., Li, D., Quan, C., Li, H.: Stress-strain relationship in axial compression for EPS concrete. Constr. Build. Mater. **105**, 377–383 (2016)
2. Fernando, P.L.N., Jayasinghe, M.T.R., Jayasinghe, C.: Structural feasibility of expanded polystyrene (EPS) based lightweight concrete sandwich wall panels. Constr. Build. Mater. **139**, 45–51 (2017)
3. Sayadi, A.A., Tapia, J.V., Neitzert, T.R., Clifton, G.C.: Effects of expanded polystyrene (EPS) particles on fire resistance, thermal conductivity and compressive strength of foamed concrete. Constr. Build. Mater. **112**, 716–724 (2016)
4. Shi, W., Miao, L., Luo, J., Wang, J., Chen, Y.: Durability of modified expanded polystyrene concrete after dynamic cyclic loading. Shock and Vibration (2016)
5. Bouvard, D., Chaix, J.M., Dendievel, R., Fazekas, A., Létang, J.M., Peix, G., Quenard, D.: Characterization and simulation of microstructure and properties of EPS lightweight concrete. Cem. Concr. Res. **37**(12), 1666–1673 (2007)
6. Liu, N., Chen, B.: Experimental study of the influence of EPS particle size on the mechanical properties of EPS lightweight concrete. Constr. Build. Mater. **68**, 227–232 (2014)

7. Dissanayake, D.M.K.W., Jayasinghe, C., Jayasinghe, M.T.R.: A comparative embodied energy analysis of a house with recycled expanded polystyrene (EPS) based foam concrete wall panels. Energy Build. **135**, 85–94 (2017)
8. Chen, B., Liu, N.: A novel lightweight concrete-fabrication and its thermal and mechanical properties. Constr. Build. Mater. **44**, 691–698 (2013)
9. Colombo, I.G., Colombo, M., di Prisco, M.: Bending behavior of textile reinforced concrete sandwich beams. Constr. Build. Mater. **95**, 675–685 (2015)
10. Assaad, J., Chakar, E., Zéhil, G.P.: Testing and modeling the behavior of sandwich lightweight panels against wind and seismic loads. Eng. Struct. **175**, 457–466 (2018)
11. Eurocode 2 (EN 1992-1-1), Design of Concrete Structure

Experimental and Numerical Vibration Analyses of Healthy and Cracked Pipes

Meriem Seguini, Djilali Boutchicha, Samir Khatir, Djamel Nedjar, Cuong-Le Thanh, and Magd Abdel Wahab

1 Introduction

Pipes need to be stronger and flexible because of the demands of safety and reliability. Crack identification becomes a popular subject for engineering. In fact, for that reason, different analyses of the behavior of the pipeline have been done [1, 2]. However, several numerical methodologies have been used to identify the crack in different types of structure. Lee et al. [3] developed a new method based on the committee network to define the location and size of the crack in a steel cantilever notched pipe. The genetic algorithm has been also used by Wang et al. [4] to identify the location of the crack. Li et al. [5] detected the pipe's crack experimentally by adding virtual masses on the substructure combined with sensitivity and frequencies. Moreover, Murigendrappa et al. [6] detected crack presence in the

M. Seguini (✉) · D. Nedjar
Faculty of Architecture and Civil Engineering, Department of Civil Engineering, Laboratory of Mechanic of Structures and Stability of Constructions LM2SC, University of Science and Technology of Oran Mohamed Boudiaf, BP 1505 Oran 31000, Algeria

D. Boutchicha
Laboratory of Applied Mechanics, University of Science and Technology of Oran Mohamed Boudiaf, BP 1505 Oran 31000, Algeria
e-mail: Djilali.boutchicha@gmail.com

S. Khatir · M. Abdel Wahab
Soete Laboratory, Faculty of Engineering and Architecture, Ghent University, Technologiepark Zwijnaarde 903, B-9052 Zwijnaarde, Belgium
e-mail: Khatir_samir@hotmail.fr

S. Khatir · C.-L. Thanh
Faculty of Civil Engineering, Ho Chi Minh City Open University, Ho Chi Minh City, Vietnam

pipe with fluid by using experimental and theoretical analyses. Owolabi et al. [7] used an analyzer of frequency to measure the acceleration frequency of a cracked aluminum beam. Song et al. [8] used a new experimental technique to identify the cracks in a long-distance natural gas pipeline. A review of damage detection in a mechanical system based on the measurement of the vibration has been also published [9]. Meshram et al. [10] studied the relationship between the measured frequencies with crack depth location in a cantilever beam where different crackdepths at different locations have been created, in order to analyze the influence of the crack damage on the frequencies of the beam. Nahvi et al. [11] developed also a finite element model of a cracked beam and determined the mode shapes. Liang et al. [12] quantified the effect of the created damage. This study was based on a new method which made use of a rotational massless spring in the beam. However, other identification methods have been recently used. Khatir et al. [13] monitored the behavior of beam-like structures both experimentally and numerically based on the variation in local flexibility near the crack position, where the naturel frequencies of cracked beam have been determined. Khatir et al. [14] carried out a numerical simulation based on genetic algorithm (GA), to identify the crack's damage where different values of natural frequencies have been determined. Another method, based on the eXtended Iso Geometric analysis and PSO, has been used by the same author in order to quantify the effect of the damage. A new approach of the vibration analysis based on the inverse problem formulation has been also used by Khatir et al. [15]. Galvanetto and Violaris [16] based their study on the POD theory to detect damage in two beams.

In this work, the Ansys software is used to model cracked and uncracked pipes, where different depths of crack are created in the middle of the pipe. Therefore, numerical and experimental analyses are done to obtain the first three mode shapes and their frequencies. A finite element method is used to model the pipe and two configurations types of the pipe are considered. The pipe is modeled using 1D and 3D beam elements in order to make a comparison. Different types of pipe's meshs are used to analyze their influence on the behavior of the pipe. Moreover, the 1D pipe is also subdivided into a different number of elements in order to perform a sensitivity study. The obtained results show the importance of the chosen mesh and configuration in the determination of the real response of the pipe.

2   Finite Element Model

This study is based on a linear dynamic analysis of a (free-free) pipe with numerical simulations based on the finite element method, where the analysis is carried out using the Ansys Software V 18.1. The characteristics of the pipe are listed in Table 1. Different depths of pipe's single crack ($d = 4$ mm, $d = 8$ mm, $d = 12$ mm and $d = 16$ mm) are created in the middle of the pipe as shown in Fig. 1.

Table 1 Pipe mechanical and geometrical properties

Notation	Parameters	Range of values	Unit
D_p	Diameter of the pipe	500	mm
L_p	Length of the pipe	1000	mm
E_p	Pipe elastic Young modulus	61950	MPa
v_p	Poisson ration of pipe	0.3	(−)
ρ	Density	7850	(Kg/m^3)
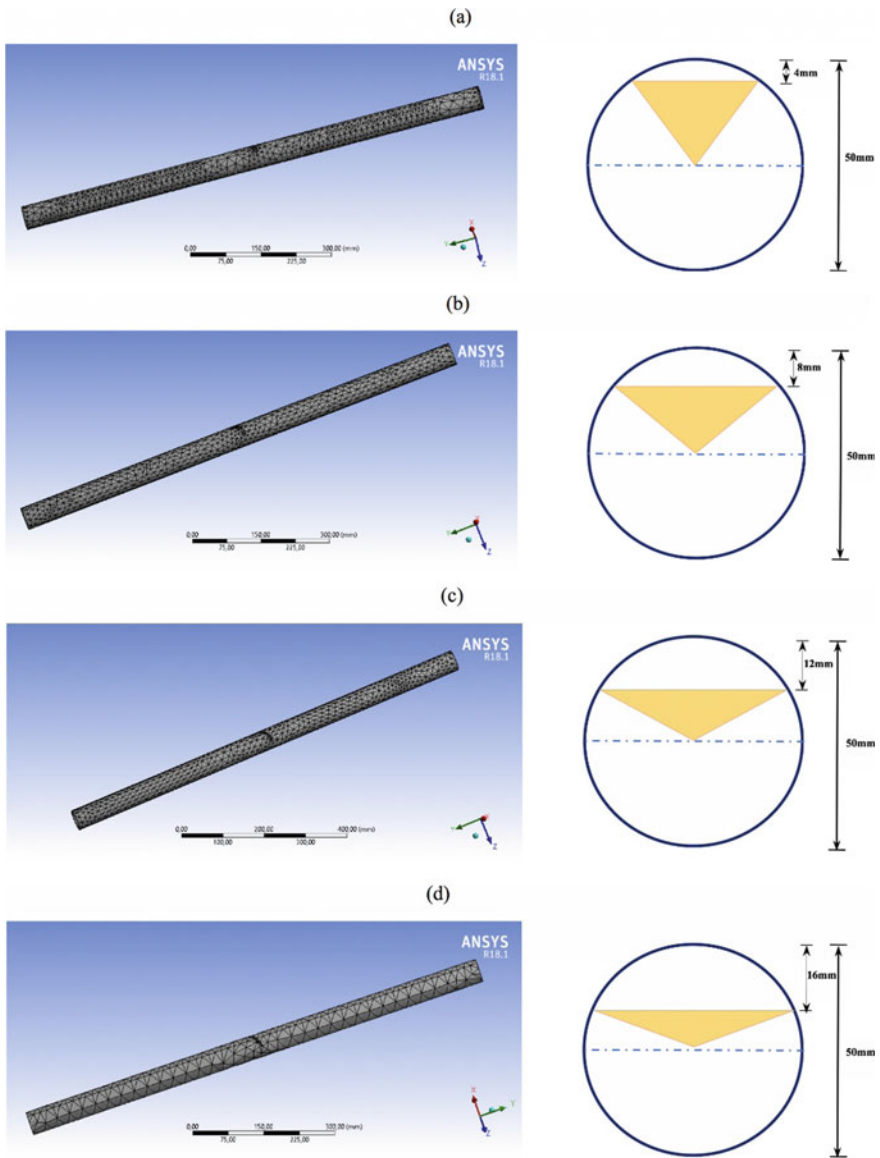
Fig. 1 Finite element models of the cracked pipe with different depths

3   Experimental and Sensitivity FE Analyses

In this work, the M + P SO Analyzer 4.3 has been used to determine the vibration of the pipe. Otherwise, the excitations have been generated by Hammer and responses were extracted using PCB Accelerometers 356A15 as shown Fig. 2. The frequencies have been measured for each depth of crack ($d = 4$ mm, $d = 8$ mm, $d = 12$ mm and $d = 16$ mm) where three modes of each depth of crack have been determined and the obtained results are listed in Table 2.

From Table 2, it can be seen that the obtained results from FEA are good compared with the experimental results. This allows us to prove the important of the developed model. From the same table, it can also be concluded that the crack's depth has a great influence on the response of the pipe. In fact, when the crack's depth increases, there is a decrease in the natural frequencies. Three mode shapes obtained from the FEA are plotted for two types of crack's depth in Figs. 3, 4.

Fig. 2 Used experimental setup for the dynamic analysis of the aluminum pipe [17]

Table 2 Numerical and experimental measured frequencies (Hz) of the cracked and uncracked pipe

Frequencies		Without crack	Crack = 4 mm	Crack = 8 mm	Crack = 12 mm	Crack = 16 mm
Mode 1	FEM	288.49	284.69	271.12	233.47	182.26
	EXP	289.38	283.75	271.56	234.06	181.56
Mode 2	FEM	774.47	776.5	770.47	757	669.29
	EXP	785	785.31	785	783.75	779.06
Mode 3	FEM	1466	1443	1394.5	1231.5	1006.7
	EXP	1463.8	1447.2	1394.7	1292.5	1185.3
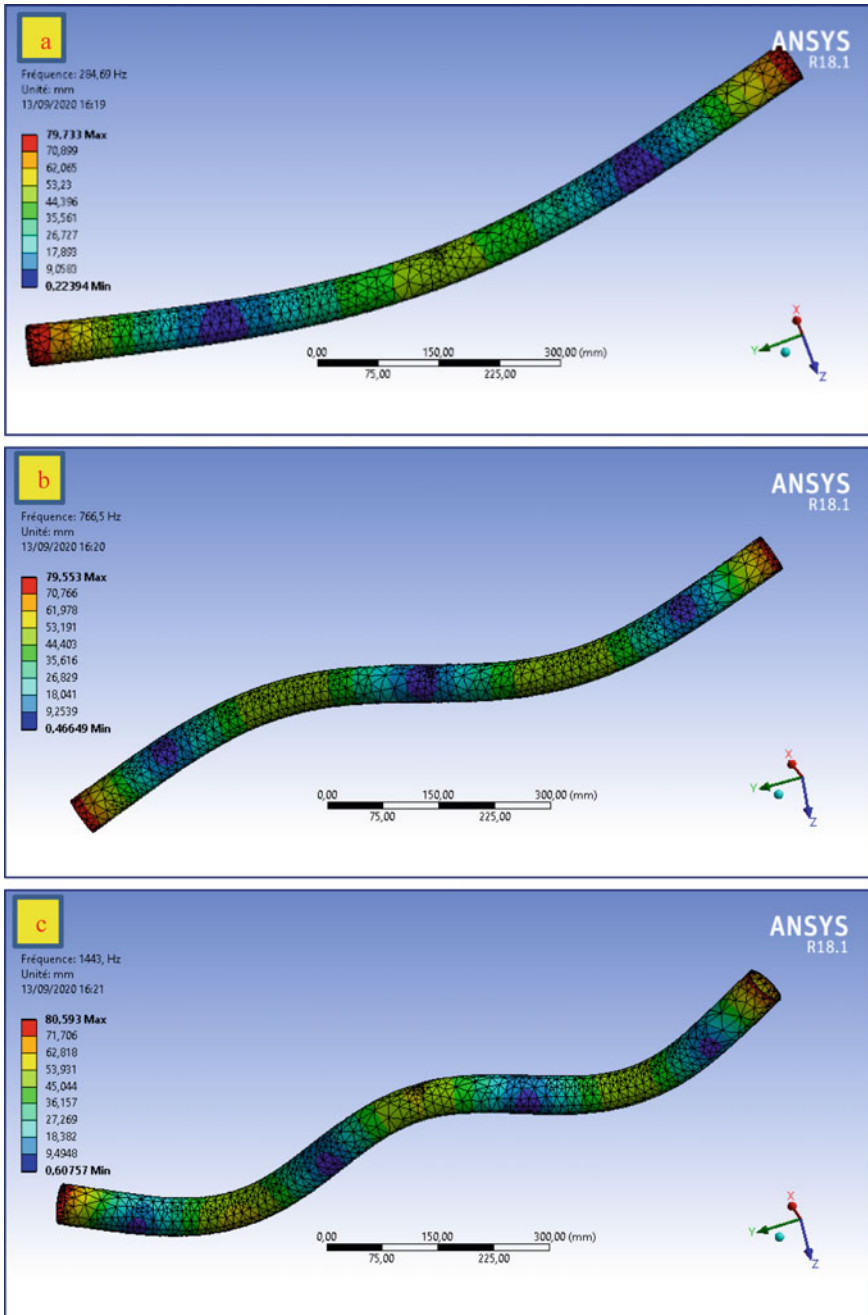
Fig. 3 Mode shapes of the cracked pipe with 4 mm of crack's depth: **a** Mode 1 **b** Mode 2 and **c** Mode 3
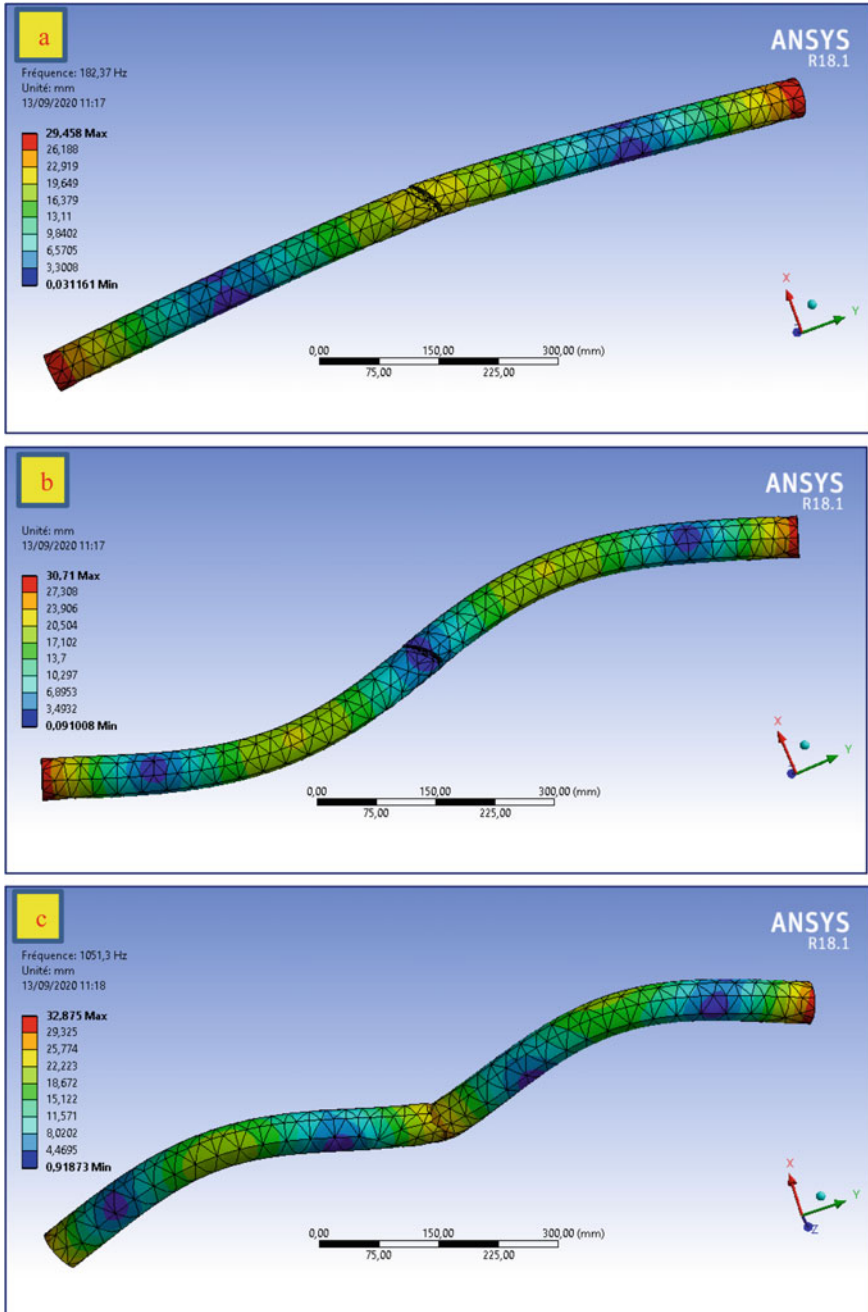
Fig. 4 Mode shapes of the cracked pipe with 8 mm of crack's depth: **a** Mode 1 **b** Mode 2 and **c** Mode 3

Table 3 Measured frequencies (Hz) of different pipe's configurations

Frequency	Pipe 1D	Pipe 3D	Experimental test
Mode 1	290.85	288.49	289.38
Mode 2	773.08	774.47	785
Mode 3	1469.5	1466	1463.8

Table 4 Measured frequencies (Hz) of 1D pipe divided into different elements

Number of elements	5	10	20	50	100
Mode 1	291.33	290.88	290.85	290.85	290.85
Mode 2	788.3	775.64	775.08	775.04	775.64
Mode 3	1513.8	1472.2	1469.5	1469.2	1469.2

Moreover, different specimens of pipe's configurations have been analyzed for which the obtained frequencies of 1D and 3D are summarized in Table 3. From this analysis, it can be observed that the 3D configuration allows us to obtain accurate results.

Next, the sensitivity of the used mesh is also studied for 1D- and 3D-based number of elements and mesh types, respectively. In Table 4, it can be observed that when the number of elements increases for 1D, the values of frequencies converge for 50 elements and there isn't any change on the values of frequencies after that.

The natural frequencies of the pipe using 3D FE model are obtained by using three types of pipe's mesh tetrahedron, quadrilateral, and hexahedron as shown in Fig. 5 and summarized in Table 5. From this table, we can conclude that the tetrahedron pipe's mesh allows us to obtain better results than the others.
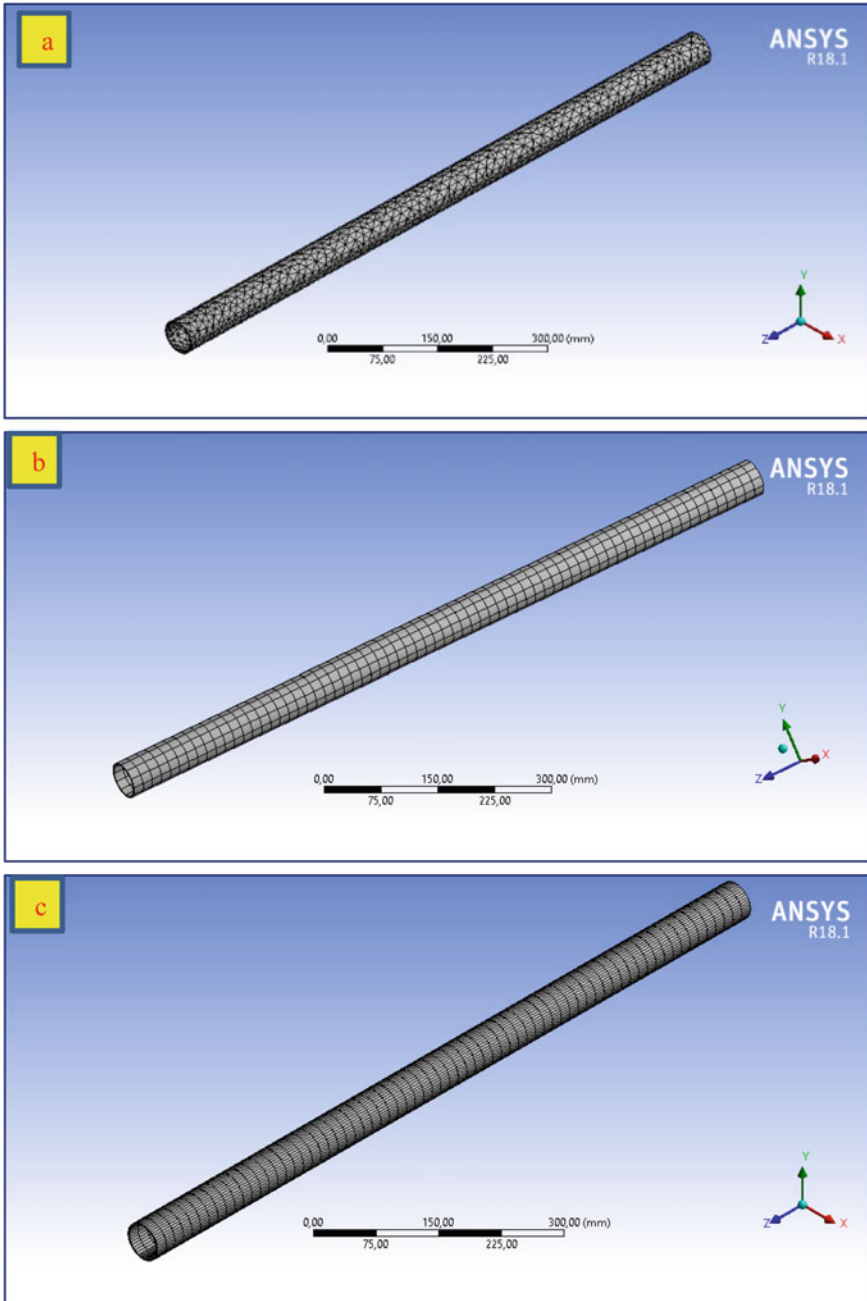
Fig. 5 Different types of pipe's meshing: **a** tetrahedron, **b** hexahedron and **c** quadrilateral

Table 5 Measured frequencies (Hz) of the uncracked pipe, obtained from different types of pipe's meshing

	Tetrahedron	Quadrilateral	Hexahedron	EXP
Mode 1	288.49	287.13	287.1	289.38
Mode 2	774.47	774.58	774.48	785
Mode 3	1466	1460.1	1459.9	1463.8

4   Conclusion

This study developed and validated an innovative finite element model of cracked and uncracked pipes. The efficiency of the developed model has been verified by making a comparison between numerical and experimental results. Many parameters have been also analyzed in this study such as the types of mesh and the pipe's configurations.

The results of this work mainly showed that:

- The depth of the crack has a strong influence on the response of the pipe where the values of the frequencies decrease with the increase of the crack's depth.
- The chosen type of pipe's configuration and meshing play a major role in the determination of the correct response of the cracked and uncracked pipes.

References

1. Seguini, M., Nedjar, D.: Modelling of soil–structure interaction behaviour: geometric nonlinearity of buried structures combined to spatial variability of soil. Eur. J. Environ. Civil Eng. **21**(10), 1217–1236 (2017)
2. Seguini, M., Nedjar, D.: Dynamic and probabilistic analysis of shear deformable pipeline resting on two parameter foundation. Periodica Polytechnica Civil Eng. **64**(2), 430–437 (2020)
3. Lee, J.-W., Kim, S.-R., Huh, Y.-C.: Pipe crack identification based on the energy method and committee of neural networks. Int. J. Steel Struct. **14**(2), 345–354 (2014)
4. Wang, Y., Chen, X., He, Z.: Daubechies wavelet finite element method and genetic algorithm for detection of pipe crack. Nondestr. Test. Eval. **26**(01), 87–99 (2011)
5. Li, D., Lu, D., Hou, J.: Pipeline damage identification based on additional virtual masses. Appl. Sci. **7**(10), 1040 (2017)
6. Murigendrappa, S., Maiti, S., Srirangarajan, H.: Experimental and theoretical study on crack detection in pipes filled with fluid. J. Sound Vib. **270**(4–5), 1013–1032 (2004)
7. Owolabi, G., Swamidas, A., Seshadri, R.: Crack detection in beams using changes in frequencies and amplitudes of frequency response functions. J. Sound Vib. **265**(1), 1–22 (2003)
8. Song, X., Huang, S., Zhao, W.: Nondestructive testing technique for cracks in long-distance natural gas pipelines. Nat. Gas. Ind. **26**, 103–106 (2006)

9. Galvanetto, U., Violaris, G.: Numerical investigation of a new damage detection method based on proper orthogonal decomposition. Mech. Syst. Signal Process. **21**(3), 1346–1361 (2007)

10. Meshram, N.A., Pawar, V.S.: Analysis of crack detection of a cantilever beam using finite element analysis. Int. J. Eng. Res. Technol. **4**(04) (2015)

11. Nahvi, H., Jabbari, M.: Crack detection in beams using experimental modal data and finite element model. Int. J. Mech. Sci. **47**(10), 1477–1497 (2005)

12. Liang, R.Y., Choy, F.K., Hu, J.: Detection of cracks in beam structures using measurements of natural frequencies. J. Franklin Inst. **328**(4), 505–518 (1991)

13. Khatir, S., et al.: Crack identification method in beam-like structures using changes in experimentally measured frequencies and Particle Swarm Optimization **346**(2), 110–120 (2018)

14. Khatir, S., et al.: Genetic algorithm based objective functions comparative study for damage detection and localization in beam structures. In: Journal of Physics: Conference Series. IOP Publishing (2015)

15. Khatir, S., et al.: Damage detection and localization in composite beam structures based on vibration analysis. J. Mech. **21**(6), 472–479 (2015)

16. Galvanetto, U., Violaris, G.: Numerical investigation of a new damage detection method based on proper orthogonal decomposition. J. Mec. Syst. Signal Process. **21**(3), 1346–1361 (2007)

17. Seguini, M., et al.: Crack prediction in pipeline using ANN-PSO based on numerical and experimental modal analysis. Smart Struct Syst. **27.3**, 507 (2021)

Cracking Behavior of Corroded Beams Repaired in Flexure by Steel Fiber-Reinforced Concrete

Linh Van Hong Bui[ID]**, Pitcha Jongvivatsakul,**
Boonchai Stitmannaithum, Phuoc Trong Nguyen[ID]**,**
Yen Thi Hai Nguyen, Nam Van Nguyen, Thi Nguyen Cao,
and Thanh-Truong Nguyen

1 Introduction

Corrosion causes substantial deterioration of reinforced concrete (RC) structures in extreme conditions [1–3]. To rehabilitate the corroded members, many researchers concerned on structural intervention techniques that could not only help to restore members' mechanical capacity but also extend service life of structures [4, 5]. Among the repairing methods, the technique patching steel fiber-reinforced concrete (SFRC) composites up the deteriorated zone of the corroded members has great potential [6]. As reported in the study by Azam and Soudki [7], the SFRC could resist significantly the cracking propagation in the repaired beams.

L. Van Hong Bui · Y. T. H. Nguyen · N. Van Nguyen
Faculty of Civil Engineering, Ho Chi Minh City Open University,
Ho Chi Minh City 700000, Vietnam

P. Jongvivatsakul · B. Stitmannaithum
Innovative Construction Materials Research Unit, Department of Civil Engineering,
Chulalongkorn University, Pathumwan, Bangkok 10330, Thailand

P. T. Nguyen
Faculty of Civil Engineering, Ho Chi Minh City Open University,
Ho Chi Minh City 700000, Vietnam

T. N. Cao
Faculty of Civil Engineering, Tien Giang University, My Tho City 860000, Vietnam

T.-T. Nguyen (✉)
Industrial Maintenance Training Center, Ho Chi Minh City University of Technology
(HCMUT), 268 Ly Thuong Kiet Street, District 10, Ho Chi Minh City, Vietnam
e-mail: thtruong@hcmut.edu.vn

T.-T. Nguyen
Vietnam National University Ho Chi Minh City, Linh Trung Ward, Thu Duc District,
Ho Chi Minh City, Vietnam

Furthermore, the SFRC might improve the interfacial connection of SFRC to steel and concrete through the interlock mechanism.

In addition, the study by Azam and Soudki [7] revealed that the shear behavior of corroded beams has changed the beam action to the arch action. This leads the enhancement in shear carrying capacity of the test specimens [8, 9]. Following available literature, the authors have conducted two studies [10, 11] to examine the shear resisting mechanism of corroded RC beams repaired using SFRC in the tension zone. However, the deformational cracking of corroded beams repaired by a tensile SFRC system has not been fully considered in previous sources.

This study investigates an experimental monitoring the cracking behavior of corroded RC beams repaired in flexure with SFRC. Four RC beams are designed to examine the influences of corrosion degree and the steel fiber volume in SFRC on deformation mechanism, such as cracking pattern and width and load–crack width trace.

2   Experimental Monitoring

The geometry dimensions and reinforcement configurations for four RC beams are presented in Fig. 1 and Table 1. The overall dimension for the test beams was $150 \times 200 \times 1400 \text{ mm}^3$. The beams used the longitudinal bars with 20 mm bar diameter, and the beams employed both compressive reinforcement and shear reinforcement with 6 mm bar diameter. The labels for four beams are 12C-1F, 12C-1.5F, 17C-1F, 17C-1.5F. There were two beams subjected to corrosion degree of 12%, and the other two beams were subjected to corrosion degree of 17%. Note that corrosion degree was derived by the percentage in reinforcement mass loss. The beams were then repaired by SFRC with volume of steel fibers of 1 and 1.5%.

The average concrete compressive strength of the tested cylinders at 28 days was 34.6 MPa. The yield strengths of the tension bar with 20 mm bar diameter and the shear and compression bars with 6 mm bar diameter were, respectively, 512 MPa and 386 MPa. The repairing SFRC was mixed between a ration of water to cement (w/c) by 0.5 and a ratio by weight of cement-to-weight of sand (c/s) by 1:3 and with steel fibers.
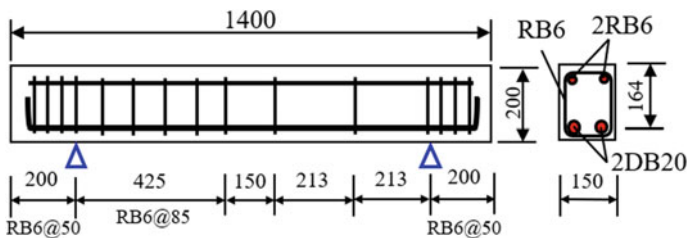
Fig. 1 Configurations for the test beams [10]

Table 1 Description of repaired beams

Specimen name	Corrosion degree (%)	Maximum crack width due to corrosion (mm)	Repairing scheme	Steel fiber volume (%)
12C-1.0F	12	0.35	SFRC	1.0
12C-1.5F	12	0.25	SFRC	1.5
17C-1.0F	17	0.95	SFRC	1.0
17C-1.5F	17	0.85	SFRC	1.5

In previous studies [10, 11], the artificial corrosion process is briefly summarized as follows. On seventh day after casting, the beams were subjected to a corrosion acceleration procedure as demonstrated in Fig. 2a. All beams were submerged in a 3% NaCl solution, and the water level was carefully identified to embed the bottom surface of beams. The prevention of the corrosion to transverse steels and compar reinforcement was intervened. The study by Jongvivatsakul et al. [10] described that direct current (DC) was attached to total of 600 Ah and 900 Ah to reach the mass losses of 12% and 17% for the tensile reinforcement, respectively.

Figure 2b depicts the repairing procedure. First, the deteriorated concrete at level of reinforcement layer was removed before the beams were diammonium-controlled to cleaning up the dust and rust. Second, the bottom layer of beams with thickness of 66 mm was prepared to fill in SFRC composites.

3 Results and Discussion

3.1 Failure of Beams Subjected to Corrosion Process

It is indicated in Fig. 3 that the beams subjected to corrosion were mainly damaged by interfacial detachment of concrete at tensile reinforcement level. This is due to the change in shape and size of steel tension bars caused by accelerated corrosion. Additionally, Fig. 3 also reveals that the beams subjected to 17% degree of corrosion were prone to detachment failure compared to corroded beams with 12% of corrosion degree. Therefore, as shown in Table 1, the maximum crack width values monitored in the beams with high corrosion degree (17%) were significantly wider than those monitored in the beams with low corrosion degree (12%).

The cracking behavior of the beams resulted by corrosion process in Fig. 3 indicates the need of repairing to restore the structural performance of the members. The repairing technique is to patch SFRC up the tensile zone, where the deteriorated parts were removed.
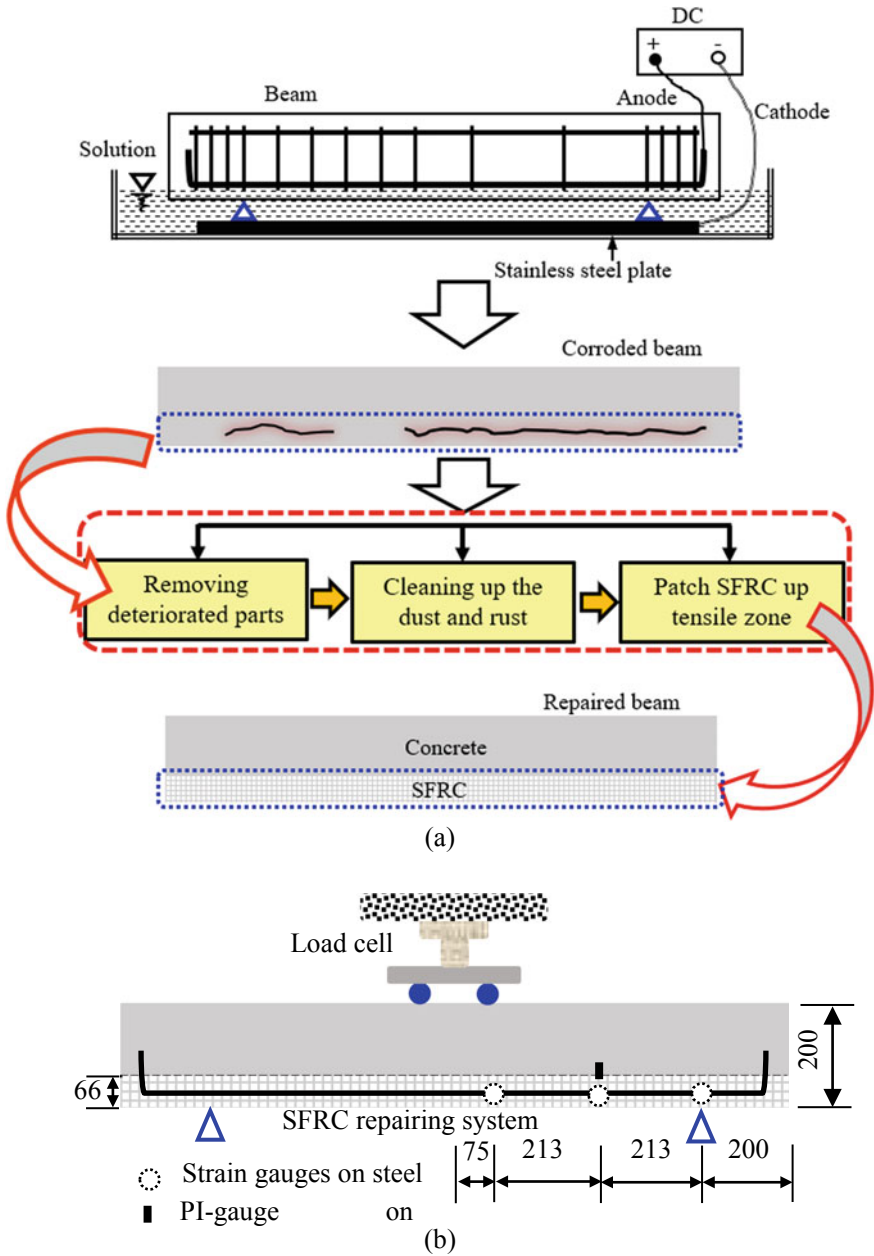
Fig. 2 **a** Corrosion process and repairing procedure; **b** scheme for test set up

Crack detachment at reinforcement level by expanding steel subject corrosion

(a) 12C-1F   (b) 12C-1.5F

(c) 17C-1F   (d) 17C-1.5F

Significant crack detachment at reinforcement level
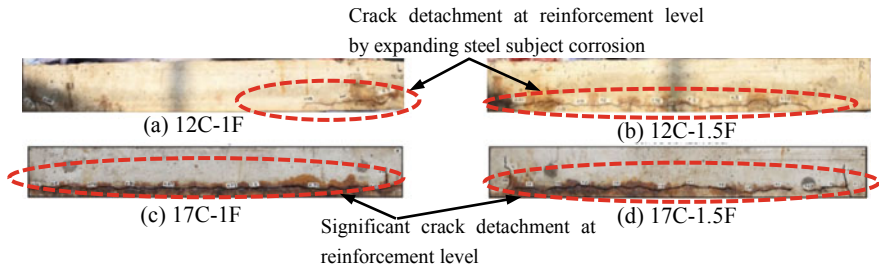
Fig. 3 Corrosion crack in beams

3.2 Load Capacity Versus Crack Width

Figure 4 presents the load capacity-crack width trace in the beams tested. The crack width measured by pi-gauge glued in concrete increased as the load increased. Owing to the same concrete properties, there is an identical response in the initial stage of the repaired beams 12C-1F, 12C-1.5F, 17C-1.5F at the load level of 70 kN. Afterward, the deformation in beams was propagated to activate the effectiveness of reinforcement and SFRC. The ultimate loads for the specimens 12C-1F, 12C-1.5F, 17C-1.5F are, respectively, 112 kN, 111 kN, 123 kN, while the crack widths at peak load for those specimens are 2.2, 1.3, 1.5 mm. In Fig. 4, the stiffness of the repaired beam with high corrosion degree is greater than the stiffness of the beam with low corrosion degree. Following the strain development in the elements, the cracks were gradually wide until the beams failed. The crack width opening by increasing load applied was found to be linear due to the elasticity of steel reinforcement.

Fig. 4 Load increase versus crack width measured at pi-gauge
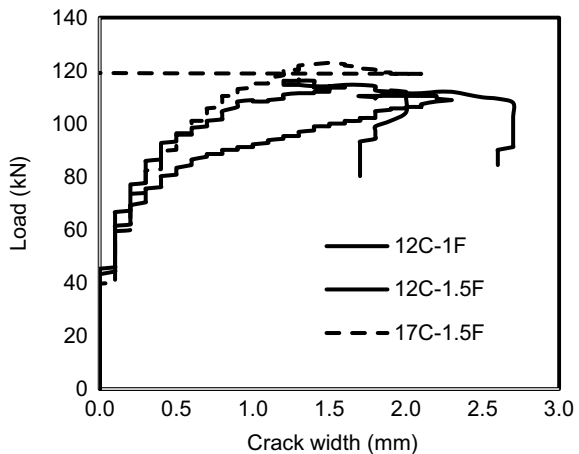
3.3 Cracking Mechanism

It can be observed in Figs. 4 and 5 that the beams repaired by SFRC that contains low percentage of steel fibers decreased the crack size and crack development in comparison with the beams repaired with SFRC that consists of large amount of steel fibers. The fact is that the number of steel fibers in SFRC improved connection at material interfaces, mitigating crack opening. Generally, the members subjected to a low corrosion degree (12%) resulted in wider crack width than crack deformation of the members subjected to 17% corrosion degree. This finding may be mainly due to the shear resisting mechanism in beams changed conventional beam action to arch action, which was effectuated by a rigid strut. Additionally, the crack width measured by pi-gauge in specimen 12C-1F is larger than the crack width monitored in specimen 12C-1.5F. These mentioned findings indicate that the beams with high corrosion degree and high volume of steel fibers in a SFRC repairing system resisted substantially the crack opening and propagation.

In Fig. 5, the lengths of main failure cracks for four repaired beams were in range of 96–122 mm. While the angles of main cracks for those members were in range of 32°–53°. These indicate that crack properties, which are length and inclination, are depended on the corrosion degree subject to the beams and the steel fiber volume in the repairing SFRC system. In fact, steel fibers could provide the resistance to crack opening, while corrosion degree could impact on the shear mechanism of beams, which affected the crack characteristics.

Figure 5a–d illustrates the deformation failure of four investigated beams. Most of specimens were failed by interfacial delamination of SFRC to old parts. However, the beam 17C-1F failed by mixed-modes of shear and delamination, as depicted in Fig. 5c. The steel fibers in SFRC could improve the adhesive bonding efficiency of SFRC to old parts (concrete and steel) through roughness mechanism. The elements concrete, SFRC, interfaces were then simultaneous to be occurred the
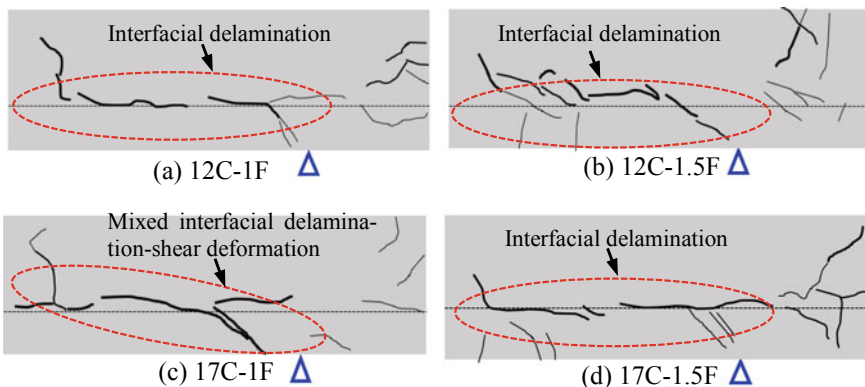
Fig. 5 Cracking patterns in investigation span of the test beams

mixed-mode failure in the beam 17C-1F. Moreover, the arch action formed in the beam 17C-1F also is a reasonable characteristic to induce the mentioned failure mode.

4 Conclusions

The primary conclusions in this study can be drawn as follows:

1. Without loading, the members subjected to high corrosion degree increased crack width and failure phenomenon compared to the members subjected to low corrosion degree. The corroded beams without loading tests failed mainly due to crack detachment at reinforcement level, where volume of steel was changed in corrosion process. With loading, the SFRC-repaired beams failed mainly by the delamination of SFRC to old parts (concrete and steel). The load-carrying capacity of the specimen 17C-1.5F, which was with high corrosion degree and following repaired by SFRC contained number of steel fibers, was greater than capacity of the other beams.
2. The beam 17C-1.5F resisted greatly the crack opening and development when the load increased. It is obvious that the increase in steel fiber amount increased tensile strength of SFRC. The maximum crack width recorded in the beams of series 12C is wider than the maximum crack width observed in the specimens of series 17C. It is because the steel fibers in SFRC were triggered in the repaired to resist the deformation.

References

1. Fu, C., Jin, N., Ye, H., Jin, X., Dai, W.: Corrosion characteristics of a 4-year naturally corroded reinforced concrete beam with load-induced transverse cracks. Corros. Sci. **117**, 11–23 (2017)
2. Wang, X.H., Gao, X.H., Li, B., Deng, B.R.: Effect of bond and corrosion within partial length on shear behaviour and load capacity of RC beam. Constr. Build. Mater. **25**(4), 1812–1823 (2011)
3. Triantafyllou, G.G., Rousakis, T.C., Karabinis, A.I.: Analytical assessment of the bearing capacity of RC beams with corroded steel bars beyond concrete cover cracking. Compos. B Eng. **119**, 132–140 (2017)
4. Ma, Y., Zhang, J., Wang, L., Liu, Y.: Probabilistic prediction with Bayesian updating for strength degradation of RC bridge beams. Struct. Saf. **44**, 102–109 (2013)

5. Liu, Y., Jiang, N., Deng, Y., Ma, Y., Zhang, H., Li, M.: Flexural experiment and stiffness investigation of reinforced concrete beam under chloride penetration and sustained loading. Constr. Build. Mater. **117**, 302–310 (2016)
6. Jongvivatsakul, P., Bui, L.V.H., Koyekaewphring, T., Kunawisarut, A., Hemstapat, N., Stitmannaithum, B.: Using steel fiber-reinforced concrete precast panels for strengthening in shear of beams: an experimental and analytical investigation. Adv. Civil Eng. **4098505**, 1–19 (2019)
7. Azam, R., Soudki, K.: Structural performance of shear-critical RC deep beams with corroded longitudinal steel reinforcement. Cement Concr. Compos. **34**(8), 946–957 (2012)
8. Safdar, M., Matsumoto, T., Kakuma, K.: Flexural behavior of reinforced concrete beams repaired with ultra-high performance fiber reinforced concrete (UHPFRC). Compsite Struct. **157**, 448–460 (2016)
9. Tanarslan, H.M.: Flexural strengthening of RC beams with prefabricated ultra high performance fibre reinforced concrete laminates. Eng. Struct. **151**, 337–348 (2017)
10. Jongvivatsakul, P., Laopaitoon, P., Nguyen, Y.T.H., Bui, L.V.H.: Assessment of shear resistance of corroded beams repaired using steel fiber-reinforced concrete in the tension zone. Comput. Concr. (2020)
11. Linh, V.H.B., Jongvivatsakul, P., Stitmannaithum, B., Nguyen, Y.T.H.: Examination on shear behavior of corroded RC beams intervened with SFRC considering interfacial bond mechanism. J. Adv. Concr. Technol. (2020)

Application for Structural Health Monitoring

Monitoring Electrical Resistivity of Strain Hardening Fiber-Reinforced Cementitious Composite Exposed to Cyclic Wetting and Drying

Phu-Cuong Nguyen and Ngoc-Thanh Tran

1 Introduction

There is a concern regarding durability of reinforced concrete structure exposed to marine environment because of the low crack resistance of concrete. Concrete with low tensile strength and brittle nature cannot be able to prevent crack formation under tensile loading. The presence of cracks obviously accelerates the immigration of harmful chemical, then causes the corrosion of steel bar and the deterioration of concrete structure [1]. Moreover, it is not easy to set up the structure health monitoring system for evaluating durability of reinforced concrete structure exposed to marine environment [2]. Thus, it is necessary to improve the crack resistance of concrete and provide a better way to monitor durability of reinforced concrete structure under marine environment.

There have been many proposed methods to improve the crack resistance of concrete and to monitor durability of reinforced concrete structure: (1) the utilization of sulfated clinker as an expanding additive to Portland cement lead to an increase in crack resistance of concrete [3]; (2) the reinforcement of steel bar to prevent crack development [4]; (3) the addition of fiber in concrete mixture to bridge crack at small crack width [5]; and (4) the use of sensor to monitor crack and embedded graphene to access chloride penetration in reinforced concrete structure [6, 7].

However, the above approaches have shown their limitations: the utilization of sulfated clinker only provide resistance to cracking caused by shrinkage; the

P.-C. Nguyen
Faculty of Civil Engineering, Ho Chi Minh City Open University, Ho Chi Minh City, Vietnam

N.-T. Tran (✉)
Faculty of Civil Engineering, Ho Chi Minh City University of Transport, Ho Chi Minh City, Vietnam
e-mail: ngocthanh.tran@ut.edu.vn

reinforcement of steel bar leads to high risk of corrosion and it is difficult to provide crack resistance at anyplace in reinforced concrete structure; fiber-reinforced concrete provides insufficient crack resistance and crack width control capacity under high value of tensile loading; and the sensor and graphene are quietly expensive and require complex connection with the data acquisition system, especially in the marine environment.

This research proposes to apply strain hardening fiber-reinforced cementitious composite (SHFRCC) to reinforced concrete structure exposed to marine environment because this material exhibits very high crack resistance and crack width control capacity owing to its high tensile strength and strain hardening behavior [8]. In addition, this material possesses self-sensing capacity obtained by measuring electrical resistivity [9]. Although the high crack-sensing capacity of SHFRCC under tensile loading has been well known [9], the measurement of electrical resistivity for evaluating the penetration of chloride in SHFRCC under marine environment is still under question. Most research has focused on the electrical resistivity of normal concrete under marine environment [10–14] while few studies have investigated electrical resistivity of fiber-reinforced concrete [15, 16]. The electrical resistivity of concrete was reduced owing to the presence of chloride [10]. The lower electrical resistivity was obtained as the immigration of chloride became faster [11]. The relationships between electrical resistivity of concrete and chloride diffusivity were introduced by many researchers [12–14]. Lehner et al. [15] concluded that the diffusion coefficient and the electrical resistivity of fiber-reinforced concrete increased with increasing fiber volume fraction. Kakooei et al. [16] reported that the electrical resistivity of fiber-reinforced concrete reduced due to the presence of chloride.

The main objective of this study is to measure electrical resistivity of SHFRCC under chloride cycle. The detail objectives include: (1) effects of number of chloride cycle on the electrical resistivity of SHFRC; (2) effect of fiber type and crack width on the electrical resistivity of SHFRCC under chloride cycle.

2   Experimental Program

In order to investigate electrical resistivity of SHFRCCs under marine environment, an experimental program was set up with 26 series of specimens, as shown in Fig. 1. Two types of steel fiber, hooked and twisted fiber, were reinforced to high-strength concrete at the fiber volume fraction of 2%. The SHFRCCs were precracked by performing direct tensile test until the strain of 0.1%. Both uncracked and precracked were subjected to 0, 7, 21, 49, 70, and 98 wet–dry cycling in 3.5% sodium chloride solution. The electrical resistivity was measured at all cycles. One series included at least three specimens.
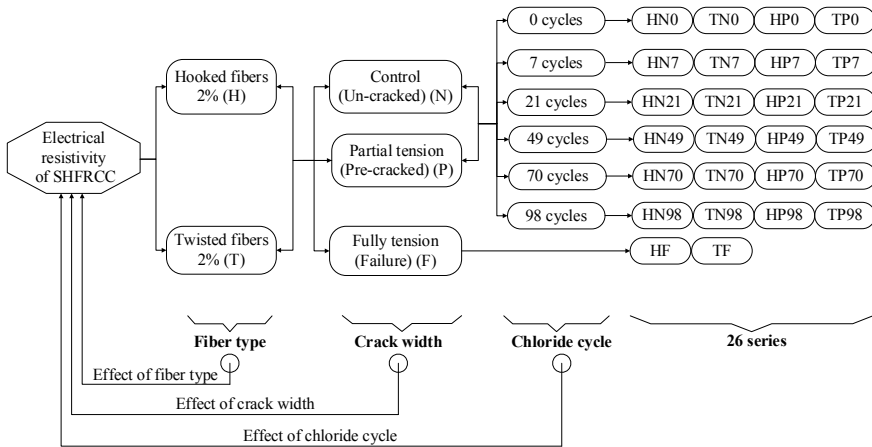
Fig. 1 Detail of test series

Table 1 Composition of high-strength concrete

Cement	Fly ash	Sand	Silica fume	Super-plasticizer	Water
0.8	0.2	1	0.07	0.04	0.26

2.1 Materials

The compositions of high-strength concrete are introduced in Table 1. The compressive of cylinder specimen after 14 days curing in water was 90 MPa [8]. On the other hand, the properties of deformed steel fibers are provided in Table 2.

In the production process of SHFRCCs, all the dry materials were mixed within 5 min. Then the water was gradually added and mixed two times with 2 min each time. After that the super-plasticizer was put and mixed until the mixture showed appreciate workability and viscosity for fiber uniform distribution. Finally, the fibers were carefully added by hand and further mixed 2 min. The mixture with fiber was poured the mold placed on vibration. After demolding, all specimens were put into water tank at room temperature until 14 days. Then specimens were divided to three groups: control, partial tension, and full tension. The specimens in group of partial tension were carried out to perform direct tensile test until strain of 0.1% while those in group full tension were tested until failure. Then all the specimen in group control and partial tension were subjected chloride cycle, and the electrical resistivity was measured at all cycles. Each chloride cycle included 8 h of wetting in 3.5 wt% chloride solution at 20 °C and 16 h of drying in chamber with constant humidity of 70% and temperature of 20 °C.

Table 2 Properties of deformed steel fibers

Type	Length (mm)	Diameter (mm)	Density (g/cm^3)	Ultimate strength (MPa)	Elastic modulus (GPa)
Hooked	30	0.375	7.9	2311	200
Twisted	30	0.3	7.9	2428	200

2.2 Test Setup

Direct tensile test was set up to create crack of specimens in group partial tension and to evaluate crack resistance of group full tension. The specimen geometry and test installation are illustrated in Fig. 2. All specimens had dog-bond shape with gage length of 200 mm. A universe transverse machine (UTM) was used to perform
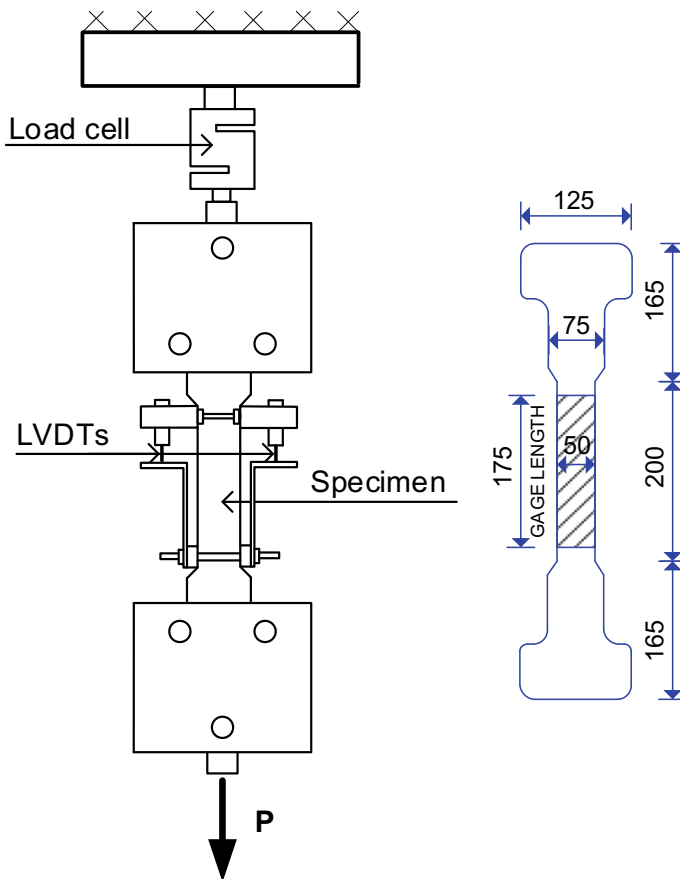
Fig. 2 Direct tensile test setup and specimen geometry

direct tensile test. The stress was obtained by load cell while the displacement was recorded by two linear variable differential transformer (LVDT) attached to specimen.

The electrical resistivity was measured to evaluate chloride penetration in SHFRCCs. Four probe method was applied by using a multimeter with a 10-mA current source, as shown in Fig. 3. The distance between two outer probes for passing the electrical current was 180 mm, whereas that of two inner probes for voltage measurement was 100 mm. At the position of probe, the specimen's surface was ground, then a silver paste was applied and followed by attached copper tapes. The electrical resistivity measurement was conducted after 16 h drying in chamber and then calculated through the below formula [9]:

$$\rho = R\frac{A}{L} \tag{1}$$

where ρ, R, and $A = 1250$ mm^2 is defined as the electrical resistivity, electrical resistance, and the cross-sectional area, respectively, while $L = 100$ mm is defined as the distance between the two inner probes.
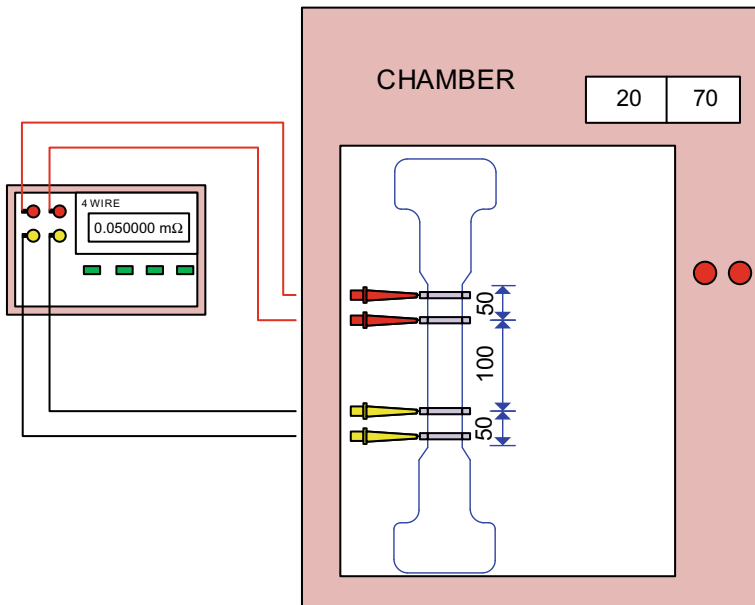
Fig. 3 Electrical resistivity measurement

3 Test Results and Discussion

3.1 *Crack Resistance of SHFRCCs*

The tensile behaviors of SHFRCCs are illustrated in Fig. 4. SHFRCCs with 2% deformed steel fibers produced very high tensile strength up to 11 MPa and the strain capacity up to 0.5%. Particularly, SHFRCCs exhibited strain hardening behavior accompanied to multiple microcracks (Fig. 4). Thus, SHFRCCs with 2% deformed steel fibers generated superior crack resistance and crack width control capacity. This is due to the fact that the addition of 2% hooked or twisted fibers in high-strength concrete was successful in bridging microcracks and delaying the formation of localized crack led to the increase of tensile strength after first cracking.

On the other hand, the direct tensile test was performed to obtain precracked SHFRCCs. All specimens of series partial tension were tested until the strain of 0.1% and their tensile behavior are shown in Fig. 5. At the strain of 0.1%, the maximum measured crack widths of precracked SHFRCCs with twisted fiber and hooked fibers were 31 μm and 70 μm, respectively.

3.2 *Relationship Between Number of Chloride Cycle and the Electrical Resistivity of SHFRCCs*

Figure 6 performs the relationship between the chloride cycle and electrical resistivity. The electrical resistivity of uncracked and precracked SHFRCCs decreased significantly with increasing number of chloride cycle. The electrical resistivity

Fig. 4 Tensile behavior and multiple microcracks behavior of SHFRCC
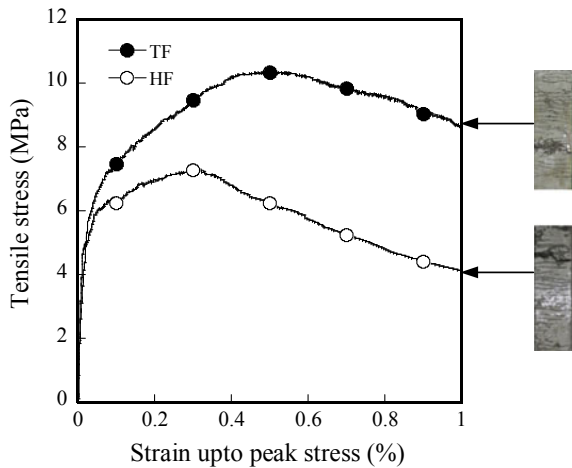
Fig. 5 Tensile behavior and maximum crack width of precracked SHFRCC
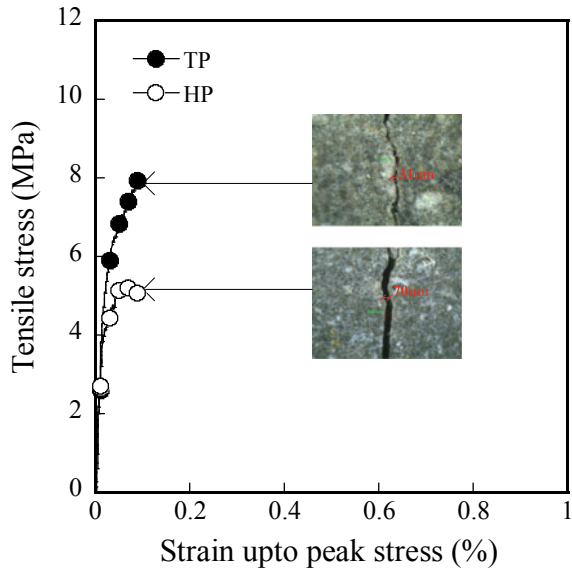
decreased rapidly as the number of chloride cycle increased from 0 to 21 cycles but reduced slowly with increasing electrical resistivity from 21 to 98 cycles. In particular, the electrical resistivity of precracked specimen reduced up to 65%, while that of uncracked specimen decreased up to 50% when the number of chloride cycle increased from 0 to 98 cycles. The reason for this behavior is that the immigration of chloride and moisture into SHFRCCs resulted in the decrease of their electrical resistivity, especially in case of precracked SHFRCCs [10].

3.3 Effect of Fiber Type and Crack Width on the Electrical Resistivity of SHFRCCs Under Chloride Environment

Twisted fibers produced lower electrical resistivity than hooked fibers in both uncracked and precrack SHFRCCs at all measured cycle, as shown in Fig. 6. Although hooked and twisted fibers were used at the same fiber volume content and fiber length, twisted fibers had smaller diameter and the number of twisted fibers per unit section area was higher than that of hooked fiber. The higher number of steel fibers per unit section area resulted in the increase of electrical conductivity and the reduction of electrical resistivity. However, the difference in the electrical resistivity between hooked and twisted fiber was dominated at 0 cycle, at higher number of cycle the difference is not significant (maximum of 8%). The reason might be that the electrical resistivity of SHFRCCs under chloride cycle was strongly dependent on the effect of chloride and moisture penetration rather than that of fiber type.
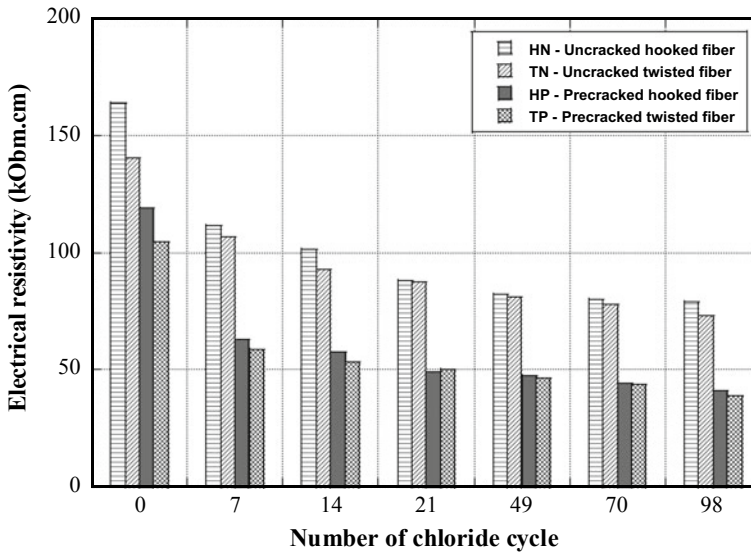
Fig. 6 Relationship between number of chloride cycle and the electrical resistivity of SHFRCCs

The precracked specimens generated much lower electrical resistivity than uncracked specimens, as indicated in Fig. 6. At the higher number of cycles, the difference in electrical resistivity between uncracked specimens and precracked specimens was more significant: the ratios between electrical resistivity of uncracked specimens and precracked specimens were 1.37 and 1.91 at 0 and 98 cycles, respectively. The formation of microcracks obviously caused the reduction of electrical resistivity and this finding was consistent with previous research [9]. At higher number of chloride cycle, the immigration of chloride cycle and moisture into precracked specimens was more significant and resulted to the more decrease of electrical resistivity.

4   Conclusion

An experimental program was conducted to evaluate the electrical resistivity of uncracked and precracked SHFRCCs under chloride environment. Based on the test results, the following conclusions can be withdrawn:

- SHFRCCs with 2% twisted or hooked fibers generated superior crack resistance and crack width control capacity.
- The electrical resistivity of uncracked and precracked SHFRCCs decreased significantly with increasing number of chloride cycle due to the immigration of chloride and moisture into SHFRCCs.

- Twisted fibers produced lower electrical resistivity than hooked fibers in both uncracked and precrack SHFRCCs at all measured cycle.
- The precracked specimens generated much lower electrical resistivity than uncracked specimens.

References

1. Montes, P., Bremner, T.W.: Influence of calcium nitrite inhibitor and crack width on corrosion of steel in high performance concrete subjected to a simulated marine environment. Cement Concr. Compos. **26**(3), 243–253 (2004)
2. Loreto, A., Benedetti, M.D., Luca, D.A., Nanni, A.: Assessment of reinforced concrete structures in marine environment: a case study. Corros. Rev. **37**(1) (2018)
3. Samchenko, S., Krivoborodov, Y.: Improving crack resistance of concrete when using expanding cements. In: IOP Conference Series: Materials Science and Engineering, p. 687 (2019)
4. Neville, A.: Chloride attack of reinforced concrete: an overview. Mater. Struct. **2**, 63–70 (1995)
5. Mangat, P.S., Gurusamy, K.: Long-term properties of steel fibre reinforced marine concrete. Mater. Struct. **20**, 273–282 (1987)
6. Zang, Q., Xiong, Z.: Crack detection of reinforced concrete structures based on BOFDA and FBG sensors. Shock Vibr. **28**, 1–10 (2018)
7. Zhao, L., Chen, S.: Preparation of graphene-cement paste anode for chloride extraction from marine reinforced concrete structures. Int. J. Electrochem. Sci. **11**, 9245–9253 (2016)
8. Kim, D.J., El-Tawil, S., Naaman, A.E.: Rate-dependent tensile behavior of high performance fiber reinforced cementitious composites. Mater. Struct. **42**(3), 399–414 (2009)
9. Nguyen, D.L., Song, J., Manathamsombat, C., Kim, D.J.: Comparative electromechanical damage-sensing behaviors of six strain-hardening steel fiber-reinforced cementitious composites under direct tension. Compos. B Eng. **69**, 159–168 (2015)
10. Sengul, O.: Use of electrical resistivity as an indicator for durability. Constr. Build. Mater. **73**, 434–441 (2014)
11. Polder, R.B.: Test methods for on site measurement of resistivity of concrete—a RILEM TC-154 technical recommendation. Constr. Build. Mater. **15**, 125–131 (2001)
12. Gowers, K.R., Millard, S.G.: Measurement of concrete resistivity for assessment of corrosion severity of steel using wenner technique. ACI Mater. J. **96**(5) (1999)
13. Bryant, J.W., Weyers, R.E., Garza J.M.: In-place resistivity of bridge deck concrete mixtures. ACI Mater. J. **106**(2) (2009)
14. Polder, R.B., Peelen, W.H.A.: Characterisation of chloride transport and reinforcement corrosion in concrete under cyclic wetting and drying by electrical resistivity. Cement Concr. Compos. **24**(5), 427–435 (2002)
15. Lehner, P., Konecny, P., Ponikiewski, T.: Comparison of material properties of SCC concrete with steel fibres related to ingress of chlorides. Crystals **220**, 1–10 (2020)
16. Kakooei, S., Akil, H.M., Jamshidi, M., Rouhi, J.: The effects of polypropylene fibers on the properties of reinforced concrete structures. Constr. Build. Mater. **27**, 73–77 (2012)

Reliability Index of a Multi-story Building Considering the Uncertainties of Monitoring System

Tham H. Duong

1 Introduction

Structural Health Monitoring (SHM) is a complicated technique in which the structure is investigated by quantitative measurement with devices and sensors installed in the structure. Information about the structural resistance and rigidity would be a base for determining what the situation of the structure is and what to be implemented to ensure the strength, stiffness, and robustness for the structure. With measurement, it is obviously to face several kinds of inherent errors such as measuring, cut off signal, errors during the process of surface treatment to mount the sensors, errors due to lack of bond and improper alignment or erection, errors due to the length of signal transferring wire, due to thermal loss, etc. These are measuring errors, and their display somehow cannot be predicted. Numerous kinds of errors were well-documented as described in detail [1, 2]. The popular approach for error removal is often to use properly the device with careful calibration and required configuration and to shift all the signals to a specific value (e.g., zero levels). Another kind of error in the monitoring system is of the model errors in which the recorded signals to be analyzed are perturbed randomly with noises. The reason for this, in general, originates from the transformation algorithm, an improper schematic diagram of the circuit of the signal data processing device, response data analyzing algorithm, etc., may lead unintentionally to a series of signals. A time-domain (TD) data of response is often transformed into the frequency-domain (FD) amplitudes in order to recognize the dominant frequency and the magnitude of the response signal.

These two kinds of errors exist in all measuring activity and should be reduced to an acceptable level so that the analyzing results will be helpful in assessing the health of the objective. The difference in the assessed data and the real responses

T. H. Duong (✉)
Ho Chi Minh City Open University, Ho Chi Minh City, Vietnam
e-mail: tham.dh@ou.edu.vn

would lead to misunderstand about the health of the structure and inaccurately assess the failure probability of the structure. Combined with uncertainties in collecting data of loading condition, structural rigidity, and other taken from the observation, it is actually a complex task to be tackled. One of the common ways to get closer to the real response, statistical data should be collected and a proper approach for error removal is necessary. The change in structural impedance is a good indicator for detecting damages and deficiencies in structure [3]. Damage or defects in a structure can be detected by applying some vibrational excitation to the structure. For reducing the cost of tests over a big amount of measurement applied to beams columns and foundations, a numerical model of the structure should be created, analyzed with various damage patterns of randomly located locations [4]. Performance function for a multi-story building will aim at the ultimate limit state (bending beams and columns) and service limit state (displacement of the building, deflection in beams, and the settlement of the foundation).

This paper would study the reliability analysis of a structure via a numerical model of a frame, through steps of structural monitoring, facing the errors due to uncertainties of data, both recording (measuring) and processing signals (model).

2   Method

2.1   Model

A six-story building plane model is assumed as in Fig. 1. There may be some randomly happened scenarios of damages. The damage is assumed to be cracks, low quality in materials, foundation settlement or being sagged seriously due to heavily loading. Structural monitoring will be responsible in detecting signals of defects or figure out whether there is damage or not. It is reasonable to model the structure subjected to impact load or vibration applied to it and analyzes the response in the conditions of such randomly occurred damages, seeing the variability of variables and parameters in TD and FD analysis. On the other hands, if a structure displays some changes in responsive signals, the structure could be assessed about the conditions of its integrity or reduction in rigidity of the system.

An excitation as a time-dependent loading $P(t) = P_o \sin (2\pi ft + \theta)$ in which f is the excitation frequency is applied to top left corner (Fig. 1). Factors to be studied are the time-dependent loading, condition of cracks (primarily occurred in beams or columns), the geometry of the cracked elements, the quality of materials and the condition of restraints, fully supported (FR) or partially restrained (PR) as springs.

The solution from time history analysis is the response in the time domain, i.e., time-dependent displacement and internal forces. The rule of the squared root of sum of squares (SRSS) is applied to obtain the most likely values of the response.

In the first stage of analysis, a set of data both in TD and FD analysis are obtained for computing the performance functions. Defects as input data are
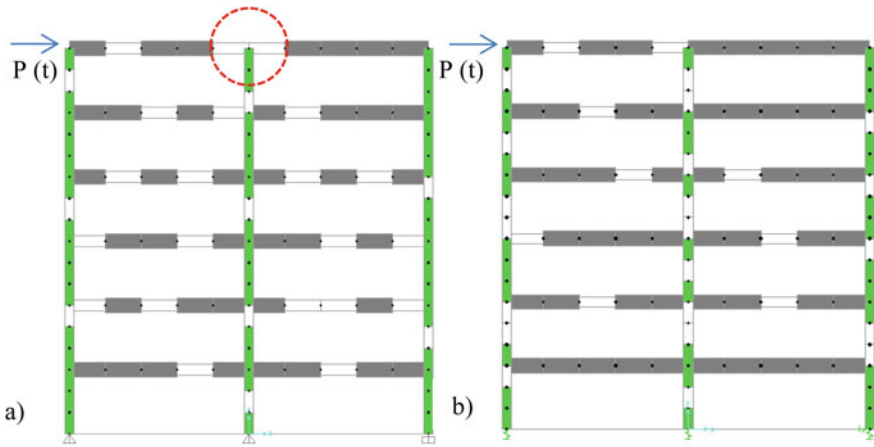
Fig. 1 Model of the building subjected to a dynamic lateral loading: **a** randomly cracked beam (CB), fully restrained (FR); **b** randomly cracked columns (CC), partially restrained (PR)

deliberately created at random locations in the frame. For reducing the number of cases but still having statistically enough data, an experimentally planned set of combined DPs is tabulated by Taguchi orthogonal matrix. Various kinds of the performance functions_ with respect to both loads: factored load and service load conditions_ are defined for some main structural elements of the frame.

In the second stage, reliability index (RI) for the system will be computed using the first-order reliability method (FORM, using Taylor's series).

A schematic diagram for the approach is described in Fig. 2.

2.2 Data for Analysis

Factors or Variables. Five input factors or variables are as follows: (a) the time-dependent excitation force $P(t)$, namely factor X1; (b) the defects due to the degradation of foundation stiffness, X2; (c) the defects due to the reduction in EJ,
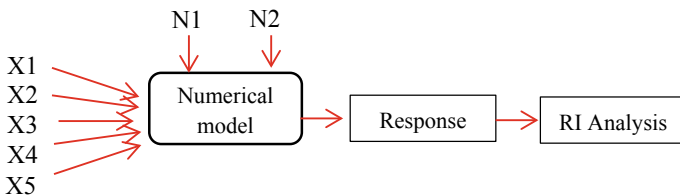
Fig. 2 Diagram showing steps for analysis in which X1 to X5 are the factors of input variables, N stands for noise or uncontrollable factors during collecting data

including the decrease in material stiffness E, factor X3; (d) the contributing effects due to the gravity loading to the performance of the structure, factor X4; and (e) the severity of damages, i.e., damages in either beams and columns, factor X5. Each factor has two levels, e.g., low or high (frequency), rigid or flexible (supports or restraints), good or poor quality (material stiffness), etc. As for X5, the unity value of this factor means cracks mostly occurred in beams, and level 2 means cracks occurred mostly in columns. There are two kinds of uncontrollable factors: modeling errors (N1, standard usage) and measuring errors (N2, the noise of output signals, 5 and 10%). Data for collection are described in Table 1.

Damage patterns. Damage patterns (DP) to be analyzed include 8 sets of the prescribed factors and 2 uncontrollable factors or noises. It is statistically sufficient to solve 32 cases ($L_8(2^5$) regarding two uncontrollable factors, N1 and N2) for taking all the possible damages into account, excluding the replicable cases. The abovementioned data collection will use Taguchi's method applied to model to have a sufficient set of statistically informative data set associated with the various combinations of factors of damage patterns [5].

The noise N1 for input uncontrollable data is the modeling errors which are originated from the standard, associated with the different limit states where the load can be factored (ultimate limit state) or unfactored (serviceability limit state) [5]. Cracked section for beams or columns is described in Fig. 3, and the recommended section for application is in Table 2. The name of each DP will be an array of five numbers standing for the level of factors in order of Table 1; for instance, DP model "22112" stands for a frame subjected to high-frequency time history load

Table 1 Factors and their levels involved in the problem

List of factors	Level 1	Level 2	COV [8]
Controllable factor			
X1 dynamic excitation $P(t)$	Low freq. f = 2 Hz	High freq. f = 20 Hz	0.30
X2 supports/springs	Rigid	Spring	Spring* 200%
X3 material stiffness	Low	High	0.1
X4 gravity loading	100% DL	50% DL	0.1
X5 damage location (occurred mostly in ∼)	∼ Beams	∼ Columns	0.3
Uncontrollable factors			
N1 load condition for cracks **	Unfactored *** load	Factored load or serviceability load	
N2 noise for signals	5%	10%	

*Spring stiffness in kN/m is computed from the wide range of the coefficient of grade; **For the limit state, the code recommends a proper condition of cracked section for beams and columns, depending on the load condition. ***Unfactored load is the service load by which the working conditioned response is designed, not the ultimate ones. This uncontrollable factor regards to the misuse in structural and numerical modeling
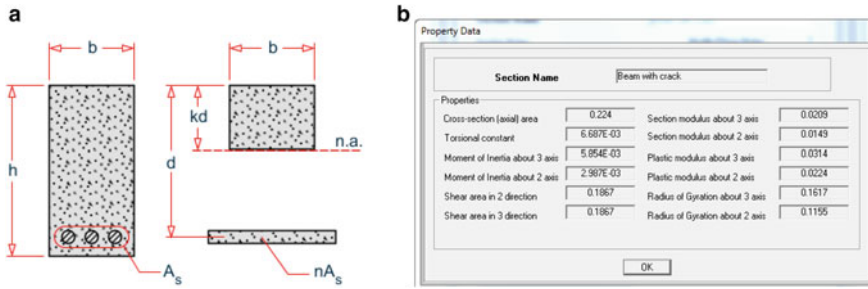
Fig. 3 a Cracked transform section of beam [6]; **b** Input data for factored load condition

(X1 = 2), partially restrained PR or spring (X2 = 2), low material stiffness (X3 = 1), subject to full factorized gravity load (X4 = 1); X5 = 2 means cracks mainly occurred in columns.

Perturbed Data. TD signal would be not filtered to artificially create the noise and then fast Fourier transformation (FFT) algorithm will be applied to determine the amplitudes of the quantities. The perturbed mode shape due to the noises [7] will be presented in the following formulation:

$$\{\Phi_j^P\}_d = \{\Phi_j\}_d(1 + N\% \times R) \tag{1}$$

The reliability index will be computed in the specific damage pattern prescribed, considering both the abovementioned uncertainties and noises. Data from the output were perturbed $\pm 5\%$ by using the formula as below:

$$\text{perturbed data} = \text{original data} + \text{scale\_factor} * (RAND() - 0.5) \tag{2}$$

2.3 Performance Function

For reliability analysis, Taylor's series is applied in the FORM in which some partial derivatives are used [9] as in the Appendix.

2.4 The FORM Reliability Index

Given a performance function g with a set of random variables $X_i Z = g(X_1, X_2, \ldots, X_n)$. Taylor's expansion for the average $g(\mu_X)$ is

Table 2 ACI 318-14R and moment of inertia for cracked section

Load condition	Beams	Columns
Factored load condition (FLC)	$0.35I_g$	$0.7I_g$
Service load condition (SLC)	$0.5I_g$	$1.01I_g$

$$Z = g(\mu_X) + \sum_{i=1}^{n} \frac{\partial g}{\partial X}(X_i - \mu_{X_i}) + \frac{1}{2}\sum_{i=1}^{n}\sum_{j=1}^{n} \frac{\partial^2 g}{\partial X_i \partial X_j}(X_i - \mu_{X_i})(X_i - \mu_{X_j}) + \cdots$$

$$(3)$$

where the average for variables X_i is $\mu_X \approx g(\mu_{X1}, \mu_{X2}, \ldots \mu_{Xn})$; disregarding the higher order derivatives and keep the first-order linear terms, and the variance is

$$\sigma_z^2 \approx \sum_{i=1}^{n}\sum_{j=1}^{n} \frac{\partial g}{\partial X_i}\frac{\partial g}{\partial X_j} \text{Cov}(X_i, X_j)$$

$$(4)$$

in which $\text{Cov}(X_i, X_j)$ is the covariance of X_i and X_j; in case there is no correlation between these two variables, the variance σ_z^2 approximately equals to

$$\sigma_z^2 \approx \sum_{i=1}^{n} \left(\frac{\partial g}{\partial X_i}\right)^2 Var(X_i)$$

$$(5)$$

For performance functions described in Table 3, and their partial derivatives on specific variables as described in Appendix.

Table 3 Moment of inertia for cracked section as per ACI 318-14R [10]

Load condition	Condition	Performance function	Checking point/ location
Flexure, beams	Factored load	$G(X) = M_{cr} - M_{max} \geq 0$	
Columns	Factored load	$H(X) = \frac{P_{max}}{\varphi P_{cr}} + \frac{M_{max}}{\varphi M_{cr}} \geq 1$	The most eccentric column
Horizontal shift	Service load	$I(X) = \frac{H}{500} - \Delta_{hor} \geq 0$	Top right corner, joint 21
Deflection at cracked section	Service load	$J(X) = \frac{L_S}{250} - \frac{5qL_S^3}{384}EI_{cr} \geq 0$	Midspan of cracked beam
Settlement	Service load	$K(X) = 8cm - \frac{N}{x} \geq 0$	Middle columns

2.5 Solution Strategy

For computing the reliability index, there are nine steps as below:
Stage 1: Preparing the model and data collection

Step 1: Creating model for structural analysis.
Step 2: Factors assigned, load cases, and preparing the cracked sections for beam and columns. Damage patterns (DP) and levels of the factors are defined (Table 1).
Step 3: Quantifying the uncertainties in all the factors involved. The coefficient of variation COV, mean values and the law of distribution must be assigned [11].
Step 3: Solving for the response of the structure associated with the individual DP.
Step 4: Investigate the perturbed mode shapes. This means outcome data will be deliberately perturbed 5 or 10% (measuring errors) and FFT data (model errors).
Step 5: Collecting statistically the variability of data in the frequency domain.
Step 6: Performance functions are prescribed, related to both limit state, serviceability state, and the robust state.

Stage 2: Post-processing

Step 7: Reliability index (RI) of the building as a system; for avoiding time-consuming and rigorous, a qualitatively based approximation should be performed [12].
Step 8: An analysis of variance for determining the order of importance and percentage of contribution for each factor.
Step 9: Regression equation $RI_{damage} = RI_{uncrack} + \alpha_1 E_m + \alpha_2 E_T + \alpha_3 E_\omega$. Assessing the probability of failure.

3 Results

3.1 Time-Domain (TD) and Frequency-Domain (FD) Analyses

Data for reliability assessment are output collected by a numerical model. They are response, in output signals and noises subjected to the errors of recordings, transferring, and transforming into other parameters. Data as output of SAP2000 model of the frame, in a variety of DPs whose name is characterized by five numbers (for instance, 11211) are collected. TD data have n_s recordings (obtained by SAP2000 output), sampling frequency f_s will be the total time of sampling divided by n_s. Nyquist frequency will be half of the f_s. The frequency of the excitation f is given (i.e., 2 Hz for low frequency and 20 Hz for high frequency), and the number of periods np_f during the time of sampling will be the time of sampling multiplied by the period. Hence, the number of samples in a period will be n_s/np_f and the frequency resolution in FD analysis equals to the sampling frequency ($f_{res} = 1/T_s$)

[13]. The minimal frequency should not exceed the frequency resolution. From SAP2000 output, $n_s = 100$; the time interval of sampling will be $T_s = 2$ s (low-frequency excitation) and 20 s (high-frequency excitation), time step $t = 0,2$ ($f = 20$ Hz), $t = 0.02$ ($f = 2$ Hz). Therefore, frequency resolution for frame subjected to low-frequency excitation is 0.5 Hz and that of high-frequency excitation is 0.05 Hz. For ensuring the correctness, all the FD domain using the Excel Data Analysis Tool will be calibrated by comparing FFT frequency to that of the spectrum response curve given by SAP2000 [14].

Displacement and bending moment at dangerous locations (i.e., the most sagged, most laterally displaced, and the weakest cross section) in TD will be transformed into FD to get the amplitude. For studying the effects of perturbed signals (noises) on the stability of the response, the signals will be randomly perturbed to 5% or 10% and transferred to frequency-domain analysis. FFT is applied to the ±5% perturbed data of signals. The dominant frequency and the magnitude at this frequency have not changed; there is some variation in FD amplitude at the other frequencies.

3.2 Effects of Fully Restrained (FR) Supports and Partially Restrained (PR) Springs on the Natural Frequency

The reduction in rigidity, both in material stiffness and weakened connectivity due to the cracks in beams and columns (damage pattern, DP 11111) results in lower natural frequencies in modal analysis. Lowering response frequency indicates displacement characteristics for the whole structure of the frame (Table 4).

3.3 Data Analysis for the Response in TD and FD

Load combination considering the randomly cracked beams and columns will be dead load, time history lateral periodic load $P(t) = 10.\sin(2\pi ft + \theta)$ exerting at joint 7. In this case, the phase angle is zero and two frequencies are studied, 2 Hz for low-frequency and 20 Hz for high-frequency excitation (Fig. 4).

Table 4 Modal frequencies, cycles per second (Hz)

Load condition	Mode 1	Mode 2	Mode 3	Mode 4
No crack structure, high E (FR)	1.58	5.03	14.11	18.86
No crack structure, low E (FR)	1.54	4.91	13.83	18.51
Cracks, mostly occurred in beams (FR)	1.35	4.42	10.76	13.97
Partially restrained supports (PR)	0.88	3.18	9.06	11.92
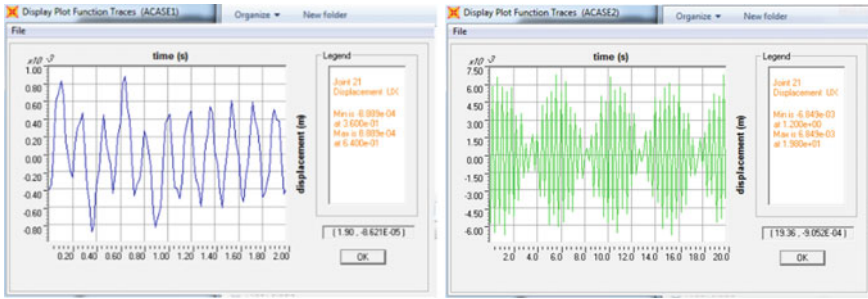
Fig. 4 Time history of displacement at top right joint 21, with respect to low-frequency (left) and high-frequency (right) excitation $P(t)$, w.r.t damage pattern 11122
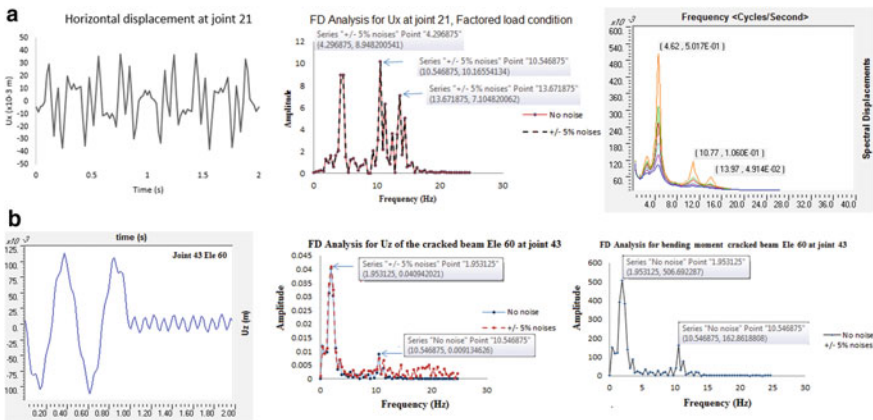
Fig. 5 **a** Ux displacement at top right joint 21; **b** Uz deflection at joint 43 cracked beam Ele#60, subjected to low-frequency $P(t)$ excitation, damage pattern 11111

The two key positions to be examined are the top right corner, joint 21 and the most deflected joint 43 of the cracked beam No 60. Response curves are displayed in Fig. 5.

Figure 5 is the SAP2000 spectral displacement of referred joint 21 and FD spectral bending moment in the most sagged beam element 60. The FD analysis indicates that perturbed ±5% signals affect significantly the spectral curve, but not change the dominant frequencies (Fig. 5b). Two dominant frequencies, i.e., $f = 1.92$ Hz and $f = 18.59$ Hz, are clearly displayed. The latter strongly refers to the cracked structure. However, perturbed data do not change the dominant frequency of the spectral displacement. In the general case of cracked beams and columns, reduced value of frequencies is found and three strange frequencies appear (Fig. 5a), $f_1 = 4.62$ Hz as fundamental frequency, $f_2 = 10.$ 56 Hz (or 10.77 Hz from SAP2000) and $f_3 = 13.67$ Hz (approx. 13.97 Hz from SAP2000 output). The reduction of the dominant frequency results in a weakening in stiffness of the

structure. Not being a harmonic vibration, the dominant values of the amplitude at some higher frequencies indicate that they are three modes of vibration, or the defects in the structure exist (Fig. 5a, centered).

3.4 Change of the Dominant Frequency Due to Perturbed Signals of Response

With ±5% noises, no dominant frequency is found, and the FD horizontal displacement Ux at joint 21 shows some peak amplitude at the intermediate frequencies, $f_1 = 9.37$ Hz, $f_2 = 17.96$ Hz ($f_3 = 19.14$ Hz (this is also $f = 20$ Hz).

Reduced stiffness and low rigidity in structural system due to cracks in both columns and beams result in a decrease of the fundamental frequency as compared to the FR supports (Fig. 6).

For a partially restrained (PR) structure, i.e., supports on springs, the response signals are shown in Fig. 7, where spectral displacement at joint 21 (top right corner) displays two peaks at the frequencies, similar to the spectral vertical displacement (or deflection) at joint 52 (the first floor, element#70). This implies two main frequencies of the cracked structure. By applying perturbed signals, there is no dominant frequency found, in both cases of horizontal displacement and deflection at cracking locations.

The response (i.e., displacement at a specific joint) in the FD depends partly on the frequency of the input time history data. The FFT from the response of the displacement at the top right corner (joint 21) due to low-frequency excitation
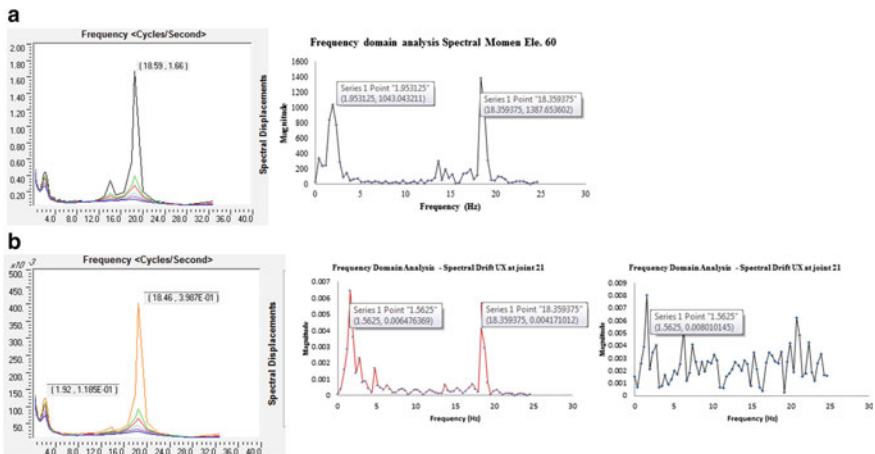
Fig. 6 In DP 11111. **a** Curves of spectral displacement (left plot) and the bending moment in FD analysis. **b** Spectral horizontal displacement at joint 21 with no noises and perturbed signal with 5% noises
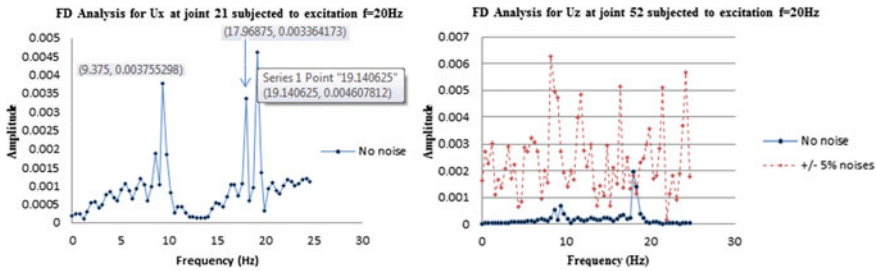
Fig. 7 In damage pattern 21221, FD analysis for Ux at joint 21 (left) and deflection Uz at joint 52 (in the midspan of the most bending and two segments of cracked beam), Element#70 with/ without noises (right)

applied at Joint 7. The signals are perturbed with ±5% noises, and the FFT is conducted on both original noise-free signals and noisy signals. A strong perturbation in dominant frequency, a lot of additional strange frequencies appears, resulting in the fact that no dominant frequency has been clearly determined. The frequency 2 Hz of the excitation cannot be recognized because of the perturbation in the range of frequency. And the change in dominant frequency is from 1.56 to 18.35 Hz (low-frequency excitation).

For bending moment at the cracked beam (Element#60, joint 43), there is no significant difference in amplitude of the response in the FD of DP 11122. There is a reduction in the FD of the response, falling from 20 to 10.54 Hz; this implies that the displacement characteristics dominate the bending moment of the cracked beams.

For service load condition (SLC), spectral displacement without noisy signal will separately display the dominant frequency is 2 Hz (dominant frequency for bending moment of element 60), 4.5 Hz (appr. 4.68 Hz), 11 Hz (secondary frequency for bending moment of element 60) and 14.87 Hz (appr. 14.45 Hz). The spectral displacement in both approaches of FD analysis is sensitive to noises in such a way that, the more percentage of the noise, the greater number of frequencies perturbed; both ±5% and much more perturbed amplitude with ±10% of noises (Fig. 8). But spectral bending moment at element 60 is not affected by noisy signals.

3.5 Reliability Index (RI) Related to Various DPs Concerning the Noise of Recording Signals and Modeling Error

The most likely failure for the frame is on limit state, with the factored load condition [15]. The most notable data in factored load condition are the bending moment at the weakest beam/column M3, the most eccentric columns $e_{max;}$ the
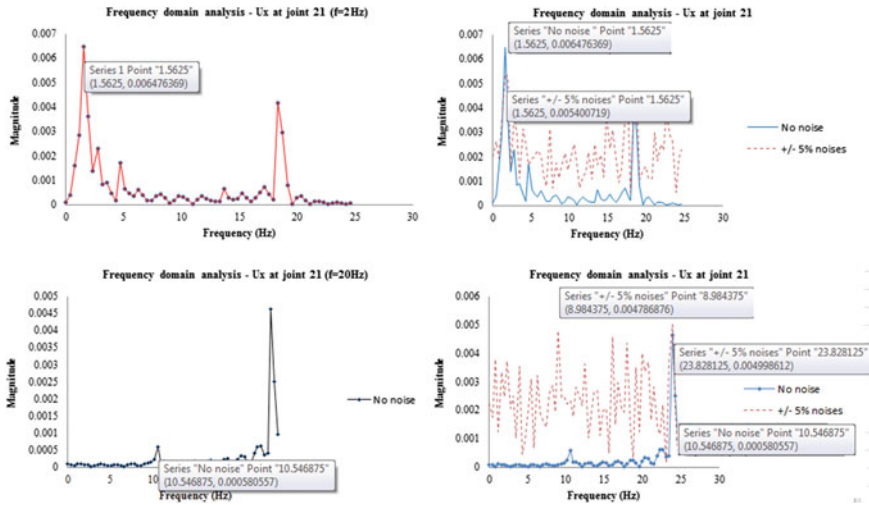
Fig. 8 Frequency-domain displacement at a specific joint 21, due to low-frequency ($f = 2$ Hz) and high-frequency ($f = 20$ Hz) excitation load case, in damage pattern 11122

Table 5 Data of the response[a]

Response					M3	e_{max}	Δ_x	δ_v	N_{max}
Domain					FD.	Output	Output	Output	Output
Performance Function					G(X)	H(X)	I(X)	J(X)	K(X)
X1	X2	X3	X4	X5	(kNm)	(m)	(m)	(m)	(m)
1	1	1	1	1	506.69 (483.45)	0.572 (0.574)	0.038 (0.002)	0.036 (0.008)	21,585 (19,633)
1	1	1	2	2	703.10 (608.87)	0.494 (0.581)	0.121 (0.032)	0.008 (0.121)	26,620 (24,221)
1	2	2	1	1	623.05 (503)	0.719 (1.64)	0.052 (0.062)	0.179 (0.21)	26,085 (23,657)
1	2	2	2	2	495 (344)	0.597 (0.698)	0.042 (0.015)	0.146 (0.022)	11,597 (16,118)
2	1	2	1	2	777 (1143)	0.762 (0.586)	0.032 (0.153)	0.116 (0.243)	21,121 (42,901)
2	1	2	2	1	596 (564)	0.626 (0.723)	0.026 (0.006)	0.086 (0.217)	16,604 (95,806)
2	2	1	1	2	1475 (306)	1.154 (0.878)	0.078 (0.046)	0.197 (0.122)	57,866 (36,139)
2	2	1	2	1	925 (1952)	0.006 (1.41)	0.515 (0.007)	0.008 (0.024)	12,036 (12,929)

[a]Values in parentheses due to Noise N1 = 2 (unfactored service load condition, SLC); values in bold refer to specified response that is recognized to be not sensitive to 5% noisy signals (signals created by the low-frequency excitation)

Table 6 Reliability index of beams and columns in ultimate limit state

				N1	1 FLC	2 SLC	1 FLC	2 SLC		
				N2	(no effect on data)*				Avr.	S/N
X1	X2	X3	X4	X5	Beam*		Col.			
1	1	1	1	1	1.49	0	0.96	0.95	0.85	−33.98
1	1	1	2	2	1.21	1.35	0.41	0.75	0.93	−3.50
1	2	2	1	1	1.33	0	0.47	0.26	0.51	−33.98
1	2	2	2	2	1.50	1.72	0.49	0.74	1.11	−2.28
2	1	2	1	2	1.11	0.60	0.73	0.42	0.71	−4.44
2	1	2	2	1	1.36	1.41	0.47	0.35	0.89	−5.35
2	2	1	1	2	0.13	1.77	0.24	0.38	0.63	−13.21
2	2	1	2	1	0.90	0	0.84	0.26	0.5	−33.98

*Noisy signal of frame forces has no effect on the data; **For a positive RI results, this value is scaled down to 20%; zero reliability means failure occurred. All the results in the table are computed by the equations in the Appendix
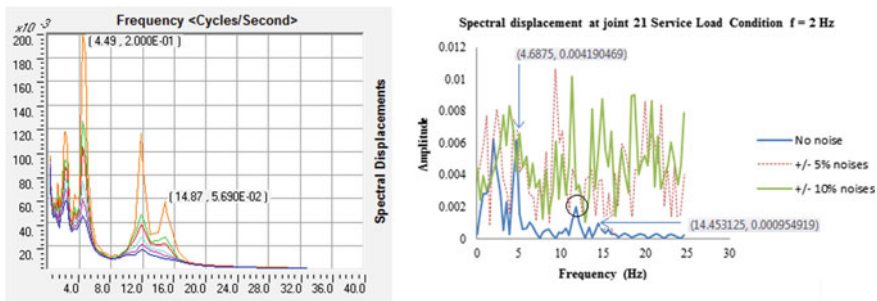
Fig. 9 Frequency-domain displacement Ux at joint 21, due to low frequency ($f = 2$ Hz) and service load condition

most sagged deflection of the cracked beam, δ_v and the most displaced lateral drift at top corner of the frame, Δ_x will be of the service load condition. Some key data are described in Table 5, and the reliability index (RI) which are computed by FORM, the equation (5), will be filled out the Table 6 as outcome. These data of displacement are sensitive to noise (Fig. 9).

Some statistical computation and analysis will be conducted to find out what the most effective factor and its percentage of contribution for the outcome. Some terms are defined as follows: $S_{X1,1} = \eta_1 + \eta_2 + \eta_3 + \eta_4$; $S_{X1,2} = \eta_5 + \eta_6 + \eta_7 + \eta_8$; $S_{X2,1} = \eta_1 + \eta_2 + \eta_{5} + \eta_6$; $S_{X2,2} = \eta_3 + \eta_4 + \eta_7 + \eta_8$; $S_{X3,1} = \eta_1 + \eta_2 + \eta_7 + eta_8$; $S_{X3,2} = \eta_3 + \eta_4 + \eta_5 + \eta_6$; $S_{X4,1} = \eta_1 + \eta_3 + \eta_5 + \eta_7$; $S_{X4,2} = \eta_2 + \eta_4 + \eta_6 + \eta_8$; $S_{X5,1} = \eta_1 + \eta_3 + \eta_6 + \eta_8$; $S_{X4,2} = \eta_2 + \eta_4 + \eta_5 + \eta_7$ where η_k is the S/N ratios in the kth trial. For each level k of the target value, the average value of η_k,

that equals to S factor, level m/n. For example, average S/N corresponding to the excitation _factor X1 _ at level 1 (i.e., dynamic excitation) is $S_{X1,1}/4 = (\eta_1 + \eta_2 + \eta_3)/4$; the average value S/N, corresponding to the excitation _factor X1_ at level 2 is $S_{X1,2}/4$, etc.

Table 7 indicates that the factor X5, or the severity of damage is the most important factor which affected most the reliability; then in order of importance is the load on beams, the material stiffness, the restrained condition, and the excitation frequency as the least of importance.

3.6 Percentage of Contribution and Regression Equation of RI in Terms of Errors

An analysis of variance (ANOVA) will be used to calculate the percentage of contribution. The formula for computing the $p\%$ is

$$p\% = \frac{SS}{SS_T} = \frac{(y_i - \overline{y}_i)^2}{\sum_{i=1}^{NV} (y_i - \overline{y}_i)^2} \tag{6}$$

where SS is the sum of square of a particular factor taken over the number of possible runs, SS_T is the total sum of square of all factors; y_i is the S/N of the factor i, at all the levels, $\overline{y}_i$ is the average of the S/N of the factor under consideration, NV is the number of the variables. Data are listed in Table 8 with the percentage of contribution of each factor shown [15].

By considering the connectivity between beams and columns, it is easy to figure out that they are in series (i.e., if one component fails then the system fails), the probability of failure for the system is $P_{f,\text{system}} = 1 - (1 - P_{f,\text{beam}})(1 - P_{f,\text{column}})$. According to FORM approximation, the relationship between the probability of failure P_f and the RI is $\beta = -\phi(P_f)$ with the function $\phi(z)$ as below:

$$\Phi(z) = \frac{1}{\sqrt{2\pi}} \int_{-\infty}^{Z} e^{-\frac{z^2}{2}} dz \tag{7}$$

Then the RI of the cracked frame is computed. An equation from the multi-variable linear regression that relates to the excitation frequency (X1), the condition of restraints (X2), the interaction between superstructure and foundation (X3), the quality of materials (X4), and the loading (X5) is given by Eq. (8).

Table 7 Results for ranking the factors associated with the reliability index

Level	Factor X1		Factor X2		Factor X3		Factor X4		Factor X5	
	Sum $(S_{X1,\,level})$	Avg S/N	Sum $(S_{X2,\,level})$	Avg S/N	Sum $(S_{X3,\,level})$	Avg S/N	Sum $(S_{X4,\,level})$	Avg S/N	Sum $(S_{X5,\,level})$	Avg S/N
1	−73.74	−18.43	−47.27	−11.81	−84.67	−21.16	−85.61	−21.40	−107.29	−26.82
2	−56.98	−14.24	−83.45	−20.86	−46.05	−11.51	−45.11	−11.27	−23.43	−5.85
$|\Delta| = |max - min|$	3.055 (5)		8.95 (4)		9.65 (3)		10.13 (2)		20.97 (1)	

Table 8 Calculation for determining the percentage of contribution

Factor	Level	S/N ratio	Aver S/N of each level	Average S/N$_X$	SS$_x$	p = SS$_x$/Σ SS	Order of importance
X1	1	−73.74	−18.43	−16.33	8.77	2.4%	5
	2	−56.98	−14.24				
X2	1	−47.27	−11.82	−16.33	40.86	11.3%	4
	2	−83.45	−20.86				
X3	1	−84.67	−21.16	−16.33	46.56	12.6%	3
	2	−46.05	−11.51				
X4	1	−85.61	−21.40	−16.33	51.31	13.9%	2
	2	−45.11	−11.27				
X5	1	−107.29	−26.82	−16.33	219.87	59.8%	1
	2	−23.43	−5.85				
ΣSS = SS$_T$ =					367.37	100%	

SUMMARY OUTPUT

Regression Statistics	
Multiple	0.994547046
R Square	0.989123827
Adjusted	0.923866791
Standard	0.044141436
Observat	8

ANOVA

	df	SS	MS	F	Significance F
Regressic	6	0.177201534	0.029533589	15.15735144	0.194128466
Residual	1	0.001948466	0.001948466		
Total	7	0.17915			

	Coefficients	Standard Error	t Stat	P-value	Lower 95%	Upper 95%	Lower 95.0%	Upper 95.0%
Intercept	0.288390238	0.32902343	0.876503652	0.541836851	-3.892248827	4.469029303	-3.892248827	4.469029303
X Variabl	-0.375943463	0.0737294	-5.098962747	0.123288042	-1.312764313	0.560877386	-1.312764313	0.560877386
X Variabl	-0.187044236	0.085967023	-2.175767278	0.274265433	-1.279358832	0.90527036	-1.279358832	0.90527036
X Variabl	0.138427299	0.150447732	0.920102264	0.526475232	-1.773192383	2.05004698	-1.773192383	2.05004698
X Variabl	0.038023577	0.033216981	1.144702961	0.457112307	-0.384038187	0.460085341	-0.384038187	0.460085341
X Variabl	0.011815565	0.035497619	0.332855153	0.795441252	-0.439224448	0.462855579	-0.439224448	0.462855579
X Variabl	0.879198865	0.55432897	1.586059744	0.35812395	-6.164218522	7.922616251	-6.164218522	7.922616251

Fig. 10 ANOVA correlates factors in the problem and a regression equation of RI

Regression equation for predicting the RI of an uncracked frame (response) in terms of factors (predictors) in the model with the damage patterns (Fig. 10) is below:

$$RI = 0.288 + 0.879(RI_{FLC,\text{crack}}) - 0.376(\text{Frequency}) - 0.187(\text{Location of Cracks})$$
$$+ 0.138(\text{Restraints}) + 0.038(\text{Material Stiffness}) + 0.012(\text{loading})$$

$$(8)$$

4   Discussions

(a) By analyzing the response in FD, there are many interesting results, as follows:

- The more flexible structural system, the lower natural frequency; damage in different components of the frame causes the appearance of higher frequencies than the fundamental one. They are indicators of damage severity. Some data of displacement in FD are more sensitive to noises as analyzed in low-frequency mode than that in high-frequency mode. However, it is contrary to spectral *acceleration*. This might lead to a viewpoint that in structural monitoring, it is recommended to use the low-frequency displacement transducer which yields a better and more stable signal than using accelerometers.
- Noisy signals of the *bending moment* in TD did not affect the FFT spectral forces in FD, using Fourier analysis in Excel. It is because ± 5 or 10% noises is negligible as compared to the big values of the bending moment.
- Damaged structures subjected to low-frequency excitation show a dominant frequency (also the fundamental frequency) and other peaks in amplitude at various frequencies of spectral displacement than the case of high-frequency excitation. This may lead to a recommendation that for flexible structure, it is reasonable to use low-frequency excitation in damage detection.
- The slight difference between the results obtained by SAP2000 and by Excel's FFT is because of the dummy data filled up to meet the required number of data recordings for Fourier analysis (i.e., power of 2). Data from SAP2000 are not enough ($ns = 100$) For having enough data to be analyzed by Fourier transformation, 27 out of 128 dummy zero data have to be added to the original data. The frequency in FD is very close to the input excitation (e.g., 1.95 Hz in SLC $\sim$ 2 Hz of the excitation).

(b) The RI for a cracked structure is computed by Eq. (8) with respect to a RI of uncracked structure and involved DPs. In FLC, the flexural capacity of beams and allowable forces in columns are considered for the reason the normal case, the ultimate limit state is more dangerous, controls the assessment due to a lower target reliability index. In other words, the index depends clearly on the uncertainties of modeling in FLC only.

- The displacement response is affected seriously by perturbed signals. For more informative assessment, the RI should be computed by the performance functions of settlement and deflection as described in the Appendix. The RI by performance function will be computed with respect to unfactored load condition (SLC). This might be a good comparison to the RI given by (8). Truncation errors (i.e., errors over finite number of Taylor series expansion) and TD to FD transformation procedure for dynamic problem are key issues in reliability of the structure. RI is computed by Taylor's series in FORM without taking the interaction between factors. For the severed cracked structure in which it is 30% out of the total number of elements are cracked elements, it is reasonably the RI

is far below the acceptable value ($\beta_T = 2.6$ for ultimate limit state). This might reduce the efficiency of regression.

- For vibration analysis, it should use the damage index (DI) as another criterion for reliability assessment. Pushover can be a relevant approach for analysis.

5 Conclusions

The paper suggests a formula for computing RI concerning the measuring errors (due to misuse of the code in structural modeling) and the recording errors (due to perturbed signals). A cracked frame obviously reduces the stiffness, resulting in a decrease in natural frequency, displays dominant frequency and clear peaks at higher frequencies. Any PR support lowers the natural frequency of the structure. Low-frequency excitation proves to be efficient in detecting the response, but more sensitive to perturbed signals than that of the high-frequency excitation. Acceleration is more sensitive to high-frequency excitation and noisy data. Noisy signals affect seriously the FD analysis of displacement, and for bending moment, spectral analysis indicates that perturbed signals did not change the dominant frequencies. Data of response are collected for computing the RI with at least five performance functions, using Taylor's series of the FORM. For practically demonstrative purposes, the ultimate limit state is studied because both the strength of beam and eccentric compression in columns are not affected by perturbed signals and govern the reliability in most cases. Finding is that the RI is strongly affected by the severity of cracks, and this is ranked as the most important factor (59,8% of contribution); in the sequential order of importance is the gravity loading on beams (13.9%), then the material stiffness (12.6% of contribution), the condition of restraints (11.3% of contribution), and finally the frequency of the excitation (only 2.4% of contribution). A regression equation with high R^2—adjusted relating to the to the RI of the uncracked structure, different the DPs (i.e., crack severity, material, restraints and load) and the load condition (i.e., modeling uncertainty) is formulated for assessing the reliability of structure.

Appendix

Partial derivatives of the performance functions and variances with respect to specific variable, reinforced concrete structure:

1. *Flexural Beams:* $G(X_i) = 0.85 f_y' (A_s - A_s')\left(d - \frac{kd}{2}\right) - \left(q \frac{L_s^2}{8}\right)$;

$\frac{\partial G}{\partial L_s} = q \frac{L_s}{4} \frac{\partial G}{\partial f_y'} = 0.85(A_s - A_s')\left(d - \frac{kd}{2}\right)$; $\frac{\partial G}{\partial d} = f_y'(A_s - A_s')\left(1 - \frac{k}{2}\right)$; $\frac{\partial G}{\partial q} = -\frac{L_s^2}{8}$;

$\sigma_X = \left[\left(\frac{\partial G}{\partial f_y'}\right)^2 \cdot Var\left(f_y' + \left(\frac{\partial G}{\partial d}\right)^2 \cdot Var\left(d + \left(\frac{\partial G}{\partial q}\right)^2\right)\right) \cdot Var(q) + \left(\frac{\partial G}{\partial L_s}\right)^2 \cdot Var(L_s)\right]^{0.5}$

2. *Eccentric Compression Columns (ACI 318):* $H(X_i) = \frac{P_u}{\varphi P_n} + \frac{M_u}{\varphi M_n} - 1 \leq 0$

$P_n = 0.8[0.85 f_c'(A_g - A_s) + (A_s f_y')]; M_n = 0.85 f_c' W$ where P_u chosen w.r.t *Max*

M_u $\quad\quad\quad\quad \frac{\partial H}{\partial f_c'} = -\frac{P \cdot A_b}{\varphi(A_b f_c' + A_s f_y')^2}; \frac{\partial H}{\partial d} = -\frac{b f_c' P}{\varphi(A_b f_c' + A_s f_y')^2} - \frac{M}{\varphi\left(0.85 \cdot f_y' \cdot A_s \left(1 - \frac{k}{2}\right)d\right)^2} \frac{\partial H}{\partial f_y'} =$

$-\frac{P \cdot A_s}{\varphi(A_b f_c' + A_s f_y')^2} - \frac{0.85 \cdot M \cdot A_s \left(d - \frac{kd}{2}\right)}{\varphi\left(0.85 \cdot f_y' \cdot A_s \left(1 - \frac{k}{2}\right)d\right)^2};$

$\sigma_X = \left[\left(\frac{\partial H}{\partial f_c'}\right)^2 \cdot Var\left(f_c'\right) + \left(\frac{\partial H}{\partial f_y'}\right)^2 \cdot Var\left(f_y'\right) + \left(\frac{\partial H}{\partial d}\right)^2 \cdot Var(d)\right]^{0.5}$

3. *Horizontal Displacement:* $I(X_i) = \Delta_{\text{Limit}} - \Delta = \frac{H}{500} - \Delta \geq 0$

4. *Vertical Deflection of beam:* $J(X_i) = f_{\text{Limit}} - f = \frac{L_s}{250} - \frac{5qL_s^4}{384 EI_{cr}} \geq 0$

$\frac{\partial J}{\partial L_s} = \frac{1}{250} - \frac{20qL_s^3}{384 EI_{cr}} = \frac{1}{250} - \frac{qL_s^3}{19.2 EI_{cr}}; \frac{\partial J}{\partial q} = -\frac{5qL_s^4}{384 EI_{cr}};$

$\sigma_X = \left[\left(\frac{\partial J}{\partial L_s}\right)^2 \cdot Var(L_s) + \left(\frac{\partial J}{\partial q}\right)^2 \cdot Var(q)\right]^{0.5}$

5. *Settlement:* $K(X_i) = s_{\text{Limit}} - \frac{N}{k} \geq 0; \frac{\partial K}{\partial N} = -\frac{1}{k^2}; \frac{\partial K}{\partial k} = -N$

References

1. Etebu, E., Shafiee, M.: Reliability analysis of structural health monitoring. In: Haugen et al. (Eds.) Safety and Reliability—Safe Societies in a Changing World, pp. 2243–2247, ISBN 978-0-8153-3682-7. Taylor & Francis, London (2014)
2. Taylor, J.R.: An Introduction to Uncertainty Analysis: The Study of Uncertainties in Physical Measurements. University Science Books, Mill Valley (1982)
3. Bernard, E.S., Xu, G.G.: Statistical distribution of fiber-reinforced concrete beam test data. J. ASTM Int. **4**(3) (2007). https://doi.org/10.1520/jai100774
4. Bandara, R.P.: Damage Identification and Condition Assessment of Building Structures using Frequency Response Function and Neural Networks. PhD Thesis in Queensland University of Technology, pp. 1–275 (2013)
5. Maru, M.B., Lee, D., Cham, G., Park, S.: Beam deflection monitoring based on genetic algorithm using lidar data. J. Sens. **20**, 2144. https://doi.org/10.3390/s20072144
6. Sarkisian, M., Mathias, N., et al.: Effective Stiffness Modeling of Shear Walls for Seismic Analysis of High-Rise Structures. In: Book chapter of the SEAOC Proceedings for Convention (2003)
7. Alberto Escobar J., Fernando Fierro, Roberto Gomez.: Proceedings of the 13th World Conference on Earthquake Engineering. Paper 2117. In Vancouver B.C, Canada (2004)
8. Duong, H.T., Khuong, V.H.: Design of experiments using Taguchi's method. J. Sci. Educ. 19–29 (2018). ISSN 2354-0567
9. Hao, G., Liang, X., Zhang, S.: The new approximation calculation method for the first order reliability. J. Appl. Math. **4**, 505–509 (2013). http://dx.doi.org/10.4236/am.2013.43075
10. Saleh, F., Supriyadi, B., Suhendro, B., Tran, D.: Damage detection in non-prismatic reinforced concrete beams using curvature mode shapes. In: SIF2004 Structural Integrity and Fracture. http://eprint.uq.edu.au/archive/00000836. Last accessed (2016)
11. Gomes, W.J.S.: Reliability analysis of reinforced concrete beams using finite element models. Conference paper. In: Faria, P.O., Lopez, R.H., Miguel, L.F.F., Gomes, W.J.S., Noronha M. (eds.) Proceedings of the XXXVIII Iberian Latin-American Congress on Computational Methods in Engineering. ABMEC, Florianópolis, SC, Brazil, 5–8 Nov 2017

12. Faber, M.H., Kubler, O., Fontana, M., Knobloch, M.: Failure Consequences and Reliability Acceptance Criteria for Exceptional Building Structure. Research collection, Swiss Federal Institute of Technology, IBK Bericht Nr 285, Jul (2004). ISBN 3-7281-2976-3, https://www.doi.org/10.3929/ethz-a-004807495

13. Telgarsky, R.: Dominant frequency extraction. Research paper. Homepage, https://www.researchgate.net/publication/237000139. Uploaded 2013/1216

14. Sap2000 User Manual. https://www.civilax.org/sap2000-manual/

15. Tham, D.H.: Some statistical techniques applied to engineering mechanics problems. Viet Nam J. Sci. Technol. **57**(6A) (2019). https://doi.org/10.15625/2525-2518/57/14006

Identification of the Bridge Pier Vibration Parameters by Rayleigh Method

Huu Hung Nguyen and Minh Hung Dam

1   Introduction

Bridge structures, after a long period of service stage, do not avoid unanticipated effects such as local scour, vessel collisions, or overloading during service stage and the deterioration of the material over time. In the face of unfavorable impacts on the bridge structure, the reassessment of structural conditions to provide solutions is very necessary. Besides, in order to be able to decide whether to reuse the substructure or not, a detailed assessment is also necessary. Among the evaluation methods, the non-destructive method has attracted more attention from scientists around the world, as shown in the study by C. Maierhofer et al. [1]. In this document, almost all the entire non-destructive methods are presented. In the group of non-destructive methods, the evaluation methods based on vibration results are more interested as shown in the research of Larry D. Olson [2]. This document presents an overview of substructure assessment techniques based on the vibration results.

Evaluation of the actual working conditions of the bridge pier has recently attracted a lot of attention from scientists around the world. In their paper, Qiang Mao et al. [3] present the feasibility of utilizing structural identification techniques to describe the substructure and bridge foundation. A simple three-span bridge in Mossy, West Virginia, USA, was used as a case study. Modal analysis and finite element model updating techniques are used to investigate and estimate structural uncertainty and conditions. This updated finite element model for the structure provides valuable information for evaluating the bridge conditions and demonstrating how to structure identification is a useful tool for the case under consideration.

H. H. Nguyen (✉)
University of Transport and Communications, Hanoi, Vietnam
e-mail: nhhunggttp@utc.edu.vn

M. H. Dam
Training, Construction and Human Resource Development JS Company No 6, Hanoi, Vietnam

A more detailed study on the bridge pier evaluation technique was presented by Masahiro Shınoda et al. [4] in their paper. In the article, the author describes the usual non-destructive evaluation of railway bridge substructures by the percussion test. By the percussion test, the natural frequency of the substructure can be measured with high accuracy and is applied to many railway bridge substructures in Japan. It has been confirmed that the natural frequency of the piers decreases with structural destruction and increases with reinforcement. The percussion inspection system includes an iron ball to apply force to the substructure, the velocity sensor measures free vibration of substructure and data acquisition system to record automatic free vibration. To actually evaluate the performance of the substructures, a criterion of the natural frequency of the substructures obtained from the results of regression analysis with many field data was presented. Finally, an application of the percussion test for the Bridge overpass Chikuma River was reported and the bridge's substructure assessment was made in this paper.

Also, research on oscillation excitation by percussion J. W. Zhan et al. [5] measured the vibration of the pier body and foundation, the pier body stiffness, the bearing stiffness, and the ground spring stiffness were used as the condition parameters. The sensitivity of longitudinal response to impulse forces was analyzed. Index signature assurance criteria (SAC) is based on a frequency response function (FRF) that is used to assess whether a failure exists and to determine global failure levels. With tested longitudinal action reactions and modal parameters as the target, the bearing stiffness parameters, pier body stiffness parameters, and underground parameters are obtained by the finite element model updating method. Hence, the working conditions of substructures can be assessed.

In the direction of damage assessment in reinforced concrete piers, Yung-Yen Ko et al. [6] used a vibration method to evaluate the failure of the pier. Through analytical transformations and validation experiments, the research group has shown a decrease in the vibration frequency proportional to the decrease in the stiffness of the pier body and the foundation of the pier. L. S. Hogan et al. [7] determined the effects of soil–structure interaction through vibration experiments and the influence of soil spring stiffness and the structural stiffness to be studied in detail.

Through the above studies, it is shown that the determination of the vibration frequency and the corresponding vibration mode can be received through field measurements. Besides, the studies also show that it is possible to determine the actual parameters of the bridge pier if the corresponding vibration frequency and mode are known, because the pier dynamic response depends a lot on the main parameters of the pier and spring link of the pier with the superstructure and the foundation. Changes in these components will lead to changes in the measured response. Furthermore, changes in structural parameters often imply risks to the superstructure as well as to the pier, so new methods of determining main structural parameters from measurement results are needed.

In this paper, the author focuses on analyzing the vibration modes of the pier, thereby selecting the vibration modes and corresponding vibration frequencies useful for diagnostic work, then determine structural parameters such as flexural

stiffness (EI), mass per unit of length, and average axial force in the pier body. The spring stiffness of the bearing and the spring stiffness of the ground have not been mentioned in this study.

2 Theoretical Basis

2.1 Vibration Theory

According to Rayleigh [8], the vibration frequency of the structure can be expressed in the following formula.

$$\omega = \sqrt{\frac{k^*}{m^*}} \tag{1}$$

where k^* is the generalized stiffness and m^* is the generalized mass depending on the structure and the shape function selected in the generalized coordinate.

$$m^* = \int_0^L m(x)[\psi(x)]^2 dx + \sum m_i[\psi(x_i)]^2 + \sum J_i[\psi'(x_i)]^2 \tag{2}$$

$$
\begin{aligned}
K* &= \int_0^L k(x)[\psi(x)]^2 dx + \int_0^L EI(x)[\psi''(x)]^2 dx \\
&+ \sum k_i[\psi(x_i)]^2 - \int_0^L N(x)[\psi'(x)]^2 dx
\end{aligned} \tag{3}
$$

In which:

$\psi(x)$ The shape function.
$m(x)$ Mass per unit of length.
m_i Lumped mass at discrete locations x_i.
J_i The moment of inertia mass at discrete locations x_i.
$k(x)$ Spring per unit of length.
$EI(x)$ Flexural stiffness.
k_i Discrete spring at discrete locations x_i.
$N(x)$ Axial force.
$\psi'(x)$ The first derivative of the variable x of the shape function.
$\psi''(x)$ The second derivative of the variable x of the shape function.

2.2 Analysis Results in Vibration Mode Shape

To clearly see the vibration mode of the pier, the paper conducts an analysis of pier vibration by FEM method and Rayleigh method for a structural system as follows: simple beam bridge, bridge cross section is composed of three 33 m long I-beams arranged 2.4 m apart; one end of the beam with fixed bearing (at pier 1), one end of the beam with movable bearing (at pier 2); The bridge pier is composed of 2 columns of reinforced concrete with 20 m long, 1 m in diameter, set apart by 2.4 m; the pier cap has cross rectangle section dimension of 1.5×1 m. The characteristics are shown in Tables 1, 2, and 3.

   The following shows the analytical results in the case of the fixed bearing and the movable bearing.

   Through the analysis of the above vibration modes, they show that the vibration mode in Fig. 1a (the pier has a fixed bearing layout), the mass of the superstructure will participate in the vibration with the pier, also with the vibration mode in Fig. 1b (the pier has movable bearing layout), only itself vibrates. The vibration mode in Fig. 2 is similar to the case of the beam with boundary conditions of fixed end and pinned end, in this case, the superstructure only affects the axial force in the pier body. To verify the above comment, the paper will calculate the vibration frequency of the pier by Rayleigh method, the parameters such as the mass of the superstructure, the pier and the axial force in the pier body due to the self-weight of the pier and of the superstructure were also taken into account.

Table 1 Geometry properties

Subjects	A (m^2)	Ixx (m^4)	Iyy (m^4)	Izz (m^4)
End cross beams	0.75000	0.04940	0.14060	0.01560
Intermediate cross beams	0.30000	0.00370	0.05630	0.00100
Girder	0.63720	0.01700	0.21360	0.01780
Pier cap	1.50000	0.29350	0.28130	0.12500
Pier body	0.78540	0.09820	0.04910	0.04910

Table 2 Material properties

E (KN/m^2)	Poisson	Density (KN/m^3)	Mass density (KN/m^3/g)
2.51E + 07	0.2	2.36E + 01	2.40E + 00

Table 3 Bearing spring stiffness

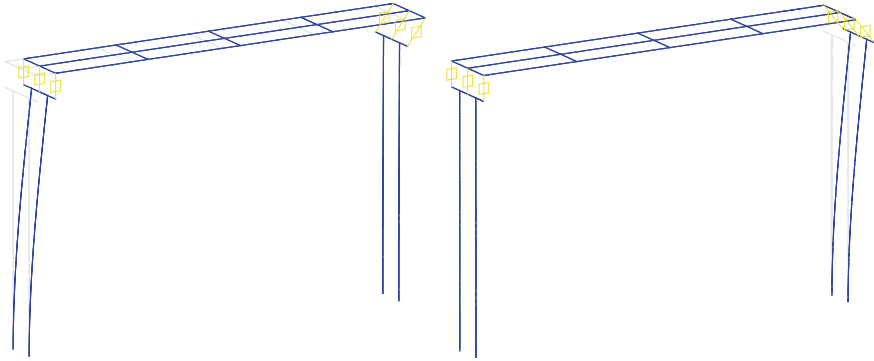| Type	Dz (KN/m)	Dy (KN/m)	Dx (KN/m)	Rz (KN m/rad)	Ry (KN m/rad)	Rx (KN m/rad)
Fixed bearing	100,000	100,000	150,000	1,000,000	1,000	100,000
Movable bearing	100,000	100,000	10	1,000,000	1,000	100,000

Fig. 1 First vibration mode of bridge pier with fixed (**a**) and movable bearing (**b**)

Fig. 2 Second vibration
mode of bridge pier with fixed
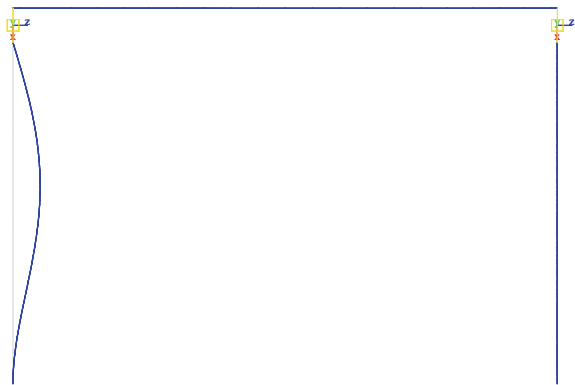
The shape function when calculating according to the Rayleigh method in the first and second figure is:

$$\psi(x) = 1 - \cos(x \cdot \pi/(2 \cdot L)) \tag{4}$$

The shape function in Fig. 2 is:

$$\psi_2 = \frac{1}{1.508}\left[\sin(\beta \cdot x) - \sinh(\beta \cdot x) - \frac{(\sin(\beta \cdot L) + \sinh(\beta \cdot L))}{(\cos(\beta \cdot L) + \cosh(\beta \cdot L))} \cdot (\cos(\beta \cdot x) - \cosh(\beta \cdot x))\right]$$
$$\tag{5}$$

$$\beta = \frac{3.926602}{L}$$

The results of the calculation compare the vibration frequency, shown in Table 4.

Table 4 Results of the calculation compare the vibration frequency

	FEM (Hz)	Rayleigh (Hz)	Error (%)
Mode 1 of pier 1	0.3282	0.3237	1.39
Mode 1 of pier 2	0.7979	0.8000	0.26
Mode 2 of pier 2	4.9311	4.9399	0.18

The results in Table 4 clearly show that the influence of the superstructure mass only affects the pier with a fixed bearing layout and little effects the pier with a movable bearing layout. This result contributes to the building of a method to determine the vibration parameters of the bridge pier.

2.3 Vibration Parameters of Bridge Pier Technique

In the case of the pier with a concentrated mass M, the above formula is presented as follows:

$$m^* = \int_0^L m(x)[\psi(x)]^2 dx + (m_{gir} + m_{cap})[\psi(x_1)]^2 + M[\psi(x_1)]^2 = \\ m_{eq} + (m_{gir} + m_{cap} + M)[\psi(x_1)]^2 \tag{6}$$

$$K* = \int_0^L EI(x)[\psi''(x)]^2 dx - N_1 \int_0^L [\psi'(x)]^2 dx - N \int_0^L [\psi'(x)]^2 dx \tag{7}$$

In which:

m_{gir}, m_{cap} The mass of the superstructure and the pier cap
M The additional mass on the bridge superstructure
N_1 The average axial force in pier body due to the pier itself and the superstructure
N Axial force in pier body due to the additional mass on the bridge superstructure

In the first case, if we arrange the mass on the top of the pier T_2 (movable bearing), then if we consider the vibration of the pier T_1, we have

$$m^* = \int_0^L m(x)[\psi(x)]^2 dx + M[\psi(x_1)]^2 + (m_{gir} + m_{cap})[\psi(x_1)]^2 \\ = m_{eq} + (m_{gir} + m_{cap} + M)[\psi(x_1)]^2 \tag{8}$$

$$K* = \int_0^L EI(x)[\psi''(x)]^2 dx - N_1 \int_0^L [\psi'(x)]^2 dx = k_{eq} - N_1 * A \qquad (9)$$

we have

$$\omega = \sqrt{\frac{k^*}{m^*}} \rightarrow \omega^2 = \frac{k_{eq} - N_1 * A}{m_{eq} + (m_{gir} + m_{cap} + M)[\psi(x_1)]^2} \qquad (10)$$

If $\psi(x_1)$= 1 (with x_1 at the top of the pier) then

$$M = \frac{k_{eq} - N_1 * A}{\omega^2} - (m_{eq} + m_{gir} + m_{cap}) \qquad (11)$$

From "Eq. (11)" we can see that M and $1/\omega^2$ will have a linear relationship with each other in the form of equations $y = a_1 * x + b_1$, so if we have the actual pair of measurements M_i and $1/\omega_i^2$ then will be able to determine $a_1 = k_{eq} - N_1 * A$ and $b_1 = -m_{eq} - m_{gir} - m_{cap}$ by their linear regression lines.

In the second case, if we arrange the mass on the top of the pier T_2 (movable bearing), then if we consider the vibration of the pier T_2, we have

$$m^* = \int_0^L m(x)[\psi(x)]^2 dx + m_{cap}[\psi(x_1)]^2 = m_{eq} + m_{cap} \qquad (12)$$

$$K* = \int_0^L EI(x)[\psi''(x)]^2 dx - N_1 \int_0^L [\psi'(x)]^2 dx - N \int_0^L [\psi'(x)]^2 dx$$
$$= k_{eq} - N_1 * A - N * A \qquad (13)$$

we have

$$\omega = \sqrt{\frac{k^*}{m^*}} \rightarrow \omega^2 = \frac{k_{eq} - N_1 * A - N * A}{m_{eq} + m_{cap}} \qquad (14)$$

From "Eq. (14)" we can see that ω^2 and N will have a linear relationship with each other in the form of equations $y = a_2 * x + b_2$, so if we have the actual pair of measurements Ni and ω_i then will be able to determine $b_2 = \frac{k_{eq} - N_1 * A}{m_{eq} + m_{cap}}$ and $a_2 = -\frac{A}{m_{eq} + m_{cap}}$ by their linear regression lines.

In this case $\psi(x) = 1 - \cos(x \cdot \pi/(2 \cdot L))$, we have $A = \int_0^L [\psi'(x)]^2 dx = \frac{\pi^2}{160}$

In the third case, if we arrange the mass on top of pier T1 (fixed bearing), then when considering the vibration form close to the fixed-pinned end beam vibration of the pier T1, we have

$$\psi_2 = \frac{1}{1.508} \left[\sin(\beta \cdot x) - \sinh(\beta \cdot x) - \frac{(\sin(\beta \cdot L) + \sinh(\beta \cdot L))}{(\cos(\beta \cdot L) + \cosh(\beta \cdot L))} \cdot \cos(\beta \cdot x) - \cosh(\beta \cdot x)) \right]$$

(15)

$$m^* = \int_0^L m(x)[\psi_2(x)]^2 dx = m_{eq2}$$

(16)

$$k^* = \int_0^L EI(x)[\psi''(x)]^2 dx - N_1 \int_0^L [\psi'(x)]^2 dx - N \int_0^L [\psi'(x)]^2 dx$$
$$= k_{eq2} - N_1 * B - N * B$$

(17)

$$B = \int_0^L [\psi_2'(x)]^2 dx$$

(18)

we have

$$\omega = \sqrt{\frac{k^*}{m^*}} \rightarrow \omega^2 = \frac{(k_{eq2} - N_1 * B) - N * B}{m_{eq2}}$$

(19)

From "Eq. (19)" we can see that ω^2 and N will have a linear relationship with each other in the form of equations $y = a_3 * x + b_3$, so if we have the actual pair of measurements Ni and ω_i then will be able to determine $b_3 = \frac{(k_{eq2} - N_1 * B)}{m_{eq2}}$ and $a_3 = -\frac{B}{m_{eq2}}$ by their linear regression lines.

From the above equations, we can determine m_{eq}, and then M, then determine N_1 and finally k_{eq}, then combine with the above shape function, we will calculate the actual m and EI of the bridge pier according to the following formula.

$$m_{eq} + m_{cap} = -\frac{A}{a_2}$$

(20)

$$m_{gir} = -m_{eq} - m_{cap} - b_1 \Rightarrow m_{gir} = \frac{A}{a_2} - b_1$$

(21)

$$a_3 = -\frac{B}{m_{\mathrm{eq}2}} \Rightarrow m_{\mathrm{eq}2} = -\frac{B}{a_3}$$
$$\Rightarrow m = \frac{m_{\mathrm{eq}2}}{\int_0^L [\psi_2(x)]^2 dx} \tag{22}$$

$$m_{\mathrm{eq}} = m \cdot \int_0^L [\psi(x)]^2 dx \Rightarrow m_{\mathrm{cap}} = -\frac{A}{a_2} - m_{\mathrm{eq}} \tag{23}$$

$$k_{\mathrm{eq}} = a_1 + N_1 \cdot A \Rightarrow EI = \frac{a_1 + N_1 \cdot A}{\int_0^L [\psi''(x)]^2 dx} \tag{24}$$

$$k_{\mathrm{eq}2} = m_{\mathrm{eq}2} \cdot b_3 + N_1 \cdot B \Rightarrow EI = \frac{m_{\mathrm{eq}2} \cdot b_3 + N_1 \cdot B}{\int_0^L [\psi_2''(x)]^2 dx} \tag{25}$$

$$N_1 = \frac{\dfrac{a_1}{\int_0^L [\psi''(x)]^2 dx} - \dfrac{-\frac{B}{a_3} \cdot b_3}{\int_0^L [\psi_2''(x)]^2 dx}}{\dfrac{B}{\int_0^L [\psi_2''(x)]^2 dx} - \dfrac{A}{\int_0^L [\psi''(x)]^2 dx}} \tag{26}$$

3 Results of Numerical Calculation

To prove the effectiveness of the proposed method, the authors used the data as described above to model by finite element method with the case of additional mass 10, 20, 30, 50, and 100 KN/g, respectively.

The results of the first mode vibration of pier 1 are obtained for the case of additional mass in pier 2 as given in Table 5.

From the above results, building a linear relationship through linear regression as shown in Fig. 3.

From the above results, based on the proposed method received $a_1 = 891.57$ and $b_1 = -209.61$.

The results of the first mode vibration of pier 2 are obtained for the case of additional mass in pier 2 as given in Table 6.

From the above results, building a linear relationship through linear regression as shown in Fig. 4.

Table 5 Results of the first mode vibration of pier 1

$1/\omega^2$	0.235118	0.246317	0.25753	0.268744	0.291174	0.347266
M (KN/g)	0.01	10	20	30	50	100

Fig. 3 Linear relationship and linear regression of M with $1/\omega^2$ of pier 1
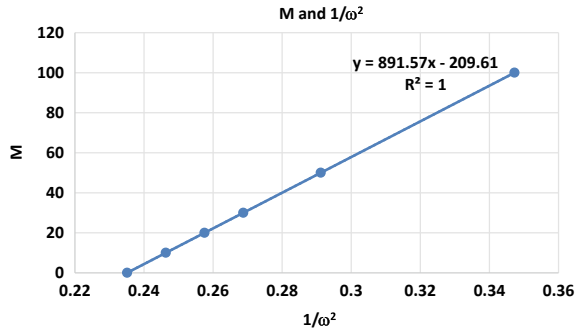
Table 6 Results of the first mode vibration of pier 2

N (KN)	0.01	10	20	30	50	100
ω^2 (rad/s)^2	25.29974	25.28287	25.26612	25.24932	25.21581	25.13233

Fig. 4 Linear relationship and linear regression of N with ω^2 of pier 2
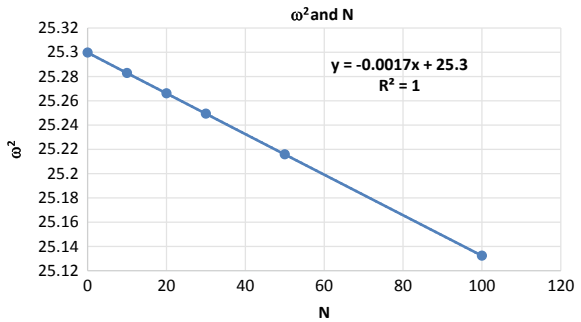
Table 7 Results of the second mode of vibration of pier 1

N (KN)	1	10	20	30	50	100
ω^2 (rad/s)^2	959.9472	959.8888	959.8071	959.7253	959.5657	959.2173

From the above results, based on the proposed method received $a_2 = -0.0017$ and $b_2 = 25.3$.

The results of the second mode vibration of pier 1 are obtained for the case of additional mass in pier 2 as given in Table 7.

From the above results, building a linear relationship through linear regression as shown in Fig. 5.

From the above results, based on the proposed method received $a_3 = -0.0074$ and $b_3 = 959.95$.

From the values a_1, b_1, a_2, b_2 and a_3, b_3 received above, instead of the equation from (Eq. 20) to (Eq. 26) calculate values such as given in Table 8.
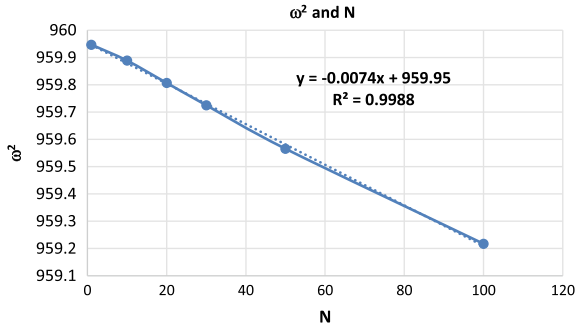
Fig. 5 Relationship and linear regression of N with ω^2 of pier 1

Table 8 Table of calculation results

Parameters	Calculating value	Assumption value	Error (%)
The mass of the superstructure (KN/g)	173.3246897	174.5667686	−0.7
Average axial force N_1 (KN)	594.7768260	653.6184413	−9.0
Pier body stiffness (EI) (KN m^2)	1.219774544*10^6	1.233369641*10^6	−2.8
mass per unit of length (KN/g/m)	1.944682568	1.886236568	3.1

The above results show that the proposed method can estimate the bending stiffness of the pier body and the mass per unit length with high accuracy, with an error of less than 5%. In addition, the proposed method can also determine the mass of the superstructure as well as the average axial force in the pier body.

4 Conclusion

The research results of the vibration modes show clear effects of the fixed or movable bearing arrangement on the top of the pier. The study also shows the parameters that mainly affect the pier vibration. The results illustrate a bridge span, but it is also the basis for studying the case of a simple multispan bridge. Because the analysis results show that only with fixed bearing, the superstructure mass participates in the vibration of the pier body also in the case of the movable bearing, the mass has little effect on the vibration of the pier.

This study is also a few studies of the pier body vibration considering the effect of the axial force in the pier body. The results also show that the axial force in the pier body significantly affects the vibration frequency of the pier.

The results of determining the vibration parameters by the proposed method give high accuracy results, especially in the case of axial force in the pier body due to the assumption that the constant force differs from the finite element model, so the results are a large difference. To overcome this case, in the near future, the team will put the axial force that changes according to the position of the pier body in the above formula.

References

1. Maierhofer, C., Reinhardt, H.-W., Dobmann, G.: Non-destructive Evaluation of Reinforced Concrete Structures. Woodhead Publishing (2010)
2. Larry, D., Olson, P.E.: Dynamic Bridge Substructure Evaluation and Monitoring. FHWA-RD-03-089, VA 22101 (2005)
3. Mao, Q., Mazzotti, M., DeVitis, J., Braley, J., Young, C., Sjoblom, K., Aktan, E., Moon, F., Bartoli, I.: Structural condition assessment of a bridge pier: A case study using experimental modal analysis and finite element model updating. Struct. Control Health Monit. **26**, e2273 (2009)
4. Shinoda, M., Haya, H., Murata, S.: Nondestructive evaluation of railway bridge substructures by percussion test. In: Fourth International Conference on Scour and Erosion (2008)
5. Zhan, J.W., Xia, H., Zhang, N..: A damage evaluation method for bridge substructures using longitudinal impact dynamic responses. In: Research and Applications in Structural Engineering, Mechanics and Computation. Taylor & Francis Group, London (2013)
6. Ko, Y.-Y., Chang, W.-K., Liu, K.-Y., Hung, H.-H., Chang, K.C.: Damage evaluation for RC bridge piers using vibration measurement. Adv. Struct. Eng. **18**(9) (2015)
7. Hogan, L.S., Wotherspoon, L.M., Beskhyroun, S., Ingham, J.M.: Vibration testing of an in-situ bridge pier to determine soil-structure interaction effects. In: 15th World Conference of Earthquake Engineering Lisbon, Portugal (2012)
8. Clough, R.W., Penzien, J.: Dynamics of Structures, Computers & Structures. Berkeley, CA 94704 (2003)

Safety Evaluation of Billboards When Considering the Random Effects of Design Parameters in the Southern Region of Vietnam

Bac An Hoang

1 Introduction

The need for advertising is indispensable, especially in Vietnam, where is under strong economic development. Outdoor advertising has been researched and evaluated to bring good communication efficiency, strong growth momentum and has increased by 6.4% from 2011. Four megacities, including Hanoi, Ho Chi Minh City, Da Nang, and Can Tho recently stand more than 17,000 billboards [1]. Outdoor large billboards are often placed on the main roads such as highways, national highways, provincial roads, etc., at bus stops, between intersections of streets, on buildings, skyscrapers, etc.

Double-sided tables and single or double columns are the main structures of the outdoor billboard design. A large billboard usually has a surface area of over 40 m^2 [2], due to the large surface, the main load of the billboard design is the wind load. The impact of the wind load is not only the effect of the static component but also the dynamic component, making billboards more complex such as oscillation, air turbulence, vibration types, etc. This study focuses on analyzing billboard structure, simulation its reliability based on the random effect of loads, construction location in the southern region, typically in Ho Chi Minh City.

According to [3, 4] southern region and Ho Chi Minh City are less affected by storms (Region IIA), but by the rainy season, the number of damaged billboards tends to increase. The billboards affected by weather, rain, and sun are the cause of steel rust, especially tornadoes that can collapse the billboards at any time [5, 6]. Ensuring safe working for billboards is an urgent issue not only for Ho Chi Minh City, where there are many billboards, but also for other provinces like Vinh Long where there are only about 50 outdoor billboards, and many of them have been

B. A. Hoang (✉)
University of Architecture Ho Chi Minh City, Ho Chi Minh City, Vietnam
e-mail: an.hoangbac@uah.edu.vn

313

degraded, resulting in a loss of safety, some of which have been built for a long time but have not been re-tested for quality [7].

Storms are usually formed from the ocean and then move to the mainland [8], from 1961 to 2014, 23 storms were affecting the southern region with the strongest wind speed is level 10, gust 12–13 [9] on the Beaufort scale [10]. Notably, in recent years, the number of storms has increased and they have been stronger. To design constructions in the southern region, the wind speed is equivalent to 12–13 on the Beaufort scale [3]. However, in the rainy season with thunderstorms, heavy rains, and strong winds (September to December are usually the strongest storms), there are significant losses such as the roof uplift, the house is collapsed, and trees and electric poles are damaged. [11–13]. With such consequences, it may be assumed that the actual wind speed during a thunderstorm may be greater than the values given in current standards, which should be considered when evaluating the safe working of construction structures.

Many studies have been researched about the reliability of large-scale structures, such as K. Ohdo analyzed the reliability of construction scaffoldings system under wind storms [14], Nguyen et al. studied the impact of wind load on large plate billboards in Vietnam [15], Giang researched about damage caused by wind load for building in Vietnam [16], Huong studied about variations and trend of maximum wind speed in Vietnam during 1961–2007 [17], the report on the zoning of wind pressure for use in the construction industry over Vietnam was written by Lien [18].

Zhu et al. [19] analyzed the effectiveness of different stiffener heights, design load, stiffener thickness, and skin thickness on the buckling of a construction structure. Their proposed method provides robust and efficient results compared to the modified iterative reliability methods. Bagheri et al. [20] proposed a numerical approach that is efficiently and robustly estimates the fuzzy time-dependent reliability index of reinforcement corrosion structures. Ho-Huu et al. [21] proposed two steps method to analyze the reliability of steel structure including a multi-objective design optimization problem is formulated and solved by a multi-objective evolutionary optimization algorithm, first. Then, reliability analysis problems are formed by taking into account the uncertainty of input data of the problem. Their results indicate that the proposed approach is reliable and more competitive compared to other methods.

In summary, reliability analysis has been applied to analysis in many structural problems, such as concrete design, steel design, buckling of structure, and large-scale structures. However, to the best of the authors' knowledge, this is the first attempt to analyze the reliability of billboard structure in Vietnam. Therefore, this study proposed a Monte Carlo simulation combine with a specific structural method to analyze the reliability of billboards under different kinds of wind loads.

2 Materials and Methods

In this study, the author calculated the typical billboard structure in the southern region (specific location is Ho Chi Minh City) according to Vietnam standards [19], then analyzed the safety of it.

2.1 Load and Action

The load used to design billboard structure was from TCVN 2737–1995 load and action-design code [4], including:

(a) Self-weight of the billboard.
(b) Wind load: Following [3] for estimating wind load value effect to buildings. In 2009, to supplement the changes, due to the environment Vietnam building code [3] was issued. However, it was not widely used because most engineers were still familiar with [4], which made the design work incompatible with the natural conditions and regulations of law.

In [4], the value of wind pressure is divided into 5 zones. Conversion factors to obtain wind speed/pressure at higher return periods, 50–100 year-return periods. According to [3], mean wind speed V_0 using in design depends on the 3-seconds mean wind speed of 10 m height in open-flat terrain (type B), with a return period of 20 years. Wind speed converted value from 10 min in 50 years (V_{10}^{50}) to 3 s in 20 years (V_3^{20}) is 37.21 m/s, and a deviation changes from 3.1 m/s $\div$ 6.6 m/s (($0.084 \div 0.18$) V_0) based on [4] and [17], respectively. Therefore, the mean and deviation of the wind load should be considered when designing the billboard structure.

The value of wind load static component W at the height Z above the reference level is determined by the formula [4]:

$$W = W_0 \cdot k \cdot c \tag{1}$$

where: W_0—the standard value of wind pressure; k—factor of wind pressure variation height; c—aerodynamic factor (reliability of wind load) is taken equal to 1.2.

2.2 Materials

Material suitable for the structure of the billboard is steel, with high strength, convenient for transportation because of its low weight, easy to erect. However, the steel billboard structure is susceptible to corrosion due to moisture, which leads to

structural damage, so steel protection measures should be taken. In Vietnam, commonly used are low carbon steel ($f_y \leq$ 290 MPa, f_u= 310 ÷ 400 MPa) such as CT34, CT38, SS400, S235, Q235, A36 and relatively high strength steel (f_y= 310 ÷ 400 MPa, f_u= 450 ÷ 540 MPa) such as Q345, A570 [22].

2.3 Limit State Design and System Reliability Evaluation

The structural design standards of Vietnam use the design method according to the limit state, this is shown in the Vietnamese standard [22]. The meaning of the method is that the structure will be safe when the load effect (U) is smaller than the structural strength (B), which can be written in inequality:

$$U < B \tag{2}$$

Assuming the occurrence of the failure of the structure when condition (2) is not satisfied; therefore, a hypothetical boundary distinguishing between the safety and failure states of the structure is given by the following equation:

$$B - U = 0 \tag{3}$$

Equation (3) is the fundamental formula of the so-called limit state (performance) function (Fig. 1).

Both U and B are generally random variables and the validity of inequality (2) cannot be guaranteed, i.e., with the probability equal to 1. The essential objective of reliability theory is to assess the probability of failure p_f and to find the necessary conditions for its limited magnitude. Thus, the probability of failure can be formulated as:

$$p_f = P(U > B) \tag{4}$$

Fig. 1 Limit state function
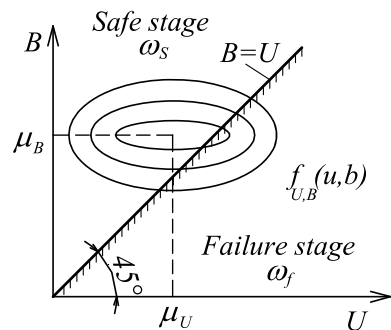
To analyze reliability, assumed that variables U and B are random variables [17, 18]. Then, the difference M (called the reliability margin) has a normal distribution:

$$M = B - U \tag{5}$$

Distribution of M has mean value, $\mu_M = \mu_B - \mu_U$ and Fig. 2 presents the standard deviation (σ_M) and probability density ($f(m)$).

When B and U are independent random variables, we have:

$$f(m) = \int_{-\infty}^{\infty} g(m+u)f(u)du \tag{6}$$

With $g(m + u)$—probability density of strength, the variable is $m + u$; $f(u)$—probability density of load effect.

Reliability of structure:

$$R = P_s = P(M > 0) = \int_0^{\infty} f(m)dm = \int_0^{\infty}\int_0^{\infty} g(m+u)f(u)dudm \tag{7}$$

Thus, the probability of failure is given:

$$P_f = P(M<0) = 1 - R = \int_{-\infty}^{0} f(m)dm \tag{8}$$

In practice, there is often not enough statistical data to determine the specific density function of each variable. To obtain an analysis of the probability of failure or safety determined by the expressions (6) and (7), using FORM and SORM can approximate reliability [23–25]. However, the disadvantage of this method is the complex state function when the number of variables is many. In that case, the Monte Carlo simulation method has the advantage of being an accurate and powerful technique to analyze this problem [25].
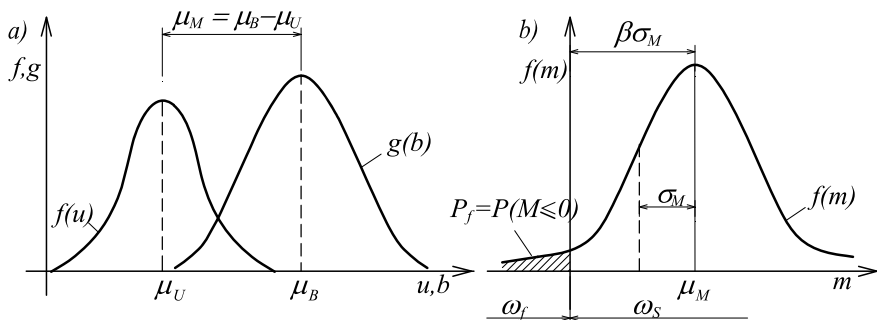

Fig. 2 Safety margin (**a**) and reliability index (**b**)

U and B often do not know in advance or have no clear mathematical expressions, or maybe they are not independent variables. In that case, it is best to represent the basic variables x_i, $i = 1, 2, \ldots, n$ which are statistically independent and have known distribution functions. The Monte Carlo method creates a set of values for independent representations of x_i for each basic variable and thereby determines the corresponding values of the safety margin.

$$m = f(x_1, x_2, \ldots, x_n) = f(\overline{x}) \tag{9}$$

By generating random numbers, this process is repeated many times to create a large set of m values, from which the probability distribution of the quantity M can be simulated. So, the probability of failure formulated as:

$$P_f = P(M \leq 0) = \lim_{n \to \infty} \frac{k}{n} \tag{10}$$

In which: n—the total number of tests, k—the number of trials with $f(x) \leq 0$.

3 Numerical Example

3.1 Example Description

Consider a typical billboard, structure consists of an open-web column lattice, each branch form is angle steel welded from two plates, and the ties are made of hot-rolled angle (Fig. 3). Impact load: self-weight of billboard (structure system, technical equipment, etc.); Wind load is calculated with region IIA [4]. All the billboard parameters are presented in Tables 1, 2, and Figs. 3, 4.

3.2 Statistic Properties of Random Variables

The random variables of reliability analysis are mean (μ), standard deviation (σ) and coefficient of variation (CV = σ/μ) are displayed in Table 3.

3.3 Structural Design Case and Reliability Estimation

With a life of a building is 20 years, the billboard structure designs have a wind speed $V_0 = 36.8$ m/s [3]. So, according to [22], the standard value of wind pressure is determined as $W_0 = 0.613 V_0^2 \cdot 10^{-3} = 0.83$ KN/m^2. Analysis results indicated
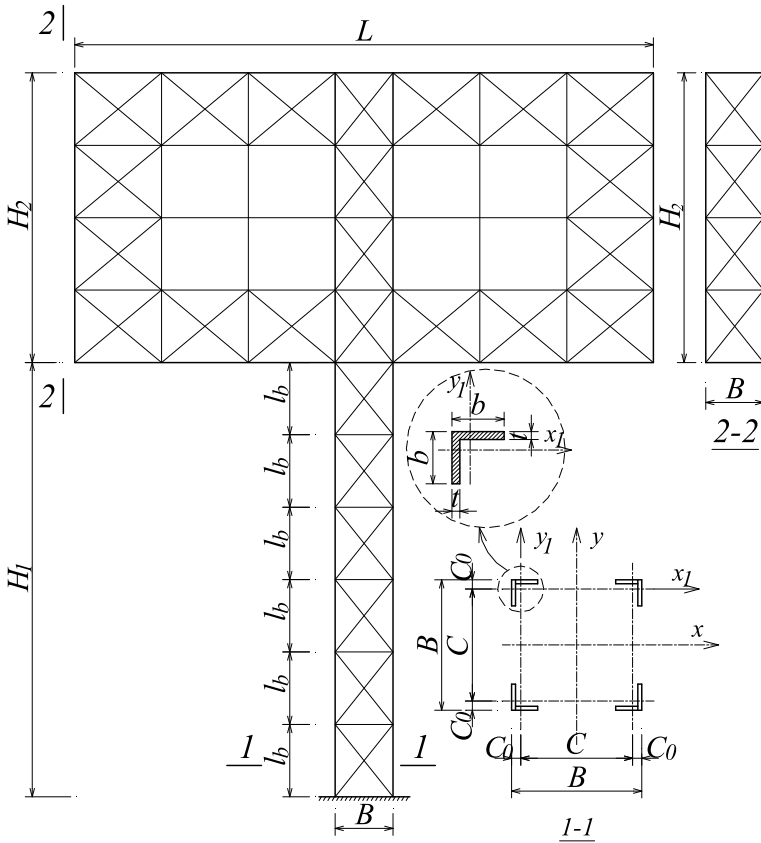
Fig. 3 Type of billboard structure

Table 1 Input parameters of the billboard analysis

Parameters of billboard (m)						Column shape branch (mm)		Material steel (MPa)	
H_1	H_2	L	B	l_b	d_1	b	t	E	f_y
15	10	20	2	2.5	L75 × 5	250	12	2.1E + 5	275

Table 2 Geometric characteristics

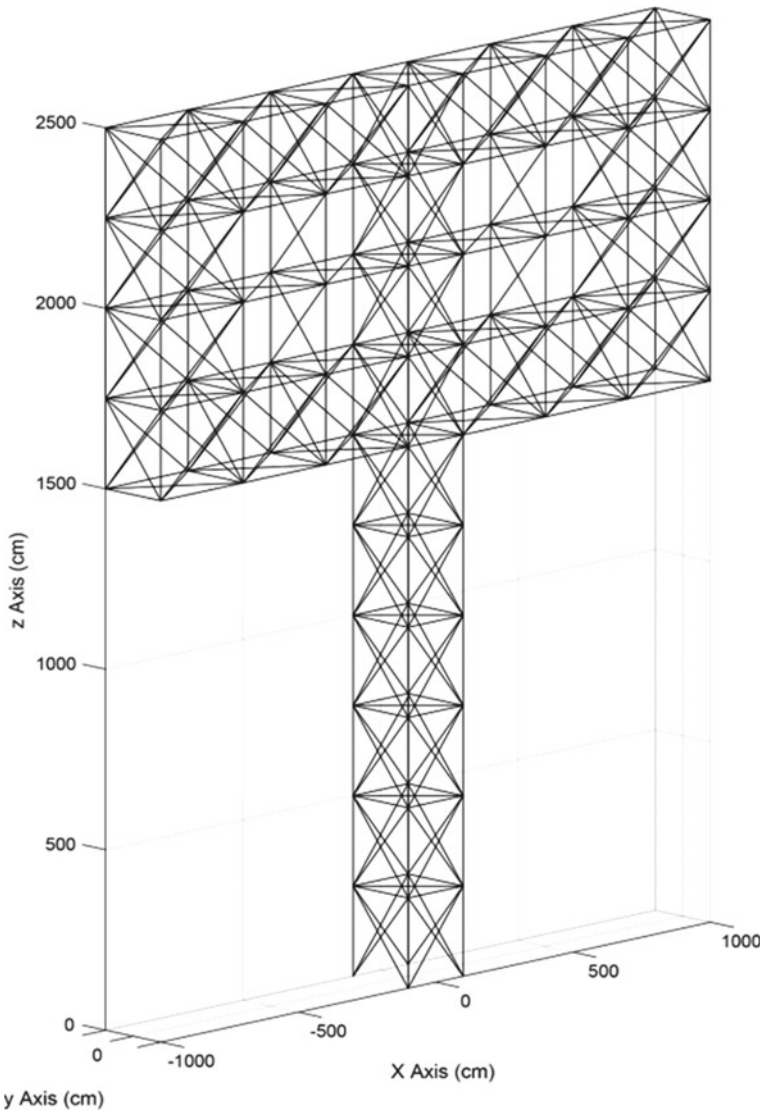| Geometric characteristics	One branch of the column	Gross section
Area, A (cm^2)	60	240
Moment of inertia, I_x/I_y (cm^4)	3639.6	2111747.2
Radius of gyration, i_x/i_y (cm)	7.79	93.8
Equivalent slenderness ratio, λ_0	32.09	26.65
Conventional slenderness ratio, $\overline{\lambda}$	1.08	1.3

Fig. 4 3-D model of the billboard

that the column foot section is the most dangerous, and it has the moment $M = 5515.39$ KNm and axial force $N = -154.52$ KN.

For billboards, the following conditions must be checked:

- Check the buckling of branch columns: $\sigma_1 = 20.15$ MPa $< f_y \cdot \gamma_c / \gamma_m = 24.43$ MPa, OK
- Check local buckling of the column: $\sigma_C = 18.07$ MPa $< \sigma_{lim} = 40.46$ MPa, OK

Table 3 Statistic parameters of random variables

S. no.	Property	Random variables	Mean, μ	Std. deviation, σ	CV	Probability distribution
1	Yield strength	f_y	270 MPa	$0.05.\mu_{fy}$	0.05	Lognormal [26]
2	Column cross-section parameters	b	25 cm	$0.05.\mu_B$	0.05	Normal [27]
		t	1.6 cm	$0.05.\mu_t$	0.05	Normal [27]
3	Wind speed	V_0	36.8 m/s	$(0.084 \div 0.18).\mu_{V0}$	$0.084 \div 0.18$	Gumbel [28]

- Check the global stability of the column (compressive strength): $\sigma_f = 21.02$ MPa $< f_y \cdot \gamma_c/\gamma_m = 24.43$ MPa, OK.
- Horizontal transfer conditions are guaranteed.

For effective design, the maximum normal stress should be $\sigma \approx f_y \cdot \gamma_c/\gamma_m$. The analysis results show that the most dangerous billboard is the loss of overall stability of the column. Therefore, this study focus on the global stability of column structure under random factors in Table 3, the limit state function has the form:

$$g(X) = \frac{f_y \cdot \gamma_c}{\gamma_m} - \sigma = \frac{f_y \cdot \gamma_c}{\gamma_m} - \frac{N_1}{\varphi_{\min} \cdot A_1} \tag{11}$$

In which: N_1—total axial force on one side of compression; A_1—the area of two branches on the side of the compressive surface; $\varphi_{\min}$—determined from the conventional slenderness $\bar{\lambda}$, equivalent slenderness λ_0.

To assess the system reliability of the billboard frame, the MATLAB program is used to implement Monte Carlo simulation [29], with $N = 10^5$ samples (Figs. 5 and 6).

With the mean of wind speed of 36.8 m/s, the standard deviation of the wind speed increase from $0.9 \div 6.1$ m/s (Table 3) and use the Gumbel density distribution [23] and Eq. (1) for an estimate. The mean, standard deviation, and coefficient of variations of wind pressure are calculated and presented in Table 4 and Fig. 7. Recognize that the standard deviation of the wind pressure increases faster than the standard deviation of the wind speed, as shown by the ratio CV_{Wo}/CV_{Vo} of 2–2.2 times.

4 Result

Analyzing the reliability of the billboard structure in the 5 different cases is displayed in Table 5. The failure probability distribution of case 3 and the safety margin M is presented in Figs. 8 and 9, respectively.
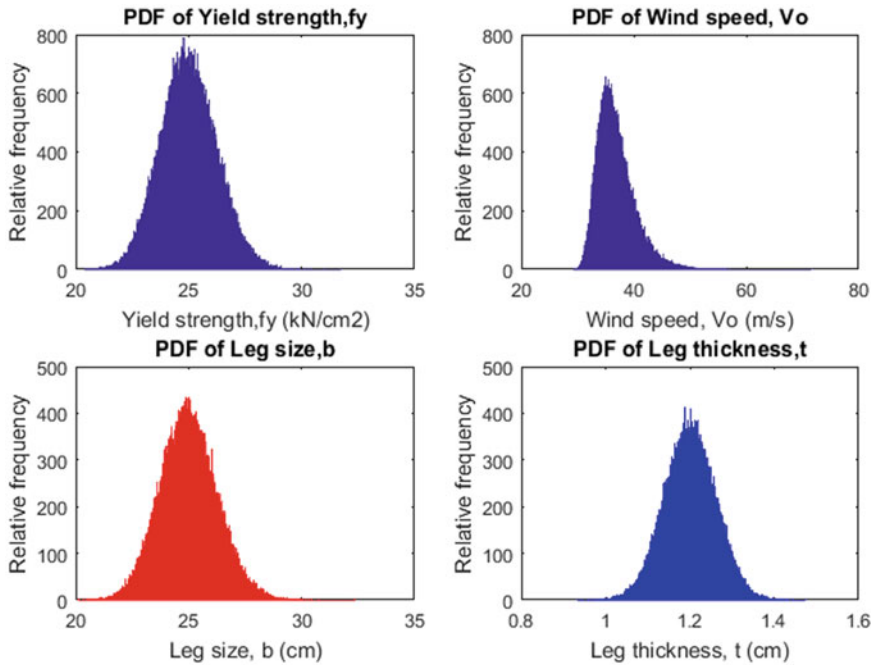
Fig. 5 Probability density function (PDF) of yield strength (f_y), wind speed (V_0), the width of column branch (b), and thickness (t)

To investigate the reliability of the structure by random parameters, we consider the cases based on the ratio (γ_i) between the safety margin and yield strength as $\gamma_i = \left(\frac{\mu_{M_i}}{\mu_{f_y}} \cdot \frac{\gamma_c}{\gamma_m} \right)$, $i = 1, \ldots, 5$, with the safety margin increasing from 10 to 30%, the values ($\gamma_1 \div \gamma_5$) are $0.9 \div 0.7$ (Table 5).

The randomness of the parameters included in the survey is expressed as a CV coefficient, in which: standard deviation of the yield strength (σ_{f_y}), branch width of column (σ_b) and thickness (σ_t) is equal to 5% of the mean (Table 5); the standard deviation of wind load (σ_{W_0}) is considered in 6 cases with values from 5 to 30% of the mean (Tables 5 and 8).

The Reliability-based design has found wide application in structural engineering [31], for example, as the basis of the partial safety factors applied in the standards [32, 33], the target reliability index (β) is given for the working life and related not only to the consequences but also to the relative costs of safety measures, see Tables 6 and 7.

According to [32], billboards can be classified into the third class (RC1), in which the target of reliability index (β) is select of 4.2 for one year. Then, the reliability level corresponding to arbitrary remaining working life can be expressed as follows:
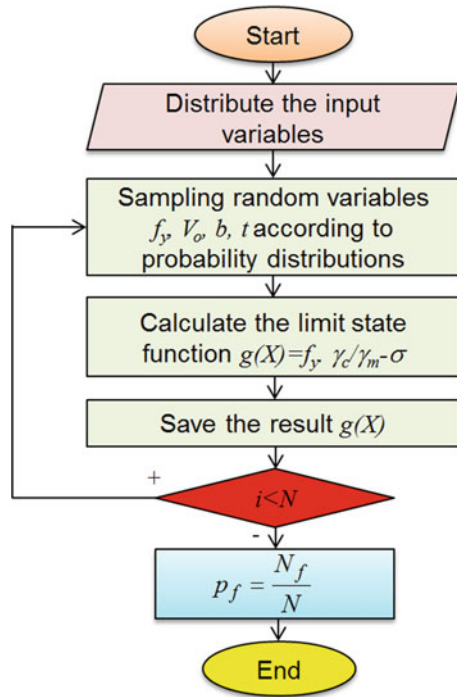
Fig. 6 Flowchart of Monte
Carlo simulation

Table 4 Relation between the mean and standard deviation of wind load/wind pressure

S. no.	μ_{V0} (m/s)	σ_{V0} (m/s)	CV_{V0}	μ_{W0} (KN/m^2)	σ_{W0} (KN/m^2)	CV_{W0}
1	36.8	0.9	0.024	0.838	0.0414	0.05
2	36.8	1.8	0.049	0.8388	0.084	0.10
3	36.8	2.7	0.073	0.8452	0.128	0.15
4	36.8	4.4	0.120	0.8577	0.2133	0.20
5	36.8	5.3	0.144	0.8667	0.2612	0.25
6	36.8	6.1	0.166	0.8765	0.3072	0.30

$$\beta_{\text{tref}} = \Phi^{-1}\left\{[\Phi(\beta_1)]^{\text{tr}}\right\} \tag{12}$$

With β_1 (target reliability index), which is taken from Table 7 for a relevant reliability class with the reference period $t_{\text{ref}} = 1$ year. Thus, $\beta \approx 3.34$ should be considered with $t_{\text{ref}} = 20$ years for the lifetime of the billboard structure.
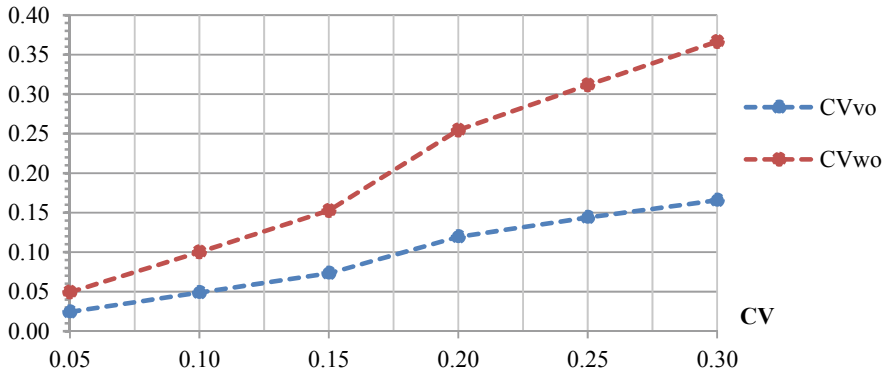
Fig. 7 Correlation between wind speed and win pressure (expressed via coefficient variation—
CV)

Table 5 Cases of analysis

S. no.	Survey cases		Coefficient of variation, *CV*			
			CV_{W0}	CV_{f_y}	CV_b	CV_t
1	Case 1:	$\gamma_1 \approx 0.9$	0.05, 0.1, 0.15, 0.2, 0.25, 0.3	0.05	0.05	0.05
2	Case 2:	$\gamma_2 \approx 0.85$	0.05, 0.1, 0.15, 0.2, 0.25, 0.3	0.05	0.05	0.05
3	Case 3:	$\gamma_3 \approx 0.8$	0.05, 0.1, 0.15, 0.2, 0.25, 0.3	0.05	0.05	0.05
4	Case 4:	$\gamma_4 \approx 0.75$	0.05, 0.1, 0.15, 0.2, 0.25, 0.3	0.05	0.05	0.05
5	Case 5:	$\gamma_5 \approx 0.7$	0.05, 0.1, 0.15, 0.2, 0.25, 0.3	0.05	0.05	0.05

5 Discussion

Table 8 shows the analyzed results, in which, reliability index (β), reliability (P_s),
probability of failure (P_f) of 5 cases correspond to different safety margins.
Figure 10 shows the relationship between reliability (P_s) and standard deviation of
wind pressure in 5 safe marginal cases.

Table 8 and Fig. 10 show that: The standard deviation of the wind pressure is
small (i.e., $CV_{W0} = 0.05$) and the case 4–5 with $\gamma_4 \approx 0.75$, $\gamma_5 \approx 0.7$ then β is 3.41
and 3.85, the reliability is 0.999 and 0.9999. When $CV_{W0} = 0.05$, the case 2–3 is
$\gamma = 0.85 - 0.8$ and $CV_{W0} = 0.1$, the safety margin is from 0.8 to 0.7, β value has a
pretty similar value $2.47 \div 2.79$, and the reliability is quite low $P_s = 0.98 \div 0.99$.
When CV_{W0} from 0.1, the reliability decreases rapidly (the slope of the lines in
Fig. 10 increases gradually), the damage of the structure is more likely. It can be
said that the choice of safety margin has a great impact on structural reliability, the
safety margin greater and the structure more secure. With the conventional design,
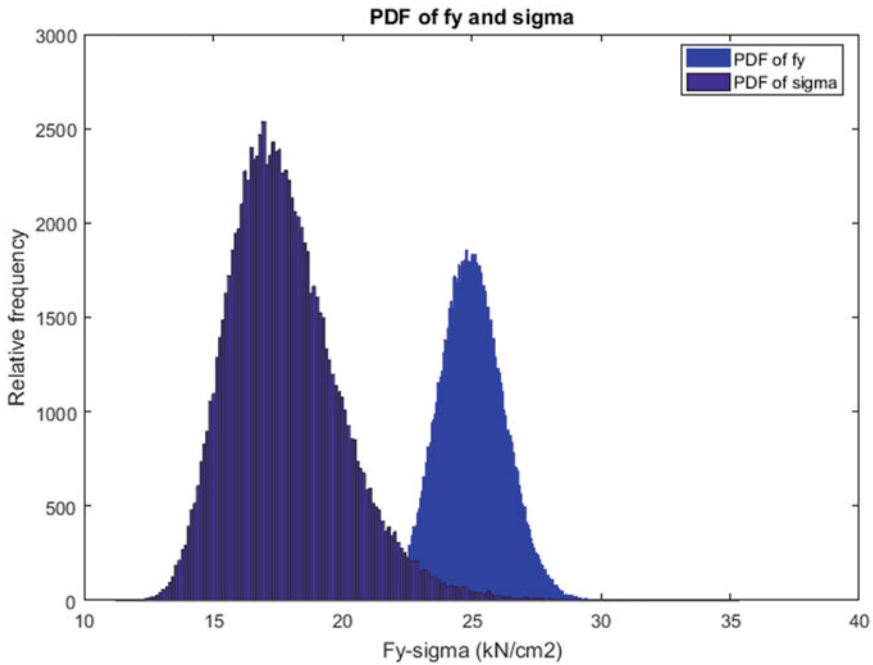
Fig. 8 PDF of strength (f_y) and stress (σ)

the safety margin is usually 0.1–0.15, but when considering the randomness of the calculated quantities, this safety margin needs to be increased [23], but the selection of the safety margins need to consider economic factors because then on it will use more materials.

6 Conclusions

This study assessed the safety of the billboard structure in the southern region (for example, in Ho Chi Minh City) by random factors. Based on the results of the studies in Sects. 3 and 4, statistical characteristics of random parameters such as wind speed, yield strength, and column section properties were developed.

The main impact on the billboard is the wind load, so the evaluation of the standard deviation of wind speed and wind pressure is taken from the standard [4, 24], and the results indicate that small changes in wind speed lead to large changes in wind pressure in unpredictable climate change conditions. Therefore, considering the value of wind load should be carefully considered for the designer.
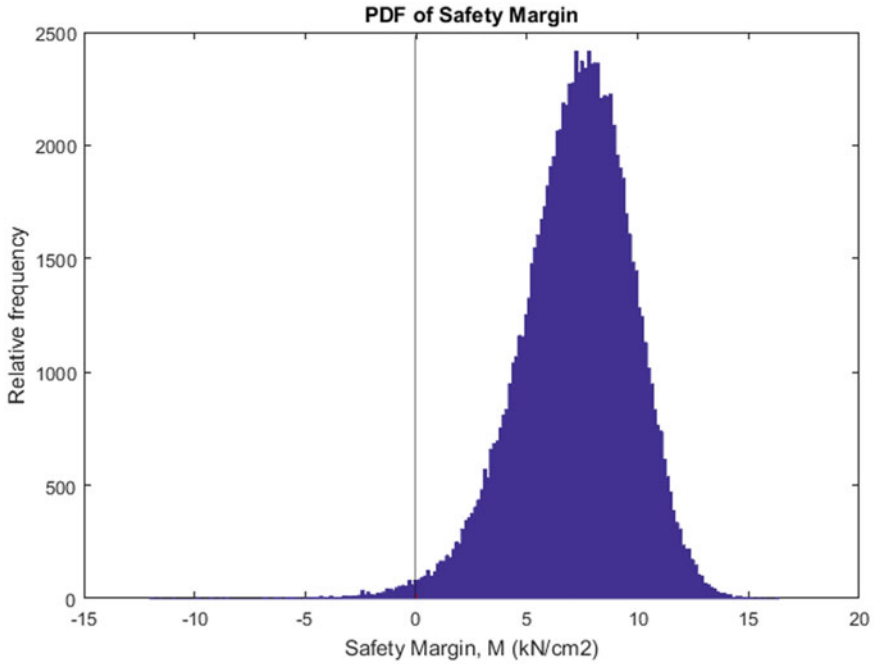
Fig. 9 PDF of safety margin, *M*

Table 6 Target β-values for elements (lifetime), ISO 2394:1998 [30]

Relative costs of safety measures	Consequences of failure			
	Small	Some	Moderate	Great
High	0	1.5	2.3	3.1
Moderate	1.3	2.3	3.1	3.8
Low	2.3	3.1	3.8	4.3

Table 7 Classification of reliability for different periods according to (EN 1990 2002) [32]

Reliability classes	Failure consequences	Reliability index		Examples
	Small	1 year	50 years	
RC3	0	5.2	4.3	Bridges, public buildings
RC2	1.3	4.7	3.8	Residences, offices
RC1	2.3	4.2	3.3	Agricultural buildings

Table 8 Characteristics of reliability of cases with variable CV_{W0}

| S. no.	Characteristic reliability		Variable coefficients of wind pressure, CV_{W0}					
			0.05	0.1	0.15	0.2	0.25	0.3
1	Case 1: $\gamma_1 \approx 0.9$	$P_s=$	0.98295	0.94382	0.89887	0.85632	0.81977	0.79462
		$P_f=$	0.01705	0.05618	0.10113	0.14368	0.18023	0.20538
		$\beta=$	2.12	1.59	1.28	1.06	0.91	0.82
2	Case 2: $\gamma_2 \approx 0.85$	$P_s=$	0.99324	0.96594	0.92869	0.88985	0.85325	0.82708
		$P_f=$	0.00676	0.03406	0.07131	0.11015	0.14675	0.17292
		$\beta=$	2.47	1.82	1.47	1.23	1.05	0.94
3	Case 3: $\gamma_3 \approx 0.8$	$P_s=$	0.99859	0.98486	0.95674	0.92735	0.89473	0.86777
		$P_f=$	0.00151	0.01514	0.04326	0.07265	0.10527	0.13223
		$\beta=$	2.97	2.17	1.71	1.46	1.25	1.12
4	Case 4: $\gamma_4 \approx 0.75$	$P_s=$	0.99968	0.99374	0.9774	0.95387	0.92577	0.90285
		$P_f=$	0.00032	0.00626	0.0226	0.04613	0.07423	0.09715
		$\beta=$	3.41	2.50	2.00	1.68	1.44	1.30
5	Case 5: $\gamma_5 \approx 0.7$	$P_s=$	0.99994	0.99739	0.98751	0.96953	0.95089	0.92638
		$P_f=$	0.00006	0.00261	0.01249	0.03047	0.04911	0.07362
		$\beta=$	3.85	2.79	2.24	1.87	1.65	1.45
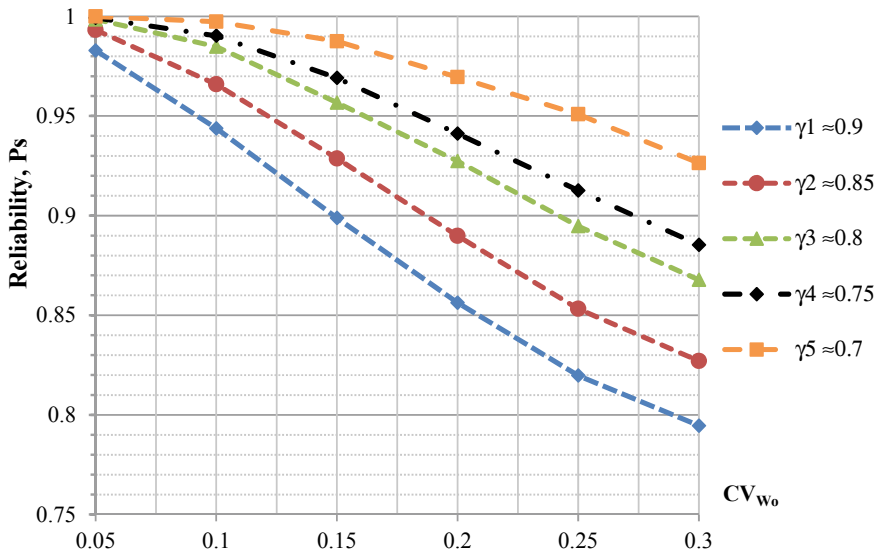
Fig. 10 Analyze the reliability of the structure according to the cases CV_{W0}

The Monte Carlo simulation is used to analyze reliability with the state function being the global stability condition of the billboard column, paying attention to the relationship between random variables (Table 3) and the safety margin.

Also, the analysis of random effects due to column shapes (2 branches, 3 branches, etc.), type of load (dynamic components of the wind, due to subsidence of the ground, etc.), and dimension factors (distance between column branches, branch length, etc.) continue in subsequent studies.

State management agencies need to have regulations and guidelines to evaluate the quality of outdoor billboards overtime to ensure safety for society.

References

1. Son, C.: Hanoi leads the way in number of outdoor billboards (in Vietnamese). Available: https://vtv.vn/kinh-te/ha-noi-dan-dau-so-luong-bien-quang-cao-ngoai-troi-108623.htm. Accessed 22 Nov 2013
2. QCVN: Vietnam building code. QCVN 17:2013/BXD, National technical regulations on the construction and installation of outdoor advertising (2013)
3. QCVN: Vietnam building code. QCVN 02:2009/BXD, Natural Physical & Climatic Data for Construction (2009)
4. TCVN: Vietnam Standard. TCVN 2737-1995, Loads and Effects—Design Standard. Construction Publishing House (1995)
5. Anh, Q.: Ho Chi Minh City: Strictly handle the deadly billboard (in Vietnamese). Available: https://dantri.com.vn/xa-hoi/tphcm-xu-ly-nghiem-vu-bang-quang-cao-do-de-chet-nguoi-20180814194112719.htm. Accessed 14 Aug 2018
6. Tuong, D.C.: Heavy rain with tornadoes overturned the billboard, causing wide power outages (in Vietnamese). Available: https://dantri.com.vn/xa-hoi/mua-lon-kem-loc-xoay-giat-do-bien-quang-cao-gay-mat-dien-dien-rong-1376385641.htm
7. Long, T.: Risk of insecurity from outdoor billboards (in Vietnamese). Available: http://www.baovinhlong.com.vn/xa-hoi/201806/nguy-co-mat-an-toan-tu-bang-quang-cao-ngoai-troi-2897815. Accessed 13 June 2018
8. Nguyen, L.: Catastrophic storms have struck and devastated Nam Bo at the end of the year (in Vietnamese). Available: https://baomoi.com/nhung-con-bao-cap-tham-hoa-tung-do-bo-tan-pha-nam-bo-dip-cuoi-nam/c/24401562.epi. Accessed 25 Dec 2017
9. Monre: Updating storm zones, identifying storm risks, storm surges and wind zones for inland areas affected by storms and super typhoons. Hanoi (2016)
10. Beer, T.: Beaufort wind scale. Encyclopedia of Earth Sciences Series (2013)
11. Khoa, H.: Tornadoes lift up the roofs of many houses in Thu Thiem (in Vietnamese). Available: https://vnexpress.net/loc-xoay-lam-toc-mai-nhieu-nha-dan-o-thu-thiem-3933197.html. Accessed 06 June 2019
12. Thuong, H.: Thunderstorms collapsed and unroofed more than 300 houses in the southwest region (in Vietnamese). Available: https://tuoitre.vn/dong-loc-lam-sap-va-toc-mai-hon-300-can-nha-o-mien-tay-20190716114209763.htm. Accessed 16 July 2019
13. Phung, T., Viet, D.: Hundreds of houses collapsed and lift up roofs due to thunderstorms in Kien Giang and Hau Giang (in Vietnamese). Available: https://www.nhandan.com.vn/xahoi/item/41095702-hang-tram-can-nha-bi-sap-va-toc-mai-do-dong-loc-o-kien-giang-hau-giang.html. Accessed 04 Aug 2019
14. Ohdo, K., Kareem, A.: Reliability analysis of construction scaffoldings system under wind storms. Indiana (2020)
15. Nguyen, L.T., Nguyen, H.S., Tran, V.Q., Nguyen, Q.H.: Impact of wind load on large plate billboards in Vietnam. Int. J. Innov. Technol. Explor. Eng. (2019)
16. Giang, L.T.: Damage cause by strong wind & wind loads standard for building in Viet Nam. Tokyo (2005)

17. Huong, C.T.: Variations and trend of maximum wind speed in Vietnam during 1961–2007 (in Vietnamese). J. Sci. - Univ. Nat. Technol. **3** (2010)
18. Lien, T.: The Report on Zoning of Wind Pressure for Use in Construction Industry over Vietnam (in Vietnamese). Hanoi (2005)
19. Zhu, S.-P., Keshtegar, B., Bagheri, M., Hao, P., Trung, N.-T.: Novel hybrid robust method for uncertain reliability analysis using finite conjugate map. Comput. Methods Appl. Mech. Eng. **371**, 113309 (2020), 01 Nov 2020
20. Bagheri, M., Hosseini, S.A., Keshtegar, B., Correia, J.A.F.O., Trung, N.-T.: Uncertain time-dependent reliability analysis of corroded RC structures applying three-term conjugate method. Eng. Failure Anal. **115**, 104599 (2020), 01 Sep 2020
21. Ho-Huu, V., Duong-Gia, D., Vo-Duy, T., Le-Duc, T., Nguyen-Thoi, T.: An efficient combination of multi-objective evolutionary optimization and reliability analysis for reliability-based design optimization of truss structures. Expert Syst. Appl. **102**, 262–272 (2018), 15 July 2018
22. TCVN: Vietnam Standard. TCVN 5575-2012, Steel structures—Design standard. Construction Publishing House (2012)
23. Rayzer, V.D.: Reliability Theory of Structures. Izd-vo ASV, Moscow (2010)
24. Rackwitz, R., Flessler, B.: Structural reliability under combined random load sequences. Comput. Struct. (1978)
25. Holický, M.: Reliability analysis for structural design (2009)
26. Bartlett, F.M., Dexter, R.J., Graeser, M.D., Jelinek, J.J., Schmidt, B.J., Galambos, T.V.: Updating standard shape material properties database for design and reliability. Eng. J. (2003)
27. Huh, J., Lee, S.Y., Haldar, A.: Reliability evaluation using finite element method. J. Cyst. Fibros. 28–33 (2003)
28. Rzhanitsyn, A.: Theory of Design of Reliable Structures. Stroyizdat, Moscow (1978)
29. Bac, A.H.: Reliability analysis of steel beam under combined bending and torsion. Vietnam J. Constr. 53–62 (2019)
30. ISO: ISO 2394:2015—General Principles on Reliability for Structures (2015)
31. Rackwitz, R.: Optimization—the basis of code-making and reliability verification. Struct. Saf. (2000)
32. Standard, E.: Eurocode 0 - Basis of structural design. Eurocode 0 (2002)
33. JCSS: Probabilistic Model Code—Part 1: Design basis. Struct. Saf. (2001)

A Novel Proposal in Using Viscoelastic Model for Bridge Condition Assessment

Thao D. Nguyen, Hung Q. Nguyen, Toan B. Pham , and Nhi K. Ngo

1 Introduction

The problem of structural health monitoring (SHM) is significant in the civil, mechanical, aerospace and military fields [1]. Generally, damage makes the structure produce abnormal changes sheltered in its measured response [2]. Vibrational responses of structures such as displacement, deformation and acceleration are measurements used commonly. In part due to the hypothesis, the damages change the mechanical parameters of a structure, which will cause changes to the vibrational characteristics of the structure. Vibration-based damage detection (VBDD) is developed rapidly, and an available number of methods have been proposed [3]. By extracting abnormalities (features), VBDD can be used to identify the damage of structures. In assessing the damage condition of a structure, VBDD is divided into four levels: remaining damage, locating damage, quantifying damage and predicting the residual service life of the structure [4]. Most of VBDD methods can be classified into two approaches: model-based methods and non-model-based methods. The model-based method [5] is a model updating procedure form a baseline model, usually a finite element model, which is representative of the healthy structure. In this procedure, the physical parameters of the mathematic model are calibrated using measurement signals as displacement, strain, acceleration or updated using traditional vibrational features such as natural frequencies, damping and mode shapes. However, a main drawback of this approach is that the

T. D. Nguyen · H. Q. Nguyen · T. B. Pham · N. K. Ngo
Laboratory of Applied Mechanics (LAM), Ho Chi Minh City University of Technology, HCMUT, Ho Chi Minh City, Vietnam

H. Q. Nguyen · T. B. Pham (✉) · N. K. Ngo
Ho Chi Minh National University, Ho Chi Minh City, Vietnam
e-mail: baotoanbk@hcmut.edu.vn

T. D. Nguyen
Ho Chi Minh City Department of Transportation, Ho Chi Minh City, Vietnam

mechanical parameters calibrated from the updating procedure may be unrelated to the real state of structural damage, although they are coherent with the measured data. In contrast, in the non-model-based methods, there is no need for a representative model of the structure, and damage is characterized by comparing features between healthy and damage scenarios. Non-model-based methods are more promising in real-life application, especially in the case of the large and complex structures.

A bridge is a typical important structure which operates in complex conditions, including overuse, dynamic load, environmental influences and aging. A bridge often suffers various types of damage such as cracking and fatigue. There are a number of approaches to the modeling of cracks in beam reported in the literature that fall into three main categories: local stiffness reduction, discrete spring model and finite element model. In past, the sensitivity of some vibration-based features to different levels of damage in bridge was evaluated by Farrar and Jauregui [6, 7], using the data collected from the I-40 Bridge on New Mexico. It is demonstrated that the model-based features were not good indicators of damage.

The study proposes an expansion of Hooke's linear elastic model by adding viscous parameter called Kelvin–Voigt's viscoelastic model [8]. In this model, material characteristics contained two parameters such as the elastic modulus E as in Hooke's law and the viscous coefficient C as in Newton's law [9]. The viscous coefficient C is a new component which illustrates changes of material characteristics during the structure's operation. At the same time, the article performs the correlation between the viscoelastic parameters of materials and the vibration parameters. This shows the generalization of the study as it assesses not only the mechanical characteristics but also the changes of materials during the operating time of a structure. Other contribution from the current work is to propose a new feature which is the loss factor function (LF) for assessment of the structure's condition. LF is a function which is easy to calculate from power spectral density function of output signals. This study will focus to establish the relationship between the change of the LF and the material parameters of the structure such as elastic modulus and viscous coefficient.

2 Theoretical Background

2.1 Problem Formulation

2.1.1 The Viscoelastic Model in Bending Vibration Bending of Beams

The governing equation for the bending of thin beams, neglecting shear deformation and rotary inertia, is established by the Euler–Bernoulli beam theory. Thus, Kelvin–Voigt model is selected to describe the viscoelastic properties of beam. The viscoelastic model is described in terms of a parallel combination of an elastic

spring and a viscous damper. The dissipation of the internal energy in the material is expressed by the differential operator of strain. Here, the total strain ε is the same for both spring and damper, whereas the total stress σ is given by the summation of individual strains of elastic and viscous elements [8] as:

$$\sigma(t) = E_b\varepsilon(t) + C_b\frac{\partial\varepsilon(t)}{\partial t} \tag{1}$$

where E_b and C_b are the Young modulus and flexural viscous coefficient of the material. The differential equation of motion for the transverse vibration of beam is formulated as below:

$$E_bJ_b(x)\frac{\partial^4 w_b}{\partial x^4} + C_bJ_b(x)\frac{\partial^5 w_b}{\partial x^4 \partial t} + \rho A(x)\frac{\partial^2 w_b}{\partial t^2} = f_b(x,t) \tag{2}$$

where A, J_b, w_b and f_b are the area of cross section, the area moment of inertia, the transverse displacement and external force of the beam, respectively.

2.1.2 The Viscoelastic Model in Torsional Vibration of Beams

The governing equation of the beams in torsion, with non-circular cross section, assumes the Saint–Venant theory. The dissipation of the internal energy in the viscoelastic material is expressed by Kelvin–Voigt model (three parameters). Here, the total angle strain γ is the same for both elastic spring and viscous damper, whereas the shear stress τ is the sum of the stresses acting on each of the two elements [9] as follows:

$$\tau(t) = E_t\gamma(t) + C_t\frac{\partial\gamma(t)}{\partial t} \tag{3}$$

where E_t and C_t are the shear modulus and torsional viscous coefficient of the material. The differential equation of motion for the torsional vibration of beam is formulated as below:

$$E_tJ_t(x)\frac{\partial^2 w_t}{\partial x^2} + C_tJ_t(x)\frac{\partial^3 w_t}{\partial x^2 \partial t} - \rho J_t(x)\frac{\partial^2 w_t}{\partial t^2} = f_t(x,t) \tag{4}$$

where E_tJ_t, ρ, w_t and f_t are the torsional rigidity and mass density per unit length, the angular displacement and external torque of the beam, respectively.

2.2 Solution Methodology

To analyze the dynamic of a structure, the mode superposition technology has been used to generate the vibration response of the beam, as a function of space and time, under the arbitrary load. The mode superposition method is used to discretize the problem in spatial coordinates and generate a system of differential equation in the time domain [10]. The displacement of the beam is considered as a linear superposition of n modal responses as

$$w = \sum_{r=1}^{n} w_r = \sum_{r=1}^{n} W_r(x)T_r(t) \tag{5}$$

where $W_r(x)$ is the rth eigenfunction, and $T_r(t)$ is the rth generalized coordinate. The generalized system of motion different equations in the time domain becomes

$$\ddot{T}_r + p_r^2 \frac{C}{E}\dot{T}_r + p_r^2 T_r = f_r \tag{6}$$

with p_r and f_r are, respectively, the natural frequency and generalized load of the rth generalized coordinate. Equation (6) is very practical as this research converts a complex problem of multiple degrees of freedom into the basic systems of one degree of freedom. With such conversion, we can understand that transposition w_r at each position x varies corresponding to time t and follows function $T_r(t)$. Therefore, to study the effects of the mechanical parameters on $w(x,t)$, we study their effects on function $T_r(t)$.

Let the generalized load be $f(t) = e^{i\omega t}$. The steady-state response will then be $T_r = H_r(\omega)e^{i\omega t}$, where $H_r(\omega)$ is a complex function. Substituting these into the differential equation and canceling $e^{i\omega t}$ from each side, the frequency response function is then

$$|H_r(\omega)| = \frac{1/p_r^2}{\sqrt{\left[1 - \left(\frac{\omega}{p_r}\right)^2\right]^2 + \left(\frac{C\omega}{E}\right)^2}} \tag{7}$$

In frequency domain, $H_r(\omega)$ can be obtained by taking the Fourier transform (FT) of the input $f_r(t)$ and output $T_r(t)$ as follows:

$$T_r(\omega) = H_r(\omega)F_r(\omega) \tag{8}$$

where $T_r(\omega)$ and $F_r(\omega)$ are the FT of $T_r(t)$ and $f_r(t)$, respectively. A graph showing the relationship between amplitude values and frequencies is called a spectrum. Spectrum value of response is high when force frequency ω approximates natural frequencies. In the analysis, we use dimensionless values by considering the ratio of the response amplitudes at frequencies to the maximum amplitude of the response.

$$\frac{T_{r,\max}}{T_r}(\omega) = \frac{F(p_r)}{F(\omega)} \frac{\sqrt{\left[1 - \left(\frac{\omega}{p_r}\right)^2\right]^2 + \left(\frac{C\omega}{E}\right)^2}}{\frac{Cp_r}{E}} \tag{9}$$

Vibration amplitude depends on mechanical properties including elastic modulus, viscous coefficient, cross section and mass density. This helps to develop a new parameter related to both the natural frequency p_r and elastic modulus E. We find that the amplitude value T_r does not only depend on mechanical properties but also is a function of the forced frequencies. If there are m force frequencies, there will also be m vibration amplitude. In practice, acceleration response will be measured because accelerator is easy to install into structures. In signal processing, continuous data are often analyzed into power spectral density (PSD). Thus, the output PSD (S_T) is equal to the square of the frequency response function multiplied by the input PSD (S_F).

$$S_T(\omega) = |H(\omega)|^2 S_F(\omega) \tag{10}$$

Following [11], PSD of acceleration is related to displacement power spectrum S_T as follows:

$$S_r(\omega) = \omega^4 S_T(\omega) \tag{11}$$

we often use dimensionless values by considering the ratio between the maximum amplitude of the acceleration PSD and the amplitude of the acceleration spectral density at other frequencies.

$$\frac{S_{r,\max}}{S_r}(\omega) = \frac{S_F(p_r)}{S_F(\omega)} \frac{\left[1 - \left(\frac{\omega}{p_r}\right)^2\right]^2 + \left(\frac{C\omega}{E}\right)^2}{\left(\frac{Cp_r}{E}\right)^2} \left(\frac{p_r}{\omega}\right)^4 \tag{12}$$

For viscoelastic material, the maximum strain energy potential Π of the structure will be linearly proportional to the square of the initial strain value ε_0 according to Eq. (13). However, in each cycle of oscillation, the strain energy will be dissipated by a determined amount D according to Eq. (14). And the ratio between the dissipated energy and the initial strain potential is called the loss factor η according to Eq. (15).

$$\Pi = \frac{1}{2} E \varepsilon_0^2 \tag{13}$$

$$D = \pi C \omega \varepsilon_0^2 \tag{14}$$

$$\eta = \frac{D}{2\pi \prod} = \frac{C\omega}{E} \tag{15}$$

Loss factor is completely dependent on basic material parameters such as viscous coefficient C, elastic modulus E and frequency ω. Hence, the loss factor generation can be used to evaluate the overall material condition. Assuming the force input function is a random white noise process, the power spectral density of the force S_F will be constant S_0. Form Eqs. (12 and 15), we have loss factor function (LF) as follows:

$$\text{LF}(\omega) = \frac{\left(1 - \left(\frac{\omega}{p_r}\right)^2\right)^2 \left(\frac{p_r^2}{\omega^2}\right)}{\left(\frac{S_{r,\max}}{S_r}\right) \cdot \left(\frac{\omega^2}{p_r^2}\right) - 1} \tag{16}$$

LF is easy to calculate from power spectral density function of output acceleration. LF is a new proposal to measure energy dispersal based on the structural monitoring data of bridge structures. This study will focus to establish the relationship between the change of the LF and the material parameters of the structure such as elastic modulus and viscous coefficient.

3 Exemplary Results

3.1 Free Vibration

In order to illustrate above-discussed model, example of viscoelastic beams subject to free decay has been performed. The beam is analyzed for the classical boundary condition (simply supported). The geometric and material properties of the beam are given in Table 1. The natural frequencies of beam are given in Table 2.

Table 1 Parameters of the viscoelastic beam

Property	Magnitude	Property	Magnitude
Length (m)	24.5 m	Young's modulus E	3.394 e^{10} Pa
Width	20.6 m	Shear modulus G	1.414 e^{10} Pa
Thickness	1.3 m	Poisson's coefficient	0.2
Material density ρ	2663 kg/m^3	Viscous coefficient C	800 MPa s

Source Laboratory of Applied Mechanics

Table 2 Natural frequencies of viscoelastic beam

Mode	Frequencies (Hz)
First bending	3.506
First torsion	5.805
Second torsion	11.61
Second bending	14.025
Third torsion	17.416

Source Laboratory of Applied Mechanics

3.2 Force Vibration

In theory, under the forces $f(t)$, the beam will undergo in the flexural or torsional state at the same time and the forces are often simplified with constant amplitude in wide frequency band. However, in practice, the vehicle acting on the bridge has random amplitude and frequency. Thus, in order to get the practical results, the study created the random force functions by the sum of the harmonic functions with random frequencies and amplitudes. PSD of the force functions is shown in Fig. 1. We see that at the same frequency, the spectral amplitude value changes randomly and irregularly. Therefore, the force functions used in this study are consistent with the reality by randomizing the PSD of force.

To test the variation of the PSD of response when material properties of beam change, the study used six elastic modulus and six viscosity coefficient (Table 3) to
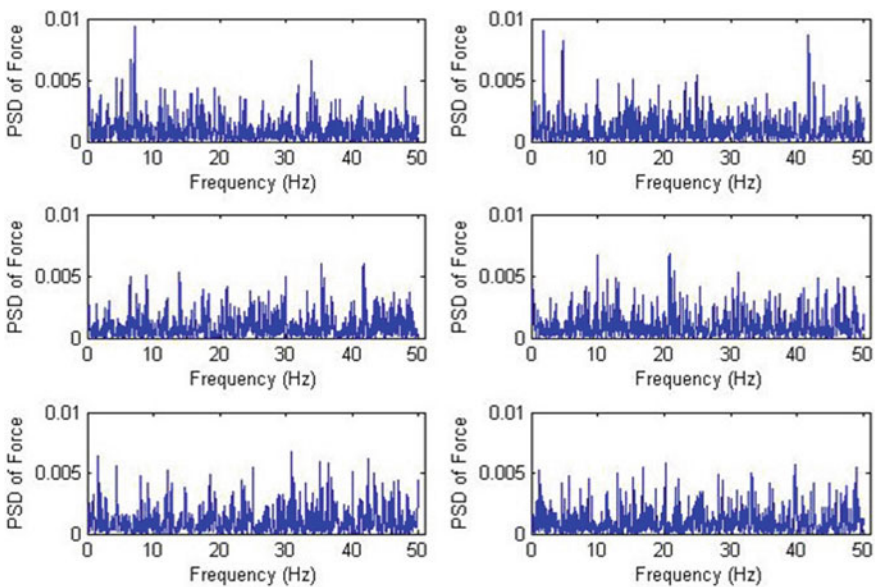

Fig. 1 PSD of random forces. *Source* Laboratory of Applied Mechanics

Table 3 Description of material property cases

Young modulus	Viscous coefficient
$E_1 = E$	$C_1 = C$
$E_2 = 0.9 E$	$C_2 = 1.2 C$
$E_3 = 0.8 E$	$C_3 = 1.4 C$
$E_4 = 0.7 E$	$C_4 = 1.6 C$
$E_5 = 0.6 E$	$C_5 = 1.8 C$
$E_6 = 0.5 E$	$C_6 = 2 C$

Source Laboratory of Applied Mechanics

create 36 pairs of different material parameter values $E_i C_j$. The influence of viscous coefficient on PSD of response is shown in Fig. 2. When viscous coefficient increases, high-frequency domain tends to change from decreasing gradually to disappearing. However, natural frequencies are not less variables.

3.3   Condition Assessment

The LF is calculated from the spectral characteristics of acceleration response, as given in Eq. (16). The LF has n values corresponding to the n pairs of amplitude and frequency in PSD. If the force function is modeled by a white noise which has constant spectral amplitude, the LF will be constant. However, due to the change of force amplitude, LF will have many different values. The LF value is due to factors influencing from the random loads, Young's modulus and viscous coefficient. In this study, each random load will give us a different set of LF values (Fig. 3).

To evaluate the distribution of LF values, the research used statistic concepts such as mean value MLF, variance VLF and coefficient of variation CLF as Eq. (17). Result of MLF, VLF and CLF when material parameters change is shown in Figs. 4, 5 and 6.
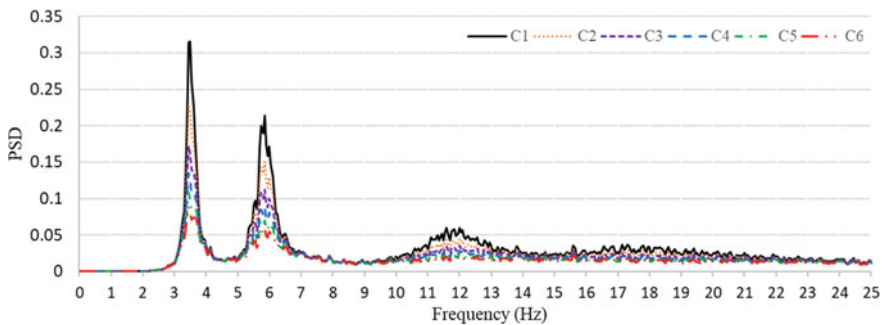

Fig. 2 PSD of response with different viscous coefficients. *Source* Laboratory of Applied Mechanics
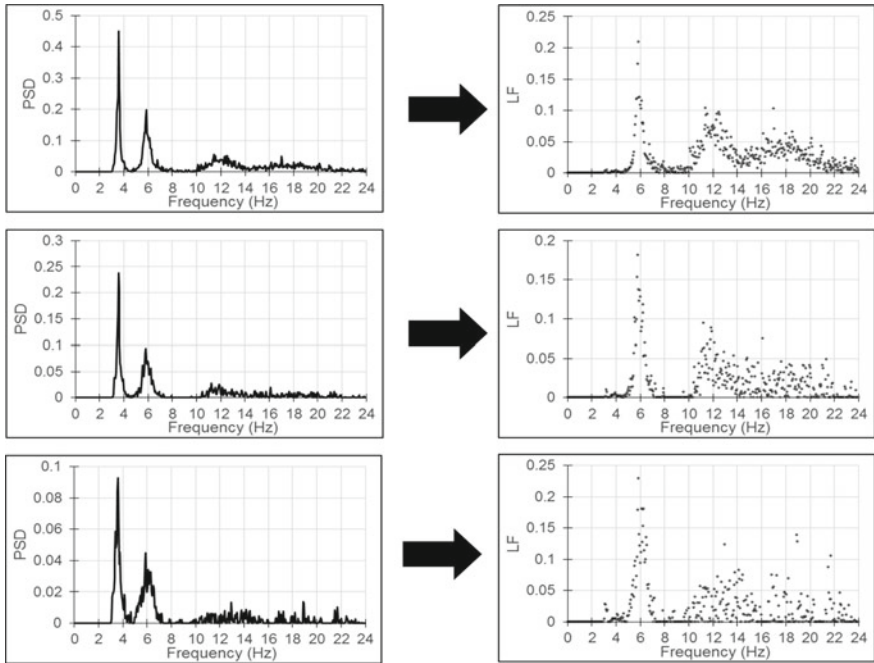
Fig. 3 LF values of some response spectral density. *Source* Laboratory of Applied Mechanics
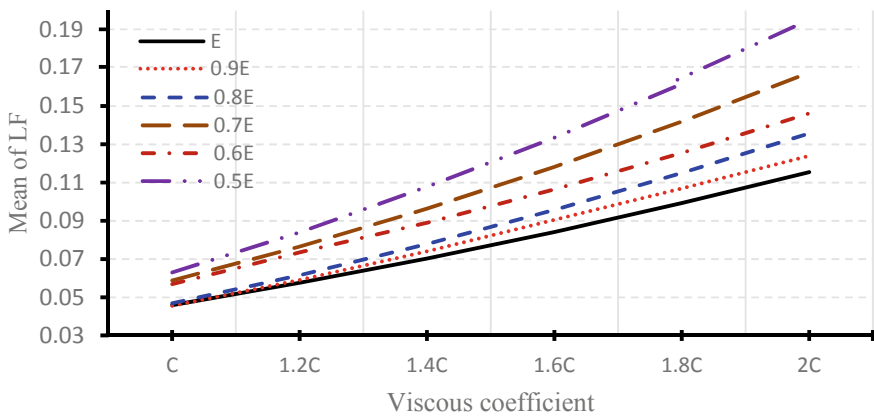

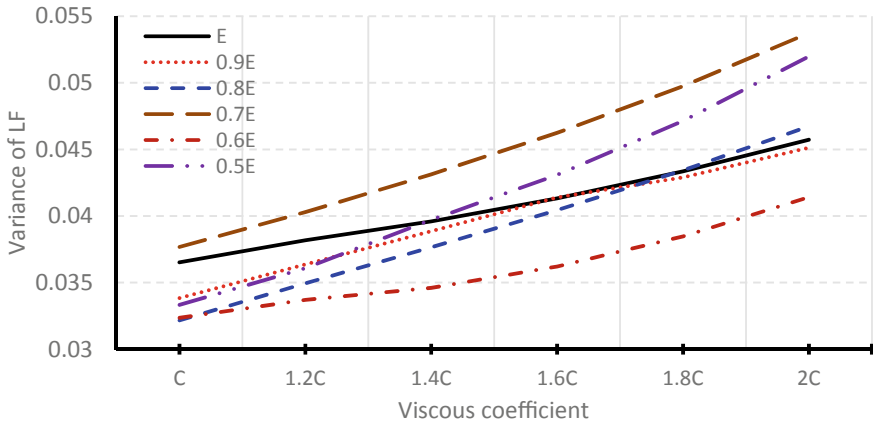**Fig. 4** MLF values when material properties change. *Source* Laboratory of Applied Mechanics

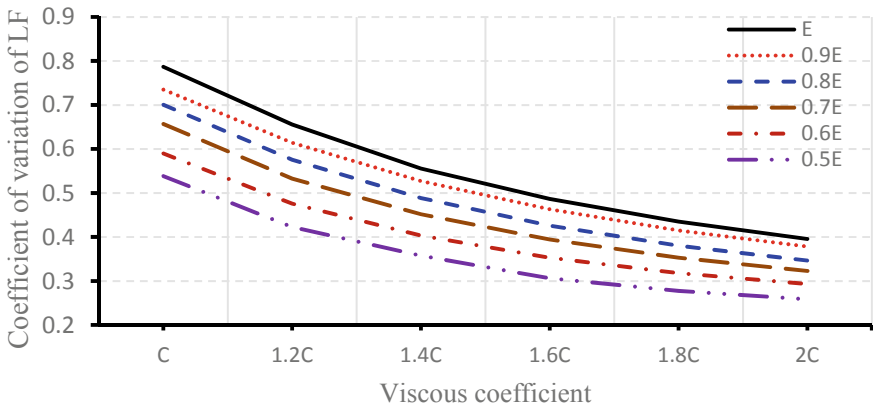**Fig. 5** VLF values when material properties change. *Source* Laboratory of Applied Mechanics

Fig. 6 CLF values when material properties change. *Source* Laboratory of Applied Mechanics

$$\mathrm{MLF} = E[\mathrm{LF}(\omega)]$$
$$\mathrm{VLF} = E\left[(\mathrm{LF} - E[\mathrm{LF}])^2\right] \qquad (17)$$
$$\mathrm{CLF} = \frac{\sqrt{\mathrm{VLF}}}{\mathrm{MLF}}$$

Among the three surveyed statistical quantities, it is easy to see that only CLF value changes clearly when elastic modulus E decreases and viscous coefficient C increases. LCF is a sensitive feature for condition assessment of the beam-like structures such as bridge span when material properties change during operation.

4   Conclusion

This study has used the viscoelastic material model to show the behavior of the mechanical system more consistent with reality. From motion differential equations of bending and torsion mode of the beam, it can be shown that the vibration amplitude of the high-order mode is usually smaller than the low-order mode under random load. In the spectrum graph, the amplitude of the torsional vibrations is declined faster than that of the flexural forms.

   This paper also proposed the concept of the loss factor function LF to track the change in the material property of structure. This LF value is based only on the output signal of the system, so it is suitable for the actual survey of real structures such as bridges. In the statistic quantity of the LF, the coefficient of variance CLF is more stable with random load than the MLF and the VLF. Therefore, this research recommends using the CLF to monitor the degradation of the structure under the effect of random loads.

References

1. Farrar, CR., Worden, K.: An introduction to structural health monitoring. In: New Trends in Vibration Based Structural Health Monitoring, pp. 1–17. Springer (2010)
2. Sinou, J.J.: A review of damage detection and health monitoring of mechanical systems from changes in the measurement of linear and nonlinear vibrations. In: Mechanical Vibrations: Measurement, Effects and Control, pp. 643–702. Nova Science, Hauppauge (2009)
3. Doebling, S.W., Farrar, C.R., Prime, M.B.: A summary review of vibration-based damage identification methods. Shock Vib. Digest **30**(2), 91–105 (1998)
4. Rytter, A.: Vibration based inspection of civil engineering structure. Earthquake Eng. Struct. Dynam. **29**, 37–62 (1993)
5. Fritzen, C.P., Jennewein, D., Kiefer, T.: Damage detection based on model updating methods. Mech. Syst. Signal Process. **12**(1), 163–186 (1998)
6. Farra, C.R., Jauregui, D.A.: Comparative study of damage identification algorithms applied to a bridge: I Experiment. Smart Mater. Struct. **7**, 704–719 (1998)
7. Farrar, C.R., Jauregui, D.A.: Comparative study of damage identification algorithms applied to a bridge: II Numerical study. Smart Mater. Struct. **7**, 720–731 (1998)
8. Amr, M.B.: Active and passive vibration damping. Wiley, Hoboken, NJ, USA (2019)
9. Chakraborty, B.C., Ratna, D.: Polymers for Vibration Damping Applications. Elsevier, New York, NY, USA (2020)
10. Praharaj, R.K., Datta, N.: Dynamic response of Euler–Bernoulli beam resting on fractionally damped viscoelastic foundation subjected to a moving point load. In: Proceedings of the Institution of Mechanical Engineers, Part C: Journal of Mechanical Engineering Science (2020)
11. Newland, D.E.: An Introduction to Random Vibrations, Spectral and Wavelet Analysis. Dover Publications, New York, NY, USA (2005)

Analysis Stability of Tunnel Using Theory Distortion Strain Energy

Vu Thi Thuy Giang and **Do Nhu Trang**

1 Introduction

The evaluation of the stability of the tunnel is a fundamental issue in tunnel engineering [1–3]. For a long time, the stability of tunnel analysis is based on elastic-plastic theory to judge stress–strain relationship and assesses strength criteria of the rock mass. However, the stress–strain of rock mass is usually not linear and scale-dependent due to the fact in the interior structures of the rocks it may be intensely inhomogeneous.

The deformation and failure of disturbed rock by excavation activities are energy-releasing processes release energy stored in the rock [4], changing the stress and strain distributions within the surrounding rock, caused the failure of the rock mass or instability of tunnel.

The ideal tunneling method is one that maintains the conditions of the surrounding rock as it was prior to the excavation. However, since tunnel excavation produces holes in the rock, the dynamic conditions of the surrounding rock are bound to change no matter what tunneling methods adopted.

Distribution of stress in the vicinity of tunnel face right after the excavation is disturbed by tunneling actions, caused locally high stress and strain to dynamic change and strength deteriorations. When strain energy stored in the rock is released completely, a rock will rupture due to over derivation or plasticized rock.

Unlike an elastic condition, a plastic condition causes the rock to undergo not only dynamic change but also a change in material properties. A so-called "loose zone" is simply a zone where plasticization has advanced, and purpose of the design tunnel support is to prevent the ground from becoming plastic [2].

V. T. T. Giang (✉)
Faculty of Civil Engineering, Hanoi Architectural University, Hanoi, Vietnam

D. N. Trang
Faculty of Civil Engineering, University of Transport Technology, Hanoi, Vietnam

Stability of tunnel is governed by the dimension of "loose zone" [2]. Depending on the method of tunnel excavation and support, tunneling may induce considerably different magnitudes of deformation to the surrounding rock, resulting as well in different rock pressure on tunnel linings.

The results of the analysis depend considerably on the modeling of the tunnel and the ranges of significant design parameters. The structural analysis is to provide the design engineer main purposes [5]:

 (i) A clear comprehension of the ground-structure interaction in tunneling.
 (ii) Prediction the principal (kinds, intensity) risks in the tunneling process.
(iii) Back analysis tool for the site observations and correction design (if necessary).

This paper using the theory of shape strain energy was developed by Prof. Matsumoto [3] taking a different look in the theory mechanism of tunnel design by applying the yield criteria for the analytical solution to the stress and the displacement of circular tunnels.

2   Theory of Distortion Strain Energy

If a tunnel is excavated in the rock, distortion strain energies arise around the tunnel corresponding to the depth and to the size of the tunnel diameter [1–3]. In this paper, we propose an analytical solution to evaluate the stress and strain state in the rock around tunnel and define the static conditions of the tunnel. This is to analyze the stability of the tunnel and design the necessary structural support system [2]. If the rock is an elastic and isotropic body, conditions for plasticization are determined by comparison of distortion strain energy arising in the rock, and the capacity of the distortion strain energy is stored in it. Yield in an isotropic substance is not generally caused by volumetric change, but changes in form, i.e., the substance always elastically acts, and the volumetric elastic strain energy stored in the substance increases limitlessly under hydrostatic pressure. The substance, however, yields, when distortion strain energy stored in rock, exceeds a certain limit determined by the yield conditions.

Calculation of yield zone (plastic zone) is analyzed based on the following assumptions.

- Circular hole under bi-axial pressure acting from far field.
- Elastic calculation.

Generally, yield function of rock is represented from six stress components.

$$f\left(\sigma_{xx}, \sigma_{yy}, \sigma_{zz}, \tau_{xy}, \tau_{yz}, \tau_{zx}\right) = C(C: \text{ constant}) \tag{1}$$

Assuming the average principle stress will not drive yield of rocks, yield condition is given as following equation.

$$F = f(\sigma, \tau) - \sigma_m \tag{2}$$

F means "deviation stress," and it will occur due to the disturbance of equilibrium like tunnel excavation. Deviation stress leads the shape strain which is important for estimation of the yield of rock which call distortion strain energy or shape strain energy [3] "U_s".

Distortion strain energy U_s is expressed using the components of the deviator of principal stress $(\sigma_1 - \sigma_m, \sigma_2 - \sigma_m, \sigma_3 - \sigma_m)$ as follows:

$$
\begin{aligned}
U_s &= \frac{1}{2G}[(\sigma_1 - \sigma_m)(\sigma_2 - \sigma_m) + (\sigma_2 - \sigma_m)(\sigma_3 - \sigma_m) + (\sigma_3 - \sigma_m)(\sigma_1 - \sigma_m)] \\
&= \frac{1}{4G}\left[(\sigma_1 - \sigma_m)^2 + (\sigma_2 - \sigma_m)^2 + (\sigma_3 - \sigma_m)^2\right] = -\frac{J_2'}{2G}
\end{aligned}
\tag{3}
$$

In which:

G: shear modulus of the rock mass J_2': second invariant of the deviator of stress.

The distortion strain energy at the time when reaches the limit is called the maximum distortion strain energy. In this paper, value of $\overline{U_s}$ which should be expressed by Von-Mises, and Drucker-Prager criteria.

Before excavation, rock pressure acts as primary stress [1–3]. In the study of elasticity body, it is general practice to adopt a plus value for tensile stress and a minus value for compressive stress. At the H depth, vertical stress is $\sigma_1 = -s = -\gamma H$, and horizontal stress acting from the side can be expressed by k called the coefficient of lateral pressure with $\sigma_2 = \sigma_3 = -ks = -k\gamma H$. Therefore, distortion strain energy stored in the rock before the excavation, as indicated in $U_s^{(1)}$, is obtained by Eq (1) under the condition of $\sigma_1 = -s$ and $\sigma_2 = \sigma_3 = -ks$

$$U_s^{(1)} = \frac{s^2}{2G}\frac{(1-k)^2}{3} \tag{4}$$

In similar, the maximum strain potential can determine $\overline{U_s^{(1)}}$ can reach values depending yield conditions:

$$\overline{U_s^{(1)}} = \frac{s^2}{2G}\frac{\left(\frac{\sigma_y}{s}\right)^2}{3} \text{ (Von Mises's)} \tag{5}$$

$$\overline{U_s^{(1)}} = \frac{s^2}{2G}\frac{\left[2(2k+1)\sin\phi + 3\left(\frac{2C}{s}\right)\cdot\cos\phi\right]^2}{3(3-\sin\phi)^2} \text{ (Drucker-Prager's)} \tag{6}$$

Minus $\Delta U_s^{(1)} = \overline{U_s^{(1)}} - U_s^{(1)}$ is called potential shape strain of rock before excavation. According $\overline{U_s^{(1)}} - U_s^{(1)}$ could judged whether rock at site is an elastic or

plastic, depending on the value $\overline{U_s^{(1)}} - U_s^{(1)}$ is positive or negative and $\Delta U_s^{(1)}$ can determine based on using the yield conditions:

$$\Delta U_s^{(1)} = \frac{s^2}{6G}\left[\left(\frac{\sigma_y}{s}\right)^2 - (1-k)^2\right] \text{ (Von Mises's)} \tag{7}$$

$$\Delta U_s^{(1)} = \frac{s^2}{6G}\left\{\left[\frac{2(2k+1)\sin\phi + 3\left(\frac{2c}{s}\right)\cos\phi}{3 - \sin\phi}\right]^2 - (1-k)^2\right\} \text{ (Drucker-Prager's)} \tag{8}$$

The term $\frac{\sigma_y}{s}$ is called rock strength ratio. When using the yield conditions of Von-Mises as a standard for judgment, the potential of the ground becomes larger as the ground as rock strength ratio $\frac{\sigma_y}{s}$ increases, and the coefficient of lateral pressure k approaches 1. On the other hand, in using the yield conditions of Drucker-Prager, the potential of the ground varies according to the values of the coefficient of lateral pressure k, internal friction angle φ, and $2C/s$ which is called the rock cohesion ratio.

3 Stability of Tunnel Using Theory Distortion Strain Energy

3.1 Stress Distribution After Tunneling

After excavation, the stress of the rock around the tunnel is redistributed. If the rock surrounding the tunnel is an infinitely elastic body (see Fig. 1), the stress distribution in the rock is determined from the plane of elastic theory in polar coordinates (r, θ).

The solution is to find airy stress function $\Phi(r,\theta)$ [1] that satisfied boundary conditions, equilibrium equation of stress, constitutive equation, and strain-displacement relationship:

The stress distribution around the circular tunnel has radius r_0 as in Fig. 1 and is obtained the boundary condition of an infinite elastic body, the vertical pressure of $-s$ is from the vertical direction, and the horizontal pressure of $-ks$ is from the side direction and boundary stress conditions $\sigma_{xx} = -ks; \sigma_{yy} = -ks; \tau_{xy} = 0$. At the perimeter of the tunnel: $r = r_0$ with $\sigma_{rr}(r_0) = 0; \tau_{r\theta}(r_0) = 0$.

If terms $X = r_o/r$, then the stress and displacement of rock surrounding tunnel are given as follows:

Fig. 1 Stress field around circular tunnel [6]
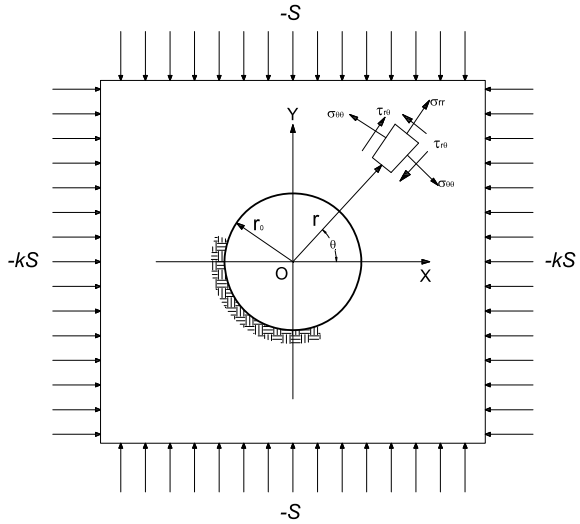
- Stresses:

$$
\begin{cases}
\sigma_{rr}^{(2)} = -\dfrac{s}{2}\left[(1+k)(1-X^2) - (1-k)(1-4X^2+3X^4)\cos 2\theta\right] \\[2mm]
\sigma_{\theta\theta}^{(2)} = -\dfrac{s}{2}\left[(1+k)(1+X^2) + (1-k)(1+3X^4)\cos 2\theta\right] \\[2mm]
\tau_{r\theta}^{(2)} = -\dfrac{s}{2}(1-k)(1+2X^2-3X^4)\sin 2\theta
\end{cases}
\tag{9}
$$

- Displacements:

$$
\begin{cases}
u_r^{(2)}(r,\theta) = -\dfrac{s(1+v_0^R)r_0}{2E_0^R}\left[(1+k)X - (1-k)\left(\dfrac{4}{1+v_0^R} - X^2\right)X\cdot\cos 2\theta\right] \\[3mm]
\qquad u_\theta^{(2)}(r,\theta) = -\dfrac{s(1+v_0^R)r_0}{2E_0^R}(1-k)\left[\dfrac{2(1-v_0^R)}{1+v_0^R} + X^2\right]X\cos 2\theta
\end{cases}
\tag{10}
$$

E_0^R and v_0^R are Young's modulus and Poisson's ratio of rock around circular tunnel under plane stress conditions. To convert to the plane strain condition, substitute the following expressions:

$$E_0^R = \frac{E_R}{1 - v_R^2}; v_0^R = \frac{v_R}{1 - v_R} \tag{11}$$

The correlation between stresses in the Cartesian coordinate system is as follows [1, 3]:

$$\sigma_{xx} = \sigma_{rr} \cos^2 \theta + \sigma_{\theta\theta} \sin^2 \theta - 2\tau_{r\theta} \cos \theta \sin \theta$$
$$\sigma_{yy} = \sigma_{rr} \sin^2 \theta + \sigma_{\theta\theta} \cos^2 \theta + 2\tau_{r\theta} \cos \theta \sin \theta \tag{12}$$
$$\tau_{xy} = (\sigma_{rr} - \sigma_{\theta\theta}) \cos \theta \sin \theta + \tau_{r\theta}(\cos^2 \theta - \sin^2 \theta)$$

The potential distortion strain energy $U_s^{(2)}$ of field stress in the unsupport excavation is obtained with state of plane stress: $\sigma_{zz} = \tau_z\theta = \tau_{zr} = 0$ and $\sigma_m = (\sigma_{rr} + \sigma_{\theta\theta})/3$:

$$U_s^{(2)} = \frac{1}{6G}\left[(\sigma_{rr} + \sigma_{\theta\theta})^2 - 3\sigma_{rr}\sigma_{\theta\theta} + 3\tau_{r\theta}^2\right] \tag{13}$$

In which:

$$U_s^{(2)}(k, X, \theta) = \frac{s^2}{24G}\begin{bmatrix}(1+k)^2(1+3X^4) + 3(1-k)^2 \\ .(1+4X^2 - 2X^4 - 12X^6 + 9X^8) \\ + 2(1-k)(1+k)(5X^2 - 6X^4 + 9X^6)\cos 2\theta \\ - 8(1-k)^2(3X^2 - 5X^4)\cos^2 2\theta\end{bmatrix} \tag{14}$$

The value of average stress σ_m:

$$\sigma_m = -\frac{s}{3}\left[(1+k) + 2(1-k)X^2 \cos 2\theta\right] \tag{15}$$

The maximum potential distortion strain energy $\overline{U_s^{(2)}}$ of the unsupported tunnel depends on yield conditions by replacing σ_m in Eqs. (5 and 6):

- Von-Mises's yield condition:

$$\overline{U_s^{(2)}} = \frac{s^2}{2G}\frac{(\sigma_y/s)^2}{3} \tag{16}$$

- Drucker-Prager's yield condition:

$$\overline{U_s^{(2)}} = \frac{s^2}{2G} \frac{4[(k+1)\sin\phi + 2(1-k)X^2\cos 2\theta.\sin\phi + 3(C/s).\cos\phi]^2}{3(3-\sin\phi)^2} \quad (17)$$

Value $\Delta U_s^{(2)} = \overline{U_s^{(2)}} - U_s^{(2)}(k,X,\theta)$ is called was stored potential distortion strain energy of rock in the unsupported tunnel, and it is possible to evaluate whether the rock around tunnel will be plasticized or not without any support by finding the potential for the rock. If $\overline{U_s^{(2)}} > U_s^{(2)}(k,X,\theta)$ is satisfied, then the surrounding rock of the tunnel will not plasticize and stability without a support system. Otherwise, $\overline{U_s^{(2)}} < U_s^{(2)}(k,X,\theta)$ the rock around the tunnel is instability and needs a support system, which can be defined as below (Fig. 2; Table 1):

$$\frac{\sigma_y}{s} > (1+k) + 2(1-k)\cos 2\theta \,(\text{Von}-\text{Mises}) \quad (18)$$

$$\frac{2(1+k)\sin\varphi + 4(1-k)\cos 2\theta \sin\varphi + 3\left(\frac{2c}{s}\right)\cos\varphi}{3-\sin\varphi} \,(\text{Druker}-\text{Prager}) \quad (19)$$
$$> (1+k) + 2(1-k)\cos 2\theta$$

Fig. 2 Displacement around circular tunnel [6]
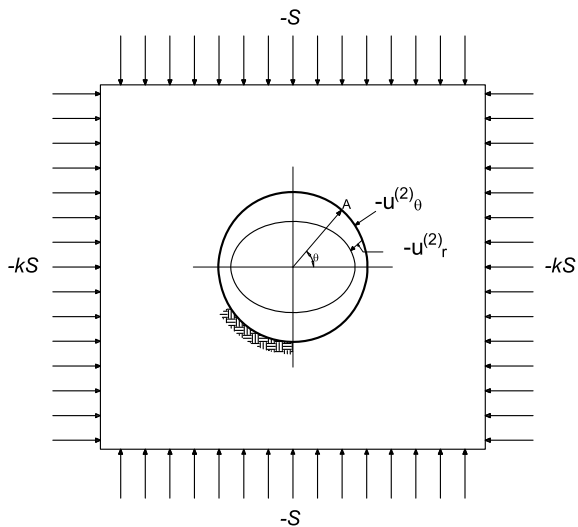
Table 1 Input data

Rock properties	Unit	Value
Vertical pressure S	MPa	5.4
Tunnel radius r_0	m	3
Tunnel depth	m	200
Elastic modulus of rock mass E_R	MPa	1822.4
Poisson's ratio of rock mass ν_R	–	0.3
Cohesion of rock C	MPa	1.638
Internal friction angle of rock φ	deg	54.43
Uniaxial yield stress σ_y	MPa	8.5

4 A Case Study Analysis Stability Tunnel

In this section, the analysis using MATLAB program for tunnel stability analysis is according to lateral earth pressure $k = 0.5$; 1; 1.2 and comparison plastic or "loosened zone" between simulation models in Von-Mises and Drukcer–Prager' yield condition (Fig. 3).

Figure 4 indicates significantly different results calculated by yield criteria (Von-Mises and Drucker-Prager); therefore, determine an appropriate yield criterion for the stability of circular tunnels. From the analysis, it is found that the Von-Mises's yield criterion is characterized by σ_y/s value, and the limit value of distortion strain energy is a function of uniaxial stress σ_y, which the higher uniaxial strength accumulates more energy before plasticization.

When the yield condition of Drucker-Prager used, the maximum distortion strain energy $\overline{U_s}$ of rock is a function of cohesion c, internal friction angle φ, and main stress σ_m. The larger value of σ_m becomes for the compression side; the more distortion strain energy is required to cause yield. That is, the deeper the excavation proceeds, the larger energy needed to plasticize the rock. However, since the rock
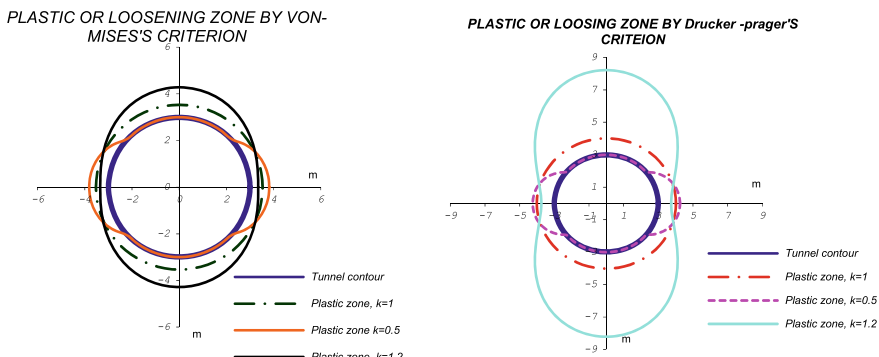

Fig. 3 Comparison "loosened zone" between Von-Mises and Drucker-Prager' yield condition
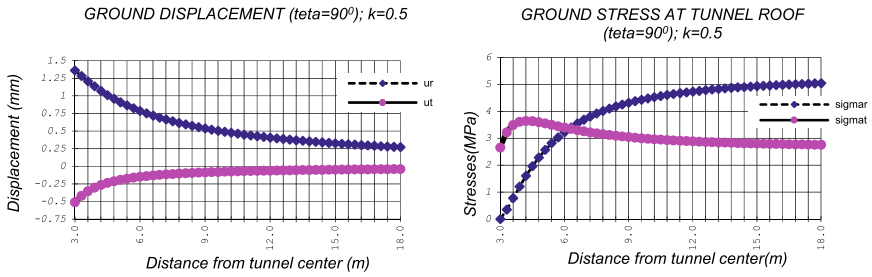
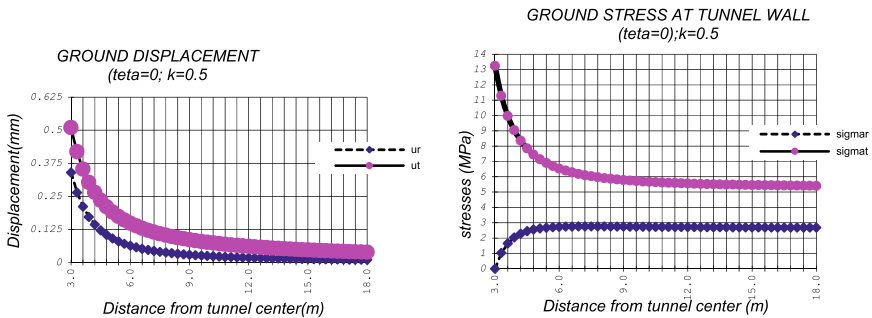**Fig. 4** Stress and displacement at tunnel roof with $k = 0.5$

Fig. 5 Stress and displacement at tunnel wall with $k = 0.5$

pressure acting against a tunnel increase in proportion to the depth of excavation, more deviator stress accumulates with depth, depending on the condition of the ground. This means that deeper tunnels are not always safer (Figs. 5 and 6).

The results in Figs. 7 and 8 indicate hydrostatic pressure is an ideal state for uniform pressure in circular tunnel, and the structural failure of rock could result in strength deterioration (Fig. 9).
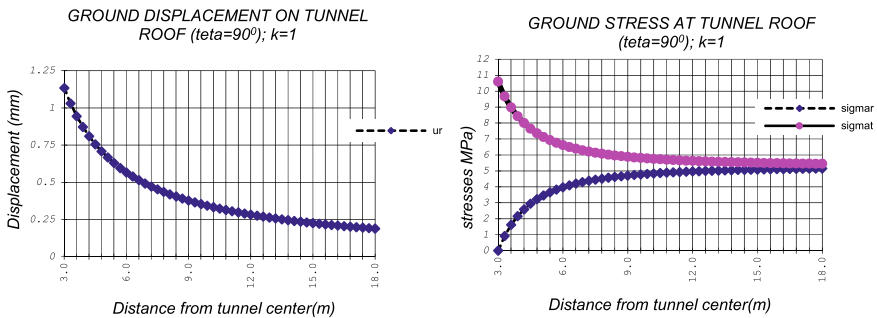

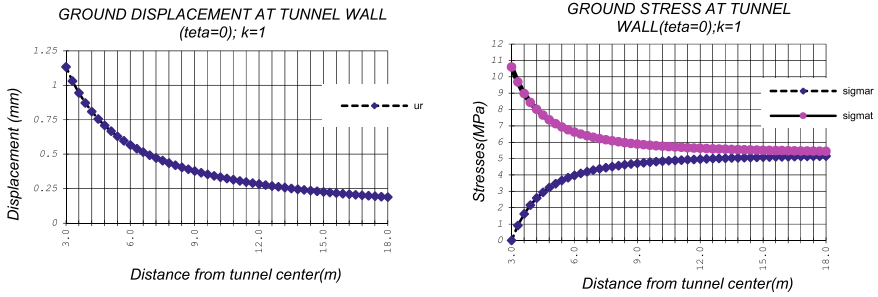**Fig. 6** Stress and displacement at tunnel roof with $k = 1$

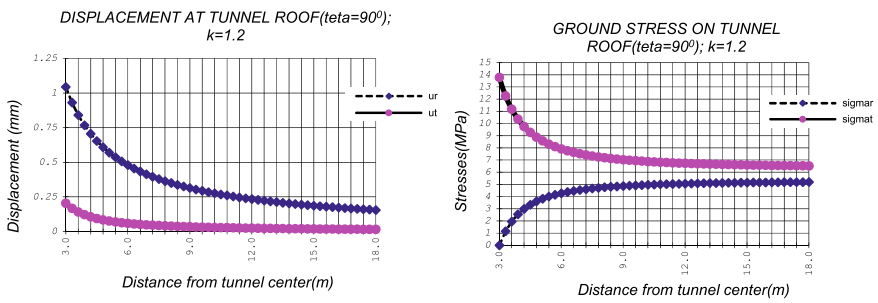**Fig. 7** Stress and displacement at tunnel wall with *k* = 1

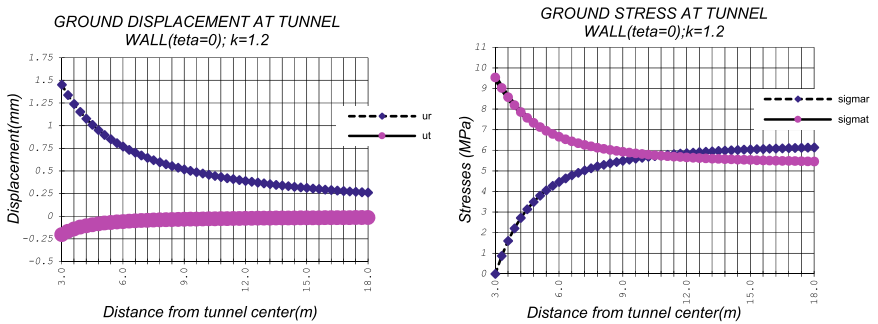**Fig. 8** Stress and displacement at tunnel roof with *k* = 1.2

Fig. 9 Stress and displacement at tunnel wall with *k* = 1.2

5 Conclusions

The strain energy released in the rock mass plays an important role in the structural failure of the rock. The analytical solutions in this paper are based on the proposed unified linear yield, and they have applicability in theory tunnel mechanics. These analytical solutions can generate a range of theoretical significances, include both stress-displacement results, and implement results that can be more comprehensive with the yield criteria.

The results also indicate the mechanism failure of the rock and effect of lateral pressure ratio in the stress–strain relationship of the rock around the circular tunnel.

The solution of the distortion strain energy theory in tunnel mechanics has great significance in analytical design of the tunnel to verify the numerical simulation analysis. The solutions result from the case study above using the distortion strain energy theory in tunnel mechanics have great significance in the analytical design of the tunnel to verify the numerical simulation analysis.

References

1. Tráng, D.H.: Rock Mechanics and Underground Structural System Interaction (Vietnamese). Army Publishing House, Hanoi (2002)
2. Xie, Heping, et al.: Energy analysis and criteria for structural failure of rocks. J. Rock Mech. Geotech. Eng. **1**, 11–20 (2009)
3. Széchy, K.: The Art of Tunnelling. Akadémiai kiadó budapest, Hungary (1970)
4. Guidelines for the Design of Tunnels. TUST **3**(3), 237–249 (1988)
5. Carranza-Torres, C., Fairhurst, C.: Application of the Convergence-Confinement method of tunnel design to rock masses that satisfy the Hoek-Brown failure criterion. Tunn. Undergr. Space Technol. **15**, 187–213 (2000)
6. Matsumoto, Y., Nishioka, T.: Theoretical Tunnel Mechanics. University of Tokyo press, Japan (1991)

Multi-Utility Tunnel (MUT) and Its Application for Urban Cities in Vietnam

Giang Thi Thuy Vu and **Trang Nhu Do**

1 Introduction

Building sustainable cities with rapid urbanization is a challenge for any country. Going underground for utility infrastructure systems has proven to be an effective solution due to benefits [1–4]:

- Reducing the needed surface area and frequency repeat surface excavation.
- Reducing traffic congestion and improving urban environmental quality: disruption to traffic and services, street maintenance requirements, noise, vibration, and dust.
- Contributing to reducing energy consumption.
- Increasing the area of land use.
- Effective producing, storing, and sharing energy: easier for maintenance, upgrading, and future expansion.
- Reducing corrosion and increasing longevity of pipelines by isolating them from the surrounding.
- Improving the water supply system and sewage treatment.

The utility tunnel has existed since the ancient period. Sewage systems in Roman Empire are known as the world's earliest utility tunnel. Such system was forgotten during the Middle Ages [1]. Until 1855, the urban utility systems of Paris were resurrected by Haussman's project incorporated several water supplies pipelines, and sewer [1] basically introduced the utility concept.

There are many different names for MUTs, such as "Utilidors" (America), common service tunnels (Singapore), common utility tunnels (Malaysia), common

G. T. T. Vu (✉)
Faculty of Civil Engineering, Ha Noi Architectural University, Hanoi, Vietnam

T. N. Do
Faculty of Civil Engineering, University of Transport Technology, Hanoi, Vietnam

utility enclosures (Hong Kong), common utility ducts (Taiwan), and les galeries multiréseaux (France) [5]. However, in general, a multi-utility tunnel is defined "any system of an underground structure containing one or more utility service which permits the placement, renewal, maintenance, repair, or revision of the service without the necessity of making excavation; this implies that the structure is traversable by people and, in some cases, traversable by some sort of vehicle as well" (after [3]).

Multi-utility tunnels are solutions in areas where traffic and densed utilities are critical. This solution allows for direct access (without trenching) to the infrastructures located in the tunnel and to operate any kind of operation (repair, maintenance, replacement of components, …). Multi-utility tunnel services accommodate pipelines (supply facilities such as electricity, gas, water supply, telecom, sewer, etc.) essential to the daily life of the urban citizens, thereby improving aesthetics, preventing disasters, preserving road structures, and smooth urban transportation.

Urban utility includes [2]:

- Water distribution system.
- Wastewater collection system.
- Landscape irrigation water supply system.
- Urban stormwater drainage system.
- Gas network medium and low pressure.
- Power supply, including high voltage that supplies primary substations, medium voltage low voltage.
- Telecommunication networks.
- Fiber optic networks including intelligent transportation system, traffic control system, closed circuit TV, and police.
- District heating/cooling network.
- Power for public street lighting.

Thus, services mentioned above, the dimension of the MUT is varied on the demand for pipelines installation, including utility type being housed, utility size, and interior requirements (features of accommodation: pipe brackets and separation sections) (Table 1).

There are two main types of utility tunnels: "searchable" and "visitable" [1] utility tunnels. "Searchable" type is the case where people can access the tunnel through removable roof panels, but personnel entry along its length is not possible due to its reduced cross section. The alternative type has accessible interior throughout their length and called "visitable."

In addition, consideration of depth, location, and connectivity is important when installing MUTs. They can be installed at different depths: burial, shallow, and deep.

Figure 1 illustrates the classification of multi-utility tunnels based on their depth.

Table 1 Typical installation, shape, and material of multi-utility tunnel [4]

Type	Installation	Shape	Material
A. Searchable	R—Road	I. Trapezoid	a. High density polyethylene (PEHD)
B. Visitable	P—Pavement	II. Rectangular	b. Cast in-situ concrete
C. Compartmentalized	M—Metro	III. Rectangular with lid	c. Pre-cast concrete sections
		IV. Circular	d. Steel
		V. Oval with gutter	e. Brick and mortar
		VI. Telescope	f. Shotcrete lining

Fig. 1 Different types of MUT construction [3]

(a) Flush-fitting

(b) Shallow

(c) Deep
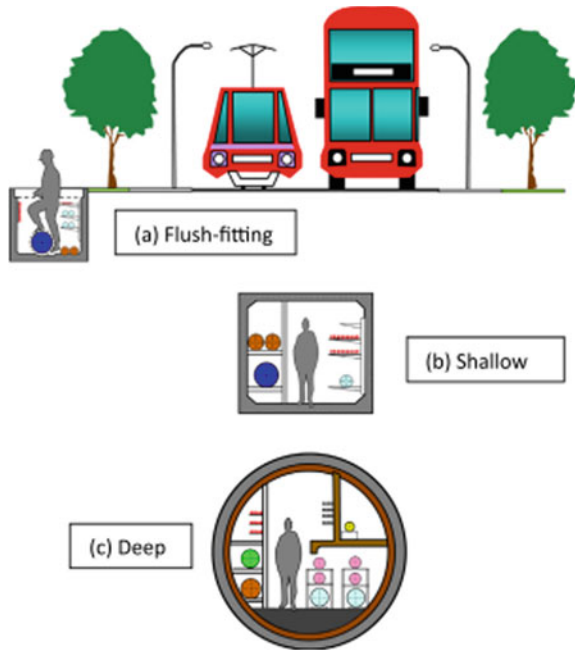
2 Characteristic Utility System in Urban of Vietnam

Sewer system like those in Paris has existed in Vietnam since the French colonial period. In 1897, Paul Doumer—the Governor-General of Indochina [6]—planned to transform Hanoi into a city of order, urbanism, and renovation and to make the first step toward building a "civilized" city including the construction of an underground sewer system. Hanoi was then successfully transformed into new urban space. The reformed, renovated, and modernized thirty-six streets old Hanoi became a symbol of civilization among the French colonies. The 14 km underground network was considered a success until it became a haven for rats to breed

in. Due to the fear of bubonic plague becoming a health crisis, and the failure of rat massacre's plan, all the sewers were closed [6].

In Saigon, the city's sewer system, one of the French colonies' greatest urban achievements, remained after 150 years [7]. The old sewers have a different width ranging from 1.8 to 2.35 m and height ranging from cramped 0.5 meters to 0.5 meters high. All is made of brick and mortar, suffering from erosion, loss of structure (brick and mortar), and degrade by cracks (Fig. 2).

Until the 90s, after "Doi moi" program [8], Vietnam has been in the process of soaring urbanization. However, the poor infrastructure planning and spontaneous urbanization induce the asymmetry of utility—transport–construction, leading to the urban infrastructure be overloaded. The rapid development and expansion of the urban areas have been boosting the need to complete the urban utility system for sustainable development.

There are two types of urbanization: planned urbanization and spontaneous urbanization in large cities such as Ho Chi Minh or Hanoi. The consequence of this is the difficulty in synchronizing the development of underground utilities in spontaneous urban areas. On the other hand, in the old quarter of Hanoi and Ho Chi Minh city where there remain many generations of families living in a cramped space, there has been no appropriate plan for construction utilities such as MUTs due to the overlap of new and old services.

The overlap of urban utility is a serious issue for the sustainable development target of Vietnam. Most urban utilities are individual burial pipelines belonging to various municipal management sectors. They are mainly constructed on side road

Fig. 2 Sewer tunnel in Saigon (in French colonies period) [7]

by the trench method called culverts, generally, type searchable box/circular shape permitted work in a manhole. Some of them have large box shape that permit people to work in.

Consequently, underground pipelines are great challenges for road maintenance and conservation of urban surface. In some cases, renewing, replacing, and extending the pipelines cause inconvenience such as noise, dust, risk, and other negative effects on the urban landscape.

The commonly seen network of electricity and telephone cables installed in messy manner in urban cities of Vietnam, disrupts the urban landscape, poses potential risks to the safety of the citizen's lives.

The situation of overlapping infrastructure sectors on the main roads causes waste in investment, repeated excavation, and frustration among the cities's resident.

In Figs. 3, 4, and 5 present potential risk and poor urban management in Vietnam.

The poor urban planning induces the lack of policy and neglect of state attention to core requirements at the correct location, scale, and on the significant issues in an underground utility network, caused an extremely mess of underground pipe. On the other hand, a recent report by the World Bank [8] states that the most adverse impacts of climate change are likely to be in urban areas where people, resources, and infrastructures are concentrated. Hanoi and Ho Chi Minh city are areas at risk regarding the lowland of the river delta and the effect of climate hazards such as floodings, subsidence surface, dewatering, and sea-level rise.

Due to its historical heritage, the biggest challenges in urban development in Vietnam are the shortage of public underground utility regulation and database management. In each sector (power, telecom, water supply, sewer….), utilities have their own regulations and do not match each other. A strong element of the centralized planning system in Vietnam was the idea of planned economies. This approach often does not consider the value and the force of market dynamics. Government interventions through urban planning and regulations, housing policy, and infrastructure investment have a great impact on the development process.

Fig. 3 Images of overhead lines—a mess for repair or replacement [9]

Fig. 4 Inconvenience of urban life in Vietnam when replacement or installation utility and road surface reimbursement [9]

a). Non break surface   b). Open cut
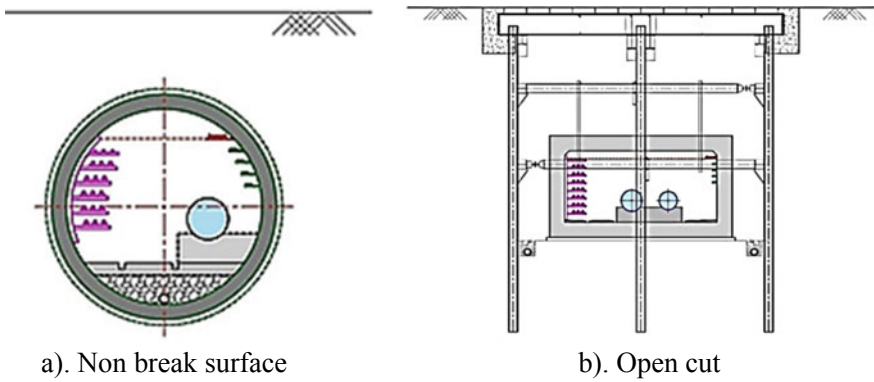
Fig. 5 Ilustration of the MUT excavation methods [5]. **a** Non-break surface. **b** Open cut

Much of the planning process in Vietnam is increasingly based on the physical design (not on socio-economic realities) without taking account of the culture, urban characteristics, and climate regions.

3 Multi-Utility Tunnel (MUT) for Sustainable Development in Vietnam's Condition

The use of multi-utility tunnels creates greater opportunities for the use of underground space in cities by sharing facilities benefits (tunnels, garages, basement, etc.). For areas where infrastructures are still burial pipes for water, gas, district heating/cooling, or are overhead lines (electricity and telecommunication cables),

the utility tunnel represents an innovation for urban cities. In addition, installing the network of multi-utility tunnels increases the reliability of its operation and allows for the repair/replacement of pipes without trenches and the obstruction of traffic. As a result, considering the lower costs of a network's operation and the lower social costs of cities resulting from the lack of communication obstacles for investments, more expensive multi-utility tunnels are technically and economically viable when considering their lifetime.

Principles for planning an urban technical underground system network [2]:

- Ensure sufficient essential space to arrange pipes during the project life cycle.
- Meet the urban development and planning according to each region and each period.
- Meet the requirements of standard lines, pipes, and equipment available.
- Can reduce the frequency of excavation.
- Ensure feasible technical tunnel works, rationally and systematically arranged, achieve the highest economic efficiency in the process of urban development.
- Combine effectively with preventing accidents and natural disasters caused by climate change.
- Combine construction with other infrastructure projects.
- Sufficient space for other underground routes or pavement structures of newly built roads.

On the other hand, when planning for a multi-utility tunnel, we need to consider other factors such as the lifecycle of infrastructure. Due to the speed of technological advancement, especially in the ICT sector, infrastructure equipment may become obsolete within 10 years [10]. Typical lifecycle of IT is 5 years, similarly, rail and signal (15-20 years), road surface (20 years), electricity (20 years), data center 20 years, stormwater drainage (30 years), water pipe (100 years), and sewerage (100 years) [2].

Furthermore, the extensive development of tunneling technology and the application of the advanced material solutions used in the construction of tunnels enable multi-utility tunnels.

The following considerations should be accounted for in designing utility tunnels according ITU [2]:

- Wet utilities should be installed in a separate compartment from the dry utilities.
- Tunnels should be designed walkway access through the system and allowing for removal and replacement of valves, expansion joints, etc.
- Tunnels may typically have a minimum height of 1.9 m and the width of 0.7 m.
- Tunnels should be accessible through entrances with a manhole or sloping walkways.
- Tunnels should be installation ventilation; ventilation shafts should be constructed at a minimum spacing of 50–75 m or as deemed necessary based on actual tunnel dimensions.

It is an challenge for planners to design their infrastructure in world where there are modern technologies such as the Internet of Things (IoT), self-driving cars, virtual reality (VR), robots, and wireless become actualization of civil life [2]. In addition, provision of stormwater drainage is a consideration for cities that are more prone to the negative impacts of climate change.

All the issues mentioned above are important parameters that must be considered at the beginning of any MUT project.

To apply MUT projects in Vietnam, there are two main issues to be proposed in this paper:

- Selection of tunneling technology and cross-section layout.
- The mechanism of cost/benefit sharing and allocation of construction management of stakeholders suitable in Vietnam's conditions.

Selection of tunneling technology and tunnel cross-section layout: In Vietnam urban's condition, construction of multi-utility tunnels must carefully consider the possibility of complicated geological conditions of soft ground and high population density. The presence of groundwater, which is a resource to the city's daily life, needs to be protected from pollution.

The trenching method adopted a traditional, cheap, and flexible method in urban areas under planning, with a large enough surface area for open excavation construction. For densely populated, traffic-critical areas, and the ditching method will be ineffective due to traffic congestion, dust, noise, and environmental pollution.

The optimal economic and technical construction method of a multi-utility tunnel needs analysis of geological conditions, geometrical characteristics, length of the tunnel and connectivity with facilities, etc.

For example, in Fig. 6 is different typical arrangement cross section of technical tunnels in National Road N032 (Hanoi) constructed by cut and cover method (shallow tunnel). The size of 1.6 m × 2.0 m and 1.6 m × 1.4 is not reasonable, with 1.6 m in height, technicians cannot move around in the tunnel, and there is no ventilation or lighting system while the inner distance from 0.65 to 0.8 m … Obviously, these systems are not suitable for the use of underground works in urban areas.

Trenchless construction methods can be implemented for new tunnel construction as well as for renewal purpose, with vary tunnel diameter depends on trenchless technology as shown in Fig. 7.

In Vietnam condition, a recommendation in this paper for choosing technology tunneling is TBM method or deep tunnel for the main utility system, constructed along the main road, and incorporated with surface management, because trenchless technologies reducing the number of surfaces (road, pavement) cuts, can help maintain order, ensure that the repairs are done, and encourage utility companies sharing resources and operations. But for detail, agencies need an elaborated study technical parameter of deep utility tunnel in aspects: technology, safety, management… from foreign experience and justified for Vietnam's condition.
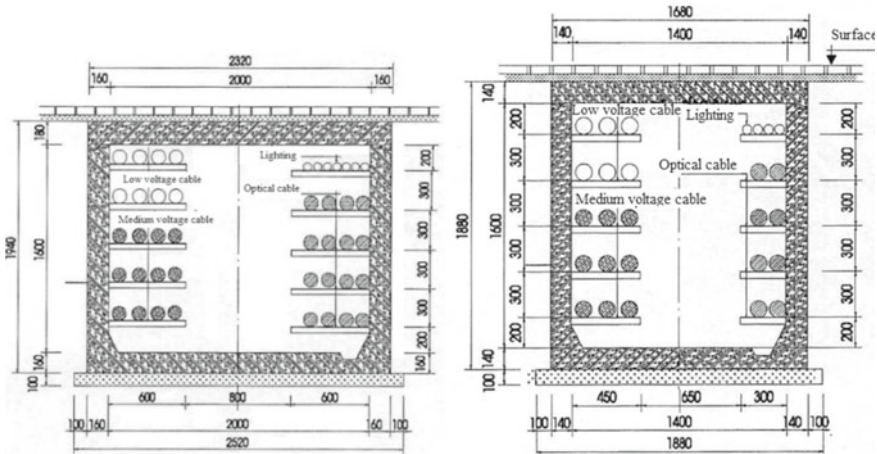
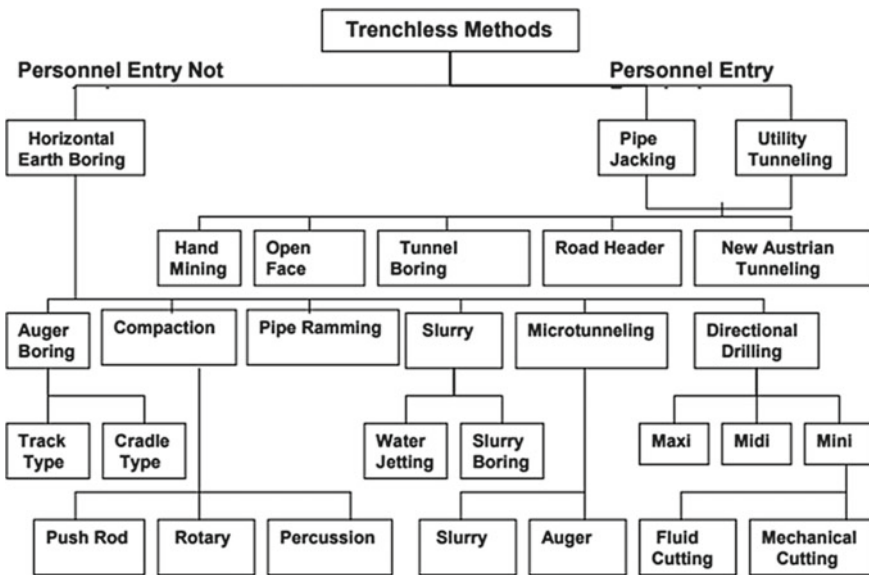**Fig. 6** The cross section of cut and cover tunnel in National Road Nᵒ32 [9]

Fig. 7 Classification systems for trenchless methods [10]

Mechanism allocation construction management: Construction and maintenance costs are the main costs of an urban utility tunnel [11]. The more pipelines are laid in the MUT, the more the underground space is needed and so the higher safety requirement that causes the expensive construction cost of a MUT project. The benefits of MUT are indirect and lying within a long-term perspective, involving special public benefits such as no disruption of the road, no traffic

interruption caused by trenching, and effective using surface land area. However, relevant data is difficult to quantitate. The concern of pipeline stakeholders is the allocation of the construction cost, which is much higher than the cost of traditionally buried pipelines. The main factors to be considered in cost allocation mechanism among companies include (i) the proportion pipelines area occupied in MUT, (ii) the cost of buried direct individual pipeline, (iii) the economic benefits of the maintenance reduction cost of laying pipeline in MUT (compared with the traditional buried pipeline) and the reasonable return on investment in MUT construction.

The infrastructure sectors need more research on evaluating investment opportunities based on the Plan–Do–Act principle. In addition, agencies need to research on technical standards, seize opportunities, and promote investment in MUTs.

4   Conclusion

In the twenty-first century, urban areas are increasingly dependent on utilities such as electricity, communications, supply water, and dispose of waste. To achieve the goal of sustainable urban, urban infrastructure must be focused and developed in which a multi-utility tunnel is a sustainable trend bringing long-term benefits to the city.

To achieve efficiency in urban sustainable development by application MUT in Vietnam, the following issues need to be of focus:

- Effective urban planning: The current planning mechanisms, inherited from the command-and-control era, are obsolete. Avoid spontaneous underground utility development in rural regions in Vietnam where continue to increase in population numbers. Updating urban planning mechanisms with the aim that will best help authorities manage the development of the city-region, involve society, and private enterprises.
- Update technology management includes financial and allocation cost mechanisms and professional tunneling technology, improving the environment and urban administration fields must be trained to ensure the ongoing implementation of the new planning MUT projects.
- Getting ready to face climate change: In the twenty-first century, global warming and seawater rise impact almost city of Vietnam, while urban management policy has been primarily designed for the short-term coping applications of infrastructure development, large neglecting the impacts, and challenges of climate change in urbanized and urbanizing areas. To have a comprehensive and sustainable solution, indeed studies on the impacts of climate change on technical infrastructure are required by managing disaster response with preventive engineering that should be carefully considered such as stormwater tunnel, restoration/expansion of groundwater drainage networks in vulnerable areas.

- Update technology tunneling: As technology advances, the ability to perform trenchless utility installation such as tunnel boring machine (TBM) and micro-tunneling and also pipejacking or HDD technology will also advance, allowing a progressively greater proportion of such work to be completed with high efficiency.
- Update and supplement to promulgate national technical regulations and specific technical standards. It is necessary to develop a mechanism to encourage utility companies (power, water supply, telecom, sewage…) to participate in MUT projects.

References

1. Cano-Hurtado, J.J., Canto-Perello, J.: Sustainable development of urban underground space for utilities. Tunn. Undergr. Space Technol. **14**(3), 335–340 (1999)
2. ITU-T: Multi-service infrastructure for smart sustainable cities in new-development areas. Focus Group Technical Specifications, ITU (2015)
3. Hunt, D.V.L., Nash, D., Rogers, C.D.F.: Sustainable utility placement via multi-utility tunnels. Tunn. Undergr. Space Technol. **39**, 15–26 (2014)
4. Rogers, C.D.F., Hunt, D.V.L.: Sustainable utility infrastructure via multi-utility tunnels. In; 1st International Construction Specialty Conference, Canada (2006)
5. Lee, S.-W., Sim, Y.-J., Na, G.-T.: A fundamental study on the development of feasibility assessment system for utility tunnel by urban patterns. J. Korean Tunn. Undergr. Space Assoc. **19**, 11–27 (2017)
6. Vann, M.G.: Of rats, rice, and race: the great Hanoi rat massacre, an episode in French colonial history. French Colonial Hist. **4**, 191–204 (2003)
7. https://plo.vn/xa-hoi/can-canh-cong-vom-lau-doi-nhat-duoi-long-sai-gon-555979.html
8. Labbé, D.: Facing the urban transition in Hanoi: recent urban planning issues and initiative. In: Institut national de la recherche scientifique Centre-Urbanisation Culture Société (2010)
9. Phong, T.L.: Construction management infrastructure of overhead lines and cable in the urban center of Hanoi (in Vietnamese). Doctoral Philosophy, Hanoi Architectural University (2017)
10. EI 07-017: Design guidance for trenchless installation of casing. Engineering instruction, New York State Department of Transportation (2007)
11. Zhang, Z., et al.: Cost allocation mechanism design for urban utility tunnel construction based on cooperative game and resource dependence theory. Energies (2019)
12. Hojjati, A., Jefferson, I., Metje, N., Rogers, C.: Sustainability assessment for urban underground utility infrastructure projects. Eng. Sustain. **171**(ES2), 68–80 (2018)

Design and Implementation of Integrated IoT System for Remote Monitoring

Nguyen Tan Khoi and Nguyen Lan

1 Introduction

With the development of cloud computing technology, IoT devices are connected to each other via Internet infrastructure, etc., and the collection of data and transmission to centralized servers has become easier and more responsive [1, 2]. Therefore, promoting the application of science and technology with smart devices is a sustainable direction that will help businesses improve performance and reduce losses in the management and operation of businesses [3, 4]. In addition, the development of cloud computing technology, sensor technology, devices connected to each other via the Internet, etc. will be more effective in operating and managing assets [5]. That is because the ability to monitor, alert, and control helps to improve labor productivity and reduce operating costs [6].

Currently, there are many solutions for the processing of data collection jobs based on IoT technology [7]. However, these solutions still have some problems such as discrete solutions, not diversified functions; an open architecture for IoT systems has not been unified; difficulty in connecting, communicating and managing devices due to the variety of different communication protocols, different device standards; the embedded software on IoT devices and the software for managing the IoT data system are not synchronously provided [8]; IoT systems have not been invested in compatible security solutions [9, 10]. Many IT companies providing technology solutions and services for collection and processing IoT data such as Microsoft, Errisson, Google, Logmein, etc., but these commercial services are expensive, and not open for the community [11, 6].

N. T. Khoi (✉) · N. Lan
Danang University of Science and Technology, The University of Danang, Da Nang, Vietnam
e-mail: ntkhoi@dut.udn.vn

N. Lan
e-mail: nlan@dut.udn.vn

Due to the need for an automated data collecting and analyzing system, which can work well in extreme weather conditions (sunshine, rain, wind, fog, etc.) with the installation located in diverse environments where there is no power source and Internet, in this paper, we propose a solution to build an integrated IoT system that allows us to collect camera image, environmental information such as temperature, humidity, precipitation, wind speed, etc.

The remainder of this paper is structured as follows: Sect. 2 presents the architecture and specifications of the components of an integrated IoT monitoring system. Section 3 presents some results of the experimental implementation of the system. Conclusions and research directions are presented in the last section.

2 Proposed System

2.1 Proposed Architecture of Integrated IoT System

The problem is the need to design an integrated IoT device system to monitor environmental changes in a large area, such as on the transportation network corridor. A remote monitoring network is formed by linking these devices together to collect different types of data. Integrated IoT devices are capable of collecting a wide variety of camera images, video data, and sensor data; transmit and store these data in real time on the server system of the IoT platform. The integrated system will exploit some important functions of IoT service provider, big data analysis function and artificial intelligence algorithms [12–14], etc. From these functions, the system will provide analysis results more accurately and specifically.

The integrated IoT system architecture is designed to meet some practical requirements such as the design in an open architecture orientation; using API libraries to communicate with many functional modules of the system; having mechanisms for data collection and aggregation from many different diverse IoT devices; having important functions such as data management, remote monitoring and warning based on image/video; support searching and retrieving data on the system quickly and accurately; providing sensor–communication–alarm function to allows users to remotely monitor in real-time management; processing and standardization of data obtained from sensor devices; the secure transmission of data from IoT terminals to the servers on IoT platform via 3G/4G mobile network; operating in adverse weather conditions and use solar energy power to operate the integrated IoT system.

We describe the proposed open IoT architecture model to solve the problems raised above. This architecture is built according to the layered model and has many corresponding functional modules in each layer. Figure 1 shows the proposed architecture of the system. This layered architecture consists of four layers: the IoT physical layer, network layer, service layer and application layer.
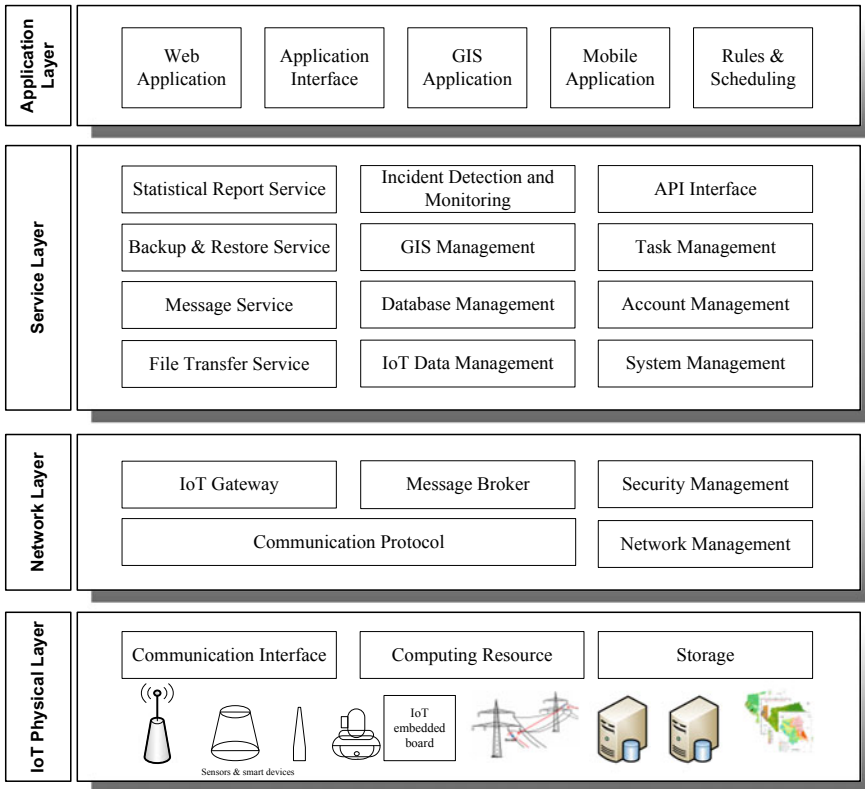
Fig. 1 Integrated IoT system architecture

a. *IoT physical layer*: This layer has the responsibility to communicate with all IoT devices and gathers the environmental data with the help of sensors. These sensors are selected according to the intent of the application. There are many types of sensors that are connected to objects to collect information such as location, changes in the air, environment, etc.

The IoT physical device layer manages and communicates with IoT devices in the system. These devices have the ability to collect data from the surrounding environment through sensors and the ability to connect to other devices based on network technologies such as LPWAN (LoraWAN, SigFox, NB-IoT) [11], WiFi, Bluetooth, Zigbee, Cellular 4G, 5G.

b. *Network layer*: This layer is responsible for data transportation from the sensing layer to the layer above it. The IoT gateways are the key component in this layer and are double-ended bridges. The network layer connects all types of IoT devices and network devices through standardized protocols such as HTTP, CoAP, and MQTT. Data is transmitted through wireless and wired transmission mediums (fiber optic cable, 3G, WiFi, etc.). The medium can be wireless or wire-based.

It also connects the network devices and networks to each other. Information IoT devices obtained are aggregated and optionally filtered before being moved to servers at the application layer.

The network layer has two main functions: controlling network connections such as accessing information resources and moving that resource to where needed, or authenticating, authorizing, etc.; connection management function is to focus on providing a connection for information transmission of IoT services/applications [12, 8].

c. Service layer: This layer is located in the middle of the IoT architecture and has an important role in the proposed four-layer IoT architecture. This layer stores and processes the data which comes from the lower layers. It has the function of complete IoT system management, including applications, user access, communication services, etc. At processing, layer can deploy the latest technologies like big data, artificial intelligence, cloud computing, etc.

d. Application layer: The application layer allows users to communicate with the system through provided application services. This layer provides access interfaces to the terminal and network IoT devices. It has the authority to provide professional services and applications to end users. The specific applications can be implemented at this layer. In an integrated IoT system, services can be different for each application because these services are based on data collected by sensors. The application layer is accessed through a dedicated network application at the end of the device such as a browser, a mobile application, or a desktop application based on protocols such as HTTP, HTTPS, SMTP, FTP, etc.

The integrated IoT architecture deployed includes main modules: digital map management module, IoT data management module, incident monitoring and warning module, operation planning module, and operation planning module. Statistic. Web site system manages and stores multimedia data and provides functions such as real-time monitoring, resource search, resource management, etc.

2.2 Deployment Model on Integrated IoT System

In this section, we present the communication model between devices in the device integrated system (Fig. 2). To connect different IoT devices in a system, we need to use intermediate network devices such as Modbus RTU, Modbus TCP and MQTT gateway.

Modbus is a serial communication method used to transmit information over the connection of electronic devices. Modbus is a master-slave system where the devices that provide information are called slaves and the devices that receive information are called masters. The master typically is a RTU, PC, PLC, etc. There are three versions of Modbus protocol used are: Modbus ASCII, Modbus RTU and Modbus TCP. In Modbus RTU and Modbus ASCII for serial lines communication, request and response data is represented in binary and communicates by byte per
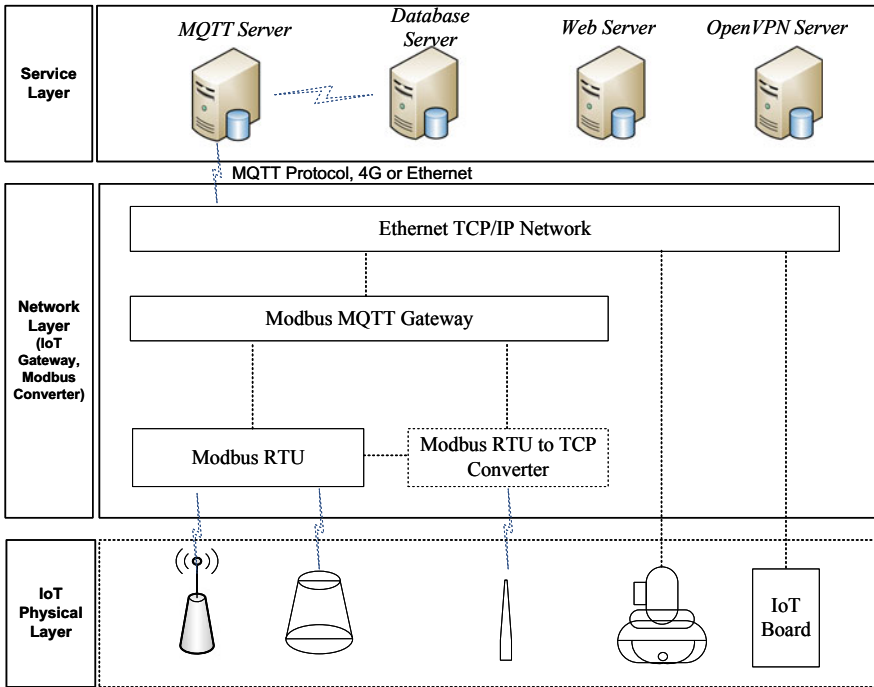
Fig. 2 Deployment model on integrated IoT system

data byte in the RS485 network. Data from the Modbus RTU are transferred to the Modbus TCP to support data transmission over Ethernet networks.

Modbus TCP is based on TCP/IP protocol to carry the data of the Modbus RTU between compatible devices in Ethernet-based networking. Modbus gateway is responsible as a protocol converter between Modbus RTU to Modbus TCP or vice versa.

MQTT gateway acts as a bridge between internal devices of integrated IoT system to cloud server. This device performs to collect data from Modbus TCP/RTU, RS485/232 and send collected data to a designated MQTT Broker Service.

API gateway has the responsibility for the routing of received requests and protocol conversion using single MQTT connection. All requests from clients will be sent to the API gateway first. It then routes the requests to the appropriate microservices in cloud server.

IoT devices can be classified into the following two categories: IoT sensor devices and IoT gateway devices. IoT sensor devices interact directly with the transmitting medium, send data to the network and can receive information from there. IoT gateway plays a role as a bridge between IoT devices and the network. Because there are many IoTs with different connection types, therefore IoT gateway must have function to communicate with many network protocols from wired to wireless, such as CAN bus, Zigbee, Bluetooth, or WiFi. Moreover, IoT gateway

devices can communicate through various technologies such as 3G/4G networks, Ethernet [14].

In order to achieve this, an integrated IoT monitoring system will need to be connected with an IoT cloud platform and meet functional requirements like collection of environmental data from various geographic locations through IoT devices; display real-time IoT data collected from the environment on the monitoring Web site and application; monitoring and detection of incidents occurring through camera image and IoT data; storing, filtering and analyzing the data collected to provide information in related fields such as agriculture, industry, etc.; using communication protocols and information processing on cloud computing platform; operation in remote and isolated areas, self-sufficient in electricity, no Internet connection, only uses 3G/4G network.

3   Results and Discussions

3.1   *Experimental Results*

Based on the proposed architectural model, we have designed and implemented an integrated IoT system in practice. With an aim of checking the reliability of the design, some experiments have been deployed in several different scenarios. The obtained results and the system functions were also analyzed. The IoT system is configured according to the device parameters to collect and exchange data on the network. The cloud server will aggregate and analyze various types of data such as temperature, humidity, precipitation, camera image and camera video from multiple integrated IoT systems.

3.2   *Experimental Environment of IoT System*

This section explains the experimentation performed in this study. Figure 3 shows our plan of integrated IoT stations in practice. These integrated IoT station are connected to a cloud-based web server. Our proposed system is deployed on private cloud for purposes of information security. Ubuntu 16.04 server is used to configure, install, and deploy IoT platform on Nitrogen8M embedded board. MongoDB is used for data storage because it stores data as JSON documents, each collection will have different sizes and different documents. MongoDB uses internal memory, so the data query speed will be very fast. Various different data are stored in database such as registered information of users, registered IoT devices and their metadata.

Nitrogen8M single-board computer is chosen for our IoT station. This embedded board includes an accessory kit option with a 5 V Power Supply, 16 GB microSD
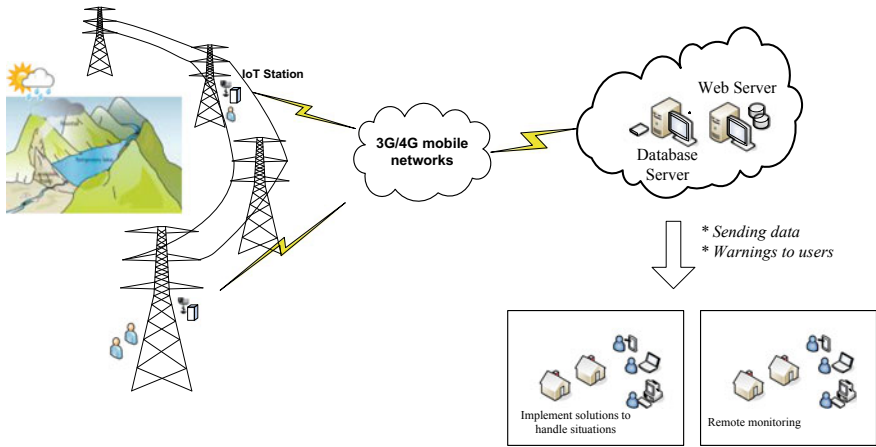
Fig. 3 Implementation of integrated IoT station in practice

card with Linux OS and have all the capabilities to perform like a computer. It consumes less power. Ubuntu operating system is configured and installed on this board for practical implementation. We have chosen the Node.js programming language for registration, connectivity, and accessibility of IoT devices.

Figure 4 shows a box of integrated IoT station and the location of this device on high voltage transmission line tower to operate the functions of the system. All the devices of the integrated IoT system are installed in a box coated with powder coating to protect all devices in extreme weather conditions.

Fig. 4 IoT station box on high voltage transmission line tower

(1) *Monitoring data from integrated IoT systems*

After logging into Web site, users will be able to observe different data types from IoT stations which are set up in many locations far away from each other (Fig. 5). Data displayed on Web site for users include: real-time images from each IoT station, temperature, precipitation measurement and wind speed. Through the analysis of received data, the system will send warnings based on the established thresholds.

(2) *Object detection*

Figure 6 illustrates the result of detection objects from the camera images at Web Server. We choose to use Mask R-CNN algorithm [12] for object detection, object localization, and object instance segmentation of images.

Mask R-CNN is a deep neural network designed for instance segmentation in computer vision. This machine learning algorithm takes the camera source image and inputs it to a CNN called a Region Prediction Network (RPN). This RPN model builds bounding boxes and segmentation masks for the objects detected in an image. It considers a large number of possible regions and uses an efficient deep learning method to predict which regions are most likely to be objects of interest.

(3) *Fire detection in observation area*

IoT data from the IoT stations will be sent continuously to server on cloud every 5 min. This time interval can be customized on the system. This data is updated to topics on the MQTT server. Captured images from camera will be analyzed through detection module using machine learning to fire detection at area far from population, or intruder object detection (Fig. 7). If the system detects an abnormal problem, it will notify to responsible user via text messages, email and alert by sending notice to the MQTT topics that the client has subscribed to. At the same
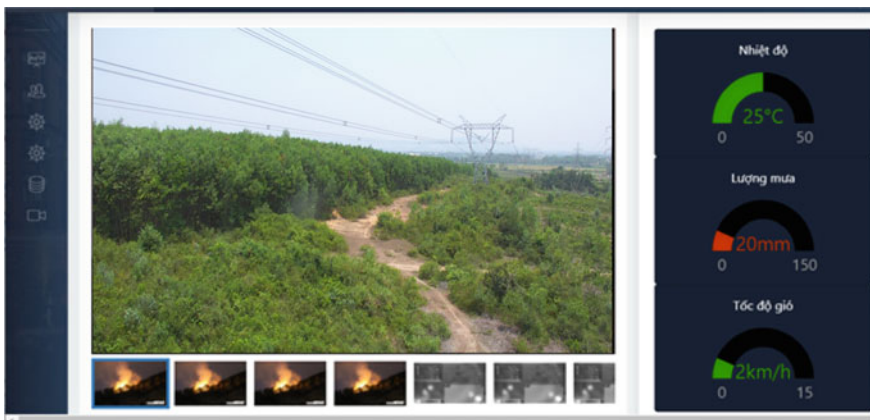

Fig. 5 View data from IoT stations on the Web site

Fig. 6 Object detection function on Web site

time, warning information will also be stored in database on system. When MQTT clients receive signal changes from topics, they will update the data.

(4) *User management*

This module has the function of defining and managing users, roles, and their access levels in system (Fig. 8). Admin user can add different user roles and manage related activity through a management dashboard in the system. A normal user management activities such as adding/deleting accounts, assigning access rights, groups, defining authentication policies, manual/automatic logout and changing user passwords.

(5) *Manage integrated IoT stations*

Figure 9 shows the web interface of the IoT platform in which a registered user can add IoT station to which they can monitor and control.
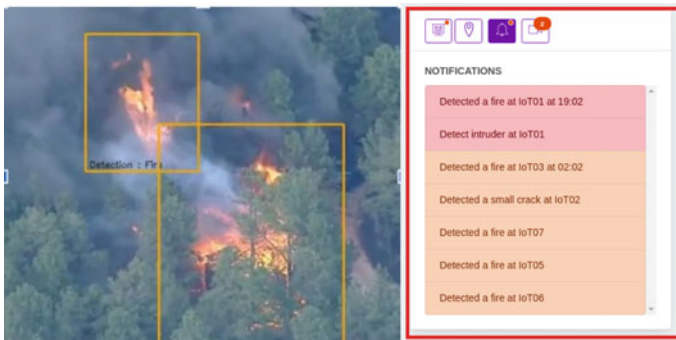

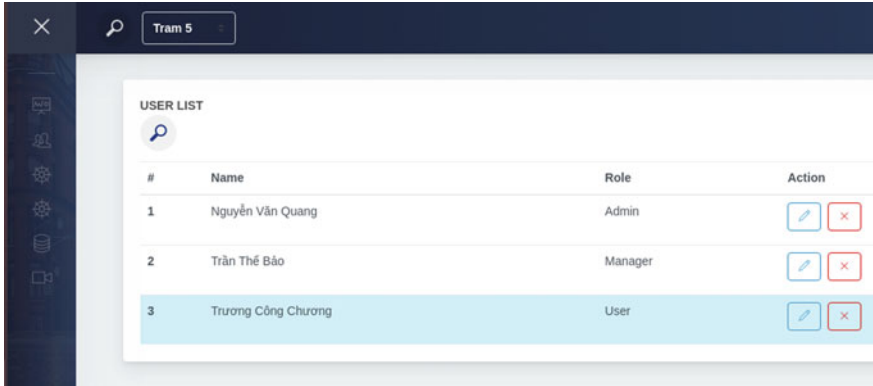**Fig. 7** Fire detection function on Web site
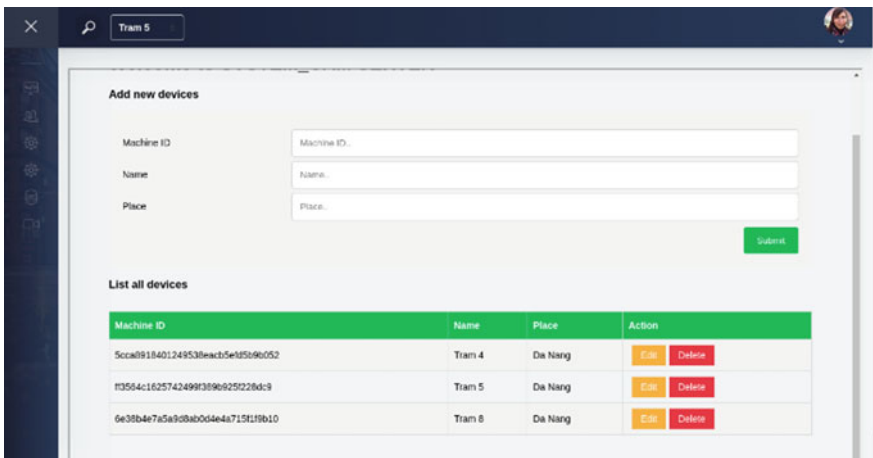
Fig. 8 User management interface

Fig. 9 IoT station management interface

(6) *IoT device management in a station*

This function shows the discovery of the IoT device. Users have access to public and private registered IoT devices. At this interface, the user can search for any IoT device and choose the category type. It will return the list of registered IoT devices. Users can select any IoT device, i.e., sensor or actuator. Besides, users can download JSON or XML format data of the IoT device to send commands to the corresponding IoT device.

(7) *View graph of IoT data statistics*

This function allows users to view statistical graphs of temperature, precipitation and wind speed for a specified time period in real time (Figs. 9, 10 and 11). At the
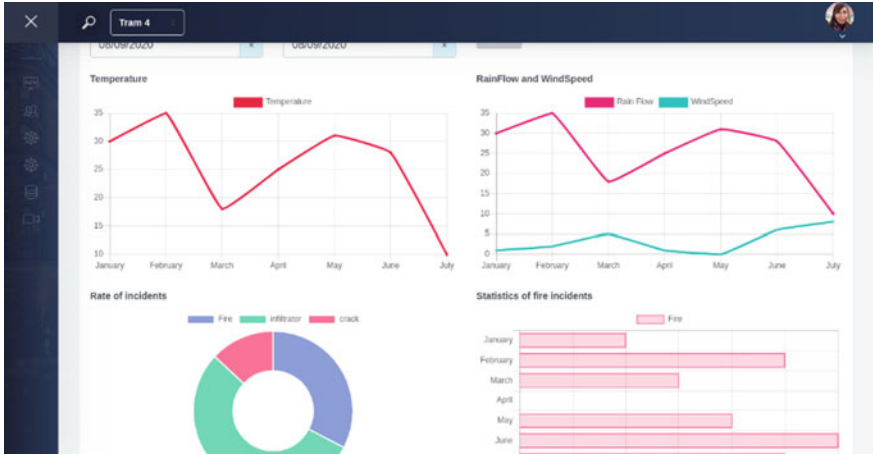
Fig. 10 Sensor data response time

Fig. 11 IoT device registration response time

same time, it also allows statistics of the rate of incidents that have occurred and detailed information about these incidents.

In this section, we present an implementation of integrated IoT systems in practice based on our proposed IoT architecture to solve the problem posed above. The IoT architecture is the foundation and basis for implementing an IoT system. The type of IoT connection is complex because of different IoT devices and software applications. There are many IoT devices and networking protocols. Therefore it is necessary to build applications and services to exploit IoT devices effectively

for different use cases in any context, i.e., user application, mobile application, enterprise IoT applications, etc.

Our approach for an integrated IoT system has the following novelties and contributions:

- This is the first approach that presents an integrated IoT system in that all IoT devices are connected and send multi-data to Server on the cloud;
- The integrated IoT system has the ability to communicate and collect data from diverse IoT devices in the system;
- The integrated IoT system allows users to remotely monitor by image and video from camera and use machine learning to detect abnormal indents;
- Our approach considers based on our proposed IoT architecture to connect all objects such as IoT devices, IoT gateway, communication networks, and cloud server technology.

4   Conclusion and Future Works

In this paper, we propose an integrated IoT system architecture model. From the proposed architecture, we perform to build a network of integrated monitoring IoT stations, distributed over geographical areas. Each integrated IoT station consists of a set of IoT devices and IoT gateways, and software installed on the embedded board. The IoT device station has the function of collecting, processing data and communicating with the server on the cloud platform, serving for remote management and monitoring. Central cloud-based servers include functional modules that allow remote data acquisition; data analysis and processing; alert to the user when an abnormal problem is detected.

Our integrated IoT system solution is useful in remote management and monitoring, especially in mountainous areas that are difficult to move, and many dangerous places. Helping businesses save costs for inspection and supervision, improve labor productivity and efficiency of workers. In addition, since the system can regularly receive real-time data from many different sources, we will have opportunities to apply the data mining problems. The purpose is to make recommendations for related fields such as agriculture, weather forecasting, tourism, etc.

In future work, we will improve the integrated IoT system in directions such as expanding the function of interacting with other IoT systems, optimizing energy consumption, building a big data management solution, improving machine learning algorithms for higher accuracy; Increased security levels for the system and detect safety of structural elements.

References

1. Botta, A., de Donato, W., Persico, V., Pescapé, A.: Integration of cloud computing and internet of things: a survey. Future Gener. Comput. Syst. **56**, 684–700 (2016)
2. Soliman, M., Abiodun, T., Hamouda, T., Zhou, J., Lung, C.: Smart home: integrating internet of things with web services and cloud computing. In: International Conference on Cloud Computing Technology and Science, IEEE (2013)
3. Andrea, M., Robert, C., Philip, T.: Dynamic line ratings deployment on the orkney smart grid. In: 21st International Conference on Electricity Distribution, Frankfurt (2011)
4. Bose, A.: Smart transmission grid applications and their supporting infrastructure. IEEE Trans. Smart Grid **1**(1), 11–19 (2010)
5. Coll-Mayor, A.D., Paget, M., Lightner, E.: Future intelligent power grids: analysis of the vision in the European Union and the United States. Energy Policy **35**(4), 2453–2465 (2007)
6. Saeed, F., Paul, A., Rehman, A., Hong, W.H., Seo, H.: IoT-based intelligent modeling of smart home environment for fire prevention and safety. J. Sens. Actuator Netw. **7**(1) (2018). https://doi.org/10.3390/jsan7010011
7. Datta, T., Apthorpe, N., Feamster, N.: Developer-friendly library for smart home IoT privacy-preserving traffic obfuscation. IoT S&P 18. In: Proceedings of the 2018 Workshop on IoT Security and Privacy, ACM, pp. 43–48 (2018)
8. Mao, J., Lin, Q., Bian, J.: Application of learning algorithms in smart home IoT system security. Am. Inst. Math. Sci (2018). https://doi.org/10.3934/mfc.2018004
9. Stergioua, C., Psannis, K., Kimb, B., Gupta, B.: Secure integration of IoT and cloud computing. Elsevier, Future Gener. Comput. Syst. **78**(3), 964–975 (2018)
10. Vijay, S., Hassan, H., Arun, V., Roksana, B., Olivier, M.: Network-level security and privacy control for smart-home IoT devices. In: IEEE 11th International Conference on Wireless and Mobile Computing, Networking and Communications (WiMob) (2015)
11. Brian R., Drew V.: Practical Internet of Things Security. Kindle Edition (2016)
12. Kaiming, H., Georgia, G., Piotr, D., Ross, G.: Mask R-CNN. In: 2017 IEEE International Conference on Computer Vision (ICCV) (2017)
13. Long, J., Shelhamer, E., Darrell, T.: Fully convolutional networks for semantic segmentation. In: Computer Vision and Pattern Recognition (2015)
14. Ren, S., He, K., Girshick, R., Sun, J.: Faster R-CNN: towards real-time object detection with region proposal networks. In: NIPS (2015)

Health Monitoring System for Long Span Bridges Across the Han River in Da Nang City, Vietnam

Lan Nguyen and Hung Huy Pham

1 Introduction of the Bridge System on Han and Da Nang Rivers

The Han River section from the river mouth to the junction of the Han–Vinh Dien–Cam Le River has a length of 9.8 km, along the river with bridges: Thuan Phuoc bridge, a suspension bridge with the main bridge diagram 125 m + 405 m + 125 m, inaugurated in 2009; Han River bridge with the main span rotating bridge form 2×60 m; Dragon bridge structural steel beam-arched structure, span diagram 128 + 200 + 128 m; It inaugurated in 2013; Nguyen Van Troi Bridge is a steel-tube bridge with midway construction since 1965, the bridge has 14 spans with a total length of 514 m; Tran Thi Ly Bridge in the form of a cable-stayed bridge, span diagram 50 m x 4 + 230 m + 45 m + 50 m x 4 + 28 m x 2 inaugurated in 2013; Tien Son Bridge is a prestressed concrete box girder bridge with a bridge length of 529 m, inaugurated in 2004 (Fig. 1).

The bridges across the Han River play a very important role in connecting between both sides of the river, it awakens potential to land on the east bank, becoming an important driving force in the transformation of economic structure to tourism—service of Da Nang city. Tien Son Bridge is a bridge connecting Tien Sa Port and National Road 14B across Southeast Asia.

Thuan Phuoc Bridge is the longest suspension bridge in Vietnam, and the bridge is located at the river mouth, so it suffers from adverse environmental loads such as wind and corrosion. Dragon Bridge belongs to arch-beam-wire combination structure so the behavior is quite complicated. Tran Thi Ly Bridge is a modern cable-stayed bridge structure with a 230 m long cable-stayed span with two-wire planes.

L. Nguyen (✉) · H. H. Pham
The University of Da Nang, University of Science and Technology, Da Nang, Vietnam
e-mail: nlan@dut.udn.vn

Fig. 1 Map of Han River and bridges in Danang city, Vietnam [https://vi.wikipedia.org/wiki]

Tran Thi Tran Bridge has been installed in a monitoring system since the construction phase (2009) including monitoring the top of the tower by GPS sensor, force in cable-stayed 13 sets by single load cell, deformation in concrete tower and host beam (32 sets), the temperature in cable-stayed and bridge tower (01 sets), beam rotation angle of tower foot position (01 sets), displacement of bearings under the tower (01 sets), wind intensity and direction (01 sets).

2 Basis Designed Bridge Health Monitoring System

Structural Health Monitoring (SHM) is a field of engineering that deals with the diagnosis and monitoring of structures during their operation. The primary goal of SHM is detection, identification, assessment, and monitoring of flaws or fault conditions that affect or may affect the future safety or performance of structures. SHM combines elements of nondestructive testing and evaluation, condition/process monitoring, statistical pattern recognition, and physical modeling (ASTM E2983-19 [1]). The modern SHM system will typically consist of six common components, namely: (1) acquisition of data (a sensory system); (2) communication of information; (3) intelligent processing and analyzing of data; (4) storage of processed data; (5) diagnostics (i.e., damage detection and modeling algorithms); and (6) retrieval of information as required [2]. Currently, some bridge structure monitoring systems also integrate some structural control systems such as vibration control, control anti-corrosion dehumidifier system in steel structure parts. The typical architecture of a bridge structure monitoring system is shown in Fig. 2.
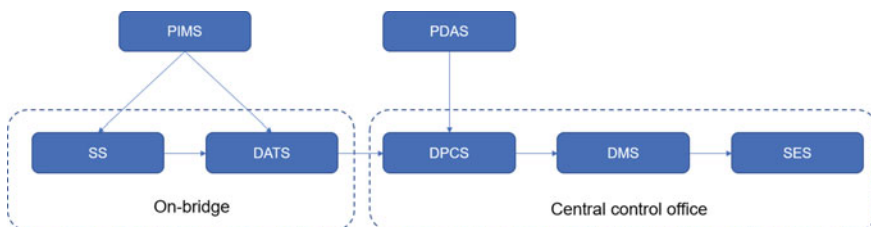

Fig. 2 Architecture of a SHM system [4]. *Note* SS: sensory system, DATS: data acquisition and transmission system, DPCS: data processing and control system, DMS: data management system, SES: structural evaluation system, PDAS: portable data acquisition system, PIMS: portable inspection and maintenance system

Currently, there are also many countries, and the organization has issued technical codes for the design of structural monitoring systems and bridges. The new Chinese technical SHM code guides the arrangement of sensor groups for the monitoring of load and environment, monitoring global and local bridge responses. This code also gives the technical requirements of different types of sensors for monitoring bridge structures [3].

The general design order of a bridge monitoring system includes the following steps:

- Define the purpose of the bridge monitoring system
- Layouts of sensor and DATS: In order to layout the sensors, the designer needs to understand the bridge's responses by analysis the bridge model to choose the type and parameters of sensors and installation location. Depending on the number of sensors, sensor distance, sensor type, sampling rate, choose the appropriate configuration of DATS connection (wired or wireless), choose the monitoring data communication model, …
- Architectural design of the software system for data collection, processing, communication and display. Design a software system capable of collecting, analyzing, diagnosing failure, alerting managers and decision support systems.
- Designing shop drawings for system installation.

The general design order of a bridge monitoring system includes the following steps:

- Define the purpose of the bridge monitoring system
- Layouts of sensor and DATS: To layout the sensors, the designer needs to understand the bridge's responses by analyzing the bridge model to choose the type and parameters of sensors and installation location. Depending on the number of sensors, sensor distance, sensor type, sampling rate, choose the appropriate configuration of DATS connection (wired or wireless), choose the monitoring data, communication model, …
- Architectural design of the software system for data collection, processing, co-communication and display. Design a software system capable of collecting, analyzing, diagnosing failure, alerting managers and decision support systems.
- Designing shop drawings for system installation.

3 Design the Health Monitoring System Thuan Phuoc Bridge, Dragon Bridge, Tran Thi Ly Bridge (Phase 2)

Based on the results of the current status survey, and the FEM model analysis, the cross-section of the monitoring equipment was arranged according to unfavorable principles, including the phasing of investment stages and capital sources, monitoring systems. Thuan Phuoc suspension bridge is installed in two stages including

the following types of sensors: Oscillating beams, host cables, cable cars; host beam deformation; rotation of host beams and bridge towers; temperature in host beams, host cables, slings and decks; environmental sensors (temperature, wind, humidity); Traffic monitoring camera sensor on the bridge (Tables 1 and 2; Figs. 3, 4, 5, and 6).

Based on the current status survey results, and the FEM model analysis, the cross-section of the monitoring equipment was arranged according to unfavorable

Table 1 Sensors deployed on the Thuan Phuoc Bridge [5]

Monitoring item	Sensor type	Sensor ID	No. of sensor	Position
Vibration of main cable, hangers, tower and girder	Accelerometer	giatoc1 to giatoc25	25	¼ and ½ main and side girder; ¼ and ½ main cable, hanger cable ZS1, ZS10, BS1, BS5; top of tower
Stress of girder and tower	Strain gauge	ungsuat1 to ungsuat12	12	¼ and ½ main and side girder, body of tower
Girder and tower rotation angle	Tiltmeters	gocxoay1 to gocxoay6	6	¼ and ½ main and side girder, top of tower
Temperature of cable, girder and tower	Thermistor	nhietdo1 to nhietdo8	8	¼ and ½ main and side girder; ¼ and ½ main cable, top of tower, asphalt concrete
Wind speed and direction	Anemometer	Tocdogio, huonggio	1	Abutment M2
Temperature and humidity	Temperature humidity sensor	Nhietdo, Doam	1	Abutment M2

Table 2 Sensors deployed on the Dragon bridge

| Monitoring item	Sensor type	Sensor ID	No. of sensor	Position
Vibration of arch and steel girder	Accelerometer	giatoc1 to giatoc6	2 (3-axis)	½ main arch and girder
Stress of steel arch and girder, reinforced concrete arch	Strain gauge	ungsuat1 to ungsuat59	59	¼, ¾ and ½ main girder, reinforced concrete arch, arch foot
Steel girder	Tiltmeters	gocxoay1 to gocxoay2	1 (2-axis)	½ main girder
Temperature of arch, girder and pile	Thermistor	nhietdoKC1 to nhietdoKC8	8	½ steel arch; ¼, ¾ and ½ main girder, reinforced concrete arch, arch foot
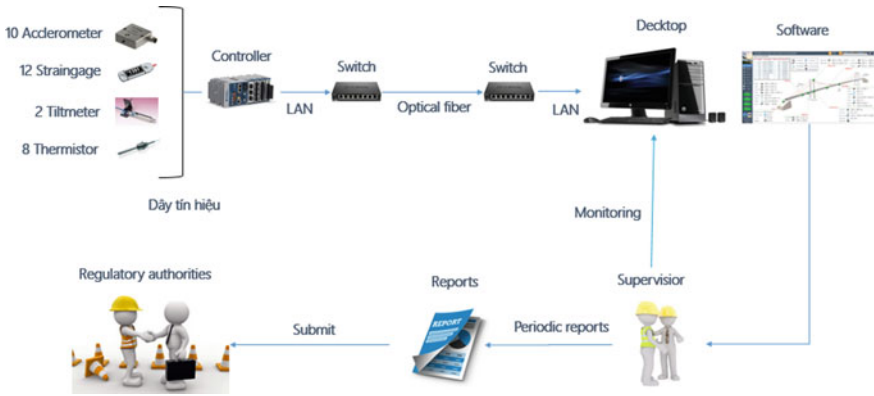
Fig. 3 Architecture of the Thuan Phuoc Bridge monitoring system [5]

principles, including the phasing of investment stages and capital sources, monitoring systems. Thuan Phuoc suspension bridge is installed in two steps including the following types of sensors: Oscillating beams, host cables, cable cars; host beam deformation; rotation of host beams and bridge towers; temperature in host beams, host cables, slings and decks; environmental sensors (temperature, wind, humidity); Traffic monitoring camera sensor on the bridge.

The cable-stayed bridge is a structure with high super-static step, large deformation, the surface is usually wide (Tran Thi Ly $B = 34.5$ m), high tower and slender structure. This structure is very sensitive due to dynamic factors such as loading, collision, wind and earthquake (Fig. 7).

4 Result of Updating Finite Element Model and Defining Warning Threshold for the SHM System of Bridges on Han River

The finite element (FE) method has become the widely accepted analysis tool in many disciplines. In bridge engineering, an accurate FE model of the bridge is often an essential tool to facilitate an effective assessment of bridge performance. This is particularly true of the prognosis of bridge performance because the performance predication of the bridge under a diversity of loadings and structural conditions could only be accomplished by an FE model-based computational approach. To obtain an accurate FE model of the bridge, appropriate modeling is essential.

Based on the initial test results and the data of the first blessed monitoring system to update the FE model.

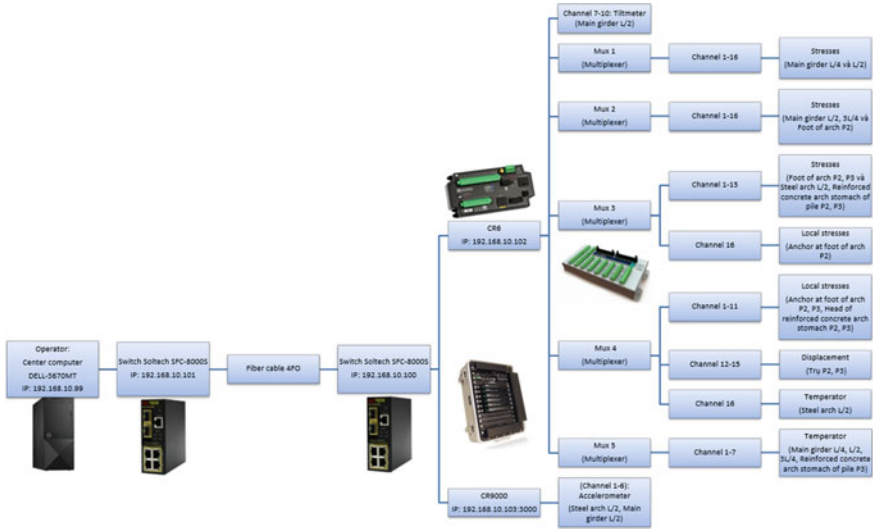**Fig. 4** Thuan Phuoc suspension bridge monitoring software and Web site (www.quantraccong-trinh.com.vn)

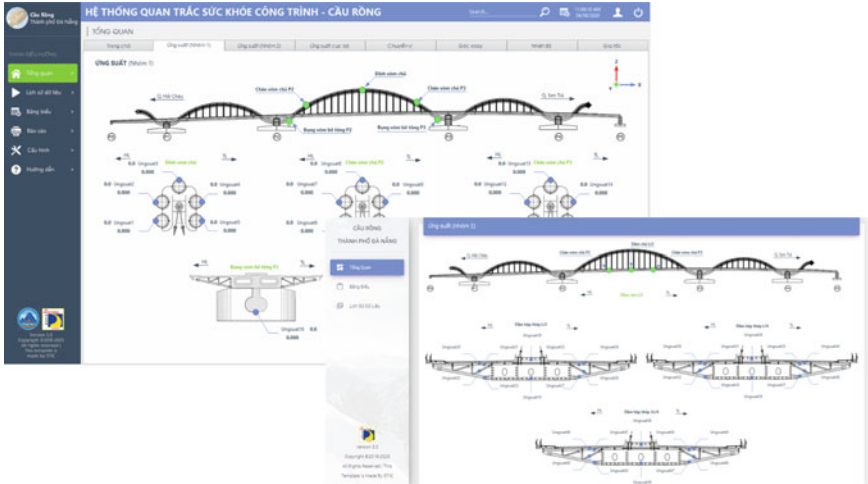**Fig. 5** Architecture of the Dragon bridge monitoring system [6]

Fig. 6 Dragon bridge monitoring software and Web site interface at control room workstation [6]
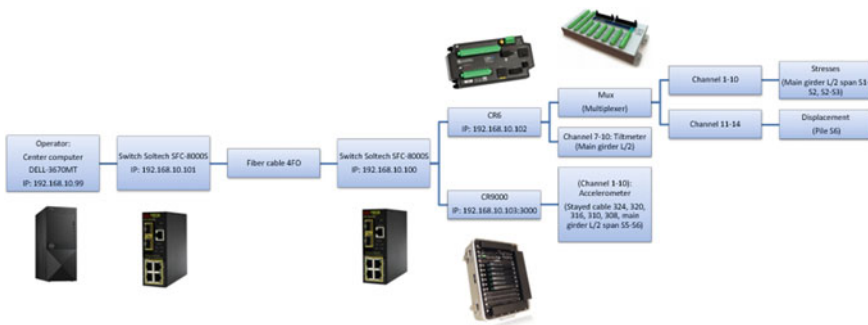

Fig. 7 Architecture of the Tran Thi Ly stayed cable bridge monitoring system [7]

Input data:

- Material:

    - Concrete: Modulus of elasticity (E), poison coefficient, modulus of shear, specific density, coefficient of thermal expansion.
    - Steel structure: Modulus of elasticity (E), poison coefficient, modulus of shear, specific density, coefficient of thermal expansion, elastic limit (F_y), tensile strength (F_u).
    - Stayed cable and prestressed cable: Modulus of elasticity (E), poison coefficient, modulus of shear, specific density, coefficient of thermal expansion, tensile strength (F_u), ultimate tensile strength.

- Load:

  - Dead load
  - Live load
  - Temperature
  - Wind load

After comparing and evaluating the results from the above calculation model, consult. Select the model using SAP 2000 V14 to calculate the alarm threshold. Threshold

The alarm is divided into two levels as follows:

- Level 1: The observed values reach the allowable material limit,

$$[\sigma]1 = [\sigma]vl - \sigma td - \sigma tt - \sigma ttk \qquad (1)$$

  therein:
  $[\sigma]_1$ the tress limit level 1
  $[\sigma]_{vl}$ the stress limit of material
  $[\sigma]_{tt}$ the stress due to static load
  $[\sigma]td$ the stress due to prestressed cable (if any)
  $[\sigma]ttk$ the stress due to another short-term load (wind).

- Level 2: The observed values reach adverse values according to the design load combination (The load considered here is HL93, temperature, wind).

$$[\sigma]2 = \sigma LL + \sigma ttk \qquad (2)$$

  therein:
  $[\sigma]2$ the stress limit level 2
  $[\sigma]LL$ the stress due to live load HL93
  $[\sigma]ttk$ stress due to other short-term loads (temperature, wind) (Fig. 8).

SAP2000/CsiBridge v20 software used to analyze the model. Results of the analysis are compared with the results of the design calculations, the results of the latest load test (2015) and the results of observations at the present time (2018). The results of model analysis and determination of warning threshold values are given in Tables 3 and 4.

Fig. 8 3D FEM model Thuan Phuoc Bridge [5]

After comparing the results from the computational model, the consultant chooses the model with Midas Civil to calculate the warning threshold. In addition, due to the calculation model, factors such as structural changes during the construction process are not taken into account; the reduction of the material intensity after 10 years of use, so the consultant recommends the warning value included in the software by 75% of the value indicated in Table 5 (Figs. 9, 10, and 11).

After comparing and evaluating the results from the above calculation model, the consultant selected the model using SAP 2000 V14 to calculate the warning threshold.

The warning is divided into two levels as follows:

- Level 1: Warning when the monitoring value reaches the given material limit allowed
- Level 2: Warning when the observed values reach the unfavorable values according to the design (The load considered here is HL93, temperature, wind) (Tables 6, 7, 8, 9, 10, and 11; Fig. 12).

Table 3 General results from the FEM model analysis [5]

Model Location	Analysis model CsiBridgeV20 (Sap2000V14)		Analysis model Midas2017	
	Max	Min	Max	Min
Stress on top fibers above of L/2 due to live load + temperature (MPa)	46.65	−138.56	48.40	−123.00
Stress on bottom fibers below of L/2 due to live load + temperature (MPa)	131.95	−48.55	120.20	−46.90
Stress on top fibers above of L/4 due to live load + temperature (MPa)	39.80	−144.70	43.90	−127.20
Stress on bottom fibers below of L/4 due to live load + temperature (MPa)	140.17	−39.73	128.00	−41.40
Vibration frequency (Hz)	0.2668		0.2375	
Tilts L/2 horizontal axis (degree)	0.928	−0.928	1.463	−1.463
Tilts L/2 longitudinal axis (degree)	–	–	0.446	−0.446

Table 4 Comparison of calculation results and dynamic test in 2015 [5]

Model Location	Analysis model CsiBridge V20 (Sap2000 V14)	Analysis model Midas2017	Analysis model RM (Accreditation 2015)	Design data (China)
Moment of L/2 due to live load 0.65HL93 (kN m)	27,910	24,238	21,000	–
Moment of L/4 due to live load 0.65HL93 (kN m)	32,710	27,335	25,918	–
Displacement of L/2 due to live load 0.65HL93 (mm)	746.3	715.9	630.0	–
Displacement of L/2 due to live load 0.65HL93 (mm)	761.9	743.3	704.9	–
Tension of main cable maximum (T)	3050.0	3492.0	3537.6	–
Tension of suspender cable maximum (T)	150.0	113.05	113.51	–
Vibration frequency (Hz)	0.2668	0.2375	0.2591	0.2456

Table 5 Warning threshold results [5]

Model Location	Analysis model by Midas2017	
	Max	Min
Stress on top fibers above of L/2 due to live load + temperature (MPa)	36.30	−92.25
Stress on bottom fibers below of L/2 due to live load + temperature (MPa)	90.15	−35.18
Stress on top fibers above of L/4 due to live load + temperature (MPa)	32.93	−95.40
Stress on bottom fibers below of L/4 due to live load + temperature (MPa)	96.00	−31.05
Tilts L/2 horizontal axis (degree)	1.10	
Tilts L/2 longitudinal axis (degree)	0.335	

5 Results of Structural Health Monitoring System

For vibration frequency of Thuan Phuoc suspension bridge, data from accelerometer calculated through FFT calculation program, it is determined frequency peak and frequency value corresponding (Fig. 13).

The results obtained from the monitoring system are similar to the results obtained on the finite element model, and the present value of the sensors in the safety value domain is calculated according to the data design.
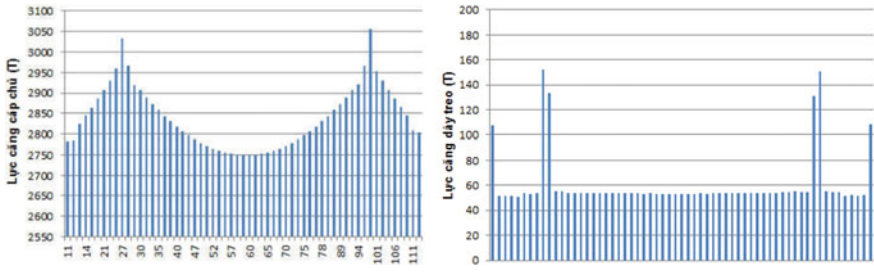
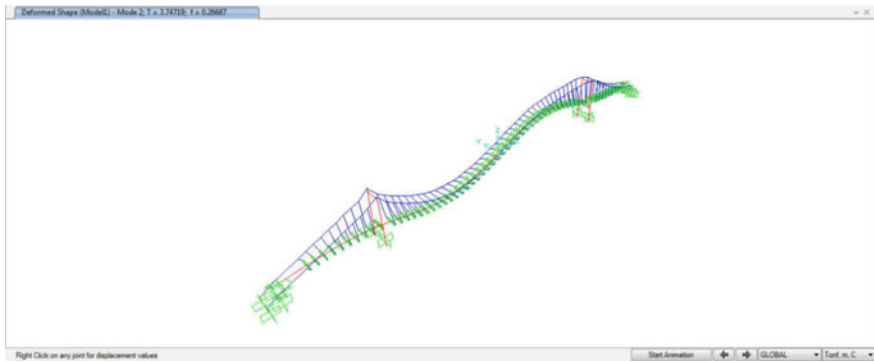**Fig. 9** Tension in main cable and suspender cable initial state [5]

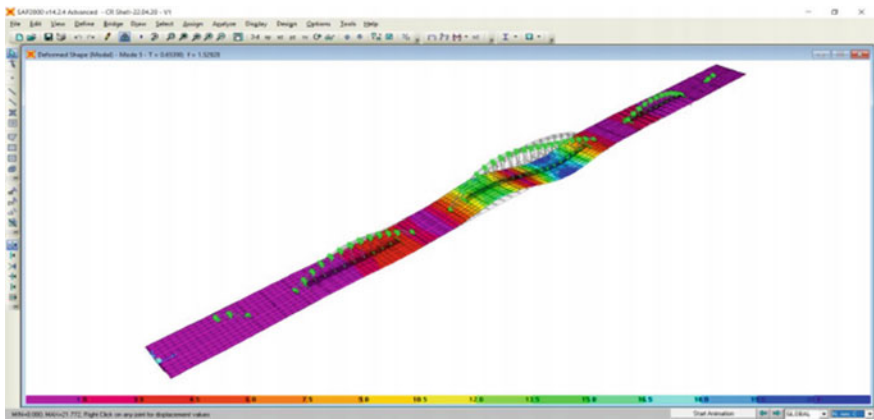**Fig. 10** Vibration on Model 1 $f = 0.267$ Hz [5]

Fig. 11 3D model Dragon bridge in SAP2000 [6]

Table 6 Compare calculation results with design documents and inspection results in 2019 [6]

No.	Results	Inspection in 2013	Inspection in 2019	Model analysis in FEM
1	Vibration frequency (Hz)	2.339	2.360	2.230
2	Total tension of tension ropes in 3 upstream beat (KN)	–	40,900	39,008
3	Total tension of rope in suspension of 3 lower section (KN)	–	40,537	39,008

Table 7 Analysis results of beam stress warning threshold [6]

Model Location	Level 1 (material limit allowed)		Level 2 (load combination)	
	Max	Min	Max	Min
Upper fiber stress L/4 and 3L/4 (MPa)	327.75	−269.68	77.01	−129.55
Lower fiber stress L/4 and 3L/4 (MPa)	294.13	−327.75	74.47	−109.78
Upper fiber stress L/2 (MPa)	327.75	−256.01	71.35	−124.59
Lower fiber stress L/2 (MPa)	277.06	−327.75	77.06	−111.51

Table 8 Results of the analysis of the steel arch stress warning threshold

Model Location	Level 1 (material limit allowed)		Level 2 (load combination)	
	Max	Min	Max	Min
Arch pipe stresses 1 and 5 L/2 section (MPa)	310.50	−205.92	19.06	−36.54
Arch pipe stresses 2 and 4 L/2 section (MPa)	310.50	−170.87	10.94	−28.83
Arch pipe stresses 3 L/2 section (MPa)	310.50	−141.33	10.29	−26.48
Arch pipe stresses 1 and 5 arch foot section (MPa)	310.50	−94.69	23.91	−39.22
Arch pipe stresses 2 and 4 arch foot section (MPa)	310.50	−93.01	33.13	−52.89
Arch pipe stresses 3 L/2 arch foot section (MPa)	310.50	−91.30	41.48	−65.00

Remote monitoring results via mobile devices in Fig. 14 show that the most unfavorable temperature in the bridge surface in May 2020 is up to 60–65 °C. With this temperature, the asphalt concrete layer on the steel bridge surface will be easily damaged when combined with a heavy truck running across the bridge.

Temperature is one of the major factors affecting the behavior of the structure, based on the stress sensor located at the top of the L/2 steel arch and the top fiber on the L/2 steel box girder of Dragon bridge, and we can see the change with the cycle of stress in 24 h (Figs. 15, 16, and 17).

Table 9 Compare calculation results with design documents and inspection results in 2019 [6]

No.	Results	Design	Inspection in 2019	Model analysis in FEM
1	Vibration frequency of tower (Hz)	0.631	–	0.636
2	Approach span vibration frequency (Hz)	–	3.40	3.347
		–	3.70	3.777
3	Vibration frequency of main span Hz)	0.414	–	0.439
		0.777	–	0.799
		1.264	–	1.235
		–	3.30	3.347

Table 10 Analysis results of beam stress warning threshold [6]

Model Location	Level 1 (material limit allowed)		Level 2 (design load combination)	
	Max	Min	Max	Min
Upper fiber stress of S1-S2 (MPa)	3.16	−14.59	2.32	−2.77
Lower fiber stress of S1-S2 (MPa)	5.44	−14.75	3.94	−3.25
Upper fiber stress of S2-S3 (MPa)	3.16	−15.14	2.75	−3.20
Lower fiber stress of S2-S3 (MPa)	5.52	−15.34	3.39	−2.66
Top of upper fiber stress of S1-S2 (MPa)	3.16	−14.69	2.93	−3.69
Bottom of lower fiber stress of S2-S3	5.46	−15.22	3.86	−2.78

Table 11 The results of the analysis of the threshold warning of cable tension, rotation [7]

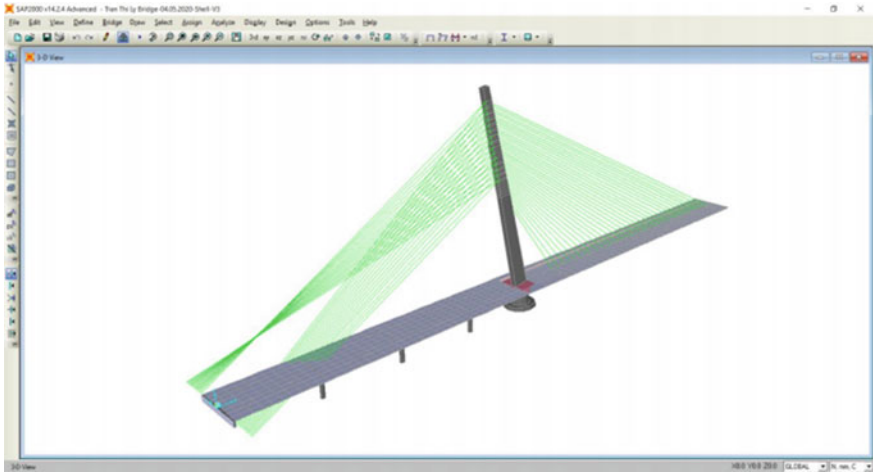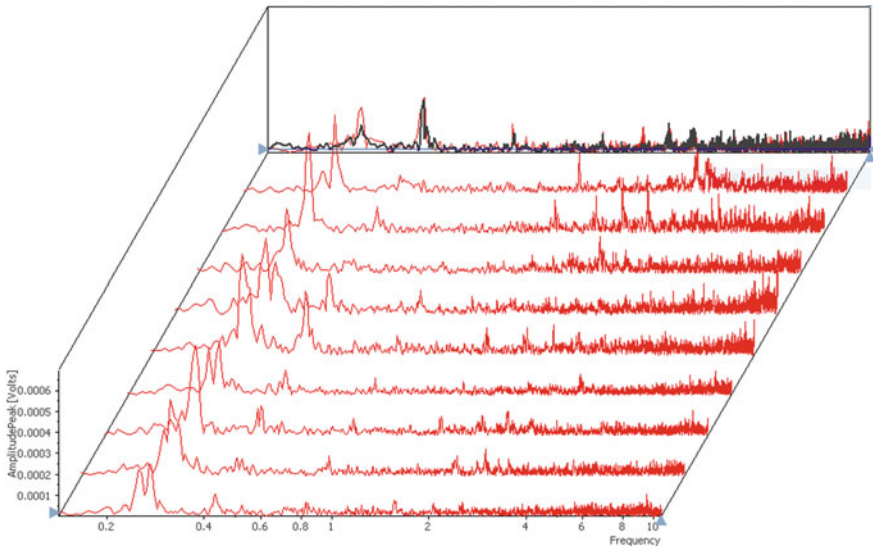| Model Location	Level 1 (material limit allowed)
	Max
Tension force 324 (KN)	8955.38
Tension force 320 (KN)	9769.50
Tension force 316 (KN)	10746.45
Tension force 310 (KN)	12049.05
Tension force 308 (KN)	12700.35
Rotation of angle L/2 horizontal bridge (degree)	0.054
Rotation of angle L/2 along the bridge (degree)	0.35

Fig. 12 3D model Tran Thi Ly bridge [7]

Fig. 13 Result of FFT $f = 0.241$(Hz) analyzed of accelerometer on ½ span main girder [5]
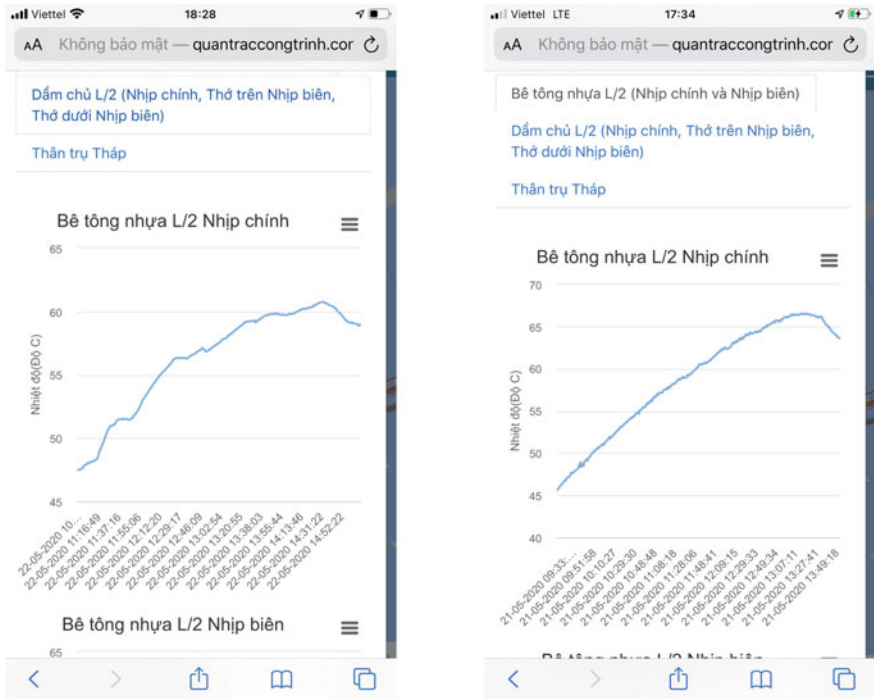
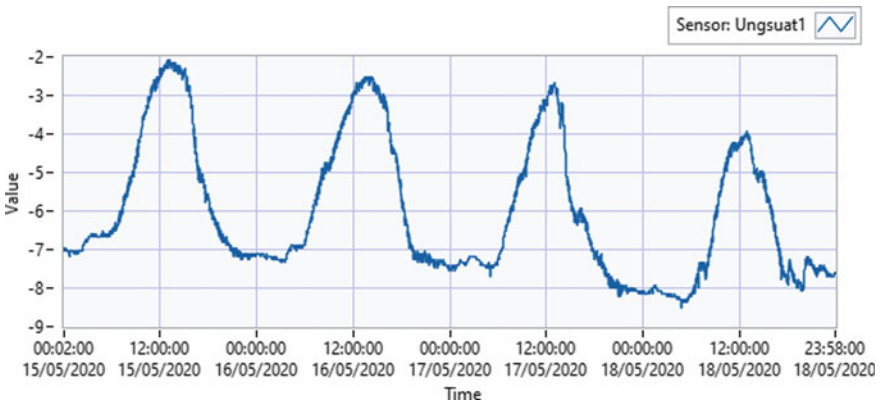**Fig. 14** Temperature of asphalt concrete is monitored via Web site on mobile devices [5]

Fig. 15 Behavior of structural stress according to temperature at the top of the L/2 steel arch—Dragon bridge [6]
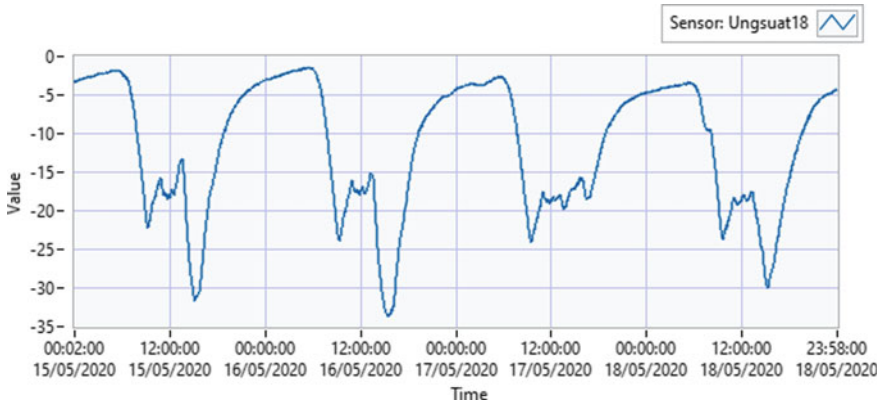
Fig. 16 Behavior of structural stress according to temperature the top fiber on the L/2 steel box girder in Dragon bridge [6]
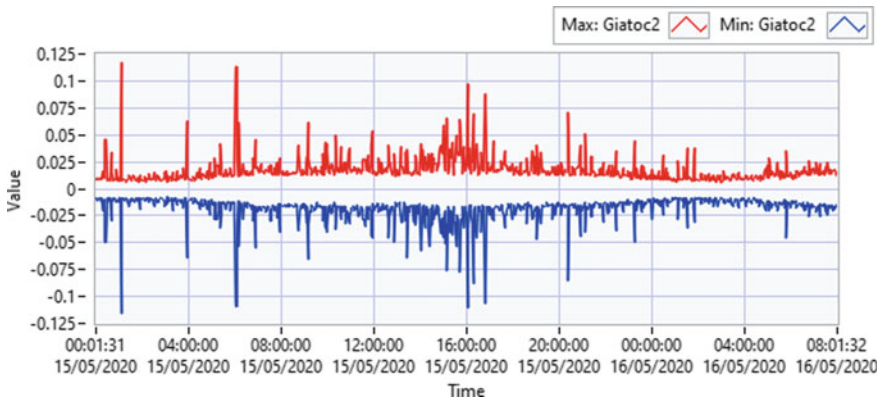

Fig. 17 Vibration spectrum of main girder of the day varies with the amount of traffic of Dragon bridge [6]

6   Conclusions

The health monitoring system for Thuan Phuoc Bridge, Dragon Bridge and Tran Thi Thi Tran Bridge over Han River in Da Nang city that is designed and installed by the authors has met the investor's targets. The construction cost of the three-bridge SHM system is quite cheap compared to similar systems that were previously installed by foreign companies.

The graphical user interface of the software for data collection, processing, display, and alarms built on the Labview environment is installed on the workstation in the monitoring room in the bridge field, allowing the display and warning of real-time monitoring data and automatic export as selected time reports. A web

portal to allow access to real-time monitoring data remotely is also set up for each bridge with integrated 3D digital map technology.

The analysis results of the warning thresholds based on the initial monitoring data and FEM model update technique show that the results of the bridge's vibration characteristics are quite consistent with the FEM model. The initial vibration monitoring data is also compared with the FEM model at the time of design and the first inspection that found at the present time the dynamic characteristics of the bridges have not changed significantly compared to the first inspection. This updated FEM model can be used with monitoring data to assess bridge health in the next future time.

The temperature monitoring data in the asphalt concrete layer on the Thuan Phuoc Bridge surface is sometimes up to 65 °C, which is the temperature that can damage the asphalt concrete when passing heavy vehicle loads.

Further research works should continue to automate updating FEM model according to optimization algorithms and damage detections based on monitoring data.

References

1. ASTM E2983-14. Standard Guide for Application of Acoustic Emission for Structural Health Monitoring (2019)
2. ISIS and SAMCO. An Introduction to Structural Health Monitoring (2006)
3. Moreu, F., Li, X., Li, S.,Zhang, D.: Technical Specifications of Structural Health Monitoring for Highway Bridges: New Chinese Structural Health Monitoring Code (2018)
4. Xu, Y.-L.,Xia, Y.: Structural Health Monitoring of Long-Span Suspension Bridges, Spon Press (2012)
5. Center for Science and Technology Investment Consultancy-DUT. As build profiles of Thuan Phuoc bridge monitoring system, Danang, Vietnam (2019)
6. Center for Science and Technology Investment Consultancy-DUT. As build profiles of Rong bridge monitoring system, Danang, Vietnam (2020)
7. Center for Science and Technology Investment Consultancy-DUT. As build profiles of Tran Thi Ly bridge monitoring system, Danang, Vietnam (2020)

Lightweight Network Communication of Railway Health Monitoring System Based on BIM Model

Zhi-cheng Wang, Chong-hui Li, Xiao-hui Cao, and Cun-rong Li

1 Introduction

Nowadays, high-speed rail has also become a popular means of transportation for people to travel, resulting in a huge flow of people at high-speed rail stations. The platform awning of high-speed railway is a large-span spatial steel structure. Therefore, more and more attention is paid to the canopy safety of high-speed railway stations. During a long-life cycle, the steel structure material is inevitably affected by the structural stress and environmental factors, resulting in the damage of structural components and the existence of certain unsafe factors [1, 2]. Mounir et al. [3, 4] determined the key role of BIM in collaborative design and construction and combined BIM with railway. The advantages of this combination include decision support, cost control, visual planning, avoiding additional losses caused by design errors, interface detection, etc. Structural health monitoring technology can effectively prevent unsafe factors. Through the combination of health monitoring system and BIM model, BIM model visualization can be well realized in real time and a large number of monitoring data can be acquired. Meanwhile, Robert [5] created most BIM software based on the Windows platform. Zhang et al. [6] found that BIM software was developed mainly by C# and Java, and the main functions of the software include model browsing and model data analysis. Later Zainab et al. [7, 8] combined sensors and BIM model, and store the sensor data in the external centralized database, so that users can see the location of each sensor, realizing the automatic alarm function. At the same time, Rebekka et al. [9, 10] have done some

Z. Wang · X. Cao · C. Li (✉)
School of Mechanical and Electrical Engineering, Wuhan University of Technology,
Wuhan, China
e-mail: zhicheng_wang_whut@163.com

C. Li
Chongqing Research Institute, Zhongxing Telecommunication Equipment Corporation,
Shenzhen, China

relevant researches on BIM model data and built structured and integrated data-bases, which is very meaningful to many related industries. On the basis of data interaction with external databases, a BIM model-based health monitoring system is developed by He et al. [11–13]. Then Ma et al. [14, 15] successfully obtained the static data of BIM model from documents and data access efficiency of BIM model is of great significance to the development of railway sector. Steel structure health monitoring plays an increasingly significant role in detecting damages to long-span steel structures to ensure their availability and sustainability, but also faces various challenges [16, 17]. Lin et al. [18] proposed the problems existing in the database storage and management of the health monitoring system. If the efficiency of data extraction is too low, the timeliness of data and alarm reliability will be affected.

The health monitoring system can effectively monitor the overall health status of the steel structure of the canopy and can accurately realize early in advance warning and alarm. So, it is very necessary to improve the performance of the system. With the in-depth study of the system, it is found that the customer service side is very slow to load BIM model and call a large amount of data. Therefore, this paper mainly calls static data from the external database to optimize, reducing the number of network communications, and improving the security and stability of the system.

2 System Architecture

In the system design process, the first part must be demand analysis. According to the actual demand and data demand analysis, the demand is transformed into the actual framework concept. Then through the framework concept, the result is transformed into the logical structure. Finally, by the logic structure, the overall structure, function and flow of the system will be finished.

Design the system according to the multi-stage networking and adopts TCP/IP protocol. The overall architecture and composition are shown in Fig. 1.

2.1 Technical Demand Analysis

Data Acquisition Demand Analysis. According to actual application and needs of users, a specific monitoring scheme was developed in this research process. The data acquisition terminal has external reporting interruption and regular inspection. Demodulation can set the data acquisition interval, and the shortest data takeover interval can be within 0.1 s.

The data information consists of user information, railway bureau information, platform information, BIM model information, component information, demodu-lator information, sensor information, monitoring information, location information, alarm information and others. The database manages all the data uniformly, and through logical transfer of each function module can realize data sharing.
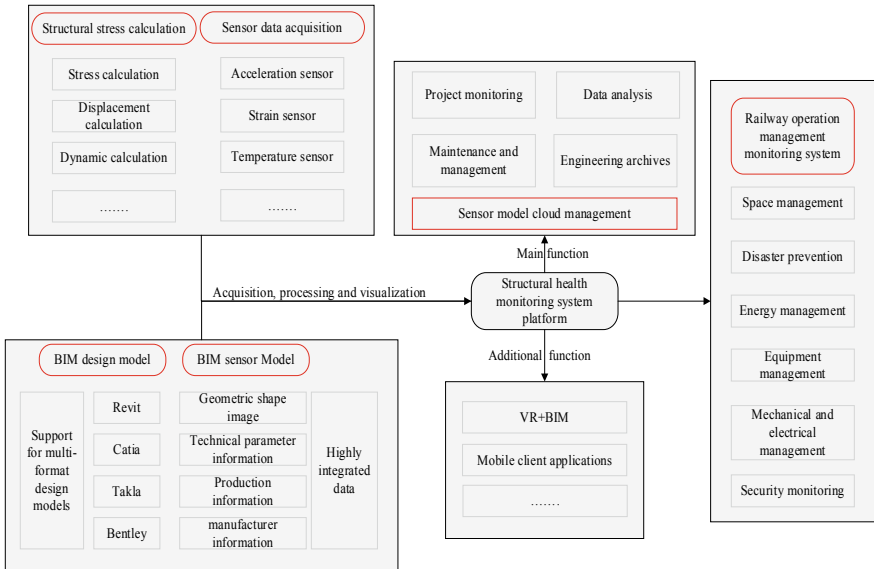
Fig. 1 Overall system architecture *Source* Authors

Functional Demand Analysis. System function mainly includes main and additional function.

Main Function. The main function of the monitoring system is divided into four modules: engineering monitoring, maintenance management, data analysis and engineering files. Each module is developed and implemented separately.

Additional Function. Additional extended function includes the implementation of BIM+VR, model re-editing; comprehensive BIM function support, lightweight processing GIS, map navigation, generating two-dimensional code and other extended development functions.

Lightweight BIM Analysis. The first step is to develop formulate unified BIM model establishment standards for steel structure of railway platform, and then standardize the storage and reading format of large amount of data resources of BIM model. Currently, IFC standard BIM model files are lightweight and processed by Navisworks in NWC format.

(1) Construct the overall structure model, the monitoring points and sensors in the model.
(2) Connect and embed BIM model and monitoring system.
(3) Implement BIM functions of structural monitoring, that is, monitoring information can be displayed on the visual interface.

2.2   Proposed System Architecture

As shown in the figure above, the overall monitoring system platform includes data acquisition and transmission system, data analysis and processing system, visual display system, operation and maintenance management monitoring system, extended functions and other parts. The work of each section and the corresponding standards are also shown in the figure. Then, according to the specific commonness and relevancy, some subsystems are integrated. The whole system framework is shown in Fig. 2.

2.3   Proposed System Workflow

Firstly, confirm the user's permission to enter the high-speed railway platform health monitoring system, and then communicate with the external database to query the relevant platform information and BIM model file information, saving it locally and displaying the relevant model information. Secondly, model artifacts are uniquely identified and bound to sensors and locations. When clicking the platform node corresponding platform sensor information is extracted. When clicking the sensor information, the sensor location information, the sensor information acquisition and corresponding data processing are acquired and displayed. Finally, compared to upper and lower limits of early warning, the function of automatic early warning is realized. The general flow chart is shown in Fig. 3.
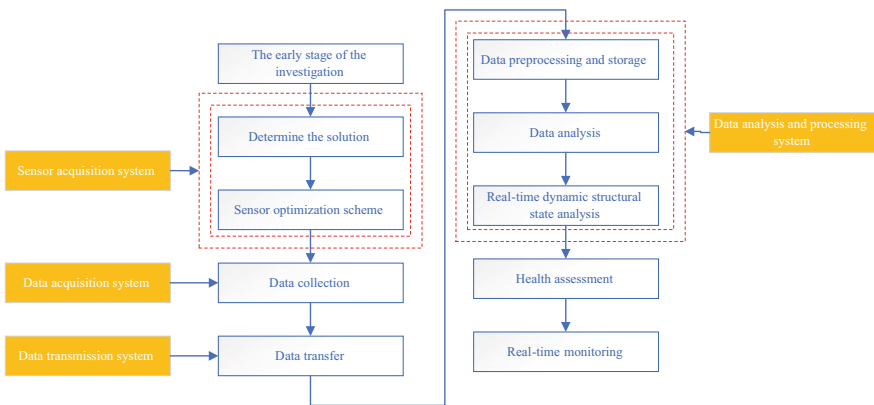
Fig. 2 System diagram *Source* Authors
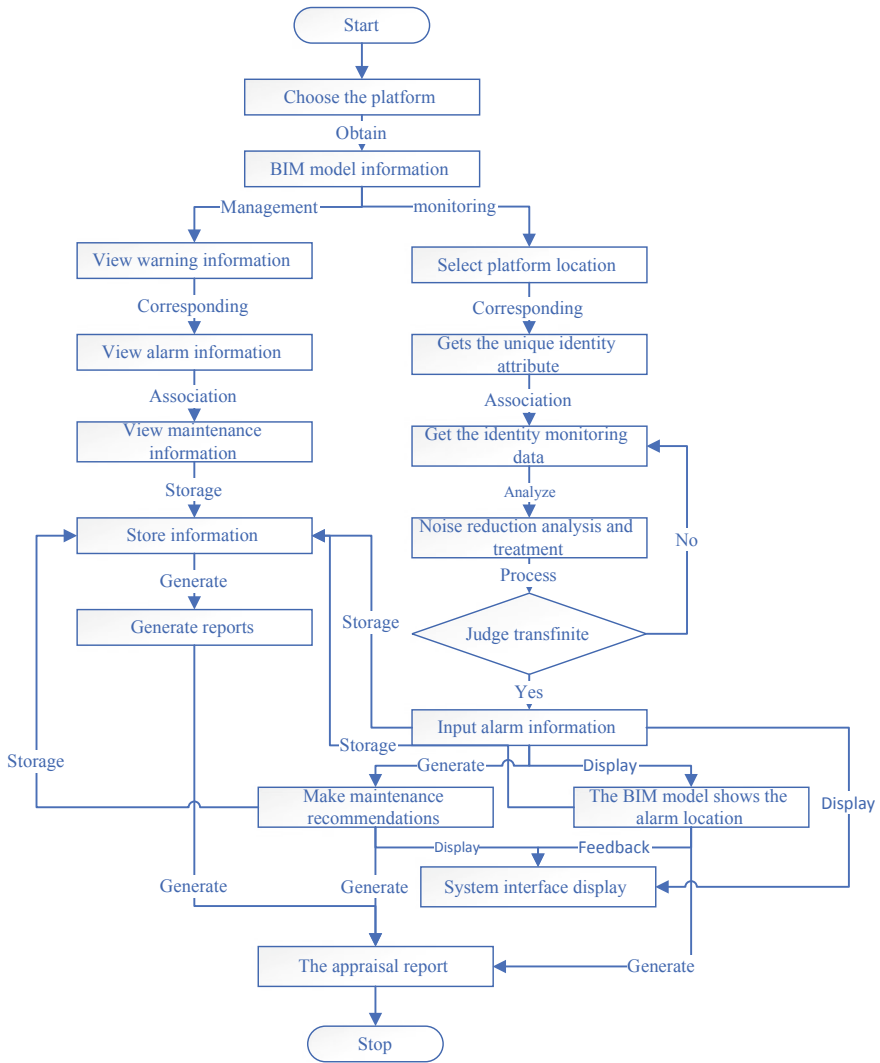
Fig. 3 System flow chart *Source* Authors

3 Optimization of Client Interaction with External Database

Since BIM model components include geometric data information, location data information and physical data information, it is difficult to meet the interactive requirements between the high-speed railway platform health monitoring and BIM model data. Therefore, it is necessary to expand the BIM model data and add an external database.

3.1 Static Data Analysis of Health Monitoring System of High-Speed Railway Platform Canopy

In this research, the ADO.NET is used to realize data between the system and the external database, and BIM model data is extracted and stored in the database. Therefore, it is inevitable in contains static data in the external database. The static data is immutable for a long time, so consistency between external database and local database data can be guaranteed.

Static data is a part of the external database data set, which consists of different information sets and is interrelated with one another. The composition of such association and static data set is expressed as follows by mathematical set relation.

Component information set: {component unique identification, geometric data, location data, physical data}.

BIM model information Set A: {component information}.

Monitoring information set: {monitoring type information, monitoring data information D}.

Data extension information set B: {user permission information, platform information, BIM model file information, location information, sensor information, monitoring information, early warning information}..

External database data information set C: $A \cup B$.

Static data Information set E: $\complement_C(C \cap D)$.

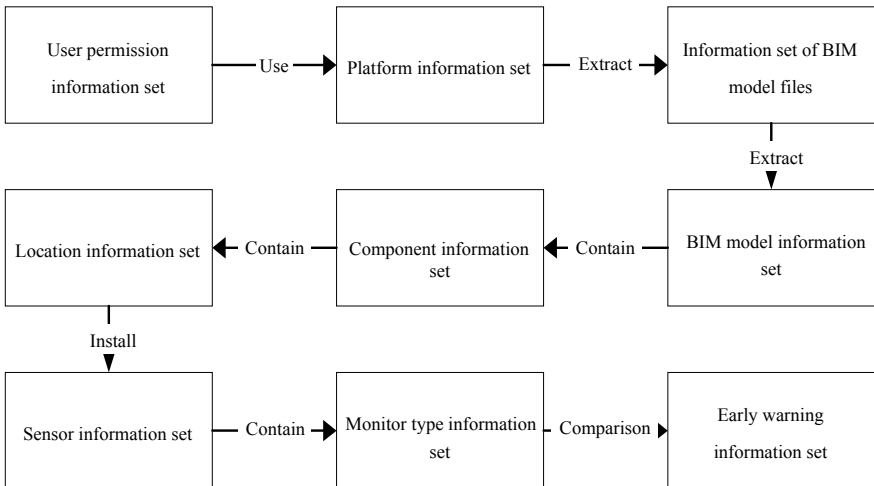Static data flow throughout the system (Fig. 4).

Fig. 4 System static data set structure *Source* Authors

3.2 Semi-static Data Analysis of Health Monitoring System of High-Speed Railway Platform Canopy

In the health monitoring system, real-time alarm function is necessary and the alarm information should be stored in the database. According to the data in the database. the health monitoring system performs real-time analysis and alarm display could be realized. The damage of steel structure of awning can be accumulated over time, so it will not alarm in a short time. However, the alarm information should be given to the staff in time, and the inspection and maintenance of steel structure should be carried out immediately. Therefore, constant query of alarm table can achieve the effect of real-time alarm, but most of the queries are invalid.

For a long-time, semi-static data has the uncertainty of changing. At the same time, it needs to ensure the real-time information, and to listen to the semi-static data table by the database. When the data table changes, the notification will update the table to convert the semi-static data into static data to achieve real-time and effective data.

3.3 Dynamic Data Analysis of Health Monitoring System of High-Speed Railway Platform Canopy

A large number of different types of sensors are installed in the platform awning of high-speed railway. By industrial control computer, the data is collected in real time in the acquisition system, and then the data is processed and stored in external databases. Types of sensors and the acquisition frequency of sensors are different.

According to the health monitoring system, BIM model can be visually displayed in real time. The data is analyzed and determined dynamically if the health status of the steel structure of the canopy is safe.

3.4 Light Weighed Network Communication

A large amount of static data in the system comes from external database and BIM model. Users need to interact with external database on the network every time they operate. Frequent operation will entail extra time cost and network change will affect the normal use of system functions. On account of the long-time invariability of static data, the consistency between external data and local data is guaranteed, which can realize the lightweight of network communication, load query, and improve the security and stability of the system. When the query operation is first executed, network communication, relevant data is extracted and stored in local and corresponding data is directly extracted locally when reused, this process is shown in Fig. 5.
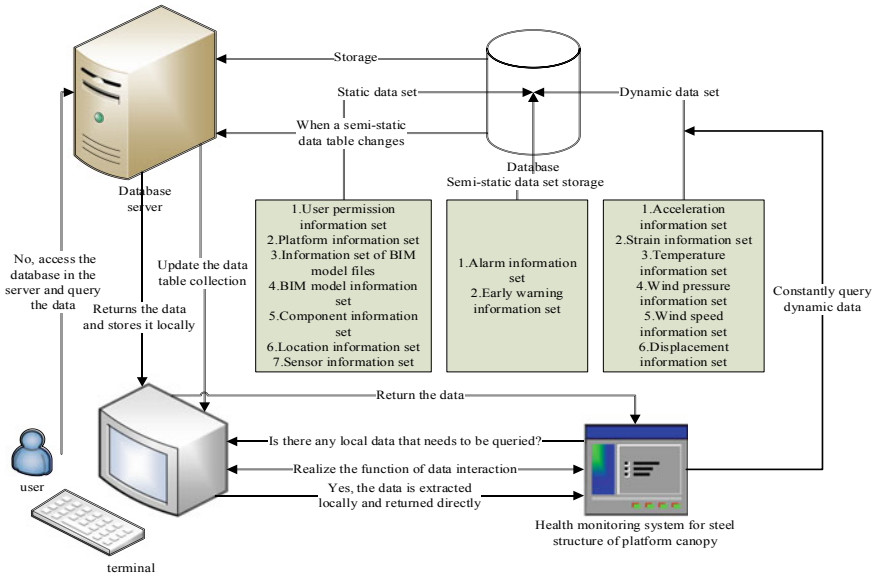
Fig. 5 Light weighted network communication *Source* Authors

Compared with loading all static data into the local area at one time, the storage space grows step by step, which can save space in a short time. Data from the same table is logically partitioned logically from static data by query and physically stored in the same collection.

4 Client and External Database Interaction Optimization Implementation

In order to realize lightweight network communication, the network communication can be greatly reduced when data is repeatedly extracted (Fig. 6).

According to the data characteristics to the system performance, the corresponding implementation method is used to determine whether the data extracted from the external database can be stored locally in a long- time, which can ensure the consistency of the data is static data. The data that may change in a certain period of time and have a high need on real-time performance is semi-static data. Finally, dynamic data changes over time.
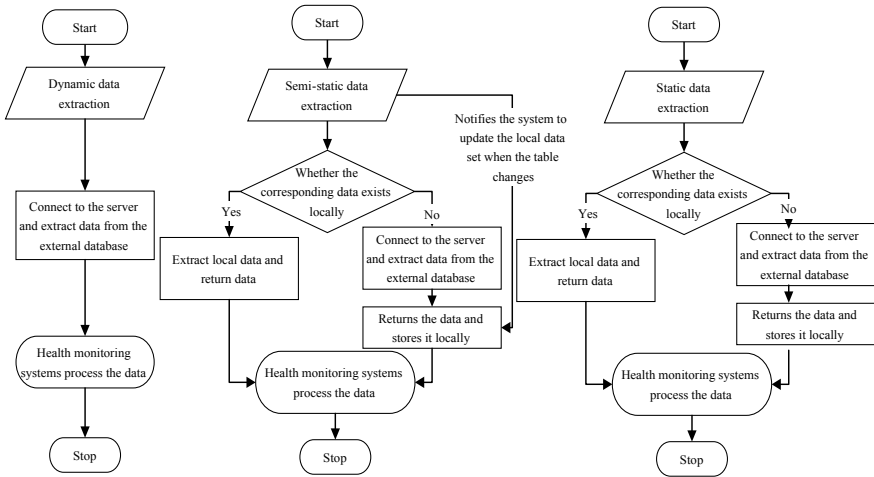
Fig. 6 System data extraction process *Source* Authors

5 Validation

5.1 Experimental Verification

Based on Visual Studio 2017 platform and SQL Server 2014, some programs of this monitoring system were tested, as shown in Fig. 7. When the platform node is clicked for the first time, sensor information is extracted and is saved locally, and then t local data flow is extracted as the same platform node is clicked again.

According to the size of data volume, the time of extracting and storing data from external database and the time of extracting local data were measured, respectively, as shown in Table 1.

5.2 Results Analysis

The external database query and local query data are processed according to different data volumes in Table 2, as shown in Fig. 8.

The total time of interaction between the client and the external database is represented as T_I and the time of query operation in the external database is expressed as T_q. The time of network communication between clients is abbreviated as T_c and external database and generic collection storage data time is expressed as T_s:

Fig. 7 System static data flow structure diagram *Source* Authors

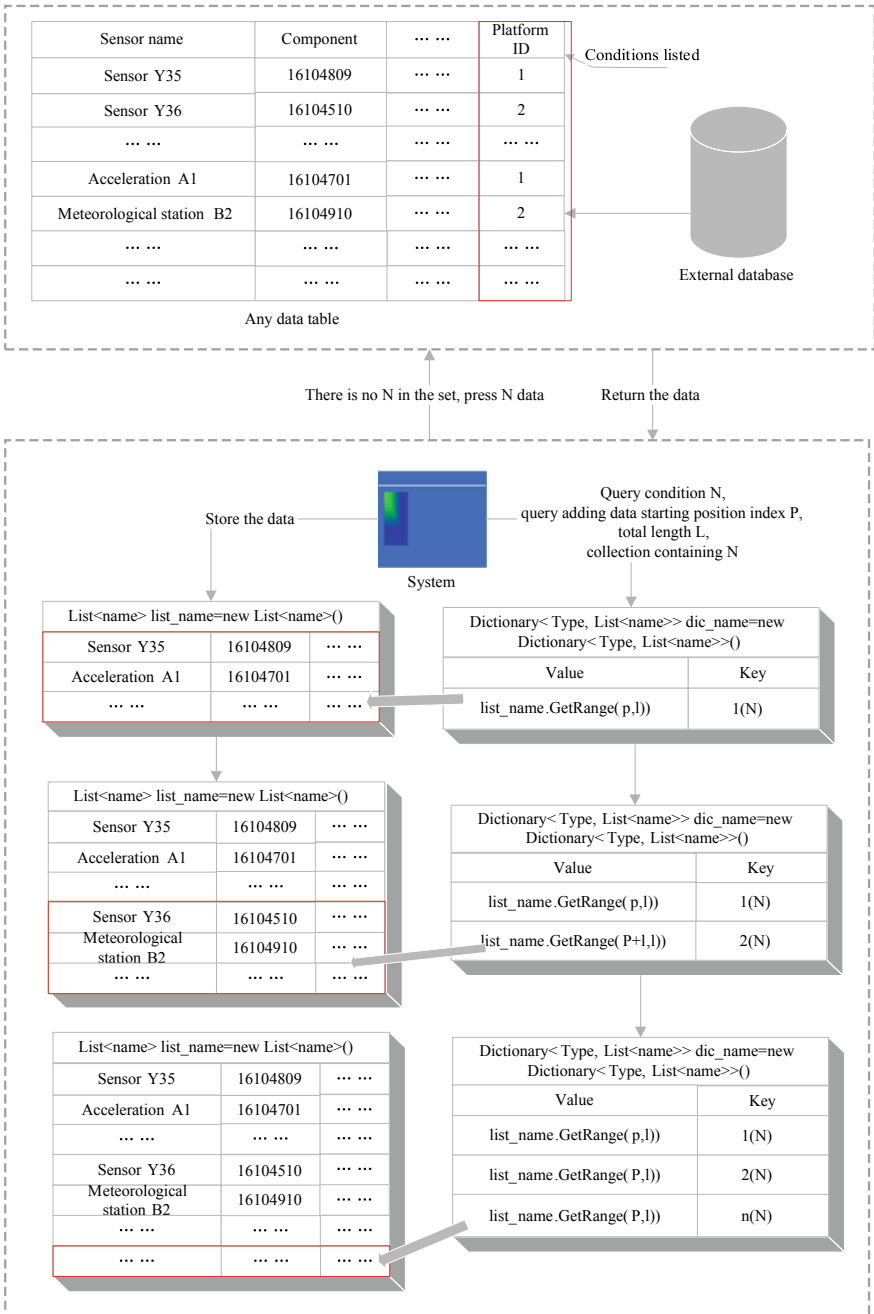**Table 1** System interaction with external databases and local interaction times *Source* Authors

Data volume	Query mode	Number of queries								
		1	2	3	4	5	6	7	8	9
777	External	20.6598	19.8569	20.3484	20.3536	20.7469	19.2667	19.8967	19.3849	20.4681
	Local	0.0015	0.0018	0.0016	0.0016	0.0016	0.0016	0.0018	0.0016	0.0019
7749	External	29.103	28.0433	28.8737	28.8726	28.6628	29.889	28.7618	28.9566	28.0868
	Local	0.0019	0.0018	0.0017	0.0016	0.0015	0.0018	0.0017	0.0019	0.0016
32,649	External	56.8264	56.4514	55.1056	54.7929	53.5237	56.8155	54.5117	55.0183	53.4201
	Local	0.0016	0.0017	0.0017	0.0018	0.0016	0.0019	0.0016	0.0018	0.0016
70,717	External	122.18	142.403	122.164	138	139.534	122.454	123.149	141.308	122.878
	Local	0.0016	0.0015	0.0015	0.0015	0.0017	0.0018	0.0016	0.0017	0.0017
103,416	External	157.232	165.015	174.374	167.969	162.026	171.344	181.256	177.828	175.373
	Local	0.0018	0.0015	0.0014	0.0014	0.0018	0.0016	0.0016	0.0016	0.002
135,984	External	210.641	223.006	217.021	211.709	225.69	213.052	209.023	208.74	209.477
	Local	0.0016	0.002	0.0015	0.0019	0.0016	0.0018	0.0017	0.0017	0.0019

Table 2 Average time for different data volumes *Source* Authors

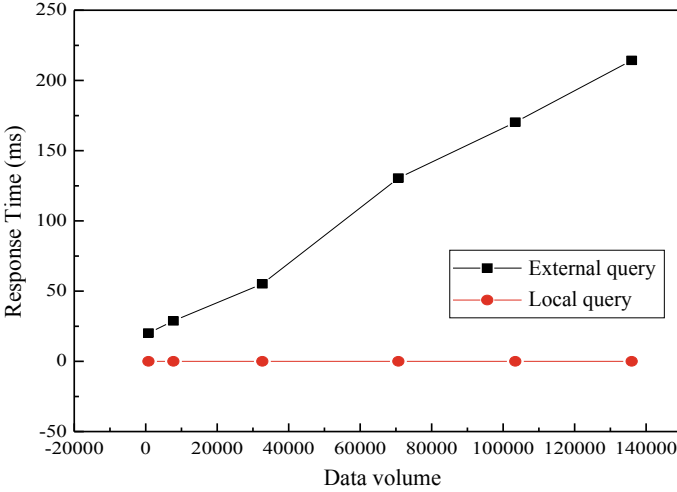| Data volumes	777	7749	32,649	70,717	103,416	135,984
External (MS)	20.1091	28.8055	55.1628	130.4521	170.2683	214.2622
Local (MS)	0.0017	0.0016	0.0017	0.0016	0.0016	0.0017

Fig. 8 Time response curves under different data volumes *Source* Authors

$$T_I = T_q + T_c + T_s \tag{1}$$

In general, T_c is generally affected by the LAN network speed and the communication distance between the client and the external database data network. The external database query data time T_q can be optimized from the database aspect, but the larger the database query data volume, the longer the query data time, which is inevitable. $T_{storage}$ is proportional to the number of items return by database interaction. The above three aspects all affect the total process time T_I for the client to interact with the external database data. As shown in Fig. 8, the general generic set only performs the addition operation when receiving data, and the internal structure of the set is a sequential linear table. So, the addition operation is performed with high efficiency and time complexity O(1) is low for this condition. The more data, the bigger the query time T_q and data storage time T_s. At the same time, the bigger the total time T_I, that is, the greater the external database query time, the lower the query efficiency.

The total time of local query data is expressed as T_{loc}, the query time of key-value pair set is represented as T_{dic}, and the data time of key-value pair set extracted from the generic set according to the key is simplified as T_{ext}. The relationship among the above three is expressed as the following equation,

$$T_{\text{loc}} = T_{\text{dic}} + T_{\text{ext}} \qquad (2)$$

In general, T_{dic} is only related to the logic partition of generic set. In this study, Hash table is adopted for key-value pair set query, average time complexity of which is expressed as O(1). There will not be a very clear difference and query time will not change significantly. According to index and time constraints of search target, the target data is extracted once in the corresponding generic set. The time complexity of extracting the data, does not change with the size of the data. As shown in Fig. 8, the total time of local query data T_{loc} is not affected by the size of data and remains keep constant.

6 Conclusion

The combination of BIM model and structural health monitoring system is also the combination of architecture and computer. ADO.NET and SQL Server are used as platforms to realize relevant requirements of health monitoring system of high-speed railway platform, which is the development trend of BIM field.

(1) Firstly, the BIM model data is extracted and stored in the external database, and then the BIM model data is read from the external database. The loading time of the model is shortened from 10 min to 10 s, which greatly improves the loading efficiency of the model.

(2) Only a small amount of related query operations is required on semi-static data and static data. The collection key value is updated according to the database notification and the local generic collection data is extracted directly from the corresponding key of the collection according to the key value when reused. Lightweight network communication is achieved, and the stability and security of this system are improved.

(3) This study clarifies how to classify according to the characteristics of data and how to query and process data in different ways so that the data structure of the entire system is getting clearer. This study can provide a theoretical reference for the optimization of railway health monitoring systems.

References

1. Xu, Y., Lu, P.: Organizational integration of large-scale construction projects based on BIM. J. Railway Sci. Eng. **13**(10), 2092–2098 (2016)
2. Xing, Y., Guo, Q., Han, Z., et al.: Simulation analysis for lifting construction of large span steel truss arch bridge based on BIM technology. Struct. Eng. **35**(01), 237–245 (2019)
3. Mounir, B., Elouadi, A., Mharzi, H.: Overview: the opportunity of BIM in railway. Smart Sustain. Built Environ. **8**(2), 103–116 (2019)

4. Liu, Y., van, N., Hertogh, M.: Understanding effects of BIM on collaborative design and construction: an empirical study in China. Int. J. Project Manage. **35**(4), 686–698 (2017)
5. Robert, B.: Evaluation of maturity of BIM tools across different software platforms. Proc. Eng. **164**, 481–486 (2016)
6. Zhang, M., Li, X., Li, Z.: An overview of international BIM software with open source. J. Eng. Manage. **31**(06), 17–22 (2017)
7. Zainab, R., Arslan, M., Kiani, A., et al.: CoSMoS: a BIM and wireless sensor based integrated solution for worker safety in confined spaces. Autom. Construction **45**, 96–106 (2014)
8. Chi, A., Zhou, F., Yi, S., et al.: The framework of BIM and sensor integrated decision-making system in the operation and maintenance period of highrise building projects. Project Manage. Technol. **15**(06), 83–89 (2017)
9. Rebekka, V., Stengel, J., Schultmann, F.: Building Information Modeling (BIM) for existing buildings—literature review and future needs. Autom. Construction **38**, 109–127 (2014)
10. Yasser, Y., Idris, O., Yani, R., et al.: BIM benefits and its influence on the BIM implementation in Malaysia. AinShams Eng. J. https://doi.org/10.1016/j.asej.2020.02.002
11. He, H., Li, C., Fan, X., et al.: Research on data model of railway rainfall steel structure health monitoring based on BIM model. Railway Standard Des. **63**(9), 115–120 (2019)
12. Hu, J., Li, H., Yang, H., et al.: Integrated design and application of structural health monitoring software system Shanghai Tower. J. Tongji Univ. (Nat. Sci. Ed.) **42**(03), 460–467 (2014)
13. Tao, W.: Research on data extraction method of BIM model based on secondary development method. Value Eng. **38**(08), 159–161 (2019)
14. Ma, Z., Teng, M., Ren, Y.: Method of extracting static data for building energy consumption monitoring from BIM. J. Harbin Inst. Technol. **12**, 187–193 (2019)
15. Yu, F., Zhang, J., Liu, Q., et al.: A semi-structured BIM database based on cloud computing platforms. J. Inf. Technol. Civil Eng. Architectural **5**(06), 1–6 (2013)
16. Tan, Y., Zhang, L.: Computational methodologies for optimal sensor placement in structural health monitoring: a review. Struct. Health Monit. https://doi.org/10.1177/1475921719877579
17. Abdulkarem, M., Samsudin, K., Rokhani, F., et al.: Wireless sensor network for structural health monitoring: a contemporary review of technologies, challenges, and future direction. Struct. Health Monit. **19**(3), 693–735 (2020)
18. Lin, J., Cheng, Y., Huang, J., Chen, S.: Massive data processing in large-scale structural health monitoring and the corresponding database development. J. Vib. Shock **29**, 55–59, 237 (2010)

Electro-Mechanical Impedance-Based Prestress Force Monitoring in Prestressed Concrete Structures

Duc-Duy Ho, Thanh-Canh Huynh, Tran-Huu-Tin Luu, and Thanh-Cao Le

1 Introduction

Nowadays, along with the outstanding development of science and technology, many complex and modern civil structures have been built. However, the occurrence of damages in the process of construction, exploitation and operation of the civil structures is inevitable. This not only has a negative impact on the structural safety and longevity, but also affects the people's lives. Therefore, regular monitoring and diagnosis of structures are essential in order to promptly detect damages and provide reasonable handling, reinforcement and repair solutions. It is nearly impossible to directly detect structural damages with the eyes. Therefore, during the last century and until now, structural health monitoring (SHM) has been playing a very important role in the safety and sustainable development for infrastructure. Many SHM technologies and methods have been developed by researchers around the world [1, 2]. In particular, the impedance-based damage detection method which utilizes electro-mechanical impedance responses is a highly effective method. The impedance-based method uses the high-frequency responses which are very effective for diagnosing the local structural damages. This method can detect

D.-D. Ho (✉) · T.-H.-T. Luu · T.-C. Le
Faculty of Civil Engineering, Ho Chi Minh City University of Technology (HCMUT), Ho Chi Minh City, Vietnam
e-mail: hoducduy@hcmut.edu.vn

D.-D. Ho · T.-H.-T. Luu · T.-C. Le
Vietnam National University Ho Chi Minh City, Ho Chi Minh City, Vietnam

T.-C. Huynh
Faculty of Civil Engineering, Duy Tan University, Da Nang, Vietnam

T.-C. Huynh
Institute of Research and Development, Duy Tan University, Da Nang, Vietnam

T.-C. Le
Faculty of Civil Engineering, Nha Trang University, Nha Trang, Vietnam

the initial damages without destructing the structure. The impedance method was first introduced by Liang et al. in 1994 [3]. After that, other researchers have proposed damage indices using impedance responses, for example the RMSD index (Root Mean Square Deviation) [4], CC index (Correlation Coefficient) [5], the CCD index (Correlation Coefficient Deviation) [6] and the MAPD index (Mean Absolute Percentage Deviation) [6]. Moreover, the impedance method has been successfully applied on many different types of structures such as truss structure [4], thin shell structure [7], steel structure [8], concrete structure [9], prestressed concrete beam [10], reinforced concrete structure strengthening with FRP [11]. In addition, some researches have been focused on the development of PZT (Lead Zirconate Titanate) interface-based impedance monitoring technique and wireless impedance sensors [2].

In civil engineering, prestressed reinforced concrete structures are very common used. For this type of structure, prestress force is an important target that needs to be monitored and diagnosed to ensure the structural safety. From the practical needs and the previous studies, the main objective of this study is to present a method of identifying the loss of the prestress force using the impedance responses. First, the basic theories of impedance responses and four damage indices (CC, CCD, RMSD, and MAPD) based on the change in impedance responses are briefly outlined. Next, a finite element model of cable anchorage system in a prestressed reinforced concrete beam is simulated using ANSYS software. In the model, the prestress loss is considered with three different levels of 20, 40, and 60%. The reliability of the simulation results is verified with experimental results. Final, the four damage indices are determined and analyzed to identify the loss of prestress force in beam.
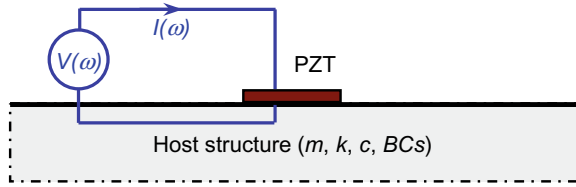
2 Impedance-Based Damage Monitoring

2.1 Electro-Mechanical Impedance Responses

For impedance-based SHM method, a PZT sensor is bonded to surface of target structure which needs to be monitored. The PZT sensor is connected to an AC power source. Electric excitation from the source and reacts in the form of an electrical signal, it is then converted to an impedance signal. The electro-mechanical interaction between the PZT sensor and the host structure is shown in Fig. 1. Consequently, the structure is described by characteristics such as mass (m), stiffness (k), damping (c) and boundary conditions. Meanwhile, the PZT sensor is described as an electrical circuit with the harmonic voltage (V) and amperage (I).

The electro-mechanical impedance $Z(\omega)$, which is a function of host structure's mechanical impedance $Z_s(\omega)$ and PZT sensor's impedance $Z_a(\omega)$, is defined as follows [3]:

$$Z(\omega) = \left[j\omega \frac{w_p l_p}{t_p} \left(\left(\overline{\varepsilon_{33}^T} - d_{31}^2 \overline{Y_{11}^E} \right) + \frac{Z_a(\omega)}{Z_a(\omega) + Z_s(\omega)} d_{31}^2 \overline{Y_{11}^E} \left(\frac{\tan k l_p}{k l_p} \right) \right) \right]^{-1} \quad (1)$$

where w_p, l_p and t_p are the width, length, and thickness of the PZT sensor, respectively; $\overline{\varepsilon_{33}^T}$ is the complex electric permittivity at constant stress; d_{31} is the PZT's piezoelectric constant when the stress is zero; $\overline{Y_{11}^E} = (1 + j\eta)Y_{11}^E$ is the PZT's elastic modulus when the electric field is zero; η and δ are the structural damping loss factor and the PZT's dielectric loss factor, respectively; $k = \omega \sqrt{\frac{\rho}{Y_{11}^E}}$ is the number of wavelengths; ρ is the PZT's mass density.

In Eq. (1), when the host structure is damaged, its mechanical impedance, $Z_s(\omega)$, will change; as a result, the electro-mechanical impedance, $Z(\omega)$, will also change. The host structure's mechanical impedance is a function of the dynamic characteristics (mass, stiffness, and damping) and the boundary conditions. Therefore, any change in the dynamic characteristics and boundary conditions (considered as damage) can lead to the change in impedance responses; and vice versa, the change in impedance responses can be used to evaluate the structural damages [12].

2.2 Impedance-Based Damage Indices

In this study, four damage indices are utilized to quantify the change in impedance responses before and after the occurrence of structural damages. The four damage indices include: CC index [5], CCD index [6], RMSD index [4], and MAPD index [6]. The effectiveness of damage diagnosis is different when using different damage index. This depends on the structural characteristics and the considered frequency range of impedance responses. The investigation of different damage indices at the same time is to find an index with good sensitivity to the prestress loss in beam.

$$CC = \frac{1}{n} \frac{\sum_{i=1}^{n} (Z^*(\omega_i) - \overline{Z^*}) \cdot (Z(\omega_i) - \overline{Z})}{\sigma_{Z^*} \sigma_Z} \quad (2)$$

$$CCD = 1 - \frac{1}{n} \frac{\sum_{i=1}^{n} (Z^*(\omega_i) - \overline{Z^*}) \cdot (Z(\omega_i) - \overline{Z})}{\sigma_{Z^*} \cdot \sigma_Z} \quad (3)$$

$$\text{RMSD} = \sqrt{\frac{\sum_{i=1}^{n}\left[Z^*(\omega_i) - Z(\omega_i)\right]^2}{\sum_{i=1}^{n}\left[Z(\omega_i)\right]^2}} \tag{4}$$

$$\text{MAPD} = \frac{1}{n}\sum_{i=1}^{n}\left|\frac{Z^*(\omega_i) - Z(\omega_i)}{Z(\omega_i)}\right| \tag{5}$$

where $Z(\omega_i)$ and $Z^*(\omega_i)$ are the impedance responses of the ith frequency for two conditions, before and after the occurrence of damage, respectively; n is the number of data in the considered frequency range; $\overline{Z}$ and $\overline{Z^*}$ are the mean values of the corresponding impedance responses, respectively; σ_Z and σ_{Z^*} are the standard deviation of the corresponding impedance responses, respectively.

In order to assess the presence of damage, the following rules are performed for each damage index. For the CC index, if the value is less than 1 then the structure is damaged; and vice versa, if the value is 1, no damage presents. For indices of CCD, RMSD, MAPD, if the value is greater than 0, the structure is damaged; and vice versa, if the value is 0, no damage presents.

3 Numerical Simulation for Cable Anchorage System

In this study, a cable anchorage system of a prestressed reinforced concrete beam was selected for numerical simulation. The details of the cable anchorage system are shown in Fig. 2 [10]. In which, an aluminum interface plate with dimensions of $100 \times 18 \times 6$ mm, with holes of $30 \times 18 \times 1$ mm, was placed on a steel bearing

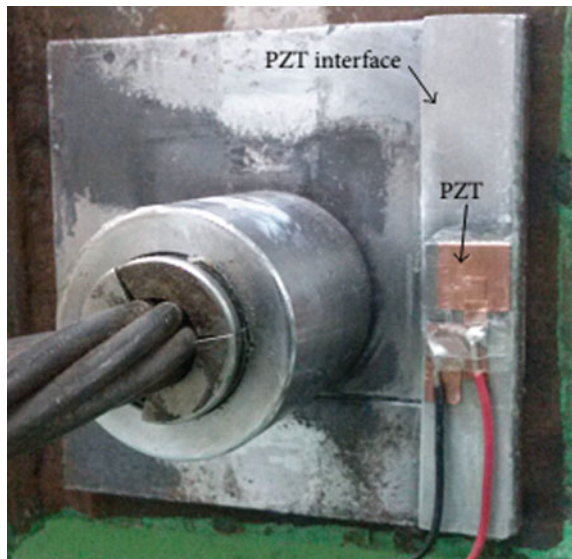**Fig. 2** Cable anchorage system [10]

Table 1 Material properties of PZT-5A sensor [13]

Parameters	Value
Elastic compliance s_{ijkl}^{E} (m²/N)	$\begin{bmatrix} 16.4 & -5.74 & -7.22 & 0 & 0 & 0 \\ -5.74 & 16.4 & -7.22 & 0 & 0 & 0 \\ -7.22 & -7.22 & 18.8 & 0 & 0 & 0 \\ 0 & 0 & 0 & 47.5 & 0 & 0 \\ 0 & 0 & 0 & 0 & 47.5 & 0 \\ 0 & 0 & 0 & 0 & 0 & 44.3 \end{bmatrix} \times 10^{-12}$
Dielectric coupling constant d_{kij} (C/N)	$\begin{bmatrix} 0 & 0 & -171 \\ 0 & 0 & -171 \\ 0 & 0 & 374 \\ 0 & 584 & 0 \\ 584 & 0 & 0 \\ 0 & 0 & 0 \end{bmatrix} \times 10^{-12}$
Permittivity ε_{jk}^{T} (F/m)	$\begin{bmatrix} 1730 & 0 & 0 \\ 0 & 1730 & 0 \\ 0 & 0 & 1700 \end{bmatrix} \times (8.854 \times 10^{-12})$
Mass density ρ (kg/m³)	7750
Damping loss factor η	0.005
Dielectric loss factor δ	0.015

plate with dimensions of $100 \times 100 \times 10$ mm. A steel anchor head with outer diameter $D = 45$ mm and inner diameter $d = 15.2$ mm was used. A PZT-5A sensor with dimensions of $15 \times 15 \times 0.51$ mm was bonded on the interface plate. The PZT sensor was excited by a harmonic voltage of 1 V. The material properties of PZT sensor and interface plate, bearing plate, anchor head are given in Tables 1 and 2 [13]. The scenarios of prestress loss are listed in Table 3.

According to the contact mechanism [14], the change in the prestress force can be considered as the variation in the structural parameters at the contact position. As a result, the prestress force was modeled through springs' stiffness [10]. When the prestress force is reduced which means the springs' stiffness is reduced proportionally. In the model, the springs' stiffness at the contact position of the anchorage is an unknown and uncertain parameter. In this study, value of the springs' stiffness was determined using trial and error method, by comparing experimental impedance responses for two cases of T0 and T3. Then the linear interpolation method was used to determine the springs' stiffness for cases of T1 and T2 [15]. In this study, ANSYS APDL software was employed to establish finite element (FE) model for the cable anchorage system. Figure 3 shows the FE model of the anchorage system in ANSYS. The bearing plate, anchor head and interface plate were modeled with elements of SOLID45. The PZT sensor was modeled with electro-mechanical elements of SOLID5. The springs were modeled with the elastic elements of COMBIN14. All of the anchorage system were simulated with 20,729 nodes and 99,318 elements, including 488 COMBIN14 elements.

From the FE model, impedance responses of the cable anchor region were analyzed. Figure 4 shows impedance responses of the prestress case of T0 in

Table 2 Material properties of cable anchorage system [13]

Parameters	Interface	Bearing plate, anchor head
Young's modulus E (N/m^2)	70×10^9	200×10^9
Mass density ρ (kg/m$^{3)}$	2700	7850
Poisson's ratio υ	0.33	0.3
Damping loss factor η	0.001	0.02

Table 3 Prestress loss scenarios

Prestress case	Prestress loss (%)	Prestress force (kN)	Springs' stiffness (N/m)
T0	0	49.05	120×10^6
T1	20	39.20	105×10^6
T2	40	29.40	90×10^6
T3	60	19.60	75×10^6

Fig. 3 FE model of the cable anchorage system

Anchor head

Bearing plate

Interface   PZT   Springs
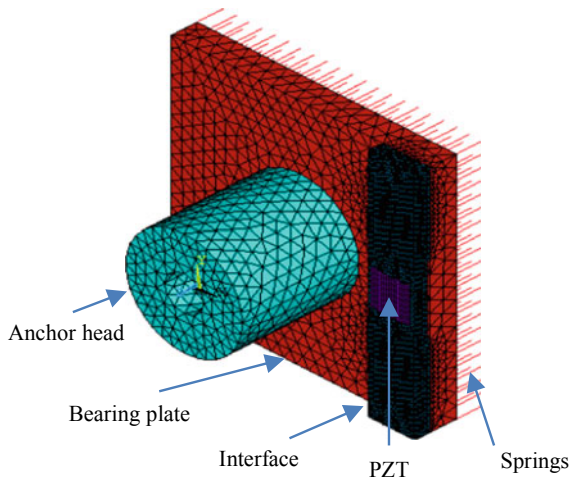
frequency range of 10–100 kHz. The numerical impedance responses are compared to the corresponding experimental ones in [10] to demonstrate the accuracy and feasibility of the simulation. The numerical results are good agreement with experimental ones. The impedance responses have two resonant peaks in the frequency domains of 15–25 and 77– 87 kHz. The numerical impedance responses are slightly different from the experimental ones. This is due to signal interference by influencing experimental factors such as temperature, wind, light, electromagnetic waves, wires, equipment, and experimenters… Meanwhile, the numerical impedance responses depend on the shape and number of meshed elements in the FE model, especially for the PZT sensor area.
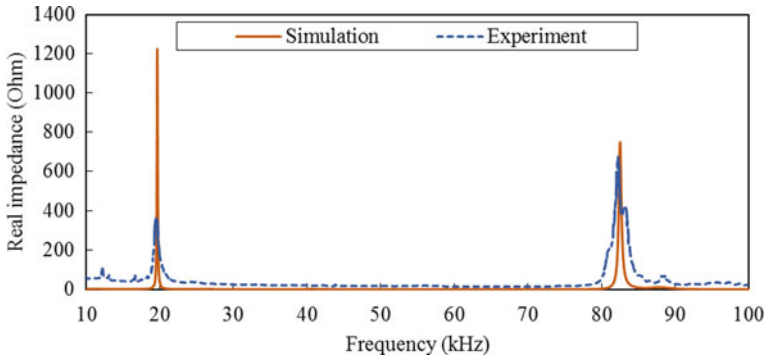
Fig. 4 Impedance responses for prestress case of T0

The results of comparing the frequency peak between simulation and experiment corresponding to the four prestress cases are summarized in Table 4. For the first resonant frequency peak in the range of 15–25 kHz, the differences are very small, ranging from 0 to 0.2%. For the second resonant frequency peak in the range of 77–87 kHz, the differences are from 0.3 to 0.6%. Thus, the differences of frequency peaks between simulation and experiment for all cases is less than 1%. This result shows that the FE model of the cable anchorage system has a very high reliability and can be used to represent the real one in monitoring of the prestress force.

Figure 5 shows the numerical impedance responses in two frequency ranges of 15–25 and 77–87 kHz for four prestress cases (i.e., T0, T1, T2, T3). When there is prestress loss, the impedance responses in the frequency range of 15–25 kHz is more sensitive than in the frequency range of 77–87 kHz. As the loss of the prestress force increases, the impedance responses tend to shift to the left with respect to decreasing frequency values. For example, the no-loss case of T0 is 19.67 kHz and the maximum loss case of T3 is 19.52 kHz. However, the decrease in frequency is negligible (less than 1%). Therefore, the change in frequency of impedance responses has been used seldom to warn the occurrence of damage; as a result, other impedance-based damage indices must be used.

4 Prestress Force Monitoring Results

The four different indices for assessing the loss of prestress force including CC, CCD, RMSD, and MAPD were determined by the corresponding Eqs. (2)–(5), with input data being the numerical impedance responses. The results are shown in Fig. 6 for the two considered frequency ranges (15–25 and 77–87 kHz). In general, all four indices correctly reflect the structural working status of the anchorage system. For the CC index, the value is less than 1 for the prestress loss cases (T1, T2, T3), and vice versa the value is 1 for no prestress loss case (T0). Meanwhile, for

Table 4 Comparison of frequency peaks between simulation and experiment

Prestress case	Prestress loss (%)	Simulation f_1 (kHz)	Experiment f_1 (kHz)	Δf_1 (%)	Simulation f_2 (kHz)	Experiment f_2 (kHz)	Δf_2 (%)
T0	0	19.67	19.63	0.20	82.51	82.23	0.34
T1	20	19.63	19.63	0.00	82.50	82.15	0.43
T2	40	19.58	19.57	0.05	82.49	82.03	0.56
T3	60	19.52	19.53	0.05	82.48	–	–

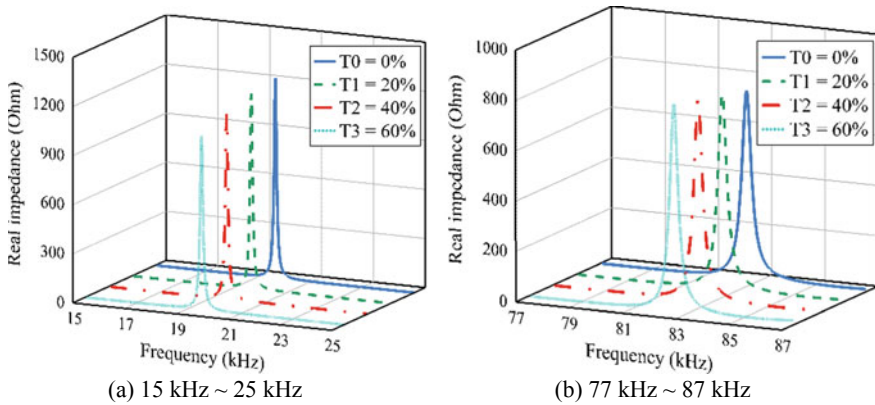(a) 15 kHz ~ 25 kHz   (b) 77 kHz ~ 87 kHz

Fig. 5 Numerical impedance responses. **a** 15– 25 kHz. **b** 77–87 kHz

the indices of CCD, RMSD, and MAPD, the value is greater than 0 for the prestress loss cases (T1, T2, T3), and vice versa the value is 0 for no prestress loss case (T0). Thus, the occurrence of prestress loss in the cable anchorage system was successfully detected by using the impedance-based damage indices.

In the frequency range of 15–25 kHz, the RMSD index has a higher sensitivity to prestress loss than the other three indices; RMSD value reaches 0.524 in case of minimum prestress loss T1 = 20%. In the frequency range of 77–87 kHz, the RMSD index is also more effective when it reaches 0.039 for the minimum prestress loss T1 = 20%. When the prestress loss increases, it means that the prestress force is decreased, the CC index tends to decrease, and the CCD, RMSD, and MAPD indices tend to increase gradually. As shown in Fig. 6a, the CC index is not effective for diagnosing the prestress loss; especially for the frequency range of 77–87 kHz, the CC index remains almost unchanged as the prestress loss increases. Three indices of CCD, RMSD, and MAPD are more effective for diagnosing the prestress loss. The indices increase synchronously as the prestress loss increases. In comparison with the frequency range of 15– 25 kHz, the CCD index is only about 1% and the RMSD index is about 10% in the frequency range of 77–87 kHz. Meanwhile, the MAPD index is not significantly different when comparing between the two considered frequency ranges.

5 Conclusions

In this study, a finite element model for monitoring the loss of prestress force in prestressed concrete structures using the electro-mechanical impedance responses was successfully developed. Impedance responses analyzed from ANSYS software were highly reliable. The analysis results from numerical simulation were in good
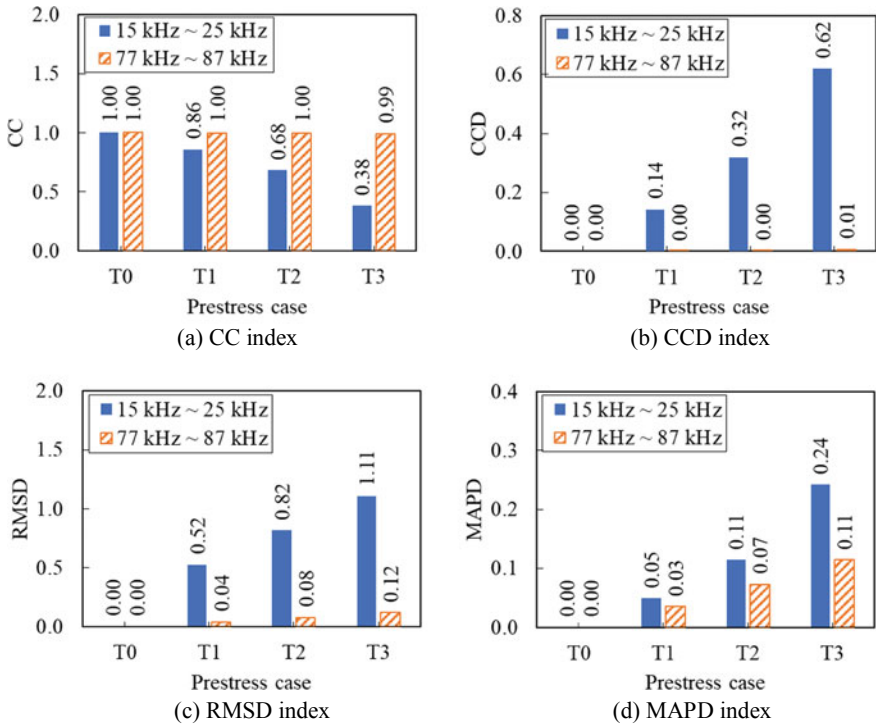
Fig. 6 Prestress force monitoring results. **a** CC index. **b** CCD index. **c** RMSD index. **d** MAPD index

agreement with experimental results. Four impedance-based damage indices were capable of detecting the loss of prestress force in the cable anchorage system. Each index had a different sensitivity to the prestress loss and depended on the considered frequency range. Three indices of CCD, RMSD, and MAPD gave better diagnostic results of prestress loss than CC index. Therefore, the impedance method is feasible, effective and potential to be applied in the problem of diagnosing the occurrence of damage to real structures. In addition, the impedance method can be combined with artificial intelligence algorithms (machine learning, artificial neural networks, genetic algorithms,…) to accurately diagnose the extent of structural damage.

References

1. Das, S., Saha, P., Patro, S.K.: Vibration-based damage detection techniques used for health monitoring of structures: a review. J. Civil Struct. Health Monit. **6**, 477–507 (2016)
2. Huynh, T.C., Dang, N.L., Kim, J.T.: Advances and challenges in impedance-based structural health monitoring. Struct. Monit. Maintenance **4**(4), 301–329 (2017)
3. Liang, C., Sun, F.P., Rogers, C.A.: Coupled electro-mechanical analysis of adaptive material systems—determination of the actuator power consumption and system energy transfer. J. Intell. Mater. Syst. Struct. **5**(1), 12–20 (1994)
4. Sun, F.P., Chaudhry, Z., Liang, C., Rogers, C.A.: Truss structure integrity identification using PZT sensor-actuator. J. Intell. Mater. Syst. Struct. **6**(1), 134–139 (1995)
5. Raju, V.: Implementing impedance-based health monitoring technique. Master's Thesis, Virginia Polytechnic Institute and State University, Blacksburg, VA (1998)
6. Zagrai, A.N., Giurgiutiu, V.: Electro-mechanical impedance method for crack detection in thin plates. J. Intell. Mater. Syst. Struct. **12**(10), 709–718 (2001)
7. Giurgiutiu, V., Zagrai, A.: Damage detection in thin plates and aerospace structures with the electro-mechanical impedance method. Struct. Health Monit. **4**(2), 99–118 (2005)
8. Park, S., Yun, C.-B., Roh, Y., Lee, J.-J.: Health monitoring of steel structures using impedance of thickness modes at PZT patches. Smart Struct. Syst. **1**(4), 339–353 (2005)
9. Park, S., Ahmad, S., Yun, C.B., Roh, Y.: Multiple crack detection of concrete structures using impedance-based structural health monitoring techniques. Exp. Mech. **46**(5), 609–618 (2006)
10. Huynh, T.C., Kim, J.T.: Impedance-based cable force monitoring in tendon-anchorage using portable PZT-interface technique. Math. Prob. Eng. (2014)
11. Li, W., Fan, S., Ho, S.C.M., Wu, J., Song, G.: Interfacial debonding detection in fiber-reinforced polymer rebar–reinforced concrete using electro-mechanical impedance technique. Struct. Health Monit. **17**(3), 461–471 (2018)
12. Bhalla, S., Kiong, S.C.: Structural impedance based damage diagnosis by piezo-transducers. Earthquake Eng. Struct. Dynam. **32**(12), 1897–1916 (2003)
13. Huynh, T.-C., Park, Y.-H., Park, J.-H., Kim, J.-T.: Feasibility verification of mountable PZT-interface for impedance monitoring in tendon-anchorage. Shock Vib. (2015)
14. Johnson, K.L.: Contact Mechanics. Cambridge University Press, New York (1987)
15. Ritdumrongkul, S., Abe, M., Fujino, Y., Miyashita, T.: Quantitative health monitoring of bolted joints using a piezoceramic actuator–sensor. Smart Mater. Struct. **13**(1), 20 (2003)

Geotechnical and Geoenvironmental Engineering

A Practicable Application of Steel Slag and Crushed Stone Together for Road-Pavement Base Layer

Duc-Trong Nguyen and Duy-Liem Nguyen

1 Introduction

Steel slag has been classified as an industrial waste formed from steel-making process, and recycling steel slag has attracted many researchers and civil engineering with various purposes as follows: decreasing construction cost, minimizing the bad environment impact, and saving natural resources. In Southern Vietnam, the demand of utilizing steel slag is more and more increasingly, this is due to a large amount of steel slag has been superabundant. For example, a province in Southern Vietnam, Ba Ria-Vung Tau, the capacity of steel slag from steel-making plants was more than four hundred thousand tons a year [1]. The excessiveness of steel slag is really an environmental risk and thus needs more applications of steel slag. Some references [2–7] reported the application of steel slag in Vietnam. Several studies [2, 3] informed the potential utilization of steel slag as aggregate for road pavement or as supplementary cementing material [4]. Some researchers suggested using steel slag aggregate to produce concrete applied for structural members [5–7]. Since the amount of steel slag used in concrete of these researches were still small, the motivation of this study is applying steel slag for road-pavement base layer with larger amount used. A road with its length of 100 km could consume a huge quantities of steel slag, consequently, it basically meets the demand of recycling steel slag. Pavement base layer plays an important role in the all thickness design of a road pavement. From a mechanical point of view, a base material characterizes a largely various heterogeneous structure. In this research, steel lag under aggregate

D.-T. Nguyen
Campus in Ho Chi Minh City, University of Transport and Communications,
Ho Chi Minh City, Vietnam

D.-L. Nguyen (✉)
Faculty of Civil Engineering, Ho Chi Minh City University of Technology and Education,
Ho Chi Minh City, Vietnam
e-mail: liemnd@hcmute.edu.vn

form would be blended with crushed stone with size within 5 mm, also by-product in making aggregate, is greatly hoped to generate a synergic effect on enhanced resilient modulus and California bearing ratio (CBR) of a pavement base.

2 Experiment

2.1 Materials

Five mixtures of the blend of steel slag and crushed stone with their weight ratios were as follows: 100/00 (named S1.0C0.0), 80/20 (named S0.8C0.2), 70/30 (named S0.7C0.3), 60/40 (named S0.6C0.4), and 50/50 (named S0.5C0.5). The steel slag materials were produced from Green Materials Co., Ltd, Ba Ria-Vung Tau Province while the crushed stone was produced from Hoa An Company, Dong Nai Province. The particle size fractions of the mixtures containing steel slag and crushed stone were provided in Table 1. Figure 1 displays the photos of steel slag and crushed stone used in experiment. Table 2 displays the physical properties of the studied mixtures including maximum density with its corresponding optimal humidity, specific gravity, and porosity. As shown in Table 2 and Fig. 2, the S0.6C0.4 exhibited the minimum porosity of 17.7%. Therefore, the experimental tests would be conducted with fraction of crushed stone by weight up to 40%, i.e., there were four mixtures, including S1.0C0.0, S0.8C0.2, S0.7C0.3, and S0.6C0.4, examined under resilient modulus and CBR test.

Table 1 Particle size fractions of the mixtures containing steel slag and crushed stone

Sieve size (mm)	Cumulative percent retained on sieve (%)					
	S1.0C0.0 100% steel slag[a]	100% crushed stone[b]	S0.8C0.2	S0.7C0.3	S0.6C0.4	S0.5C0.5
50.0	100.00	100.00	100.00	100.00	100.00	100.00
37.5	100.00	100.00	100.00	100.00	100.00	100.00
25.0	98.16	100.00	98.53	98.71	98.90	99.08
19.0	90.00	100.00	92.00	93.00	94.00	95.00
9.5	60.60	100.00	68.48	72.42	76.36	80.30
4.75	37.54	95.89	49.21	55.05	60.88	66.71
2.36	21.36	72.12	31.51	36.59	41.66	46.74
0.425	5.98	23.30	9.44	11.18	12.91	14.64
0.075	1.62	5.40	2.38	2.75	3.13	3.51
<0.075	0.00	0.00	0.00	0.00	0.00	0.00

[a]Steel slag from Green Materials Co., Ltd., Ba Ria-Vung Tau Province
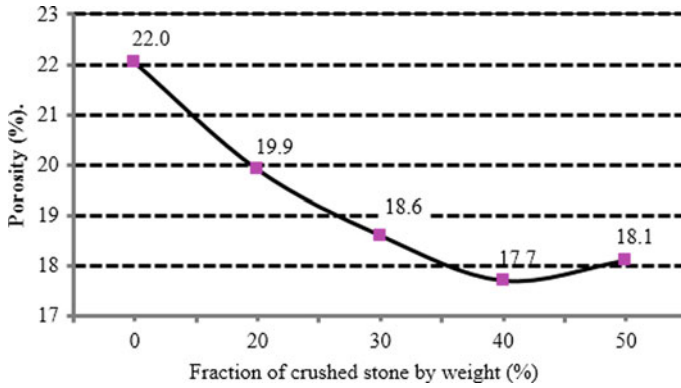[b]Crushed stone from Hoa An, Dong Nai Province

Fig. 1 Dependence of mixture porosity on fraction of crushed stone by weight

Table 2 Physic properties of the mixtures

Parameter	Name of mixtures				
	S1.0C0.0	S0.8C0.2	S0.7C0.3	S0.6C0.4	S0.5C0.5
Maximum density, γ^k_{max} (g/cm^3)	2.651	2.637	2.635	2.621	2.565
Optimal humidity, W_{opt} (%)	8.7	8.2	7.8	7.5	6.7
Specific gravity	3.400	3.292	3.238	3.184	3.130
Porosity (%)	22.0	19.9	18.6	17.7	18.1

(a) Steel slag   (b) Crushed stone

Fig. 2 Photos of steel slag and crushed stone used in experiment. **a** Steel slag. **b** Crushed stone

2.2   Test Setup

Figure 3 presents the photos of a typical preparation of a sample for CBR test while Fig. 4 displays the CBR test set up. To investigate the CBR and resilient modulus of the studied mixtures, each series were examined at least three samples and then

a) Preparing a sample for CBR test

b) Water curing for the tested sample

Fig. 3 Typical preparation of a sample for CBR test. **a** Preparing a sample for CBR test. **b** Water curing for the tested sample

Fig. 4 CBR test set up

averaged for evaluating and discussing. The CBR experiments were conducted according to 22 TCN 333-2006 (Method II-D) [8], while resilient modulus tests were examined according to 22 TCN 211-2006 [9].

2.3 Testing Result and Discussion

Table 3 provides the experimental results of the tested mixtures. The CBR was measured at compactness coefficients of $K = 0.98$ and $K = 1.00$, while the resilient modulus was only measured at compactness coefficients of $K = 0.98$.

Figures 5 and 6 show the influences of crushed stone content on CBR and resilient modulus of the studied mixtures. As shown in Figs. 5 and 6, the S0.7C0.3 with crushed stone content of 30% produced the highest values in both CBR and resilient modulus of the mixtures, although the lowest porosity was observed at crushed stone content of 40%, as displayed in Fig. 1. At the peaks of the curves in Fig. 6, the compactness coefficient of $K = 0.98$ produced the lower CBR, about 15%, in comparison with the compactness coefficient of K = 1.00. The order in terms of CBR was observed as follows: S1.0C0.0 < S0.8C0.2 < S0.6C0.4 < S0.7C0.3 for $K = 0.98$, S1.0C0.0 < S0.6C0.4 < S0.8C0.2 < S0.7C0.3 for $K = 1.00$. The order in terms of resilient modulus was as follows: S0.6C0.4 < S1.0C0.0 < S0.8C0.2 < S0.7C0.3 for $K = 0.98$.

Table 3 Experimental results of the tested mixtures

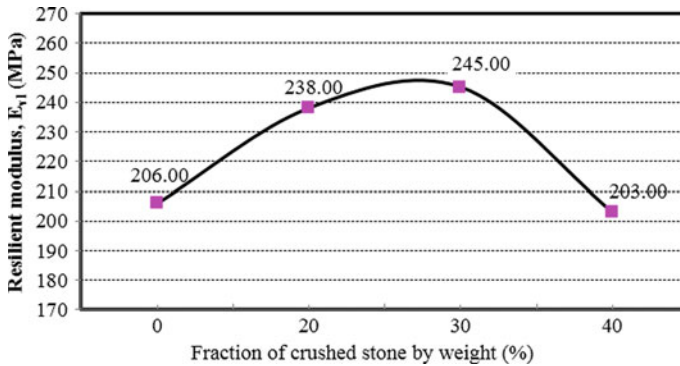| Parameter	Name of mixtures			
	S1.0C0.0	S0.8C0.2	S0.7C0.3	S0.6C0.4
CBR at $K = 0.98$ (%)	168.8	184.5	192.8	186.0
CBR at $K = 1.00$ (%)	201.4	210.8	227.0	205.8
E_{vl} at $K = 0.98$ (MPa)	206.0	238.0	245.0	203.0

Fig. 5 Influences of crushed stone content on resilient moduli of the studied mixtures
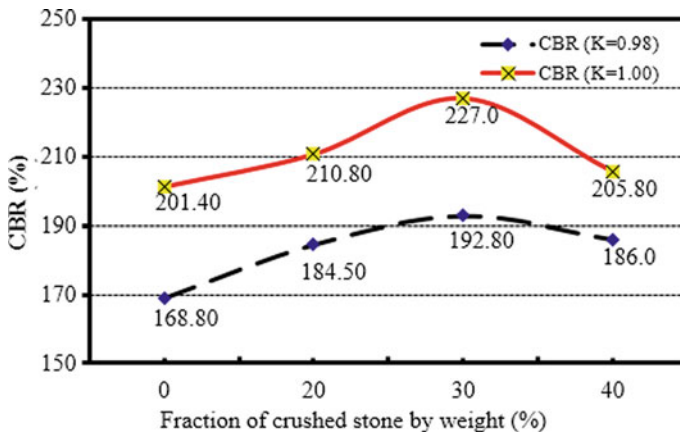

Fig. 6 Influences of crushed stone content on CBR of the studied mixtures

The experimental results also revealed that the combination between steel slag and crushed stone generated a synergistic validity in mechanical resistances of the mixture, i.e., there was a mechanical performance of the hybrid system exceeding that of a mono system with the same weight content [10]. The various particle sizes

were thought to produce the mixture porosity, as illustrated in Fig. 7, the denser microstructure resulted higher mechanical properties of the mixture.

A linear scale relationship between CBR and resilient modulus (E) was reported [11, 12], as given by Eq. (1):

$$E = \psi \; CBR \tag{1}$$

In Eq. (1), where ψ is the empirical parameter that can be drawn using experimental results. Based on the data in Table 5, $\psi = 1.054$ was derived for the five studied mixtures, as described in Fig. 8. Equation (1) can be used to estimate CBR or resilient modulus from an experimental one.
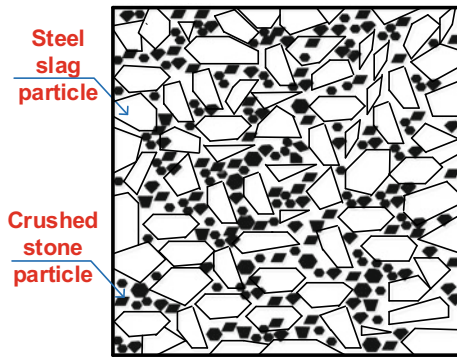

Fig. 7 Combination between steel slag and crushed stone resulted the reduction in porosity of the mixture
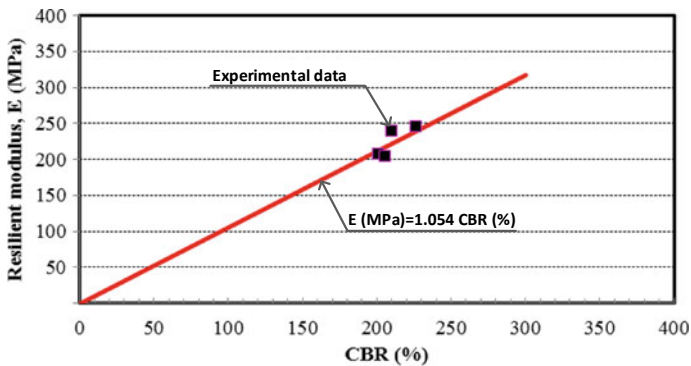

Fig. 8 Deriving the empirical parameter ψ in relationship between CBR and resilient modulus of the mixtures

3 Conclusion

This experimental study could be provided some conclusions as follows:

- The S0.6C0.4 produced the lowest porosity of the mixtures with its optimal humidity of 7.5% and maximum density 2.621 g/cm^3.
- The blend of steel slag and crashed stone may improve mechanical properties of the mixture, which was proposed to use as a road-pavement base layer. The S0.7C0.3 produced the highest CBR and resilient modulus of the mixtures.
- A correlation between CBR and resilient modulus of the mixtures was built to estimate the each other.
- It was practicable to utilize the steel slag and crushed stone together for road-pavement base.

References

1. Nguyen, T.T.H., Phan, D.H., Mai, H.H., Nguyen, D.L.: Investigation on compressive characteristics of steel-slag concrete. Materials **13**, 1928 (2020). https://doi.org/10.3390/ma13081928
2. Lam, M.N.T., Jaritngam, S., Le, D.H.: Roller-compacted concrete pavement made of electric arc furnace slag aggregate: mix design and mechanical properties. Constr. Build. Mater. **154**, 482–495 (2017)
3. Nguyen, T.T.H., Mai, H.H., Tran, V.T.: Study on using recycle steel slag-fine sand treated with cement for road pavement subbases. J. Sci. Technol. Civil Eng., NUCE **13**(5V), 93–101 (2019)
4. Nguyen, K.S., Nguyen, V.P., Le, T.D.H., Huynh, N.M., Le, M.S., Nguyen, T.H.: EAF steel slag as supplementary cementing material. ASEAN Eng. J. Part B, **4** (2), 34–43 (2015). ISSN 2286-7694
5. Nguyen, T.T.H., Mai, H.H., Phan, D.H., Nguyen, D.L.: Responses of concrete using steel slag as coarse aggregate replacement under splitting and flexure. Sustainability **12**, 4913 (2020). https://doi.org/10.3390/su12124913
6. Le, A.T., Hoang, T.Q., Nguyen, T.T.: Analysis behavior of reinforcement in a reinforced concrete beam using steel slag replacing crushed-stone aggregate. In: Congrès International de Géotechnique–Ouvrages–Structures, pp. 329–337 (2017)
7. Nguyen, N.T., Nguyen, V.V.: Partial replacement of natural sand by granulated blast furnace slag (GBFS) in fine aggregate for concrete: practical application in Vietnam. In: Conference of 18th International Multidisciplinary Scientific GeoConference—SGEM2018, pp. 523–530. https://doi.org/10.5593/sgem2018/1.2/s02.066
8. 22 TCN 333-2006. Standard of compaction of soil and aggregate
9. 22 TCN 211-2006. Standard of flexible pavement design
10. Banthia, N., Soleimani, S.M.: Flexural response of hybrid fiber-reinforced cementitious composites. ACI Mater. J. **102**(6), 382–389 (2005)
11. Tuleubekov, K., Brill, D.R.: Correlation between subgrade reaction modulus and CBR for airport pavement subgrades. In: T&DI Congress 2014 (2014). https://doi.org/10.1061/9780784413586.079

12. Dione, A., Fall, M., Yves, Berthaud, Benboudjema, F., Michou, A.: Implementation of resilient modulus—CBR relationship in Mechanistic-Empirical (M. -E) pavement design. Revue Cames—Sci. Appl. de l'Ing. **1**(2), 65–71 (2015). ISSN 2312-8712

Solutions for Underground Drainage and Stability of High Embankment Slope at Nhan Co. Industrial Zone, Dak Nong, Vietnam

Truong Linh Chau and Thanh Quang Nguyen

1 Overview of Research Area

1.1 Introduction

The high embankment slope is situated in the Nhan Co Industrial Zone of the DakR'Lap District, Dak Nong Province, Vietnam (Fig. 1). The landslide of high embankment slope is shown in Fig. 2.

1.2 Descriptions

The recent landslide has occurred on an almost "tributary stream" (Fig. 3). The research area is located in the Central Highlands region, where receives large-scale extreme rainfall for a long time from May to September 2019. The greatest measurement of rainfall recorded was approximately 2073 mm. The prolonged rainfall will infiltrate into the soil in the tributary stream with an about 14 ha area. The infiltration of rainwater forms a stable seepage over time. Based on the survey results, the seepage has risen more than the data design [1].

Landslide description and situation:

- On April 4th, 2020, there is a 150 m-in-length, 70 m-in-width and 40 m-in-height landslide (Fig. 4a). The pit crest has a 15-meter subsidence. The landslide is moved out of the embankment slope covering the wall. The expected movement is about 10÷15 m long. The groundwater is stagnant in the landslide. The soil is liquefied in some positions (Fig. 4b).

T. L. Chau (✉) · T. Q. Nguyen
University of Science and Technology, The University of Da Nang, Da Nang, Vietnam
e-mail: chau-linh@dut.udn.vn

Fig. 1 Research area

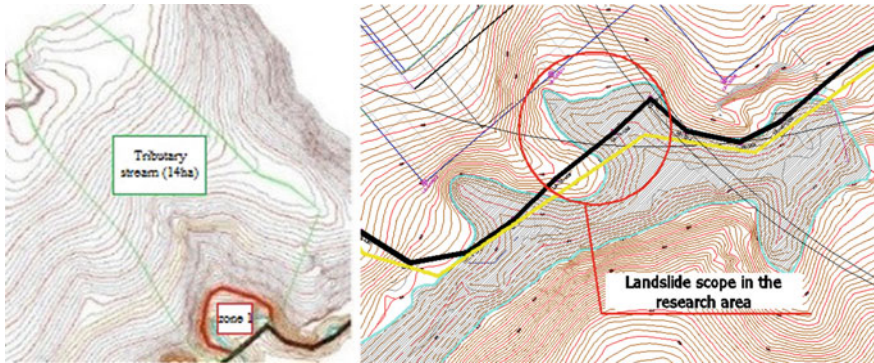**Fig. 2** A panoramic view of the landslide of Nhan Co

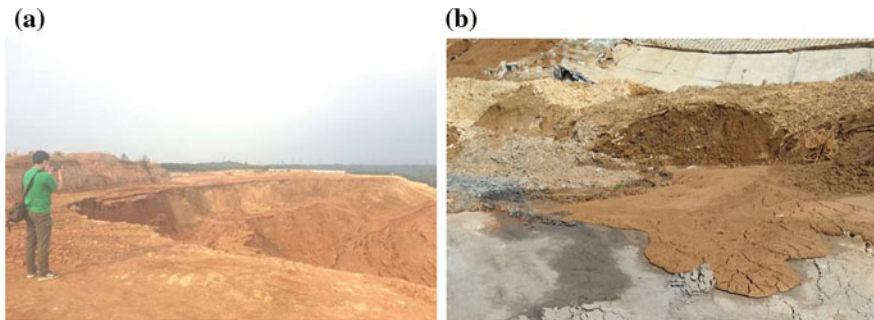**Fig. 3** Tributary stream (zone 1)—Landslide scope in the research area

Fig. 4 The situation of 15 m-in-length subsidence on the leveling ground

- The sloped roof slabs are shoved, cracked, and broken (Fig. 2).

1.3 Geological Survey After Landslide—Cause Analysis

1.3.1 Geological Survey

Based on the preliminary survey, the geology is composed of embankments on the weathered, cracked, fine-grained, dark-colored Basalt rocks with the hardness of from 4 to 7 (Layers D1, D2). In order to redefine the physical properties of embankment for subsidence cause assessment, we have reconducted the survey works such as drilling (with 3 boreholes) and laboratory works including the experimental determination of physical properties (9 properties), consolidation test, and shear test. The results are shown in Table 1 (Fig. 5).

Table 1 Summary of physical properties of embankment in the subsidence scope

| TT	Properties	Unit	DD1	DD2	DD3	DD4	DD5	K90	Change (%)
1	Natural moisture content	%	48.40	43.50	55.20	45.00	51.00	29.78	increase (51.11÷85.36)
2	Specific gravity	g/cm^3	2.850	2.841	2.840	2.850	2.843	2.850	decrease (0.00÷0.35)
3	Dry density	g/cm^3	1.112	1.179	1.063	1.220	1.160	1.377	decrease (11.40÷22.80)
4	Natural density	g/cm^3	1.650	1.692	1.650	1.770	1.752	1.787	decrease (0.95÷7.67)
6	Cohesion (natural state)	kG/cm^2	0.24	0.32	0.3	0.39	0.37	1.4	decrease (72.14÷82.86)
7	Friction angle (natural state)	degree	13°45'	15°35'	14°13'	19°45'	15°08'	38°27'	decrease (48.63÷64,24)
8	Cohesion (saturation)	kG/cm^2	0.18	0.265	0.22	0.292	0.254	0.36	decrease (18.89÷50.00)
9	Friction angle (saturation)	degree	9°56'	11°28'	11°28'	11°04'	11°28'	24°24'	decrease (53.01÷59.29)
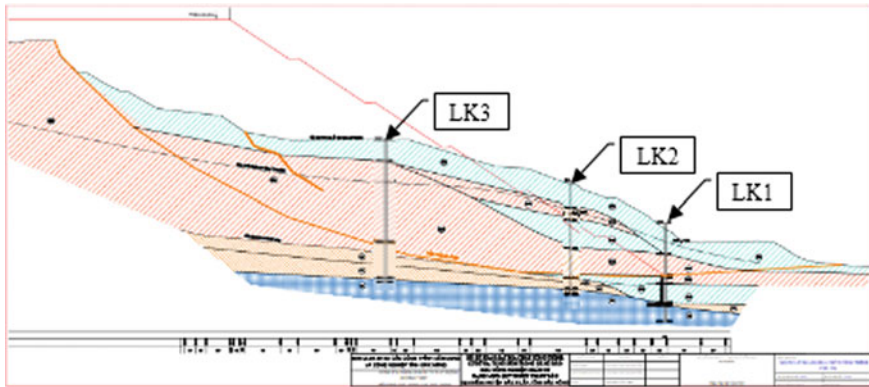
Fig. 5 Landslide cross-sections show the position of 3 boreholes

The geological survey results consisting of three boreholes on three cross-sections in order to specify the physical properties of embankment after landslide show that the embankment with the seepage effect is divided into 5 types including DD1, DD2, DD3, DD4, and DD5. The physical properties of these types of embankment are shown in Table 1 [2].

The changes in physical properties of the embankment due to seepage effect over time have also been mentioned in this research [3]. Layers DD1, DD2, DD3, DD4, DD5 locate in the MH groups which are types of weak soil with the low bearing capacity. Thus, when making the new embankment, the measures should be taken to improve the bearing capacity of this new one.

1.3.2 Cause Analysis

The landslide in this position may be result from many reasons, but the main one is due to high embankment (56 m) in a wide "troughed tributary streams" (14 ha). The seepage is derived from rainwater that has infiltrated into the soil over time. After that, it cannot drain away but accumulates behind the retaining wall for a long time and builds up which has resulted in the water saturation and the reduction of soil shear strength for the soil behind the wall. The lower soil layers will exhibit a plastic deformation and loss of ultimate bearing capacity.

Summary of landslide problems

- Changes in physical properties of the embankment due to seepage effect over time;
- The designed slope coefficient of 1:1.50 is not suitable for the high embankment and solutions.

In this article, we have proposed the solutions based on the above two main reasons for the slope stability.

2 Solutions for the Slope Stability in the Research Area

2.1 Solutions

2.1.1 Solution of Drainage Structure

- Chimney drains are used in attempt to prevent horizontal flow along relatively impervious stratified layers, and to intercept seepage water before it reaches the downstream slope. Chimney drains are often incorporated in high homogeneous dams which have been constructed with inclined or vertical chimney drains (Fig. 6) [4]. The horizontal distance of chimney drains meets the construction conditions but it must not be under 1.5 m;
- Use the waterproofing membrane (HDPE) which is a similar system to replace chimney drains in order to limit the seepage effect to the embankment landslide (Fig. 7) [5].

2.1.2 Solutions for Slope Stability Reinforcement

- Change the slope coefficient of 1:1.50–1:1.75–1:2.00 respectively corresponding to the cross Sects. 1, 2 and 3;
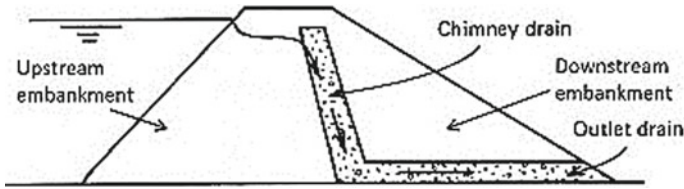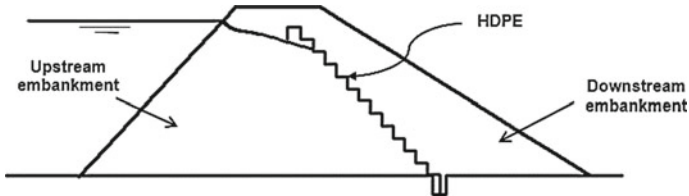
Fig. 6 Chimney drains

Fig. 7 The waterproofing membrane (HDPE)

- Replace the embankments DD1, DD2, DD3, DD4, DD5 with the other embankment materials including K90 and K95 or reinforced soil with the geogrid corresponding to the solutions 1 and 2.

2.2 Calculations

2.2.1 Requirements for Calculations

(a) Calculations of slope stability before and after the incident;
(b) Calculations of slope stability and retaining wall when the work is put into use and calculations of maximum tensile stress in the geogrid (if any) with solutions for the slope stability in the research area.

2.2.2 Calculation Conditions

The following two cases of working conditions have been taken into account during the stability calculations as fundamental load combination:

- **Case 1**: The downstream water level is 621.68 m (design flood level condition); the seepage flow is in accordance with the surveys on April 27th, 2020.
- **Case 2**: The downstream water level is 610.00 m (dead water level condition); the seepage flow is in accordance with the surveys on April 27th, 2020.

Conduct the inspection for the cross sections in the C334 representing landslide in the research area.

2.2.3 Input Variables

a. *Embankment geometry*. Based on the geological survey after the landslide (Sect. 1.3) and solutions (Sect. 2.1), Figs. 8 and 9 have shown the calculated sections in the C334.
b. *Geological materials*. Based on the geological reports in the landslide position, the basic physical properties of embankments and the reinforced materials are shown in Tables 2, 3, and 4.
c. *Water level*. Based on the construction design documents:

- Design flood level ($P = 1\%$) condition (DFL) = +621.68m
- Dead water level condition (DWL) = +610.00 m

d. *Vehicle load conversion*. The vehicle loads converted into equivalent embankments are defined in accordance with the formula (1), for the vehicle with the largest load as designed [6]:

$$hx = \frac{n.G}{\gamma.B.l} \tag{1}$$

The converted equivalent embankment thickness: 0.88(m).
e. *Allowed stability coefficient*. In accordance with the standard AASHTO LFRD 2012 [7]:

- Safety factor (general stability coefficient) [SF] = 1.00;
- Figures of shear strength of the embankment decrease 1.25 times of its value;
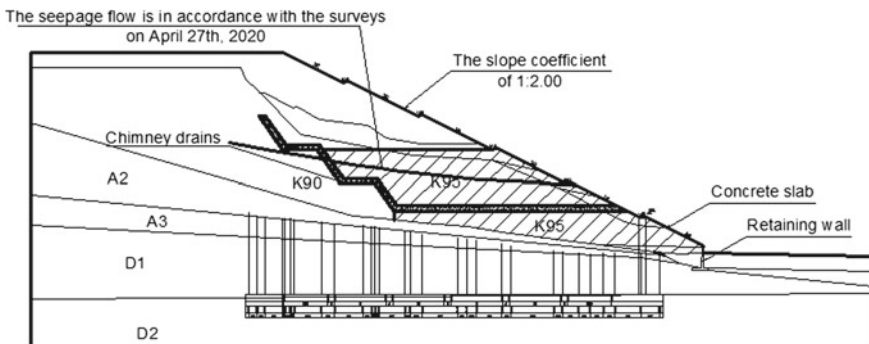- Regarding the figures of level and anchor:

Fig. 8 Cross section according to the change of slope coefficient and embankment material
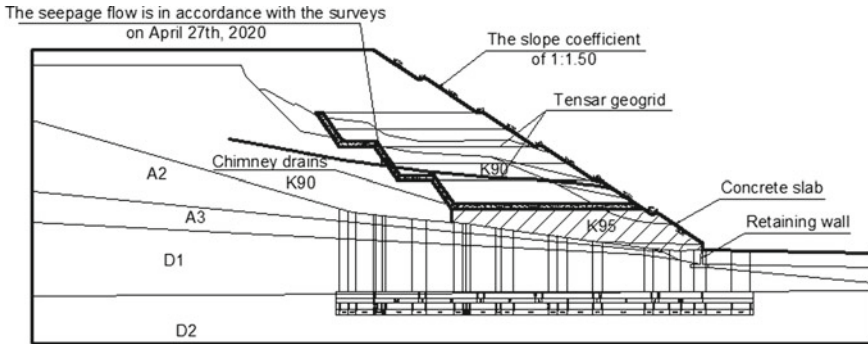
Fig. 9 Cross section according to the tensar reinforced geogrid-based embankment material

- Intensity coefficient $\varphi = 0.60 \div 0.65$ for the strength-based limit state
- Intensity coefficient $\varphi = 1.00$ for the critical state.

2.2.4 Analysis Program

In the design of an embankment, it is important to consider not only the final stability, but also the stability during the construction. PLAXIS is a finite element software, specifically used for stability and deformation analysis in geotechnical applications. A safety analysis in PLAXIS can be executed by reducing the strength parameters of the soil. This process is called Phi-c reduction. The reduction of strength parameters is controlled by the total multiplier ΣMsf with the formula (2) [8].

$$\sum Msf = \frac{\tan \varphi_{input}}{\tan \varphi_{reduce}} = \frac{c_{input}}{c_{reduce}} \tag{2}$$

This parameter is increased in a step-by-step procedure until failure occurs. The safety factor is then defined as the value of ΣMsf at failure, provided that at failure a more or less constant value is obtained for a number of successive load steps.

2.2.5 Analysis Results

Design Calculations

The design calculations have the slope coefficient 1:1.50 and embankment material is K90. The results have not considered the reduction of shear strength of embankment due to seepage effect (Fig. 10) and takes into account the seepage effect (Fig. 11).

Table 2 Parameters of soil models

Parameter	Name	Unit	K90 (unsat)	K90 (sat)	A3	A4	D1	D2	Chimney drains	Gravel aggregate	K95 (unsat)	K95 (sat)
Material model	Model	[–]	MC	MC	MC	MC	LE	LE	MC	MC	MC	MC
Drainage type	Type	[–]	Dr.	Dr.	Dr.	Dr.	Dr.	Dr.	Dr.	Dr.	Dr.	Dr.
Unsaturated weight	γ_{unsat}	g/cm^3	1.787	1.787	1.710	1.722	1.880	2.280	1.800	2.230	1.874	1.874
Saturated weight	γ_{sat}	g/cm^3	1.894	1.894	1.900	1.892	–	–	1.950	2.500	1.937	1.937
Permeability	k	m/day	0.09	0.09	0.86	0.86	–	–	86.40	8.64	0.09	0.09
Young's modulus	E	kG/cm^2	5.0E2	5.0E2	17.0	16.0	1.1E2	2.1E2	50.0	3.5E3	5.5E2	5.5E2
Poisson's ratio	ν	[–]	0.35	0.35	0.30	0.30	0.25	0.25	0.20	0.20	0.35	0.35
Cohesion	c	kG/cm^2	1.40	0.36	0.064	0.061	–	–	0.00	0.00	1.48	0.40
Friction angle	φ	degree	38.45	24.4	16.48	18.68	–	–	30.00	40.00	41.67	36.73
Dilatancy angle	ψ	degree	5.45	0	0	0	–	–	0	6.00	7.00	6.73

Table 3 Material properties of retaining wall and concrete slab

Parameter	Name	Unit	Retaining wall	Concrete slab
Material model	Model	[–]	Elastic	Linear elastic
Material behavior	Type	[–]	–	Non porous
Unsaturated weight	γ_{unsat}	kN/m^3	–	25.00
Young's modulus	E	kN/m^2	–	2.9E6
Poisson's ratio	v	[-]	0.15	0.15
Normal stiffness	EA	kN/m	3.00E6	–
Flexural rigidity	EI	kNm^2/m	2.25E4	–
Thickness	D	m	0.3	–
Weight	w	kN/m/m	8.4	–

Table 4 Material properties of geomembrane and tensar geogrid

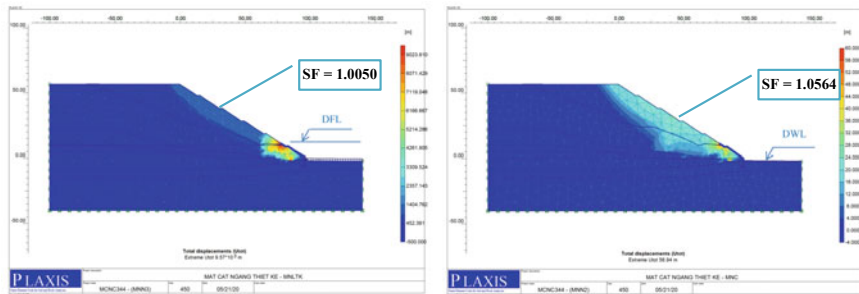| Parameter	Name	Unit	TT060	TT090	HDPE
Material model	Model	[–]	Elastic	Elastic	Elastic
Normal stiffness	EA	kN/m	60.0	90.0	43.0
Ultimate tensile strength	N_p	kN/m	28.3	42.4	23.0

Fig. 10 Failure surface and safety factor (SF = 1.0050) at the design flood level and the other one (SF = 1.0564) at the dead water level

Comment: We have audited for both cases at the design flood level and dead water level with the corresponding saturation line in the embankments and slope as designed that they all have SF > 1.00 which meets the general stability condition.

Comment: The analysis results showed that when the slope is subject to the seepage effect, the stability coefficient rapidly decreases and the slope is lack the sliding stability (SF < 1.00), the sliding shape and weight are similar to the actual one.
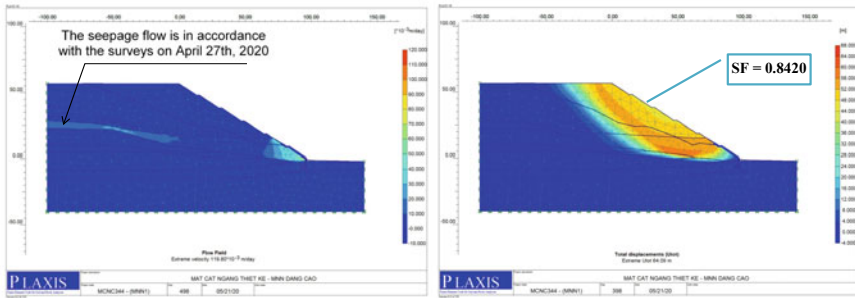
Fig. 11 Failure surface and safety factor (SF = 0.8420) with consideration to the seepage effect

Solution 1

Remarks

- Cross-Sects. 1, 2, 3: the slope coefficients are 1:1.50, 1:1.75, 1:2.00 respectively;
- Condition 1 is the embankment material = K90;
- Condition 2 is the embankment material = K90 and chimney drains;
- Condition 3 is the embankment material = K90 and chimney drains. Bench 1 = Gravel aggregate, benches 2,3 = K95;
- Condition 4 is the embankment material = K90 and chimney drains. Benches 1,2,3 = K95;
- Condition 5 is the embankment material = K90 and the waterproofing membrane (HDPE). Benches 1,2,3 = K95 (Table 5).

The analysis results corresponding to the cross-Sect. 3 according to conditions 4, 5 are shown in Figs. 12 and 13.

Comment: As can be seen from 22 calculation cases, it showed that the change of slope coefficient into 1:2.00, the removal of the first bench in the landslide area and replacement with the K95 well-compacted one, combining with underground drainage solutions (chimney drains or the waterproofing membrane (HDPE) may be used) all leads to the stability assurance. We have proposed to select one of two conditions (conditions 4 and 5).

Solution 2

Remarks

- Condition 1 is the embankment material = K90 and chimney drains. Use the TT060 tensar uniaxial geogrid to reinforce soil;

Table 5 Analysis results according to solution 1

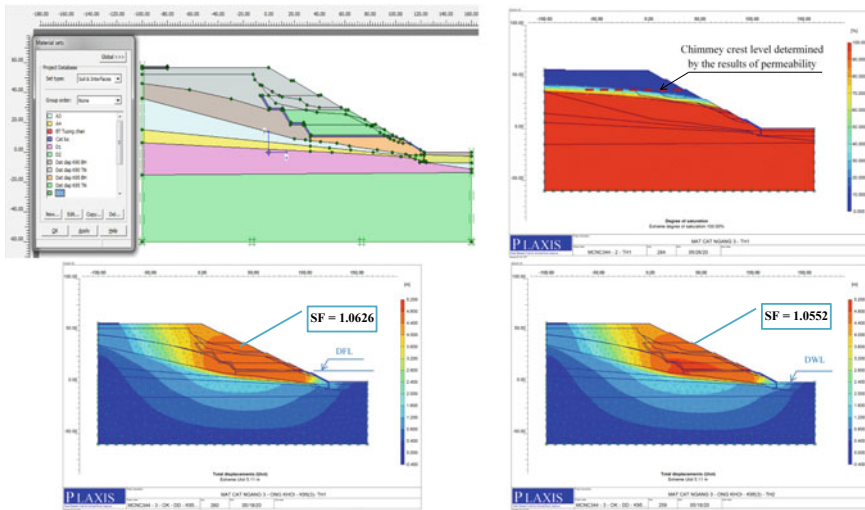| Cross-section	Case	Safety factor					[SF]
		Condition 1	Condition 2	Condition 3	Condition 4	Condition 5	
1	1	0.6275	0.8359	0.9031	–	–	1.00
	2	0.6169	0.9337	0.9610	–	–	
2	1	0.6544	0.8534	0.9311	–	–	
	2	0.6471	0.9689	1.0074	–	–	
3	1	0.6813	0.9001	1.0260	1.0626	1.0642	
	2	0.6752	1.0014	1.0259	1.0552	1.0358	

Fig. 12 Failure surface and safety factor (SF = 1.0626) at the design flood level and the other one (SF = 1.0552) at the dead water level according to condition 4—solution 1

- Condition 2 is the embankment material = K90 and chimney drains. Use the TT090 tensar uniaxial geogrid to reinforce soil (Table 6).

The analysis results corresponding to the cross-Sect. 3 according to condition 1are shown in Fig. 14.

Comment: The uses of tensar uniaxial geogrid calculated according to the conditions 1 and 2 all meet the slope stability requirements. With the high tensile strength, the K90 in-place materials can be simultaneously used to form a solid embankment, therefore we have proposed to select one of two conditions (conditions 1 and 2).
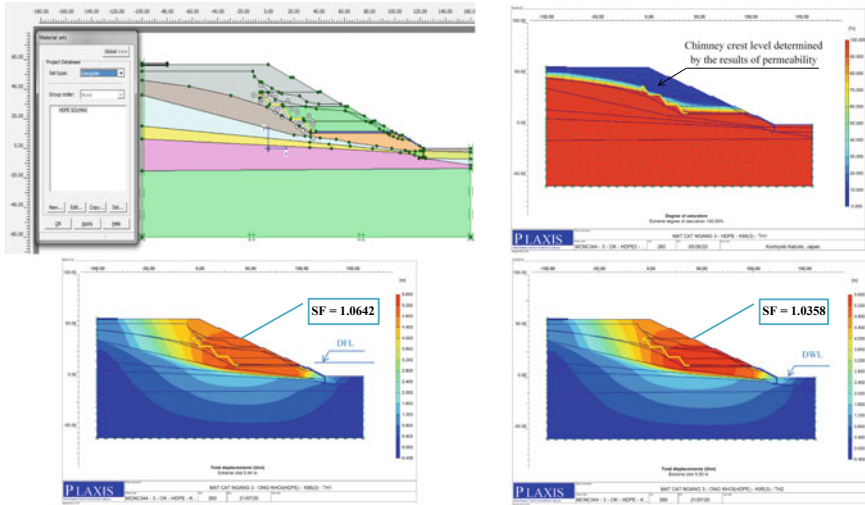
Fig. 13 Failure surface and safety factor (SF = 1.0642) at the design flood level and the other one (SF = 1.0358) at the dead water level according to condition 5—solution 1

Table 6 Analysis results according to solution 2

Cross-section	Case	Safety factor		[SF]
		Condition 1	Condition 2	
3	1	1.0648	1.0779	1.0
	2	1.0664	1.0963	

3 Summary of Solutions

3.1 Solution 1

The landslide in the calculated area occurs for many reasons. In order to thoroughly solve the problems, the main contents of this solution are as follows:

1. Design and construct chimney drains; you can use and the waterproofing membrane (HDPE) to replace the vertical drain (consideration for the durability over time).
2. Change the slope coefficient into 1:2.00;
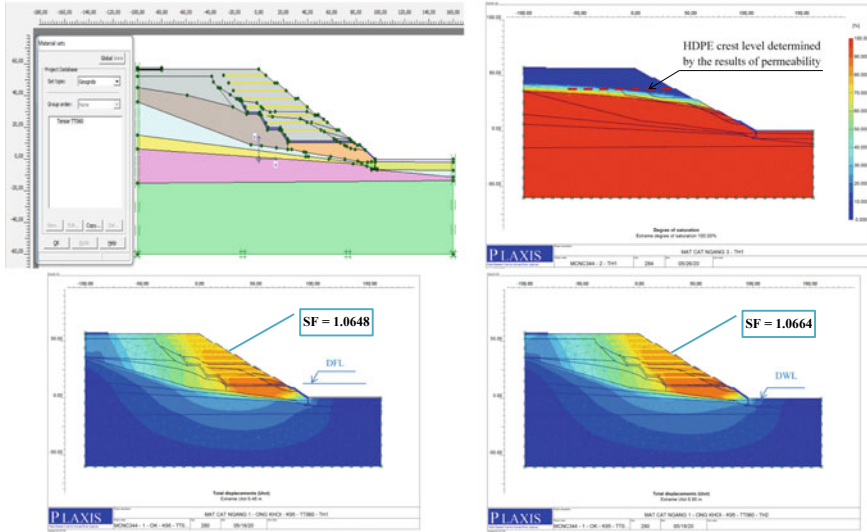3. Replace the embankments DD1÷DD5 with K90 and benches 1,2,3 = K95.

Fig. 14 Failure surface and safety factor (SF = 1.0648) at the design flood level and the other one (SF = 1.0664) at the dead water level according to condition 1—solution 2

3.2 Solution 2

Subject to the ground level of the Plant and the high embankment (about 56 m), in order to maintain the (designed) slope coefficient 1:1.50, a measure of high slope reinforcement should be taken. The reinforced tensar uniaxial geogrid can be used for the landslide solution.

4 Conclusion

The high embankment in the project of Nhan Co Industrial Zone, DakRap District, Dak Nong Province, Vietnam made of local materials have currently had a serious failure. As can be seen from the topographical, geological and hydrogeological survey data right after the landslide, the physical properties of embankment have been reduced, especially the groundwater has risen. Based on the stimulation with the Plaxis software, the safety factor (SF) of embankment is stable with SF = 1.0564 and it is unstable when the groundwater level rises in rainy seasons with SF = 0.8420. Therefore, the solutions for underground drainage and slope stability for high embankment in this area should be taken.

Two slope stability solutions have been proposed. In both of them, the solution for underground drainage has selected chimney drains or the waterproofing membrane (HDPE) to ensure the technical efficiency in limiting the seepage effect to the

slope landslide. Regarding the solution 1, we have proposed to consider the solution in accordance with the conditions 4 or 5. Corresponding to this one, the solution 2 in accordance with the condition 1 needs to be taken in order to make a technical and economical comparison.

References

1. Preliminary report of Nhan Co alumina slope failure—Item: slope failure Lot 3, May 2020
2. Summary of testing results of embankments—Item: slope failure Lot 3, LAS-XD425, May 2020
3. Nguyen, T.Q., Chau, T.L., Nguyen, T.H.: Experimental and numerical assessments of seepage effect on embankment behaviours by the time. Lecture Notes in Civil Engineering (Scopus). ISSN: 2366-2557 E-ISSN: 2366-2565. CIGOS 2019, Innovation for Sustainable Infrastructure. pp. 709-714. Springer Nature (2019)
4. Ministry of Science & Technology: National standards TCVN 10396:2015: Hydraulic structures - Compacted earth rock fill dams—Design requirements, Hanoi (2015)
5. Ministry of Agriculture and Rural Development: National standards TCVN 11322:2018 on hydraulic structures—HDPE geomembrane—Design, construction, inspection, Hanoi (2018)
6. Ministry of Transport: Specifications of surveying and designing road embankment on soft ground 22TCN 262—2000 (2000)
7. American Association of State Highway and Transportation Officials (AASHTO): LRFD Bridge Design Specifications, 6th edn. AASHTO, Washington, DC (2012)
8. Brinkgreve, R.B.J., Broere, W., Waterman, D.: Plaxis 2D-tutorial manual: Version 8.0, The Netherlands (2006)

Analyse Vertical and Horizontal Coefficient of Consolidation of Nha Be District's Soft Soil, Ho Chi Minh City

Nguyen Minh Tam and Vo Nguyen Phu Huan

1 Introduction

With the development of urban in Ho Chi Minh City, Vietnam, the demands of increased land and population are faced of limited landscape and infrastructures. To solve that matters, the movement of industries, port and infrastructures installation are carried out to suburban zone with soft soil foundation. Therefore, the large scale infrastructures over soft soils normally demand an improvement of soft sub-ground. Among a lot of soft soil treatment techniques, the use of preloading technique with prefabricated vertical drains (PVDs) is very useful in clay deposits, which decrease post-infrastructures settlement and improve the stability and the bearing capacity of soft soil [1].

The permeability and compressibility are two phenomena of consolidation process, which controls the rate of settlement, the rate of leaving excess pore water and the consolidation duration. In Terzaghi's theory, in which a constant compressibility is assumed and linear stress-strain relative, the coefficient of vertical consolidation C_v is the important parameter which can determine the consolidation process. Besides that, in Barron's theory, to design the PVD spacing, one essential parameter that can be effected to vertical drain system is the coefficient of horizontal consolidation C_h [2].

For determining C_v, the standard oedometer is normally carried out and the collected data are analysed by two method, namely Taylor method (the square root of time) and the Casagrande method (the logarithm of time) [3]. That is routinely used for determining C_v of soft soils in soil mechanics engineering applications and

---

N. M. Tam · V. N. P. Huan (✉)
Ho Chi Minh City Open University, Ho Chi Minh City, Vietnam
e-mail: huan.vnp@ou.edu.vn

N. M. Tam
e-mail: tamnm.19ac@ou.edu.vn

is allowed as standard methods. In the three decades, many researchers attempted to proposed simpler and more reliable methods for definition that parameter [4–8]. However, these alternative methods are not mentioned in any recommendations of standards on consolidation tests. However, their researches also contributed a possibility of applications in geotechnical works.

In these previous researches, laboratory tests; Asaoka's method and CPTu dissipation tests are three ways to define the horizontal coefficient of consolidation of soft sub-gound. Newly, the C_h can be determined by pressuremeter test and pressure dissipation tests [7].

From these literature researches, the research on the parameters of C_v during the different load; the C_h value of different soils types, of environment conditions, the origin of soil; and the relationship between C_v and C_h is still not mentioned exactly. In Vietnam, there are very few research on C_h value and colleration C_h with C_v. Therefore, the aim of this studies is to display these results based on laboratory tests and site test; then to compare and back analysis C_h and C_v in soft soil improvement process at Nha Be District, Ho Chi Minh City.

2 Case Study

2.1 General Information

Hiep Phuoc Port belongs to Nha Be District, Ho Chi Minh City with a large flat deposit alluvia. The soft soil profile at Hiep Phuoc has a high thickness from 10 to 45 m with almost of soil is in saturated and unconsolidation; moisture is high rank from 50 to 100%. The figure below to show relief plan of Hiep Phuoc area (Figs. 1 and 2).

2.2 Test Results and Discussion

(a) Coefficient of vertical consolidation

- Coefficient of vertical consolidation results from oedometer test of Casagrande method is less than Taylor method 7–23%.
- Casagrande method is just suitable with normally consolidated soil and overconsolidated soil. Lean clay with sand and silty clay is difficult to determine by the logarithm of time graph.
- Taylor method (the square root of time) can only provide the exactly C_v results for overconsolidated soil.
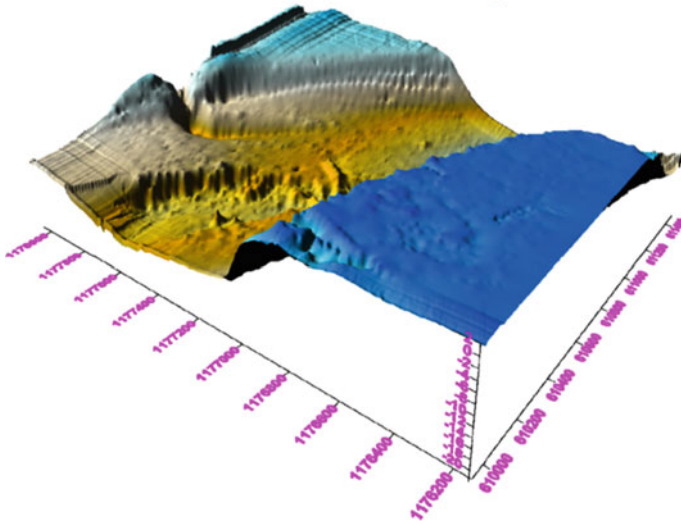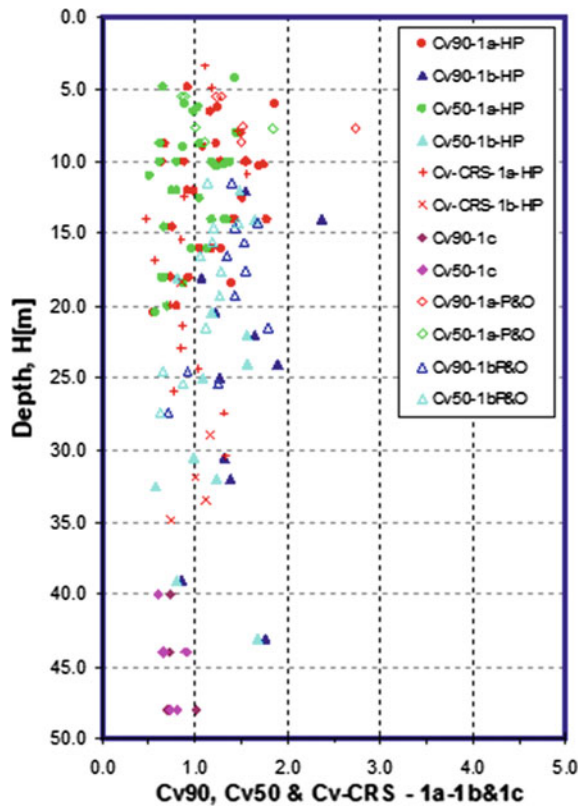- C_v results from CRS test give less values than the standard oedometer test: 17–23%.

Fig. 1 Relief plan of Hiep Phuoc area in 3D picture

Fig. 2 Summary of C_v result from lab test [log(t); $\sqrt{t}$; CRS]

- Coefficient of vertical consolidation is decreasing value when effective vertical stress increase with correlative depth.

(b) Coefficient of horizontal consolidation

   See Fig. 3.

- I_r value will increase with correlative depth when using (OCR, I_p) method.
- Decline trend of C_h value in both methods. The reason is the reduction of void ratio that make more time to dissipate (growth t_{50}).
- The C_h results from CU test and the relationship (OCR, I_p) in soil layer 1a, 1b, 1c are not much difference.
- In the same soil layer, I_r value is more growth, C_h value is also more increase. That is demonstrated in the results of soil layer 1a, 1b and 1c.
- Beside definition of C_h, CE-CSSM method also helps to determine OCR coefficient in site and contrary to Strain path method.
- The excess pore water curve in CE-CSSM method and Strain path method is made to accommodate that help to find the typical C_h for soil layer.

3 Conclusion

Based on the results of these tests, the characteristics of Cv and Ch has been demonstrated to be a guideline for the next relative research about this area.

- The characteristics of C_v:
  - C_v value in elastic phase normally is bigger than plastic phase. When effective pressure is higher than pre-consolidation pressure, then C_v is reduced quickly. After this period, the C_v value is almost no change.
  - To Nha Be soft soil, the difference of Cv value in elastic phase and plastic phase is about 3.8–8.7 times. When in Terzaghi, Peck and Mersi (1996), the number is from 5 to 10 times.

- The C_v results form CRS test have a small value than Oedometer test from 17 to 23%.

  - Suggestion of deformation rate is 0.01–0.03% per minute. This number is suitable with standard Oedometer test.
  - With suggestion of deformation rate, the ration when excess pore pressure divides vertical pressure from 5 to 20% is reasonable. Therefore, the suggestion ratio in ASTM (D4186-89) is bigger than ration in soft clay at Nha Be area.

- CE-CSMM method and Strain path method have much more advantage than traditional method. The excess pore water curve in CE-CSSM method and Strain path method is made to accommodate that help to find the typical C_h for
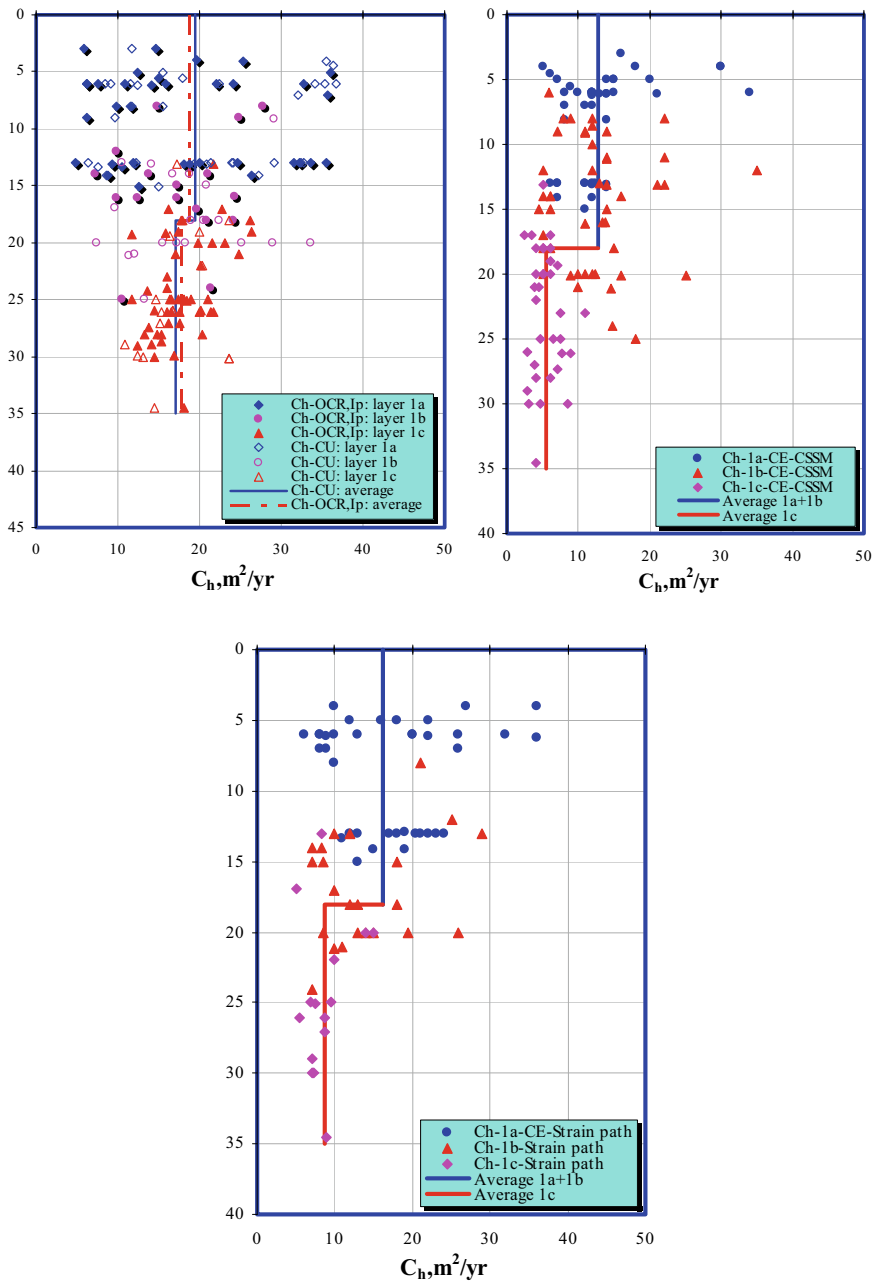
b)   Coefficient of horizontal consolidation

Fig. 3 Summary of C$_h$ result from lab test [CU; CE-CSSM; Strain path]

soil layer. C_h value in CE-CSSM and Strain path is smaller than CU test. For safety, CE-CSSM and Strain path method should be applied to determine C_h in CPTu test.

– CE-CSSM and Strain path method have much strongpoint: can define historical pressure, overconsolidation ratio, etc.
– Almost Ch value in 3 methods is in overconsolidation state. Therefore, the correction C_h value in overconsolidation state to normal consolidation state is very real coherence.

References

1. Walker, R.T., Indraratna, B.: Vertical drain consolidation with parabolic distribution of permeability in smear zone. J. Geotech. Geoenviron. Eng. **132**(7), 937–941 (2006)
2. Barron, R.A.: Consolidation of fine-grained soils by drain wells. Trans. Am. Soc. Civ. Eng. **113**(1), 718–742 (1948)
3. ASTM Standard D2435, Standard testmethod for one dimensional consolidation properties of soils (2004)
4. Chai, et al.: Coefficient of consolidation from non-standard piezocone dissipation curves. Comput. Geotech. **41**, 13–22 (2012)
5. Zhang, X.W., Wang, C.M.: Effect of soft clay structure on secondary consolidation coefficient. Rock and Soil Mechanics (2012)
6. Feng, W.-Q., Yin, J.-H.: A new simplified hypothesis B method for calculating consolidation settlements of double soil layers exhibiting creep. Int. J. Numer. Anal. Meth. Geomech. **41**(6), 899–917 (2017)
7. Ganesalingam, D., Sivakugan, N., Read, W.: Inflection point method to estimate C_h from radial consolidation tests with peripheral drain. Geotech. Test. J. **36**(5), 1–6 (2013)
8. Balachowski, L.: Soft soil over consolidation and CPTu Dissipation test. Arch. Hydro-Eng. Environ. Mech. **53**(2), 155–180 (2006)

Analysis of Increase in Bearing Capacity of Shaft-Grouted Bored Piles at a Project in Ho Chi Minh City

Thanh Danh Tran and **Van Than Tran**

1 Introduction

In recent years, more and more high-rise buildings have been built in Vietnam. Bored pile is one of the pile types with large load capacity commonly used for high-rise projects. However, in a few cases this pile also appears to be limited in its load capacity. To increase the bearing capacity for bored piles, many projects have applied high-pressure grouting technology to improve the soil strength around the pile.

Many studies related to the shaft-grouting piles have been carried out. Stocker [8] showed that the shaft-grouting method increased the shaft resistance from 1.5 to 3 times. Littlechild et al. [4] compared the pile load test results of the shaft-grouted and non-grouted bored piles carried out at a project in Bangkok and found that the measured friction resistance values for shaft-grouted bored piles in clay and sand layers were approximately double those without shaft grouting. Another study by Littlechild et al. [5] on the barrettes and bored piles using the shaft grouting technique at a project in Hong Kong shows that the measured friction resistance values for both barrettes and bored piles in the completely weathered granites and volcanics were 2–3 times higher than corresponding piles without shaft grouting. In Vietnam, Duong and Pham [1] compared the pile load test results of barrettes with and without shaft grouting in 3 different projects and concluded that the friction resistance measured in shaft-grouted barrettes was almost twice that in non-grouted barrettes. After comparing the O-Cell load test results of shaft-grouted and non-grouted large-diameter bored piles at a project in Ho Chi Minh City, Nguyen and Fellenius [6] showed that the grouting method increased the average unit friction resistance of the shaft-grouted pile by about 2–3 times that of the non-grouted pile. Recently, based on the analysis of pile load test data of bored

T. D. Tran (✉) · V. T. Tran
Ho Chi Minh City Open University, Ho Chi Minh City, Vietnam
e-mail: danh.tt@ou.edu.vn

piles and barrettes using grouting technique of many different projects in Ho Chi Minh City, Nguyen et al. [7] showed that the ultimate unit friction resistance of the shaft-grouted piles increased by about 2 times compared to the non-grouted piles.

Currently, to estimate the axial load capacity of pile, people often use formulas based on the results of soil tests including of laboratory tests or field tests. Similar to ordinary piles, previous studies on estimation of unit friction resistance of the shaft-grouted piles also proposed formulas based on soil test results. Some models can be mentioned here: $f_s = \alpha C_u$ (with $\alpha = 1$ and undrained shear strength $C_u = 5\ N$ (kPa), N-mean SPT value) and $f_s = \beta \sigma'_v$ (with $\beta = 0.55$) (Littlechild et al. [4]); $f_s = 0.36\ N + 112$ (kPa) and $f_s = 0.11 \sigma'_v + 104.5$ (Zhang and Chu [9]). Many studies found that the ratio of unit friction resistance to the mean SPT value for shaft-grouted piles in Hong Kong varied from 1.4 to 5.5 (Littlechild et al. [5]; GEO [3]). Studying on shaft-grouted barrettes of many projects in Vietnam, Duong and Pham [2] found this ratio was 7.8 for clay and 7.9 for sand.

Thus, the studies above demonstrated that the increase in friction resistance of the shaft-grouted piles compared to the non-grouted piles varied from 1.5 to 3 times. In addition, the studies that proposed the models for estimating the unit friction resistance mainly used the back analysis method of the pile load test results in relation to the SPT value. However, the mobilized friction resistance of shaft-grouted piles is affected by many factors such as soil type or geological condition of the construction site (Littlechild et al. [5]), grout properties (Zhang et al. [10]), applied load (Duong and Pham [2]) … So, the increase in friction resistance of the shaft-grouted piles as well as the correlation to estimate unit friction resistance in terms of SPT value has changed from one study to another. Therefore, the study of the increase in friction resistance of the shaft-grouted piles and the correlation to estimate the unit friction resistance for this type of pile given the specific geological conditions in Ho Chi Minh City is crucial.

2   Methods

Two trial piles used for analysis in this study are from Lancaster Lincoln project which is a 40-floor and 3-basement building in district 4, Ho Chi Minh City, Vietnam. These two trial bored piles have the same diameter and length, of which one (TP01) is non-grouted and the other (TP03) is shaft-grouted. The O-Cell test data of these both trial piles was used in this study.

The soil profile at the site is reported to consist of clay and sand, and is presented in Fig. 1. The water table varies from −0.88 m to −1.14 m below the ground surface. The two test piles TP01 and TP03 have a diameter of 1.5 m and a length of 85 m (Fig. 1). The working load for TP01 and TP03 pile is 20 MN and 21 MN, respectively. For the TP03, the shaft of pile is grouted from an elevation of −36.0 to −85.0 m.

The loading method was performed by raising the O-cell load. The maximum load for TP01 corresponds to 200% working load (cycle 1) and 100% working load
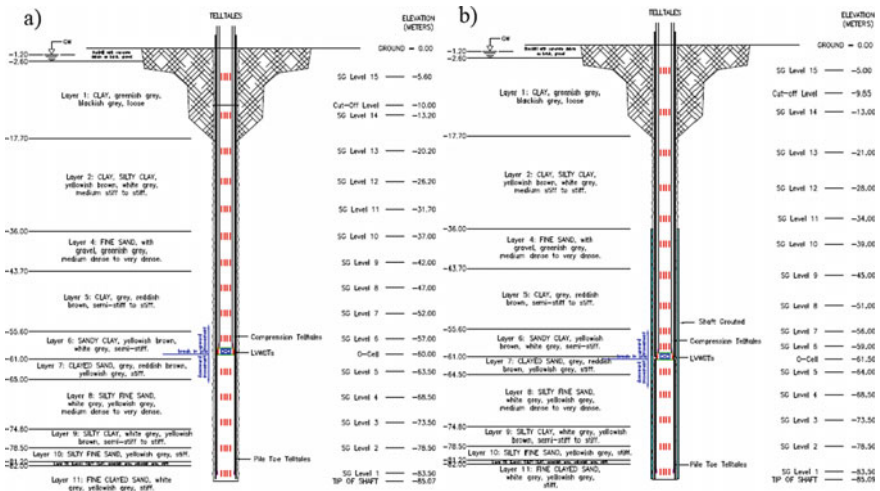
Fig. 1 Schematic section of **a** TP01 and **b** TP03

(cycle 2). The maximum load for TP03 corresponds to 387.5% working load. The loading assembly for TP01 consists of two 610 mm diameter O-cells, located at an elevation of −60.0 m. For TP03, the loading assembly consists of four 510 mm diameter O-cells, located at an elevation of −61.5 m. Two test piles were instrumented over its full depth. 15 levels of four sister bar vibrating wire strain gauges (Geokon model 4150 series) were attached to the reinforcement cage (Fig. 1).

Firstly, the load-displacement curves of the O-Cell test results were analyzed to interpret the load capacity of TP01 and TP03. Secondly, the strain gauge readings at each level were averaged to deduce the vertical strain. Any gauges giving anomalous results were not included in the analysis. The axial load along the depth of the piles was obtained by multiplying the average vertical strain with pile Young's modulus with pile cross section. The Young's modulus of piles was obtained by calibration against the applied load and the average vertical strain of gauges above the top of the O-Cell assembly. The unit friction resistance was calculated by dividing the axial load difference between the two ends of the segment by the perimeter surface area of the segment. For the purpose of the analysis, it is assumed that the O-Cell assembly did not impose an additional upward load until its expansion force exceeded the buoyant weight of the pile above the O-Cell assembly. Therefore, net load, which was defined as gross O-Cell load minus the buoyant weight of the pile above, was used to determine friction resistance above the O-Cell. For both TP01 and TP03, a pile buoyant weight of 1.5 MN above the O-Cell was calculated. Finally, the calculated friction resistance of TP01 and TP03, of which one is non-grouted and the other is shaft-grouted, were compared to deduce the increase in bearing capacity of the shaft-grouted pile.

Particularly for the TP03, the calculated unit friction resistance results of the shaft-grouted pile segments were analyzed in correlation with the SPT value of the

respective soil layers. Hence, the correlation between the unit friction resistances with the SPT value for the bored pile using shaft-grouting method was deduced. In which, the SPT value of the soil around the pile segments is weighted average according to the thickness of the soil layers involved.

To determine the ultimate bearing capacity of the TP01 and TP03, two O-Cell tests described above were simulated by the finite element method (FEM) using Plaxis 2D software. An axisymmetric model with 15-node triangular elements was used. The parameters of soil, pile, and grout material are in Table 1. All soil and grout layers were simulated using the Hardening soil (HS) model in which the grout layer was simulated with a thickness of 25 cm, from the elevation of −36.0 to −85.0 m.

The O-cell part was simulated as solid elements of 60 cm thick at −60 m depth for the TP01 and −61.5 m for the TP03. When the O-cell assembly was not in operation such as in the case of static load test with load applied at the pile top, the material properties of the O-cell were made identical to those of pile materials (i.e. concrete). When the O-cell was in use, its material properties were deactivated so that the interaction between the shaft upward and downward movement as well as the tip movement of the pile can be de-coupled.

The load-displacement curves of the TP01 and TP03 from Plaxis 2D were compared and back analyzed with the measured ones from the O-Cell tests to confirm the rationality of the finite element model input parameters. Then, the ultimate bearing capacity of the TP01 and TP03 were determined using the above models by increasing O-Cell load until the soil around each pile portion (upper and lower portion) reach the ultimate state.

3   Results

Figure 2a shows the load—displacement curves of O-Cell test on the TP01. These load—displacement curves show that at the maximum load of 21.64 MN, the upward and downward displacement of the O-Cell were 16.8 mm and 10.6 mm, respectively. For the upper pile portion, the upper friction resistance corresponds to the applied net load of the O-Cell of 20.14 MN. For the lower pile portion, the combined end bearing and lower friction resistance corresponds to the applied gross load of the O-Cell of 21.64 MN. Thus, the total mobilized load capacity of the TP01 corresponding to the maximum loading increment is 41.78 MN.

Similarly, Fig. 2b shows the load—displacement curves of O-Cell test on the TP03. These load—displacement curves show that at the maximum load of 42.46 MN, the upward and downward displacement of the O-Cell were 23.3 and 33.8 mm, respectively. For the upper pile portion, the upper friction resistance corresponds to the applied net load of the O-Cell of 40.96 MN. For the lower pile portion, the combined end bearing and lower friction resistance corresponds to the applied gross load of the O-Cell of 42.46 MN. Similarly, the total mobilized load

Table 1 Material properties of soil, pile and grout

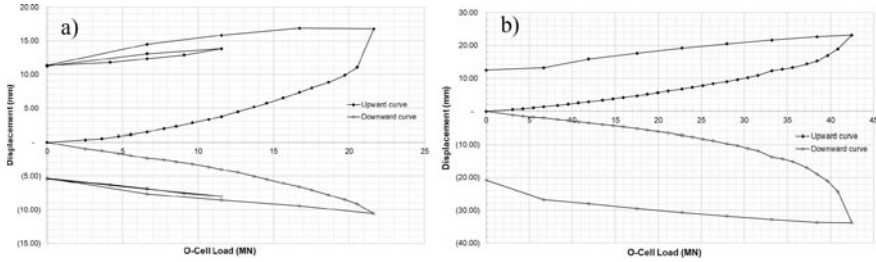| Layer	0. Backfill	1. Clay	2. Clay, silty clay	3. Clayed sand	4. Fine sand	5. Clay	6. Sandy clay	7. Clayed sand	8. Silty fine sand	9. Silty clay	10. Silty fine sand	11. Clayed sand	Shaft grouting	Pile
Type	HS Drained	HS UnDrained	HS UnDrained	HS UnDrained	HS Drained	HS UnDrained	HS UnDrained	HS UnDrained	HS Drained	HS UnDrained	HS Drained	HS UnDrained	HS UnDrained	Concrete
γ_{unsat} (kN/m³)	18	14.7	18.7	20	20.7	20.5	20	20.6	21.2	20	21.2	21.1	21	25
γ_{sat} (kN/m³)	18.5	15.2	19.2	20.5	21.2	21	20.5	21.1	21.7	20.5	21.7	21.6	21	–
E_{50}^{ref} (kN/m²)	8000	6000	16,800	14,000	61,600	49,000	21,000	50,400	58,800	35,000	60,200	65,800	90,000	3.45 × 107
E_{oed}^{ref} (kN/m²)	8000	6000	16,800	14,000	61,600	49,000	21,000	50,400	58,800	35,000	60,200	65,800	90,000	–
E_{ur}^{ref} (kN/m²)	24,000	24,000	50,400	42,000	184,800	147,000	63,000	151,200	176,400	105,000	180,600	197,400	270,000	–
m	0.6	0.9	0.95	0.7	0.5	1	0.9	0.7	0.5	1	0.5	0.7	0.8	–
ν	0.2	0.2	0.2	0.2	0.2	0.2	0.2	0.2	0.2	0.2	0.2	0.2	0.2	0.2
c (kN/m²)	5	15.7	38.3	8.2	2	68.4	46.6	14.2	2	55.3	2	14.3	65	–
φ (°)	25	14.6	15.9	28.5	32	19.5	25.8	27.4	32	18.6	32	33.5	42	–
ψ (°)	0	0	0	0	2	0	0	0	2	0	2	1	5	–
R_{inter}	0.7	0.7	0.75	0.75	0.8	0.8	0.85	0.85	0.9	0.9	0.95	0.95	0.95	1

Fig. 2 Load—displacement curves of O-Cell test on **a** the TP01 and **b** the TP03

capacity of the TP03 corresponding to the maximum loading increment is 83.42 MN.

The results of the mobilized unit friction resistance at the maximum loading increment of the O-Cell tests on the TP01 and TP03 are presented in Table 2. Note that for the TP03, the pile segments using grouting method are from the elevation of −36.0 m to the pile tip corresponding to the load transfer zones from the level 10 to the level 1 of strain gauge position.

For the TP01, strain gauge level 2 and 4 yield unusual load and are not included in the analysis. Table 2 shows that unit friction resistance values vary according to

Table 2 Unit friction resistance values corresponding to maximum load of TP01 and TP03

TP01			TP03		
Load transfer zone (strain gauge level)	Length of pile segments (m)	f_{si} (kPa)	Load transfer zone (strain gauge level)	Length of pile segments (m)	f_{si} (kPa)
GL–15	5.60	3.00	GL–15	5.00	10.87
15–14	7.60	8.15	15–14	8.00	16.16
14–13	7.00	25.30	14–13	8.00	61.54
13–12	6.00	72.50	13–12	7.00	159.66
12–11	5.50	46.02	12–11	6.00	56.42
11−10	5.30	128.20	10	–	–
10−9	5.00	149.00	11−9	11.00	144.46
9–8	5.00	115.03	8	–	–
8–7	5.00	109.00	9–7	11.00	436.65
7–6	5.00	101.00	7–6	3.00	121.55
6–O-Cell	3.00	101.00	6–O-Cell	2.50	121.55
O-Cell–5	3.50	119.80	O-Cell–5	2.50	386.87
4	–	–	4	–	–
5–3	10.00	151.20	5–3	9.50	241.85
2	–	–	3–2	5.00	172.31
3–1	10.00	228.05	2–1	5.00	585.90

the measured pile segments or to the soil layers around these pile segments. The total mobilized friction resistance of the soil around the upper pile portion and the lower pile portion corresponding to the maximum loading increment are equal to 20.2 MN and 21.53 MN, respectively (Table 2). It can be deduced that the mobilized tip resistance at this loading increment is 0.11 MN. Similarly, for the TP03, unit friction resistance values also vary according to the measured pile segments or to the soil layers around these pile segments. Strain gauge level 4, 8 and 10 yield unusual load and are not included in the analysis. The total mobilized friction resistance of the soil around the upper pile portion and the lower pile portion corresponding to the maximum loading increment are equal to 41.1 MN and 37.64 MN, respectively (Table 2). It can be deduced that the mobilized tip resistance at this loading increment is 4.82 MN.

Thus, it can be seen that, at the same depth or soil layer, the mobilized unit friction resistance of the soil around the TP03 is greater than that of the TP01 except at some unusual measurement locations. The difference in the unit friction resistance of the soil around the TP03 compared to the TP01 mainly occurs in the pile segments that are grouted from the elevation of −36.0 m to the pile tip.

The results of the field test analyzed in the above section have just determined the bearing capacity corresponding to the mobilized soil resistance at the maximum loading increment, not the ultimate bearing capacity of the two test piles TP01 and TP03. Therefore, the FEM is used to simulate the field tests for both TP01 and TP03 to determine the ultimate bearing capacity of these two piles.

Figure 3a and b show a comparison between the back-analyzed load-displacement curves with the measured ones on the TP01 and TP03, respectively. The comparison shows that the FEM calculations agree well with the actual field measurements for both TP01 and TP03. The difference between the calculations and measurements becomes significant only at some loading increments at the end of the cycle.

The comparison results show that the FEM model can achieve a satisfactory simulation of the O-cell tests with adopted parameters, which can be used to extrapolate the ultimate bearing capacity of the two test piles. The simulation results of TP01 show that the upper ultimate friction resistance of the soil around the upper
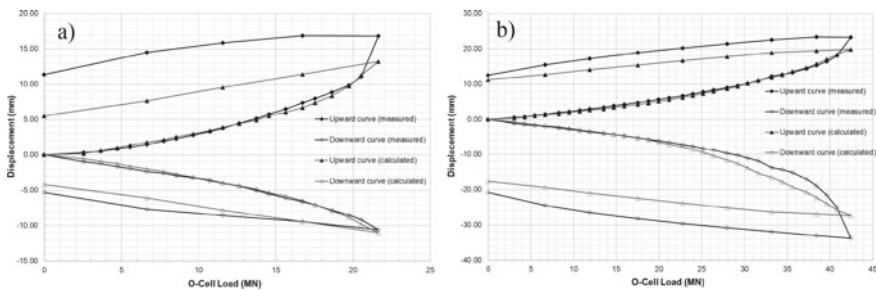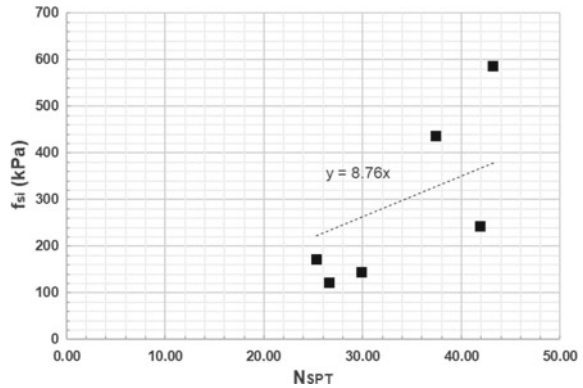

Fig. 3 Comparison of load—displacement curves for **a** the TP01 and **b** the TP03

Fig. 4 Unit friction resistance versus N_{SPT} for pile segments using grouting method of TP03

pile portion reaches 24 MN, the combined ultimate end bearing and lower ultimate friction resistance reaches 28 MN. For the TP03, the simulation results show that the upper ultimate friction resistance of the soil around the upper pile portion reaches 42 MN, the combined ultimate end bearing and lower ultimate friction resistance reaches 44 MN. It can be deduced that the ultimate bearing capacity of the TP01 is 52 MN and that of the TP03 is 86 MN.

To model the relationship between the unit friction resistance with the standard penetration test (SPT) results for the piles using shaft-grouting method, the calculated unit friction resistance values at the maximum loading increment of the O-Cell test on the TP03 from the elevation of −36.0 m to the pile tip (Table 2) were used to analyze together with the weighted average SPT values. According to Fig. 4, the correlation of unit friction resistance with SPT value is determined as $f_{si} = 8.76 N_{SPT}$ (kPa).

4   Discussion

The results of the O-Cell tests compared, the mobilized load capacity of the TP03 is 2 times that of the TP01, in which these two test piles have the same size in length and diameter. Therefrom, the grouting method in this case increases 2 times the bearing capacity of the shaft-grouted pile compared to the non-grouted pile. However, the load-displacement curves of the O-Cell test of the TP01 in Fig. 2a show that at the maximum loading increment, the upper friction resistance as well as the combined end bearing and lower friction resistance have not been fully mobilized. In fact, the mobilized end bearing resistance under the TP01 pile tip calculated from Table 2 is only 0.11 MN, much smaller than 11.5 MN, which is the ultimate end bearing resistance value estimated by the formula of the Architectural Institute of Japan (TCVN 10304: 2014). The values of the ultimate bearing capacity of the TP01 and the TP03, determined then by the FEM, show that the ultimate bearing capacity of the shaft-grouted pile is 1.7 times that of the non-grouted pile. In addition, this simulation results of the FEM also shows that the load capacity

mobilized in the O-Cell test on the TP01 reaches 80.3% of the ultimate load capacity (corresponding to 41.78 MN) and that on the TP03 reached 97.0% of the ultimate load capacity (corresponding to 83.42 MN).

It can be seen that the increase in bearing capacity of the TP03 compared to the TP01 is mainly from the increase in the friction resistance of the soil around the grouted pile segments from the elevation of −36.0 m to the pile tip. In the soil layers around the non-grouted pile segments, there is a slight difference in friction resistance on the TP03 compared to that on the TP01. This difference can be explained by the difference in the maximum loading increment in the 2 tests, leading to different mobilization of friction resistance on the two respective non-grouted pile segments (Duong and Pham [2]). For a more detailed comparison, the total friction resistance of the soil layers mobilized around the pile segments from the elevation of −36.0 m to the tip of both TP03 and TP01 is calculated from Table 2 by 72.9 MN and 34.7 MN, respectively. It infers that the grouting method using on these pile segments increases the friction resistance by more than 2 times (110%). This result is consistent with the studies of Littlechild et al. [4], Duong and Pham [1], Nguyen et al. [7].

With the results above, the model to estimate the unit friction resistance in correlation with the SPT value for the shaft-grouted bored piles proposed in this study is $f_s = 8.76 N_{SPT}$. This model shows that the greater the SPT value or the harder the surrounding soil layers, the greater the mobilized unit friction resistance. This correlation between the unit friction resistance and the SPT value of the shaft-grouted bored pile is similar to that of conventional bored piles, the effect of grouting only increases the mobilized unit friction resistance or increases the correlation coefficient in the model compared with the non-grouted pile. This correlation is completely consistent with previous studies (Littlechild et al. [4]; Nguyen and Fellenius [6]) and with the design model of Bachy Soletanche Vietnam (Duong and Pham [1]). However, if compared with the back analysis results of Duong and Pham [2] on the pile load tests of the barrettes using grouting method in other projects in Vietnam, the model in this study gives the correlation between the unit friction resistance and the SPT value with a larger coefficient than that in the study of Duong and Pham [2]. It can be explained by the difference in the study subject, as the bored pile segments chosen to grout in this study have quite hard surrounding soil with an average SPT of 25–44 while the shaft-grouted barrettes studied in Duong and Pham [2] have that with an average SPT of 12 to over 50.

In addition, the unit friction resistance values of the pile segments using the grouting method varies from 122 to 586 kPa, depending on the surrounding soil layers. This range of unit friction resistance values is consistent with that calculated in the study of Duong and Pham [2]. Some studies by Littlechid et al. [4], Littlechid et al. [5] based on load test data of bored piles and barrettes using shaft grouting method in Bangkok and Hong Kong show that the maximum unit friction resistance of surrounding soil on these types of pile ranges from 150 to 320 kPa. However, the mobilized unit friction resistance value depends on the maximum loading increment of the test. The larger loading increment, the greater the unit friction resistance will

be mobilized. The unit friction resistance values from this study only correspond to the maximum loading increment of the O-Cell tests achieved in the field.

In conclusion, the comparison of the bearing capacity determined from the O-Cell tests of two test piles with the same length and diameter, of which one is non-grouted and the other is shaft-grouted in this study shows that the shaft-grouting method increases the shaft resistance of the corresponding pile section by more than 110%, which increases the pile's bearing capacity. Moreover, the correlation $f_s = 8.76 N_{SPT}$ deduced from the back analysis of the O-Cell test and the SPT result can be used to reliably estimate the unit friction resistance for bored piles using shaft-grouting technique in the studied area.

References

1. Duong, M.T., Pham, Q.D.: The Use of Shaft-Grouted Friction Barrettes in Vietnam. In: Proceedings of the International Conference on High-rise buildings and Underground structures (CIGOS). Paris (2010)
2. Duong, M.T., Pham, Q.D.: Comprehensive Analysis of Shaft Grouted Barrettes in Vietnam. In: Proceedings of the 1st International Conference on Geotechnics for Sustainable Development (GEOTEC), pp. 7–13. Hanoi (2011)
3. GEO: The Hong Kong Geotechnical Engineering Office: Foundation design and construction. 1st edn. GEO publication, Hong Kong (2006)
4. Littlechild, B.D., Plumbridge, G.D.: Free, M. W.: Shaft grouted piles in sand and clay in Bangkok. In: Proceedings of the 7th International conference and exhibition on piling and deep foundations, pp. 171–178. DFI, Vienna (1998)
5. Littlechild, B.D., Plumbridge, G.D., Hill, S.J., Lee, S.C.: Shaft grouting of deep foundations in Hong Kong. New technological and design developments in deep foundations, pp. 33–45. Dennis ND, Houston (2000)
6. Nguyen, H.M., Fellenius, B.H.: Bidirectional cell tests on non-grouted and grouted large-diameter bored piles. J. Geo-Eng. Sci., IOS Press. **2**(3–4), 105–117 (2015)
7. Nguyen, T.D., Lai, V.Q., Phung, D.L., Duong, T.P.: Shaft resistance of shaft-grouted bored piles and barrettes recently constructed in Ho Chi Minh city. Geotech. Eng. J. SEAGS & AGSSEA **50**(3), 155–162 (2019)
8. Stocker, M.: The influence of post-grouting on the load-bearing capacity of bored piles. In: Proceedings of the 8th European Conference on Soil Mechanics and Foundation Engineering, pp. 167–170. Helsinki (1983)
9. Zhang, L.M., Chu, L.F.: Calibration of methods for designing large-diameter bored piles: ultimate limit state. Soils Found. **49**(6), 883–895 (2009)
10. Zhang, Z.M., Yu, J., Zhang, G.X., Zhou, X.M.: Test study on the characteristics of mudcakes and in situ soils around bored piles. Can. Geotech. J. **46**(3), 241–255 (2009)

Experimental and Numerical Investigation for Engineering Structure

The Factors Affecting the Toxicity of Fire Products Evolved by Burning Pinaceae Wood Materials

Khuc Quang Trung, Do Minh Thao, and Nguyen Nhu Dung

1 Introduction

Nowadays, wood materials have been widely used in construction and civil due to many advantages such as low price, being easily adapted to requirements, being easy to decorate [1]. However, wood materials have a high risk of fire and explosion. When wood materials are burned, there cause a lot of toxic fire products. The toxicity of these fire products is determined according to the models in ISO 13571 [2]).

The toxicity of fire products can be determined according to the model of asphyxiant gas (FED) in Eq. (1) or the model of irritant gas (FEC) in Eq. (2).

$$FED = \sum_{t_1}^{t_2} \frac{[\text{CO}]}{35000 ppm \cdot \min} \Delta t + \sum_{t_1}^{t_2} \frac{\exp([\text{HCN}]/43)}{220 \min} \Delta t \tag{1}$$

where, [CO] is the average concentration of CO over the time increment (ppm); [HCN] is the average concentration of HCN over the time increment (ppm); Δt: is the time increment (minute).

$$FEC = \frac{[HCl]}{F_{HCl}} + \frac{[HBr]}{F_{HBr}} + \frac{[HF]}{F_{HF}} + \frac{[SO_2]}{F_{SO_2}} + \frac{[NO_2]}{F_{NO_2}} + \frac{[acrolein]}{F_{acrolein}} + \frac{[formaldehyde]}{F_{formaldehyde}} \tag{2}$$

K. Q. Trung (✉) · D. M. Thao
The University of Fire Prevention and Fighting, Hanoi, Vietnam

N. N. Dung
Hanoi Architectural University, Hanoi, Vietnam

where [FEC] is irritant gas concentration (ppm); F: is irritant gas concentration that are expected to seriously compromise occupants' ability to take effective action to accomplish escape (ppm). This value is determined according to [2, 3] as follows: $F_{HCl} = 1000$ ppm; $F_{NO_2} = 250$ ppm; $F_{HBr} = 1000$ ppm; $F_{acrolein} = 30$ ppm; $F_{HF} = 500$ ppm; $F_{formaldehyde} = 250$ ppm and $F_{SO_2} = 150$ ppm.

In fact, the toxicity of fire products is often determined based on the model with higher value. Currently, study on the determination of the toxicity of fire products evolved when burning materials has attracted the participation of several research groups. G. Prado et al. [4] studied fire products evolved when burning polymer materials. Bert et al. [5] studied fire products in the burning process of PVC materials and wood materials. These studies showed that burning plastic materials produce highly toxic fire products. However, these research groups have still focused on determining the effects of inhaling toxic smoke in fires on human's health [6–8]. To the best of our knowledge, there is not a comprehensive study on fire products in the burning process of Pinaceae wood materials, therefore, in this work, we determine the toxicity of fire products that evolved when burning Pinaceae wood materials.

2 Experiment

We used the experimental process according to ISO 5659 as follows [9] to determine the toxicity of fire products, generated when wood materials are burned. Figure 1 shows the experiment processes: preparing the sample (with a size of $75 \times 75 \pm 1$ mm); checking before measuring; starting the system; cleaning the chamber; and starting and connecting FTIR with the SDC device (see Fig. 2). Firstly, the tray is placed into the center of the rack (this must be done exactly to ensure the accuracy of the measurement); press 'Load Cell' and 'Tare' to be at the standard value of 0. Secondly, the tray containing the sample is inserted; close the Lower vent and Upper vent before closing the SDC device. The measurement is started by simultaneously pressing 'Ignition', pressing the 'Foot switch', and selecting the 'Smoke chamber' on the touch screen of the FTIR device. The time of measurement is set to 600 s (=10 min). When the measurement is finished, for the SDC device, press 'Ignition', Lower Vent (Upper Vent opens automatically), and press Extraction. For FTIR machine, select 'Air Sample' and press Ok → Record → Ok.
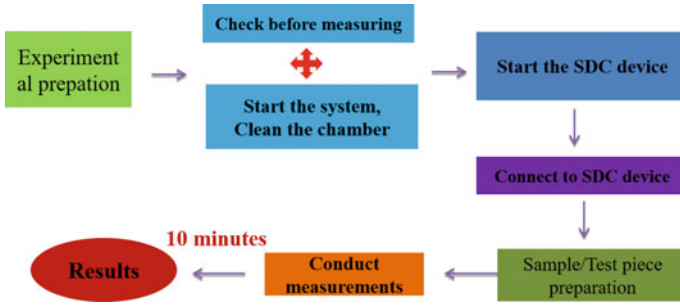
Fig. 1 Procedure for determining the toxicity of fire products generated when burning wood materials on DSC and FTIR device

Fig. 2 SDC device, which was made in Britain, is currently used at the University of Fire, Vietnam

3 Results and Discussion

3.1 The Toxicity of Fire Products Produced When Burning Pinaceae Wood Materials

We conducted experiments to determine the toxicity of fire products that are generated when samples of Pinaceae wood materials are burned. In our experiments, the heat intensity is 25 kW/m^2 and the sample thickness is 9 mm. The experimental results show that the fire products of burning samples of Pinaceae wood materials consist of various gases such as CO_2, CO, HCHO, and SO_2; the concentration varies over time. Figure 3 plots the concentration of several toxic gases that were produced when the samples of Pinaceae wood materials are burned.
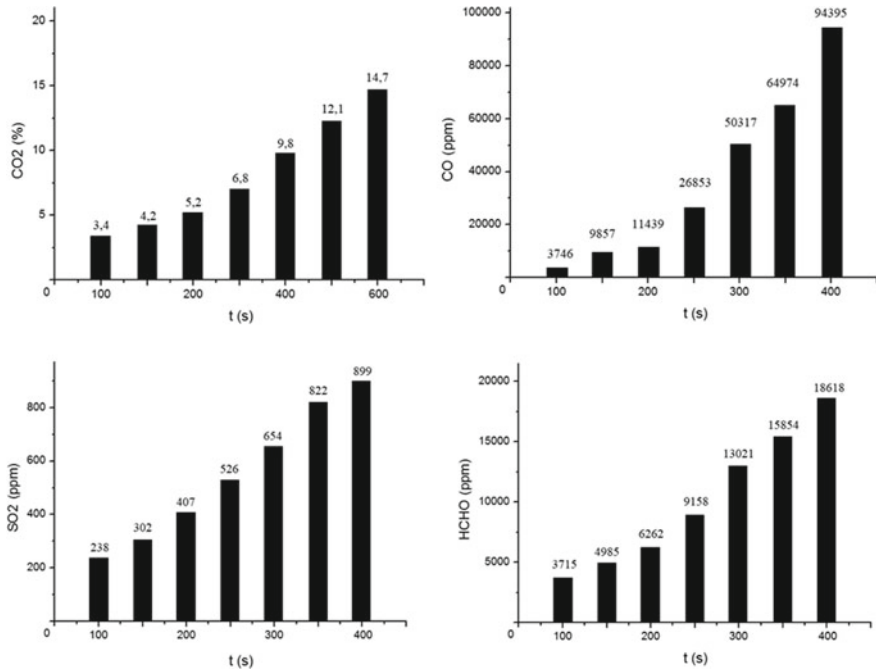
Fig. 3 Concentration of CO_2, CO, SO_2, and HCHO in fire products measured in the combustion of Pinaceae wood samples

From the concentration of the toxic gases (i.e., CO_2, CO, HCHO, SO_2), we determine the toxicity of fire products of the burning process of Pinaceae wood materials according to the asphyxiant gas model (FED) and irritant gas model (FEC). As shown in Fig. 4, the toxicity of fire products according to the FEC model (Fig. 4a) is much higher than that according to the FED model (Fig. 4b). Therefore, we choose to determine the toxicity of fire products based on the FEC model (irritant gas model).

3.2 Factors Affecting the Toxicity of Fire Products Produced When Burning Pinaceae Wood Materials

Impact of different wood types on the toxicity of fire products. In order to study the impact of different wood materials on the toxicity of fire products, we conducted the experiments with 4 different wood samples (these wood types are commonly used in Vietnam, including Pinaceae wood), Prunus arborea wood, Taulauma wood, and Parashorea chinensis wood. Figure 5 shows the toxicity of fire products produced when burning 4 types of wood materials. From the results, the toxicity of
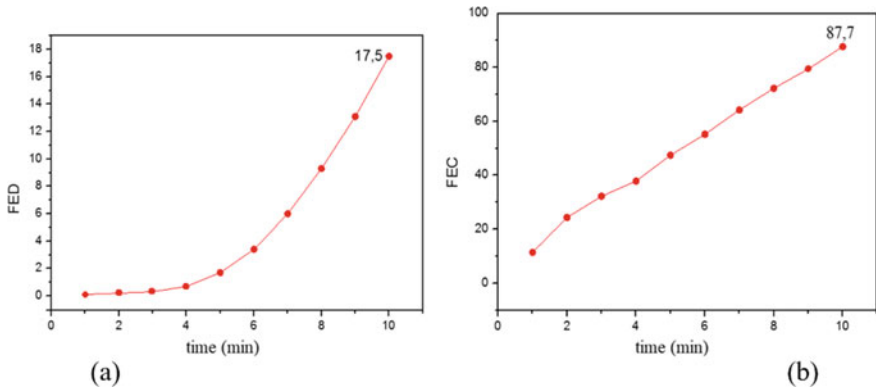
Fig. 4 Toxicity of fire products evolved when burning Pinaceae wood samples according to asphyxiant gas model (**a**) and irritant gas model (**b**)

fire products evolved when burning Pinaceae wood samples is higher than that when burning the three other wood samples.

The different concentration of toxic gases is due to the composition of each wood type. Specifically, each wood types has different proportion of basic components (e.g., Cellulose, Hemi-Cellulose, and Ligin). In case of softwood trees, the content of Ligin and Hemi-Cellulose is higher than that of hardwood trees. Therefore, Pinaceae wood is classified as softwood tree while Prunus arborea, Taulauma, and Parashorea chinensis are classified as hardwood tree. Because the proportion Ligin and Hemi-Cellulose in the Pinaceae wood sample is larger than
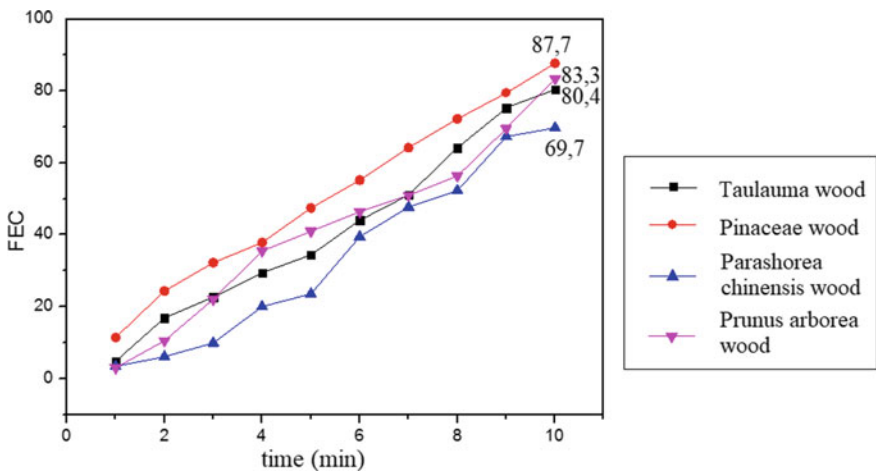

Fig. 5 Results of the determination of the toxicity of fire products when burning 4 types of wood materials

that in the three remaining wood samples, the toxicity generated by burning the Pinaceae wood is greater than that generated by burning the three remaining wood samples.

Impact of heat intensity on the toxicity of fire products. To study the impact of heat intensity on the toxicity of fire products, we conducted the experiments on 2 Pinaceae wood samples with different heat intensities. From the concentration of the toxic gases obtained by burning process of Pinaceae wood materials, we can determine the toxicity of the fire products according to irritant gas model (FEC), as shown in Fig. 6.

In fire conditions, wood is thermally decomposed leading to different types of fire products. The amount of gas and vapor increases directly proportional to the increase of heat since the thermal decomposition occurs more rapidly. When wood is heated to 250 °C, the decomposition of wood will release gases such as CO, CH_4, H_2, CO_2, and H_2O. The mixture of these gases may be combusted due to the ignition source. Wood is partially decomposed at the temperature from 280 to 300 °C; the decomposition of wood increases significantly when the temperature reaches 350–450 °C. We can see that, under the same condition, the higher heat intensity leads to more quickly thermal decomposition of the material, and thus increasing the toxic gas concentration when Pinaceae wood is burned.

Impact of coating material on the toxicity of fire products. To study the impact of coating materials, we conducted the experiments on 3 Pinaceae wood samples under the following experimental condition: one Pinaceae wood sample without coating materials, one Pinaceae wood sample painted with PU, and one
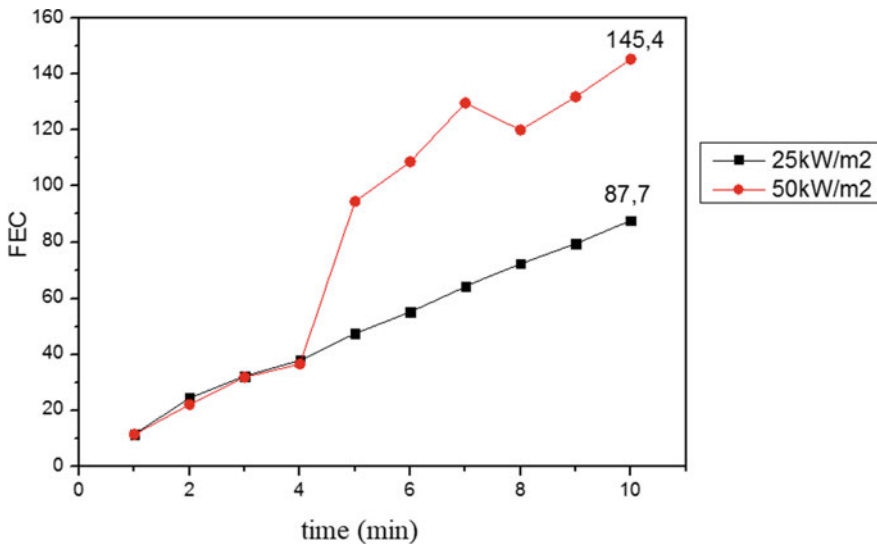

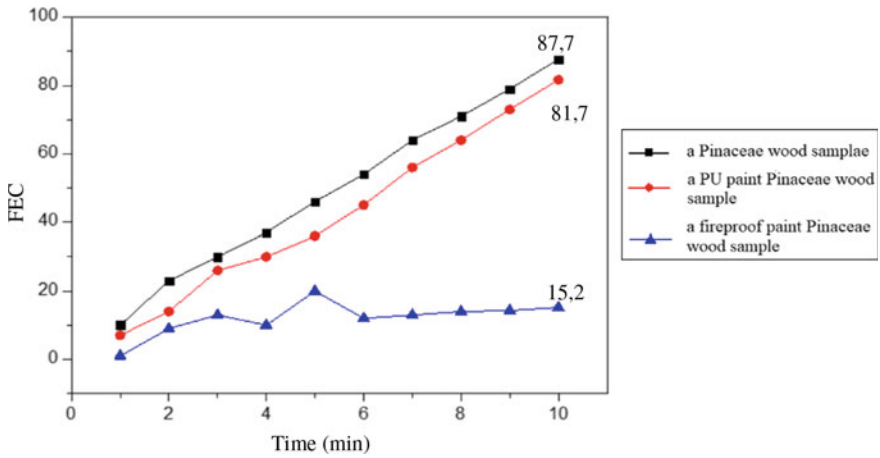**Fig. 6** Toxicity of fire products produced when burning Pinaceae wood with different heat intensity

Fig. 7 Toxicity of fire products produced when burning Pinaceae wood samples with different coating materials

fire-resistant painted Pinaceae wood sample. From the concentration of toxic gases, the toxicity of smoke evolved by burning Pinaceae wood materials with different coating materials is determined by irritant gas model (FEC), as shown in Fig. 7. We can see that the toxicity of fire products in case of the Pinaceae wood sample without coating materials is higher than that in cases of the Pinaceae wood sample painted with PU, and the fire-resistant painted Pinaceae wood sample. The difference is due to the compositions of coating materials and their functions.

Based on some research, there are 3 basic components in paint, including film forming agents, solvents, and additives. Film forming agent is the main ingredient in paint, which determines the properties of the paint film, normally called original paint. Solvents are volatile liquids (ethers, ketones, esters, alcohols, … chlorinated hydrocarbons, nitrates, paraffin) which are capable of dissolving the film forming agent and evaporating gradually in the process of forming paint film. Solvents directly affect stability, machining methods and quality of paint film. Additives are ingredients that are put into paint to improve certain features in the process of processing, preserving, or creating paint film. The additives are different in each type of paint. They are the ingredients of additives that change the concentration of toxic gas produced.

Besides, the coating material reduces the impact of heat on the surface of the Pinaceae wood material, thus slowing down the thermal decomposition process on the surface, and reducing the concentration of toxic gases in fire products. Since the fire-resistant paint prevents the thermal impact effectively, the concentration of toxic gases from the combustion of a Pinaceae wood sample coated by fire-resistant paint is lower than that with the two remaining Pinaceae wood samples. Sample 3 without coating material was decomposed the most, thus causing more toxicity.

4 Conclusion

The toxicity of fire products generated when burning Pinaceae wood materials according to the irritant gas model was much higher than that according to the asphyxiant gas model. Hence, in this case, the toxicity of fire products produced in the combustion of Pinaceae wood was determined according to the irritant gas model with the results were 87.7 after 10 min. In addition, we investigated the factors affecting the toxicity of fire products created during the burning process of Pinaceae wood materials. The results are as follows:

– The toxicity of fire products produced when burning the Pinaceae wood sample was higher than that when burning three remaining wood samples.
– The greater the heat intensity is, the higher the toxicity is.
– The toxicity in fire products produced when burning Pinaceae wood sample without coating material is higher than that when burning Pinaceae wood samples painted with PU and fire-resistant paint.

References

1. Từng, D., Hợp, D.Q., Phong, C.D.: Theory of combustion process, Science and Technichs Publishing House (2004)
2. ISO 13571:2012 Life-threatening components of fire—Guidelines for the estimation of time to compromised tenability in fires
3. Purser, D.A.: Toxicity Assessment of Combustion Products. In: SFPE Handbook of Fire Protection Engineering, National Fire Protection Association, Quicy, MA, Sect. 2, pp. 85–146 (1995)
4. Prado, G., Jagoda, J., Lahaye, J.: Smoke formation by combustion of Polymeric Materials. Fire Res. 1, 229–235 (1977/1978)
5. Bert, M., Michel, A., Guyot, A.: Reduction of smoke Generation in Poly (vinyl chloride) Combustion. Fire Res. 1, 301–311 (1977/1978)
6. Chen, K., Mackie, J.C., Kennedy, E.M., Dlugogorski, B.Z.: Determination of toxic products released in combustion of pesticides. Prog. Energy Combust. Sci. 38, 400–418 (2012)
7. Rybiński, P., Bradło, D., Żukowski, W., Syrek, B.: Determination of toxic products emissions of polymers thermal decomposition using fluidised bed reactor and FTIR analysis. Polymer Testing 79, 106040 (2019)
8. Wang, J., Zhang, D., Zhang, Y., Cai, W., Weizhao, H.: Construction of multifunctional boron nitride nanosheet towards reducing toxic volatiles (CO and HCN) generation and fire hazard of thermoplastic polyurethane. J. Hazard. Mater. 362, 482–494 (2019)
9. ISO 5660-1:2015 Reaction to fire tests—Heat release, smoke production and mass loss rate—Part 1: Heat release rate (cone calorimeter method) and smoke production rate (dynamic measurement)

The Fabrication of a Liquefied Petroleum Gas-Leak Detection Device with Sensor Made from α-Fe$_2$O$_3$ Nanorod/SnO$_2$ Nanorod Composites

Khuc Quang Trung, Do Minh Thao, Le Quang Hai, and Nguyen Nhu Dung

1 Introduction

In recent years, liquefied petroleum gas (LPG) has become a very important source of fuel for our country. With low price compared to other fuels, the ability to burn completely, the relatively high combustion heat, LPG is commonly used in various fields such as: industry, agriculture, household activities and transportation. However, LPG is also a source of fuel with a high risk of fire and explosion. It not only causes economic losses but also affects people's lives. Therefore, limiting the explosion due to gas leakage is a matter of concern for the whole society in general and for fire police forces in particular. Under these circumstances, many scientists have conducted research which aimed at fabricating gas sensors capable of detecting gas leaks. Due to their advantages, namely being simple and low cost, gas sensors made from semiconductor metal oxide materials have been commonly used to detect combustible gases and toxic gases.

Studies in the world have shown that semiconductor metal oxide materials such as SnO$_2$ [1, 2], Fe$_2$O$_3$ [3, 4], ZnO [5] and WO$_3$ [6, 7] have been widely utilized to make gas-sensitive materials in gas sensors. Specifically, the SnO$_2$ material with superior features of chemical resistance, heat resistance as well as sensitivity has been studied and put into use in life [8, 9]. However, studies in the world are now focusing on controlling the size of nanoparticles and finding suitable impurities to improve gas sensitivity characteristics [10, 11]. Hence, in this paper, we present the results of research and fabrication of a LPG- leak detection device, which is based on a sensor made of α- Fe$_2$O$_3$ nanorod/SnO$_2$ nanorod composites, to detect and warn the risks of fire and explosion.

K. Q. Trung (✉) · D. M. Thao · L. Q. Hai
University of Fire Prevention and Fighting, Hanoi, Vietnam

N. N. Dung
Hanoi Architectural University, Hanoi, Vietnam

2 Experiment

### 2.1 Fabrication of the α-Fe₂O₃ Nanorod/SnO₂ Nanorod Composites Material

A typical synthesis procedure of nanostructured SnO_2 rod material is described in Fig. 1. First, the mixture of $SnCl_4$ (0.15 M) and NaOH is dissolved in deionized water and stirred at room temperature. After stirring for about 10 min, C_2H_5OH is dropped slowly into the mixture to obtain a white precipitation. The solution is then transferred into Teflon-linked autoclave to hydrolyze for 24 h at temperature of 190 °C. After being treated by hydrothermal method, the sample is naturally cooled to room temperature. The resulting product is a white precipitate, which is washed with ethanol and distilled water several times to remove all Na^+ and Cl^- ions. The precipitate was finally dried at 80 °C for 24 h to obtain a powder sample [10]. These powder samples were analyzed and surveyed to determine their crystal structure and morphology.

To improve the sensitivity of the sensor, Fe_2O_3 nanorods were doped with SnO_2 nanorods. The α-Fe_2O_3/SnO_2 composite was synthesized by doping α-Fe_2O_3 nanorods with SnO_2 nanorods with different mass ratios. The α-Fe_2O_3 nanorod was made from $Fe(NO_3)_3$ and Na_2SO_4 by hydrothermal treatment method.

2.2 The Measurement of Gas-Sensing Properties of the Sensor

To make sensor components, the above α-Fe_2O_3/SnO_2 composite material was rotated on a Si substrate attached to a comb-tooth electrode. Then, a thin film was

Fig. 1 SnO₂ rod material preparation process by hydrothermal
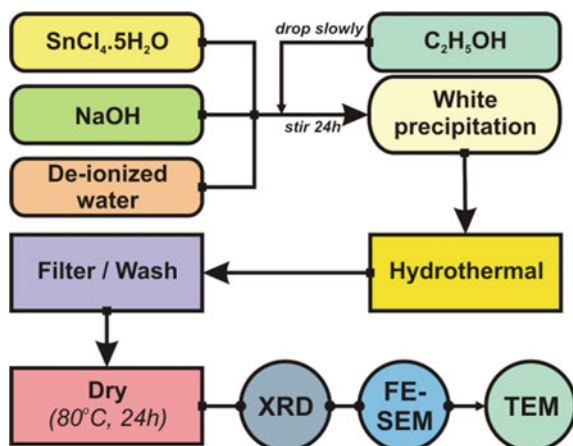
formed on the surface of the electrode. The thin films were baked at 100 °C for 24 h. The sensitivity of the sensor (S) is defined as the ratio of the resistance of the sensor film in the air (R_a) and the resistance of the sensor film when the test gas appears (R_g). Sensor components were measured in the range of 0.1–1% of the volume for LPG. The surveyed working temperature range was 220–400 °C.

2.3 The Design of Principle Circuits and Printed Circuits with Proteus 7 Professional Software

The design of principle circuits. The principle circuit is one of the basic, important parts for designing and manufacturing warning devices. Based on the principle circuit, the designer as well as the reader can understand part or all of the circuit's operation principle. We used the ISIS Professional of Proteus 7 Professional software program to design the principle circuit for the device. Proteus VSM software is written by Labcenter Electronics and widely used in 35 countries. Proteus has confirmed its strength in simulating principle circuits which are close to reality. In addition, Proteus provides a full range of tools and libraries of electronic components, allowing users to easily design and simulate electronic circuits from simple to complex in a short period of time. By using this software, we designed a gas-leak warning device based on the principle of comparing the voltage on the sensor with a threshold voltage to output a dangerous warning signal using LEDs, speakers and to control fan and magnetic valve.

The design of printed circuits. After developing the principle diagram of the measurement circuit, we designed the printed circuit for the gas warning device based on the ARES Professional item of the Proteus 7 Professional software program. Some components already available in Vietnam were used to ensure the convenience and reduce the cost of the device. LM 324 algorithm, 7805 voltage regulator IC, C828 transistor, exhaust fan system, electromagnetic gas valve, LED lights, capacitors and different types of resistors were used to design the circuit for the device.

3 Results and Discussion

3.1 Morphology and Structure of the Material

The SnO_2 nanorod materials were formed by hydrothermal treatment method using precursors such as $SnCl_4.5H_2O$, NaOH and C_2H_5OH solvent. The results of the study on the structure of SnO_2 nanorod material by X-ray diffraction method (XRD) are shown in Fig. 2. It is noticed that the nanorod samples were treated at 400 °C for 3 h; the crystal existed in the form of rutile phase with diffraction angles

which correspond with the theoretical results. It can be easily observed from the XRD spectrum that the peak appears with the strongest intensity at the scanning angle of $2\theta = 33.7°$ for the face (101), and the next vertices have the weaker intensity corresponding to the face (211) at $2\theta = 51.7$ °C and face (110) at 26.65 °C.

The TEM image of SnO_2 nanorods after thermal treatment at 120 °C for 24 h is illustrated in Fig. 3. It can be seen in Fig. 3a1 that the SnO_2 nanorods were synthesized quite uniformly and relatively small in size. Besides, the density of rods in the samples is very high. The synthesized SnO_2 nanorods have the diameter of about 10–13 nm and the length of about 30 nm. In addition, it seems that SnO_2 particles with a size of about 6 nm still exist interspersed among rods as shown in Fig. 3a2. However, the density of the particles collected in the sample was not high. Figure 3c1, c2 and c3 show FE-SEM images of nanostructured $\alpha\text{-}Fe_2O_3$ rods after thermal treatment at 600 °C for 2 h. The results indicated that the synthesized $\alpha\text{-}Fe_2O_3$ rods were fairly uniform and the density of the rods in the sample was very high. The obtained $\alpha\text{-}Fe_2O_3$ nanorods have the diameter of about 50 nm and the length of about 300 nm. In addition, the $\alpha\text{-}Fe_2O_3$ rods are uniformly arranged from the center of the hollow sphere structure with the size of about 2–3 µm.

The images in Fig. 3b5–b7 illustrate that SnO_2 nanorods with relatively small size tend to stick to $\alpha\text{-}Fe_2O_3$ rods in the $\alpha\text{-}Fe_2O_3/SnO_2$ composite sample, which is clearly shown in TEM b2 image, b4. At the same time, hierarchical sphere structures tend to be broken down into $\alpha\text{-}Fe_2O_3$ rods because the sample was vigorously stirred for 24 h.

3.2 Gas-Sensing Properties of Nanorod $\alpha\text{-}Fe_2O_3$/Nanorod SnO_2 Composite

To investigate the gas-sensitive characteristics of the $\alpha\text{-}Fe_2O_3/SnO_2$ composite film, the material was covered on Pt comb electrode system. The sample was then thermally treated at 100 °C for 24 h, and the survey about its sensitivity for LPG in

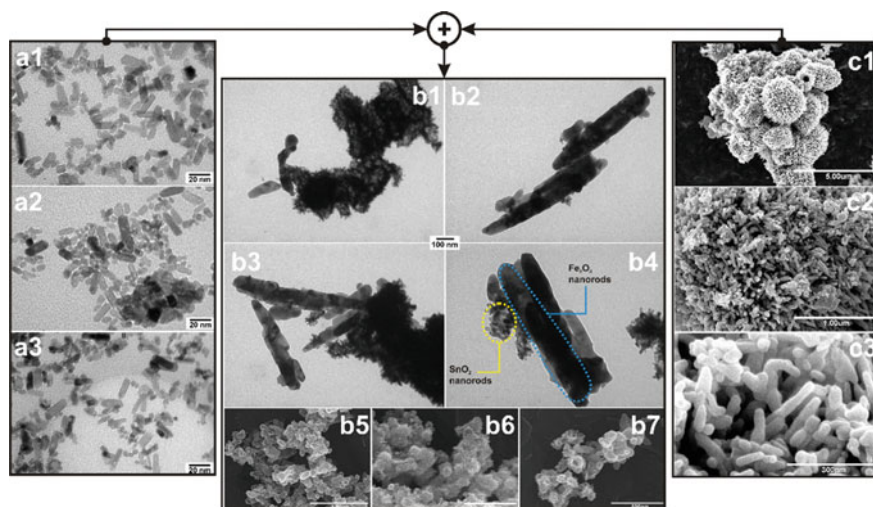**Fig. 2** XRD pattern of SnO_2 nanorods powder samples incubated at 400 °C in 3 h
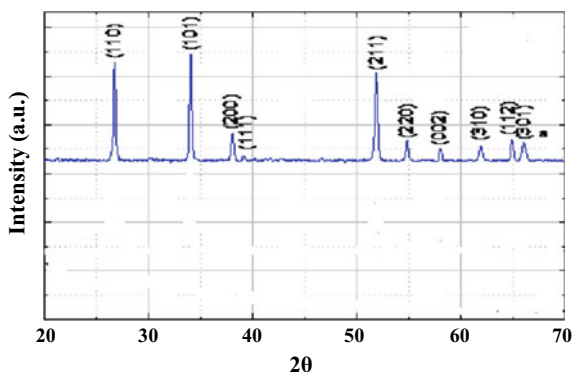
Fig. 3 TEM and FE-SEM images of SnO$_2$ nanorods, α-Fe$_2$O$_3$ rods and the α-Fe$_2$O$_3$/SnO$_2$ composite samples with different scales

the temperature range of 220–390 °C was carried out. The dependence of sensitivity of the film samples on the working temperature for 1% of LPG is shown in Fig. 4. Experimental results indicate that the sensitivity of the sensors based on α-Fe$_2$O$_3$/SnO$_2$ composites strongly depends on the working temperature. The sensitivity of film samples has not increased significantly in the temperature range from 220 to 300 °C. However, the sensitivity of the sensor increases sharply when the temperature is greater than 300 °C, and the optimum temperature of the sensor reaches 370 °C. As the working temperature continues to increase, the sensitivity of the film samples tends to decrease. The results show that the composite film sample with the ratio of Fe: Sn equal to 75:25 has the highest sensitivity (with 32 times at 370 °C). Compared with pure material film samples, the sensitivity of the sensor based on SnO$_2$ nanorod and Fe$_2$O$_3$ nanorod materials was 14 and 9.6 times, respectively. It can be seen that the sensitivity of the sensor based on α-Fe$_2$O$_3$/SnO$_2$ nanorod composite materials gives a much higher sensitivity than the sensors using pure SnO$_2$ nanorod or α- Fe$_2$O$_3$ nanorod materials.

The influence of LPG concentration on the sensitivity of the sensor made from α-Fe$_2$O$_3$/SnO$_2$ composites was also investigated. The dependence of the film sample sensitivity on LPG concentration at 370 °C is shown in Fig. 5. Experimental results indicate that the sensitivity of the sensor made from α-Fe$_2$O$_3$/SnO$_2$ composites greatly depends on the tested LPG concentration. The sensitivity of the sensor increases as the tested LPG concentration increases. Especially for composite samples with the ratio of Fe:Sn equal to 75:25, the sensitivity of the sensor reaches 32 times for 1% LPG at 370 °C. Besides, the dependent function of the sensitivity of the sensor according to the concentration in the range of 0.2–1.0%

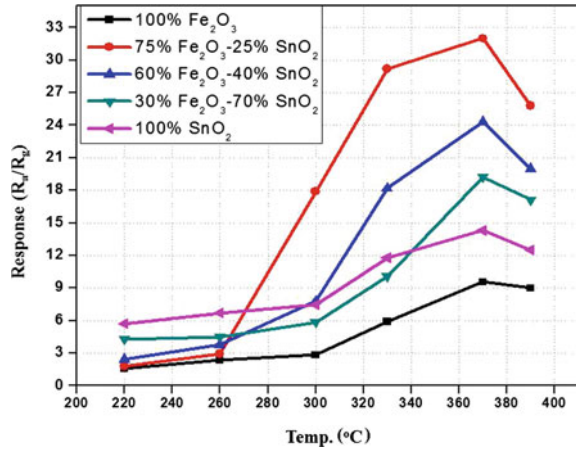**Fig. 4** Dependence of sensitivity of the film samples on the working temperature for 1% of LPG
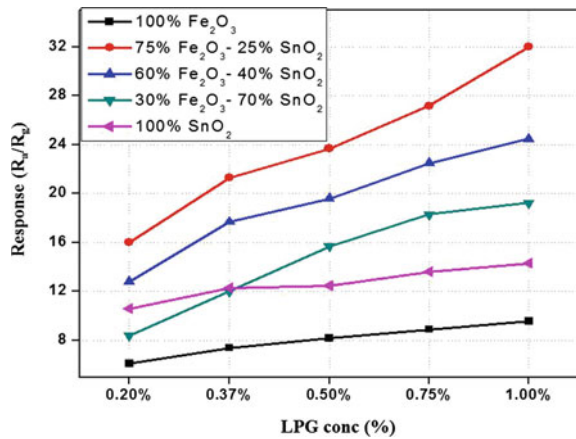

Fig. 5 Dependence of the film sample sensitivity on LPG concentration at 370 °C

LPG is nearly linear. These results are favorable for practical application because the working temperature of about 370 °C is not very high (low energy consumption) and the dependence of sensitivity on linear concentration makes it easy for processing display results in electronic circuits.

3.3 Fabrication of a LPG—Leak Detection Device Based on a Sensor Made from the Composites of α-Fe_2O_3 Nanorods/SnO_2 Nanorods

Principle circuits of the device. After researching and calculating the necessary components, a LPG—leak detection device was designed based on Proteus
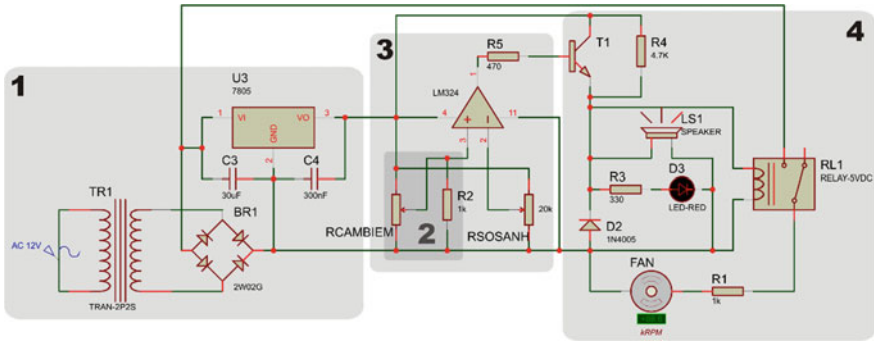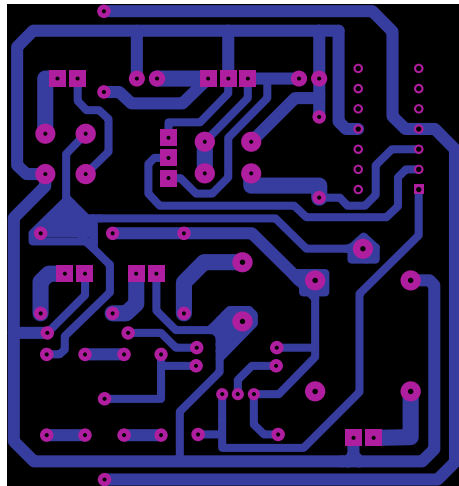
Fig. 6 Principle circuit diagram of the device

Fig. 7 Upper-layer printed
circuit diagram

software. The design of the device consists of 4 basic blocks as follows: power unit
(1); sensor unit (2); comparison block (3); alarm and peripheral connecting devices
unit (4). The principle diagram of the warning device is shown in Fig. 6.

Printed circuits of the device. After studying the principle diagram of the
device, the printed circuit was designed based on ARES Professional item of the
Proteus 7 Professional software program. The 7805 voltage stabilizer IC is used to
supply a stable voltage to the microheater. The comparative signal circuit is taken
on IC LM 324. The device gives the alarm sound at the same volume as interna-
tional devices (>85 dB at a distance of 3 m). Figures 7 and 8 illustrate the printed
circuit diagram of the LPG-leak detection device.

Fig. 8 Lower-layer printed
circuit diagram
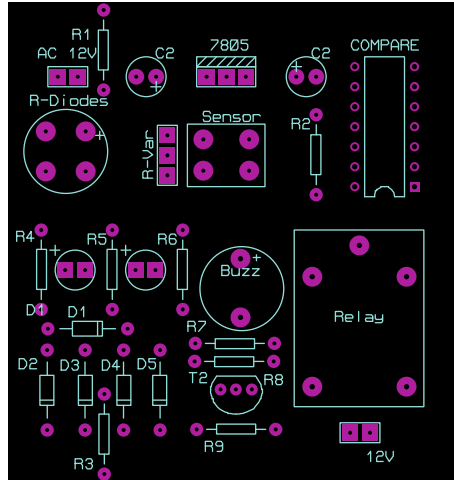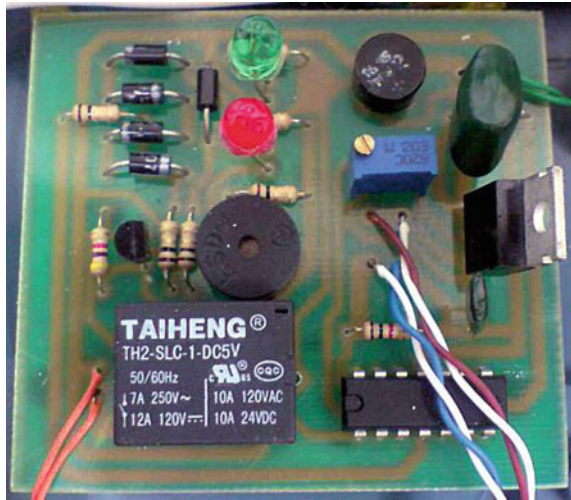

Fig. 9 Component footer
layout

Component footer layout and LPG-leak detection device. The performance of
the device was tested after the complete installation. The technical specifications are
as follows (Figs. 9 and 10; Table 1).

Fig. 10 LPG-leak detection device

Table 1 Technical specifications

Sensor	Electrical power	Gas	Display	Alarm threshold	Size (mm)	Weight (g)
Conductivity	220 V	Gas	Horn, light	15% LEL[a]	170 × 130 × 40	400

[a]LEL: Lower explosive limit

4 Conclusion

SnO_2 nanorods have been successfully synthesized from $SnCl_4$ and NaOH by hydrothermal treatment method. The synthesized rods have the diameter of about 13 nm and the length of about 30 nm. Besides, α-Fe_2O_3/SnO_2 nanocomposites with the dispersion of SnO_2 nanorods into α-Fe_2O_3 nanorods were successfully synthesized by hydrothermal treatment method. Sensors based on α-Fe_2O_3/SnO_2 nanorods composite materials have shown good sensitivity to LPG. The results show that the composite film with Fe:Sn ratio equal to 75:25 has the highest sensitivity with 32 times at 370 °C. Sensors based on α-Fe_2O_3/SnO_2 composites give much higher sensitivity than sensors using pure SnO_2 or Fe_2O_3 materials. In addition, we have also successfully fabricated a LPG-leak detection device based on the sensor made from α-Fe_2O_3/SnO_2 composite with the following specifications: Source: AC-220 V; power consumption: 1.5 W; size: 170 × 130 × 40 mm; weight: 400 g; warning display: sound, light alarm; alarm threshold: 15% LEL.

References

1. Zhang, D.F., Sun, L.D., Xu, G., Yan, C.H.: Size-controllable 1D SnO_2 nanocrystals: synthesis, growth mechanism, and gas sensing properties. Phys. Chem. Chem. Phys. **8**, 4874–4880 (2006)
2. Xi, L.J., Qian, D., Tang, X.C., Chen, C.J.: High surface area SnO2 nanoparticles: synthesis and gas sensing properties. Mater. Chem. Phys. **108**, 232–236 (2008)
3. Wang, Y., Cao, J., Wang, S., Guo, X., Zhang, J., Xia, H., Zhang, S., Wu, S.: Facile synthesis of porous α-Fe_2O_3 nanorods and their application in ethanol sensors. J. Phys. Chem. C **112**, 17804–17808 (2008)
4. Patil, D., Patil, V., Patil, P.: Highly sensitive and selective LPG sensors based on α-Fe2O3 nanorods. Sens. Actuators, B **152**, 299–306 (2011)
5. Peng, L., Xie, T.F., Yang, M., Wang, P., Xu, D., Pang, S., Wang, D.J.: Light induced enhancing gas sensitivity of copper-doped zinc oxide at room temperature. Sens. Actuators, B **131**, 660–664 (2008)
6. Hieu, N.V., Quang, V.V., Hoa, N.D., Kim, D.: Preparing large-scale WO3 nanowirelike structure for high sensitivity NH3 gas sensor through a simple route. Curr. Appl. Phys. **11**, 657–661 (2011)
7. Balázsi, C., Wang, L., Zayim, E.O., Szilágyi, I.M., Sedlacková, K., Pfeifer, J., Tóth, A.L., Gouma, P.I.: Nanosize hexagonal tungsten oxide for gas sensing applications. J. Eur. Ceram. Soc. **28**, 913–917 (2008)
8. Yamazoe, N.: New approaches for improving semiconductor gas sensors. Sensors and Actuators B: Chemical **5**, 1–4 (1991)
9. Yamazoe, N.: Toward innovations of gas sensor technology. Sensors and Actuators B: Chemical **108**, 1–2 (2005)
10. Vuong, D.D., Trung, K.Q., Hung, N.H., Hieu, N.V., Chien, N.D.: Facile preparation of large-scale α-Fe_2O_3 nanorod/SnO_2 nanorod composites and their LPG-sensing properties. J. Alloy. Compd. **599**, 195–201 (2014)
11. Yamazoe, N., Kurokawa, Y., Seiyama, T.: Effects of additives on semiconductor gas sensors. Sensors and Actuators. **4**, 283–289 (1983)
12. Baik, N.S., Sakai, G., Shimanoe, K., Miura, N., Yamazoe, N.: Hydrothermal treatment of tin oxide sol solution for preparation of thin—film sensor with enhanced thermal stability and gas sensitivity. Sensors and Actuators B, **65** (2000)
13. Baik, N.S., Sakai, G., Miura, N., Yamazoe, N.: Hydrothermal treated sol solution tin oxide for thin- film gas sensor. Sensors and Actuators B **63**, 74–79 (2000)

Three-Dimensional Study on Aerodynamic Drag Coefficients of Cable-Stayed Bridge Pylons by Finite Element Method

Van-My Nguyen, Thanh-Hoang Phan, Hoang-Nam Phan, Duc-Anh Nguyen, Minh-Nhat Ha, and Dinh-Tuan Nguyen

1   Introduction

In recent years, many long-span bridges have been constructed as a result of the development of the bridge construction industry. In 1940, the Tacoma Narrows bridge was collapsed in the low-speed wind due to the resonant frequency of the bridge. Since this noteworthy incident, the aerodynamic instability has been paid more attention to long-span bridges, especially cable-supported bridges. A series of studies have been carried out to improve the aerodynamic stability of the bridges subjected to wind loads by either wind tunnel tests or computer models. With the development of computer techniques, the computational approach, known as computational fluid dynamics (CFD), has been used more and more widely because it is possible to numerically simulate wind flows and their effects on structures. Many studies have been carried out to simulate aerodynamic forces of bridge decks using different numerical methods [1–3]. On the other hand, there are a few numbers of studies devoted to the aerodynamic characteristics of a single bridge pylon, especially one of cable-stayed bridges. Ying et al. [4] investigated aerodynamic forces on a bridge pylon by a 3-D CFD model using the Large Eddy Simulation (LES) technique. Their work aims to identify the wind load parameters of the pylon and examine the accuracy of the LES model applied to the bluff-body flows. Recently, Wang et al. [5] studied the characteristics of the flow field in the vicinity of the bridge pylon that effects the vehicle control stability by both experimental and numerical methods. Their numerical model is based on the FLUENT software, where the steady Reynolds-averaged Navier-Stokes (RANS) simulation method is applied and the discretization finite volume method is used to

V.-M. Nguyen (✉) · H.-N. Phan · D.-A. Nguyen · M.-N. Ha · D.-T. Nguyen
University of Danang, University of Science and Technology, Da Nang, Vietnam
e-mail: nvmy@dut.udn.vn

T.-H. Phan
School of Mechanical Engineering, Pusan National University, Busan, South Korea

solve the flow field. The above works emphasize the importance of the turbulence model in CFD simulations, which plays a significant role in achieving realistic predictions of flow characteristics.

Based on the above discussions, the present work mainly aims at simulating the flow field around cable-stayed bridge pylons with different shapes and identifying their aerodynamic drag coefficient, which is based on a 3D finite element wind flow model. The model is first validated with the experimental data available in the literature and the selection of the optimal turbulent model for the wind flow around a bridge pylon is also investigated. The numerical analyses are then carried out on three different pylons of cable-stayed bridges in Vietnam. The analysis results in terms of drag coefficients and surface pressures acting on the pylons are obtained and discussed in detail.

2 Basic Background

In fluid dynamics, the Navier-Stokes equations govern the flow velocity and pressure of the fluid flow, expressed by Eq. (1) in convective form, where ρ, $\frac{D}{Dt}$, p, $\mathbf{u}$, μ, $\mathbf{I}$, ζ, and $\mathbf{g}$ are fluid density, material derivative, pressure, flow velocity, dynamic viscosity, identity tensor, second viscosity, and acceleration gravity, respectively.

$$\rho \frac{D\mathbf{u}}{Dt} = -\nabla p + \nabla \cdot \left\{ \mu \left(\nabla \mathbf{u} + (\nabla \mathbf{u})^T - \frac{2}{3}(\nabla \cdot \mathbf{u})\mathbf{I} \right) + \zeta(\nabla \cdot \mathbf{u})\mathbf{I} \right\} + \rho \mathbf{g} \quad (1)$$

The numerical solution of the Navier–Stokes equations for turbulent flow is difficult. Time-averaged equations such as the Reynolds-averaged Navier–Stokes equations (RANS), supplemented with turbulence models, are commonly used in practical CFD applications when modeling turbulent flows. Some models include k-epsilon, k-omega, shear stress transport, BSL Reynolds stress, and SSG Reynolds stress, which add a variety of additional equations to bring closure to the RANS equations.

Since the flow velocity and pressure quantities are obtained as the solution of the Navier-Stokes equations. Aerodynamic force coefficients on an object under the flow can be then obtained, including lift, moment, and drag forces.

The drag coefficient is one of the three coefficient characteristics of aerodynamic stability. The drag coefficient can be calculated from the surface pressure, pressure coefficient, or estimated by Eq. 2. Here, C_d, D, ρ, A, and v are drag coefficient, drag force, fluid density, reference area, and fluid velocity.

$$C_d = \frac{2D}{\rho A v^2} \quad (2)$$

3 Numerical Simulations

In this study, the finite element ANSYS CFX software is used to determine drag coefficients of various objects under the flow field, including simple objects (cube, hemisphere, thin disk, and cylinder) and pylons of three bridges in Vietnam. The first one is an H-shape pylon of Cao Lanh bridge in Dong Thap province. This bridge is 650 m long with a central span of 350 m. The total length of the bridge including the approach viaducts is 2010 m. The second pylon is of Vam Cong bridge and is more likely A-shape. The Vam Cong bridge is also in Dong Thap province and is a cable-stayed bridge with 450 m length of the main span and 840 m total length. The bridge deck is a composite edge girder type with an overall width of 25.8 m. The last examined pylon is an I shape of Tran Thi Ly bridge. This is a cable-stayed bridge in Danang City with a length of 731 m and a width of 35.5 m.

3.1 *Simulation of Flow Around a Simple Object*

At first, the drag coefficient of simple shapes is calculated with the aim to validating the numerical model with respect to the available wind tunnel test in the literature. For this purpose, a 3-D box computational domain is used for simulating the flow through the cube with 1 m of dimension, as shown in Fig. 1. The length, width, and height of the domain are 10 meters, 5 meters, and 5 meters, respectively.

The flow velocity and flow type are defined in the inlet boundary condition. The outlet boundary and the opening condition are specified with zero pressure. Three flow velocities including 0.1 m/s, 10 m/s, and 20 m/s, corresponding to Reynold numbers of 6.62×10^3, 6.62×10^5, and 1.32×10^5, respectively, are chosen for simulations. This leads to a total of 15 cases of simulation.

Fig. 1 The dimension and boundary condition of the flow domain
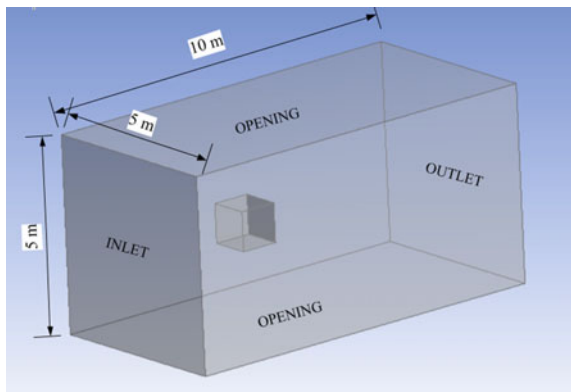
3.2 Simulation of Flow Around a Single Bridge Pylon

In order to evaluate the effect of the pylon shape on the aerodynamic drag coefficient, three different bridge pylons are simulated. The 3D schematics of Cao Lanh, Vam Cong, and Tran Thi Ly pylons are shown in Fig. 2.

The fluid domain is created so that the streamline at the boundary condition is steady. The dimension of the flow domain is shown in Fig. 3, where a 3D box computational domain is formed. The length, width, and height of the domain are 10H, 2H, and 2H, respectively, where H is the total height of pylon. In these cases, the magnitude of wind velocity is considered as a uniform distribution along with the pylon high. In addition, the bottom of the domain is assumed to be flat and there is no rough.

In computational fluid dynamics, mesh quality plays an important rule; the finer of mesh, the more accuracy of the result. However, a finer mesh model commonly consumes more computational effort. The ANSYS manual recommends the mesh quality for users to apply in their model to get enough fine mesh, as shown in Table 1. In this study, to improve the results, the fine mesh is created at the area near the object, and the coast mesh is created at the side of the domain. The fine mesh and the coast mesh are converted so that the mesh has good quality. All models of this study have the same mesh quality, this means that the mesh is excellent or very good if checking by skewness or orthogonal, respectively, as shown in Table 2.
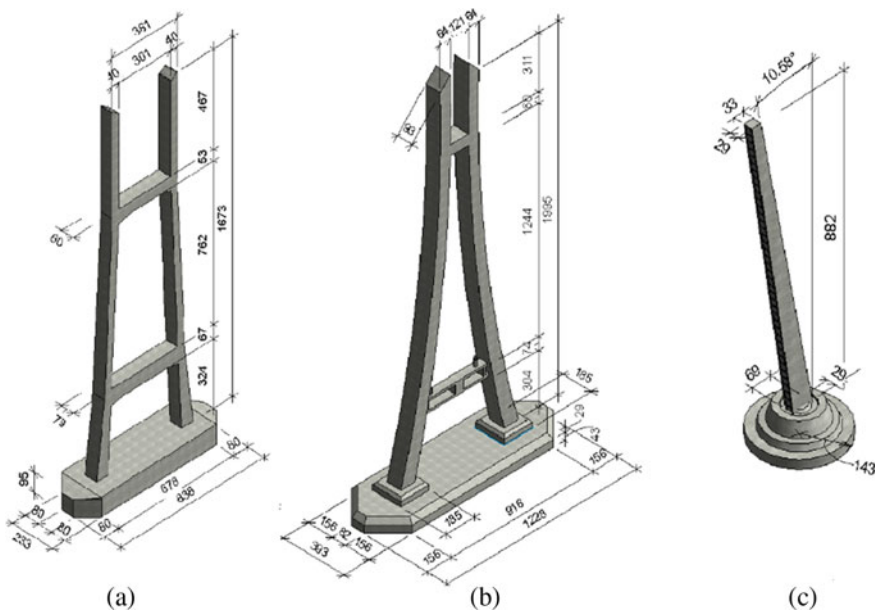

Fig. 2 Model dimensions of the three pylons: **a** Cao Lanh, **b** Vam Cong, and **c** Tran Thi Ly
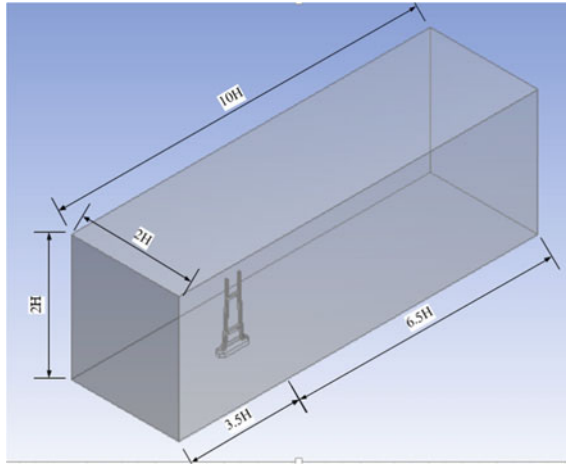
Fig. 3 Computational domain of pylon

Table 1 Mesh qualities

Skewness mesh metrics spectrum (Skw)					
Excellent	Very good	Good	Acceptable	Bad	Unacceptable
0–0.25	0.25–0.50	0.50–0.80	0.80–0.94	0.95–0.97	0.98–1.00
Orthogonal quality mesh metrics spectrum (Oq)					
0–0.001	0.001–0.14	0.15–0.20	0.20–0.69	0.70–0.95	0.95–1.00

Table 2 Mesh information

Bridge	Number of elements	Number of nodes	Mesh quality by Skw/Oq
Cao Lanh	2,320,315	426,759	0.221/0.778
Vam Cong	5,602,497	1,012,391	0.214/0.784
Tran Thi Ly	2,420,474	444,676	0.219/0.779

For more detail, the mesh size at boundary conditions as a bottom side, top side, inlet, and outlet is 0.05 m and the mesh size of the pylon is 0.02 m, as shown in Fig. 4.

4 Numerical Results

4.1 Drag Coefficients of Simple Shapes

Drag coefficients of five simple shapes are obtained from 15 CFD simulations, as shown in Table 3. Here, Cube 0 is denoted for the cube when the angle of wind
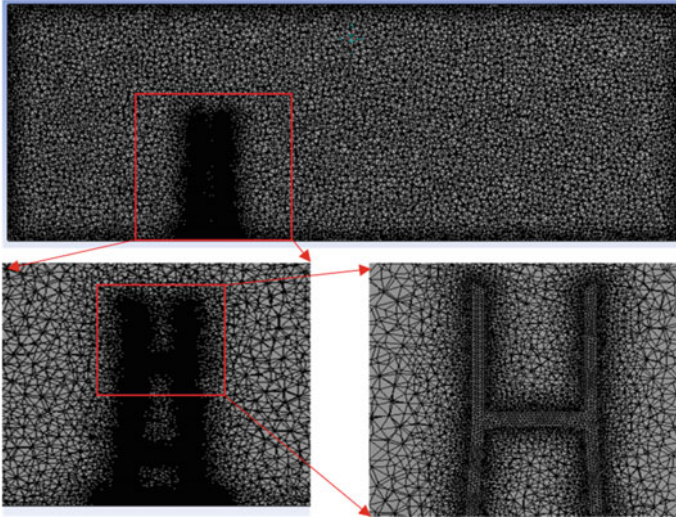
Fig. 4 Mesh distribution near the pylon region of Cao Lanh bridge

flow and the plane perpendicular to the front of the cube is 0 degrees and 45 degrees for Cube 45. Hemisphere, thin disk, and cylinder are also chosen to calculate the drag coefficient. A good agreement in comparison with the theory [6] method is obtained except for the third case of cube 0 that has an error larger than 5% (8.095%). The remaining cases have errors lower than 5%. The results of the simple objects demonstrate the capacity of the present model to determine the drag coefficient on an object under the flow field.

4.2   On the Influence of Turbulence Models

The next simulation is carried out with the Cao Lanh bridge pylon with different turbulence models, in order to find the best suitable model for the analysis of the flow characteristic. Five turbulent flow models including k-epsilon, k-omega, shear stress transport, BSL Reynolds Stress, and SSG Reynolds Stress are used. The results in terms of the drag coefficient are compared with one obtained from the tunnel test [7]. The comparative study shows that the k-omega and the shear stress transport model exhibit a good agreement with the tunnel test data. The same observation is also found in Rezaeiha et al. [8] (Table 4).

Table 3 Drag coefficient of the simple shape
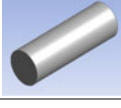
Name	Shape	Reynold number	Drag coefficient	Theory	Error (%)
Cube 0		6.62E+03	1.017	1.05	3.143
		6.62E+05	1.052		0.190
		1.32E+06	0.965		8.095
Cube 45		6.62E+03	0.800	0.80	0.000
		6.62E+05	0.804		0.500
		1.32E+06	0.805		0.625
Hemisphere		6.62E+03	1.189	1.17	1.624
		6.62E+05	1.204		2.906
		1.32E+06	1.207		3.162
Thin disk		6.62E+03	1.087	1.10	1.182
		6.62E+05	1.085		1.364
		1.32E+06	1.086		1.273
Cylinder		6.62E+03	0.859	0.82	4.756
		6.62E+05	0.837		2.073
		1.32E+06	0.829		1.098

Table 4 Drag coefficients of Cao Lanh pylon calculating from five turbulence models [7]

Model	Velocity (m/s)	Drag force (N)	Area (m^2)	C_d from simulation	C_d from experiment
k-Omega	14.4	21.023	0.140	1.223	1.22
k-epsilon	14.4	20.534	0.140	1.195	
SST	14.4	21.028	0.140	1.224	
BLS	14.4	19.067	0.140	1.068	
SSG	14.4	18.350	0.140	1.110	

4.3 On the Influence of Pylon Shapes

The three pylons of Cao Lanh, Vam Cong, and Tran Thi Ly bridges are finally simulated to investigate the pylon shape effect on the aerodynamic drag coefficient. The domain flow is created so that the streamline at boundary condition is steady. The k-omega model, demonstrating the most suitable model for the case study, is used. The results in terms of the drag coefficient for the three pylons are shown in Tables 5 and 6.

As seen from Table 5, the Tran Thi Ly bridge pylon shows the highest value of the drag coefficient, i.e. 1.344 while that of Cao Lanh bridge is 1.233 and the lowest one is of Vam Cong bridge. The drag coefficient is one of three coefficients that

Table 5 Drag coefficients of three pylons

Bridge	Velocity (m/s)	Drag force (N)	Area (m^2)	C_d
Cao Lanh	14.4	21.023	0.140	1.223
Vam Cong	14.4	17.799	0.141	1.029
Tran Thi Ly	14.4	9.287	0.056	1.344

Table 6 Pylon characteristics

Characteristics	Cao Lanh	Vam Cong	Tran Thi Ly
The angle between wind flow and windbreak plane	Almost perpendicular	Slope	Perpendicular
The flatness of pylon section	No hole	No hole	1 hole

characterize the aerodynamic stability of bridges. Therefore, from the analysis results, it can be observed that the Vam Cong bridge pylon exhibits high performance in terms of aerodynamic stability among three examined pylons.

The pressure distribution on the surface of the pylons is also investigated. In Fig. 5, the surface pressure value of the Vam Cong pylon is lowest, so it is reasonable when the lowest drag coefficient of this pylon is observed before. The difference with the angle between the wind flow and the windbreak plane and the flatness of the pylon section are also the significant factors leading to different drag coefficients. In the case of Tran Thi Ly bridge, the wind flow and the windbreak plane are perpendiculars, this results in a maximum surface pressure acting on the pylon surface. Hence, the drag coefficient is the largest. On the other hand, those values of Vam Cong and Cao Lanh pylons are smaller due to a smaller attached angle (less perpendicular).
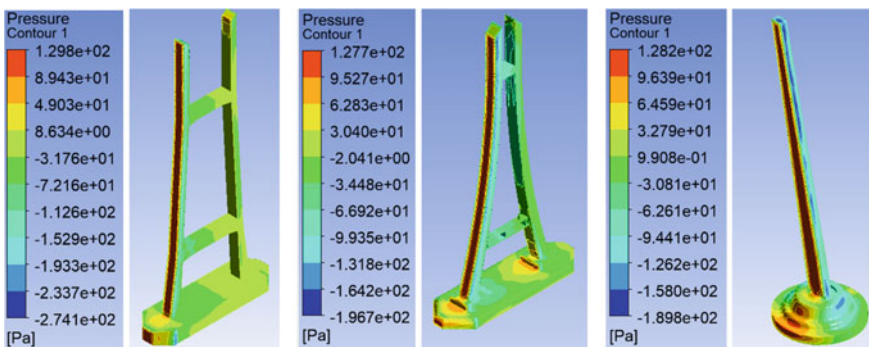

Fig. 5 Surface pressure at pylons, Cao Lanh bridge (left side), Vam Cong bridge (center), and Tran Thi Ly bridge (right side)
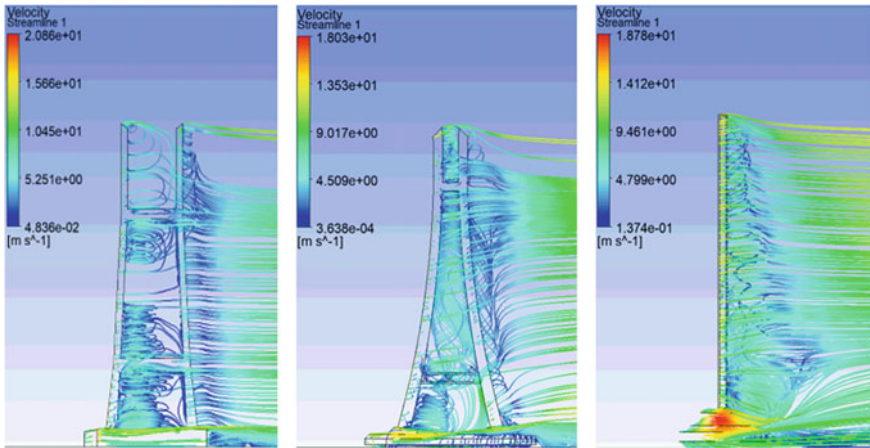
Fig. 6 The vortex flow behind three pylons, Cao Lanh bridge (left side), Vam Cong bridge (center), and Tran Thi Ly bridge (right side)

In addition, the flatness of the pylon section is also an important factor affecting the pressure distribution and the drag coefficient. Tran Thi Ly bridge has a hole on its side (irregular pylon section); this leads to an increase in the pressure distribution.

The downwind of the pylon is the wake galloping region and it affects the flutter and galloping stability of the bridge [9, 10]. Figure 6 shows the direction and magnitude of the vortex flow behind three pylons. It can be seen that, for the same initial velocity, the vortex flow behind the pylon of three bridges are different. The magnitude of vortex flows is in turn about 5.2 m/s, 4.5 m/s, and 4.8 m/s, and its flow directions are also distinctive. In Cao Lanh bridge, the vortex tends to flow in horizontal, so the magnitude is large, it can be explained by the large distance between two columns of the pylon so there will be no obstructions in the airflow. In Vam Cong bridge, because the column shape tends to cluster on the top of the pylon, so the vortex flows from the bottom to the top of the pylon. Both these cases have less turbulent than the case of Tran Thi Ly pylon. Despite the simple shape of the pylon, the vortex flow is complex when horizontal and vertical flows appear behind pylon with high magnitude. So, galloping phenomena more likely to appear in Tran Thi Ly bridge than two other bridges.

5 Conclusion

This paper presents a numerical model of the flow field around a single cable-stayed bridge pylon. The model is based on the finite element ANSYS CFX software, where the flow domain and the object are modeled using the finite element method.

In order to validate the present numerical model, 15 cases of the wind flow around simple objects are simulated and compared with the available wind tunnel test. A good agreement is observed.

The influence of the turbulence model on the drag coefficient of the bridge pylon also is investigated in the study. As a result, the k-omega and shear stress transport turbulence models are the most suitable.

The aerodynamic stability of the three pylons is then assessed in terms of the pressure distribution and the drag coefficient. It can be observed that those quantities depend on the angle between the wind flow and the windbreak plane and the flatness of the pylon section. In the case of Tran Thi Ly bridge, the flow is perpendicular to the windbreak plane and the pylon has a hole on the side, hence the surface pressure and the corresponding drag coefficient show the higher value as compared with Cao Lanh and Vam Cong bridges.

The galloping phenomenon is finally evaluated through the vortex appearing behind the pylon. This phenomenon is expected to strongly appear in Tran Thi Ly bridge because of the high magnitude and direction of the vortex flow in the wake galloping region of the pylon.

References

1. Larsen, A., Walther, J.H.: Aeroelastic analysis of bridge girder sections based on discrete vortex simulations. J. Wind Eng. Ind. Aerodyn. **67–68**, 253–265 (1997)
2. Vairo, G.: A numerical model for wind loads simulation on long-span bridges. Simul. Model. Pract. Theory **11**(5–6), 315–351 (2003)
3. Lin, H., Liao, H.: Identification of Flutter Derivatives of Bridge Deck Under Multi-Frequency Vibration. Eng. Appl. Comput. Fluid Mech. **5**, 16–25 (2010)
4. Ying, X.Y., Xu, F.Y., Zhang, Z., Tan, Y.G.: Large Eddy Simulation of Aerodynamic Forces on a Bridge Pylon. Adv. Mater. Res. **243–249**, 1578–1582 (2011)
5. Wang, D., Zhang, Y., Sun, M., Chen, A.: Characteristics of the Wind Environment above Bridge Deck near the Pylon Zone and Wind Barrier Arrangement Criteria. Appl. Sci. **10**, 1437 (2020)
6. Hoerner, S.F.: Fluid-dynamic Drag: Theoretical, Experimental and Statistical Information. Hoerner Fluid Dynamics; 2nd edition (1965)
7. Tae, Y.K. et al.: Final report, detailed design (Cao Lanh bridge), Central Mekong delta region connectivity project (2013)
8. Rezaeiha, A., Montazeri, H., Blocken, B.: On the accuracy of turbulence models for CFD simulations of vertical axis wind turbines. Energy **180**, 838–857 (2019)
9. Jung, H.J., Lee, S.W.: The experimental validation of a new energy harvesting system based on the wake galloping phenomenon,. Smart Mater. Struct. **20**(5) (2011)
10. Buljac, A., Kozmar, H., Pospíšil, S., Macháček, M.: Flutter and galloping of cable-supported bridges with porous wind barriers. J. Wind Eng. Ind. Aerodyn. **171**, 304–318 (2017)

On the Representative Volume Element of Dense Granular Assemblies Made of 2D Circular Particles

Trung-Kien Nguyen

1 Introduction

The concept of the representative volume element (RVE) is widely used in various mechanics, geomechanics, civil engineering issues, especially in multi-scale problems [1–5]. By its description, RVE has the following characteristics: It is elementary because it considers a material point of the homogenized equivalent medium; it is representative because it can reproduce macroscopic behavior of material by taking into account the heterogeneous characteristics of its constituents. To properly meet the elementary and representative criteria, the RVE must be neither too large nor too small. Relative to the size of the structure, it is small because it is elementary; however, it is large enough to ensure a representative set of the material's microscopic heterogeneities. It means that $e \ll l \ll L$ where L, l, e are, respectively, the characteristic dimensions of the structure, RVE, and the heterogeneities [5].

A common and important feature of a RVE is that it must contain sufficient information to represent the material's behavior, and it is significantly smaller than the macroscopic problem. Hence, the RVE must be large enough and behave as homogeneously as possible. Previous studies also revealed that the use of periodic boundary conditions (PBC) when considering RVE would make it easier to achieve this purpose by eliminating the undesired effect of other types of boundary conditions [4, 6]. Especially in the context of multi-scale modeling when the behavior of materials is considered at different scales [5]. In that case, RVE is commonly assumed to exist and is of a given size. However, RVE existence is not evident as demonstrated in several publications [7, 8].

T.-K. Nguyen (✉)

Faculty of Building and Industrial Construction, National University of Civil Engineering, 55 Giai Phong Road, Hanoi, Vietnam

e-mail: kiennt3@nuce.edu.vn

To address the questions about the existence of periodic-RVE consisted of 2D circular particles by means of a combined study by discrete element modeling and statistical analysis, the paper is laid out as follows: Sect. 2 describes the RVE sample preparation process and test setup. Section 3 presents numerical results and statistical analysis. The paper ends with some conclusions in Sect. 4.

2 Samples Preparation and Numerical Simulations

2.1 Contact Model

In order to simulate the RVE behavior using discrete element method (DEM), it is necessary to define the grain interaction laws at contact level. The contact laws represent the relationship between contact forces and displacements of grains in contact. DEM formulations are limited to 2D circular grain in the present study.

The normal force f_n is related to the interpenetration δ via a normal stiffness k_n. The interpenetration δ is assumed to be small compared with grain size [9]. To model cohesive-frictional material, a normal cohesive force f_c is introduced. The normal force is calculated as follows:

$$f_n = -k_n \cdot \delta + f_c \tag{1}$$

The approach suggested by Cundall and Strack [10] is used for calculating tangential forces f_t at grain contact. This method requires the definition of tangential stiffness k_t at contact point. The contact tangential force at instant $T + \Delta T$ is defined by:

$$f_t^{T+\Delta T} = f_t^T + \Delta f_t^{\Delta T} \tag{2}$$

In which f_t^T is the tangential force at the instant T; $\Delta f_t^{\Delta T} = -k_t \cdot \Delta u_t$ is the increment of tangential force function of the tangential stiffness k_t and the tangential relative displacement Δu_t.

In this model, the tangential force is bounded by Coulomb's condition with μ which is the coefficient of intergranular friction.

$$|f_t| < \mu \cdot f_n \tag{3}$$

The RVE stress results from interaction forces between grains in contact as follows:

$$\sigma_{ij} = \frac{1}{S} \sum_{(i,j) \in C} \overrightarrow{f}^{i/j} \otimes \overrightarrow{r}^{ij} \tag{4}$$

With $\overrightarrow{f}^{i/j} = (f_n, f_t)$ is the contact forces and $\overrightarrow{r}^{ij}$ is the vector joining the center of two particles (i, j) in contact. S is the surface of RVE.

2.2 Samples Preparation

The present paper uses DEM simulations combined with statistical methods to analyze and evaluate the existence of RVE. For this purpose, a series of granular assembly is prepared with specific numbers of particles. They are initially dense and have the same ratio between the maximum and minimum radii of grains. RVE series are labeled *RVExy*, where *x* indicates the number of particles in the RVE sample (*x* equals to 100, 225, 400, 625), and *y* distinguish between different realizations with the same number of particles (*y* is denoted as a, b, c, d, e). For example, RVE100*a* means that the *RVE* contains *100* grains, realization *a*. A total of 20 RVEs (5 realizations per RVE size) are generated for this study. The RVEs are then subjected to isotropic compression loading with confining stress σ_0.

Examples of RVE at the end of isotropic compression loading (i.e., *RVE at isotropic condition*) are shown in Fig. 1. In these sub-figures, the width of red line connecting the center of two grains in contact is proportional to the normal force. Periodic boundary conditions are used. Microscopic parameters of contact law are given in Table 1.

2.3 Test Setup and Simulations

RVE sample is considered to be subjected to biaxial loading with constant confining pressure $\sigma_2 = \sigma_0$ and constant axial strain rate $\dot{\varepsilon}_1$. The inertial number is related to the imposed strain rate as follows:

$$I = \dot{\varepsilon}_1 \sqrt{\frac{m}{\sigma_0 \cdot \overline{a}^{D-2}}} \tag{5}$$

In Eq. (5), $\sigma_0, D, \overline{a}$ are, respectively, the confining pressure, the dimension of the problem, and the average diameter of the granular assembly. In 2D, $D = 2$ Eq. (5) is reduced to:

$$I = \dot{\varepsilon}_1 \sqrt{\frac{m}{\sigma_0}} \tag{6}$$

Numerical experiences by DEM suggested that the quasi-static regime persists for I value below 10^{-4} [6, 9]. By imposing a sufficiently low value of I, the imposed strain rate $\dot{\varepsilon}_1$ is calculated.
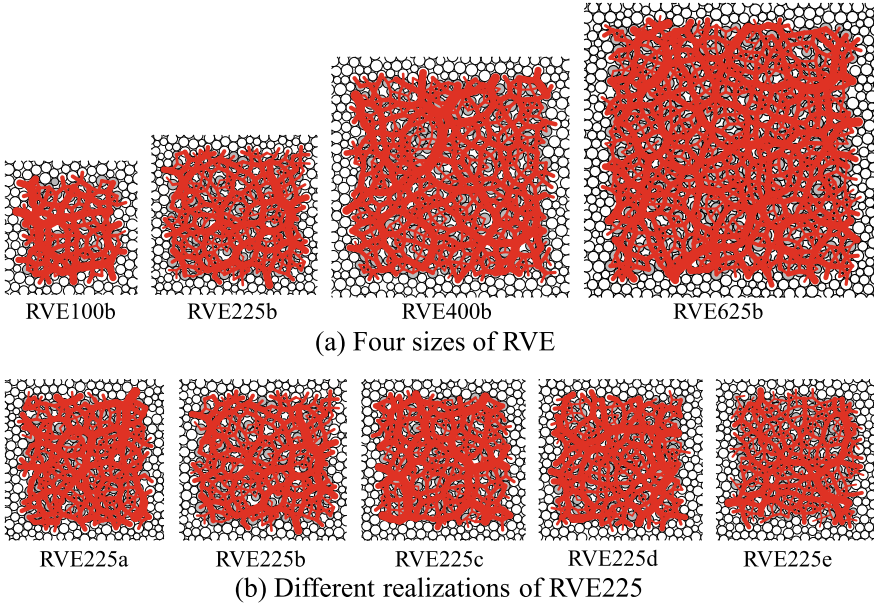
(a) Four sizes of RVE

(b) Different realizations of RVE225

Fig. 1 RVEs contain 2D circular grains

Table 1 Microscopic parameters of contact law

Parameters		Value
$k = k_n/\sigma_0$	Stiffness level	1000
k_n/k_t	Normal/tangential stiffness	1
μ	Intergranular coefficient of friction	0.5
$c = f_c/(\overline{a}\cdot\sigma_0)$	Cohesion level	1

DEM simulations are used to study the RVE behavior. The periodicity of boundary conditions (PBC) is employed. By using PBC, if a particle on the right edge is out of RVE, the picture of that particle will appear on the opposite side of RVE at the same time. Therefore, the number of particles is conserved. The interested readers are invited to reference [6] for more details about PBC in DEM simulations. The principle of the biaxial elementary test and other conditions is displayed in Fig. 2.

Fig. 2 Principle of the elementary test
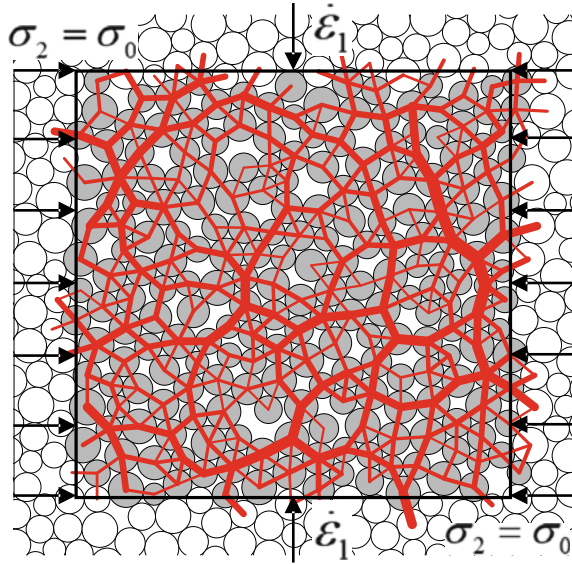
3 Numerical Results and Statistical Analysis

Numerical results for different RVE sizes (RVE100, RVE225, RVE400, and RVE625) are plotted in Fig. 3. These curves represent the relationship between normalized deviatoric stress $q/\sigma_0 = (\sigma_1 - \sigma_2)/\sigma_0$ versus axial strain ε_{11}. Each subfigure reflects the responses of 5 realizations with the same RVE number of grains, and the bold black continuous curve represents the mean value of these 5 realizations. It can be observed that the deviatoric stress and axial strain relationship have the same tendency for all samples: From the isotropic state, the deviatoric stress increases to reach a peak at around 0.7% of axial strain ($\varepsilon_{11} = 0.7\%$), then decreases to the plateau at about 6.5–8% of axial strain ($\varepsilon_{11} = 6.5 - 8\%$). This response is typical, as a result of the inherent strain-softening exhibited by the material. The behavior of RVE can be divided into three phases: elastic linear ($\varepsilon_{11} = 0 - 0.3\%$), hardening ($\varepsilon_{11} = 0.3 - 0.7\%$), and softening phases ($\varepsilon_1 > 0.7\%$). The variation between these realizations is highly considerable for RVE with limited number of particles (RVE100 and RVE225). As expected, by increasing the RVE size (RVE400 and RVE625), this scattering range is getting smaller.

The amount of variation expressed by standard deviation varies considerably according to RVE size (Fig. 4). Particularly in the phase between 0 and 2% of axial strain. The results suggest that the responses vary greatly with RVE of small size (RVE100, RVE225), while this variation is decreased in the case of RVE400 and RVE625.

Before performing the statistical analysis, we recall again the concept of RVE. This concept was commonly introduced to obtain the macroscopic behavior from
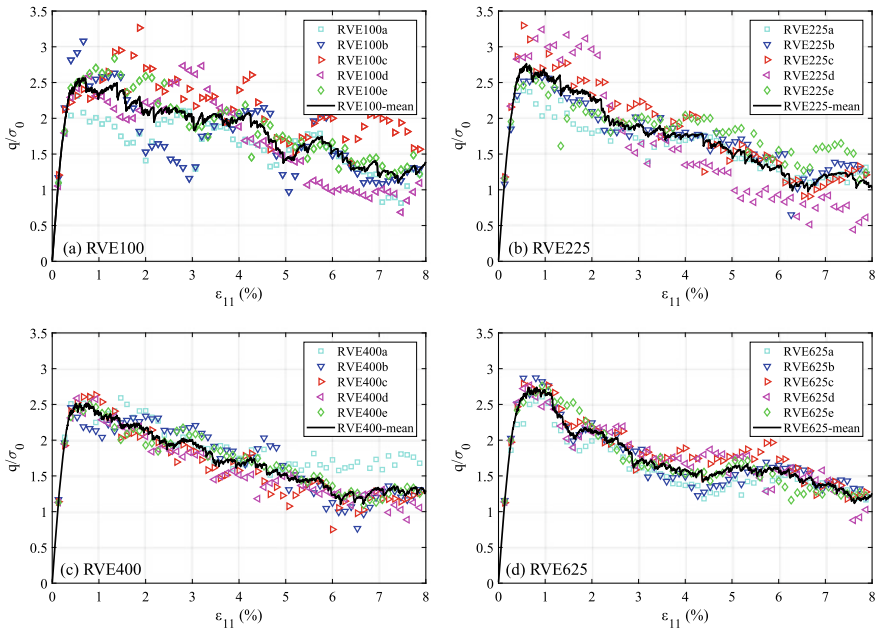
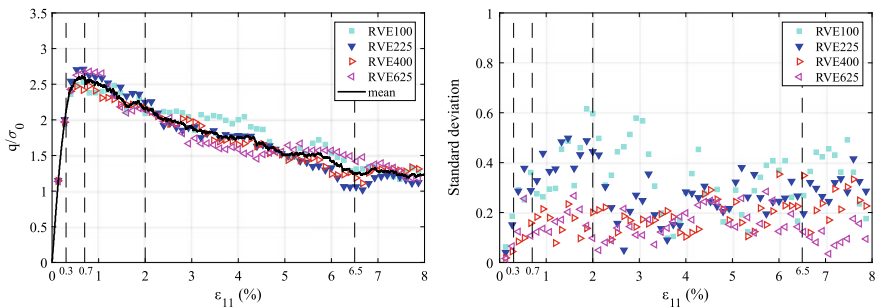**Fig. 3** Stress–strain responses of RVE subjected to biaxial loading

Fig. 4 Mean responses (left) and standard deviation (right)

microscopic constituents of materials [11]. As mentioned by [8], "*RVE is defined as a sufficient volume to be statistically representative of a heterogeneous medium.*" It means that this volume is not only large enough to contain sufficient heterogeneities but also small enough compared to the scale of the problem. Based on these definitions, the paper presents in its next paragraph statistical analysis based on numerical responses obtained by DEM to evaluate the existence and size of RVE. The mean value of the different responses for each RVE size is determined from the data as shown in Fig. 3. The desired precision, which is represented by the error

number defined in Eq. (7), indicates the normalized difference between simulated and mean value.

$$\text{err}\,(\%) \;=\; \frac{|R - \overline{R}|}{\overline{R}} \times 100 \ \text{ with } \ R \;=\; \frac{q}{\sigma_0} \;=\; \frac{\sigma_2 - \sigma_1}{\sigma_0} \tag{7}$$

Desired precision of 95% (err = 5%) and 90% (err = 10%) (horizontal continuous and dashed lines in Fig. 5) is set to verify the existence and RVE size. As clearly shown in this figure, the error number is strongly influenced by RVE size.

If the desired precision is set as 90% (dashed line), in linear elastic regime $(\varepsilon_{11} = 0 - 0.3\%)$, the RVE always exists and the minimum RVE size is 100 particles. However, if 95% of desired precision is set, this limit decreases to $(\varepsilon_{11} = 0 - 0.1\%)$ for RVE100 and $(\varepsilon_{11} = 0 - 0.15\%)$ for RVE225. Moreover, it can be observed that in linear elastic behavior phase $(\varepsilon_{11} = 0 - 0.3\%)$, if the desired precision is 95%, the existence of RVE is verified and RVE size is 400 grains.

In the hardening phase $(\varepsilon_{11} = 0.3 - 0.7\%)$, it can be seen that the accuracy increases with increasing in the RVE size. With RVE less than 400 grains, the error number exceeds 12.5% while if the number of grain greater or equal 400 (i.e., RVE400, RVE625), no value greater than 5% is found. The result confirms the
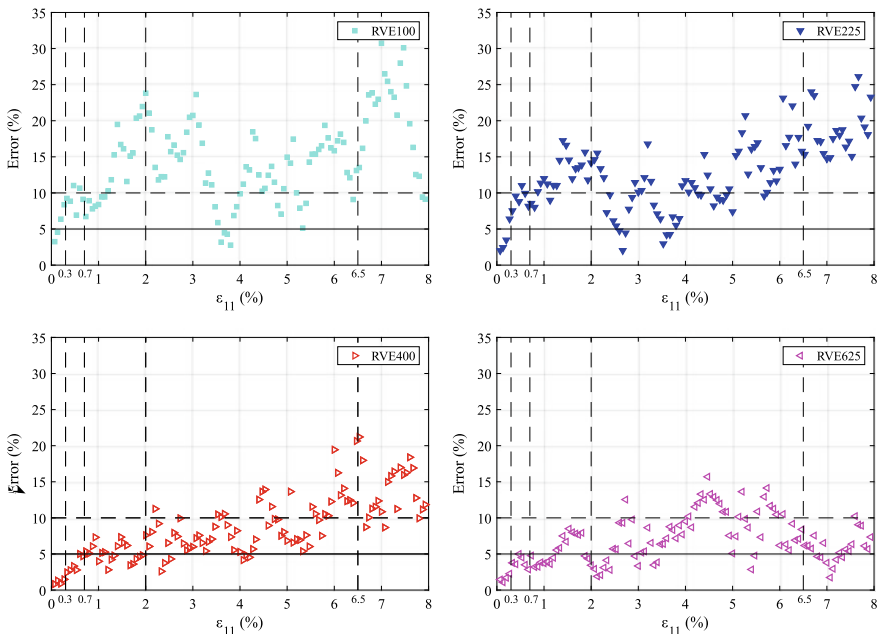

Fig. 5 Statistical analysis

Table 2 RVE existence and size

Regime	Precision 95%		Precision 90%	
	Existence	Size	Existence	Size
Linear Elastic	Yes	400	Yes	100
Hardening	Yes	400	Yes	400
Softening (0.7–2%)	No	–	Yes	400
Softening (>2%)	No	–	No	–

RVE existence and suggests that the RVE size is 400 grains. This observation is in agreement with the visual inspection in Fig. 3.

After reaching the peak at ($\varepsilon_{11} = 0.7\%$), between 0.7 and 2.0% of axial strain, with RVE100 and RVE225, the error number is found above the dashed line (90%), which means that the required precision for RVE existence is not achieved. Whereas the error number for RVE400 and RVE625 is in between 5% and 10% error lines. The RVE existence is not found with the precision of 95% but 90% of precision. It is because of a *sensitive situation*. In fact, the cohesive-frictional materials in softening regime are well known to exhibit strain localization. In that case, the material behavior loses their uniqueness. As observed in the previous study, the bifurcation occurred indeed in this phase and localized band where deformation was concentrated in a narrow band exhibited [4]. From this point of view, between ($\varepsilon_{11} = 0.7 - 2.0\%$), the existence of RVE could be verified or not, which depends on the occurrence of bifurcation. After ($\varepsilon_{11} > 2.0\%$), the values of error number are very scattered, higher than the previous stage, obtain sometimes up to 25% as shown in Fig. 5. The existence of RVE could not be found after 2% of axial strain. These observations are summarized in Table 2.

The non-existence of RVE, especially in the softening regime, has a strong implication in multi-scale FEM×DEM modeling. In that case, when bifurcation occurs, loss of uniqueness solution is observed. This induces mesh dependency when the macro problem is treated by finite element method [4]. To preserve the mesh independence and objectivity of the problem, enhanced models are necessary. Several approaches are possible, particularly in the case of FEMxDEM multi-scale modeling, and second gradient model has been applied and proved to efficiently resolve the mesh dependency. Details of the local second gradient model can be found in [12–14].

4 Conclusions

The combined numerical–statistical investigation on the RVE made of 2D circular particles was presented in the paper. A total of 20 RVEs, with different sizes (100, 225, 400, 625 grains, and 5 realizations for each RVE size), were generated and simulated under biaxial loading with bi-periodic boundary conditions.

The results show that the overall response varies from RVE to RVE, which is statistically homogeneous with the increase of RVE size. Based on numerical results, statistical analysis was conducted in terms of the error number. We found that the existence of RVE could be verified in the phases of linear and hardening response. In these regimes, RVE size is 400 grains with precision desired precision set as 95%. After reaching the peak in stress–strain response, the material behavior changes into softening regime. The findings reveal that there is a transition zone ($\varepsilon_{11} = 0.7 - 2.0\%$) where the existence of RVE could be verified, or not. This latter relates to the loss of the uniqueness of materials behavior and the moment that bifurcation occurs. In the phase of strong softening of the material, the existence of RVE composed of 2D circular grains could not be verified. The non-existence of RVE in the softening regime has a strong implication in the multi-scale FEMxDEM framework. This implies the mesh dependency on finite element macrolevel. To preserve the objectivity of the solution, second gradient model has to be considered.

References

1. Feyel, F., Chaboche, J.L.: FE2 multiscale approach for modelling the elastoviscoplastic behaviour of long fibre SiC/Ti composite materials. Comput. Methods Appl. Mech. Eng. **183** (3–4), 309–330 (2000)
2. Kouznetsova, V., Brekelmans, W.A.M., Baaijens, F.P.T.: An approach to micro-macro modeling of heterogeneous materials. Comput. Mech. **27**(1), 37–48 (2001)
3. Miehe, C., Dettmar, J.: A framework for micro–macro transitions in periodic particle aggregates of granular materials. Comput. Methods Appl. Mech. Eng. **193**(3–5), 225–256 (2004)
4. Nguyen, T.K., Combe, G., Caillerie, D., Desrues, J.: FEM × DEM modelling of cohesive granular materials: numerical homogenisation and multi-scale simulations. Acta Geophys. **62** (5), 1109–1126 (2014)
5. Desrues, J., Argilaga, A., Caillerie, D., Combe, G., Nguyen, T.K., Richefeu, V., Dal Pont, S.: From discrete to continuum modelling of boundary value problems in geomechanics: An integrated FEM-DEM approach. Int. J. Numer. Anal. Meth. Geomech. **43**(5), 919–955 (2019)
6. Radjaï, F., Dubois, F., Dubois, F.: Discrete-element modeling of granular materials. ISTE Ltd. and Wiley (2011)
7. Kanit, T., Forest, S., Galliet, I., Mounoury, V., Jeulin, D.: Determination of the size of the representative volume element for random composites: statistical and numerical approach. Int. J. Solids Struct. **40**(13–14), 3647–3679 (2003)
8. Gitman, I.M., Askes, H., Sluys, L.J.: Representative volume: existence and size determination. Eng. Fract. Mech. **74**(16), 2518–2534 (2007)
9. Nguyen, T.K.: Modelisation multi-echelle des materiaux granulaires frottant-cohesifs (Doctoral dissertation, Université de Grenoble) (2013)
10. Cundall, P.A., Strack, O.D.: A discrete numerical model for granular assemblies. Geotechnique **29**(1), 47–65 (1979)
11. Nguyen, T.K., Pouya, A., Rohmer, J.: Integrating damage zone heterogeneities based on stochastic realizations of fracture networks for fault stability analysis. Int. J. Rock Mech. Min. Sci. **80**, 325–336 (2015)

12. Chambon, R., Caillerie, D., Matsuchima, T.: Plastic continuum with microstructure, local second gradient theories for geomaterials: localization studies. Int. J. Solids Struct. **38**(46–47), 8503–8527 (2001)
13. Nguyen, T.K., Claramunt, A.A., Caillerie, D., Combe, G., Dal Pont, S., Desrues, J., Richefeu, V.: FEM $\times$ DEM: a new efficient multi-scale approach for geotechnical problems with strain localization. In EPJ Web of Conferences (140). EDP Sciences (2017)
14. Desrues, J., Argilaga, A., Dal Pont, S., Combe, G., Caillerie, D., Kien Nguyen, T.: Restoring mesh independency in FEM-DEM multi-scale modelling of strain localization using second gradient regularization. In International Workshop on Bifurcation and Degradation in Geomaterials (pp. 453–457). Springer (2017)

Investigate the Energy Absorption Capacity of EPS with Different Thicknesses in the Motorcycle Helmet

Le Phuoc Son Huynh, Thanh Au Vo, and Tuong Long Nguyen

1 Introduction

According to National Traffic Safety Committee in the first six months of 2020, Vietnam had 6790 traffic accidents in totals, killing 3165 and injuring 1918 people [1]. It is a result of the violation of traffic safety regulations by drivers and passengers. The Global status report on road safety published by WHO in 2018, Vietnam is a country that has the highest percentage of people wearing a helmet among the Indochinese countries (driver and passenger with 81% and 60.4%, respectively) [2].

For people wearing a qualified helmet, their head and brain can protect better from 63 to 88% against serious injury [3]. Standards are used for testing the level of comfort, the safety of helmet was developed in the world for a long time ago such as (ECE 22 (United Nations, 2003b), Snell M95-M2000 (Snell Memorial Foundation, 2003), DOT (Federal Motor Vehicle Standard No 218, 1997), and BS6658 (BSI, 1999). In Vietnam, QCVN-02-2008/BKHCN is a national standard for helmet testing developed to conduct quality and safety checks. Specially shock absorption test is one of the key factors to estimate the protective ability.

Today helmets are produced the diverse design for different needs and purposes, but in general, their principal architecture which consists of two main liners shown in Fig. 1a. The first is ABS shell protecting against falling objects and penetration by sharp objects. The second is EPS liner which undertakes reducing the shock to

L. P. S. Huynh (✉) · T. L. Nguyen
Centre of Computational Mechanics, Department of Engineering Mechanics,
Ho Chi Minh City University of Technology, Ho Chi Minh City, Vietnam

T. A. Vo
Testing Lab, HCMC Technical Center of Standards Metrology and Quality,
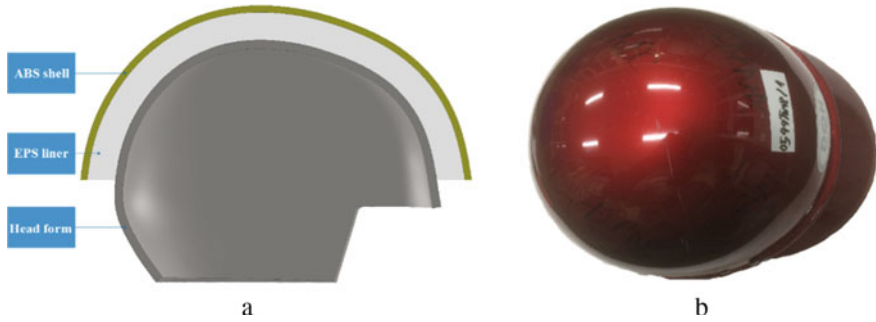Ho Chi Minh City, Vietnam

509

Fig. 1 Helmet structure and head form (**a**) and the half type protective helmet (**b**)

the head by absorbing energy impact. Besides, nowadays helmets are equipped with some accessories to make the user feel comfortable such as chin strap, interior cushion, face shield, etc.

There are many researchers investigating the shock absorption of EPS foam both by experiment and by simulation. Typical of them include the study of Wensu Chen [4] for the static and dynamic characteristics via compressive and tensile experimental tests to evaluate the energy absorption of two EPS foams at different strain rates. Another study observes the performance of this material of Michael F. Ashby, which was written in Materials Selection in Mechanical Design book [5]. It concluded that EPS foam is better optimization of energy absorption, cost, and volume than some other materials.

In Vietnam until the end of 2018, there are six centers of quality evaluation approved to evaluate helmet by the government:

- Quality Assurance and Testing Center 1—QUATEST 1
- Quality Assurance and Testing Center 2—QUATEST 2
- Quality Assurance and Testing Center 3—QUATEST 3
- Ho Chi Minh City Technology Center for Standard, Measurement and Quality—SEMQ
- CanTho Technical Center of Standards Metrology and Quality
- Lang Son Department for Standards, Metrology and Quality.

With the support of SMEQ center, this paper conducted the quality evaluation of helmets in shock absorption tests in order to get the peak acceleration. In parallel with the test helmet, the cylindrical cores of EPS foam liner in helmets were extracted to determine their density and stress-strain curve which are used as foam material parameters in FEA model. The goal of this study is to compare the result of FEA model and practical test to figure out the best model which is developed to investigate the behavior of the helmet changed the various thickness of EPS layer.

2 Experiment

Two same helmets are selected to conduct the experiment whose diagram is shown in Fig. 2. In the up row of this diagram, the EPS liner is dissociated in a helmet for the weight density measurement as well as the determination of the material properties of EPS liner. Another helmet is tested shock absorption following the bottom row of the diagram at SMEQ center to find out the impact acceleration to compare with the FEM simulation result expressed in Sect. 3.

2.1 Determination of EPS Material Properties

Five cylindrical cores in EPS liner are extracted at positions where the helmet tends to be impact tested. They are located and numbered as Fig. 3a which four points are from 1 to 4 within the test range separating from each other at least one-fifth of maximum perimeter of the helmet and another one is in the front or rear point of the foam liner. The height and the diameter of the cores depend on the extracting position, which has the diameter range from 20 to 25 mm and 10 to 12 mm height of the cylinder.

Each EPS core is weighted by 8028-series scale with 0.001-gram resolution and the maximum weight is 50 grams (Fig. 3b). Its thickness and diameter are determined via Thickness Gauge WMT and Mitutoyo 530-312 (shown in Fig. 3c–d) having their minimum reading with 0.01 mm and 0.02 mm, respectively. Every sample is measured 3 times and found the average value so that the volume of cores is calculated by these values. The core density is respectively 93.5 kg/m^3 determined following British standard BS EN ISO 845.

According to the research from Shannon G. Kroeker [6] indicating the affection of the age of EPS material in helmets on its properties, 63 cores, whose density varied from 58 to 100 kg/m^3, are extracted to find a stress-strain curve at a strain rate of 195 s^{-1}. These data are measured of the relation between it and the density of EPS by using Thin-plate method (the result shown in Fig. 4a with $R^2 = 0.9864$). By finding out the density of EPS used in the helmet, the paper interpolates the stress-strain curve at a density of 93.5 kg/m^3. This curve is shown in Fig. 4b with a maximum stress of 7.26 MPa at 0.9 strain. From this curve, the elastic modulus is
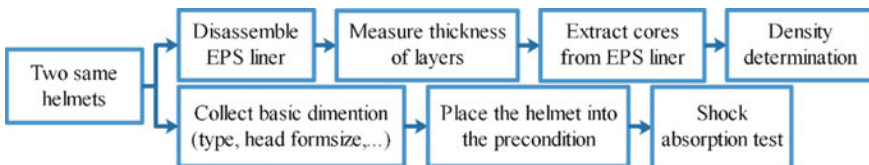

Fig. 2 Experiment diagram with density determination (up) and shock absorption test (bottom)
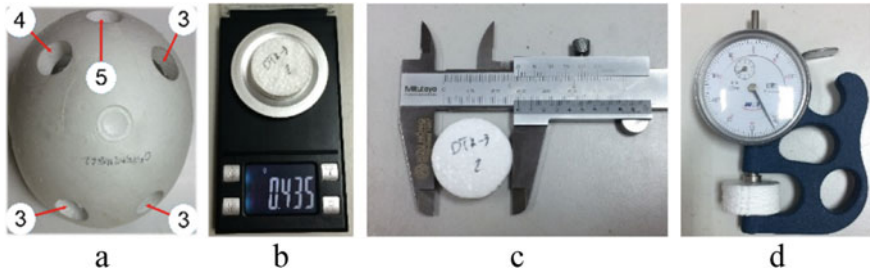
Fig. 3 EPS liner of the helmet with the numbered locations to extract (**a**) and instruments: weight scale (**b**), thickness (**c**) and diameter meter (**d**) used for measuring the size of cores
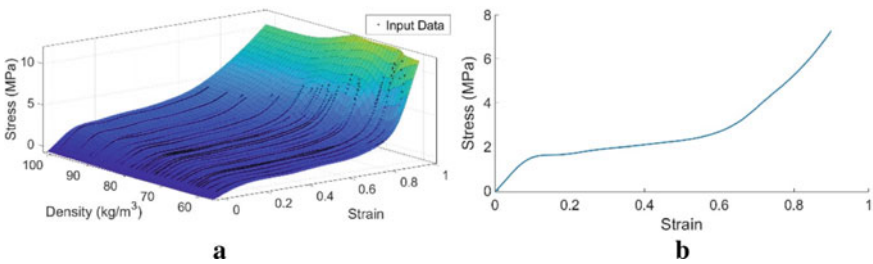

Fig. 4 Regression surface from the experimental stress-strain with various densities (**a**) and Stress-Strain of EPS at a density of 93.5 kg/m^3 interpolated from the regression surface (**b**)

obtained equally 22.29 MPa. At this point, the determination of the properties of EPS liner in the paper has been completed, next another helmet is needed to undergo an impact test at SMEQ center to find out the acceleration value presented above.

2.2 Shock Absorption Test

The helmet tested (shown in Fig. 1b) is a half-type protective helmet. Following the procedure before testing, it is the sample preparation including 2 steps. Firstly, the head form size and the weight of the helmet are determined respectively 570 mm and 0.51 kg. Secondly, although according to QCVN 2:2008/BKHCN, a helmet needs to be undergone at least one of two pre-conditions for 4–6 h either in high temperature (at 50 °C) or immersed in water (at 25 °C), the paper does not carry out prior these preconditions. Because of the most radical preservation of material consistent with the samples in the research of Shannon G. Kroeker [6], the helmet is placed under the condition of 20–25 °C at for 4 h and tested at an ordinary temperature within 2 min after taking out it from the preconditioning apparatus.

After finishing the precondition, it is brought out and worn on the head form of the helmet impact test machine. The information of the helmet is defined in IP-Machine Software on PC which controls the test process. The head form wearing the helmet is guided drop from a height of 1830 mm onto a fixed flat steel anvil, an accelerometer into the head form records to determine the shock absorption. The test is carried out at 3 other-remain positions, resulting in that the average peak acceleration is 344.5 g (g is gravitational acceleration on the earth) at a dropping velocity of 5.58 m/s and the acceleration signal is indicated in Fig. 9. The reports of the tests show that the helmet does not meet the requirement of QCVN-2008 standard because the allowable maximum acceleration must be 300 g or less. The total information of this step is used to build the FEA model in LS-DYNA to simulate the impact process presented in the next section.

3 Simulation

In this section, Fig. 5 shows the steps of this section, a 3D impact test model, which is created from the outer surface of 3D scanned head form, is imported into LS-DYNA to mesh and rebuild a virtual drop test helmet as closely as the practical circumstances at SMEQ. This model is modified and optimize so that its peak acceleration of simulation result obtains the deviation from a real value less than or equally 5%. Only after this requirement is met, the speed normalization process following TCVN 5756:2017 at 5.8 m/s before impact is applied in order to simulate other FEA models based on this model but with different EPS thicknesses and their consequences are discussed at the end of this section.

3.1 Modeling

In the beginning, a 3D head form model, shown in Fig. 6b is built by scanning the practical head form size 570 mm at SMEQ center (Fig. 6a) and put it into
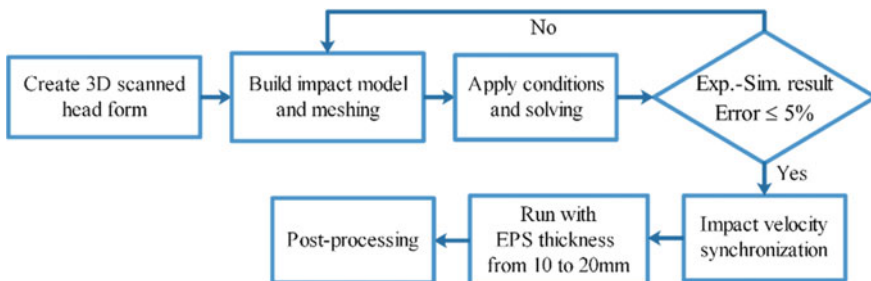

Fig. 5 Simulation diagram

Fig. 6 The practical head form (**a**), 3D scan model in Solidworks (**b**) a cross-section view of the wear of helmet on the head form (**c**) and a fully assembled model with a flat anvil (**d**)

Solidworks to create a simple geometric model including head form including EPS liner and ABS shell. Base on the outside surface of the head form, the EPS layer is constructed by using Offset Surface with a distance equal to the thickness of this layer (11 mm) and this step is repeated to create the ABS layer (4 mm). The middle section view in Fig. 6c showed visually the layers and, moreover, it is the head form layer in which the volume is declined to 72.5% of its original value. This is because, after meshing, it is model as a rigid body and instead of the use of many elements, it is replaced with mass elements (an element type in LS-DYNA) to reduce the solving time.

In the next step, the head form worn the helmet is set up, as closely as possible, when testing at SMEQ center. Here, the collision point if on the axis line of the anvil, the front plane of the head form is 30 degrees off the front plane of the fixed anvil. Similarly, the angle between the right plane of the head form and the one plane of the anvil is 30 degrees (the result shown in Fig. 6d). After completing this constructional model, it is imported to LS-DYNA in order to mesh and run.

The head form has meshed with an element thickness equal to the layer thickness (5 mm) and the edge length not less than 5 mm. This is also done with the anvil, but the element edge length is 20 mm, and both are model as a rigid body. By using sweep method, the EPS is divided into ten layers of equal height and the ABS is two layers. The edge lengths of these elements are related to the distance from the center of impact, for a 50 mm radius around the center of impact, these lengths would be 2 mm and 5 mm in the outer region. Figure 7a shows the section at the

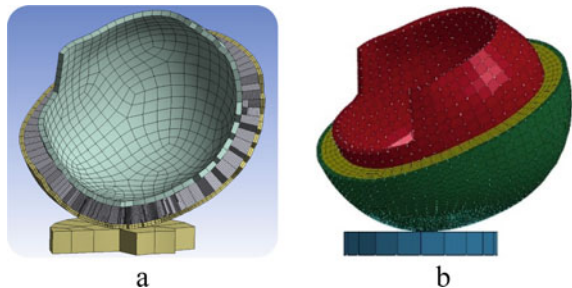**Fig. 7** Section view of meshed (**a**) and full FEA model (**b**)

Table 1 Information of parts in simulation model

Part	Density (kg/m³)	Young's modulus (GPa)	Poisson's ratio	Weight (kg)	Number of elements
Head form	2700	69	0.33	4.7	711
Anvil	7850	207	0.3	–	33
ABS shell	1030	1.7	0.35	0.63	6282
EPS liner	93.5	22.29	0	0.07	5256

impact point of the meshed model and the number of elements of each part is shown in Table 1.

3.2 Finite Element Analysis

Base on the result of the shock absorption test indicated in Sect. 2, the boundary conditions applied to the FEA model are three types: boundary SPC, contact, and mass element. The Head form and the anvil are used 020-RIGID from the material library of LS-DYNA as well as the research of Tso-Liang Teng [7]. They have some constraints as follows:

- The anvil is steel material and the bottom plane of the anvil is fixed in all directions.
- The head form is an aluminum alloy and fixed all directions except for the Y-axis (the direction of impact). It is defined as the initial velocity of 5.58 m/s equal to the velocity of the practical test. It is also put on mass elements to ensure that the mass of the head form is equal to the real one at SMEQ center (about 4.7 kg).

In addition, because this paper investigates the elastic behavior of ABS shell, the 001-ELASTIC material model is applied to this layer and its specifications are shown in Table 1, which is obtained from previous research [8]. Besides, a shock absorption material model is referenced from Andrej Sˇkrlec's paper [9] used MAT_Low_Density_Foam (MAT57) to study the loading-unloading behavior of EPS. Similarly, Tso-Liang Teng [7] used it in the virtual impact test of helmets based on the EN1078 standards. Furthermore, Gerhard Slik [10] compared between MAT57 and CRUSHABLE_FOAM (MAT63) in Quasi-static and dynamic compression test, resulting in the approximated energy-absorption capacity of two material models. This material type requires a stress-strain curve, which is interpolated in Sect. 2, and some parameters (density, Young's modulus, etc.) also shown in Table 1.

*CONTACT_AUTOMATIC_SURFACE_TO_SURFAFE is used for all contacts of the model, such as anvil—ABS shell, ABS shell—EPS layer, and EPS layer—head form. The static and dynamic coefficients of friction are declared to prevent

slipping during impact, with a value of 0.2, according to N. J. Mills [11] and Tso-Liang Teng [7] also applied this value to the research.

All elements of parts are applied solid element, in more detail, element formulation is 1-point corotational for *MAT_MODIFIED_HONEYCOMB. In parallel, every node of head form and ABS has defined a mass element m_N with its value determined by the ratio of the real and virtual weight (m_P and m_L) to number of nodes N of this part following Eq. (1):

$$m_N = \frac{m_P - m_L}{N} \tag{1}$$

Besides, the gravity acceleration is applied to three motion parts and the termination time in *CONTROL_TERMINATION keyword is 0.01 s with a time interval between outputs is 0.00001 s in *DATABASE_BINARY_D3PLOT. And as a result, Fig. 7b shows the full FEA model with conditions, mass elements, and contacts. Finally, the result of simulation with running time about from 4.5 to 7 h and optimization is indicated in the next subsection below.

3.3 Result

With the support of LS-PrePost-4.3, this paper exports the result of the FEA model, and the max compression state of EPS layer shown in Fig. 8a. The compress strain reaches a value of more than 90% at the center of the impact and gradually decreases away. In more detail, the stress field of ABS shell in Fig. 8b shows that the max stress (up to 91.35 MPa) on the shell tends to move from the center impact point to the edge of the helmet with the shortest distance. This expands that the crack has often appeared in this region.

Continuously, the comparison between the practical test and simulation of acceleration data in Fig. 9 indicates that it is quite similar in shape and their difference is the time when the peak value is reached. From this curve, the deviation of peak acceleration (337.8 g of FEA and 344.5 g of experiment result) is about
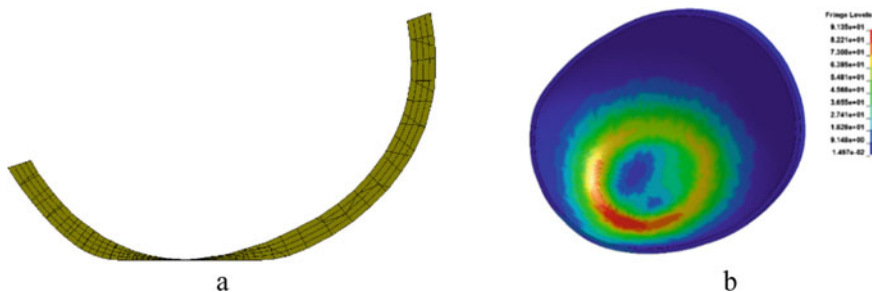

a   b

Fig. 8 The deformation of EPS layer (a) and stress of ABS (b) at maximum compression
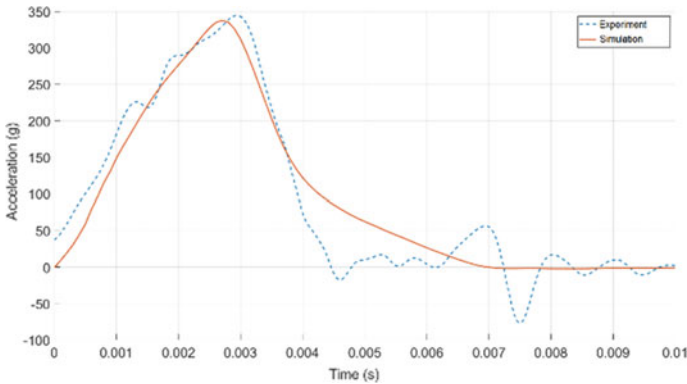
Fig. 9 Acceleration-time as a result of experiment and simulation

1.9% less than 5%, so this model is suitable to develop the EPS layers of various thickness. Before, the model is run at a velocity of 5.8 m/s in order to conduct the speed synchronization according to TCVN 5756:2017. Next step, the results of this process are discussed.

4 Discussion

After solving the models with thicknesses from 10 to 20 mm, Fig. 10 shows their deformation of EPS layer (10–13 mm) in the state of maximum compression. Moreover, Fig. 12 is the maximum strain of these layers, they show that their initial thickness affects the one after compression, in other words, if the initial value is larger, at the time of maximum deformation, the greater the residual value will be. For helmet below 12 mm thick, the strain of this layer is most likely greater than 90%, especially for 10 and 11 mm, the head form mostly collides directly with the ABS shell because the EPS layer at this point has compressed to the maximum (about 98–99%). It also explains that if this layer is compressed more and more, the pressure on the contact surface of the EPS and ABS layers increases.
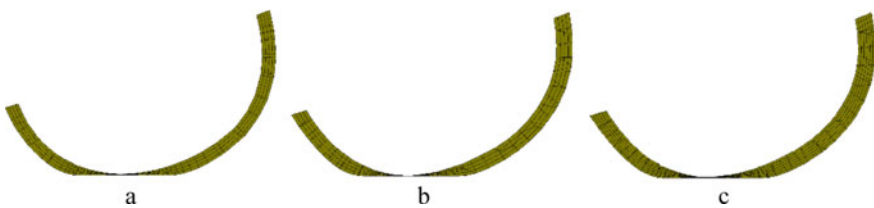

Fig. 10 The deformation of EPS layers at maximum compression with EPS thickness of 10 mm (**a**), 11 mm (**b**), and 12 mm (**c**)
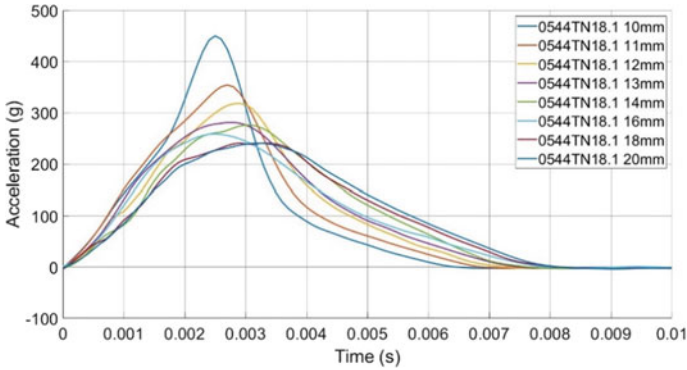
Fig. 11 Acceleration – time result of multi-thickness solving
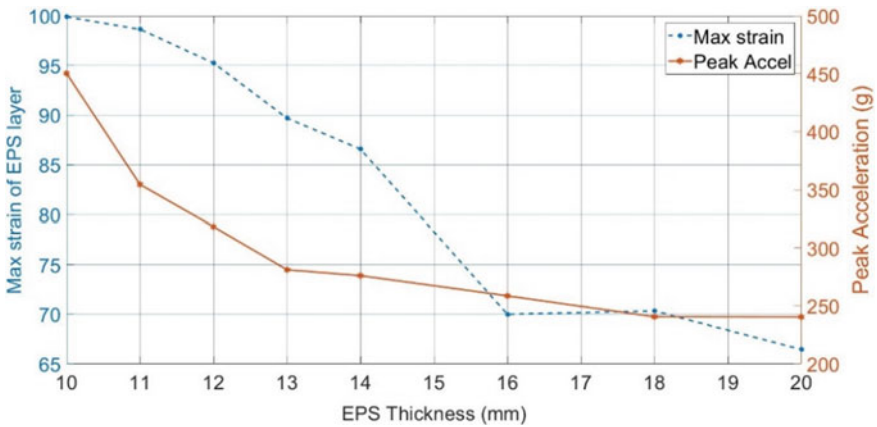
Fig. 12 Maximum strain of EPS layer and peak acceleration following EPS thickness

Similarly, in Fig. 11, it shows that when EPS layer changes from 10 to 12 mm, their acceleration curve steeply rises and they reach peak values greater than 300 g, especially at 10 mm its peak is 450.3 g. The others at the beginning push as well but then they remain quite stable over the top and go down to zero. Figure 12, right side, clearly shows the change in peak acceleration which collapses from 450.3 to 354.4 g at 10 mm and 11 mm. Then it drops linearly (11–14 mm) to 276.2 g and approaches a limit value (240 g at 18–20 mm). Therefore, peak acceleration and max strain tend to approach a certain value as the thickness of the EPS layer increases, especially when the thickness is 16 mm or more. So, whether this changes according to the density of the EPS? If so, for each type of EPS there will be an upper limit value, if the thickness is greater than this value, the redundant part will be unnecessary and wasteful. Conversely, if it is less than a lower limit, the

helmet does not meet standard quality (QCVN-02-2008/BKHCN) because the peak acceleration will exceed the allowable maximum acceleration. In this study, the lower and upper values are about 13 mm and 16 mm, respectively.

References

1. National Traffic Safety Committee Homepage. http://antoangiaothong.gov.vn/. Last accessed 20 July 2020
2. World Health Origination (WHO): Global status report on road safety 2018. Table A6: helmet laws, enforcement and wearing rates by country/area, 346–357 (2016)
3. Thompson, D.C., Rivara, F., Thompson, R.: Helmets for preventing head and facial injuries in bicyclists. In: Cochrane Database of Systematic Reviews, (1999)
4. Wensu, C., Hong, H., Dylan, H., Yanchao, S., Jian, C., Zhong-Xian, L.: Static and dynamic mechanical properties of expanded polystyrene. Mater. Des. **69**, 170–180 (2015)
5. Michael, F.: Ashby: Materials Selection in Mechanical Design, 2nd edn. Butterworth-Heinemann, New York, NY, USA (2011)
6. Shannon, G.K., Stephanie, J.B., Alyssa, L.D., Craig, A.G., Gunter, P.S.: Age Does Not Affect the Material Properties of Expanded Polystyrene Liners in Field-Used Bicycle Helmets. J. Biomech. Eng. **138** (2016)
7. Tso-Liang, T., Cho-Chung, L. and Van-Hai, Ng.: Innovative design of bicycle helmet liners. J. Mater.: Des. Appl. **228**, 341–351 (2013)
8. Khoa, H.B., Vinh, P.Q., Hung, C.P., Thanh. P.M., Son, H.L. P., Quoc, N.T.M., Long, N.T.: Research a numerical method to determine the impact resistance and shock absorption of motorcycle helmet. In: The 12th National Conference on Solid Mechanics, 770–777 (2015)
9. Andrej, Š., Jernej, K., Matija, F.: Parameter identification for a low-density-foam material model using numerical optimisation procedures. Eng. Comput.: Int. J. Comput.-Aided Eng. Softw. **31**, 1532–1549 (2014)
10. Gerhard, S., Gavin, V., Virendra, C.: Material model validation of a high efficient energy absorbing foam. In: 5th LS-DYNA Forum, 3 (2006)
11. Mills, N.J., Gilchrist, A.: Finite-element analysis of bicycle helmet oblique impacts. Int. J. Impact Eng **35**, 1087–1101 (2008)

Dynamic Analysis of the Duct Drilling Structure to the Wave and Wind Loadings Considering the Ballast Water

Duc Minh Nguyen, Duy Khanh Doan, and Trong Phuoc Nguyen

1 Introduction

Tuned liquid damper (TLD) is commonly used to reduce the dynamic response of structures. One of the adopts liquid damping system for construction damping with the proposal to use rectangular tanks containing two types of non-mixed fluids to reduce behavior for structure [1]. Number model for solving Navier–Stokes equations and continuity equations is based on shallow water wave theory to disassemble the main equations and solve them numerically [2]. The effectiveness of TLD, TLCD installed in structures, is presented in previous studies such as Nagasaki Aviation Tower, Yokohama Marine Tower and Shin Yokohama Prince Hotel [3, 4]. TLD with shallow water dissipates energy through the wave motion mechanism at the surface leading to wave breaking. Therefore, the energy dissipation in TLD with deep water levels depends on the mechanism of action of the liquid, the position of the partition, the size and type of the baffle [5]. The equivalent mass damping model includes mass quantities, hardness and resistance from experimental data of rectangular, circular and annular tanks subjected to harmonic stimuli [6]. Studying the damping system consists of many TLDs with frequency adjusted to match the frequency of vibration modes of the structure. Results showed that using more TLD was more efficient than a TLD. Furthermore, this study showed that the working of the TLD is highly dependent on natural stimulation and installation site [7]. Mass damping model is equivalent to stiffness, and nonlinear resistance is calculated based on energy similarity. This model can describe the

D. M. Nguyen
Graduate student, Ho Chi Minh City Open University, Ho Chi Minh City, Vietnam

T. P. Nguyen (✉)
Ho Chi Minh City Open University, Ho Chi Minh City, Vietnam
e-mail: phuoc.nguyen@ou.edu.vn

D. K. Doan
National University of Forestry—Southern Campus, Hanoi, Vietnam

behavior of TLD under stimulation with large amplitude and also when wave breaking occurs [8, 9]. The digital study takes into account the nonlinear behavior of TLD, including the effect of wave dispersion as well as the boundary layer friction at the tank wall, the interaction between the floating objects at the surface and the wave breaking. However, there is a big difference between calculated and experimental results [10].

Research on the behavior of agitated TLD has a large amplitude through experiment, and the results are compared with a numerical model based on the nonlinear shallow water wave equation. The study shows that the frequency of TLD increases as the excitation amplitude increases, and for the best TLD to achieve the best effect, the frequency of the TLD is adjusted to be less than the natural frequency of the structure [11]. Theoretical and experimental study to determine the optimum parameters of TLD installed on top of a structure subjected to vortex agitation (a special case of wind load) is shown in [11]. A series of wind tunnel experiments with different types of TLD is performed; a ratio between the TLD frequency and the structural frequency is proposed [12]. Optimal value of liquid depth, ratio between TLD mass and total structural mass, ratio of tank frequency retention to natural vibration frequency of the structure are determined experimentally. Thereafter, a practical TLD design procedure is recommended to reduce the dynamic response of the structure to earthquakes [13]. Expanding the idea by studying the behavior of TLD with a slope of 300, experimental studies show that the more liquid mass involved in wave motion, the more energy dissipated in this model [14]. The continuity equation and the kinetic equation of the shallow water level liquid using the finite element method are solved [15]. This study simplifies the problem in three dimensions by considering the problem in one direction, which has many advantages in the computation process. TLD's nonlinear behavior attached to elastic structures subjected to vertical harmonic stimulation is also proposed [16]. In [17], it is proposed to use multiple TLDs to reduce the response of multiple modes of oscillation of high-rise structures subjected to earthquakes stimulation. TLDs are tuned for the very first structural vibrations. Theoretical and experimental results show that with the same mass ratio, a system with many TLDs will have better efficiency than a system with only one TLD [17]. The dynamic characteristics of the water in the tank are described by the movement of the open surface, shear force and dissipation energy; the results show that TLD behaves separately in two directions; this allows the use of rectangular tanks to reduce the dynamic response of the structure [18].

In the field of offshore structural structures, up to now, there have been many studies applying liquid damping systems to various types of offshore structures, typically. Fluid shock resistance to control the response of the fixed rig under earthquake load is presented in [19]. Application study of liquid column seismic resistance system for offshore wind turbines is shown in [20, 21]. It is recommended to use the internal baffles to increase the drag ratio of the TLD and to calculate the coefficient of stress loss for the screens and estimate the energy dissipated by the screens and develop a model that describes the steady state of the liquid. That model also shows that a TLD equipped with adjustable baffles can

produce a constant drag ratio over a range of excitation amplitudes [22–24]. The numerical model uses simultaneously the finite volume method for the liquid and the finite element method for the tank and structure; the model has been verified experimentally, a number of models have been proposed previously, and the results show that the model describes almost accurately the behavior of TLD under the effects of agitation and earthquake [25]. Research and proposed S-shaped liquid column reduction system to reduce vibrations for offshore structures [26] and application of fluid for vibration control of tension leg platform vertical stretch anchor rig structure [27] are studied.

The dynamic analysis of duct drilling structure (Tam Dao 05 self-jacking rig) to the wave loading with consideration of the ballast water inside is studied in this paper. The structural system of offshore structure with the ballast water inside is modeled by finite element method in ANSYS Workbench. The analysis results show the effect of ballast water height inside to dynamic response of the structures.

2 Formulation

The model of the Tam Dao 05 self-lifting drilling rig is presented as in Fig. 1 [28]. This is the second jack-up rig that has been designed in detail and manufactured by Vietnam, completed and handed over to Vietsovpetro Vietnam–Russia Joint Venture at the end of 2016. The structural members of the rig's body, base and water in the rig are modeled by ANSYS Workbench software. The interaction of fluid in ballast water and structure is simultaneously analyzed via the acoustic expansion tool (ACT). This model of drilling rig Tam Dao 05 is shown in Fig. 2 [28]. The tools "Mass Point" using in unmodeled structures and weight of the base in ANSYS are applied.

Ballast water in the rig is expressed as follows. A jack-up rig is a combination of two elements of marine engineering and structural engineering. To ensure stability in duration moving as well as loading for truss legs, inside the truss body is always designed to accommodate ballast water with a volume of up to thousands of cubic meters according to the principles and regulations of the engineering industry. Total calculated volume of Tam Dao 05 self-lifting drilling rig is 21,386 tons, including: weight of foot base: 1239 tons; weight of foot part: 3855 tons; body weight: 13,007 tons; transport volume: 3285 tons. The volumes of transport are the volume of goods, equipment and fluids serving the extraction and operation of the rig, including fuel, drinking water and especially ballast water. The weight of the rig itself body and foot weights is considered constant throughout the life of a jack-up rig, the weight portion carried varies depending on cargo conditions, carriage of truss. Carrying volume of 3285 tons is the maximum volume that Tam Dam 05 rig can carry. The effects of ballast water on the vibration of Tam Dao 05 self-lifting rig, and the volume of added ballast water are surveyed with different heights with total ballast water volume less than 3285 tons.

Fig. 1 Model of drilling rig structure in Tam Dao 05
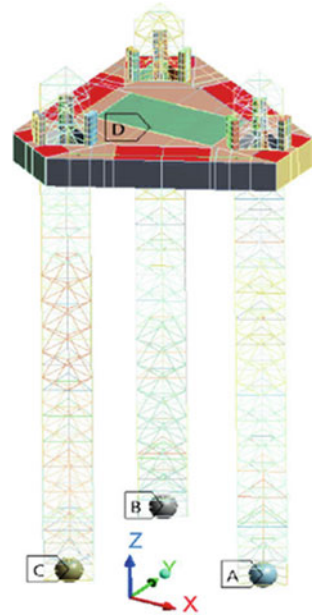
Fig. 2 Division inside the drilling rig Tam Dao 05
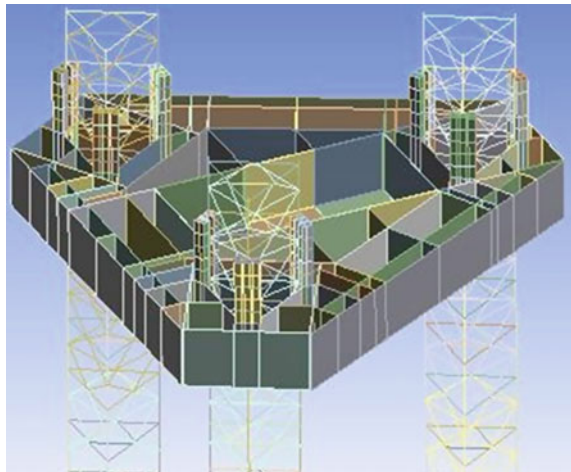
In ANSYS software, the ANSYS Geometry (Design Modeler) module is used to model structures and fluids. The ANSYS acoustic ACT extender enables fluid simulation and consideration of structural interaction in specific vibrational analysis. Fluid elements are simulated by mass elements and corresponding boundary conditions for interaction analysis. In addition, the contact surface between the liquid block and the wall of the tank is also considered the interaction between the structure and the liquid (fluid–structure interaction [FSI]).

Wind load acting on the rig on Tam Dao 05 is applied under two different conditions as operating conditions corresponding to wind speed 36 m/s and storm conditions with wind speed of 51.4 m/s (Petroleum Rig Manufacturing Joint Stock Company, 2016). According to the API rule, the wind load per unit area of the structure projected onto the square with wind direction is calculated as follows:

$$F = 0.473\gamma_{zt}^2 C_s \tag{1}$$

Loading of waves acting on the rig Tam Dao 05 self-lifting is designed to meet the needs of operations in the coastal area of Vietnam. The predetermined wave load acting on the rod element of the truss is determined by Morison's equation as

$$F(t) = 0.5\rho C_D D|v|v + \rho C_M A v \tag{2}$$

ANSYS Design Modeler and ANSYS Meshing are two important modules used to model and mesh the problem, serving for this simulating process. The main modules used to simulate fluid motion inside a self-lifting rig are the ANSYS Geometry (Design Modeler) module and the meshing module for meshing and the modal module for structural and fluid modeling. In addition, to consider the co-working of liquids and structures, this paper uses the acoustic ACT extension toolkit, developed by ANSYS to help users easily simulate fluid vibration problems. The simulation of liquid vibration problem (ballast water) inside the rig body considering sloshing inside the tank is very important in this problem; it has helped the problem of dynamics of self-lifting rig structure system to be solved more accurately in actual working conditions.

3 Numerical Investigations

3.1 Effect of Ballast Water on Rig Frequency

In this section, a ballast water tank as shown in Fig. 3 with a rectangular bottom, width 18.25 m and length 36.58 m, is used to investigate the effect of the ballast water mass on the natural frequency of the structure. The previous results show that the maximum allowable load weight is 3285 tons, based on the size of the water tank and the above maximum carrying volume, to ensure that the allowable load of the rig is not exceeded. Ballast water height in the chamber is investigated to a maximum height of 5 m (equivalent to 3310 tons). Based on the structure of Tam Dao 05 self-lifting drilling rig modeled and verified as mentioned above, simulating ballast water volume at water depths from 0.2 to 5 m in turn at the selected water tank location is approved. The results of analysis of individual oscillation of the Tam Dao 05 self-lifting rig corresponding to the different ballast water heights are presented in Table 1.
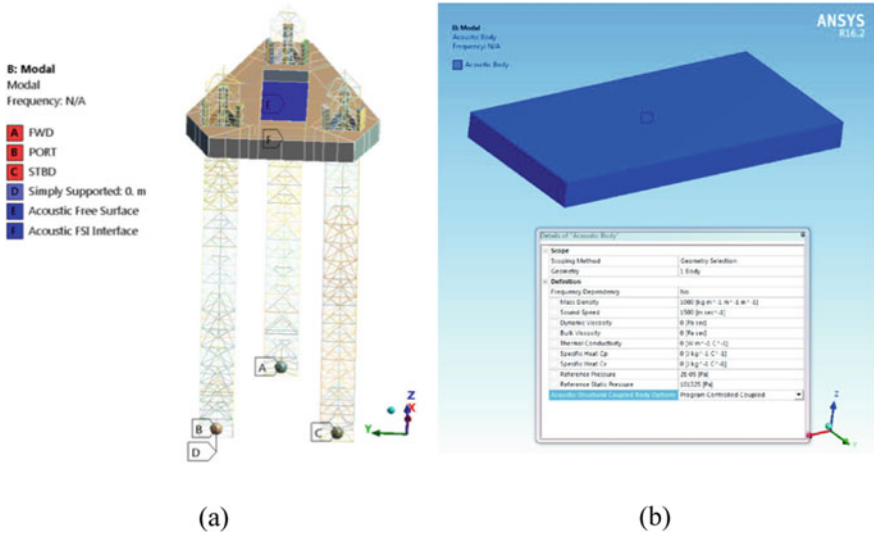
Fig. 3 Location of the water reservoir under consideration

Table 1 First natural period of drilling rig at various water levels

Ballast water depth (m)	T_1 (s)	Ballast water volume (tons)
0	11.07	0
0.2	14.42	132.4
0.4	18.28	264.8
0.6	19.17	397.2
0.8	21.18	529.6
1.0	**23.34**	662.0
1.2	21.43	794.4
1.4	19.08	926.8
1.5	19.27	993.0
1.6	18.62	1059.2
2.0	16.89	1324
2.5	15.39	1655
3.0	14.40	1986
3.5	13.76	2648
4.0	13.35	2317
4.5	13.11	2979
5.0	12.88	3310

The result of the relationship between ballast water volume and individual oscillation cycle of self-lifting drilling rig is shown in Fig. 4. It is found that, in general, when considering fluid vibrations, the rigging cycle of the rig structure is increased compared to the analysis of the oscillation without considering the fluid vibration. The liquid makes the system "softer" overall due to its interactive inertial force. The difference is more if the amount of water decreases. When the water level is at 1 m, the oscillation cycle of the system is 23.34 s maximum (peak), and when the water level rises to 5 m, the cycle continues to decrease closer to the cycle of the system without water (11.07 s).

3.2 Effect of Ballast Water on Gantry Movement Displacement

From the wave and wind load data obtained in the previous section, the dynamic analysis of the structure drilling rig model Tam Dao 05 is carried out by using ANSYS software. At the same time, wind and waves are predetermined to evaluate the effects of changes in ballast water on the overall analysis of self-lifting drilling rig under two operating conditions and extreme maintenance conditions as shown in Fig. 4. The maximum of horizontal displacement corresponding to the cases operating conditions and extreme maintenance conditions is presented as Table 2 and Fig. 5.

Fig. 4 Declaring boundary conditions and loads
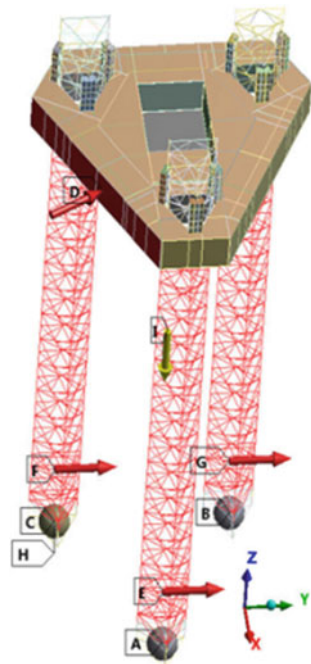
Table 2 Maximum horizontal displacement corresponding to the cases operating conditions and extreme maintenance conditions (mm)

Ballast water depth (m)	Horizontal displacement operating conditions (mm)	Horizontal displacement extreme warranty conditions (mm)
0	324.42	730.82
0.2	295.34	690.12
0.4	278.12	654.31
0.6	222.31	621.36
0.8	200.16	560.17
1.0	**195.72**	**530.76**
1.2	197.23	556.27
1.4	210.41	562.10
1.5	214.02	560.36
1.6	241.32	590.72
1.8	226.17	600.31
2.0	234.78	610.17
2.5	316.03	640.00
3.0	400.38	721.63
3.5	420.79	**740.55**
4.0	**470.41**	719.50
4.5	444.79	695.52
5.0	401.10	634.37

Fig. 5 Maximum horizontal displacement of the rig at 1 m ballast water under operating and extreme conditions (mm)

The results show that the effect of ballast water for the structure is significant when the ballast water level height is between 0.6 m and 2 m under the working conditions of the rig. The response of the rig structure is minimizing at the ballast water level height approximately 1.0 m.

4   Conclusion

The effect of the level of the ballast water inside to the natural frequency has been investigated. In this structure, Tam Dao 05, as water level increasing (0–1.0 m), the natural frequency of the system is decreased and minimize at water level of 1.0 m. However, the natural frequency is increasing with water level ranking from 1.0 to 5.0 m.

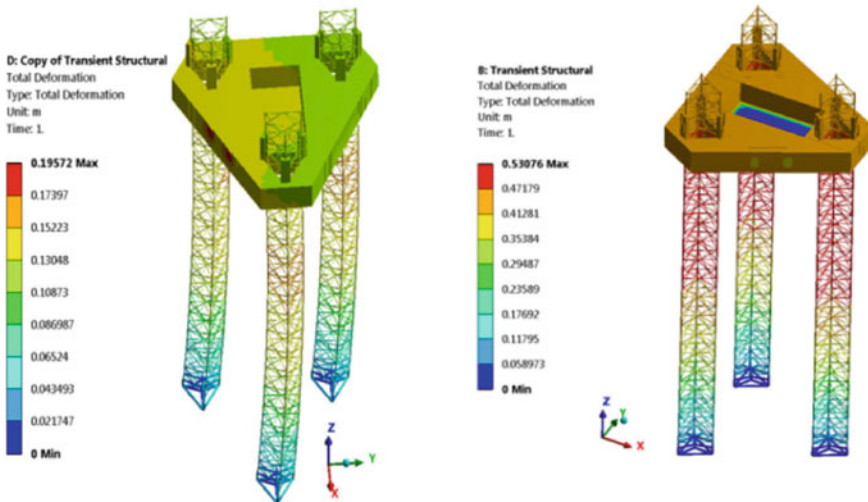Similarly, the effect of the level of the ballast water inside to the dynamic response of the structure to wind and wave loading with operating and extreme conditions has been also carried out. Besides the positive effects in the ranking water level from 0.6 to 1.8 m to reduce dynamic responses, ballast also brings negative effects, increasing the dynamic response to the system, causing negative effects to the structure. In the water level from 3.0 to 4.0 m, the maximum horizontal displacement of the system increases significantly, causing disadvantages for the project.

References

1. Bauer, H.F.: Oscillations of immiscible liquids in a rectangular container: A new damper for excited structures. J. Sound Vib., 117–133 (1984)
2. Shimisu, T., Hayama, S.: Nonlinear response of sloshing based on the shallow water wave theory. The Japan Society of Mechanical Engineers, No. 86-0385A (1986)
3. T.Wakahara et al (1992), "Suppression of Wind-Induced Vibration of a Tall Building using TLD," Journal of Wind Engineering and Industrial Aerodynamics, pp. 1895–1906
4. Nguyen, T.P., et al. Effectiveness of multi tuned liquid dampers with slat screens for reducing dynamic responses of structures. In: IOP Conference Series, 143(1), 012023 (2018)
5. Sun, M. et al.: Modeling of Tuned Liquid Damper (TLD). J. Wind. Eng. Ind. Aerodyn., 1883–1894 (1992)
6. Sun, L.M. et al.: Properties of tuned liquid dampers using a TMD analogy. Earthq. Eng. Struct. Dyn. **24**, 967–976 (1995)
7. Koh, C.G., et al.: Reduction of structural vibrations by multiple-mode liquid dampers. Eng. Struct. **17**, 122–128 (1995)
8. Yu, J.K.: Nonlinear Characteristic of Tuned Liquid Dampers. PhD Thesis, University of Washington (1997)
9. Yu, J.K., et al.: A Nonlinear Numerical Model of the Tuned Liquid Dampers. Earthq. Eng. Struct. Dyn. **28**, 671–686 (1999)
10. Modi, V.J., Seto, M.L.: Suppression of flow-induced oscillations using sloshing liquid dampers: analysis and experiments. J. Wind Eng. Ind. Aerodynamics, 611–625 (1997)

11. Reed, D., et al: Tuned liquid dampers under large amplitude excitation. J. Wind. Eng. Ind. Aerodyn., 923–930 (1998)
12. Chang, C.C., Gu, M.: Suppression of Vortex-Excited Vibration of Tall Buildings using Tuned Liquid Damper. J. Wind. Eng. and Industrial Aerodynamic, 225–237 (1999)
13. Banerji, P., et al.: Tuned liquid dampers for controlling earthquake response of structures. Earthquake Engng Struct. Dyn, 587–602 (2000)
14. Gardarsson, S., et al.: Behavior of Sloped-Bottom Tuned Liquid Dampers. J. Eng. Mech. **127**, 26–271 (2001)
15. Li, S.J., et al.: Shallow rectangular TLD for structural control implementation. Applied Acoustics, 1125–1135 (2002)
16. Ikeda, T.: Nonlinear parametric vibrations of an elastic structure with a rectangular liquid tank. Nonlinear Dyn. **33**, 43–70 (2003)
17. Li, H.N., et al.: Theoretical and Experimental studies on reduction for multi- modal seismic response of high-rise structure by TLD. J. Vib. Control **10**, 1041 (2004)
18. Tait, M.J. et al.: An investigation of tuned liquid dampers equipped with damping screen sunder 2D excitation. Earthquake Eng. and Structural Dyn. **34**, 719–735 (2005)
19. Jin, Q., et al.: Experimental and numerical study on TLDs for controlling earthquake response of jacket offshore platform. Marine Struct. **20**, 238–254 (2007)
20. Colwell, S., Basu, B.: Tuned liquid column dampers in offshore wind turbines for structural control. Eng. Struct. **31**, 358–368 (2009)
21. OceanMetriX Ltd.: Metocean Criteria and Statistics, 8 to 9°N, 107 to 109°E, Offshore South Vietnam (2010)
22. Cassolato, M.R., et al.: Modelling of a tuned liquid damper with inclined damping screens. Struct. Control. Health Monit. **18**, 674–681 (2010)
23. Ikeda, T.: Non-Linear Dynamic Responses of Elastic Two-Story Structures with Partially Filled Liquid Tanks. Inter J. Non-Linear Mech. 263–278 (2010)
24. Love, J.S., Tait, M.J.: Equivalent Mechanical Model for TLD of Complex tank geometry coupled to a 2D structure. Struc. Control. Health. Mon. **21**(1), 43–60 (2013)
25. Malekghasemi, H., et al.: Experimental and numerical investigations of the dynamic interaction of TLD -structure systems. J. Vibration and Control **21**, 32707–32720 (2013)
26. Zeng, X. et al.: A new energy-absorbing device for motion suppression in deep-sea floating platforms. Energies, **8**, 111–132 (2014)
27. Jaksic, V. et al.: Performance of a Single liquid column damper for the control of dynamic responses of a tension leg platform. In: 11th Int. Conf Damage Ass. of Structures (2015)
28. Petroleum Rig Manufacturing Joint Stock Company (PVMS), "Tam Dao 05 Leg Global In-place Analysis" (2016)

Developing an Apparatus to Determine Thermal Diffusivity of Paving Materials

Thao T. T. Tran, Hai H. Nguyen, Phuc Q. Nguyen, Phuong N. Pham, and Viet T. Tran

1 Introduction

Extreme environments significantly influence on performance and properties of pavement structures and materials, especially the change in temperature affects the durability of pavement materials during the operation period, such as inducing cracking, fracture due to high and low temperature, and thermal aging [1]. Pavement temperature is an important parameter used to evaluate workability of pavement materials. In addition, it is also used to determine basic properties of materials for pavement structural design such as modulus of elasticity, temperature markers for checking and forecasting pavement failures (crack, spalling, and sliding) [2–4]. Therefore, determining and forecasting accurately temperature distribution in pavement materials and structures during operation is necessary.

Currently, there are two research lines to predict heat distribution in pavement structure based first on statistical theory from actual pavement temperature monitoring models [5–7] and second on the theory of heat transfer [8–12]. For the first one, it is difficult to fully consider all factors affecting the heat distribution such as material properties due to costly and complicated large-scale investigations. The second research direction can be done in a laboratory to determine necessary parameters in the heat transfer model. Therefore, it will be simpler and less expensive to investigate the effect of material properties on the thermal distribution in pavements. For this research line, thermal diffusivity is a necessary parameter, which characterizes the rate of thermal propagation in materials. This factor combines two material properties: thermal conductivity and heat accumulation [13].

T. T. T. Tran (✉) · H. H. Nguyen · P. N. Pham · V. T. Tran
University of Danang, University of Science and Technology,
54 Nguyen Luong Bang str, Danang City, Vietnam
e-mail: tttthao@dut.udn.vn

P. Q. Nguyen
University of Transport and Communications, 3 Cau Giay str, Hanoi City, Vietnam

Thermal diffusivity is an important parameter to indirectly determine the temperature distribution of pavement materials [14]. However, it is difficult to determine thermal diffusivity in pavement materials. The thermal diffusivity (α) is mainly determined indirectly through other material properties via Eq. (1), such as specific heat capacity (C), thermal conductivity (K), and density (ρ) [15, 16].

$$\alpha = \frac{K}{\rho \cdot C} \tag{1}$$

The coefficient of thermal conductivity of pavement materials finds difficulties to determine due to the composites mainly consisting of blending granular aggregates with heterogeneous grain size [17]. Conventional methods to determine the coefficient of thermal conductivity are just designed for homogeneous materials with small sample sizes [18–20]. Meanwhile, the parameter is greatly affected by the material density, so small testing samples cannot provide an accurate coefficient of thermal conductivity [17]. Hou et al. [21] used hot oil to create an initial source of heat in their experiments of determining thermal conductivity in order to avoid the problems of uneven heat distribution in conventional wires. However, oil may penetrate into the material affecting the specimen. Therefore, it is not recommended for aggregates and composites. Wei Geng et al. [22] used a cylindrical core asphalt concrete sample drilled a small hole in the center, and a rubber holder was used to place thermocouples outside the core. Sand and water were finally filled the inner hole after a cartridge heater was installed. Nevertheless, the authors found non-uniform heat distribution and difficulties to locate the drilled hole in the center of the tested sample. Yan et al. [17] created an apparatus to determine coefficient of thermal conductivity for pavement materials including asphalt concrete and cement-treated aggregates. Their experimental method mitigated the above-mentioned disadvantages as large test specimens were used as well as easily and uniformly heated. However, the study did not mention what method of making 30×30 cm specimens to ensure density of samples suitable for determining other material properties. The ISO 22007-2: 2015 method [23] helps to determine the heat diffusion coefficient for homogeneous materials without the need for specific heat conduction and heat capacity. The heat diffusion coefficient can be determined via the applied heat and the obtained thermal data using the theory of heat transfer. As recommended, this method is only suitable for homogeneous materials such as metals, ceramics, polymers, and insulating materials.

Therefore, this study aims to create a suitable device in order to obtain the thermal diffusivity of paving materials without determining thermal conductivity. Samples can be easily fabricated by current methods such as Marshall and Proctor. Then the device was applied to determine thermal diffusivity of hot mixed asphalt concrete type 19 (19 mm nominal maximum size mixtures) with air void content of 9.7%, bitumen content of 4%, and density of 2.14 (T/m^3).

2 Developing an Experimental Device

2.1 Manufacturing Principles

The device is manufactured to simulate the condition of the 1-D heat equation from the top to the lower positions of a sample. The boundary conditions are as following: (i) the temperature provided at the top of the sample is constant and can vary as long as being higher than the original temperature of the tested sample when measuring, (ii) as for one-way heat transfer, the sample container must be made of insulating material; (iii) no heat exchanges available at the bottom of the tested sample so the underside of a specimen container will also be made of insulating material (Fig. 1).

2.2 Device Description

The device includes major components such as (1) Heater; (2) Specimen container; (3) Data recorder.

(1) Heater

   Heating part has two main units: heating plate and temperature controller.

–   Heating plate is capable of providing heat from the top of a tested sample to the bottom one. It is a copper slab attached rows of wires, so when connected to the source will generate heat. The hot plate is designed to move along the 10 mm
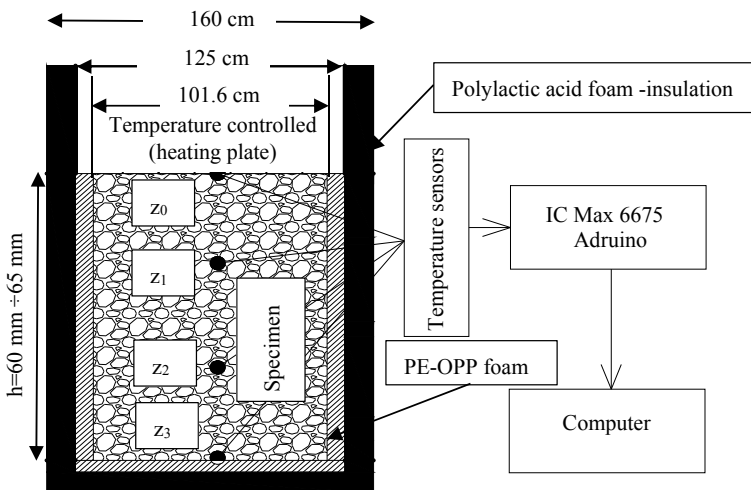

Fig. 1 Design of an experiment device to determine thermal diffusivity

vertical axis to match the height of tested samples. The external image of the hot plate is shown in Fig. 2a.

– Temperature controller is to adjust the heater, to keep the hot plate thermally stable or stabilize the supplied electrical pulse to the hot plate in order to suit different measuring temperatures. An image of temperature controller is shown in Fig. 2b.

(2) Specimen Container

A specimen container is to create an insulating environment in order to limit the amount of heat escaping. A container is made of 3D printed polylactic acid in combination with insulated hollow frame. The container size is suitable for a sample fabricated by Marshall method. For specimen processed according to Proctor mold, after curing, specimens will be cut to obtain the appropriate size. The diameter of the specimen container is 125 mm larger than the one of specimen. The remaining space between a specimen and the insulating cover is inserted with the PE-OPP insulated foam to ensure the test specimen is well insulated. There are drilled holes around the specimen container to attach temperature sensors. The location of the bores to attach the temperature sensor is on the surface of the specimen (z_0), and the others are at lower positions (z_1, z_2, z_3). The specimen container is detailed in Fig. 3.

(3) Data Recorder

A data receiving device includes temperature sensors, a data logger, and a computer. The thermocouple sensor-type K thermocouple (type K) is used. The
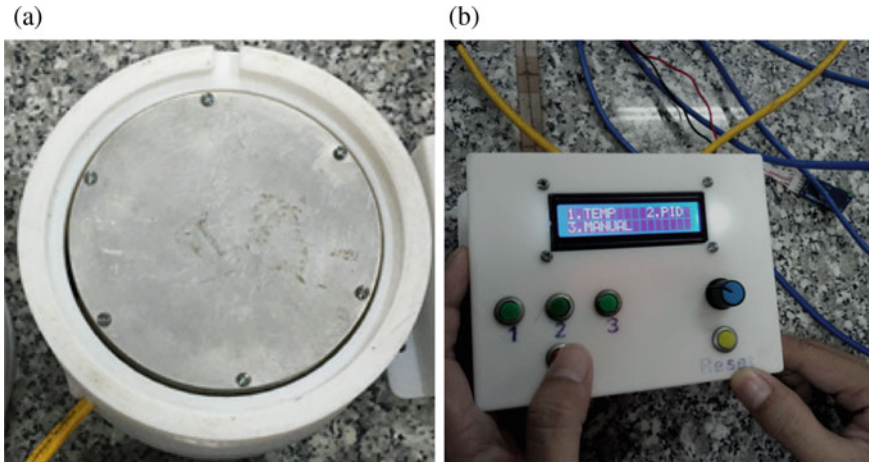
Fig. 2 Heater: **a** Heating plate, **b** Temperature controller
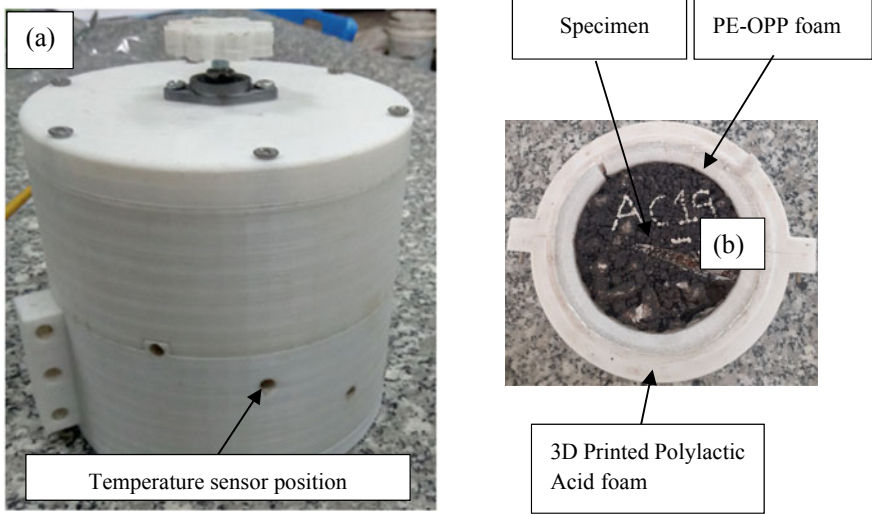
Fig. 3 Specimen container details: **a** specimen container, **b** Cross section of the container
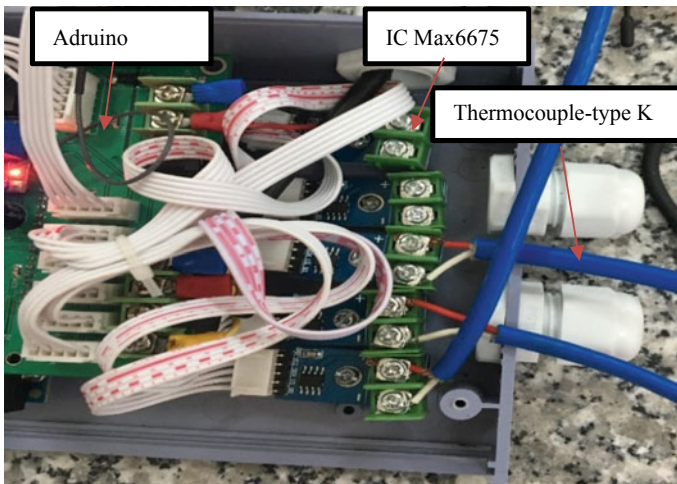
Fig. 4 Data receiving device

thermocouple sensors will be attached to the sample through the positioning position on the sample container. Adruino circuit with the IC Max6675 is used to record temperature over a measuring period, and data was displayed on the computer using a software. Details of the data acquisition are shown in Fig. 4.

2.3 Device Calibration

Calibration Method

Water in Marshall thermostats was set up at different temperature levels. The first step is to place a mercury thermometer and two thermocouples simultaneously under the thermostat in order to measure water temperature, in which the thermocouple-type K was connected to TDS 303 reader and another one connected to the homemade Adruino reader. Then the temperature of the thermostatic tank was set up at 10 different temperature points, namely 20, 25, 30, 35, 40, 45, 50, 55, 60, and 65 °C. The selected temperature range is suitable for the working conditions of pavement materials in Vietnam.

Calibration Results

The results illustrated in Fig. 5 exhibited a negligible difference in measured temperature between the Adruino reader circuit and the mercury thermometer (error is approximately ±0.4 °C). This difference can be explained by reading error and an accuracy of the mercury thermometer of 0.5 °C. The difference in recorded temperature between the Adruino reading circuit and the TDS 303 one is also not significant, only ±0.25 °C. Hence, it is possible to use the homemade Adruino reading circuit to measure the temperature in order to determine thermal diffusivity.

2.4 Test Procedure and Result Processing Method

Temperature measurement was conducted as following steps:

Step 1: First, create and do curing for specimens and then drill specimen to fix temperature sensors. Boreholes are positioned according to their positions on the specimen container. The bore diameter and length are equal to the sensor wire size and to radius of tested samples, respectively.

Fig. 5 Data test result between Arduino device and TDS303 and mercury thermometer
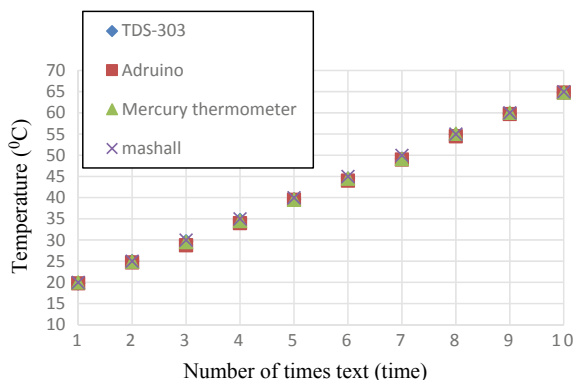
Step 2: Clean the hole, place the tested sample in the specimen container and attach temperature sensors.

Step 3: Set temperature for heating plate, wait for the temperature to stabilize, and mount the heater to the specimen container.

Step 4: Record data through connecting data acquisition to a personal computer.

Step 5: Process test results to determine thermal diffusivity

Apply the 1-D heat equation to determine thermal diffusivity α by solving the inverse problem.

The 1-D heat equation [14]:

$$\frac{\partial T}{\partial t} = \alpha \cdot \frac{\partial^2 T}{\partial Z^2} \tag{2}$$

where z is the distance from specimen surface to the position of the specimen being determined temperature; t is the time of keeping constant temperature on the specimen surface; T temperature specimen at depth z.

Because the sample is heated according to the simulation of the temperature diffusion from the top to different lower positions of the sample, Eq. (2) can be therefore solved to calculate the temperature $T = T(z, t)$ with boundary conditions as well as the initial ones as below:

– Initial conditions:

$$t = 0, \; T(z, t = 0) = T_0 \tag{3}$$

where T_0 is the start-up temperature ($t = 0$) of the specimen at position z.

– On the top of the tested sample:

$$T(z = 0, t = t_1) = T_{suf} = const \, (during \, the \, time \, t) \tag{4}$$

where T_{suf} is the constant temperature at the sample surface ($z = 0$) during the test t.

$$\frac{\partial T(z = h, t)}{\partial T(z = h)} = 0 \tag{5}$$

– At the bottom of tested sample (no heat transfer and exchange):

From the initial conditions (3) and the boundary conditions (4 and 5), Eq. (2) can be solved to obtain temperatures at different depths in the sample after the time t (6):

$$T(z, t) = T_{suf} + (T_0 - T_{suf})k_q; \qquad (6)$$

$$k_\theta = \sum_{n=0}^{\infty} \frac{\sin\frac{2n+1}{2h}\Pi z}{2n+1} \cdot \exp\left[-\alpha \frac{(2n+1)^2 \Pi^2}{4h^2} \cdot t\right] \qquad (7)$$

where h is the height of sample; t is the duration to remain a uniform temperature on the surface of the specimen (at $z = 0$).

Therefore, a 1-D thermal equation can be used to determine the heat diffusion α by solving the inverse problem and using the least squared average method to evaluate the accuracy.

3 Measuring Temperature and Determining Thermal Diffusivity of Asphalt Concrete

3.1 Sample Preparation and Measurements

To apply the manufactured equipment as well as evaluating the measurement method, asphalt concrete was used for these purposes. The asphalt concrete samples were manufactured by Marshall method. The gradation curve of asphalt concrete mixture was taken according to the median curve prescribed in Vietnamese standards [24]. This asphalt concrete specimen meets the prescribed technical specification requirements [24], in which bitumen content is 4% and resulting air void content and density are 9.7% and 2.14 (T/m^3), respectively. Thermal sensors are installed at three positions $z = 1.8$ cm, $z = 3.7$ cm, and $z = 6.05$ cm. Figure 6 shows all the prepared specimens.
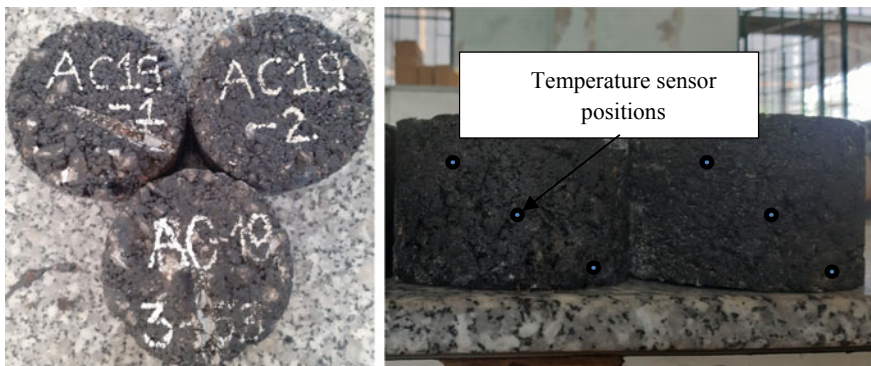

Fig. 6 Prepared specimens

3.2 Results and Discussion

A number of different values α were first assumed based on the previous studies [4, 25], and the temperature at tested positions was then calculated based on Eqs. (6 and 7) depending on the measuring time. The calculated temperature (T_{cal}) was compared with the experimental one (T_{exp}). The least squares method was used to find thermal diffusivity. The obtained least squares versus thermal diffusivity at different test positions is shown in Table 1 and Fig. 7.

It can be seen clearly from Table 1 and Fig. 7 that:

(1) Even maintaining similar surface temperature at the same time, the least squares values are still changing at different positions. This observation can be explained by the fact that the temperature sensors at different locations could be attached to aggregates having different particle sizes and distribution.

(2) The thermal diffusivity (α) corresponding to the least squares (χ^2) at different positions are as follows: $z = 1.8$ cm: $\chi^2 = 1.024$ and $\alpha = 0.00116$ (m^2/h); $z = 3.7$ cm: $\chi^2 = 0.178$ and $\alpha = 0.00164$ (m^2/h); $z = 6.05$ cm: $\chi^2 = 0.870$ and $\alpha = 0.0014$ (m^2/h). The results indicate that position 3.7 cm gives the most accurate α value. Hence, the thermal diffusivity of the investigated of asphalt concrete α is 0.00164 (m^2/h) or 4.556×10^{-7} (m^2/s). The values are consistent with the one from the previous studies [4, 13, 16, 25].

Table 1 Least squares versus thermal diffusivity

Thermal diffusivity, α (m^2/hour)	Least squares $\chi^2 = \frac{1}{n}\sum_{k=0}^{n}\left(T_{exp} - T_{cal}\right)^2$		
	$z = 1.8$ cm	$z = 3.7$ cm	$z = 6.05$ cm
0.0008	0.866	5.760	5.457
0.00092	0.444	3.690	3.249
0.00104	0.246	2.222	1.758
0.00116	0.205	1.217	0.828
0.00128	0.276	0.570	0.334
0.0014	0.428	0.197	0.174
0.00152	0.637	0.035	0.268
0.00164	0.886	0.036	0.553
0.00176	1.163	0.160	0.980
0.00188	1.458	0.379	1.513
0.002	1.764	0.668	2.120
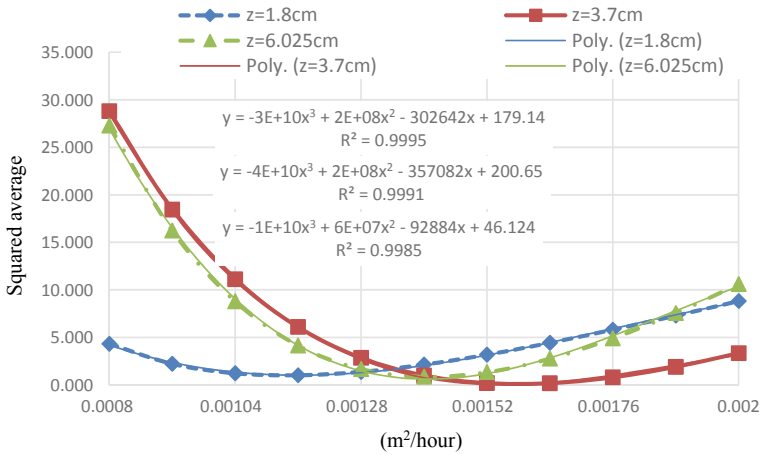
Fig. 7 Thermal diffusivity versus least squares
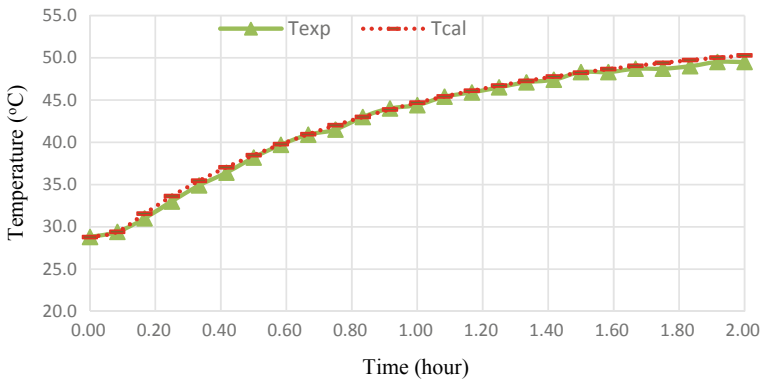
Fig. 8 Recorded temperature versus calculated temperature

Figure 8 shows the correlation between recorded temperature and the calculated one. As can be seen that:

(1) The measured temperature appeared to be lower than the one from calculation. This may be due to temperature loss. Therefore, on-going studies now focus on determining the amount of experimental temperature which compensates for the loss.

(2) There is quite different in temperature between measured and calculated values in the first one-hour testing period. It can be explained by large heat loss at the beginning. After this period, heat transfer in material is stable, the difference is therefore negligible.

4 Conclusions and On-Going Works

The experimental equipment to determine thermal diffusivity for pavement materials has been proposed and verified for asphalt concrete. The obtained results were consistent with the ones from the previous studies, namely the thermal diffusivity α of asphalt concrete type 19 with air void content of 9.7%, bitumen content of 4%, density of 2.14 (T/m^3) is 4.556×10^{-7} (m^2/s). Therefore, it is strongly recommended this device for thermal diffusivity test of pavement materials.

On-going studies are as follows:

(1) Investigating impacts of paving material compositions on thermal diffusivity.
(2) Determining optimal testing time to perform the equipment for different pavement material specimens.

References

1. Hassn, A., Chiarelli, A., Dawson, A., Garcia, A.: Thermal properties of asphalt pavements under dry and wet conditions. Mater. Des. **91**, 432–439 (2016)
2. AASHTO: Pavement Design Guide A Manual of Practice (2008)
3. 211-06, I. standards of V. 22TCN: Pavement structural design. Hanoi (2006)
4. Industry standards of Russia 01, O. 218. 06, Pavement structural design (2001)
5. Hassan, H.F., Al-Nuaimi, A.S., Taha, R., Jafar, T.M.A.: Development of Asphalt Pavement Temperature Models for Oman. J. Eng. Res. [TJER]. **2**, 32 (2005). https://doi.org/10.24200/tjer.vol2iss1pp32-42
6. Ariawan, I.M.A., Subagio, B.S., Setiadji, B.H.: Development of Asphalt Pavement Temperature Model for Tropical Climate Conditions in West Bali Region. Procedia Eng. **125**, 474–480 (2015). https://doi.org/10.1016/j.proeng.2015.11.126
7. Chao, J., Jinxi, Z.: Prediction Model for Asphalt Pavement Temperature in High-Temperature Season in Beijing. Adv. Civ. Eng. (2018). https://doi.org/10.1155/2018/1837952
8. Yavuzturk, C., Ksaibati, K., Chiasson, A.D.: Assessment of temperature fluctuations in asphalt pavements due to thermal environmental conditions using a two-dimensional, transient finite-difference approach. J. Mater. Civ. Eng. **17**, 465–475 (2005). https://doi.org/10.1061/(ASCE)0899-1561(2005)17:4(465)
9. Minhoto, M.J.C., Pais, J.C., Pereira, P.A.A., Picado-Santos, L.G.: Predicting asphalt pavement temperature with a three-dimensional finite element method. Transp. Res. Rec. 96–110 (2005). https://doi.org/10.3141/1919-11
10. Chen, J., Zhang, M., Wang, H., Li, L.: Evaluation of thermal conductivity of asphalt concrete with heterogeneous microstructure. Appl. Therm. Eng. **84**, 368–374 (2015). https://doi.org/10.1016/j.applthermaleng.2015.03.070
11. Athukorallage, B., Dissanayaka, T., Senadheera, S., James, D.: Performance analysis of incorporating phase change materials in asphalt concrete pavements. Constr. Build. Mater. **164**, 419–432 (2018). https://doi.org/10.1016/j.conbuildmat.2017.12.226

12. Basheer Sheeba, J., Krishnan Rohini, A.: Structural and Thermal Analysis of Asphalt Solar Collector Using Finite Element Method. J. Energy. **2014**, 1–9 (2014). https://doi.org/10.1155/2014/602087

13. Tan, S.A., Low, B.H., Fwa, T.F.: Determination of thermal conductivity and diffusivity by transient heating of a thin slab. Build. Environ. **27**, 71–76 (1992). https://doi.org/10.1016/0360-1323(92)90010-M

14. Islam, M.R., Tarefder, R.A.: Determining thermal properties of asphalt concrete using field data and laboratory testing. Constr. Build. Mater. **67**, 297–306 (2014). https://doi.org/10.1016/j.conbuildmat.2014.03.040

15. Nguyen, Q.T., Di Benedetto, H., Sauzéat, C.: Determination of thermal properties of asphalt mixtures as another output from cyclic tension-compression test. Road Mater. Pavement Des. **13**, 85–103 (2012). https://doi.org/10.1080/14680629.2011.644082

16. Hassn, A., Aboufoul, M., Wu, Y., Dawson, A., Garcia, A.: Effect of air voids content on thermal properties of asphalt mixtures. Constr. Build. Mater. **115**, 327–335 (2016). https://doi.org/10.1016/j.conbuildmat.2016.03.106

17. Yan, X., Chen, L., You, Q., Fu, Q.: Experimental analysis of thermal conductivity of semi-rigid base asphalt pavement. Road Mater. Pavement Des. **20**, 1215–1227 (2019). https://doi.org/10.1080/14680629.2018.1431147

18. C177, A.S.: Standard Test Method for Steady-State Heat Flux Measurements and Thermal Transmission Properties by Means of the Guarded-Hot-Plate Apparatus (2004)

19. ASTM-International-C518: Standard Test Method for Steady-State Thermal Transmission Properties by Means of the Heat Flow Meter Apparatus (2015)

20. C1113, A.S.: Standard Test Method for Thermal Conductivity of Refractories by Hot Wire (2019)

21. Hou, T., Huang, S., Hsu, C.: A new approach for determination of the coefficient of thermal expansion of asphalt con-crete. Measurement **85**, 222–231 (2016)

22. Geng, A.P.W.: Measuring the Thermal Properties of Pavement Materials A. P. Wei Geng 1,2 ; and Michael Heitzman, Ph.D., P.E. 31. 109–116 (2016))

23. ISO 22007: INTERNATIONAL STANDARD conductivity and thermal diffusivity —. Int. Stand. ISO 22007-12017(E) (2017)

24. Vietnam Ministry of Transport: TCVN 8819:2011—Specification for Construction of Hot Mix Asphalt Concrete Pavement (2011)

25. Joseph Luca and Donath Mrawira, P.E.: New Measurement of Thermal Properties of Superpave Asphalt Concrete. Mater. Civ. Eng. **17** (2005)

Influences of Ground Motion Frequency on the Seismic Vulnerability of Nonstructural Components

Thanh-Tuan Tran[ID]**, Anh-Tuan Cao, Phu-Cuong Nguyen**[ID]**,
Dookie Kim, and Thi-Mai-Trang Le**

1 Introduction

Nonstructural components (NSCs) as the electrical cabinets are one of the important parts of the nuclear industry; therefore, the seismic response of this equipment should be considered carefully. Evidence from the previous earthquake events has indicated that the damage of the NSCs affected the operant condition of building structures or NPP [1, 2]. Some researchers investigated the behavior of column-base connections of steel structures under earthquake time history loading [3, 4], and the buckling behavior of steel structures [5]. Many works in recent years have been

T.-T. Tran
Institute of Offshore Wind Energy, Kunsan National University,
558 Daehak-ro, Gunsan-si, Jeollabuk-do, Republic of Korea
e-mail: tranthanhtuan@kunsan.ac.kr

T.-T. Tran · T.-M.-T. Le
Faculty of Technology and Technique, Quy Nhon University,
170 An Duong Vuong St, Quy Nhon, Binh Dinh, Vietnam

A.-T. Cao
Department of Civil and Environmental Engineering, Kunsan National University,
558 Daehak-ro, Gunsan-si, Jeollabuk-do, Republic of Korea

P.-C. Nguyen (✉)
Advanced Structural Engineering Laboratory, Faculty of Civil Engineering,
Ho Chi Minh City Open University, 97 Vo van Tan St, Ho Chi Minh City, Vietnam
e-mail: henycuong@gmail.com

D. Kim
Department of Civil and Environmental Engineering, Kongju National University,
1223-24 Cheonan-Daero, Seobuk-gu Cheonan, Chungcheongnam-do, Republic of Korea

T.-M.-T. Le
Department of Ocean Science and Engineering, Kunsan National University,
558 Daehak-Ro, Gunsan-si, Jeollabuk-Ddo, Republic of Korea

conducted to research the seismic performance of this equipment [6, 7]. Furthermore, the electrical cabinet is known as the high-frequency NSC, and its failure is directly affected by dynamic characteristics of ground motions (i.e., frequency content, amplitude, and duration). According to Tran et al. [6], the seismic response of the electrical cabinet can be amplified under the high-frequency ground motions. Based on the frequency contents, which is represented by dominant frequency, the earthquakes can be classified into two groups: ground motion high-frequency (GMHF) and ground motion low-frequency (GMLF) [8].

The present work aims to examine the seismic performance of a cabinet facility due to earthquake frequency contents and compare the seismic behavior of the cabinet facility in terms of structural acceleration. This work is essential for designing nuclear power plants.

2   Numerical Modeling

The 3D simulation of the electrical cabinet, which is described in Fig. 1, is carried out using SAP2000 software. The modeling is constructed based on the prototype provided by Innose Tech Company in Korea. The external dimensions including the width, depth, and height are 800 mm, 800 mm, and 2100 mm, respectively, whereas its weight is about 290 kg. The structure is assembled by the frames and plates, which are assigned SS400 steel. The main specifications of steel material including Young's modulus ($E = 200$ GPa), Poisson's ratio ($v = 0.3$) and density ($\rho = 7850$ kg/m^3). Plate and mainframes are modeled using the shell and beam elements, respectively. The rigid link elements are used to simulate the connection between frames and plates. Furthermore, the boundary condition of the electrical cabinet is assumed to be fixed at eight locations corresponding to the real places of bolts connected to the floor.

3   Selection of Ground Motion

In this research, eighty ground motions from PEER and historical ground motions in Korea are selected to analyze the seismic responses of the cabinet. These data are classified into two categories via the dominant frequency obtained from the response spectra analysis (i.e., GMHF, GMLF), as shown in Fig. 2. As the peak frequency of ground motion in the response spectra is greater than 10 Hz, it is considered as a high-frequency motion. In contrast, it will belong to the low-frequency case. For a better comparison of the structural seismic behavior, the value of PGA 0.5 g is chosen to scale all these recorded time history ground motions.
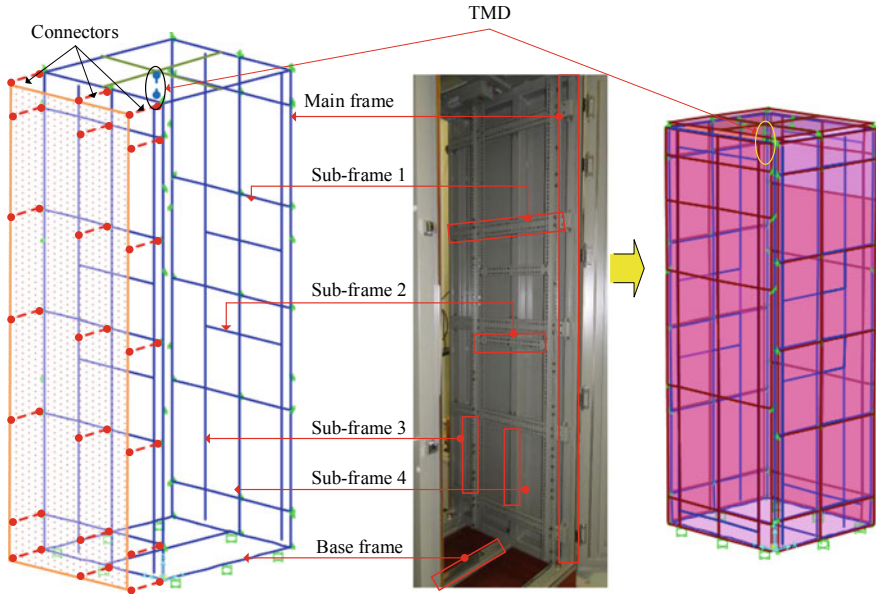
Fig. 1 Numerical modeling of the electrical cabinet

4 Fragility Analysis

The vulnerability of the electrical cabinet can be evaluated through the fragility curves, which is widely applied in many works. Various approaches can be used for the fragility analysis depending on the process applied to obtain the structural response [9]. In this study, the incremental dynamic analysis (IDA) method is applied to estimate the parameter values of the fragility curve.

To carry out the fragility analysis, all of the selected earthquakes are scaled into various intensity levels to ensure that the limitation of structural collapse can be defined [9, 10]. The fragility curves of the cabinet are calculated using a lognormal cumulative distribution function as follows [10].

$$P(F|\text{PFA} = a) = \Phi\left[\frac{\ln\left(\frac{a}{\sigma}\right)}{s}\right] \tag{1}$$

where $P(F|\text{PFA} = a)$ is the probability of failure of the structure at intensive measure PGA = a, σ and s are the mean and the standard deviation of ln PGA, which causes 50% of the collapse. These values are expressed as the following equations.

Fig. 2 Ground motion
selection

(a) GMHF

(b) GMLF
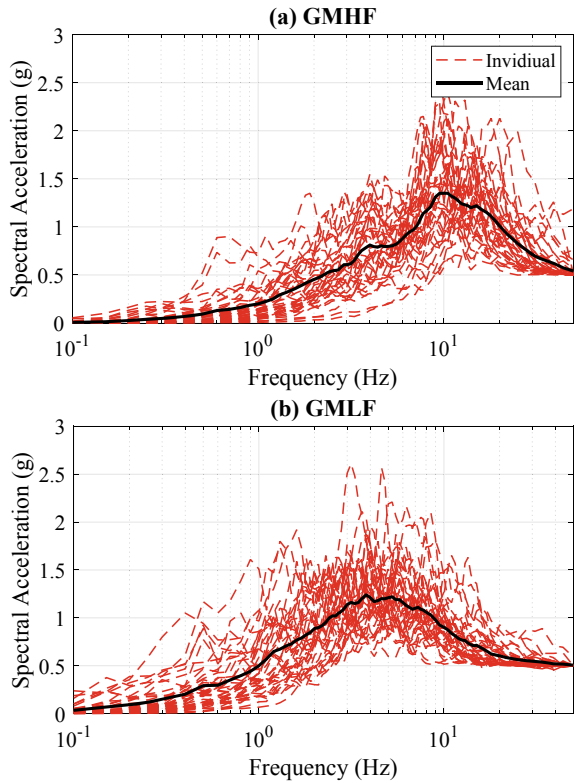
$$\ln \sigma = \frac{1}{n} \sum_{i=i}^{n} \ln \mathrm{PGA}_i \tag{2}$$

$$s = \sqrt{\frac{1}{n-1} \sum_{i=1}^{n} (\ln(\mathrm{PGA}_i/\sigma))^2} \tag{3}$$

For the performance criteria, the U.S. Nuclear Regulatory Commission [11] stated that the acceleration response is the critical engineering demand parameter to apply the fragility analysis. Thus, a maximum top acceleration of 1.8 g is considered as the damage state.

5   Results and Discussions

Figure 3 shows a comparison of the maximum acceleration of the cabinet subjected to two groups of ground motions. The scatter points represent the responses for each earthquake, and horizontal lines illustrate the average values for each group. From this figure, it can be seen that the response of the electrical cabinet in the case of GMLF earthquakes are lower compared to the GMHF group, which is expressed clearly through the mean curves. As a result, the high-frequency ground motions substantially amplify the seismic response of the electrical cabinet. Furthermore, the probability of failure of the electrical cabinet is illustrated in Fig. 4 for both GMHF and GMLF groups of ground motions, 50% of the collapse was found at the acceleration of 0.521–1.699 g for GMHF and GMLF groups, respectively. Consequently, the cabinet subjected to high-frequency earthquakes shows more vulnerability compared to low-frequency motions, this can be explained by the fact that the collapse value of the electrical cabinet for the GMHF group is much smaller than that of the GMLF group (0.512 g < 1.699 g).

Fig. 3 Maximum acceleration response of the nonstructural component
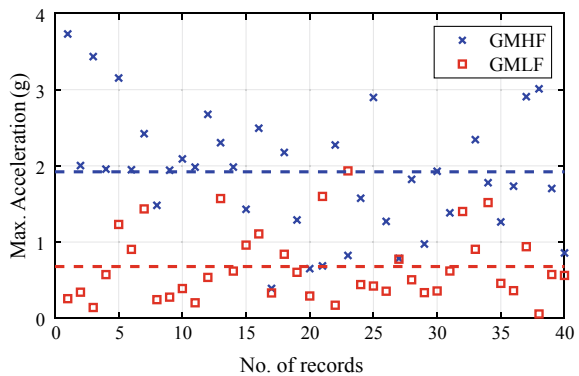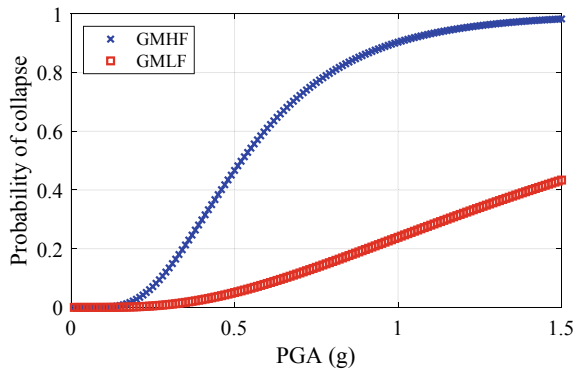

Fig. 4 Fragility curves of the nonstructural component

6   Conclusions

In this study, it can be seen that the probabilistic method plays an important role to quantify the effects of the earthquake frequency on the seismic response of the electrical cabinet in NPP. To make it more understandable, eighty selected ground motions are divided into two sets including high- and low-frequency earthquakes group which are used to examine the differences in its seismic performance. Based on the fragility analysis, the probabilities of failure are compared to assess the influences of earthquake frequency contents.

The obtained results concluded that the frequency content of the earthquake significantly affects the seismic response of the electrical cabinet, which is considered as a high-frequency nonstructural component. The fragility curves indicate that the electrical cabinet subjected to high-frequency motions is more vulnerable, as the consequence of the amplification of the structural responses.

References

1. Singh, M.P., Moreschi, L.M., Suarez, L.E., Matheu, E.E.: Seismic design forces. II: Flexible nonstructural components. J. Struct. Eng., **132**(10), 1533–1542 (2006)
2. Adam, C., Furtmüller, T.: Response of nonstructural components in ductile load-bearing structures subjected to ordinary ground motions. In: Proceedings of the 14th world conference on earthquake engineering, paper (No. 05-01, p. 0327) (2008, January)
3. Nguyen, P.C., Kim, S.E.: Investigating effects of various base restraints on the nonlinear inelastic static and seismic responses of steel frames. Int. J. Non-Linear Mech. **89**(3), 151–167 (2017)
4. Nguyen, P.C., Kim, S.E.: Second-order spread-of-plasticity approach for nonlinear time-history analysis of space semi-rigid steel frames. Finite Elem. Anal. Des. **115**(11), 1–15 (2015)
5. Nguyen, P.C., Kim, S.E.: A new improved fiber plastic hinge method accounting for lateral-torsional buckling of 3D steel frames. Thin-Walled Struct. **127**(6), 666–675 (2018)
6. Tran, T.T., Cao, A.T., Kim, D., Chang, S.: Seismic Vulnerability of Cabinet Facility with Tuned Mass Dampers Subjected to High-and Low-Frequency Earthquakes. Appl. Sci. **10**(14), 4850 (2020)
7. Tran, T.T., Nguyen, P.C., So, G., Kim, D.: Seismic behavior of steel cabinets considering nonlinear connections and site-response effects. Steel Compos. Struct. **36**(1), 17–29 (2020)
8. Nguyen, D.D., Thusa, B., Han, T.S., Lee, T.H.: Identifying significant earthquake intensity measures for evaluating seismic damage and fragility of nuclear power plant structures. Nucl. Eng. Technol. **52**(1), 192–205 (2020)
9. Baker, J.W.: Efficient analytical fragility function fitting using dynamic structural analysis. Earthq. Spectra **31**(1), 579–599 (2015)

10. Cao, A.T., Tran, T.T., Nguyen, T.H.X., Kim, D.: Simplified Approach for Seismic Risk Assessment of Cabinet Facility in Nuclear Power Plants Based on Cumulative Absolute Velocity. Nucl. Technol. **206**(5), 743–757 (2020)
11. Bandyopadhyay, K.K., Hofmayer, C.H., Kassir, M.K., Pepper, S.E.: Seismic fragility of nuclear power plant components: Phase 2, Motor control center, switchboard, panelboard and power supply (No. NUREG/CR–4659-vol. 2). Brookhaven National Lab (1987)

Analysis of Steel Columns Deteriorated Two-Directionally During Seismic Loading

Tran Tuan Nam

1   Introduction

Shake-table is a useful facility to test the seismic behavior of structures. In September 2007, a full-scale four-story steel building was shaken to collapse on the E-Defense, one of the largest worldwide shake-table located in Japan. [1] provided an overview of the project, and [2–4] reported the experimental responses of the building specimen under the increasing shaking levels up to collapse state.

This study additionally compares and details the different progress of column strength deterioration in the structure. During the seismic excitation, axial forces developed in columns are either compression or tension loads, therefore affecting the bending moment capacity. Moreover, the initial movements of the building tended toward a particular direction, however later changed to a significantly rotated direction. This study emphasizes the progress of two-directional deteriorations of those columns during the change of building movement. On the other hand, this paper provides further interpretation of the building response in terms of energy, in which energy input and the dissipation mechanism at the collapse excitation state are evaluated.

2   Collapse Test Summary

2.1   *Full-Scale Steel Building and Input Ground Motion*

A full-scale 4-story steel building (Fig. 1a) was used as the specimen of the collapse test. The total height of the building is 14 m (Fig. 1b). Beams and columns are

T. T. Nam (✉)
Ho Chi Minh City University of Technology (HUTECH), Ho Chi Minh City, Vietnam
e-mail: tt.nam@hutech.edu.vn

(a) Building speciman

(b) Building plan

(c) Post-collapse frame
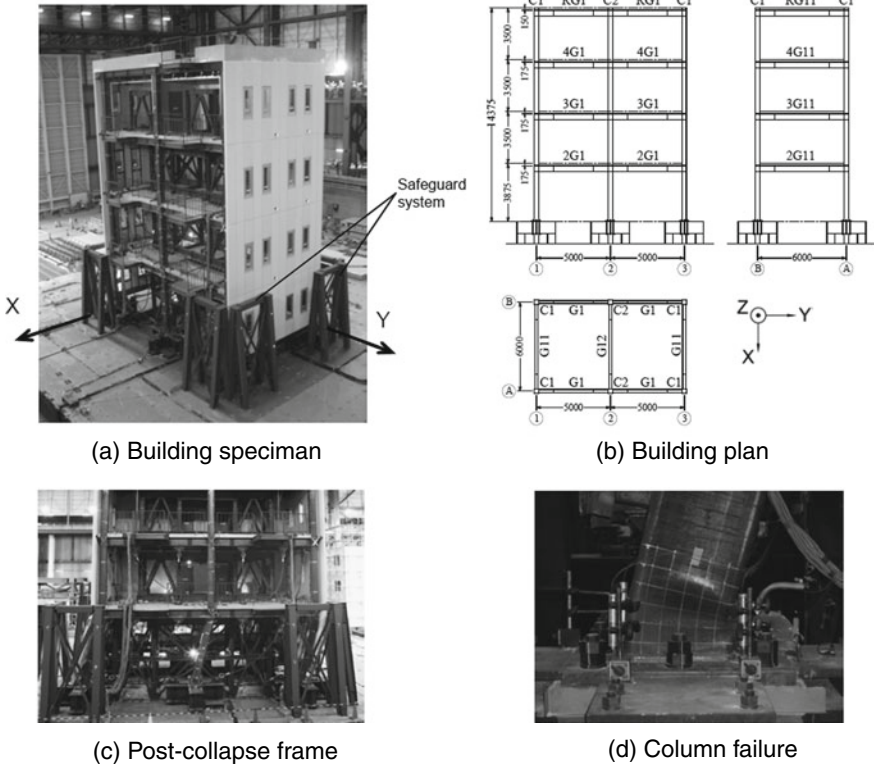
(d) Column failure

Fig. 1 Shake-table test on a full-scale steel moment frame (**a**) Building specimen, (**b**) Building plan, (**c**) Post-collapse frame, (**d**) Column failure

constructed using SN400B and BCR295 steel material, respectively. Three sides of the structure are covered with autoclaved lightweight concrete (ALC) external cladding panels. The column section is $300 \times 300 \times 9$ cold-formed square tube with relatively large width-to-thickness ratios ($b/t = 33$). The column base connection composes of a 50 mm thick base plate and 8 anchor bolts of M36.

The input motion applied in the test is the ground acceleration during the 1995 Kobe earthquake recorded at the JR Takatori station, namely *Takatori motion*. In this test, various increasing scales of the excitation such as 20, 40, 60, and 100% magnitude were input to the specimen. Finally, the building completely collapsed (Fig. 1c) at the motion scale of 100% Takatori motion because local buckling occurred at column ends (Fig. 1d).

2.2 Building Collapse Due to Column Deterioration

After experiencing the increasing shaking levels, the building completely collapsed when subjected to 100% Takatori motion. Deterioration and local buckling of the 1st story column ends played an important role in weakening the story and determining the unbounded translational displacement toward Y direction. Although the building initially deformed quite similarly in both directions, story drift along Y direction (r_Y) eventually increased rapidly, as shown in Fig. 2. The rapid displacement occurred from 5.7 to 6.5 s. The building then collided with the surrounding fence and completely settled on the supporting table at 6.5 s when r_Y became 0.2 rad.

However, levels of column deterioration were different from one another, closely related to the axial force developed seismically in columns. The larger compression force, the more significantly those columns deteriorated. The moment hysteretic curves of two representative columns (A1 and B1) are plotted in Fig. 3. Column A1 is on the tension side, whereas column B1 is on the compression side according to the time of collapse displacement. Figure 3 shows apparently that the consequent deterioration was different between two columns during the last movement prior to collapse, from 5.7 to 6.5 s.

3 Earthquake Energy Dissipation

3.1 Earthquake Input Energy

The building response can be assessed in terms of energy. The earthquake input energy E_{in} (in either the X or Y direction) is calculated using the following equation, where m_i and $\dot{u}_i$ represent the lumped mass and the relative velocity of the ith floor with respect to the shake table, respectively; n is the total floor number; and $\ddot{u}_g$ is the input acceleration:

Fig. 2 Drift ratio orbit of the 1st story (at 100% Takatori—collapse level)
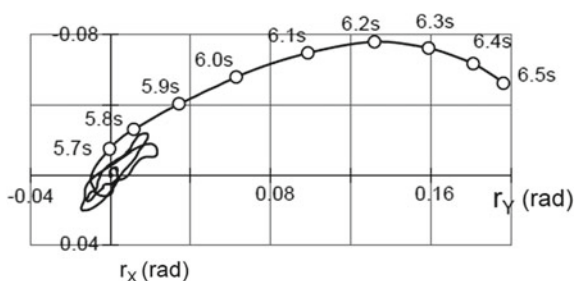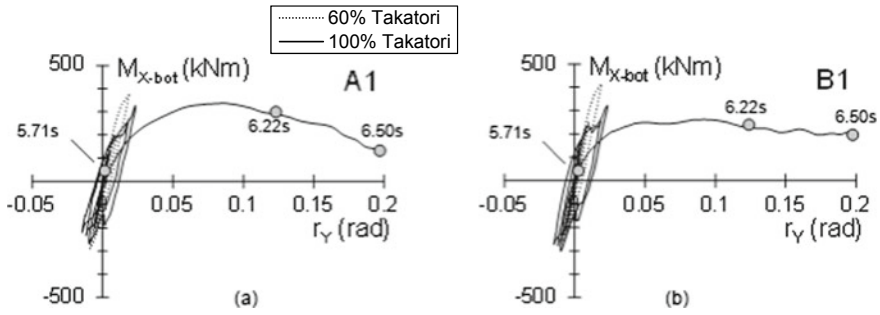
Fig. 3 Column bottom moment versus first-story drift ratio with respect to the Y direction (dotted: 60% Takatori, solid: 100% Takatori)

Fig. 4 Time histories of normalized **a**, **b** input energy, **c**, **d** instantaneous input energy, and **e**, **f** first-story relative velocity: scale factor $\alpha = 1$, 1/2, 1/3, and 1/5 for 20, 40, 60, and 100% Takatori levels, respectively

$$E_{in} = -\int \sum_{i=1}^{n} \dot{u}_i m_i \ddot{u}_g dt \qquad (1)$$

The input and response energy quantities for 40, 60, and 100% Takatori motion levels are scaled to 20% Takatori motion for direct comparison (Fig. 4) using the scale factor $\alpha = 1/2$, $1/3$, and $1/5$, respectively. As indicated by Eq. (1), because there are two time-dependent quantities, i.e., the input ground acceleration $\ddot{u}_g(t)$ and the ith-floor response velocity $\dot{u}_i(t)$, the scaled earthquake input energy $\alpha^2 E_{in}$ is used in the graphical presentation in Fig. 4a and b for the X and Y directions. Up to 40% Takatori level, $\alpha^2 E_{in}$ during the cycles (a) and (b) were similar for all levels for both the X and Y directions. As yielding occurred, especially at the 100% Takatori level, $\alpha^2 E_{in}$ started to increase to nearly twice the values at previous levels. However, at each shaking level, the input energy in the X direction during these two cycles was approximately two to three times the input energy in the Y direction due to the stronger ground motion as well as larger response.

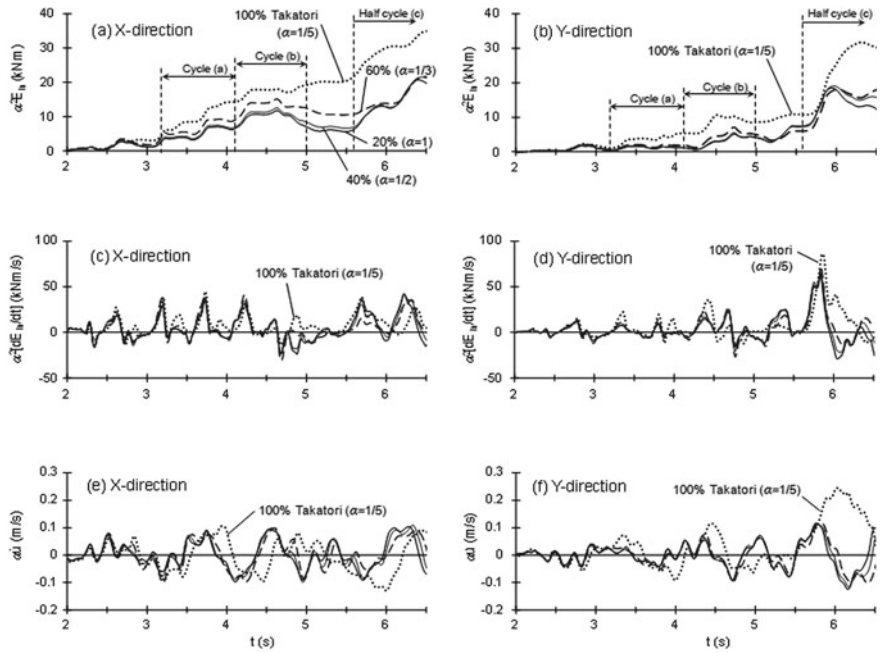The instantaneous input energy defined as dE_{in}/dt, in the X direction (Fig. 4c) was also very high during the first two main cycles and much larger than that in the Y direction (Fig. 4d). Moreover, from 5.7 to 6.0 s, dE_{in}/dt in the Y direction increased to a remarkable peak (Fig. 4d) and was similar for all excitation levels. As a result, $\alpha^2 E_{in}$ in the Y direction rapidly increased during this shaking period (Fig. 4b), thereby causing greater dissipation demand in the frame and consequently very large displacements due to the deteriorated strength in the Y direction. Figure 4a and b also show that $\alpha^2 E_{in}$ at collapse are similar for the X and Y directions, thus suggesting that the above behavior cannot be predicted by such total input energy.

3.2 Energy Dissipation at the Collapse Excitation Level

The building response during the half cycle (c) at the 100% Takatori level can be interpreted using energy equilibrium. Because the 100% Takatori motion is 1.66 times greater than the 60% Takatori motion, its input energy should be $1.66^2 = 2.76$ times greater if the structure is elastic (see Eq. (1)).

However, because the exceedingly large amount of instantaneous input energy in the Y direction needed to dissipate within a short time, the peak $\dot{u}_Y$ at 6.0 s (Fig. 4f) was more than twice that of $\dot{u}_X$ (Fig. 4e). Consequently, the building rapidly translated and collapsed in the Y direction, although the total input energies in the X and Y directions were nearly equal (Fig. 4a and b, respectively). Therefore, this is an important issue in evaluating and predicting the vulnerable side of the building displacement response; *maximum instantaneous input energy* is thought to play a more important role than *total input energy* in determining the main response of the structure.

4   Conclusions

From the results above, various conclusions can be stated as follows.

– Deteriorating situations of bending moments are different among columns because their axial forces differed considerably based on their locations on the building plan.
– The sudden increase in the damage in the Y direction could be explained based on input energy, which depends on not only ground motion but also response velocity. Although the total accumulated input energies were very similar in both directions, a large amount of instantaneous input energy in the Y direction had to be dissipated within a short time by the frame with limited strength due to deterioration, thereby resulting in the rapid translational response of the first story.
– As the P-Δ effect increased, the building consequently lost stability and eventually collapsed. Therefore, the maximum instantaneous earthquake input energy should be of greater interest in predicting structural response in seismic design.

References

1. Suita, K., Matsuoka, Y., Yamada, S., Shimada, Y., Tada, M., Kasai, K.: Experimental procedure and elastic response characteristics of shaking table test—complete collapse test of full-scale 4-story steel building part 1 (in Japanese). J. Struct. Constr. Eng., AIJ **74**(635), 157–166 (2009)
2. Yamada, S., Suita, K., Matsuoka, Y., Shimada, Y.: Elasto-plastic responses and process leading to a collapse mechanism—complete collapse test of full-scale 4-story steel building part 2 (in Japanese). J. Struct. Constr. Eng., AIJ **74**(644), 1851–1859 (2009)
3. Shimada, Y., Suita, K., Yamada, S., Matsuoka, Y., Tada, M., Ohsaki, M., Kasai, K.: Collapse behavior on shaking table test—complete collapse test of full-scale 4-story steel building part 3 (in Japanese). J. Struct. Constr. Eng., AIJ **75**(653), 1351–1360 (2010)
4. Kasai, K., Nam, T., Maison, B.: Structural collapse correlative analysis using phenomenological fiber hinge elements to simulate two-directional column deteriorations. Earthquake Eng. Struct. Dynam. **45**(10), 1581–1601 (2016)

Eigenfrequencies Calculation of Rotating Multilayer Beams Using the Asymptotic Numerical Method

Faiza Boumediene, Hadjila Bournine, and Ferhat Bekhoucha

1 Introduction

Studying the vibration of rotating structures is of great importance in the process of designing and evaluating the performance of many mechanical systems, such as turbine blades and helicopters. Rotating beams are subjected to complex elastic vibrations that can induce noise and resonance, which made the determination of eigenfrequencies as well as the loss factors very important. Actual rotating structures are generally twisted, curved, and non-homogeneous, giving rise to a coupling between the two transverse bending movements and that of torsion.

The linear and nonlinear vibratory behavior of rotating and non-rotating twisted isotropic beams has been studied at length. We can cite, for example, the work of Yoo et al. [1] where the authors considered rotating Euler–Bernoulli beams and the work of Yardimoglu et al. [2] who studied non-rotating Tymoshenko beams. An interesting review of modeling methods can be found in reference [3]. In these works, the authors often simplified dynamic models under restrictive assumptions, such as the neglect of the coupling terms of the Coriolis effect, or the neglect of the torsional deformations in the bending vibrations. In applications requiring lightweight structures, viscoelastic materials are often used as interlayers to introduce passive damping induced by the shear effect. Twisted, rotating and non-rotating viscoelastic sandwich beams have been the subject of several research works [4, 5]. In these last references, the authors supposed that the complex Young's modulus is constant.

F. Boumediene (✉) · H. Bournine
University of Sciences and Technology Houari Boumediene, BP 32 El Alia,
16111 Bab Ezzouar, Algeria
e-mail: fboumediene@usthb.dz

F. Bekhoucha
Polytechnic National School, 10 Ave Hassen Badi, BP 182, 16200 El Harrach, Algeria

557

Recently, the authors Bekhoucha et al. [6] published a study on the calculation of the eigenfrequencies and the loss factors of rotary sandwich beams taking into account the variation of Young's modulus of the viscoelastic material with respect to frequency, using the Newton–Raphson method. The objective of our present work is to resolve the problem using homotopy technic and asymptotic numerical method. These two methods have proven their efficiency in diverse fields. The beam is supposed to be clamped-free with a rectangular cross section and linear twist along its axis. At the end of this paper, we present the effect of the twist angle on natural frequencies and damping coefficients.

2 Problem Formulation

Consider a twisted sandwich beam with a constant cross section (Fig. 1), where the central layer is viscoelastic of thickness h_c and the face layers are elastic, isotropic, and symmetric of thickness h_f. The beam, of length L and width b, is attached to a hub of radius r_h. The whole structure revolves around the axis of the hub. To describe the movement, three references are used:

- the fixed reference $R_0(O; x_0; y_0; z_0)$ whose axis z_0 is the axis of the hub;
- the reference related to the structure $R(O; x; y; z)$; whose x-axis passes by the geometric centers of the core layer and the two axes z_0 and z are coincident;
- the reference related to the cross section located at the x position $R_x(G_2; X; Y; Z)$, such that the X-axis overlaps with the x-axis of the reference R and the Y- and Z-axes are the main inertia axes of the cross section.
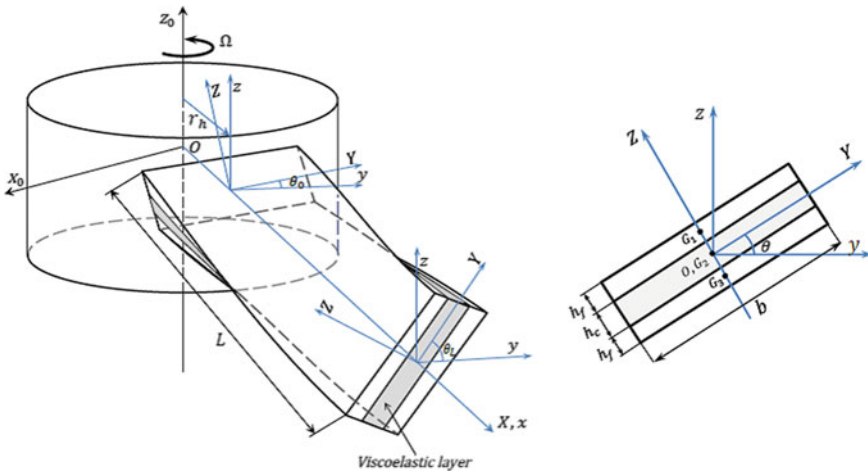
Fig. 1 Rotating twisted sandwich beam

It is assumed that the twist of the beam varies linearly. Therefore, the Y-axis of a cross section located at position x is inclined with respect to the y_0-axis by an angle θ (Fig. 1) given by the following expression:

$$\theta(x) = \theta_0 + \Delta\theta \cdot x/L$$

with $\Delta\theta = \theta_L - \theta_0$; θ_0 and θ_L are the twist angles of the two end sections of the beam in positions $x = 0$ and $x = L$.

The structure rotates in the horizontal plane, around the z-axis, with a constant rotational speed Ω. The equations of motion are determined in the Galilean coordinate system $R_0(O; x_0; y_0; z_0)$ and expressed in the reference $R(O; x; y; z)$ linked to the structure. It is considered that the three layers are perfectly bonded, the transverse deformations are negligible and the central layer deforms mainly in shear.

The transverse displacements $v(x, t)$ and $w(x, t)$ (t indicate the time), following y and z, are common for all three layers. Due to shear deformation, the rotation around the y axis of the core layer is defined by $\beta(x, t)$. The longitudinal displacement of the geometric centers of each layer (1, 2, or 3) is noted $u_i(x, t)$, where $i = 1$, 2, or 3. The equations of motion of the system in free vibration are obtained by applying the Hamilton principle

$$\int_{t_1}^{t_2} (\delta T - \delta U)dt = 0 \tag{1}$$

where δT and δU are the changes in kinetic energy and potential energy. To have more details about the computation of δT and δU, the reader can consult reference [6].

Using the continuity equations at the interfaces, we can write the equation of motion as a function of the variables: $u_2(x, t)$; $v(x, t)$; $w(x, t)$ and $\beta(x, t)$. The bending displacements $v(x, t)$; $w(x, t)$ and $\beta(x, t)$ are decoupled from the longitudinal displacements $u_2(x, t)$. In this study, we are only interested in deflection movements. Hence, the approximate solutions $v(x, t)$; $w(x, t)$; and $\beta(x, t)$ are assumed to be as follows:

$$v(x, t) = \sum_{i=1}^{m} \Phi_i(x)q_{v_i}(t) \tag{2}$$

$$w(x, t) = \sum_{i=1}^{m} \Phi_i(x)q_{w_i}(t) \tag{3}$$

$$\beta(x, t) = \sum_{i=1}^{m} \Phi_i'(x)q_{\beta_i}(t) \tag{4}$$

where q_{v_i}, q_{w_i} and q_{β_i} are the generalized coordinates, m is the number of modes taken into account, $\Phi_i(x)$ are approximation functions that satisfy the boundary

conditions and $\Phi'_i(x)$ are their derivatives with respect to x. For our study we use the known semi-analytical eigenform of a clamped-free beam given as follows:

$$\Phi_i(x) = \cosh(B_i x) - \cos(B_i x) - \sigma_i(\sinh(B_i x) - \sin(B_i x))$$

where

$\sigma_1 = 0.7341$, $\sigma_2 = 1.0185$, $\sigma_3 = 0.9992$, $\sigma_i = 1$ for $i > 3$
$B_1 = 1.87510407/L$, $B_2 = 4.69409113/L$, $B_3 = 7.85475744/L$,

$B_4 = 10.99554073/L$, $B_5 = 14.1376839/L$, and $B_i = \frac{(2i-1)\pi}{(2L)}$ for $i > 5$.

After the substitution of these functions into the equation of motion, we obtain the eigenvalue problem defined by:

$$\left[K_0 + E_2^*(\omega)K_v - \lambda M\right]\{q\} = 0 \tag{5}$$

where K_0; K_v are the elastic and viscoelastic total stiffness matrices; M is the mass matrix; $E_2(\omega) = E_2^0 + E_2^*(\omega)$ is Young's modulus of the central layer as a function of the frequency; λ is the eigenvalue; q is the generalized coordinates vector.

This nonlinear problem is solved using two methods: the homotopy technique with the asymptotic numerical method [6]. The homotopy technique consists of introducing a parameter ε to problem (5) as follows:

$$\Re(q, \lambda) = \Re_1(q, \lambda) + \varepsilon\Re_2(q, \lambda) \tag{6}$$

where $\Re_1(q, \lambda) = [K_0 - \lambda M]\{q\}$ and $\Re_2(q, \lambda) = \left[E_2^*(\omega)K_v\right]\{q\}$

After that, the asymptotic numerical method is applied to this new problem (6). The unknowns q and λ are developed in the form of integer series according to the parameterization ε up to a truncation order n, as follows:

$$\begin{cases} q = \sum_{j=0}^{n} \varepsilon^j q_j \\ \lambda = \sum_{j=0}^{n} \varepsilon^j \lambda_j \end{cases} \tag{7}$$

such that the following orthogonality condition is satisfied:

$$^T q_0(q - q_0) = 0 \tag{8}$$

Inserting series (7) into (6) and (8) gives a set of recurring linear problems, as follows:

- at $\varepsilon = 0$, Eq. (6) represents the problem with undamped eigenvalues:

$$[K_0 - \lambda_0 M]\{q_0\} = 0 \tag{9}$$

giving the starting point of the ANM iterations, namely the undamped eigenvector q_0 and the undamped eigenvalue λ_0.

- and at each order i, we calculate the unknown parameters (q_i, λ_i); by solving the following linear problem:

$$L(q_i, \lambda_i) = f_i^{nl} \tag{10}$$

where $L(q_i, \lambda_i)$ is a linear operator of the unknown parameters at order i and f_i^{nl} depend only on the known parameters calculated in the previous orders.

After the computations of all values q_i and λ_i at each order $i(i = 1\ to\ n)$, one can compute the solution using the expression (7). This solution is satisfied up to the value:

$$\varepsilon_{max} = \left(\delta\frac{q_1}{q_n}\right)^{1/(n-1)} \tag{11}$$

where δ is the tolerance given by the user.

After several iterations of the ANM and when the parameter ε reaches the value of $\varepsilon = 1$, the solution of the nonlinear damped problem (5) will be reached, too. The eigenvalue λ is complex:

$$\lambda = \omega_d^2(1 + i\ \eta) \tag{12}$$

where ω_d is the damped frequency and η is its associated loss factor.

So, from the expression (12), one can compute the damped frequency ω_d and the loss factor as follows:

$$\omega_d = \sqrt{\mathrm{Re}(\lambda)}/2\pi \tag{13}$$

$$\eta = \mathrm{Im}(\lambda)/\mathrm{Re}(\lambda) \tag{14}$$

where $\mathrm{Re}(\lambda)$ is the real part of λ and $\mathrm{Im}(\lambda)$ its imaginary parts.

3   Code Validation

To test our calculation code, we consider a twisted isotropic beam studied in [2]. The beam properties are given as follows: Length $= 15.24$ cm, width $b = 2.54$ cm, thickness $h = 0.17272$ cm, Young modulus $E = 206.85 \times 10^9$ N/m^2, Poisson ratio $v = 0.25$, density $\rho = 7857.6$ kg/m^3, and twist angle $\Delta\theta = 45°$. Authors in the reference [2] considered the Timoshenko hypotheses in their studies. The results are given in Table 1. For our calculation, ten modes ($m = 10$) are taken to approximate the eigenform $\Phi_i(x)$. One can remark that our results are in perfect accordance with those of the references [2, 7].

4   Sandwich Beam with a Variable Shear Modulus

In this example, we study a sandwich beam with aluminum faces and a core of a viscoelastic material (3 M ISD112) at 27 °C. The material and geometrical characteristics are given in Table 2. The core has a variable shear modulus expressed with a generalized Maxwell model as follows:

$$G_2(\omega) = G_c \left(1 + \sum_{j=1}^{3} (\Delta_j \omega) / (\omega - \mathrm{i} \, \delta_j) \right) \tag{15}$$

where G_c is the delayed shear modulus of the (3 M ISD112) viscoelastic material and (Δ_j, δ_j) is the parameters of the generalized Maxwell model. These coefficients as well as the properties of the beam are grouped together in Table 2.

Figure 2 illustrates the twist angle effect on the fundamental frequency and the corresponding loss factor η in two cases:

– The beam does not rotate, stationary case ($\Omega = 0$)
– The beam rotates at a constant speed ($\Omega = 146$ rd/s).

We can notice, in both cases, that:

– when the twist angle increases, the damped fundamental frequency and the corresponding loss factor are almost stable up to the angle 49.5°,
– after this angle, increasing the twist angle makes the beam more flexible.

Note that, for this example, the initial angle at $x = 0$ is zero $\theta_0 = 0$.

Table 1 First four natural frequencies of a twisted isotropic beam

	ω_1[Hz]	ω_2[Hz]	ω_3[Hz]	ω_4[Hz]
Present work	62.10	305.78	1009.55	1229.60
Subrahmanyam et al. [7]	62.0	305.1	955.1	1214.7
Yardimoglu et al. [2]	61.8	304.8	944.5	1193.0

Table 2 Characteristics of the sandwich beam *Al/ISD112/Al* at 27 °C

Length	$L = 177.8\,\mathrm{mm}$	
width	$b = 12.7\,\mathrm{mm}$	
Hub radios	$r_h = 0.5\,L$	
Young modulus	$E_f = 6.9 \times 10^{10}\,\mathrm{N/m^2}$	$G_c = 0.5 \times 10^6\,\mathrm{N/m^2}$
Poisson ratios	$v_f = 0.3$	$v_c = 0.5$
Densities	$\rho_f = 2766\,\mathrm{kg/m^3}$	$\rho_c = 1600\,\mathrm{kg/m^3}$
Thickness	$h_f = 1.524\,\mathrm{mm}$	$h_c = 0.127\,\mathrm{mm}$
$\Delta_1 = 0.746$	$\Delta_2 = 3.265$	$\Delta_3 = 43.284$
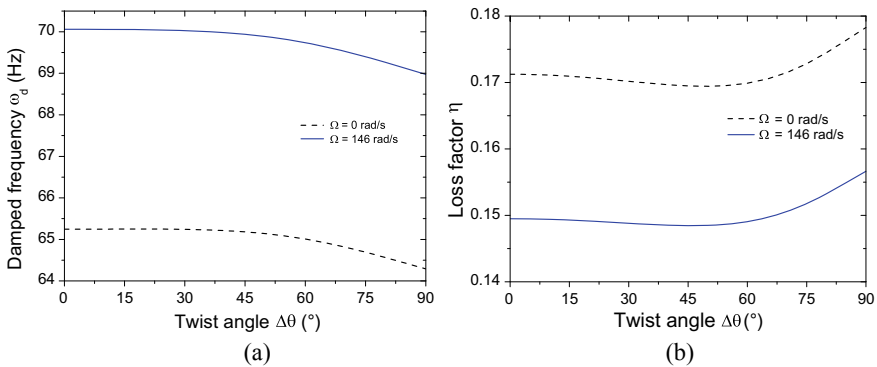
Fig. 2 Modal parameters variation of the sandwich beam with respect to the twist angle for two rotational speeds **a** the first damped frequency **b** the first loss factor

5 Conclusion

In this work, we calculated the natural frequencies and their corresponding loss factors of a clamped-free twisted viscoelastic sandwich beam with a uniform cross section that revolves at a constant rotating speed. We have presented only one validation example in this paper, but different examples have been studied showing the effectiveness of the method used and the consistency of our results with those in the literature and commercial codes. Our calculation code makes it possible to directly find the natural frequencies and the loss factors of the viscoelastic rotary sandwich beams having a Young modulus which varies with respect to frequency.

This fast and efficient calculation is not possible with commercial software. The results show that for low twist angles, the variation of the dynamic parameters is not significant. However, at a certain angle, increasing the twist angle tends to increase the damping effect and makes the beam more flexible.

References

1. Yoo, H.H., Park, J.H., Park, J.: Vibration analysis of rotating pre-twisted blades. Comput. Struct. **79**, 1811–1819 (2001)
2. Yardimoglu, B., Yildirim, T.: Finite element model for vibration analysis of pre-twisted Timoshenko beam. J. Sound Vib. **273**, 714–754 (2004)
3. Kim, H., Yoo, H.H., Chung, J.: Dynamic model for free vibration and response analysis of rotating beams. J. Sound Vib. **332**, 5917–5922 (2013)
4. Rao, D.K.: Transverse vibrations analysis of pre-twisted sandwich beams. J. Sound Vib. **44**(2), 159–168 (1976)
5. Lin, C.Y., Chen, L.W.: Dynamic stability of rotating pre-twisted blades with a constrained damping layer. Compos. Struct. **61**, 235–245 (2003)
6. Bekhoucha, F., Boumediene, F.: Modal analysis of rotating pre-twisted viscoelastic sandwich beams. Comput. Mech. **65**, 1019–1037 (2020)
7. Subrahmanyam, K.B., Kulkarni, S.V., Rao, J.S.: Coupled bending-bending vibration of pre-twisted cantilever blading allowing for shear. Int. J. Mech. Sci. **23**, 517–530 (1981)

Application of Polygonal Finite Element for Incompressible Steady Navier–Stokes Fluid Flow Over Obstacle

T. Vu-Huu, Sy Pham-Van, Q. Hoan Pham, and Thanh Cuong-Le

1   Introduction

Recently, PFEM—a special finite element method is emerging as one of the most robust numerical methods which can be performed on almost mesh families, e.g. triangular, quadrilateral, random Voronoi mesh, etc. This method has a desirable advantage of applying the properties of Voronoi diagrams mesh generation algorithms [1, 2]. This paper is to apply this method, to solve the incompressible steady N-S fluid flow over a domain with an obstacle. Because of this purpose, a polygonal finite element (PFE), named Pe_1Pe_1 [3, 4], is employed.

For the goal mentioned above, a well-known classical benchmark problem of two-dimensional (2D) incompressible steady N-S equations (i.e. lid-driven cavity flow) is re-utilised in this research to present a validation. This benchmark is early and widely applied by many researchers, e.g. Ghia et al. [5]; Botella and Peyret, 1998 [6], Bruneau and Saad [7], etc. to evaluate the numerical methods in solving the N-S equations. Because of this benchmark, we benefit from its geometrical simplicity for the straightforward coding in terms of applying of numerical methods on this flow [6, 8]. Then, the extension application of this method is executed through the second test of flow over an obstacle; see Ref. [9].

This research takes the advantages of the PFEM by applying the meshing algorithms of Voronoi diagrams [1, 2]. In addition, in order to handle the bottleneck of generating quality polygonal meshes, the technique introduced in [2, 10] are deployed. Besides, the Wachspress coordinates [11, 12] are utilised to create the basis shape functions of polygons.

T. Vu-Huu · S. Pham-Van · Q. Hoan Pham
Faculty of Civil Engineering, Vietnam Maritime University, Hai Phong, Vietnam

T. Cuong-Le (✉)
Faculty of Civil Engineering, Ho Chi Minh City Open University,
Ho Chi Minh City, Vietnam
e-mail: cuong.lt@ou.edu.vn

The paper is divided into three sections, as follows: Sect. 2 introduces the brief information for the strong, weak and discretisation form of the incompressible steady N-S flows. In Sect. 3, an illustration of the equal-order PFE is presented. Section 4 presents the results of numerical tests. Finally, Sect. 5 gives the conclusions for this paper.

2   Incompressible Steady Navier–Stokes Equations

Incompressible steady N-S fluid flow is normally written as following [9, 13, 14]:

$$\nabla p - v\nabla^2 u + \boldsymbol{u} \cdot \nabla u = \boldsymbol{f} \tag{1}$$

$$\nabla \cdot u = 0 \tag{2}$$

where v is a given positive constant called the fluid kinematic viscosity; $\boldsymbol{f}$ is the forcing term; $\boldsymbol{u}$ and p are the fluid velocity in $H^1(\Omega)$ and the modified pressure (after dividing by water density) of the fluid in $L^2(\Omega)$, respectively. For more simplification, body force vector $\boldsymbol{f}$ is set to zero with a little loss of generality. In this case, the conservation term of body force (gravity force) is the gradient of a scalar field, that is, $\boldsymbol{f} = -\nabla \Xi$, and thus can be incorporated into the system by redefining the pressure ($p \rightarrow p + \Xi$). Then, by choosing the test spaces:

$$\boldsymbol{H}^1 = \left\{ \boldsymbol{u} \in \mathcal{H}^1(\Omega)^2 | \boldsymbol{u} = \boldsymbol{w} \text{ on } \Gamma^D \right\} \tag{3}$$

$$\boldsymbol{H}_0^1 = \left\{ \boldsymbol{v} \in \mathcal{H}^1(\Omega)^2 | \boldsymbol{v} = 0 \text{ on } \Gamma^D \right\}, \tag{4}$$

the standard weak formulations of Eqs. (1 and 2) are:

$$v \int_\Omega \nabla \boldsymbol{u} : \nabla \boldsymbol{v} \mathrm{d}\Omega + \int_\Omega (\boldsymbol{u} \cdot \nabla \boldsymbol{u}) \cdot \mathbf{v} \mathrm{d}\Omega - \int_\Omega p(\nabla \cdot \boldsymbol{v}) \mathrm{d}\Omega = 0 \quad \forall \boldsymbol{v} \in \boldsymbol{H}_0^1, \tag{5}$$

$$\int_\Omega q(\nabla \cdot \boldsymbol{u}) \mathrm{d}\Omega = 0 \quad \forall q \in L_0^2, \tag{6}$$

where $\boldsymbol{v}$ and q are test functions; $v \int_\Omega \nabla \boldsymbol{u} : \nabla \boldsymbol{v} \mathrm{d}\Omega$ is diffusive term; $\int_\Omega (\boldsymbol{u} \cdot \nabla \boldsymbol{u}) \cdot \mathbf{v} \mathrm{d}\Omega$ denotes the convective term what is the nonlinear term of convection identified by a trilinear form $: \boldsymbol{H}_0^1 \times \boldsymbol{H}_0^1 \times \boldsymbol{H}_0^1 \rightarrow \mathbb{R}$ as:

$$(\boldsymbol{z}; \boldsymbol{u}, \boldsymbol{v}) = \int_\Omega (\boldsymbol{z} \cdot \nabla \boldsymbol{u}) \cdot \boldsymbol{v} \mathrm{d}\Omega \tag{7}$$

Now, establish the subspace of divergence-free velocities as:

$$V_0 \sim \ = \ \{z \in H_0^1; \ \nabla \cdot z \ = \ 0 \ \text{in} \ \Omega\} \tag{8}$$

Based on the mixed scheme method of two finite spaces $M^h \subset L_0^2(\Omega)$ and $X^h \subset H_0^1$ of fluid pressure and velocity, respectively, and with the given spaces of velocity, X^h, and pressure, M^h, the discretisation system now becomes:

$$\begin{aligned} v \int_\Omega \nabla u_h : \nabla v_h d\Omega + \int_\Omega (u_h \cdot \nabla u_h) \cdot v_h d\Omega \\ - \int_\Omega p_h (\nabla \cdot v_h) d\Omega = \int_\Omega \mathbf{f} \cdot v_h \quad \forall v_h \in \mathbf{X}^h, \end{aligned} \tag{9}$$

$$\int_\Omega q_h (\nabla \cdot u_h) d\Omega \ = \ 0 \quad \forall q_h \in M^h. \tag{10}$$

Then, based on the set of vector-valued basis functions $\{\phi_j\}$ for velocity and a set of pressure basis functions $\{\psi_k\}$ for pressure:

$$u_h \ = \ \sum_{j=1}^{n_u} u_j \phi_j + \sum_{j=1+n_u}^{n_u+n_\partial} u_j \phi_j, \ \delta u_h \ = \ \sum_{j=1}^{n_u} \Delta u_j \phi_j, \tag{11}$$

$$p_h \ = \ \sum_{k=1}^{n_p} p_k \psi_k, \delta p_h \ = \ \sum_{k=1}^{n_p} \Delta p_k \psi_k. \tag{12}$$

The approximation solution is achieved by the system of linear equations as:

$$\begin{bmatrix} vA + N + W & B^T \\ B & 0 \end{bmatrix} \begin{bmatrix} \Delta u \\ \Delta p \end{bmatrix} = \begin{bmatrix} f \\ g \end{bmatrix} \tag{13}$$

Here, A is the vector-Laplacian matrix, B is the divergence matrix. Besides, N is the vector–convection matrix, and W is the Newton derivative matrix, defined as follows:

$$A \ = \ [a_{ij}], \ a_{ij} \ = \ \int_\Omega \nabla \phi_i : \nabla \phi_i d\Omega \quad \forall i, j \ = \ 1, \ldots, n_u, \tag{14}$$

$$B \ = \ [b_{kj}], \ b_{kj} \ = \ - \int_\Omega \psi_k \nabla \cdot \phi_j d\Omega \quad \forall k \ = \ 1, \ldots, n_p. \tag{15}$$

$$N \ = \ [n_{ij}], n_{ij} \ = \ \int_\Omega (u_h \cdot \nabla \phi_j) \cdot \phi_i d\Omega, \tag{16}$$

$$\boldsymbol{W} = \begin{bmatrix} w_{ij} \end{bmatrix}, \; w_{ij} = \int_{\Omega} \left(\boldsymbol{\phi}_j \cdot \nabla \boldsymbol{u}_h \right) \cdot \boldsymbol{\phi}_i \mathrm{d}\Omega, \tag{17}$$

In this paper, because of the simplicity, Picard is chosen to handle the nonlinear term in N-S equations. For Picard iteration, by omitting the Newton derivative matrix, the mixed finite discretisation system becomes:

$$\begin{bmatrix} v\boldsymbol{A} + \boldsymbol{N} & \boldsymbol{B}^T \\ \boldsymbol{B} & 0 \end{bmatrix} \begin{bmatrix} \Delta \boldsymbol{u} \\ \Delta \boldsymbol{p} \end{bmatrix} = \begin{bmatrix} \boldsymbol{f} \\ \boldsymbol{g} \end{bmatrix} \tag{18}$$

In case of unstable problem, it is necessary to eliminate the zero block in the system Eq. (13) as well as the system Eq. (18) by a stabilisation matrix to get the stable results. Therefore, the stabilised analogue of the system Eq. (18) is:

$$\begin{bmatrix} v\boldsymbol{A} + \boldsymbol{N} & \boldsymbol{B}^T \\ \boldsymbol{B} & -\frac{1}{v}\boldsymbol{C} \end{bmatrix} \begin{bmatrix} \boldsymbol{u} \\ \boldsymbol{p} \end{bmatrix} = \begin{bmatrix} \boldsymbol{f} \\ \boldsymbol{g} \end{bmatrix} \tag{19}$$

Here, $\boldsymbol{C}$ is the stabilisation matrix provided by $c(\cdot,\cdot) : M^h \times M^h \to \mathbb{R}$. The local stabilisation matrix, c_e, of elements becomes [4, 15]:

$$\begin{aligned} c_e(q_h, p_h) &= \frac{1}{v} \int_{\Omega_e} \left(q_h - \prod q_h \right) \left(p_h - \prod p_h \right) \mathrm{d}\Omega \\ &= \sum_{i,j=1}^{n_{ne}} \frac{1}{v} q_i \int_{\Omega_e} \left(\psi_i - \frac{1}{n_{ne}} \right) \left(\psi_j - \frac{1}{n_{ne}} \right) \mathrm{d}\Omega q_j, \end{aligned} \tag{20}$$

for all $\Omega_e \in \mathfrak{I}_h$. In which, the basis functions ψ_i and ψ_j does not vanish on the element Ω_e. Thus, the global stabilisation matrix $\boldsymbol{C}$ can be assembled from contribution matrices c_e by:

$$\boldsymbol{C} = \mathop{\mathrm{A}}_{e=1}^{n_e} \sum_{i,j=1}^{n_{ne}} \frac{1}{v} \int_{\Omega_e} \left(\psi_i - \frac{1}{n_{ne}} \right) \left(\psi_j - \frac{1}{n_{ne}} \right) \mathrm{d}\Omega, \tag{21}$$

where A is the assembly operator, e is the eth element, n_e is the total number of the elements in the domain $\mathfrak{I}_h$.

3 Equal-Order Mixed Polygonal Finite Element

The equal-order mixed PFE, $\mathrm{Pe}_1\mathrm{Pe}_1$ [3, 4] is introduced in this section. This PFE applies the similar polygonal basis shape functions [11, 12] to represent for both velocity and pressure fields; see Fig. 1.

Fig. 1 Equal-order mixed PFE, Pe$_1$Pe$_1$ [3, 4]

□ Pressure nodes
● Velocity nodes
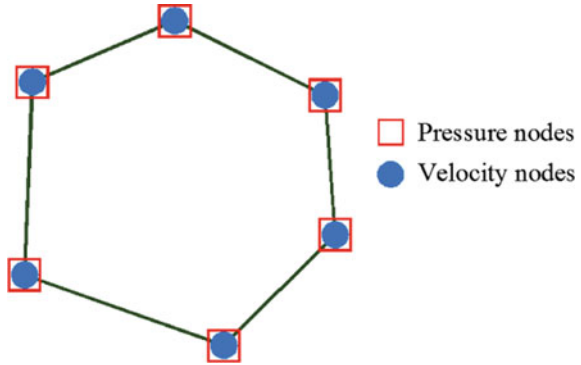
Firstly, consider a representative polygonal mesh $\Im_h = \{\Omega_e\}_{e=1}^{N}$ of the domain Ω. In which, h is the maximum diameter of the elements. Then, the fluid pressure is approximated by the set of barycentric basis functions in $\Im_h$ [16] on the discrete space, M^h, i.e.

$$M^h \quad = \quad \left\{\, q_h \in L_0^2(\Omega) : q_h|_{\Omega_e} \in \mathrm{P}(\Omega_e), q_h|_{\Gamma_e} \in C^0, \quad \forall e = 1, \ldots, M \,\right\}, \quad (22)$$

where $\mathrm{P}(\Omega_e)$ is the generalised barycentric coordinates. For polygonal element, Ω_e, with n_{ne} nodes and n_s edges so that $\Omega = \sum\limits_{e=1}^{n_e} \Omega_e \approx \Im_h$. The approximation pressure, $q_h \in M^h$ with $\forall \Omega_e \in \Im_h$, is:

$$q_h(\mathbf{x}) \quad = \quad \sum_{i=1}^{n_{ne}} q_i \psi_i^e(\mathbf{x}), \tag{23}$$

in which, q_i is DOFs of $q^h(\mathbf{x})$ and ψ_i^e is the basis test functions on polygons.

Secondly, the representative space $\mathbf{X}^h$ of velocity field [16]:

$$\mathbf{X}^h \quad = \quad \left\{\boldsymbol{u}_h \in \left(\boldsymbol{H}_0^1\right)^2 : \boldsymbol{u}_h|_{\Omega_e} \in [\mathrm{P}(\Omega_e)]^2, \boldsymbol{u}_h|_{\Gamma_{\Omega_e}} \in C^0, \quad \forall e = 1, \ldots, M\right\}. \tag{24}$$

The approximation velocity $\boldsymbol{u}_h \in V^h$ with $\forall \Omega_e \in \Im_h$ is now expressed by:

$$\boldsymbol{u}_h(\boldsymbol{x}) \quad = \quad \sum_{i=1}^{n_{ne}} \phi_i^e(\boldsymbol{x}) \boldsymbol{I}_2 \boldsymbol{d}_{e_u}^i. \tag{25}$$

where $\boldsymbol{d}_{e_u}^i$ is DOFs of $\boldsymbol{u}^h(\boldsymbol{x})$ and ϕ_e^i stand for the test function at the ith vertex of polygons. $\boldsymbol{I}_2$ is the identity matrix, or sometimes ambiguously called a unit matrix of the second rank.

4   Numerical Tests

The first test of this is an extensive well-known classical benchmark (i.e. lid-driven cavity flow; see Fig. 2). The properties of this test are as follows:

–   Its domain is defined by a unit square $\Omega = (0, 1)^2$.
–   The boundary condition of velocity along the estuary of the cavity $(0 \leq x \leq 1 \, (m), y = 1(m))$ is $u_x = -1(m/s)$ and $u_y = 0$. Besides, the velocity condition on left, right wall and bottom are zero; see Fig. 2.
–   In addition, the fluid density is assumed $\rho = 1 \, (kg/m^3)$.
–   The viscosity, v, is 0.01 (m^2/s).
–   For this test, four progressively finer hexagonal meshes are utilised, i.e. Mesh 1 with 4046 elements, Mesh 2 with 16,491 elements, Mesh 3 with 36,977 elements and Mesh 4 with 66,102 elements.

The initial results of this test are the velocity of fluid flows; see Fig. 3. The detail of the comparison is based on the velocity values on the centrelines of the cavity domain; see Fig. 3b and c. From the figure, the complete coincidence of our results to the Ghia et al. [5] is visible. Moreover, the good convergence from the present results is also proved through the results of fluid pressure and velocity values at the domain centre; see Table 1 (Fig. 4).

The second test is presented in Fig. 5 with the following properties: The inlet velocity is u_x 1.0 m/s and u_y 0 m/s. The flow velocity at the upper and bottom boundary is zero as shown in Fig. 5. Besides, the kinematic pressure at the outlet boundary is zero. In addition, the fluid density is assumed $\rho = 1 \, (kg/m^3)$. The viscosity, v, is: 0.01 (m^2/s).

The velocity and pressure results of this test are shown in Fig. 6. And the convergence of this test is checked through the comparison of velocity and pressure at the local point (2.0, 1.5) in the domain. For this aim, five progressively finer hexagonal meshes are employed, i.e. Mesh 1 with 3000 elements, Mesh 2 with
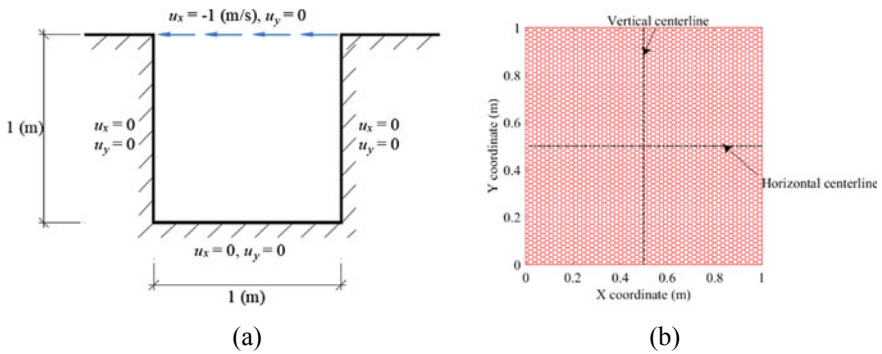
Fig. 2 **a** Lid-driven flow over cavity square and **b** Hexagonal mesh
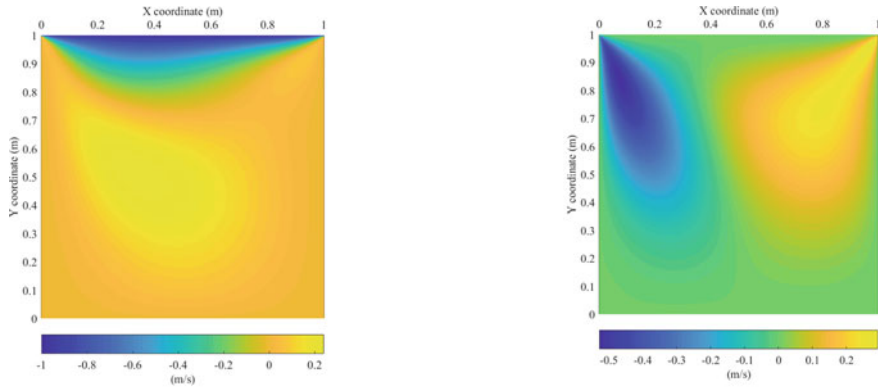
(a) Results of velocity field on whole domain.
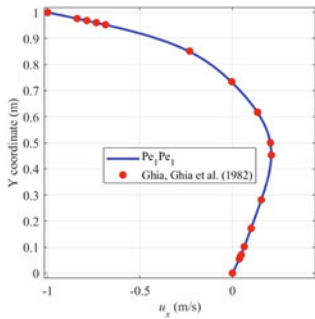
(b) The horizontal velocity on the
vertical centreline.
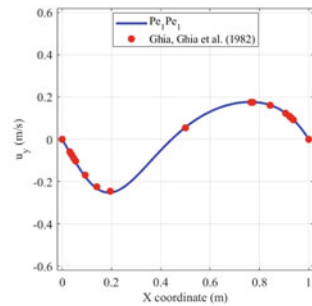
(c) The vertical velocity on the
horizontal centreline.

Fig. 3 Velocity results

Table 1 Velocity results at the centre of the domain (0.5, 0.5)

Mesh	Velocity		Pressure, p (kPa)
	u_x (m/s)	u_y (m/s)	
Mesh 1	0.195982	0.053876	−0.021810
Mesh 2	0.201646	0.053830	−0.021689
Mesh 3	0.205567	0.055145	−0.021142
Mesh 4	0.205958	0.056892	−0.021189
[5]	0.20581	0.05454	−0.021189

4000 elements, Mesh 3 with 5000 elements, Mesh 4 with 8000 elements and Mesh 5 with 10,000 elements. The detail of results is illustrated in Table 2. From the table, it clearly realises a good convergence from both the results of fluid pressure and velocity values.
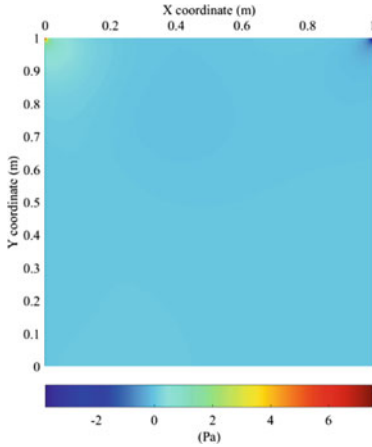
(a) The pressure fields.
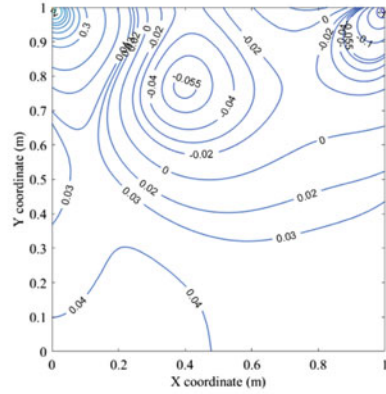
(b) Contour of the pressure result.

Fig. 4 Pressure result
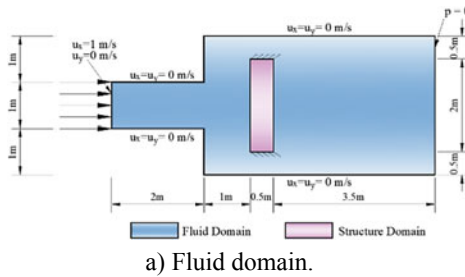
a) Fluid domain.
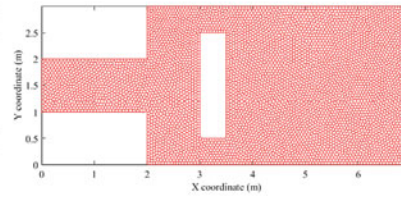
b) Polygonal mesh sample .

Fig. 5 Second benchmark

5 Conclusion

In this research, we successfully applied a PFE to solve the incompressible steady N-S fluid problems. This contribution is based on the equal-order mixed scheme method presented in Ref. [4]. In this research, we can see a drawback of meshing technique introduced in [2, 10], particularly, the low-quality mesh at the corners (0, 1), (2, 0), (3, 0.5), (3.5, 0.5), etc. This problem can cause bad effects to the accuracy of the method. Therefore, for the next step of this work, we would like to improve the technique of polygonal meshing to discretise the more complicated domain.

Fig. 6 Results of the second benchmark

a) Horizotal velocity.

b) Vertical velocity.
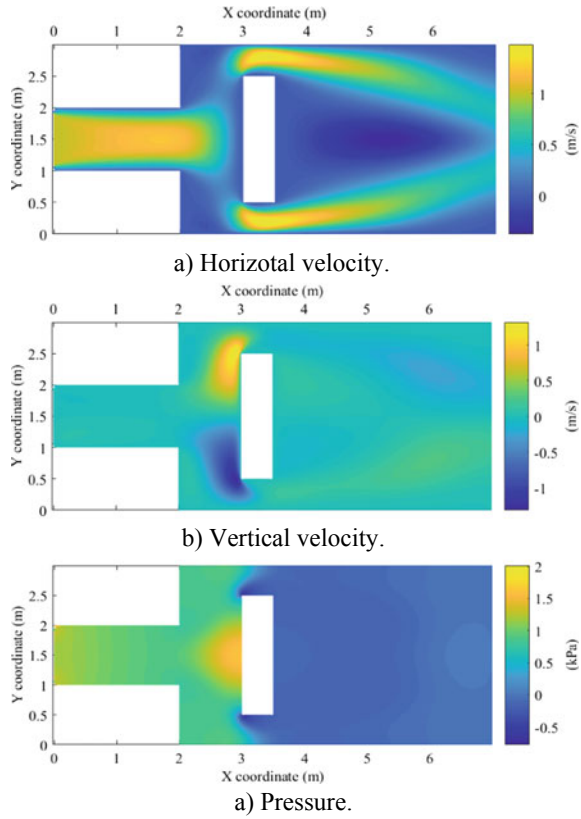
a) Pressure.

Table 2 Velocity results at the point (2.0, 1.5)

Mesh	Velocity		Pressure, p (kPa)
	u_x (m/s)	u_y (m/s)	
Mesh 1	1.3078	0.0077	1.2628
Mesh 2	1.2974	0.0017	1.1973
Mesh 3	1.1106	0.0026	0.8087
Mesh 4	1.2302	−0.0068	0.9800
Mesh 5	1.1970	−0.0066	0.9290

References

1. Sieger, D., Alliez, P., Botsch, M.: Optimizing voronoi diagrams for polygonal finite element computations. In: The 19th International Meshing Roundtable, Springer, pp. 335–350 (2010
2. Talischi, C., Paulino, G.H., Pereira, A., Menezes, I.F.: PolyMesher: a general-purpose mesh generator for polygonal elements written in Matlab. Struct. Multidiscip. Optim. **45**, 309–328 (2012)

3. Vu, H.T., Le, T.C., Nguyen-Xuan, H., Abdel Wahab, M.: Stabilization for Equal-Order Polygonal Finite Element Method for High Fluid Velocity and Pressure Gradient, CMC-Computers. Materials & Continua **62**, 1109–1123 (2020)

4. Vu-Huu, T., Le-Thanh, C., Nguyen-Xuan, H., Abdel-Wahab, M.: An equal-order mixed polygonal finite element for two-dimensional incompressible Stokes flows. Eur. J. Mech.-B/ Fluids **79**, 92–108 (2020)

5. Ghia, U., Ghia, K.N., Shin, C.: High-Re solutions for incompressible flow using the Navier-Stokes equations and a multigrid method. J. Comput. Phys. **48**, 387–411 (1982)

6. Botella, O., Peyret, R.: Benchmark spectral results on the lid-driven cavity flow. Comput. Fluids **27**, 421–433 (1998)

7. Bruneau, C.-H., Saad, M.: The 2D lid-driven cavity problem revisited. Comput. Fluids **35**, 326–348 (2006)

8. Erturk, E., Corke, T.C., Gökçöl, C.: Numerical solutions of 2-D steady incompressible driven cavity flow at high Reynolds numbers. Int. J. Numer. Meth. Fluids **48**, 747–774 (2005)

9. Vu-Huu, T., Phung-Van, P., Nguyen-Xuan, H., Wahab, M.A.: A polytree-based adaptive polygonal finite element method for topology optimization of fluid-submerged breakwater interaction. Comput. Math Appl. **76**, 1198–1218 (2018)

10. Tabarraei, A., Sukumar, N.: Application of polygonal finite elements in linear elasticity. Int. J. Comput. Methods **3**, 503–520 (2006)

11. Wachspress, E.L.: A rational finite element basis, Elsevier (1975)

12. Floater, M.S.: Wachspress and mean value coordinates, in: Approximation Theory XIV: San Antonio 2013, Springer, pp. 81–102 (2014)

13. Elman, H.C., Silvester, D.J., Wathen, A.J.: Finite elements and fast iterative solvers: with applications in incompressible fluid dynamics, Numerical Mathematics and Scientific Computation (2014)

14. Förste, J., Girault, V., Raviart, P.A.: Finite Element Methods for Navier-Stokes Equations. ZAMM-J. Appl. Mathematics and Mech. **67**, 579 (1987)

15. Vu-Huu, T., Le-Thanh, C., Nguyen-Xuan, H., Abdel-Wahab, M.: A high-order mixed polygonal finite element for incompressible Stokes flow analysis. Comput. Methods Appl. Mech. Eng. **356**, 175–198 (2019)

16. Nguyen-Xuan, H., Nguyen-Hoang, S., Rabczuk, T., Hackl, K.: A polytree-based adaptive approach to limit analysis of cracked structures. Comput. Methods Appl. Mech. Eng. **313**, 1006–1039 (2017)

Investigating the Influence of Pre-existing Crack on the Failure of High Carbon Steel Girders

The Truyen Tran, Sy Quan Tu, Duc Hieu Nguyen, Tung Thanh Bui, and Ngoc Hoa Tran

1 Introduction

Crack on steel beams could derive from different causes. The crack could originate from the welding process of parts of section; particularly, it could be met more fluently in the welding process of low ductile steel material. The crack could originate from the collision in the process of conveyance or launch. Besides, its origination could stem from fatigue, chemical erosion, or over-loads in the operation process. From these causes, on steel beams, cracks could appear variedly in forms from position or shape to dimension so forth. Initially, crack is a result of causes; however, it tends to cause the failure of the steel beam within later working periods.

Investigation of defects in the behavior of steel structures has been mentioned in researchers' lots of studies in the world; among them, there were studies about the behavior of steel members on which cracks appeared [1–5]. Influence from the pre-crack appearance with different Modes on fatigue behavior of steel beam was analyzed for evaluation of the fatigue lifespan of steel members [6] and fracture mechanics theory was often applied in the estimation of the fatigue lifespan.

The failure event of the steel beam of Vam Cong Bridge in Viet Nam has raised issues needed to explain clearly. In those issues, interpretation of the failure mechanism of steel beam made of high carbon steel with appearance and propagation of cracks at certain positions on the beam needs to be encountered. This study aims to clarify the influence of pre-existing crack on the behavior of steel beam by investigating by experimental work and numerical simulation. Equivalent calculation results in the case of integrity steel beams without pre-crack would be used to be referent results. ANSYS software Mechanical/Workbench 2019R1 was used to model calculation [7].

T. T. Tran · S. Q. Tu · D. H. Nguyen (✉) · T. T. Bui · N. H. Tran
University of Transport and Communications, Hanoi, Vietnam
e-mail: hieund_ph@utc.edu.vn

2   Beam Samples for Investigation

The failure feature of the I beam could be effected by pre-cracks. There are influence parameters namely: the position of cracks on the beam, the length of cracks, the width of cracks, and the depth of cracks so on. Designing different experimental beam samples is to assess the influence of initial crack parameters on failure features of beams under static load. A combination of beam samples to investigate includes pre-crack and no pre-crack beams. Samples also have the same geometry features which are 2000 mm length, a simply supported beam, 1800 mm calculation length, 176 mm height and 4 mm thickness of beam web, 90 mm width and 4 mm thickness of upper and lower flanges, stiffening ribs with 4 mm thickness arranged at bearing positions and positions of one third calculation length. Beam samples were made of high carbon steel. Among samples, While one with no pre-crack was used as a reference sample, others with pre- cracks were designed at different positions as follows Table 1.

Investigation of influence parameter on failure feature through sample groups, specifically:

Sample group 1: To investigate the influence of the parameter of the crack position including sample units: Sample unit 1 contains Form 2, Form 3, Form 4, and Form 5; Sample unit 2 contains Form 6, and Form 7.

Table 1 Investigated beam sample

Form	Crack position	Length (mm)	Width (mm)	Depth (mm)	Investigation parameters
1	No crack	–	–	–	
2	At the middle of span	90	4	3	P1-G1, P3
3	Underneath loading position	90	4	3	P1-G1
4	150 mm distance from the middle of span	90	4	3	P1-G1
5	225 mm distance from the middle of span	90	4	3	P1-G1
6	At the middle of span and on edge of flange	45	4	2	P1-G2
7	At the middle of span and amid flange	45	4	2	P1-G2, P2
8	At the middle of span	60	4	2	P2
9	At the middle of span	90	4	2	P2
10	At the middle of span	90	3	3	P3
11	At the middle of span	90	2	3	P3, P4
12	At the middle of span	90	2	2	P4
13	At the middle of span	90	2	1	P4

Notes P1—parameter of crack position; P2—parameter of crack length; P3—parameter of crack width; P4—parameter of crack depth; G—sample unit

Sample group 2: To investigate the influence of parameter of crack length including sample units: Form 7, Form 8, and Form 9.

Sample group 3: To investigate the influence of parameter of crack width including sample units: Form 2, Form 10, and Form 11.

Sample group 4: To investigate the influence of parameter of crack depth including sample units: Form 11, Form 12, and Form 13.

3 The Study Model in the Laboratory

Experimental beam samples include Sample 1, Sample 2, and Sample 3, shown in Table 2. Detailed geometry and dimension are shown in Fig. 1.

Parts of the steel beam section were cut from steel plates with 4 mm homogenous thickness. Parts of the steel beam section were combined by welding lines to make an I- combination beam.

The bending experiment of beam samples was four-points bending. Two same concentrated loads were put on every position of one-third calculation length of span by an incremental loading machine. Instruments measuring the deflection of the beam were arranged on the bottom side of steel beams at the mid-span and positions where loads were subjected on beam. In the middle of the span, electronic tensometers were glued on the lower and upper sides of the beam to measure longitudinal deformations of lower and upper flanges of the steel beam. Measurement instruments were connected to a computer to record values according to the time as shown in Fig. 2.

Loads put on the steel beams are gradually increased from zero to value which at the moment, large cracks appear on the beam, and the loading capacity of the beam would not remain yet. Datum of deflection and deformation are updated with corresponding load grades in the period of loading increase.

Table 2 Physio-mechanical properties of steel material

Label	Description	Value
E	Young's modulus	210,000 MPa
υ	Poisson's ratio	0.3
α	Thermal expansion coefficient	0.0000117 1/$^{\circ}$C
γ	Specific density	7850 kg/m^3
f_y	Yield strength	665 MPa
f_u	Ultimate strength	1060 MPa

a. Form 1 - Beam with no pre-crack

b. Form 2 - Beam with pre-crack on the bottom side at the mid span

c. Form 3 - Beam with pre-crack on the bottom side at the underneath loading
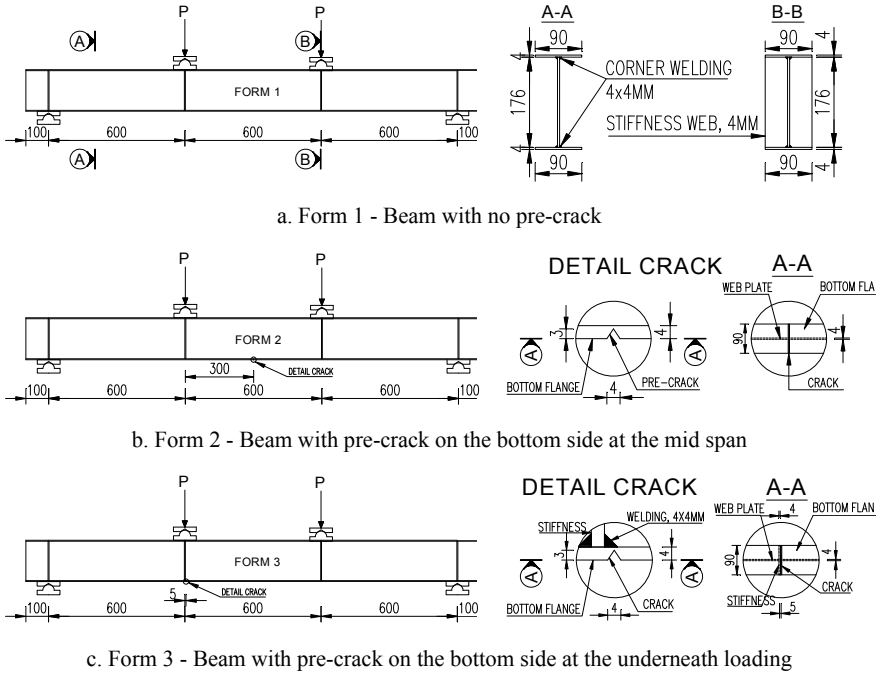
Fig. 1 The dimension of beam samples

Fig. 2 Arrangement of four-points bending experiment

4 Numerical Simulation and Appraisal of Experimental Results

4.1 Numerical Simulation in ANSYS Software

Numerical simulations of experimental steel beams were modeled by the finite element method used to verify experimental results. Achieved results of numerical simulation and experiments are used to evaluate the behavior of steel beam with and without pre-crack.

ANSYS software Mechanical/Workbench 2019R1 was used to make virtual models of steel beams with pre-cracks and their behavior according to the theory of linear elastic fracture mechanics. Three samples of steel beam were modeled with dimensions and pre-cracks like experimental beam samples. The steel beam in the model was divided into elements. The density of element mesh was increased at the vicinity of pre-crack to increase the accuracy of the analysis result as shown in Fig. 3.

The properties of steel material are taken from experiments in the laboratory. Physio-mechanical properties of steel material are performed in Table 2.

Beam samples were analyzed with an increase in loading grades. Analysis results for a typical beam sample are shown in Fig. 4 (sample 2). Analysis results consist of deflection under loading grades, Stress Intensity Factor (SIF) K_I, K_{II}, and K_{III} corresponding to damage Mode consisting of Mode I, Mode II, and Mode III with loading grade $P = 110$ kN.

Diagram in Fig. 4 shows the alteration of Stress Intensity Factor K_{III} of the points on the bottom flange at the vicinity of the pre-made crack tip. The pre-made crack continues on the whole width of the bottom flange with a length of 90 mm. The ends of the crack side correspond to values of abscissa of the diagram which are 0 mm and 90 mm long while the abscissa of position right under the web is 45 mm long. Stress Intensity Factors are the greatest at the ends of the crack side after that extremely reduce inward. Points at the ends of the crack side thus can be failed first in comparison with points at an internal position.
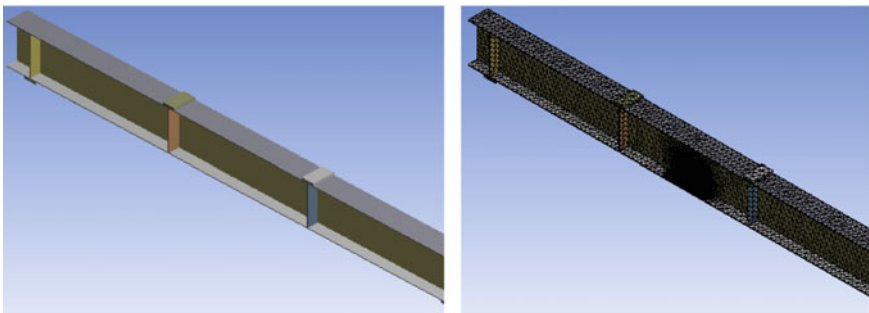
Fig. 3 Element nets of three beam samples are modeled in ANSYS software

a. Deflection.

b. Stress Intensity Factor K_I

c. Stress Intensity Factor K_{II}

d. Stress Intensity Factor K_{III}
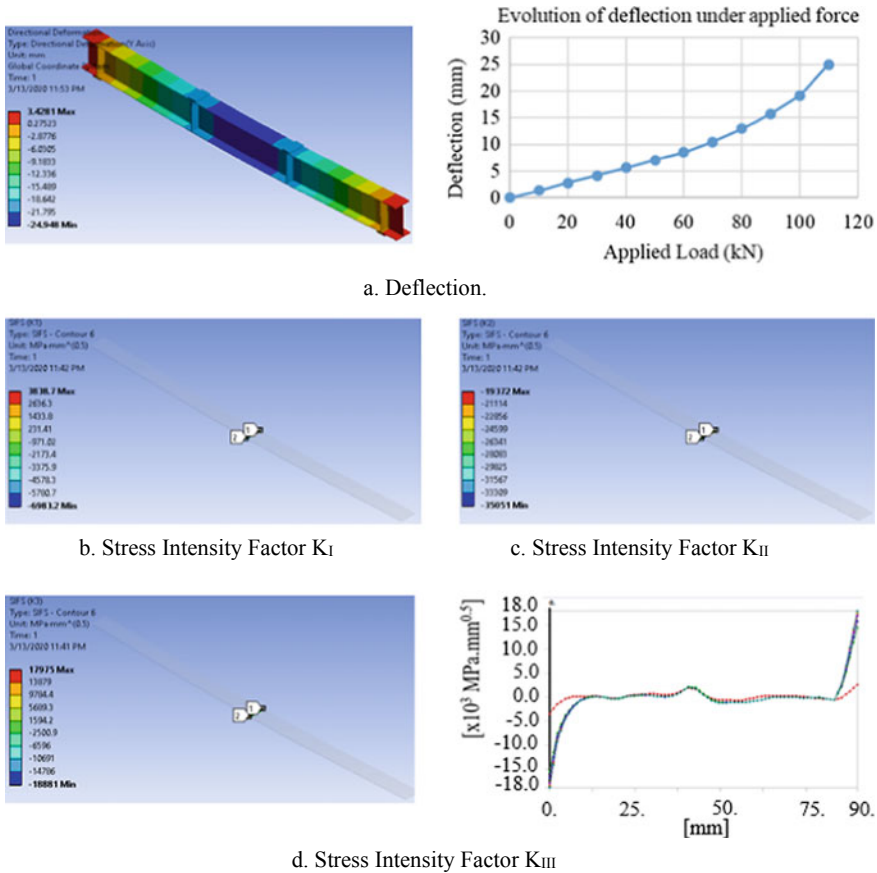
Fig. 4 Analysis result of sample 2 with loading grade $P = 110$ kN

4.2 Comparison of Experimental Results

A comparison of deflection in the middle of the beam for sample 1, sample 2, and sample 3 under loading increase to damage state of beams between experimental and numerical results is specifically shown in Fig. 5.

Damage loads of the beam in the numerical model are less from 5% to 9% than in the experiment. Curves of deflection in the numerical model have changed the direction when loads were more than 60 kN, meanwhile, those were not clear in the experiment. Deflections corresponding to maximum loading grades were different from 15 to 23% between numerical simulation and experimental results. From reference to experimental results, it shows that the analysis results of numerical simulation are quite reliable. Therefore, achieved results from numerical simulation could be used to evaluate the behavior of beam samples.
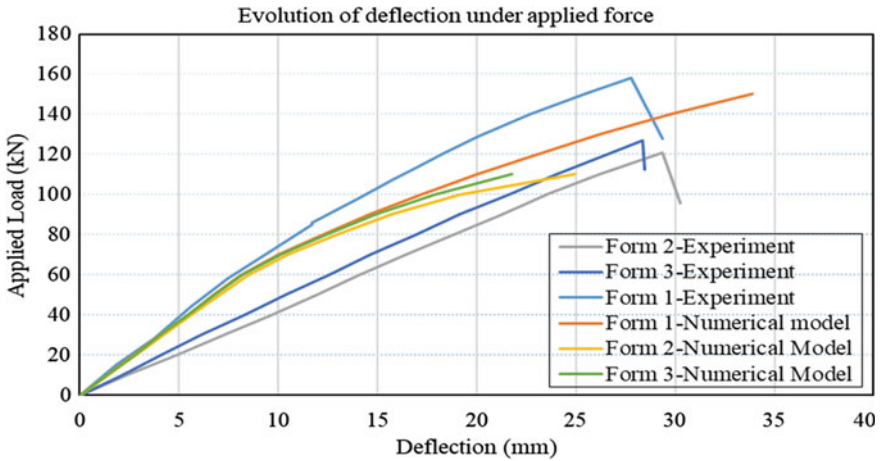
Fig. 5 Comparison between experimental and numerical results

5 Investigation of Crack Parameters

5.1 Influence from Position Parameter of Cracks

Influence from position parameters of cracks was investigated through Sample unit 1 and Sample unit 2. Sample unit 1 containing Form 1, Form 2, Form 3, Form 4, and Form 5 is steel beams without pre-crack and with pre-crack at different positions according to the longitudinal direction of the beam, while Sample unit 2 containing Form 1, Form 6, and Form 7 was steel beams without pre-crack and with pre-crack at different positions according to transverse direction on the flanges of beams.

Influence of Crack Position According to the Longitudinal Direction in Sample Unit 1

Pre-cracks on samples all have the same dimensions with 90 mm length on the whole width of flanges, 4 mm width, and 3 mm depth; however, the positions of the pre-cracks are different from the longitudinal direction of the beam. The positions of cracks are at the middle of the span, immediately underneath of loading position, 150 mm and 225 mm distance from the middle of the span corresponding to Form 2, Form 3, Form 4, and Form 5, respectively.

Deflection and increase of deflection of beam samples which have pre-crack in comparison with beam sample without pre-crack according to loading grades are shown in Table 3.

The failure feature of beam samples with pre-cracks in which the length of the crack is different is shown in Table 4.

Table 3 Influence of crack length to deflection at the middle of the span

P (kN)	Form 1 (mm)	Form 2 (mm)	Form 3 (mm)	Form 4 (mm)	Form 5 (mm)	Percentage increase (%)			
						Form 2	Form 3	Form 4	Form 5
0	0.00	0.00	0.00	0.00	0.00	0.00	0.00	0.00	0.00
10	1.36	1.41	1.36	1.37	1.37	3.63	0.51	0.82	0.71
20	2.70	2.80	2.72	2.73	2.72	3.65	0.53	0.87	0.75
30	4.05	4.20	4.08	4.09	4.09	3.72	0.57	0.92	0.80
40	5.41	5.61	5.44	5.46	5.45	3.85	0.64	1.03	0.89
50	6.76	7.04	6.81	6.84	6.83	4.13	0.75	1.24	1.06
60	8.12	8.50	8.20	8.25	8.23	4.67	0.97	1.62	1.38
70	10.01	10.51	10.12	10.19	10.16	4.93	1.08	1.78	1.46
80	12.22	12.93	12.40	12.51	12.45	5.79	1.47	2.33	1.89
90	14.59	15.72	14.92	15.20	15.01	7.75	2.30	4.18	2.90
100	17.20	19.15	17.87	18.57	18.08	11.34	3.87	7.97	5.13
105	18.57	21.39	19.59	20.77	19.97	15.23	5.52	11.86	7.57
110	20.01	24.95	21.78		22.74	24.67	8.83		13.66
120	23.04								

Table 4 Stress Intensity Factor according to loading grades

P kN	Form 2 (MPa mm$^{0.5}$)	Form 3 (MPa mm$^{0.5}$)	Form 4 (MPa mm$^{0.5}$)	Form 5 (MPa mm$^{0.5}$)
0	0.00	0.00	0.00	0.00
10	122.50	107.65	109.46	123.67
20	250.46	219.94	226.47	251.62
30	381.64	337.36	346.05	377.07
40	481.62	448.50	451.15	500.16
50	576.13	557.14	578.53	654.58
60	689.74	659.28	709.99	820.99
70	827.32	775.11	837.56	927.93
80	935.23	904.64	972.68	962.70
90	1352.22	1297.63	1475.69	1384.70
100	3265.30	2767.61	3447.45	3405.57
105	4843.11	4392.25	4579.16	4292.46
110	6983.16	6546.82		5667.84

Beam samples with pre-crack at the middle of the span (Form 4) and immediately underneath loading position were damaged at minimum loading grade (105 kN). The other samples were damaged at equivalent loading grades (110 kN) along with the maximum stress intensity factor. The closer pre-cracks were in the

middle of the span, the greater deflection of beams. The deflection was the greatest when pre-crack in the middle of the span well matching experimental results.

Influence of Crack Position According to the Transverse Direction in Sample Unit 2

Pre-cracks on samples all have similar dimensions with 45 mm length corresponding to a half of flange width, 4 mm width, and 3 mm depth. However, the positions of cracks are different from the transverse direction. The position of the crack of Form 6 is complete on one side in comparison with the centreline of the beam from the edge of flange while the position of the crack of Form 7 is symmetric through the centreline of the beam. Deflection and Stress Intensity Factor K_I of the sample are shown in Table 5.

The crack position according to transverse direction did not make significant differences of deflections between samples but took drastic degradation of loading capacity. Beam samples with cracks at the edge of the flange were larger stress intensity factor and far smaller failure loading grade than ones with cracks amid flange.

Table 5 Failure feature of samples according to loading grades and crack position

P (kN)	SIF K_I Form 6 (MPa mm$^{0.5}$)	Deflection Form 6 (MPa mm$^{0.5}$)	SIF K_I Form 7 (MPa mm$^{0.5}$)	Deflection Form 7 (mm)
0	0.00	0.00	0.00	0.00
10	80.95	1.37	60.17	1.36
20	165.36	2.73	119.82	2.70
30	257.67	4.09	184.75	4.05
40	352.59	5.46	252.16	5.41
50	461.41	6.83	324.26	6.76
60	606.14	8.21	414.81	8.13
70	764.90	10.12	526.64	10.02
80	926.05	12.35	631.62	12.23
90	1107.67	14.76	744.07	14.60
100	1324.67	17.44	867.44	17.22
110	1569.68	20.38	990.70	20.04
120	1880.31	23.70	1125.79	23.09
130	2127.01	28.31	1296.48	26.37
140			1411.76	30.35
150			1618.22	

5.2 *Influence of Crack Length*

The influence of crack length parameter was investigated through a combination of four samples: Form 1 without pre-crack, Form 7, Form 8, and Form 9 with pre-crack at the middle of the span on the bottom side of the beam which lengths are 45 mm, 60 mm, and 90 mm, respectively. These pre-cracks have the same width of 4 mm and a similar depth of 2 mm.

The deflection and increase of deflection of samples according to loading grades in comparison with the beam sample without pre-crack are shown in Table 6.

The failure feature of beam samples with pre-crack having differences of lengths is illustrated in Fig. 6.

Crack length influenced insignificantly deflection of the steel beam. However, deflection rose drastically (about 7.76%) with the crack on the whole width of the bottom side of the flange at the failure moment of the beam.

The failure load of the beam declines when cracking length increases. Failure loads of Form 7, Form 8, and Form 9 were 140 kN, 135 kN, and 130 kN, respectively. The stress intensity factor of the beam sample with the crack on the whole width of the bottom side of the flange was much higher than that of the

Table 6 Influence of crack length to deflection at the middle of the span

| P (kN)	Form 1 (mm)	Form 7 (mm)	Form 8 (mm)	Form 9 (mm)	Percentage increase (%)		
					Form 7	Form 8	Form 9
0	0.00	0.00	0.00	0.00	0.00	0.00	0.00
10	1.36	1.36	1.36	1.37	0.01	0.17	0.93
20	2.70	2.70	2.71	2.73	0.01	0.16	0.90
30	4.05	4.05	4.06	4.09	0.01	0.17	0.90
40	5.41	5.41	5.42	5.46	0.02	0.19	0.94
50	6.76	6.76	6.77	6.83	0.04	0.23	1.00
60	8.12	8.13	8.15	8.21	0.12	0.35	1.13
70	10.01	10.02	10.04	10.12	0.06	0.26	1.02
80	12.22	12.23	12.25	12.35	0.05	0.21	1.02
90	14.59	14.60	14.62	14.76	0.08	0.21	1.16
100	17.20	17.22	17.24	17.44	0.09	0.22	1.36
110	20.01	20.04	20.07	20.38	0.12	0.28	1.85
120	23.04	23.09	23.14	23.70	0.21	0.44	2.88
130	26.27	26.37	26.49	28.31	0.37	0.81	7.76
135	28.13	28.53	28.66		1.42	1.88	
140	29.73	30.35			2.08		
145	31.66						
150	33.88						
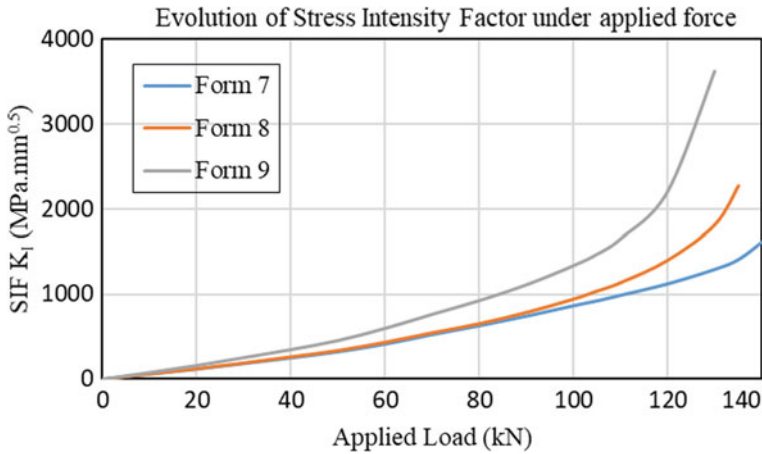
Fig. 6 Comparison between experimental and numerical results

others. Therefore, cracks lengthen on the whole width of the flange are dangerous to the operation of the steel beam.

5.3 Influence of Crack Width

The influence of the crack width parameter was investigated through a combination of three samples: Form 2, Form 10, and Form 11, all of which have pre-crack at the middle of the span with the length of 90 mm on the whole width of flange, 3 mm depth. Nevertheless, these pre-cracks are different in width which is 4 mm, 3 mm, and 2 mm in turn. The calculation results of deflection and Stress intensity factor K_I of beam samples are shown in Table 7.

Crack width influences insignificantly failure feature of beams. The deflection and failure load of beam samples were the same. Nevertheless, beam samples with a larger width of pre-cracks are greater deflections.

5.4 Influence of Crack Depth

The influence of crack depth was investigated through a combination of three samples: Form 11, Form 12, and Form 13, all of which have pre-crack at the middle of the span with the length of 90 mm on the whole width of the flange, 2 mm width. However, these pre-cracks are different from the depth which is 3 mm, 2 mm, and 1 mm in turn. The calculation results of deflection and Stress intensity factor K_I of beam samples are shown in Table 8.

Table 7 Failure feature of beam samples according to loading grades and crack width

P (Kn)	SIF KI Form 2 (MPa mm$^{0.5}$)	Deflection Form 2 (mm)	SIF K$_I$ Form 10 (MPa mm$^{0.5}$)	Deflection Form 10 (mm)	SIF K$_I$ Form (MPa mm$^{0.5}$)	Deflection Form 11 (mm)
0	0.00	0.00	0.00	0.00	0.00	0.00
10	122.50	1.41	122.49	1.40	101.43	1.40
20	250.46	2.80	250.23	2.80	205.62	2.80
30	381.64	4.20	379.74	4.20	311.54	4.20
40	481.62	5.61	507.43	5.61	406.34	5.61
50	576.13	7.04	663.26	7.03	514.90	7.03
60	689.74	8.50	845.21	8.49	634.72	8.48
70	827.32	10.51	960.67	10.49	772.16	10.48
80	935.23	12.93	956.45	12.89	890.94	12.86
90	1352.22	15.72	1395.99	15.62	1864.50	15.56
100	3265.30	19.15	4160.66	18.96	4687.62	18.78
110	6983.16	24.95	9271.43	24.25	8558.95	23.25

Table 8 Failure feature of beam samples according to loading grades and crack depth

P (Kn)	SIF K$_I$ Form 11 (MPa mm$^{0.5}$)	Deflection Form 11 (mm)	SIF K$_I$ Form 12 (MPa mm$^{0.5}$)	Deflection Form 12 (mm)	SIF K$_I$ Form 13 (MPa mm$^{0.5}$)	Deflection Form 13 (mm)
0	0.00	0.00	0.00	0.00	0.00	0.00
10	101.43	1.40	78.50	1.37	24.25	1.36
20	205.62	2.80	155.12	2.72	48.24	2.70
30	311.54	4.20	236.39	4.08	72.31	4.05
40	406.34	5.61	321.79	5.44	100.01	5.40
50	514.90	7.03	412.61	6.81	128.03	6.75
60	634.72	8.48	519.17	8.18	164.81	8.11
70	772.16	10.48	646.06	10.08	203.77	10.01
80	890.94	12.86	775.70	12.29	239.13	12.21
90	1864.50	15.56	911.04	14.67	276.84	14.58
100	4687.62	18.78	1062.76	17.31	318.49	17.19
110	8558.95	23.25	1237.08	20.16	367.40	19.99
120			1462.91	23.30	420.16	23.02
130			1751.50	26.78	479.18	26.26
140					564.67	29.92

The stress intensity factor and deflection of the beam increased together when crack depth rose but the increment of the stress intensity factor was faster than that of deflection. Crack depth affected considerably loading capacity of the steel beam. The larger the crack depth was the faster degradation of loading capacity was.

6 Conclusion and Recommendation

Pre-crack affects steel beam on deflection and loading capacity. There are many parameters of crack with the influence rate on the failure feature of the steel beam.

Cracks at the middle of the span of the steel beam generate the maximum deflection meanwhile cracks at immediately underneath loading positions make the minimum loading capacity of the steel beam. Besides,

Cracks at the flange edge more dangerous than those amid flange. The crack causing the maximum deflection is not dangerous to loading capacity.

Loading capacity declines with an increase of crack length, the behavior of beam under loading is the most dangerous when the crack is on the whole width of the beam flange. This enhances danger to the appearance of crack at the flange edge.

Crack width influences the deflection and loading capacity of the steel beam insignificantly.

Crack depth affects roughly loading capacity. The larger the crack depth is the faster decrease of loading capacity is.

References

1. El Abdi, R., Samrout, H.: A non-linear kinematic hardening model for a steel under complex loadings. Comput. Struct. **76**(5), 675–681 (2000)
2. Chung, W., Sotelino, E.D.: Nonlinear finite-element analysis of composite steel girder bridges. J. Struct. Eng. **131**(2), 304–313 (2005)
3. Song, Q.Y., Heidarpour, A., Zhao, X.L., Han, L.H.: Experimental and numerical investigation of ductile fracture of carbon steel structural components. J. Constr. Steel Res. **145**, 425–437 (2018)
4. Tarigopula, V., Hopperstad, O.S., Langseth, M., Clausen, A.H.: An evaluation of a combined isotropic-kinematic hardening model for representation of complex strain-path changes in dual-phase steel. Eur. J. Mech.-A/Solids **28**(4), 792–805 (2009)
5. Haghani, R., Al-Emrani, M., Heshmati, M.: Fatigue-prone details in steel bridges. Buildings **2** (4), 456–476 (2012)
6. Truyen, T.T., Hieu, N.D., Tung, B.T., Quoc, D.B., Anh, N.T., Anh, N.T.: Fracture Analysis of Crack Propagation on the Diaphragm of Steel Bridge Structures, CIGOS 2019. Innovation for Sustainable Infrastructure, Lecture Notes in Civil Engineering book series (LNCE, volume 54) (2019)
7. Duchaczek, A., Mańko, Z.: The influence of a cracking mode on fatigue crack propagation in steel girders in military bridges. Eur J Environ Civ En **20**(1), 1–18 (2016)